frontiers | Research Topics

Functional surfaces and biomaterials

Edited by
Yuangang Liu, Rumen Krastev, Junchao Wei and Min Jiang

Published in
Frontiers in Bioengineering and Biotechnology
Frontiers in Materials

ISSN 1664-8714
ISBN 978-2-83251-506-8
DOI 10.3389/978-2-83251-506-8

About Frontiers

Frontiers is more than just an open access publisher of scholarly articles: it is a pioneering approach to the world of academia, radically improving the way scholarly research is managed. The grand vision of Frontiers is a world where all people have an equal opportunity to seek, share and generate knowledge. Frontiers provides immediate and permanent online open access to all its publications, but this alone is not enough to realize our grand goals.

Frontiers journal series

The Frontiers journal series is a multi-tier and interdisciplinary set of open-access, online journals, promising a paradigm shift from the current review, selection and dissemination processes in academic publishing. All Frontiers journals are driven by researchers for researchers; therefore, they constitute a service to the scholarly community. At the same time, the *Frontiers journal series* operates on a revolutionary invention, the tiered publishing system, initially addressing specific communities of scholars, and gradually climbing up to broader public understanding, thus serving the interests of the lay society, too.

Dedication to quality

Each Frontiers article is a landmark of the highest quality, thanks to genuinely collaborative interactions between authors and review editors, who include some of the world's best academicians. Research must be certified by peers before entering a stream of knowledge that may eventually reach the public - and shape society; therefore, Frontiers only applies the most rigorous and unbiased reviews. Frontiers revolutionizes research publishing by freely delivering the most outstanding research, evaluated with no bias from both the academic and social point of view. By applying the most advanced information technologies, Frontiers is catapulting scholarly publishing into a new generation.

What are Frontiers Research Topics?

Frontiers Research Topics are very popular trademarks of the *Frontiers journals series*: they are collections of at least ten articles, all centered on a particular subject. With their unique mix of varied contributions from Original Research to Review Articles, Frontiers Research Topics unify the most influential researchers, the latest key findings and historical advances in a hot research area.

Find out more on how to host your own Frontiers Research Topic or contribute to one as an author by contacting the Frontiers editorial office: frontiersin.org/about/contact

Functional surfaces and biomaterials

Topic editors

Yuangang Liu — Huaqiao University, China
Rumen Krastev — Reutlingen University, Germany
Junchao Wei — Nanchang University, China
Min Jiang — Nanjing Tech University, China

Citation

Liu, Y., Krastev, R., Wei, J., Jiang, M., eds. (2023). *Functional surfaces and biomaterials.* Lausanne: Frontiers Media SA. doi: 10.3389/978-2-83251-506-8

Table of contents

06 Editorial: Functional surfaces and biomaterials
Yuangang Liu, Rumen Krastev, Junchao Wei and Min Jiang

08 Regulation of Magnesium Matrix Composites Materials on Bone Immune Microenvironment and Osteogenic Mechanism
Xiaojing Nie, Xueyan Zhang, Baozhen Lei, Yonghua Shi and Jingxin Yang

17 Regulation of T Cell Responses by Nano-Hydroxyapatite to Mediate the Osteogenesis
Fangze Guo, Changqing Yuan, Hailin Huang, Xuyang Deng, Zirui Bian, Danyang Wang, Keke Dou, Li Mei and Qihui Zhou

26 Bone Quantification Around Chitosan-Coated Titanium Dental Implants: A Preliminary Study by Micro-CT Analysis in Jaw of a Canine Model
Nansi López-Valverde, Antonio López-Valverde, Marta Paz Cortés, Cinthia Rodríguez, Bruno Macedo De Sousa and Juan Manuel Aragoneses

38 pH/Redox/Lysozyme-Sensitive Hybrid Nanocarriers With Transformable Size for Multistage Drug Delivery
Zhe Liu, Dong Zhou and Lan Liao

52 Peptide-Grafted Microspheres for Mesenchymal Stem Cell Sorting and Expansion by Selective Adhesion
Shuo Wu, Zongliang Wang, Yu Wang, Min Guo, Mengyang Zhou, Liqiang Wang, Jie Ma and Peibiao Zhang

68 Fucoidan-Mediated Anisotropic Calcium Carbonate Nanorods of pH-Responsive Drug Release for Antitumor Therapy
Pei Wang, Fei Tong, Jun Luo, Zhihua Li, Junchao Wei and Yuangang Liu

78 Bone Response to Osteopontin-Functionalized Carboxyethylphosphonic Acid-Modified Implants. Experimental Study in a Minipig Model
Javier Aragoneses, Nansi López-Valverde, Antonio López-Valverde, Cinthia Rodríguez, Bruno Macedo De Sousa and Juan Manuel Aragoneses

89 Gold Nanoparticle-Functionalized Diatom Biosilica as Label-Free Biosensor for Biomolecule Detection
Tongtong Chen, Feifei Wu, Yang Li, Hussein E. Rozan, Xiguang Chen and Chao Feng

101 Liquid Crystal Modified Polylactic Acid Improves Cytocompatibility and M2 Polarization of Macrophages to Promote Osteogenesis
Zexiang Zheng, Renqin Wang, Jianjun Lin, Jinhuan Tian, Changren Zhou, Na Li and Lihua Li

115 **Development of Biomimetic Hepatic Lobule-Like Constructs on Silk-Collagen Composite Scaffolds for Liver Tissue Engineering**
Lina Guo, Ziqing Zhu, Chuanzhou Gao, Kaiwen Chen, Shenzhou Lu, Hexin Yan, Wenming Liu, Mingqi Wang, Yanfang Ding, Lin Huang and Xiuli Wang

132 **Tumor Cell-Specific and Lipase-Responsive Delivery of Hydrogen Sulfide for Sensitizing Chemotherapy of Pancreatic Cancer**
Libing Tian, Rui Pei, Xiaojun Zhang, Kun Li, Yuting Zhong, Yougen Luo, Shu-Feng Zhou and Lichan Chen

143 **Directed Self-Assembly of Heterologously Expressed Hagfish EsTKα and EsTKγ for Functional Hydrogel**
Ruishuang Sun, Ruonan Zheng, Wenlong Zhu, Xiqin Zhou, Luo Liu and Hui Cao

153 **Heparin/Collagen-REDV Modification of Expanded Polytetrafluoroethylene Improves Regional Anti-thrombosis and Reduces Foreign Body Reactions in Local Tissues**
Yaping Shan, Gang Chen, Qiqi Shi, Jiaxi Huang, Yaping Mi, Wenbo Zhang, Huifeng Zhang and Bing Jia

167 **Encapsulated vaterite-calcite $CaCO_3$ particles loaded with Mg^{2+} and Cu^{2+} ions with sustained release promoting osteogenesis and angiogenesis**
Lu Fan, Fabian Körte, Alexander Rudt, Ole Jung, Claus Burkhardt, Mike Barbeck and Xin Xiong

183 **Ultrasound combined with glial cell line-derived neurotrophic factor-loaded microbubbles for the targeted treatment of drug addiction**
Feng Wang, Hongwei Wu, Azhen Hu, Lei Dong, Xiaoxia Lin, Menghao Li, Yongling Wang, Wenjun Li, Liansheng Chang, Yuqiao Chang, Hanqing Liu, Yu Shi and Nana Li

194 **Phase-change materials-based platforms for biomedicine**
Biao-Qi Chen, Yu-Jing Pan, Da-Gui Zhang, Hong-Ying Xia and Ranjith Kumar Kankala

202 **Effectiveness of biomolecule-based bioactive surfaces, on os-seointegration of titanium dental implants: A systematic review and meta-analysis of *in vivo* studies**
Nansi López-Valverde, Javier Aragoneses, Antonio López-Valverde, Norberto Quispe-López, Cinthia Rodríguez and Juan Manuel Aragoneses

219 **Soft integration of a neural cells network and bionic interfaces**
Jixiang Zhang, Ting Wang, Yixin Zhang, Pengyu Lu, Neng Shi, Weiran Zhu, Chenglong Cai and Nongyue He

229 3D cell culture based on artificial cells and hydrogel under microgravity for bottom-up microtissue constructs
Ruimin Long, Linrong Shi, Peng He, Jumei Tian, Shibin Wang and Jun Zheng

239 Antibacterial intraosseous implant surface coating that responds to changes in the bacterial microenvironment
Xin Bai, Jiawei Yu, Jie Xiao, Yanping Wang, Zhe Li and Hao Wang

frontiers | Frontiers in Bioengineering and Biotechnology

TYPE Editorial
PUBLISHED 17 January 2023
DOI 10.3389/fbioe.2023.1138172

Editorial: Functional surfaces and biomaterials

Yuangang Liu[1]*, Rumen Krastev[2], Junchao Wei[3] and Min Jiang[4]

[1]College of Chemical Engineering, Huaqiao University, Xiamen, China, [2]Faculty for Life Sciences, Reutlingen University, Reutlingen, Germany, [3]School of Stomatology, Nanchang University, Nanchang, China, [4]School of Biotechnology and Pharmaceutical Engineering, Nanjing Tech University, Nanjing, China

KEYWORDS

surface modification, coating, cell-material interaction, functionalized materials, functionalized surfaces, drug delivery systems, immobilization of biomolecules, miniaturized biosensor and bioreactors

OPEN ACCESS

EDITED AND REVIEWED BY
Hasan Uludag,
University of Alberta, Canada

*CORRESPONDENCE
Yuangang Liu,
✉ ygliu@hqu.edu.cn

SPECIALTY SECTION
This article was submitted to Biomaterials, a section of the journal Frontiers in Bioengineering and Biotechnology

RECEIVED 05 January 2023
ACCEPTED 09 January 2023
PUBLISHED 17 January 2023

CITATION
Liu Y, Krastev R, Wei J and Jiang M (2023), Editorial: Functional surfaces and biomaterials.
Front. Bioeng. Biotechnol. 11:1138172.
doi: 10.3389/fbioe.2023.1138172

Editorial on the Research Topic
Functional surfaces and biomaterials

Functional surfaces and biomaterials

At the beginning of 2022, Frontiers in Bioengineering and Biotechnology - Biomaterials Section has published a Research Topic on “Functional Surfaces and Biomaterials.” The aim of this Research Topic is to summarize the current state of research and development in the field of functional surfaces and biomaterials with a particular focus on biotechnological and medical applications.

The guest editorial team would like to thank all colleagues from around the world who submitted their reviews and research articles for the Research Topic. By the end of August 2022, we have successfully collected 20 articles by 138 participating authors following the peer review process. We also tried to select manuscripts from different research areas to cover the most relevant Research Topic of interest, from drug delivery systems to bone tissue engineering to biosensors and general aspects in biomedicine. By the end of December, the 20 articles had been viewed for more than 21000 times with downloads more than 4,000 times, and 11 articles have reached more than 1,000 views.

Among the 20 articles, the interests mainly focus on tissue engineering, especially bone tissue engineering, including the influence of divalent cations on osteogenic mechanism (L. Fan et al.; X. Nie et al.), the modification of materials on cell response and osteogenesis promotion (F. Guo et al., Z. Zheng et al.), and the antibacterial coating on the surface of intraosseous implants (X. Bai et al.). For example, L. Fan et al. described the synergistic effects on osteogenesis and angiogenesis by the controlled release of Ca^{2+}, Mg^{2+}, and Cu^{2+} ions. The simple technique used in this article served to address the adverse effects of using biologics in bone tissue engineering, the availability of which is quite limited due to regulatory issues. In addition, the osseointegration of tianium dental implants also has been investigated by N. López-Valverde et al., A. López-Valverde et al. and J. Aragoneses et al., which could be of general interest as titanium oxide-based materials are widely used in orthopedic treatments. The article by L. Guo et al., reported a biomimetic hepatic lobule-like model that could be a robust platform for various medical applications. The article by Y. Shan et al. reported modification of ePTFE with heparin/collagen-REDV can promote the cytocompatibility and antiplatelet property.

Drug delivery system is another intensive field. Researchers prepared carriers with different modes such as stimuli-responsive nanocarriers with transformable size for multistage drug delivery (Z. Liu et al.). The contribution from P. Wang et al. described $CaCO_3$ nanorods for tumor therapy demonstrates a possible rethinking of the use of fundamental and widely studied materials to address medical challenges. Gas–involved chemosensitization strategy is also proposed for cancer treatment. For example, L. Tian et al. prepared a tumor-specific lipase-responsive nanomedicine based on aptamer-conjugated DATS/Dox co-loaded PCL-b-PEO micelle for pancreatic cancer, F. Wang et al. reported magnetic resonance imaging-guided low-frequency focused ultrasound combined with GDNF microbubbles was used to target BBB opening in the ventral tegmental area (VTA) region. New materials such as Hagfish proteins (R. Sun et al.), and phase-change materials (B. Chen et al.), as well as diatom biosilica label-free biosensor (T. Chen et al.), and bionic neural interfaces (J. Zhang et al.), are also reported in this Research Topic.

An interesting work is about cell expansion and microtissue construction. S. Wu et al. developed a unique magnetic peptide-grafted sorting microsphere to obtain relatively pure and high-yield MSCs in an economical and effective way, which can also be used for the expansion of MSCs. (R. Long et al.) introduced a novel tissue construction strategy using 3D cell culture based on artificial cells and hydrogel under microgravity for bottom-up microtissue constructs, which is beneficial for cell distribution and of great significance for tissue construction research *in vitro*.

In summary, given their importance, it is perhaps not surprising that the functional surfaces and functionalization using biomaterials are highly interesting areas in the biomedicine. The main reasons are the cellular behavior and the reactions to differently structured and chemically presented surfaces. To control these effects and to use them for the improvement of clinical outcomes, research and development in the fields of materials, process engineering and analytical strategies are required. With the new trend of circular economy, resource efficiency and value chain becoming a driving force for innovation, active collaboration between researchers, clinicians and industry is essential and increasingly important. The close collaboration was also evident in the research articles, as various laboratories and hospitals were engaged in the contributed papers. It is anticipated that the better understanding of the functional surfaces and biomaterials will promote the applications of biomaterials in the future.

Author contributions

YL drafted the manuscript, and other authors discussed and revised the manuscript.

Acknowledgments

YL thanks the National Natural Science Foundation of China (32171337).

Conflict of interest

The authors declare that the research was conducted in the absence of any commercial or financial relationships that could be construed as a potential conflict of interest.

Publisher's note

frontiers
in Bioengineering and Biotechnology

REVIEW
published: 14 March 2022
doi: 10.3389/fbioe.2022.842706

Regulation of Magnesium Matrix Composites Materials on Bone Immune Microenvironment and Osteogenic Mechanism

Xiaojing Nie[1], Xueyan Zhang[2,3], Baozhen Lei[2,3], Yonghua Shi[1] and Jingxin Yang[2,3]**

[1]Department of Pathology, School of Basic Medical Sciences, Xinjiang Medical University, Urumqi, China, [2]Beijing Engineering Research Center of Smart Mechanical Innovation Design Service, Beijing Union University, Beijing, China, [3]College of Robotics, Beijing Union University, Beijing, China

Edited by:
Yuangang Liu,
Huaqiao University, China

Reviewed by:
Qiang Lu,
Soochow University, China
Fengxuan Han,
Soochow University, China
Junchao Wei,
Nanchang University, China

***Correspondence:**
Xiaojing Nie
2441209094@qq.com
Jingxin Yang
myxin825@163.com

Specialty section:
This article was submitted to
Biomaterials,
a section of the journal
Frontiers in Bioengineering and
Biotechnology

Received: *24 December 2021*
Accepted: *10 February 2022*
Published: *14 March 2022*

Citation:
Nie X, Zhang X, Lei B, Shi Y and Yang J (2022) Regulation of Magnesium Matrix Composites Materials on Bone Immune Microenvironment and Osteogenic Mechanism. Front. Bioeng. Biotechnol. 10:842706. doi: 10.3389/fbioe.2022.842706

Despite magnesium based metal materials are widely used in bone defect repair, there are still various deficiencies, and their properties need to be optimized. Composites synthesized with magnesium based metal as matrix are the research hotspot, and the host immune response after biomaterial implantation is very important for bone binding. By studying the immunoregulation of bone biomaterials, it can regulate the immune response in the process of osteogenesis and create a good local immune microenvironment, which is conducive to biomaterials to reduce inflammatory response and promote good bone binding. This article introduces the osteogenic mechanism of magnesium based metal materials and its regulation on bone immune microenvironment in detail.

Keywords: magnesium, functionalmaterials, coating, osteogenesis, osteogenic mechanism, bone immunity

INTRODUCTION

Applications of Magnesium(Mg) Matrix Composites

Mg is a light metal with low density, high strength/weight ratio, in addition Mg and its alloys exhibit good biocompatibility as a kind of degradable and absorbable biomaterials (Qi et al., 2019). Compared with metallic materials that are now widely used in the clinic, the elastic modulus of Mg based metallic materials is closer to the bone cortex, structurally and mechanically similar to trabecular bone, favoring the growth of bone tissue toward its interior and obtaining early fixation effects, thus reducing the “stress shielding effect”. However, Mg based metal is a double-edged sword as a biomaterial. Due to the poor corrosion resistance, Mg alloys degrade too fast and do not match the time of bone tissue healing, making it difficult to exert the osteogenic effect of Mg alloys, and the gas generated during the degradation process may cause a local inflammatory response, which greatly limits the application of Mg alloys in the clinic. There are many methods to reduce the degradation rate of Mg metal materials, such as Mg purity, alloying components, surface modification and increasing coatings (Kato et al., 2019).

High Purity Mg

Since the purity of Mg metal reached higher (99.99% or 99.999%), it can have a degradation rate suitable for the internal fixation material of bone repair. At the same time, high-pure Mg *in vivo* degradation will not release other alloying elements, avoiding the disadvantages of other non degradable elements aggregation *in vivo*, these advantages make the application of high-pure Mg in bone repair gradually attract attention. In the related research process, it was found that pure Mg has a series of problems, such as pitting corrosion, degradation rate faster so that hydrogen gas accumulation around the implant delays the healing of the tissue (Mahapatro et al., 2015; Siddiqui et al., 2019).

Mg Alloys

Alloying is a general and effective method to improve the corrosion resistance and mechanical properties of Mg, and considerable work has focused on this method, such as the addition of aluminum (Al), zinc (Zn), strontium (Sr), yttrium (Y), and cerium (Ce) elements (Alvarez-Lopez et al., 2010; Seitz et al., 2015; Wu et al., 2016). However, the use of some alloying elements is still potentially hazardous to human body, such as the high concentration of Ce, the hepatotoxicity of Y as well as the neurotoxicity of Al (Zain et al., 2012). As a neurotoxicant, the accumulation of Al is associated with various neurological diseases, such as dementia, senile dementia and Alzheimer's disease (Wang et al., 2017a).

Calcium (Ca) is a major component of bone, and Ca ions are also necessary for each cell they regulate various biochemical reactions *in vivo*, such as in the absence of serum in culture medium, and the addition of Ca ions can enhance the proliferation of stem cells and induce osteogenic differentiation (MarmionCeline et al., 2014; Lei et al., 2015). Multiple *in vitro* studies have also reported the enhancing effects of Mg or Ca on osteoblast activity, such as improving cell growth status and alkaline phosphatase (ALP) expression (Streckova et al., 2018).

Both oral and *in vitro* studies confirm that Sr can pharmacologically increase bone formation and decrease bone resorption at the cellular level (Reginster et al., 2010; Reginster et al., 2013) and Sr compounds can activate osteoblast and osteoclast activity through different signaling pathways (Saidak and Marie, 2012). Li studies proved that Sr can promote osteogenic differentiation of stem cells, and up regulation of several osteogenic genes as well as an increase in ALP protein expression was observed when rat mesenchymal stem cell (MSCs) were cultured in Sr supplemented medium (Li et al., 2012). An increase in the gene and protein expression of various osteogenic markers was detected in osteogenic human stem cells (hMSCs) cultures treated with Sr by Sila et al. (Munisso et al., 2012). In addition to this small amount of strontium can promote the regeneration of grains and thus improve the mechanical properties of pure Mg (Brar et al., 2012).

Surface Modification/Coating Treatment of Mg Alloy

Pure Mg or Mg alloys can be treated physically or chemically to form a "protective film" on their surface that can reduce the degradation rate of the substrate, which can include micro arc oxidation coating (MAO), chemical conversion coating, electroplating coating, biomimetic deposition coating, polymer coating, etc. (Lin et al., 2013). Among all these methods, MAO is a promising new surface treatment method, and the MAO technique shows excellent adhesion to the base metal. In addition, this technique has many advantages, such as simple surface pretreatment, simple process, low cost, and comprehensive properties, which can improve corrosion resistance, wear resistanceand microhardness of Mg alloys (Zhu et al., 2016). In immersion tests, the mechanical properties of MAO coated samples remain unchanged and have good biocompatibility. However, MAO coatings on Mg alloys are composed of micro pores and cracks, which may affect the protective properties of the coatings and accelerate the corrosion rate (Dima et al., 2014; Golshirazi et al., 2017). The coating process of the self-assembly technique resulted in the formation of a double-layer PEI/KC: Mao coating on the surface of AZ91 Mg alloy, which led to an increase in the thickness of the coating and improved the coating and filling of pores, and the bonding strength of the double-layer PEI/KC: MAO coating was significantly higher (about 1.3-fold) than that of the MAO coating, the double-layer PEI/KC: MAO coating improved the anti-corrosion ability of AZ91 Mg alloy with the potential for application in biomedicine by prohibiting the corrosive ion transport. In some studies, zirconia (ZrO_2) materials have been used in biomedicine to obtain implants or various coatings. It is bioneutral, and its result is equivalent to titanium, but it does not affect the growth rate of osteoblasts. At the same time, ZrO_2 nanoparticles have antibacterial properties. ZrO_2 is an important biomaterial, widely used in applications such as dental implants, where osteointegration is of minor importance compared to the requirements. The effects of 100 nm thick titanium dioxide (TiO_2), ZrO_2 and hafnium oxide (HfO_2) coatings on the corrosion behavior and cytotoxicity of AZ31Mg alloy were evaluated. The results show that ZrO_2 has the higher corrosion resistance and cell viability (Peron et al., 2021).

Other Types of Composites

Recent studies have shown that customized poly lactic-co- glycolic acid (PLGA)/MgO alendronate microspheres are used to study the bone immune regulation of extracellular bioactive cations (Mg^{2+}) in the bone tissue microenvironment. The microspheres give a controllable release of Mg^{2+}. The results show that Mg^{2+} controlled tissue microenvironment can enhance anti-inflammatory (IL-10) and promote bone protein (BMP-2 and TGF-β1). The production of cytokines effectively induced macrophages to polarize from M0 phenotype to M2. It can also produce a good bone immune microenvironment. The newly formed bone tissues in the Mg TME possess a superior microstructure, bone mineral density, and mechanical property (Lin et al., 2021). In addition, injectable *in-situ* formed hydrogels have been extensively studied in bone regeneration applications. This hydrogel can not only be quickly and locally formed in any geometric target, but also play an important role in minimally invasive treatment, and it is also used to enhance the damage of bone tissue as a carrier for delivery of therapeutic drugs and cells. Gelatin, collagen, gelatin, hyaluronic acid and alginate, injectable hydrogels, which are prepared from natural polymers, have been widely used in bone tissue engineering due to their physical and chemical properties, excellent biocompatibility and structural similarity with extracellular matrix. Studies have shown that Injectable *in-situ* formed hydrogels as a carrier of Mg matrix composites helps to promote osteoblast differentiation (Chen et al., 2021).

THE ROLE OF MG MATRIX COMPOSITES IN MACROPHAGE-MEDIATED INFLAMMATORY RESPONSE

Biomaterials trigger a foreign body response (FBR) upon implantation, involving a series of inflammatory events and repair processes including protein adsorption, immune cell

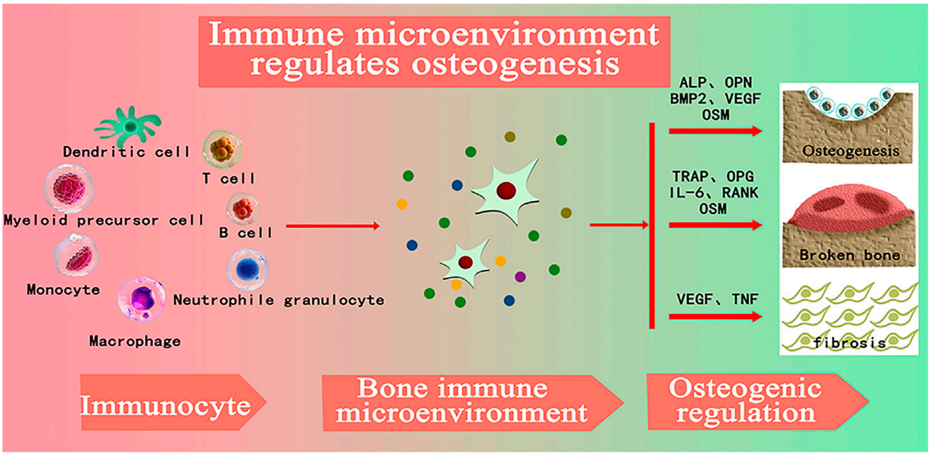

FIGURE 1 | (ALP: alkaline phosphatase; OPN: Bone bridge egg white, BMP-2: Bone morphogenetic protein-2, VEGF: vascular endothelial growth factor, OSM: tumor suppressant M, TRAP: Tartrate-resistant acid phosphatase, OPG: osteoprotectin; Il-6: Interleukin-6, RANK: nuclear factor κβ receptor activation factor, TNF: Tumor necrosis factor) (Chen et al., 2018).

infiltration, cytokine and chemokine release, cell recruitment, and fiber encapsulation (Zhang et al., 2016). Therefore, the study of "bone immune microenvironment" of bone repair materials is a major issue to be faced. Timely and appropriate protection and adequate immune response will promote the integration of implant surface and host bone tissue, creating a microenvironment that promotes osteogenesis, which is conducive to promoting bone repair of implant materials (Ping et al., 2021). The development of bone immunology has become one of the greatest achievements in the field of bone biology, which reveals the important role of immune cells in regulating bone dynamics (Cui et al., 2018). By studying the immune regulation of bone biomaterials, it can regulate the immune response in the process of osteogenesis, create a good local immune microenvironment, and help biomaterials reduce inflammatory response and promote good bone binding (Haggerty et al., 2018). As shown in **Figure 1**, with the introduction of the concept of bone immunity and its development in the field of bone regeneration, researchers gradually found that immune cells play a central role in the formation of local bone microenvironment. By regulating the expression of growth factors, chemokines, inflammatory factors and other factors, osteogenic differentiation, osteoclast differentiation, fibrosis, vascularization and other processes closely related to bone regeneration are regulated in bone regeneration. Moreover, immune cells are the central regulators of bone immune microenvironment, and affect the process of osteogenesis, osteofragmentation and fibrosis in the process of bone regeneration by secreting various cytokines into the bone regeneration microenvironment (Chen et al., 2018).

Polarization of Macrophage Phenotype Plays a Central Role in the Regulation of Inflammatory Response

Macrophages, especially monocyte derived macrophages, are key regulators. Traditionally, these cells have been known to remove foreign bodies and cell debris—both pathogens and tiny matter.

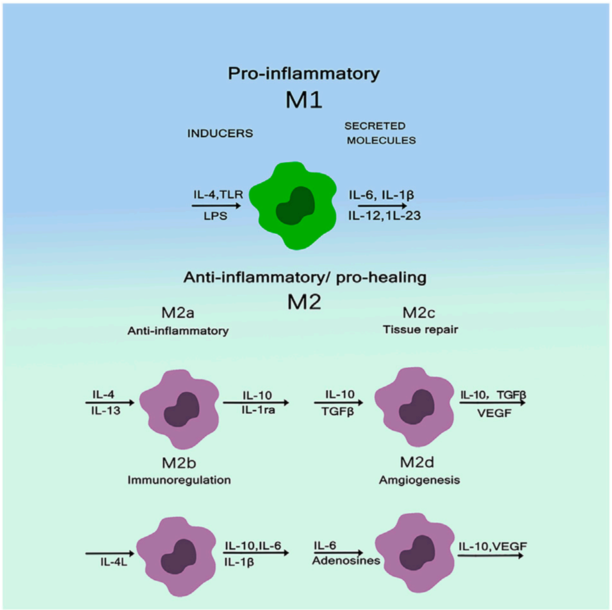

FIGURE 2 | Macrophages have high plasticity and exhibit pro-inflammatory M1 or anti-inflammatory M2 types (Italiani and Boraschi, 2014).

Increasingly, they are found to play important roles in a wide range of processes from host defense, inflammation, wound healing, and tissue remodeling (Nenasheva et al., 2020). When exposed to external stimuli, Macrophages are activated into different phenotypes and secrete various chemokines, inflammatory mediators, matrix metalloproteinases (MMPs), and growth factors (Zhao et al., 2020; Sharma et al., 2020). Among all cells in the immune system, macrophages are innate immune cells and play an important role in the immune response induced by substances. Macrophages participate in bone physiological processes and secrete some important regulatory molecules to influence bone remodeling (Jetten et al., 2013). Biomaterial implants induced polarization of macrophages towards different phenotypes M1 and M2. M1 is a pro-inflammatory macrophage that can be "classically activated" and M2 is an anti-inflammatory macrophage that can be "selectively activated" to its microenvironment (Murray et al., 2014; Piccolo et al., 2017). **Figure 2** shows macrophages are usually (induced by TH1 cytokines such as IFN-G and LPS) or selectively activated (induced by TH2 cytokines such as IL-4/IL-13), called M1 or M2, respectively. M1 macrophages polarize to perform their pro-inflammatory and pathogen-killing functions, secreting high levels of TNF-α, IL-12, and IL-23. M2 macrophages resolve inflammation and organize tissue repair, producing IL-10 and arginase. M2 are further subdivided into M2a (IL-4 and IL-13 triggers), M2b (FcgR/TLR triggers), and M2c (IL-10, TGF-β, glucocorticoid triggers). All of these subtypes have anti-inflammatory properties. While M2a and M2b are more immunomodulatory, M2c cells are considered as inactivated macrophages and participate in tissue remodeling (Italiani and Boraschi, 2014; Nahrendorf and Swirski, 2016). The interaction between macrophage polarization and biomaterial composition significantly affects bone regeneration. Thus, macrophages can be used as a cellular model to evaluate the osteogenic process of biomaterials implanted *in vitro*. Unlike osteomas, inflammatory macrophages are established during fetal development and are derived from monocyte precursors circulating in the blood. Macrophages have high plasticity and exhibit pro-inflammatory M1 or anti-inflammatory M2 type depending on the polarization phenomenon according to microenvironmental cues. M1 cells are involved in acute inflammation and, therefore, they are more closely related to the early stages of tissue repair. In contrast, M2 cells play a role in the later stages of bone healing, leading to positive repair or fibrous tissue production. Over time, the two types of macrophages release different factors and cytokines that interact with other coordinating factors of bone healing, such as endothelial cells, mesenchymal cells, osteoclasts and osteoblasts (Moeser et al., 2011; Wu et al., 2013). It is noteworthy that both M1 and M2 are required to restore the function of injured bone tissue, and timely switching between these two phenotypes may determine the success of active bone regeneration and implant.

Regulatory Role of Mg in Macrophage-Mediated Inflammatory Response

Studies have shown that Mg^{2+}, a major degradation product of Mg, is the most abundant divalent cation in cells, which can regulate cell growth, metabolism, proliferation and other cellular functions, and has the function of anti-inflammatory regulation of bone immune microenvironment (Bockstaller et al., 2005; Lee et al., 2016). For example, Mg^{2+} is used to improve the prevention of obstetric epileptic seizures. Mg^{2+} promote the conversion of macrophages to the M2 phenotype, and M2 macrophages also produce growth factors, including transforming growth factor (TGF-β) and VEGF, which support the migration and osteogenic differentiation of MSC. In addition, the inflammatory NF-κβ signaling pathway was down-regulated by inhibiting TLR pathway, and the activated macrophages were promoted to secrete anti-inflammatory cytokines IL-10 and IL-1, and the expressions of osteogenic genes BMP2 and VEGF were up-regulated. Suitable concentration of Mg^{2+} (100 mg/L) can promote osteogenic differentiation of MSC. The mechanism may be that Mg^{2+} promote the secretion of BMP2 by macrophages, by activating the BMP2/Smad signaling pathway of MSC to enhance its osteogenic differentiation ability. Mg^{2+} release concentration (about 100 mg/L) can overcome the harmful bone immunomodulatory properties of Mg-based biomaterials and make them more favorable for bone marrow. Specifically, microscale Mg^{2+}induces phenotypic switching in M2 macrophages, and most likely induces an anti-inflammatory environment by inhibiting the TLR-NF-κβsignaling pathway. Microscale Mg^{2+} stimulates macrophage BMP-2 expression and activates BMP-2 signaling pathway in bone MSC, promoting osteogenic differentiation. Therefore, manipulating the concentration of in Mg-based bone scaffolds can make biomaterials have good bone immunomodulatory properties. In short, Mg matrix composites promote the transformation of macrophages to M2 phenotype, and M2 macrophages can produce TGF-β and VEGF, supporting the migration and osteogenic differentiation of BMSC and down regulate inflammatory NF by inhibiting TLR pathway-κB signaling pathway promotes activated macrophages to secrete anti-inflammatory factors IL-10 and IL-1ra, and up regulates the expression of osteogenesis related genes BMP2 and VEGF to promote osteogenesis (Mele et al., 2014).

MECHANISMS OF OSTEOGENESIS OF MG MATRIX COMPOSITES

Promotion of ERK Signaling Pathway in Osteoblasts by Degradation Products From Mg-Ca-Sr Alloys

In osteoblasts, a critical member of mitogen-activated protein kinase cascades (MAPK) plays an important role in cell proliferation and differentiation. ERK1/2 is a positive regulator for osteoblast differentiation and bone formation. Studies have shown that C3G may act through ERK1/2 signaling pathways in various cells (Hu et al., 2021; Ibarra et al., 2021). Li et al. (2016) developed ternary Mg-1Ca-xwt% Sr (x = 0.2, 0.5, 1.0, 2.0) Alloys as degradable implant materials in orthopedic field. Its results showed that Mg-1Ca alloy with different amounts of Sr added during the melting process could refine the alloy grains. The extracts of the obtained cast alloys could stimulate cell viability and osteogenic differentiation, and the degree of stimulation varied according to the Sr content. The addition of 2.0 wt% Sr in Mg-1Ca alloy could induce higher proteins adsorption, and improve cell proliferation and ALP activity as a marker of osteogenic differentiation, collagen secretion, etc. ECM mineralization and osteogenesis related genes are expressed through the ERK1/2 pathway. The MAPK family is involved

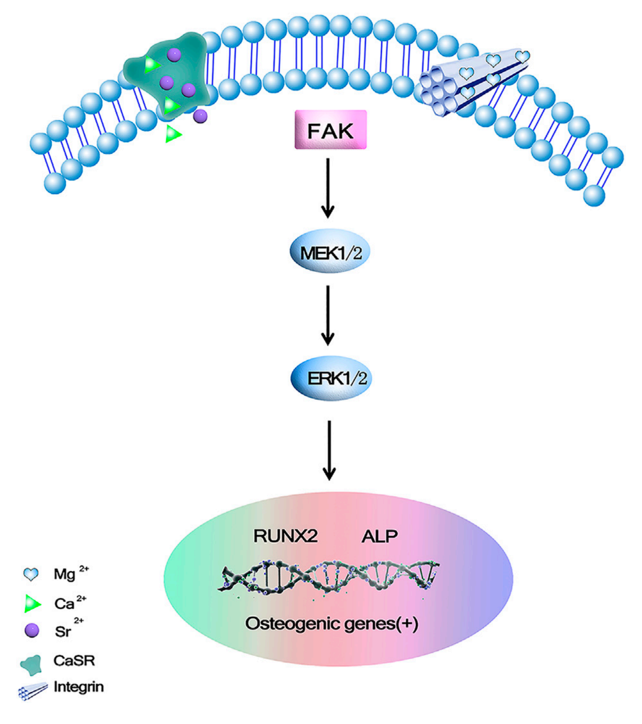

FIGURE 3 | Mg^{2+}, Ca^{2+} and Sr^{2+}could promote osteogenic gene expression *via* binding to calcium-sensing receptor (CaSR) and activating ERK signaling pathway through Ras/Raf/MEK/ERK pathway (Li et al., 2016).

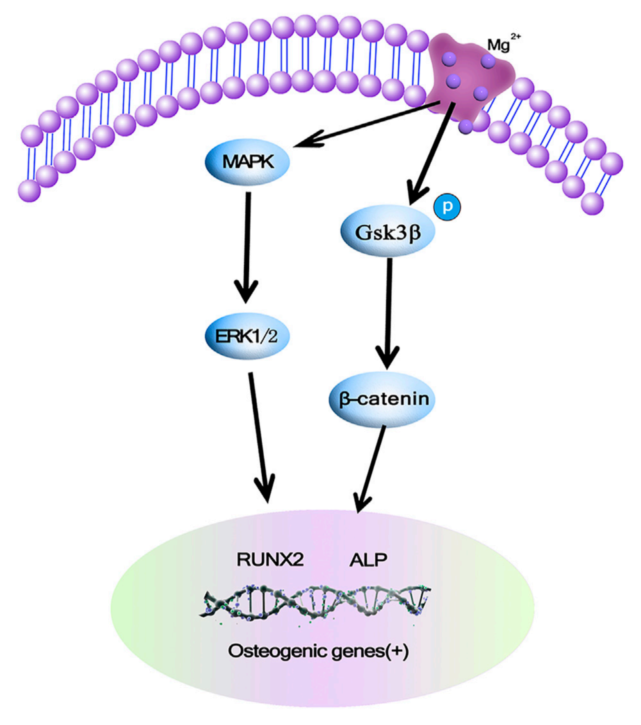

FIGURE 4 | Mg ions promoting osteogenesis may be achieved by activating the MAPK/ERK signaling pathway or promoting osteoblast proliferation and differentiation *via* Wnt/β-Catenin (Iezaki et al., 2016).

in regulating many cellular physiological functions, such as proliferation, differentiation, inflammation, and apoptosis, and MAPKs are indispensable factors in the process of osteoblast initiation, especially the ERK/MAPK pathway (Yang et al., 2018), in which ERK1/2 mediated the phosphorylation and transcriptional activity of Runx2 in bone (Wang et al., 2010; Park et al., 2021). Without increasing the total ERK level, it was found that Mg-1Ca-2Sr alloys induced ERK1/2 activation as well as upregulation of Runx2 expression in osteoblasts significantly, however there was no obvious difference in the amount of total and phosphorylated JNK or P38 between the treatment and control groups, and its further study found Ras/Raf/MEK of MAPK signaling pathway, ERK plays an essential role in the differentiation and maturation of osteoblasts cultured on Mg-1Ca-2Sr alloys. **Figure 3** shows these alloys release Mg^{2+}, Ca^{2+}, and Sr^{2+}. Mg^{2+} can bind to the subunits of integrins and activate the MEK/ERK pathway. $Ca^{2+}$and Sr^{2+}bind to Ca^{2+}receptors (CaSR) Binding. Once the CaSR is activated by the increased divalent cation, the intracellular signaling pathways start to activate different G proteins. This leads to the activation of tyrosine kinases, phospholipase C and adenylate cyclases, which activates the ERK signaling pathway through the RAS/Raf/MEK/ERK pathway (Li et al., 2016). The Mg^{2+} integrin subunits bind, upregulate the expression of integrins in osteoblasts, and in turn activate focal adhesion kinase (FAK). FAK in integrin signal integration can directly activate ERK signaling and promote osteogenic gene expression. Berglund et al. (2017). Effects of novel Mg-Ca-Sr alloys on cellular mechanisms during degradation ion concentrations of alloy degradation products were found to be specific to hMSCs had a dual effect, increasing cell proliferation and possibly inducing osteogenesis, the effect on proliferation was attributed to the presence of Sr, whereas the addition of Mg appeared to induce osteogenesis. HMSCs differentiation was examined by changes in ALP and Runx2 genes expression, and further concluded that alloy degradation products affected the osteogenic process. ALP gene expression in osteogenic induced cultures showed that the alloy extracts had different effects on osteogenesis.

The Underlying Mechanism of Mg Ions Promoting Osteogenesis May be Achieved by Activating the MAPK/ERK Signaling Pathway or Promoting Osteoblast Proliferation and Differentiation *via* Wnt/β - Catenin

MAPK/ERK is an important signaling pathway that regulates the processes of bone development, bone remodeling, and bone metabolism (Ishii et al., 2019). The main pathways of MAPK/ERK signaling include β-Catenin and GSK-3β. β-Catenin is a positive regulatory protein, which is able to promote proliferation and differentiation of osteoblasts. GSK-3β acts as a signaling protein and transcription factor to monitor cell growth (Liu et al., 2011). β-Catenin is an important positive regulator of osteoblasts and promotes osteoblast differentiation and bone formation, and several studies have also suggested different observations on the effects of Mg^{2+} on the β-Catenin pathway, which may be due to different cells. The current study gives an explanation that Mg exerts anabolic effects on bone, and in this study, Mg^{2+}increased ERK phosphorylation and then enhanced the level of c-fos may help promote the proliferation of MC3T3 cells, in addition Mg^{2+} induced GSK3β phosphorylation, so the level of β-Catenin was increased due to the Mg^{2+}-induced phosphorylation of GSK3β and Ca^{2+}impedes GSK3β binding to β-Catenin in order to increase the level of β-Catenin and stimulate β-Catenin to form new bone. *In vitro* studies have shown that at least two pathways are involved in Mg^{2+} stimulation of bone formation, as shown in **Figure 4** (Iezaki et al., 2016).

Mg Ions is Involved in the PI3K/Akt Signaling Pathway Through the Ion Channel Functional Protein Kinase TRPM7

Two cation channels of the transient receptor potential hormone (TRPM) family have been characterized as Mg^{2+} transporters: TRPM6 and TRPM7. TRPM7 is both an ion channel and a phosphokinase active transmembrane protein, it has been implicated in cell proliferation and cell motility in various normal tissues (Yang et al., 2013; Na et al., 2018). As a divalent cation channel, TRPM7 participates in the process of cellular uptake of Mg^{2+} in the external environment, TRPM7 is also involved in Mg^{2+} absorption, and the absence of TRPM7 kinase activity can lead to the same phenotype as hypomagnesemia, which indicates that Mg^{2+} can activate TRPM7 kinase activity to mediate downstream signaling pathways and regulate cell biological functions and activities (Zhao et al., 2019). In many tissues, TRPM7 mediates the PI3K signaling pathway to regulate the proliferative activity of cells and increase the extracellular Mg^{2+} content, which relieves the growth inhibition caused by TRPM7 gene deletion. Zhang et al. (2017) human studies have confirmed that Mg^{2+}promote bone repair by recruiting osteoblasts and promoting osteogenesis in osteoblasts. Inhibition of TRPM7 gene expression by siRNA gene interference found that Mg^{2+} induced ossification, mineralization migration, and chemotaxis were significantly inhibited after TRPM7 knockdown, demonstrating that the TRPM7 gene mediates the osteogenic induction by Mg^{2+} in human osteoblasts. Its data suggest that Mg ions induce osteogenesis byTRPM7/PI3K signaling upregulates the expression of Runx2 and ALP, which are markers of osteogenic differentiation, and can significantly improve the osteogenic activity of human osteoblasts. Furthermore, TRPM7/PI3K signaling increases MMP2, MMP9, and vascular endothelial growth factor (VEGF). The expression level of PI3K, a key signal transduction molecule downstream of TRPM7, induces osteoblasts from a low to a high Mg^{2+} environment by inducing cell migration. It can activate Akt protein and regulate cell proliferation, differentiation, apoptosis, and glucose transport in many tissues (Guntur and Rosen, 2011). The PI3K/Akt signaling pathway plays a crucial role in osteogenesis, and Akt phosphorylation upregulates the Runx2 gene, which induces genes associated with bone repair and remodeling, such as osteocalcin, type I collagen, osteopontin, and ALP. (Choi et al., 2014; Wang et al. (2017b)) incubation of rat calvarial osteoblasts with three different concentrations of Mg ions (6, 10, and 18 mM) revealed that appropriate concentrations of Mg^{2+} (6–10 mM) promoted osteoblast viability and differentiation, whereas excessively high Mg concentrations (18 mM has an inhibitory effect on osteoblast viability and differentiation. Blocking the PI3K/Akt signaling pathway using wortmannin, a specific inhibitor of the PI3K/Akt signaling pathway, wortmannin significantly attenuated the enhancement of cell adhesion, cell viability, ALP activity, ECM mineralization, and osteogenesis related gene expression induced by 10 mM Mg^{2+}. Our study showed that 6 and 10 mM Mg^{2+} exerts stimulatory effects on cell adhesion, cell viability, ALP activity, ECM mineralization, and expression of osteogenesis related genes, and this process has been attributed, at least in part, to the activated PI3K/Akt signaling pathway.

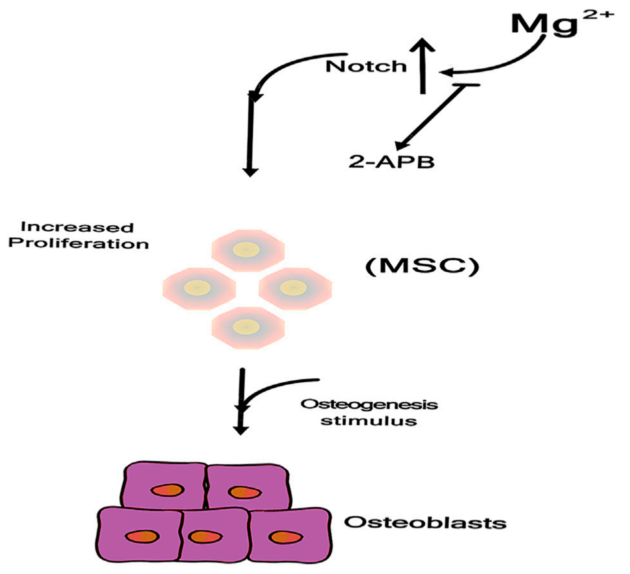

FIGURE 5 | Mg ions enter into MSC through TRPM7 channel, increasing Notch Intracellular Domain (NICD) nuclear translocation (Díaz-Tocados. et al., 2017).

Mg Ions Promote Osteogenic Differentiation *via* the Notch Signaling Pathway

As shown in **Figure 5**, these effects were not observed after inhibition of the Mg^{2+} channel TRPM7 by 2-APB confirming the crucial role of intracellular Mg^{2+} during MSCs osteogenesis, and Mg supplementation enhances MSCs proliferation. Mechanistically, Mg ions enter MSCs through TRPM7 channels and increase Notch intracellular domain (NICD) nuclear translocation. Proliferation of MSCs contributes to subsequent osteogenesis, and inhibition of 2-APB channels decreases the osteogenic potential of Mg (Díaz-Tocados. et al., 2017; Niapour et al., 2019).

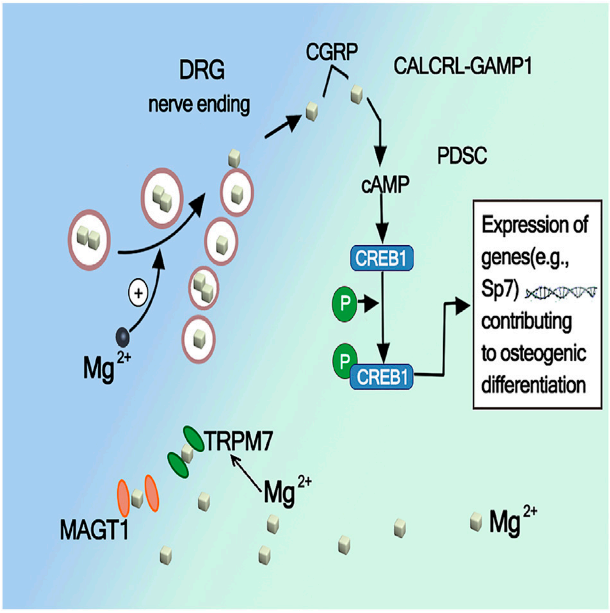

FIGURE 6 | Activation of CREB1 and SP7 by Mg mediated CGRP (Zhang et al., 2016).

Activation of CREB1 and SP7 by Mg Mediated CGRP

Calcitonin peptide (CGRP) primarily located in small sensory fibers, most usually found in nerves that are closely associated with blood vessels. The periosteum contains sensory nerves and releases neuropeptides, such as CGRP, which are known as involving in bone healing (). It has been demonstrated that magnesium ion release implantation enhances the synthesis of CGRP in the dorsal root ganglion (DRG) and its release at the end of the sensory nerve periosteum, and the CGRP mediated pathway has been identified as a major mechanism of potential magnesium to promote bone formation in fracture healing. Some study also demonstrates that CGRP processes an equal effect on migration and tube formation compared with VEGF, accompanied by increased VEGF expression, and activation of focal adhesion kinase (FAK), thereby acting as a strong proangiogenic growth factor during bone healing (Sun et al., 2020; Ye Li et al., 2021). Zhang et al. (2022) demonstrated through *in vitro* and *in vivo* studies that the promotion of bone formation by Mg is largely mediated by CGRP released from the sensory neuron terminals of the periosteum of the long bone axis, CGRP mediated periosteal nerves, and periosteal stem cells. The crosstalk pathway between them was identified as the main mechanism underlying Mg induced bone formation. Mg^{2+}enters neurons through the ion channels MAGT1 and TRPM7 and promotes CGRP vesicle clustering and secretion in spinal root ganglion phosphorylates cyclic adenosine monophosphate (cAMP) by coupling with the CGRP receptor on periosteal stem cells, which in turn activates CREB1 and SP7 (transcription factors essential for osteogenesis) to promote osteogenesis. As shown in **Figure 6**, CGRP or Mg implants only upregulate SP7 and not Runx2, another downstream target of CREB1 important for bone formation, which suggests that specific activation of CREB1 and SP7 leads to the differentiation of osteoblasts *in vitro* and *in vivo*.

CONCLUSION

In conclusion, The synthesis of Mg matrix composites is a hot research topic nowadays, and the host immune response is very important for bone bonding after biomaterial implantation. By studying the immune regulation of bone biomaterials, it can regulate the immune response in the process of osteogenesis, create a good local immune microenvironment, and help biomaterials reduce inflammatory response and promote good bone bonding. This study provides basic evidence for the development or modification of advanced Mg-based bone biomaterials and suggests new strategies. It has broad prospects and application value in the field of bone repair. It will provide experimental basis for exploring new bone tissue engineering materials with good antibacterial activity, excellent bone conductivity and suitable biodegradability, and further improve the application effect and scope of guided bone regeneration technology and bone tissue engineering materials in the field of implantation, It lays a good foundation for the final development of international advanced domestic bone tissue engineering materials.

AUTHOR CONTRIBUTIONS

XN: Formal analysis, Writing Reviewing and Editing. XZ, YS: Literature review. JY: Examination and polishing of articles. All authors contributed to the article and approved the submitted version.

FUNDING

This work was supported by the Academic Research Projects of Beijing Union University (No.ZK70202006) and Beijing Youth top individual project (2016000026833ZK04), the National Natural Science Foundation of China (No. 5177050098), the collaborative innovation project of Chaoyang District, Beijing (CYXC2102). Xinjiang Uygur Autonomous Region Youth Science Foundation Project (2022D01C208).

ACKNOWLEDGMENTS

The authors are grateful for the Xinjiang Medical University and College of Robotics, Beijing Union University.

REFERENCES

Alvarez-Lopez, M., Pereda, M. D., del Valle, J. A., Fernandez-Lorenzo, M., Garcia-Alonso, M. C., Ruano, O. A., et al. (2010). Corrosion Behaviour of AZ31 Magnesium alloy with Different Grain Sizes in Simulated Biological Fluids☆fferent Grain Sizes in Simulated Biological FLuids. *Acta Biomater.* 6, 1763–1771. doi:10.1016/j.actbio.2009.04.041

Berglund, I. S., Dirr, E. W., Ramaswamy, V., Allen, J. B., Allen, K. D., and Manuel, M. V. (2017). The Effect of Mg-Ca-Sr alloy Degradation Products on Human Mesenchymal Stem Cells. *J. Biomed. Mater. Res.* 106, 697–704. doi:10.1002/jbm.b.33869

Bockstaller, M. R., Mickiewicz, R. A., and Thomas, E. L. (2005). Block Copolymer Nanocomposites: Perspectives for Tailored Functional Materials. *Adv. Mater.* 17, 1331–1349. doi:10.1002/adma.200500167

Brar, H. S., Wong, J., and Manuel, M. V. (2012). Investigation of the Mechanical and Degradation Properties of Mg-Sr and Mg-Zn-Sr Alloys for Use as Potential Biodegradable Implant Materials. *J. Mech. Behav. Biomed. Mater.* 7, 87–95. doi:10.1016/j.jmbbm.2011.07.018

Chen, X., Tan, B., Wang, S., Tang, R., Bao, Z., Chen, G., et al. (2021). Rationally Designed Protein Cross-Linked Hydrogel for Bone Regeneration via Synergistic Release of Magnesium and Zinc Ions. *Biomaterials* 274, 120895. doi:10.1016/j.biomaterials.2021.120895

Chen, Z., Wang, X., and Zhang, L. (2018). The Concept of "osteoimmunomodulation" and its Application in the Development of "Osteoimmune-Smart" Bone Substitute Materials. *J. Prev. Treat. Stomatological Dis.* 26, 688. doi:10.12016/j.issn.2096-1456.2018.11.002

Choi, Y. H., Kim, Y.-J., Jeong, H. M., Jin, Y.-H., Yeo, C.-Y., and Lee, K. Y. (2014). Akt Enhances Runx2 Protein Stability by Regulating Smurf2 Function during Osteoblast Differentiation. *Febs J.* 281, 3656–3666. doi:10.1111/febs.12887

Cui, X., MoralesQian, R.-T. T. W., Qian, W., Wang, H., Gagner, J.-P., Dolgalev, I., et al. (2018). Hacking Macrophage-Associated Immunosuppression for Regulating Glioblastoma Angiogenesis. *Biomaterials* 161, 164–178. doi:10.1016/j.biomaterials.2018.01.053

Díaz-Tocados., J. M., Herencia, C., Martínez-Moreno, J. M., Montes de Oca, A., Rodríguez-Ortiz, M. E., Vergara, N., et al. (2017). Magnesium Chloride Promotes Osteogenesis through Notch Signaling Activation and Expansion of Mesenchymal Stem Cells. *Sci. Rep.* 7, 7839. doi:10.1038/s41598-017-08379-y

Dima, C., Cotârlet, M., Alexe, P., and Dima, S. (2014). Microencapsulation of Essential Oil of Pimento [Pimenta Dioica (L) Merr.] by Chitosan/k-Carrageenan Complex Coacervation Method. *Innovative Food Sci. Emerging Tech.* 22, 203–211. doi:10.1016/j.ifset.2014.07.00810.1016/j.ifset.2013.12.020

Golshirazi, A., Kharaziha, M., and Golozar, M. A. (2017). Polyethylenimine/kappa Carrageenan: Micro-arc Oxidation Coating for Passivation of Magnesium alloy. *Carbohydr. Polym.* 167, 185–195. doi:10.1016/j.carbpol.2017.03.025

Guntur, A. R., and Rosen, C. J. (2011). The Skeleton: a Multi-Functional Complex Organ. New Insights into Osteoblasts and Their Role in Bone Formation: the central Role of PI3Kinase. *J. Endocrinol.* 211, 123–130. doi:10.1530/JOE-11-0175

Haggerty, A. E., Maldonado-Lasunción, I., and Oudega, M. (2018). Biomaterials for Revascularization and Immunomodulation after Spinal Cord Injury. *Biomed. Mater.* 13, 044105. doi:10.1088/1748-605X/aaa9d8

Hu, B., Chen, L., Chen, Y., Zhang, Z., Wang, X., and Zhou, B. (2021). Cyanidin-3-glucoside Regulates Osteoblast Differentiation via the Erk1/2 Signaling Pathway. *ACS Omega* 6, 4759–4766. doi:10.1021/acsomega.0c05603

Ibarra, B. A., Machen, C., and Atit, R. P. (2021). Wnt-Dependent Activation of ERK Mediates Repression of Chondrocyte Fate during Calvarial Development. *Jdb* 9, 23. doi:10.3390/jdb9030023

Iezaki, T., Onishi, Y., Ozaki, K., Fukasawa, K., Takahata, Y., Nakamura, Y., et al. (2016). The Transcriptional Modulator Interferon-Related Developmental Regulator 1 in Osteoblasts Suppresses Bone Formation and Promotes Bone Resorption. *J. Bone Miner Res.* 31 (3), 573–584. doi:10.1002/jbmr.2720

Ishii, A., Furusho, M., Macklin, W., and Bansal, R. (2019). Independent and Cooperative Roles of the Mek/ERK1/2-MAPK and PI3K/Akt/mTOR Pathways during Developmental Myelination and in Adulthood. *Glia* 67, 1277–1295. doi:10.1002/glia.23602

Italiani, P., and Boraschi, D. (2014). From Monocytes to M1/M2 Macrophages: Phenotypical vs. Functional Differentiation. *Front. Immunol.* 5, 1–22. doi:10.3389/fimmu.2014.00514

Jetten, N., Verbruggen, S., Gijbels, M. J., Post, M. J., De Winther, M. P. J., and Donners, M. M. P. C. (2013). Anti-inflammatory M2, but Not Pro-inflammatory M1 Macrophages Promote Angiogenesis *In Vivo*. *Angiogenesis* 17, 109–118. doi:10.2741/269210.1007/s10456-013-9381-6

Kato, K., Ikeda, Y., and Ito, K. (2019). Direct Determination of Cross-Link Density and its Correlation with the Elastic Modulus of a Gel with Slidable Cross-Links. *ACS Macro Lett.* 8, 700–704. doi:10.1021/acsmacrolett.9b00238

Lee, J.-W., Han, H.-S., Han, K.-J., Park, J., Jeon, H., Ok, M.-R., et al. (2016). Han Hyung-Seop., Han Kyeong-JinLong-Term Clinical Study and Multiscale Analysis of *In Vivo* Biodegradation Mechanism of Mg alloy. *Proc. Natl. Acad. Sci. USA* 113, 716–721. doi:10.1073/pnas.1518238113

Lei, Q., Chen, J., Huang, W., Wu, D., Lin, H., and Lai, Y. (2015). Proteomic Analysis of the Effect of Extracellular Calcium Ions on Human Mesenchymal Stem Cells: Implications for Bone Tissue Engineering. *Chemico-Biological Interactions* 233, 139–146. doi:10.1016/j.cbi.2015.03.021

Li, M., He, P., Wu, Y., Zhang, Y., Xia, H., Zheng, Y., et al. (2016). Stimulatory Effects of the Degradation Products from Mg-Ca-Sr alloy on the Osteogenesis through Regulating ERK Signaling Pathway. *Sci. Rep.* 6, 322–323. doi:10.1038/srep32323

Li, Y., Li, J., Zhu, S., Luo, E., Feng, G., Chen, Q., et al. (2012). Effects of Strontium on Proliferation and Differentiation of Rat Bone Marrow Mesenchymal Stem Cells. *Biochem. Biophysical Res. Commun.* 418, 725–730. doi:10.1016/j.bbrc.2012.01.088

Lin, X., Tan, L., Wan, P., Yu, X., Yang, K., Hu, Z., et al. (2013). Characterization of Micro-arc Oxidation Coating post-treated by Hydrofluoric Acid on Biodegradable ZK60 Magnesium alloy. *Surf. Coat. Tech.* 232, 899–905. doi:10.1016/j.surfcoat.2013.06.121

Lin, Z., Shen, D., Zhou, W., Zheng, Y., Kong, T., Liu, X., et al. (2021). Regulation of Extracellular Bioactive Cations in Bone Tissue Microenvironment Induces Favorable Osteoimmune Conditions to Accelerate *In Situ* Bone Regeneration. *Bioactive Mater.* 6, 2315–2330. doi:10.1016/j.bioactmat.2021.01.018

Liu, R., Shi, Y., Yang, H. J., Wang, L., Zhang, S., Xia, Y. Y., et al. (2011). Neural Cell Adhesion Molecule Potentiates the Growth of Murine Melanoma via β-Catenin Signaling by Association with Fibroblast Growth Factor Receptor and Glycogen Synthase Kinase-3β. *J. Biol. Chem.* 286, 26127–26137. doi:10.1074/jbc.M111.237297

Mahapatro, A., Negron, T. M. D., Arshanapalli, S. A., Gomes, A. S., and Yao, L. (2015). Fabrication, Biofunctionality and Biocompatibility Evaluations of Octadecyltrichlorosilane Nano Coatings on Magnesium Alloy. *J. Nanoengng Nanomfg* 5, 294–303. doi:10.1166/jnan.2015.1255

MarmionCeline, C. J., Sigel, H., and Sigel, R. O. (2014). A. Sigel, H. Sigel, R. K. O. Sigel (Eds): Interrelations between Essential Metal Ions and Human Diseases. Vol. 13 of Metal Ions in Life Sciences. *Transit. Met Chem* 39, 971–972. doi:10.1146/annurev.pa.15.040175.00135510.1007/s11243-014-9883-0

Mele, E., Bayer, I. S., Nanni, G., Heredia-Guerrero, J. A., Ruffilli, R., Ayadi, F., et al. (2014). Biomimetic Approach for Liquid Encapsulation with Nanofibrillar Cloaks. *Langmuir* 30, 2896–2902. doi:10.1021/la4048177

Moeser, A. J., Bond, S., Russo, S., Elloumi, H. Z., and Plevy, S. E. (2011). Early Life Stress Triggers Persistent Colonic Barrier Dysfunction and Exacerbates Colitis Inil-10(-/-) Mice. *Gastroenterology* 140, 696. doi:10.1016/S0016-5085(11)62890-4

Munisso, M. C., Kang, J.-H., Tsurufuji, M., and Yamaoka, T. (2012). Cilomilast Enhances Osteoblast Differentiation of Mesenchymal Stem Cells and Bone Formation Induced by Bone Morphogenetic Protein 2. *Biochimie* 94, 2360–2365. doi:10.1016/j.biochi.2012.05.031

Murray, P. J., Allen, J. E., Biswas, S. K., Fisher, E. A., Gilroy, D. W., Goerdt, S., et al. (2014). Macrophage Activation and Polarization: Nomenclature and Experimental Guidelines. *Immunity* 41, 14–20. doi:10.1016/j.immuni.2014.06.008

Na, C., Liping, L., and Namariq, A. S. (2018). The Kinase Activity of the Channel-Kinase Protein TRPM7 Regulates Stability and Localization of the TRPM7 Channel in Polarized Epithelial Cells. *J. Biol. Chem.* 293 (29), 11491–11504. doi:10.1074/jbc.RA118.001925

Nahrendorf, M., and Swirski, F. K. (2016). Abandoning M1/M2 for a Network Model of Macrophage Function. *Circ. Res.* 119, 414–417. doi:10.1161/CIRCRESAHA.116.309194

Nenasheva, T., Gerasimova, T., Serdyuk, Y., Grigor'eva, E., Kosmiadi, G., Nikolaev, A., et al. (2020). Macrophages Derived from Human Induced Pluripotent Stem Cells Are Low-Activated "Naïve-like" Cells Capable of Restricting Mycobacteria Growth. *Front. Immunol.* 11, 1016. doi:10.3389/fimmu.2020.01016

Niapour, A., Ghasemi Hamidabadi, H., Niapour, N., Mohammadi, P., Sharifi Pasandi, M., and Malekzadeh, V. (2019). Pharmacological Notch Pathway Inhibition Leads to Cell Cycle Arrest and Stimulates Ascl1 and Neurogenin2 Genes Expression in Dental Pulp Stem Cells-Derived Neurospheres. *Biotechnol. Lett.* 41, 873–887. doi:10.1007/s10529-019-02687-1

Park, K.-R., Lee, J.-Y., Cho, M., Hong, J.-T., and Yun, H.-M. (2021). Paeonolide as a Novel Regulator of Core-Binding Factor Subunit Alpha-1 in Bone-Forming Cells. *Ijms* 22, 4924. doi:10.3390/ijms22094924

Peron, M., Cogo, S., Bjelland, M., Bin Afif, A., Dadlani, A., Greggio, E., et al. (2021). On the Evaluation of ALD TiO2, ZrO2 and HfO2 Coatings on Corrosion and Cytotoxicity Performances. *J. Magnesium Alloys* 9, 1806–1819. doi:10.1016/j.jma.2021.03.010

Piccolo, V., Curina, A., Genua, M., Ghisletti, S., Simonatto, M., Sabò, A., et al. (2017). Opposing Macrophage Polarization Programs Show Extensive Epigenomic and Transcriptional Cross-Talk. *Nat. Immunol.* 18, 530–540. doi:10.1038/ni.3710

Ping, J., Zhou, C., Dong, Y., Wu, X., Huang, X., Sun, B., et al. (2021). Modulating Immune Microenvironment during Bone Repair Using Biomaterials: Focusing on the Role of Macrophages. *Mol. Immunol.* 138, 110–120. doi:10.1016/j.molimm.2021.08.003

Qi, H., Heise, S., Zhou, J., Schuhladen, K., Yang, Y., Cui, N., et al. (2019). Electrophoretic Deposition of Bioadaptive Drug Delivery Coatings on Magnesium Alloy for Bone Repair. *ACS Appl. Mater. Inter.* 11, 8625–8634. doi:10.1021/acsami.9b01227

Reginster, J.-Y., Badurski, J., Bellamy, N., Bensen, W., Chapurlat, R., Chevalier, X., et al. (2013). Efficacy and Safety of Strontium Ranelate in the Treatment of Knee Osteoarthritis: Results of a Double-Blind, Randomised Placebo-Controlled Trial. *Ann. Rheum. Dis.* 72, 179–186. doi:10.1136/annrheumdis-2012-202231

Reginster, J.-Y., Hiligsmann, M., and Bruyere, O. (2010). Strontium Ranelate: Long-Term Efficacy against Vertebral, Nonvertebral and Hip Fractures in Patients with Postmenopausal Osteoporosis. *Ther. Adv. Musculoskelet.* 2, 133–143. doi:10.1177/1759720X10362824

Saidak, Z., and Marie, P. J. (2012). Strontium Signaling: Molecular Mechanisms and Therapeutic Implications in Osteoporosis. *Pharmacol. Ther.* 136, 216–226. doi:10.3390/ijms2120762310.1016/j.pharmthera.2012.07.009

Seitz, J.-M., Durisin, M., Goldman, J., and Drelich, J. W. (2015). Recent Advances in Biodegradable Metals for Medical Sutures: A Critical Review. *Adv. Healthc. Mater.* 4, 1915–1936. doi:10.1002/adhm.201500189

Sharma, A., Liaw, K., Sharma, R., Spriggs, T., Appiani La Rosa, S., Kannan, S., et al. (2020). Dendrimer-Mediated Targeted Delivery of Rapamycin to Tumor-Associated Macrophages Improves Systemic Treatment of Glioblastoma. *Biomacromolecules* 21, 5148–5161. doi:10.1021/acs.biomac.0c01270

Siddiqui, D. A., Sridhar, S., Wang, F., Jacob, J. J., and Rodrigues, D. C. (2019). Can Oral Bacteria and Mechanical Fatigue Degrade Zirconia Dental Implants *In Vitro*? *ACS Biomater. Sci. Eng.* 5, 2821–2833. doi:10.1021/acsbiomaterials.9b00223

Streckova, M., Sopcak, T., Stulajterova, R., Giretova, M., Medvecky, L., Kovalcikova, A., et al. (2018). Needle-less Electrospinning Employed for Calcium and Magnesium Phosphate Coatings on Titanium Substrates. *Surf. Coat. Tech.* 340, 177–189. doi:10.1016/j.surfcoat.2018.02.063

Sun, J., Zhang, W., Tan, Z., Zheng, C., Tang, Y., Ke, X., et al. (2020). Zika Virus Promotes CCN1 Expression via the CaMKIIα-CREB Pathway in Astrocytes. *Virulence* 11, 113–131. doi:10.1080/21505594.2020.1715189

Wang, J., Hua, Z. S., and Ma, H. (2017). Research Progress on Preparation of RareEarth Magnesium Alloys by Molten Salt Electrolysis. *Chin. Rare Earths* 38, 100–113. doi:10.16533/J.CNKI.15-1099/TF.201702015

Wang, J., Ma, X.-Y., Feng, Y.-F., Ma, Z.-S., Ma, T.-C., Zhang, Y., et al. (2017). Magnesium Ions Promote the Biological Behaviour of Rat Calvarial Osteoblasts by Activating the PI3K/Akt Signalling Pathway. *Biol. Trace Elem. Res.* 179, 284–293. doi:10.1007/s12011-017-0948-8

Wang, X., Harimoto, K., Xie, S., Cheng, H., Liu, J., and Wang, Z. (2010). Matrix Protein Biglycan Induces Osteoblast Differentiation through Extracellular Signal-Regulated Kinase and Smad Pathways. *Biol. Pharm. Bull.* 33, 1891–1897. doi:10.1248/bpb.33.1891

Wu, A. C., Raggatt, L. J., Alexander, K. A., and Pettit, A. R. (2013). Unraveling Macrophage Contributions to Bone Repair. *Bonekey Rep.* 2, 1–7. doi:10.1038/bonekey.2013.107

Wu, Y., He, G., Zhang, Y., Liu, Y., Li, M., Wang, X., et al. (2016). Unique Antitumor Property of the Mg-Ca-Sr Alloys with Addition of Zn. *Sci. Rep.* 6, 21736. doi:10.1016/j.actbio.2009.04.04110.1038/srep21736

Yang, X., Yang, Y., Zhou, S., Gong, X., Dai, Q., Zhang, P., et al. (2018). Puerarin Stimulates Osteogenic Differentiation and Bone Formation through the ERK1/2 and P38-MAPK Signaling Pathways. *Cmm* 17, 488–496. doi:10.2174/1566524018666171219101142

Yang, Y.-M., Jung, H.-H., Lee, S. J., Choi, H.-J., Kim, M. S., and Shin, D. M. (2013). TRPM7 Is Essential for RANKL-Induced Osteoclastogenesis. *Korean J. Physiol. Pharmacol.* 17, 65–71. doi:10.4196/kjpp.2013.17.1.65

Ye Li, Y., Xu, J., Mi, J., He, X., Pan, Q., Zheng, L., et al. (2021). Biodegradable Magnesium Combined with Distraction Osteogenesis Synergistically Stimulates Bone Tissue Regeneration via Cgrp-Fak-Vegf Signaling axis. *Biomaterials* 275 (502), 120984. doi:10.1016/j.biomaterials.2021.120984

Zain, M. Z. M., Illias, S., Salleh, M. M., Ismail, K. A., and Nooraizedfiza, Z. (2012). Improvement of Corrosion Resistance of Rare Earth Element (REE)-Based Anodic Oxidation Coating on AZ91D Magnesium Alloy. *Amm* 187, 210–214. doi:10.4028/www.scientific.net/AMM.187.210

Zhang, L., Li, M., Li, X., Liao, T., Ma, Z., Zhang, L., et al. (2022). Characteristics of Sensory Innervation in Synovium of Rats within Different Knee Osteoarthritis Models and the Correlation between Synovial Fibrosis and Hyperalgesia. *J. Adv. Res.* 35, 141–151. doi:10.1016/j.jare.2021.06.007

Zhang, X., Zu, H., Zhao, D., Yang, K., Tian, S., Yu, X., et al. (2017). Ion Channel Functional Protein Kinase TRPM7 Regulates Mg Ions to Promote the Osteoinduction of Human Osteoblast via PI3K Pathway: *In Vitro* Simulation of the Bone-Repairing Effect of Mg-Based alloy Implant. *Acta Biomater.* 63, 369–382. doi:10.1016/j.actbio.2017.08.051

Zhang, Y., Xu, J., Ruan, Y. C., Yu, M. K., O'Laughlin, M., Wise, H., et al. (2016). Implant-derived Magnesium Induces Local Neuronal Production of CGRP to Improve Bone-Fracture Healing in Rats. *Nat. Med.* 22, 1160–1169. doi:10.1038/nm.4162

Zhao, F., Wu, H., Reinach, P. S., Wu, Y., Zhai, Y., Lei, Y., et al. (2020). Up-Regulation of Matrix Metalloproteinase-2 by Scleral Monocyte-Derived Macrophages Contributes to Myopia Development. *Am. J. Pathol.* 190, 1888–1908. doi:10.1016/j.ajpath.2020.06.002

Zhao, L., Li, M., and Sun, H. (2019). Effects of Dietary Calcium to Available Phosphorus Ratios on Bone Metabolism and Osteoclast Activity of the OPG/RANK/RANKL Signalling Pathway in Piglets. *J. Anim. Physiol. Anim. Nutr.* 103, 1224–1232. doi:10.1111/jpn.13115

Zhu, L. H., Xu, X. J., Chen, T. Z., Niu, X. Y., and Xu, L. (2016). Cell Compatibility of the Micro-arc Oxidized Surface of Large Plastic Deformed TA2 *In Vitro*. *Msf* 852, 1220–1226. doi:10.4028/www.scientific.net/msf.852.1220

Conflict of Interest: The authors declare that the research was conducted in the absence of any commercial or financial relationships that could be construed as a potential conflict of interest.

frontiers | Frontiers in Bioengineering and Biotechnology

ORIGINAL RESEARCH
published: 04 April 2022
doi: 10.3389/fbioe.2022.884291

Regulation of T Cell Responses by Nano-Hydroxyapatite to Mediate the Osteogenesis

Fangze Guo[1,2], *Changqing Yuan*[1,2]*, *Hailin Huang*[1,2], *Xuyang Deng*[1,2], *Zirui Bian*[2], *Danyang Wang*[1,2], *Keke Dou*[1,2], *Li Mei*[1,2,3] *and Qihui Zhou*[1,2,3]*

[1]*Department of Stomatology, The Affiliated Hospital of Qingdao University, Qingdao University, Qingdao, China,* [2]*School of Stomatology, Qingdao University, Qingdao, China,* [3]*Institute for Translational Medicine, The Affiliated Hospital of Qingdao University, Qingdao University, Qingdao, China*

Nano-hydroxyapatite (nHA) has been widely applied as a tissue-engineering biomaterial and interacted with osteoblasts/stem cells to repair bone defects. In addition, T cells that coexist with osteoblasts/stem cells in the bone modulate the regulation of osteoimmunology by cytokine formation. However, the effects of nHA on T cells and the following regulatory interplay on osteogenic differentiation have been rarely examined. In this work, the physicochemical properties of needle-like nHA are characterized by field emission scanning electron microscopy, zeta potential, Fourier transform-infrared and X-ray diffraction. It is found that as the concentration of nHA increases, the proliferation of T cells gradually increases, and the proportion of apoptotic T cells decreases. The percentage of CD4$^+$ T cells is higher than that of CD8$^+$ T cells under the regulation of needle-like nHA. Furthermore, the supernatant of T cells co-cultured with nHA significantly inhibits the osteogenic differentiation of MC3T3-E1 by downregulating the formation of alkaline phosphatase and calcium nodule compared with the supernatant of nHA. Thus, our findings provide new insight into the nHA-mediated T cell and osteoblast interactions.

Keywords: nano-hydroxyapatite, T cell, osteogenesis, osteoimmunology, nanomaterials

Edited by:
Junchao Wei,
Nanchang University, China

Reviewed by:
Jiaolong Wang,
Affiliated Stomatological Hospital of Nanchang University, China
Guicai Li,
Nantong University, China

Correspondence:
Changqing Yuan
yuancq@qdu.edu.cn
Qihui Zhou
qihuizhou@qdu.edu.cn

Specialty section:
This article was submitted to Biomaterials, a section of the journal Frontiers in Bioengineering and Biotechnology

Received: *26 February 2022*
Accepted: *17 March 2022*
Published: *04 April 2022*

Citation:
Guo F, Yuan C, Huang H, Deng X, Bian Z, Wang D, Dou K, Mei L and Zhou Q (2022) Regulation of T Cell Responses by Nano-Hydroxyapatite to Mediate the Osteogenesis. Front. Bioeng. Biotechnol. 10:884291. doi: 10.3389/fbioe.2022.884291

1 INTRODUCTION

Hydroxyapatite (HA) is one of the most remarkable biomaterials and has been widely used in bone tissue engineering and regenerative medicine owing to its good biocompatibility and osteoinductive activity (Wei and Ma, 2004; Santos et al., 2012; Wang et al., 2012; Akram et al., 2014; Pepla, 2014; Yu et al., 2022). Particularly, nano-HA (nHA) particles gained increasing attention from the viewpoint of fundamental research and clinical applications due to their enhanced (bio)physicochemical properties compared with HA, including solubility, surface energy and bioactivity (Wang et al., 2004, 2021a; Guo et al., 2007; Mokabber et al., 2019; Ji et al., 2021). In addition, nHA is more similar to apatite of biological bone and dental tissues in terms of morphology, crystal structure and crystallinity (Fathi et al., 2008; Barros et al., 2019). It has been demonstrated that nHA can greatly promote osteoblast proliferation and osteogenesis, as well as accelerate osseointegration (Wang et al., 2021a). In addition, T cells that coexist with osteoblasts in the bone modulate the regulation of osteoimmunology by cytokine formation. Osteoimmunology is an emerging field for investigating the interaction between the immune system and bone tissue (Kumar and Roger, 2019; Yu et al., 2022). Osteoblasts have the capacity to communicate with the immune cells and vice versa (Gruber, 2019; Tsukasaki and Takayanagi, 2019; Zhang et al., 2020). Therefore, as a key regulator in

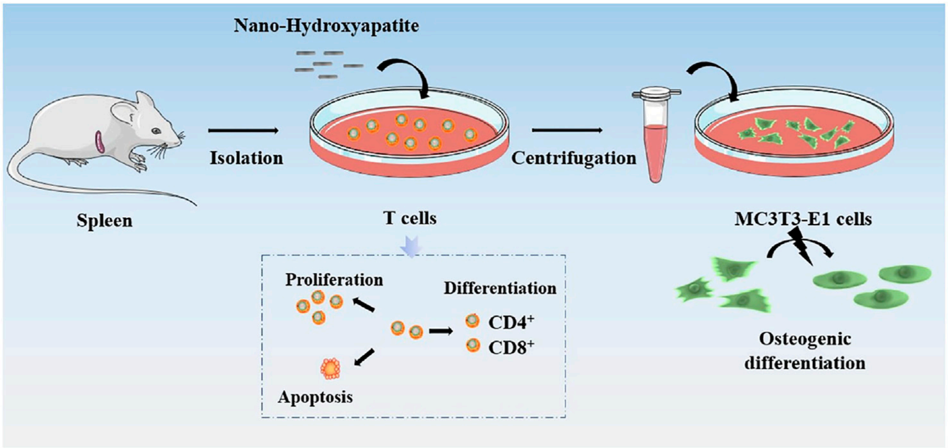

FIGURE 1 | Schematic diagram of the effects of nHA on T cell responses, differentiation, and the following regulatory on osteoblasts.

the process of bone regeneration, it is vital to elicit how nHA mediates the interplay between osteoblasts and T cells.

The bone marrow is the major location of haematopoiesis, harboring haematopoietic stem cells, myeloid and lymphoid progenitors, and mature immune cells such as B cells, neutrophils, macrophages, and T lymphocytes (Tsukasaki and Takayanagi, 2019). Osteoblasts/stem cells and immune cells share the same microenvironment and interact to complete the function of the "bone immune system" (Kumar and Roger, 2019). Osteoblast maturation is triggered by T lymphocytes (Croes et al., 2016; Khassawna et al., 2017). The formation and activity of osteoclasts are affected by some cytokines and growth factors secreted by T lymphocytes (Gillespie, 2007). Activated conventional $CD4^+$ and $CD8^+$ T lymphocytes control bone homeostasis *via* surface-bound molecules that bind to cognate molecules expressed in osteoblasts and their stromal cell precursors and by producing osteoclastogenic cytokines such as receptor activator of nuclear factor-κB ligand, tumor necrosis factor α (TNF-α), interleukin 1 (IL-1), IL-6, and IL-17 (Pacifici, 2016). In addition, T cell subsets and their released factors may influence bone regeneration outcomes differentially. $CD4^+$ and $CD8^+$ T lymphocytes affect osteoprogenitor cell development in various ways (Kumar and Roger, 2019; Shao et al., 2020). Nanoparticles are known to be able to interact with and affect the immune system (Liu et al., 2009). Nanoparticles could induce T cell activation and differentiation (Items et al., 2018). The effect of nHA with different aspect ratios on T cells has been investigated and greatly affected $CD3^+$ T cells as percentages of total cells (Yu et al., 2022). However, the effects of various nHA concentrations on T cells and the following regulatory interplay on osteogenic differentiation have been rarely examined.

Inspired by the introduction above, nHA was applied to investigate their effects on T cell responses, differentiation, and the following regulatory on osteoblasts (**Figure 1**). First, the physicochemical properties of needle-like nHA are characterized by field emission scanning electron microscopy (FE-SEM), zeta potential, Fourier transform-infrared (FT-IR) and X-ray diffraction (XRD). The viability, apoptosis and differentiation of T cells were treated with different nHA concentrations (i.e., 0, 10, 100, and 1,000 μg/ml), and cell viability was determined. In addition, the supernatant after co-culturing nHA and T cells was used to test its effect on the osteogenic capacity of osteoblasts by measuring the formation of alkaline phosphatase and calcium nodule. Thus, this work could offer new insight into the nHA-mediated T cell and osteoblast interactions.

2 MATERIALS AND METHODS

2.1 Materials

The nHA (purity >97%, CAS 1306-06-5) was purchased from Aladdin Industrial Inc. (Shanghai, China). Cell Counting Kit-8 (CCK-8), Annexin V-FITC/PI apoptosis detection kit, bicinchoninic acid (BCA) protein assay kit, Dulbecco's modified Eagle's medium (DMEM), trypsin, fetal bovine serum (FBS), penicillin and streptomycin were supplied by Meilunbio (Dalian, China). EasySep™ mouse T cell isolation kit was obtained from StemCell Technologies (Vancouver, CA, United States). Anti-mouse CD3 (Clone 17A2), anti-mouse CD28 (Clone 37.51) were purchased from Peprotech (Westlake Village, CA, United States). Anti-mouse CD4, phycoerythrin (PE, Clone GK1.5), Anti-mouse CD8α, phycoerythrin-cyanine 7 (PE-Cy7, Clone 53-6.7) and flow cytometry staining buffer was purchased from Multi Sciences Biotech, Co., Ltd. (Hangzhou, China). 5-(and-6)-Carboxyfluorescein diacetate, succinimidyl ester (CFSE) was obtained from Abbkine Bioadvisers. Alizarin red S (ARS) staining kit for osteogenesis was purchased from Beyotime (Shanghai, China). Dimethyl sulfoxide (DMSO) and RPMI 1640 culture medium were obtained from Solarbio (Beijing, China). Deionized (DI) water was used in all experiments. All chemicals were used without additional purification.

2.2 Physicochemical Characterization of nHA

2.2.1 FE-SEM

The size and morphology of nHA were evaluated using an FE-SEM (Sigma500, Zeiss, Germany). The nanoparticles were diluted in DI water and placed in an ultrasonic bath for 30 min to disperse the particles. The entire observation procedure was carried out in a vacuum atmosphere with a constant accelerating voltage of 5 kV, at magnification of 50,000. The average crystal size was determined by ImageJ software. The size was determined statistically by averaging data from 100 unique particles from different images.

2.2.2 FT-IR Spectroscopy

To measure the FT-IR spectra of the nHA, a Nicolet iN10 FT-IR spectrometer (Thermo Fisher Scientific, Waltham, MA, United States) was utilized over the range of 500–4,000 cm^{-1} at a scanning resolution of 2 cm^{-1} during 32 scans.

2.2.3 XRD Spectroscopy

The crystal structures of nHA were measured using XRD spectroscopy (Ultima IV Japan). The nHA was examined between 20° and 60° (2θ) at a scanning rate of 0.02° (2θ) per min operating with voltage 40 kV and current 40 mA equipped with Cu Kα radiation (λ = 1.5418 Å).

2.2.4 Zeta Potential

Dynamic light scattering on a Zetasizer Nano ZSE (United Kingdom) was used to assess the zeta potential of nHA samples. At the same concentration, the nHA were disseminated in DI water and 1640 RPMI complete medium.

2.3 Cell Assays

2.3.1 Isolation and Culture of Mouse T Cells

Spleens were dissected from C57BL/6 mice. Following mechanical digestion, the tissue suspension was filtered to produce a leukocyte single-cell suspension. T cells were isolated from this suspension by a mouse T cell isolation kit (19851; StemCell). These separated T lymphocytes were then used in the following cellular assays.

T cells (10^5 cells/ml) were cultured in 1640 RPMI complete medium (with FBS) in the presence of anti-mouse CD3 and anti-mouse CD28 antibodies. T cells co-cultured in the presence of 10, 100, and 1,000 μg/ml nHA. T cells were cultivated under the same conditions without the addition of nHA as the control.

The Cell Culture Centre of Shanghai Institutes for Biological Science Chinese Academy of Sciences (Shanghai, China) contributed a murine osteoblastic cell line (MC3T3-E1). MC3T3-E1 cells were incubated at 37°C in 5% CO_2 and the medium was changed every 2 days. Cells were subcultured when they achieved 80%–90% confluence by using Dulbecco’s phosphate buffered saline and trypsin/ethylenediaminetetraacetic acid. The studies listed below were carried out in duplicate across three different experiments ($n = 3$). This research was approved by the Ethics Committee of the Affiliated Hospital of Qingdao University (approval number: QYFYWZLL 26848).

2.3.2 T Cell Viability

The CCK-8 was used to assess cellular viability. Briefly, nHA samples were added into T cells medium (10^5 cells/well in 96-well plates) for 1, 2 and 3 days. Subsequently, 10 μl of CCK-8 solution was added to each well. The option density (OD_{450}) was measured using a microplate reader (SynergyH1/H1M, Bio-Tek, China) after 4 h of incubation.

2.3.3 Flow Cytometry

T cell apoptosis was examined by using the Annexin V-FITC/PI Apoptosis Assay Kit according to the manufacturer’s instructions. Briefly, T cells were incubated with or without nHA samples for 48 h. T cells were collected, washed with phosphate buffer solution (PBS), and resuspended at a concentration of 10^6 cells/ml in 1 × binding buffer. Then 100 μl of the solution (10^5 cells) was moved to a 2.5 ml Eppendorf tube, and 5 μl of annexin V-fluorescein-5-isothiocyanate (FITC) and 5 μl of propidium iodide (PI) were added. T cells were gently vortexed and incubated in the dark for 15 min. All samples were analyzed using FACScan flow cytometry (ACCURI C6, Becton Dickinson, United States). 10,000 ungated events were collected for each sample. The early apoptotic populations were represented by Annexin V^+ PI^- cells. The late apoptotic or secondary necrotic populations were represented by Annexin V^+ PI^+ cells.

T cells were stained with PE-conjugated anti-mouse CD4 and PE-cy7 conjugated anti-mouse CD8 antibodies after 5 days of incubation. T cells were washed and resuspended in flow cytometry staining buffer. FACScan flow cytometry was used to analyze the samples.

T lymphocytes were isolated, stimulated with anti-mouse CD3 and anti-mouse CD28 and labeled with 2.5 μM CFSE. These cells were cultured in the presence of nHA in 96-well plates at an equal ratio. After 72 h, the proliferation was assessed using flow cytometry based on CFSE dilution in gated T cells. Flow Cytometry samples were analyzed using FlowJo software.

2.3.4 MC3T3-E1 Cell Viability

DMEM (CON), the supernatant of nHA in 1640 RPMI complete medium (nHA), the supernatant of T cells (T), T cells and 100 μg/ml nHA co-culture supernatant (T + nHA) were respectively added into MC3T3-E1 cells medium (5 × 10^3 cells/well in 96-well plates) for 1 and 3 days culture. Then 10 μl CCK-8 solution was added to each well. The OD_{450} was measured using a microplate reader after 1 h of incubation.

2.3.5 Alkaline Phosphatase Activity

ALP activity was used to estimate the osteogenic performance of T cells and 100 μg/ml nHA co-culture supernatant, for evaluating the early osteogenic differentiation of MC3T3-E1 cells. MC3T3-E1 cells (2 × 10^4 cells/well in 24-well plates) were seeded on the samples and incubated with the osteogenic induction medium. The osteogenic induction medium (CON), the supernatant of nHA in 1640 RPMI complete medium (nHA), the supernatant of T cells (T), T cells and 100 μg/ml nHA co-culture supernatant (T + nHA) were respectively added into MC3T3-E1 cells medium. Following a 14 days culture

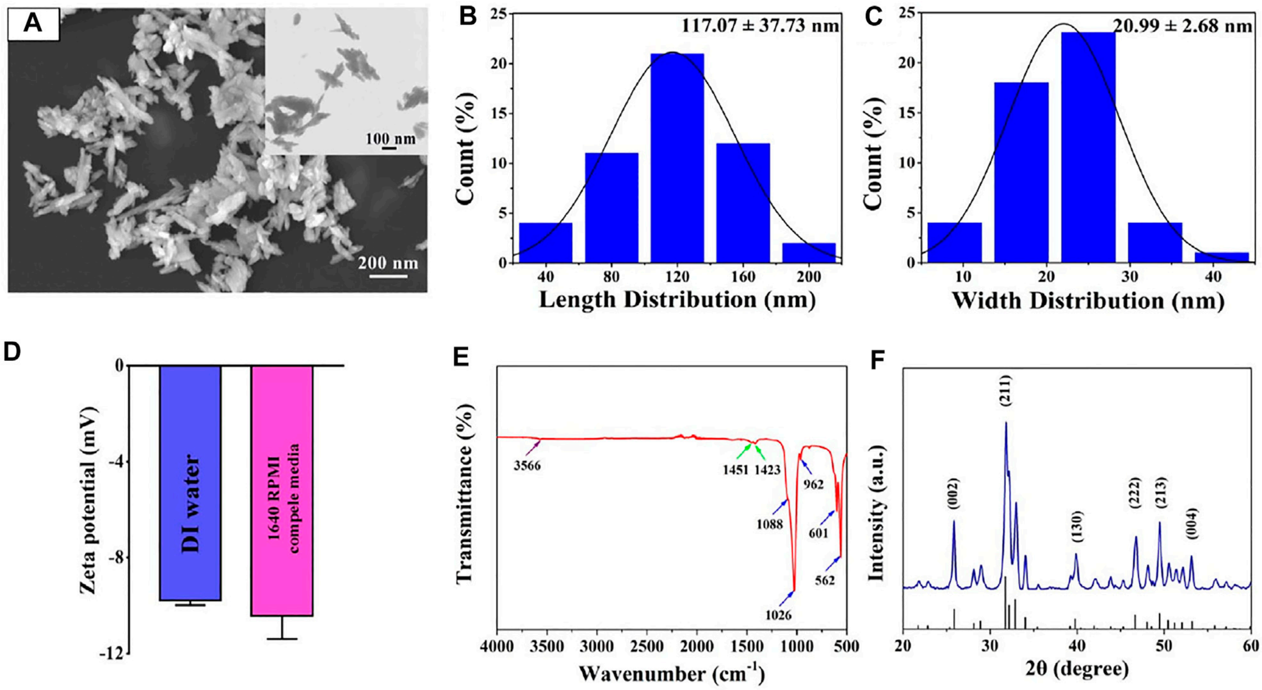

FIGURE 2 | (A) FE-SEM image of nHA. **(B,C)** Length and width size distribution of nHA. **(D)** Zeta potential of nHA in DI water and 1640 RPMI complete medium. **(E)** FT-IR spectrum of nHA. The purple, green and blue arrows indicated OH-, CO32- and PO43- groups, respectively. **(F)** XRD pattern of nHA.

period, the ALP activity of MC3T3-E1 cells was determined using an ALP test kit and the manufacturer's instruction. A BCA protein assay kit was used to standardize the total protein content of cells (king unit/g prot), which was used to calculate ALP activity.

2.4 ARS Staining

To examine matrix mineralization qualitatively, at the differentiation days of 14, MC3T3-E1 cells were washed with PBS, and then fixed and stained with ARS Staining Kit for Osteogenesis (C0148, Beyotime) as the manufacturer's instructions. The cells were examined by light microscopy (VIYEE, China).

2.5 Statistical Analysis

All data were presented as mean ± standard deviation (SD). GraphPad Prism 8.0 or Origin 9.0 software was used for statistical analysis. To determine differences between groups, one-way analysis of variance (ANOVA) with Tukey's test was used. A value of $p < 0.05$ was considered to be statistically significant.

3 RESULTS AND DISCUSSION

3.1 Physicochemical Characterization of nHA

Accumulating evidence suggested that the morphology and size of nanomaterials play a critical role in cell behaviors, including adhesion, viability, proliferation, migration, functionalization or differentiation (Nguyen et al., 2016; Zhou et al., 2018; Li et al., 2020; Liu M. et al., 2021; Wang et al., 2021b; Yang et al., 2021; Yao et al., 2021). **Figure 2A** shows that the nanosized HA particles possessed uniform distribution and needle-shaped morphology. **Figures 2B,C** displays that the length of the needle-like HA nanoparticle was 117.07 ± 37.73 nm and their width was 20.99 ± 2.68 nm. Previous studies have demonstrated that the needle-shaped nHA were biocompatible with bone marrow mesenchymal stem cells, enhanced cell proliferation and facilitated osteogenic differentiation (Paquin et al., 2015). Also, it was reported that the size (20–40 nm) of apatite nanoparticles could promote biomineralization in the bone tissue (Cai et al., 2007).

In addition, the surface charge and functional group in the nanomaterials significantly affected their interplay with cells (Thian et al., 2010). As shown in **Figure 2D**, it was found that the zeta potential of nHA in the DI water is −9.78 ± 0.2 mV. The nHA with negative charges was consistent with results reported in other studies (Huang et al., 2014). When nanoparticles were suspended in the cell culture medium, additional proteins were attached to their surface, which could affect their zeta potential (Thian et al., 2010; Sabuncu et al., 2012; Patel et al., 2017). In the 1640 RPMI complete medium, the zeta potential of the nHA was −10.43 ± 0.97 mV. The result indicates that nHA in the 1640 RPMI complete medium had no effect on their surface charge.

Moreover, FT-IR spectra were acquired to detect the functional group of the nHA sample. As indicated in **Figure 2E**, the spectroscopy of nHA displayed characteristic bands, including PO_4^{3-} (1,088, 1,026, 962, 601 and 562 cm^{-1}) and OH^- (3,566 cm^{-1}). In addition, the

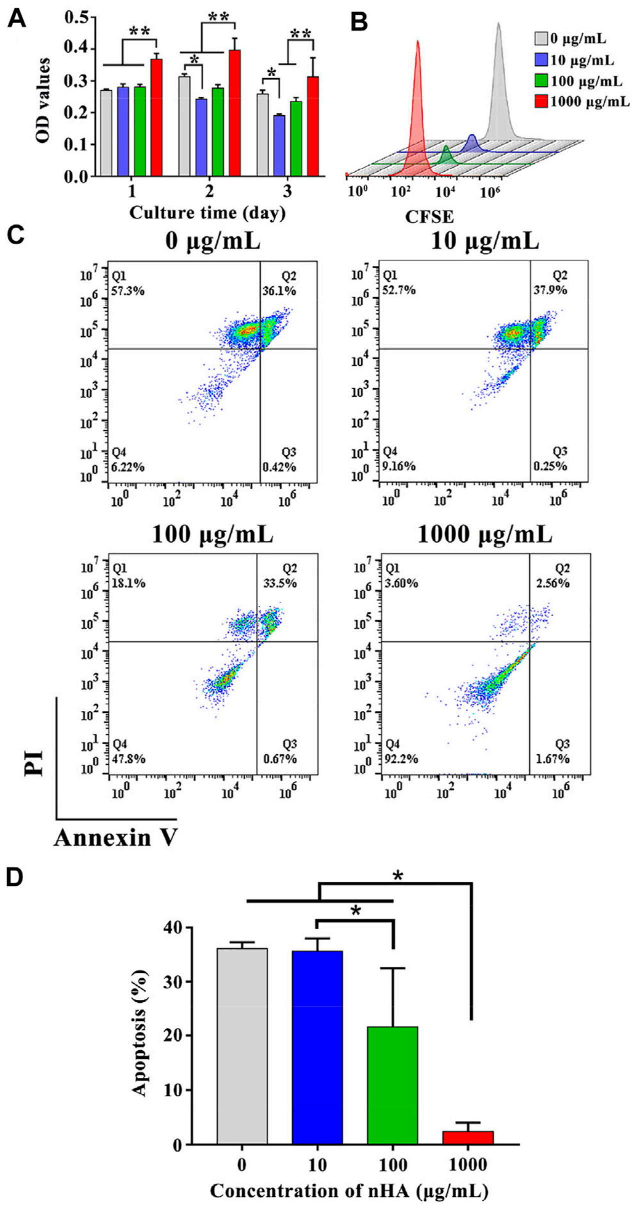

FIGURE 3 | (A) T cells viability on various samples for 1, 2 and 3 days. * represents $p < 0.05$ and ** represents $p < 0.01$. **(B)** Effect of nHA on T cell proliferation. **(C)** Flow cytometry analysis of the effect of nHA on T cell apoptosis. **(D)** Quantitative analysis of apoptosis.

ion stretching vibration at 1,451 and 1,423 cm^{-1} confirmed the presence of the CO_3^{2-} group. The functional groups of nHA from FT-IR spectra analysis are compared with the results in other studies (Cipreste et al., 2016). The XRD pattern of nHA showed several sharp peaks, indicating good crystallinity (**Figure 2F**). The characteristic XRD peaks (25.8°, 31.8°, 39.8°, 46.7°, 49.5°, and 53.2°) corresponded to the (002), (211), (130), (222), (213) and (004) crystal planes of the nHA structure, respectively. The peak positions are in good agreement with the ICSD card no. 74-0566.

3.2 The Interactions Between nHA and T Lymphocytes

T cells were co-cultured with various concentrations of nHA to assess the effect of nHA on T cell viability. After 1, 2, and 3 days of cell culture, CCK-8 viability assays were performed. After 1 day, the cell viability in 1,000 μg/ml nHA was greatly higher than those in other groups, as shown in **Figure 3A**. There were no significant differences among control, 10 and 100 μg/ml nHA. After 2 and 3 days, the cell viability in 10 μg/ml nHA was lower than that in the control group. However, in the 100 μg/ml nHA group, the cell viability was similar to the control group. The cell viability in the 1,000 μg/ml nHA group was higher than 10 and 100 μg/ml groups. In addition, as the incubation time increased from 1 to 3 days, the cell viability in 10 μg/ml nHA significantly decreased and the cell viability of the 100 μg/ml nHA group remained unchanged. These results imply that the viability of T cells was dependent on the concentrations of nHA. Importantly, 1,000 μg/ml nHA greatly enhanced the viability of T cells. We added different concentrations of nHA to the cell culture medium to explore the influence of nHA content on T cell proliferation after 3 days. As shown in **Figure 3B**, there was only one CFSE signal peak in each group, which represented the same number of generations of cell proliferation in each group. However, the CFSE signal of the 1,000 μg/ml nHA group was the strongest, indicating that the number of cells in the sample was the most among other groups, which was consistent with the result of T cell CCK-8. Furthermore, the effect of nHA on the apoptosis of T cells with different concentrations of nHA was shown in **Figure 3C**. It was found that the percentages of apoptotic cells in control, 10 and 100 μg/ml groups were 36.1%, 37.9% and 33.5%, respectively. The percentage of apoptosis cells in the 1,000 μg/ml nHA group (2.56%) was the lowest than those in other groups. The percentages of viable cells in control, 10, 100 and 1,000 μg/ml groups were 6.22%, 9.16%, 47.8% and 92.2%, respectively. Taken together, as the concentration of nHA increased, the proportion of apoptotic T cells gradually decreased after 48 h culture, and the proportion of normal living cells gradually increased (**Figure 3D**).

To evaluate the effect of nHA on the differentiation of T cells to $CD4^+$ or $CD8^+$ T cells, we used different concentrations of nHA to co-culture with T cells for 5 days. As indicated in **Figure 4**, in the presence of 100 μg/ml nHA, the proportion of differentiated T cells was more than those of the other groups. In each group, the proportion of $CD4^+$ T cells was greater than that of $CD8^+$ T cells. Interestingly, the 1,000 μg/ml group had the most undifferentiated and normal living cells than other groups. This may be due to the effect of feedback-regulated balance of growth and differentiation (Bocharov et al., 2011). We found that 100 μg/ml of nHA had a large effect on T cell differentiation, with 50.9% $CD4^+$ and 32.9% $CD8^+$ T cells. This concentration of nHA has the greatest effect on T cell differentiation compared with other groups. The differentiated T cells may produce more various cytokines, which may offer interesting information for the regulation on osteogenic differentiation. Therefore, it is essential to further investigate the effect of this condition on T cells on osteogenic differentiation. Therefore, 100 μg/ml of nHA was selected in subsequent experiments.

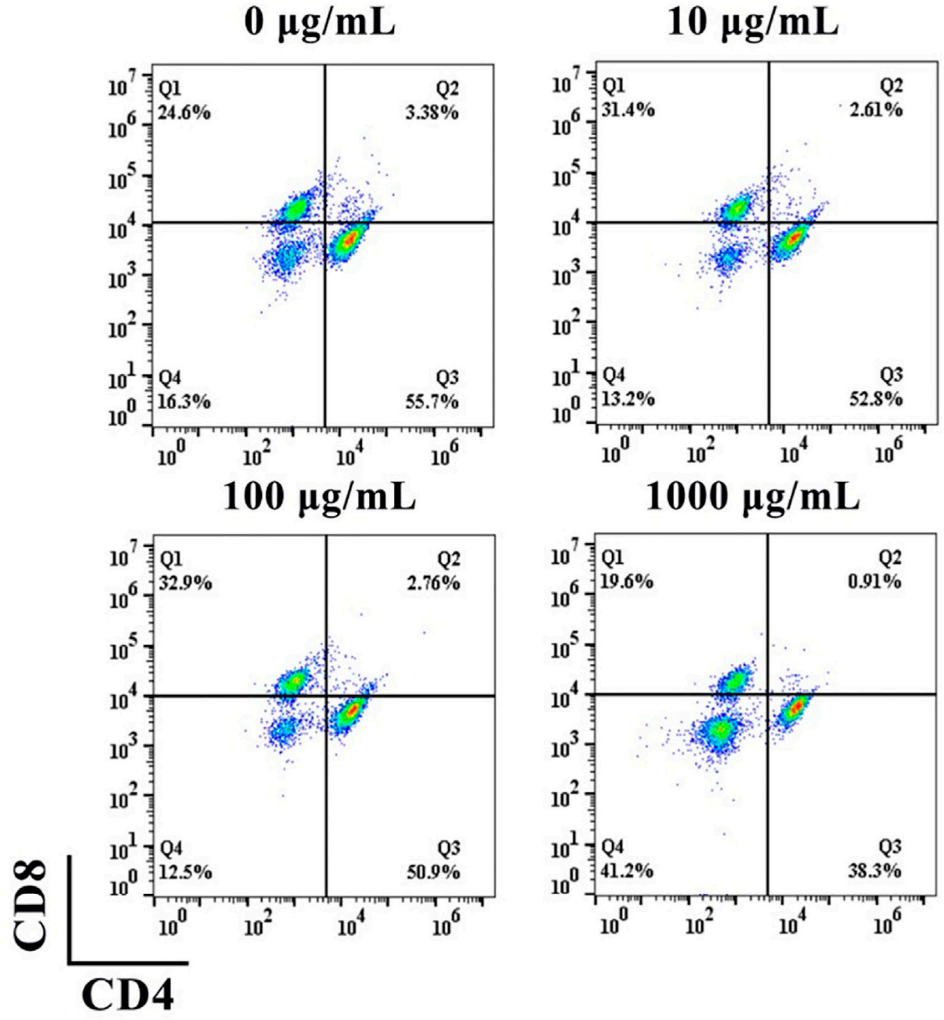

FIGURE 4 | Flow cytometry analysis of the effect of nHA on T cell differentiation.

3.2.1 MC3T3-E1 Cell Viability and Osteogenic Differentiation

The impact of T cell supernatant co-cultured with nHA (T + nHA) on the viability of MC3T3-E1 cells was investigated. After 1 and 3 days of cell growth, the CCK-8 viability test was conducted. With the increase of culture time, the viability of MC3T3-E1 cells was significantly increased. However, after 3 days culture, the supernatant of T + nHA significantly affected the viability of MC3T3-E1 cells, compared with the control and the supernatant of T cells (**Figure 5**).

ALP is the most significant biological marker of osteogenic differentiation and new bone production (Seo et al., 2010; Zhou et al., 2020; Liu X.-W. et al., 2021). MC3T3-E1 cells were cultured in the supernatant of T + nHA for 14 days and subsequently stained for detecting alkaline phosphatase activity. As shown in **Figures 6A,B**, it was found that in the group of nHA supernatant, the number of stained cells and the staining area was larger than other groups, and the staining in the group of nHA supernatant is deeper. The other groups had similar staining. Further, the ALP activity of MC3T3-E1 cells was analyzed by an ALP assay kit (Ehara et al., 2003). As depicted in **Figure 6C**, the supernatant of

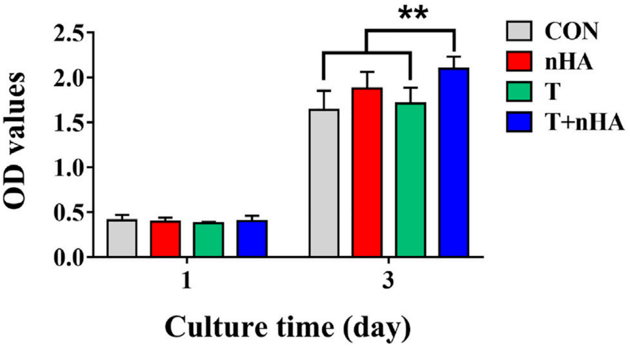

FIGURE 5 | MC3T3-E1 cells viability on various samples for 1 and 3 days. ** represents $p < 0.01$.

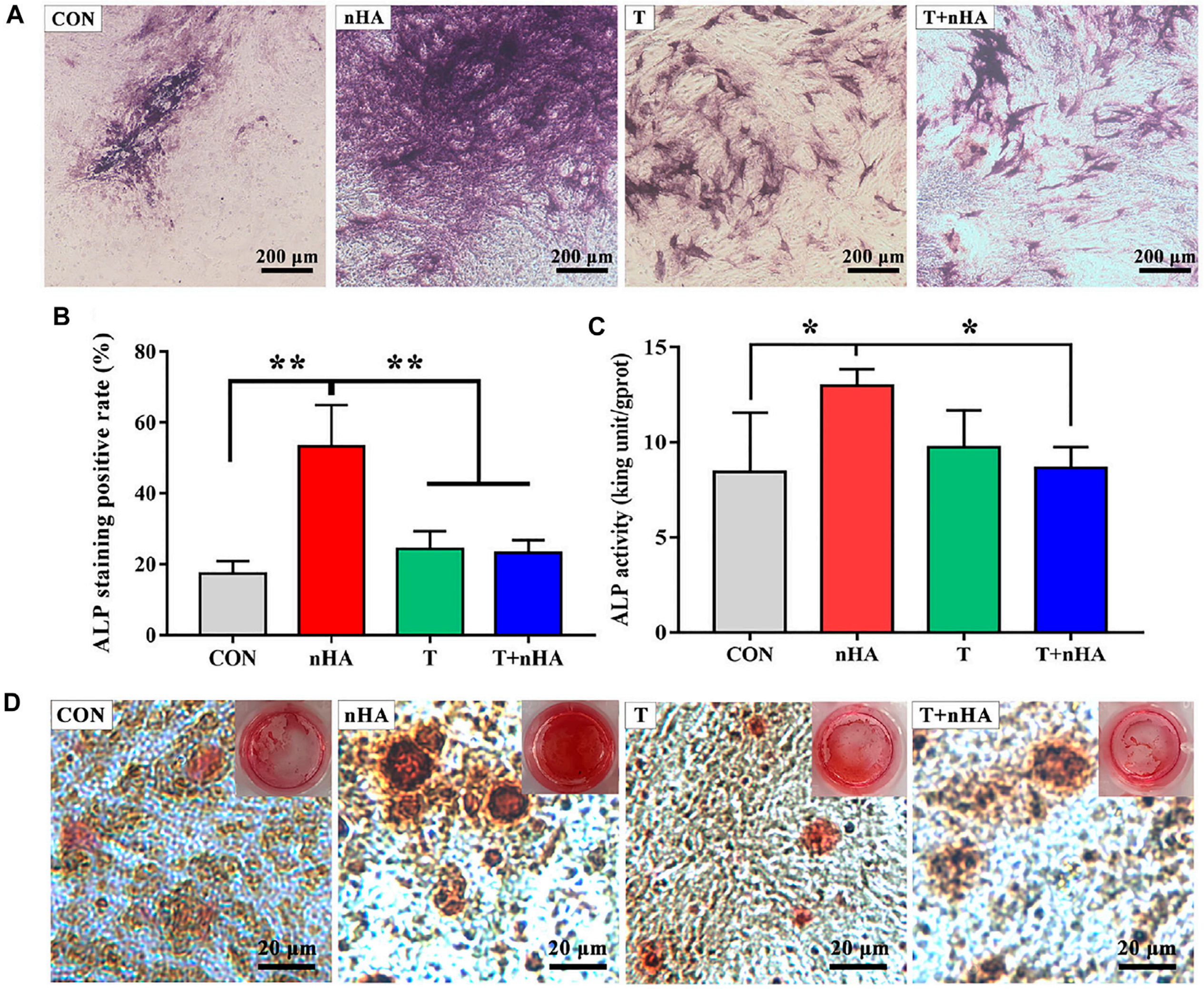

FIGURE 6 | (A) ALP staining images. **(B)** The quantitative assessment of the ALP staining results was performed using ImageJ. **(C)** ALP activity of MC3T3-E1 cells on different samples after 14 days of culture. * represents $p < 0.05$ and ** represents $p < 0.01$. **(D)** ARS stained images of MC3T3-E1 cells on different samples after 14 days culture.

T + nHA significantly inhibited the ALP expression of MC3T3-E1 cells compared with the supernatant nHA.

In addition, mineralized nodules formed by extracellular matrix Ca deposition were stained with ARS, a dye that binds to Ca ions. By the ARS staining, bright red color of calcified nodules was found in all groups (**Figure 6D**). However, in the group containing supernatants of T + nHA, the ARS staining showed that the number of calcified nodules was less, and the area of calcified nodules was smaller than in the other groups. The above indicates that the supernatant of T + nHA inhibited the stromal mineralization of MC3T3-E1 cells. Based on the results of ALP and ARS, we found that the supernatant of 100 μg/ml nHA co-cultured with T cells inhibited the osteogenic differentiation of MC3T3-E1 cells. This concentration of needle-like nHA mediated the most differentiation of T lymphocytes into $CD4^+$ cells. It may be due to cytokine secretion by total $CD4^+$ T cells that inhibited osteogenic differentiation (Shao et al., 2020). And the specific cytokine secretion needs to be further explored in future studies.

4 CONCLUSION

In summary, compared with 0–100 μg/ml nHA, 1,000 μg/ml nHA significantly promoted the growth of T cells and inhibited their apoptosis. In addition, 100 μg/ml nHA was more favorable to cell differentiation into $CD4^+$ T cells. Moreover, the supernatant of T cells co-cultured with nHA greatly suppressed the osteogenic differentiation of MC3T3-E1 by reducing the production of ALP and calcium nodule compared with the supernatant of nHA. Therefore, this work offers new insight into the nHA-mediated T cell and osteoblast interactions.

DATA AVAILABILITY STATEMENT

The raw data supporting the conclusion of this article will be made available by the authors, without undue reservation.

ETHICS STATEMENT

The animal study was reviewed and approved by the Ethics Committee of the Affiliated Hospital of Qingdao University (approval number: QYFYWZLL 26848).

AUTHOR CONTRIBUTIONS

QZ and CY contributed to the conception and design of the study. FG, HH, XD, ZB and DW performed the experiments. FG, LM and CY performed the statistical analysis. FG, CY and KD wrote the first draft of the manuscript. QZ reviewed the draft of the manuscript. QZ and CY provided the funding. All authors contributed to manuscript revision, read, and approved the submitted version.

ACKNOWLEDGMENTS

The authors are very grateful for the financial support by National Natural Science Foundation of China (Grant No. 31900957), Shandong Provincial Natural Science Foundation (Grant No. ZR2019QC007), Innovation and technology program for the excellent youth scholars of higher education of Shandong province (Grant No. 2019KJE015), and Traditional Chinese Medicine Science and Technology Project of Shandong province (Grant No. 2021Q069).

REFERENCES

Akram, M., Ahmed, R., Shakir, I., Ibrahim, W. A. W., and Hussain, R. (2014). Extracting Hydroxyapatite and its Precursors from Natural Resources. *J. Mater. Sci.* 49, 1461–1475. doi:10.1007/s10853-013-7864-x

Barros, J., Ferraz, M. P., Azeredo, J., Fernandes, M. H., Gomes, P. S., and Monteiro, F. J. (2019). Alginate-nanohydroxyapatite Hydrogel System: Optimizing the Formulation for Enhanced Bone Regeneration. *Mater. Sci. Eng. C* 105, 109985. doi:10.1016/j.msec.2019.109985

Bocharov, G., Quiel, J., Luzyanina, T., Alon, H., Chiglintsev, E., Chereshnev, V., et al. (2011). Feedback Regulation of Proliferation vs. Differentiation Rates Explains the Dependence of CD4 T-Cell Expansion on Precursor Number. *Proc. Natl. Acad. Sci. U.S.A.* 108, 3318–3323. doi:10.1073/pnas.1019706108

Cai, Y., Liu, Y., Yan, W., Hu, Q., Tao, J., Zhang, M., et al. (2007). Role of Hydroxyapatite Nanoparticle Size in Bone Cell Proliferation. *J. Mater. Chem.* 17, 3780–3787. doi:10.1039/b705129h

Cipreste, M. F., Gonzalez, I., Maria Da Mata Martins, T., Goes, A. M., Augusto De Almeida Macedo, W., and Barros De Sousa, E. M. (2016). Attaching Folic Acid on Hydroxyapatite Nanorod Surfaces: An Investigation of the HA-FA Interaction. *RSC Adv.* 6, 76390–76400. doi:10.1039/c6ra14068h

Croes, M., Öner, F. C., van Neerven, D., Sabir, E., Kruyt, M. C., Blokhuis, T. J., et al. (2016). Proinflammatory T Cells and IL-17 Stimulate Osteoblast Differentiation. *Bone* 84, 262–270. doi:10.1016/j.bone.2016.01.010

Ehara, A., Ogata, K., Imazato, S., Ebisu, S., Nakano, T., and Umakoshi, Y. (2003). Effects of α-TCP and TetCP on MC3T3-E1 Proliferation, Differentiation and Mineralization. *Biomaterials* 24, 831–836. doi:10.1016/S0142-9612(02)00411-8

El Khassawna, T., Serra, A., Bucher, C. H., Petersen, A., Schlundt, C., Könnecke, I., et al. (2017). T Lymphocytes Influence the Mineralization Process of Bone. *Front. Immunol.* 8. doi:10.3389/fimmu.2017.00562

Fathi, M. H., Hanifi, A., and Mortazavi, V. (2008). Preparation and Bioactivity Evaluation of Bone-like Hydroxyapatite Nanopowder. *J. Mater. Process. Tech.* 202, 536–542. doi:10.1016/j.jmatprotec.2007.10.004

Gillespie, M. T. (2007). Impact of Cytokines and T Lymphocytes upon Osteoclast Differentiation and Function. *Arthritis Res. Ther.* 9, 103–109. doi:10.1186/ar2141

Gruber, R. (2019). Osteoimmunology: Inflammatory Osteolysis and Regeneration of the Alveolar Bone. *J. Clin. Periodontol.* 46 (Suppl. 2), 52–69. doi:10.1111/jcpe.13056

Guo, X., Gough, J. E., Xiao, P., Liu, J., and Shen, Z. (2007). Fabrication of Nanostructured Hydroxyapatite and Analysis of Human Osteoblastic Cellular Response. *J. Biomed. Mater. Res.* 82A, 1022–1032. doi:10.1002/jbm.a.31200

Huang, X., Liu, X., Liu, S., Zhang, A., Lu, Q., Kaplan, D. L., et al. (2014). Biomineralization Regulation by Nano-Sized Features in Silk Fibroin Proteins: Synthesis of Water-Dispersible Nano-Hydroxyapatite. *J. Biomed. Mater. Res.* 102, 1720–1729. doi:10.1002/jbm.b.33157

Items, R., Rose, W., Rose, W., If, T., and Rose, W. (2018). This Is a Repository Copy of Non-functionalized Ultrasmall Silica Nanoparticles Directly and Size-Selectively Activate T Cells. *White Rose Res. Online URL this paper : Version : Accepted Version Article : Vis, B, Hewitt, RE, Faria, N al.* 12 (11), 10843–10854. doi:10.1021/acsnano.8b03363

Ji, Y., Han, Z., Ding, H., Xu, X., Wang, D., Zhu, Y., et al. (2021). Enhanced Eradication of Bacterial/Fungi Biofilms by Glucose Oxidase-Modified Magnetic Nanoparticles as a Potential Treatment for Persistent Endodontic Infections. *ACS Appl. Mater. Inter.* 13, 17289–17299. doi:10.1021/acsami.1c01748

Kumar, G., and Roger, P.-M. (2019). From Crosstalk between Immune and Bone Cells to Bone Erosion in Infection. *Ijms* 20, 5154. doi:10.3390/ijms20205154

Li, D., Li, S., Liu, J., Zhan, L., Wang, P., Zhu, H., et al. (2020). Surface Modification of Carbon Nanotube with Gelatin via Mussel Inspired Method. *Mater. Sci. Eng. C* 112, 110887. doi:10.1016/j.msec.2020.110887

Liu, M., Wang, D., Gu, S., Tian, B., Liang, J., Suo, Q., et al. (2021a). Micro/nano Materials Regulate Cell Morphology and Intercellular Communication by Extracellular Vesicles. *Acta Biomater.* 124, 130–138. doi:10.1016/j.actbio.2021.02.003

Liu, X.-W., Ma, B., Zi, Y., Xiang, L.-B., and Han, T.-Y. (2021b). Effects of Rutin on Osteoblast MC3T3-E1 Differentiation, ALP Activity and Runx2 Protein Expression. *Eur. J. Histochem.* 65, 1–6. doi:10.4081/ejh.2021.3195

Liu, Y., Jiao, F., Qiu, Y., Li, W., Lao, F., Zhou, G., et al. (2009). The Effect of Gd@C82(OH)22 Nanoparticles on the Release of Th1/Th2 Cytokines and Induction of TNF-α Mediated Cellular Immunity. *Biomaterials* 30, 3934–3945. doi:10.1016/j.biomaterials.2009.04.001

Mokabber, T., Zhou, Q., Vakis, A. I., van Rijn, P., and Pei, Y. T. (2019). Mechanical and Biological Properties of Electrodeposited Calcium Phosphate Coatings. *Mater. Sci. Eng. C* 100, 475–484. doi:10.1016/j.msec.2019.03.020

Nguyen, A. T., Sathe, S. R., and Yim, E. K. F. (2016). From Nano to Micro: Topographical Scale and its Impact on Cell Adhesion, Morphology and Contact Guidance. *J. Phys. Condens. Matter* 28, 183001. doi:10.1088/0953-8984/28/18/183001

Pacifici, R. (2016). T Cells, Osteoblasts, and Osteocytes: Interacting Lineages Key for the Bone Anabolic and Catabolic Activities of Parathyroid Hormone. *Ann. N.Y. Acad. Sci.* 1364, 11–24. doi:10.1111/nyas.12969

Paquin, F., Rivnay, J., Salleo, A., Stingelin, N., and Silva-Acuña, C. (2015). Multi-phase Microstructures Drive Exciton Dissociation in Neat Semicrystalline Polymeric Semiconductors. *J. Mater. Chem. C* 3, 10715–10722. doi:10.1039/b000000x10.1039/c5tc02043c

Patel, S., Patel, P., and Bakshi, S. R. (2017). Titanium Dioxide Nanoparticles: an *In Vitro* Study of DNA Binding, Chromosome Aberration Assay, and Comet Assay. *Cytotechnology* 69, 245–263. doi:10.1007/s10616-016-0054-3

Pepla, E. (2014). Nano-hydroxyapatite and its Applications in Preventive, Restorative and Regenerative Dentistry: a Review of Literature. *Ads* 5 (3), 108–114. doi:10.11138/ads/2014.5.3.108

Sabuncu, A. C., Grubbs, J., Qian, S., Abdel-Fattah, T. M., Stacey, M. W., and Beskok, A. (2012). Probing Nanoparticle Interactions in Cell Culture media. *Colloids Surf. B: Biointerfaces* 95, 96–102. doi:10.1016/j.colsurfb.2012.02.022

Santos, C., Gomes, P. S., Duarte, J. A., Franke, R. P., Almeida, M. M., Costa, M. E. V., et al. (2012). Relevance of the Sterilization-Induced Effects on the Properties of Different Hydroxyapatite Nanoparticles and Assessment of the Osteoblastic Cell Response. *J. R. Soc. Interf.* 9, 3397–3410. doi:10.1098/rsif.2012.0487

Seo, H.-J., Cho, Y.-E., Kim, T., Shin, H.-I., and Kwun, I.-S. (2010). Zinc May Increase Bone Formation through Stimulating Cell Proliferation, Alkaline Phosphatase Activity and Collagen Synthesis in Osteoblastic MC3T3-E1 Cells. *Nutr. Res. Pract.* 4, 356. doi:10.4162/nrp.2010.4.5.356

Shao, B.-Y., Wang, L., Yu, Y., Chen, L., Gan, N., and Huang, W.-M. (2020). Effects of CD4+ T Lymphocytes from Ovariectomized Mice on Bone Marrow Mesenchymal Stem Cell Proliferation and Osteogenic Differentiation. *Exp. Ther. Med.* 20, 1. doi:10.3892/etm.2020.9212

Thian, E. S., Ahmad, Z., Huang, J., Edirisinghe, M. J., Jayasinghe, S. N., Ireland, D. C., et al. (2010). The Role of Surface Wettability and Surface Charge of Electrosprayed Nanoapatites on the Behaviour of Osteoblasts. *Acta Biomater.* 6, 750–755. doi:10.1016/j.actbio.2009.08.012

Tsukasaki, M., and Takayanagi, H. (2019). Osteoimmunology: Evolving Concepts in Bone-Immune Interactions in Health and Disease. *Nat. Rev. Immunol.* 19, 626–642. doi:10.1038/s41577-019-0178-8

Wang, L., Zhou, G., Liu, H., Niu, X., Han, J., Zheng, L., et al. (2012). Nano-hydroxyapatite Particles Induce Apoptosis on MC3T3-E1 Cells and Tissue Cells in SD Rats. *Nanoscale* 4, 2894–2899. doi:10.1039/c2nr00044j

Wang, Y. F., Yan, Y. H., Ren, W., Cao, X. Y., and Li, S. P. (2004). Preparation and Characterization of Nano Hydroxyapatite Sol. *Trans. Nonferrous Met. Soc. China (English Ed.* 14, 29–32. doi:10.4028/www.scientific.net/kem.330-332.235

Wang, Z., Mei, L., Liu, X., and Zhou, Q. (2021a). Hierarchically Hybrid Biocoatings on Ti Implants for Enhanced Antibacterial Activity and Osteogenesis. *Colloids Surf. B: Biointerfaces* 204, 111802. doi:10.1016/j.colsurfb.2021.111802

Wang, Z., Wang, X., Wang, Y., Zhu, Y., Liu, X., and Zhou, Q. (2021b). NanoZnO-modified Titanium Implants for Enhanced Anti-bacterial Activity, Osteogenesis and Corrosion Resistance. *J. Nanobiotechnol* 19, 1–23. doi:10.1186/s12951-021-01099-6

Wei, G., and Ma, P. X. (2004). Structure and Properties of Nano-Hydroxyapatite/polymer Composite Scaffolds for Bone Tissue Engineering. *Biomaterials* 25, 4749–4757. doi:10.1016/j.biomaterials.2003.12.005

Yang, L., Pijuan-Galito, S., Rho, H. S., Vasilevich, A. S., Eren, A. D., Ge, L., et al. (2021). High-Throughput Methods in the Discovery and Study of Biomaterials and Materiobiology. *Chem. Rev.* 121, 4561–4677. doi:10.1021/acs.chemrev.0c00752

Yao, H., Zhu, M., Wang, P., Liu, Y., and Wei, J. (2021). Combination of Mussel Inspired Method and "Thiol-Michael" Click Reaction for Biocompatible Alginate-Modified Carbon Nanotubes. *Nanomaterials* 11, 2191. doi:10.3390/nano11092191

Yu, F., Lian, R., Liu, L., Liu, T., Bi, C., Hong, K., et al. (2022). Biomimetic Hydroxyapatite Nanorods Promote Bone Regeneration via Accelerating Osteogenesis of BMSCs through T Cell-Derived IL-22. *ACS Nano* 16, 755–770. doi:10.1021/acsnano.1c08281

Zhang, W., Dang, K., Huai, Y., and Qian, A. (2020). Osteoimmunology: The Regulatory Roles of T Lymphocytes in Osteoporosis. *Front. Endocrinol.* 11, 1–8. doi:10.3389/fendo.2020.00465

Zhou, Q., Chen, J., Luan, Y., Vainikka, P. A., Thallmair, S., Marrink, S. J., et al. (2020). Unidirectional Rotating Molecular Motors Dynamically Interact with Adsorbed Proteins to Direct the Fate of Mesenchymal Stem Cells. *Sci. Adv.* 6, 1–14. doi:10.1126/sciadv.aay2756

Zhou, Q., Zhao, Z., Zhou, Z., Zhang, G., Chiechi, R. C., and van Rijn, P. (2018). Directing Mesenchymal Stem Cells with Gold Nanowire Arrays. *Adv. Mater. Inter.* 5, 1800334. doi:10.1002/admi.201800334

Conflict of Interest: The authors declare that the research was conducted in the absence of any commercial or financial relationships that could be construed as a potential conflict of interest.

frontiers | Frontiers in Bioengineering and Biotechnology

ORIGINAL RESEARCH
published: 07 April 2022
doi: 10.3389/fbioe.2022.858786

Bone Quantification Around Chitosan-Coated Titanium Dental Implants: A Preliminary Study by Micro-CT Analysis in Jaw of a Canine Model

Nansi López-Valverde[1], Antonio López-Valverde[2]*, Marta Paz Cortés[3], Cinthia Rodríguez[4], Bruno Macedo De Sousa[5] and Juan Manuel Aragoneses[3]

[1]Department of Medicine and Medical Specialties, Faculty of Health Sciences, Universidad Alcalá de Henares, Alcalá de Henares, Spain, [2]Department of Surgery, University of Salamanca, Instituto de Investigación Biomédica de Sala-manca (IBSAL), Salamanca, Spain, [3]Faculty of Dentistry, Universidad Alfonso X El Sabio, Villanueva de la Cañada, Spain, [4]Department of Dentistry, Universidad Federico Henríquez y Carvajal, Santo Domingo, Dominican Republic, [5]Institute for Occlusion and Orofacial Pain Faculty of Medicine, University of Coimbra, Polo I-Edifício Central Rua Larga, Coimbra, Portugal

OPEN ACCESS

Edited by:
Min Jiang,
Nanjing Tech University, China

Reviewed by:
Sara Ferraris,
Politecnico di Torino, Italy
Atakan Tevlek,
Middle East Technical University, Turkey

****Correspondence:***
Antonio López-Valverde
alopezvalverde@usal.es

Specialty section:
This article was submitted to Biomaterials,
a section of the journal Frontiers in Bioengineering and Biotechnology

Received: *20 January 2022*
Accepted: *17 March 2022*
Published: *07 April 2022*

Citation:
López-Valverde N, López-Valverde A, Cortés MP, Rodríguez C, Macedo De Sousa B and Aragoneses JM (2022) Bone Quantification Around Chitosan-Coated Titanium Dental Implants: A Preliminary Study by Micro-CT Analysis in Jaw of a Canine Model. Front. Bioeng. Biotechnol. 10:858786. doi: 10.3389/fbioe.2022.858786

Surface treatments of Ti in the dental implant industry are performed with the aim of increasing its bioactivity and osseointegration capacity. Chitosan (Cht) is a polysaccharide that has been proposed as a promising biomaterial in tissue engineering and bone regeneration, due to its ability to stimulate the recruitment and adhesion of osteogenic progenitor cells. The aim of our preliminary study was to evaluate, by micro-computed tomography (micro-CT), the osseointegration and bone formation around Cht-coated implants and to compare them with conventional surface-etched implants (SLA type). Four im-plants (8.5 mm length × 3.5 mm Ø) per hemiarch, were inserted into the jaws of five dogs, divided into two groups: chitosan-coated implant group (ChtG) and control group (CG). Twelve weeks after surgery, euthanasia was performed, and sectioned bone blocks were obtained and scanned by micro-CT and two bone parameters were measured: bone in contact with the implant surface (BCIS) and peri-implant bone area (PIBA). For BCIS and PIBA statistically significant values were obtained for the ChtG group with respect to CG ($p = 0.005$; $p = 0.014$ and $p < 0.001$ and $p = 0.002$, respectively). The results, despite the limitations, demonstrated the usefulness of chitosan coatings. However, studies with larger sample sizes and adequate experimental models would be necessary to confirm the results.

Keywords: titanium dental implant, chitosan-coating, micro-computed tomography, canine model, osteointegration

INTRODUCTION

Dental implant treatments have now become indispensable in clinical dental practice. The survival rate exceeds 90%, although studies on success rates are difficult to interpret, mainly due to a large number of variables, such as the surgical techniques used and the follow-up periods, in addition to the different criteria that have been proposed to define implant success (Simonis et al., 2010). Modern oral im-plantology uses different devices, in terms of size, shape, length, thickness and composition, from pure titanium (Ti) to titanium-aluminum-vanadium alloys (Ti-Al-V), due to their biocompatibility and high corrosion resistance (von Wilmowsky et al., 2014). However, the biological response of tissues can be improved by different surface treatments that provide both bioactivity and osseointegration capacity (Jemat et al., 2015). The first materials used in implantology provoked marked inflammatory reactions that led to the formation of fibrous tissue around the implant, with consequent failure; however, the latest generation materials, in addition to awakening metabolic activities, do not affect the normal biological metabolism, being considered as bioinductive materials (Li et al., 2019a; Hotchkiss et al., 2019), it is currently considered that certain changes on the surface of Ti play an active role in the control of the cellular response, resulting in reduced healing times and improved healing of the peri-implant area (Le Guéhennec et al., 2007a; Alfarsi et al., 2014). Current trends are directed not only towards achieving optimal osseointegrative surfaces, but also towards surfaces with antibacterial activity for prolonged periods of time, either by blocking microbial adhesion or by preventing late infections (Palla-Rubio et al., 2019).

Chitosan (Cht) is a polysaccharide derived from partially deacetylated chitin, formed by copolymers of glucosamine and N-acetylglucosamine. It possesses several amino groups attached to the main chain of the polysaccharide, which are readily available for chemical reaction and formation of salts with acids (Singla and Chawla, 2001). In recent years, it has been proposed as a promising biomaterial in certain dental and tissue engineering applications, in addition to being used as a cholesterol-lowering agent, hemostatic, drug carrier etc. (Ylitalo et al., 2002; Rojo and Deb, 2015; Ahsan et al., 2018; Hu et al., 2018; Ahn et al., 2021; Yu et al., 2022).

Some studies consider it as bactericidal and others as bacteriostatic, although its mechanism of action in both situations is not exactly known, since different factors have been proposed as contributing to its antibacterial action, among them, the amino groups of its structure and the origin of the chitin (Rabea et al., 2003; Matica et al., 2019). Likewise, its high biocompatibility, hydrophilicity and biodegradability, in addition to being non-toxic (Tajdini et al., 2010), are noteworthy. For all these reasons, its ability to increase cell adhesion and protein adsorption in Ti coatings has been highlighted, which would be beneficial for improving the osseointegration of dental implants (Bumgardner et al., 20032003; Bumgardner et al., 2003; López-Valverde et al., 2021). Muzzarelli et al. (Muzzarelli et al., 1994) demonstrated in a clinical trial on 10 patients, bone neoformation and mineralization of post-extraction sockets, due to the cationic nature and chelating ability of Cht; these results would highlight the potential of Cht coatings to support and facilitate osseointegration of orthopedic and craniofacial implants. Cht-based implants have been found to elicit minimal foreign body reaction, with little or no fibrous encapsulation and promote a rapid healing response (Kim et al., 2008). Most implant failures are due to poor early bone healing at the bone-implant interface (Sakka et al., 2012) and in this aspect, Cht has been proposed as a biomaterial with good bioactivity for osteogenesis (Hu et al., 2009).

However, as implant surface modifications have changed, investigations have become multifactorial in an attempt to develop detailed information on design optimization, resulting in difficulty in capturing the detailed bone response in a timely manner and with sufficient resolution by current conventional methods (Vandeweghe et al., 2013a).

The good film-forming ability of Cht allows its use in the coating of dental implants and the coated surfaces show good cell compatibility with osteoblastic and fibroblastic cells (Shukla et al., 2013a). Numerous studies of Ti coatings with Cht have been performed, with the attachment of Cht to the metal substrate being considered a challenge, either by electrophoretic deposition, layer-by-layer deposition, casting methods, spin coating and dip coating methods (Bumgardner et al., 20032003; Reddy Tiyyagura et al., 2016; Chen et al., 2017; Höhlinger et al., 2017). Dip coating of a substrate, used in our study, is a simple form of deposition, especially for small substrates, forming thin layer deposits, which can be further compacted, by heat treatment. Moreover, it is an economical way to deposit thin layers from chemical solutions, with relatively fair control over the layer thickness (Grosso, 2011). Dip coating is based on a steady flow condition, and the coating thickness is determined by the competition between viscous force, surface tension, gravity and substrate withdrawal rate (Scriven, 1988).

On the other hand, some researchers have pointed out the limitations of histomorphometry in providing quantitative and qualitative bone information, due to the dependence on slice position and possible interface damage during sample cutting and grinding procedures, in addition to relying on a small number of sections, which means a limited subset of the entire sample. All this, together with the sample preparation time, the destructive nature of the method and its cost, has led to the proposal of new evaluation techniques, such as micro computed tomography (micro-CT) analysis, which increase the performance of the evaluation, providing the same resolution capacity as conventional techniques and, above all, because they take advantage of the non-destructive nature of the specimens (Kampschulte et al., 2016; Becker et al., 2017; He et al., 2017).

In addition, micro-CT produces an improved resolution in the range approximately 1,000,000 times smaller than normal CT scanning, allowing a three-dimensional (3D) evaluation of the specimen in high resolution and providing 3D reconstructed images, to obtain a better understanding of the bone architecture, generated within the area of interest (AoI) (Szmukler-Moncler et al., 2004; Boyd et al., 2006; Peyrin et al., 2014).

Therefore, the aim of our study, was to evaluate the osseointegration and bone formation at crestal, mid and apical levels of Cht-coated Ti implants in the mandible of a canine model and to compare them with conventional implants with an etched surface (SLA type) without coating. The null hypothesis was that uncoated implants, with a conventional SLA-type etched surface, have the same osseointegration and bone formation capacity as implants coated with Cht.

MATERIALS AND METHODS

Study Design

Forty implants (8.5 mm length x 3.5 mm Ø) were inserted in the jaws of 5 Foxhound dogs, four per hemiarch. They were randomly

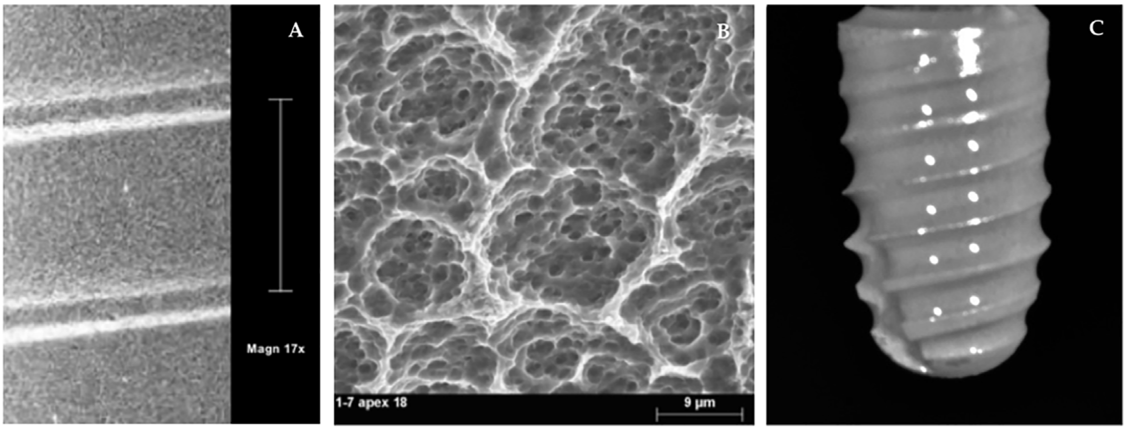

FIGURE 1 | Implant surface topography. CG surface **(A,B)**. ChtG coated implant surface **(C)**.

divided into two groups: a group of im-plants re-coated with chitosan (ChtG) and a group of control implants without coating (CG). Two bone parameters were measured around the implant, Bone in Contact to the Implant Surface (BCIS) and Peri-Implant Bone Area (PIBA) at three levels: crestal, middle and apical of each implant. The study protocol was approved on 24 July 2020 by the Ethics Committee of the Catholic University of Murcia (Spain) with code CE072004.

Implant Surface Topography

Bioner® Ti implants, grade 5 (TiAl6V4) (Sant Just Desvern, Barcelona, Spain) (CG), were etched by the proprietary Bioetch® method, which provides a homogeneous macro- and microtextured macropore surface in the 15–20 µm range (Höhlinger et al., 2017) (**Figures 1A,B**)

Implant Surface Preparation

The chitosan coating (ChtG) was prepared according to the procedure described by Vakili et al. with slight modifications (Vakili and Asefnejad, 2020). 0.5% (w/v) chitosan was prepared in 0.5% (v/v) acidic solution by stirring the solution for 12 h on a magnetic stirrer. The film-forming solution was prepared following the procedure described by Zhang et al. with slight modifications (Zhang et al., 2019). Glycerol (0.4 g) was dispersed in 80 ml of acetic acid (1%, w/v) by stirring for at least 12 h (4°C). The prepared chitosan solution was added to the film-forming solution using a syringe pump (Infusomat® Space, Braun, Barcelona, Spain), at a rate of 50 ml/h, stirring by mechanical shaker at 800 rpm. The implants were coated with Cht by immersion in the prepared solution, coating the entire implant surface. The coated implants were then dried in a drying oven with rotary drum and air blowing at 25°C for the formation of a uniform film, with a relative humidity of 50%, to avoid cracking and deformation of the coating (**Figure 1C**). CG implants did not receive any surface coating. Both CG and ChtG implants were sterilized by gamma irradiation. This method of sterilization in ChtG was preferred so as not to give rise to sterilization biases with GC. Other methods, such as ethylene oxide, in addition to leaving residues detrimental to health, could damage the molecular structure of the coating and its susceptibility to degradation, although the effects of sterilization on the stability of the molecular structure and the mechanical properties of the coating itself are unclear. Certain *in vitro* studies have shown that the early stages of mineralization are essentially independent of the sterilization method (Ueno et al., 2012; Türker et al., 2014).

Surgical Protocol

The surgical procedures, supervised by a veterinary surgeon, were performed under general anesthesia, infusing Propofol® (Propovet, Abbott Laboratories Ltd., Queens-borough, Kent, United Kingdom), through a catheter installed in the cephalic vein. Anesthetic maintenance was performed by means of a volatile anesthetic (Isoflurane, IsoVet 1000 mg/g®, Piramal Critical Care B.V. Voorschoten, NL). In addition, a local anesthetic was administered to the surgical sites (articaine 40 mg, with 1% epinephrine, Ultracain®, Normon, Madrid, Spain). Three premolars and the first mandibular molar (P2, P3, P4 and M1) of each animal were extracted by odontosection (**Figure 2**). The placement of the implants in the empty sockets (**Figure 2**) was determined by the randomization program (http://www.randomization.com). The experimental animals were assigned to the two different implant surfaces: 20 implants with Cht from the test group (ChtG) and 20 uncoated implants from the commercial company Bioner (Bioetch®, Bioner Sistemas Implantológicos, Barcelona, Spain) (CG), randomly distributed among five dogs. Each dog received eight screw implants (8.5 mm length x 3.5 mm Ø in the premolar and molar area), four per hemiarch. Cover screws were placed to allow a submerged healing protocol (**Figure 2**). The implants were placed in the post-extraction sockets without friction of the implant with the alveolar walls (**Figure 2**), achieving primary stability of the implants in the apical area, so as not to damage the coating with the insertion forces, leaving the cylindrical part of the implant in contact with the blood clot and only the conical apical part in contact with the bone. Healing abutments were not

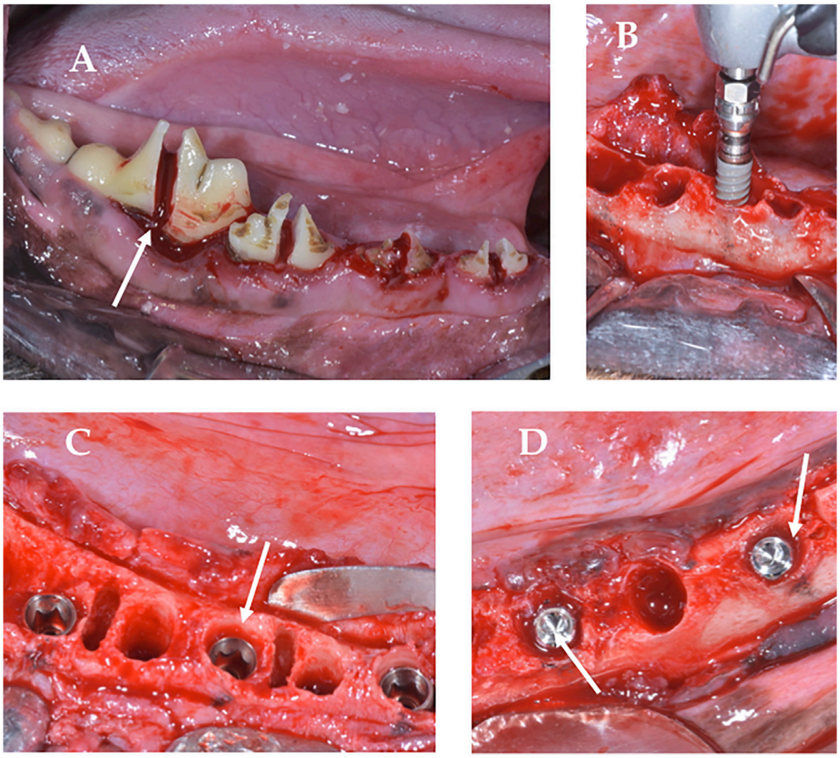

FIGURE 2 | Surgery. **(A)**, Odontosection; **(B)**, Implant insertion; **(C)**, Implant placed in subcrestal position with cover screws for submerged curing; **(D)**, Lack of friction between the implant and the bone wall.

placed to avoid bacterial contamination and contact with the antagonist teeth during chewing and to avoid disturbing the rest period of the implants. No grafting materials were used in the spaces between the alveolar walls and the placed implants (**Figure 2**). The flaps were closed with simple sutures (Silk 4-0®, Lorca Marín, Lorca, Spain). The animals were maintained on a soft diet from the time of surgery until the end of the study. Sacrifice was performed after 12 weeks, using pentothal natrium (Abbot Laboratories, Madrid, Spain) perfused through the carotid artery, after anesthesia of the animal. Sectioned bone blocks were obtained.

Micro-Computed Tomography Analysis

After euthanasia of animals (after 12 weeks of implants placement), the sections of the block were preserved and fixed in 10% neutral formalin. Image acquisitions were per-formed using a multimodal SPECT/CT Albira II ARS scanner (Bruker® Corporation, Karksruhe, Germany). The acquisition parameters were 45 kV, 0.2 mA, and 0.05 mm voxels. The acquisition slices were axial, 0.05 mm thick, and 800 to 1,000 images were obtained from each piece through a flat panel digital detector with 2,400 × 2,400 pixels and a FOV (field of view) of 70 mm × 70 mm. The implants were grouped according to the three axes (transverse, coronal, and sagittal). The sagital axis was used for BCIS and PIBA measurements. In all images the same color scale was used (0 min and 3 max) with the same parameters in FOV (%): 90 and zoom 0.6, with a hardness of 1. The areas of interest (AoIs) were manually fixed by three micro-CT cross-sections at crestal, mid and apical levels; the apical section avoided the conical area of the implant (**Figure 3**). The voxels in contact with the implant surface were excluded in the measurements because they were considered artifact zones, estimating a value of 0.5 mm higher than the implant diameter for the calculation of the BCIS AoI (4 mm Ø) and 2 mm for the calculation of the PIBA AoI (5.5 mm Ø) (**Figure 4**).

The AMIDE tool allowed us to obtain the data in statistical form (Hounsfield Units), with maximums, minimums and deviations. AMIDE is a tool for visualizing, analyzing and registering volumetric medical image data sets (AMIDE, UCLA University, Los Angeles, CA, USA). It allows drawing two-dimensional and three-dimensional AoIs directly on the images and generating statistical data for these AoIs. 3D Slicer program (http://www.slicer.org) provided the 3D images of the bone-to-implant contact area (**Figure 5**).

Statistical Analysis

SPSS Statistics 26.0 (IBM, Chicago, IL, USA) was used as the statistical analysis program. Statistical analysis of the BCIS and PIBA variables in the crestal, mid and apical areas was performed for the experimental and control groups. The normality of the data generated by the microtomographic analyses was examined using the Shapiro-Wilk test. The mean and standard deviation of each group were proposed; the *p*-value and p for trend derived from the differences and changes in each group were presented, with a significance level of ≤0.05.

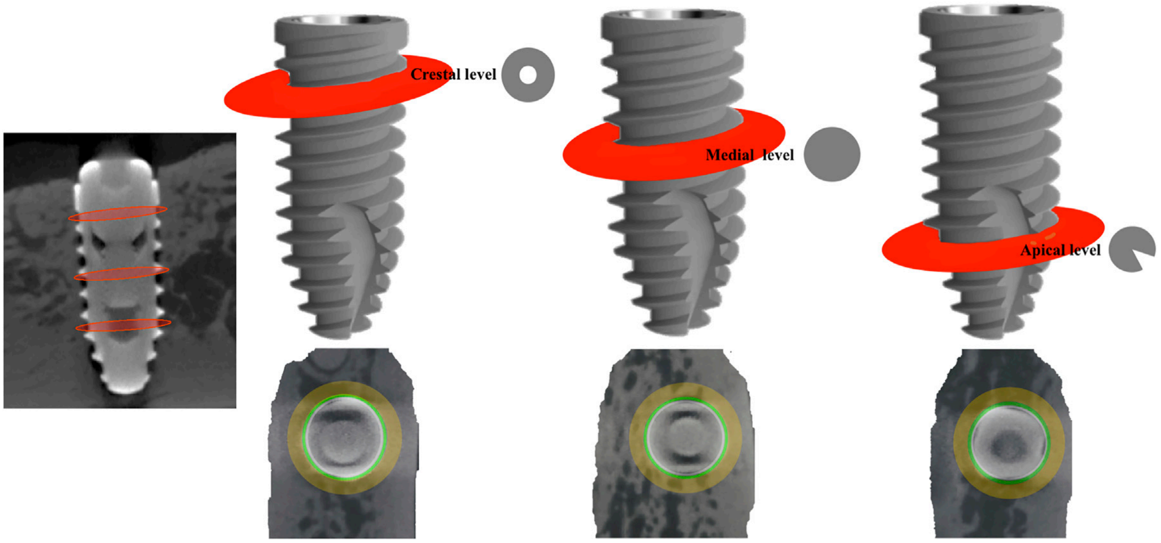

FIGURE 3 | Areas of interest (AoI) delimited by three micro-CT slices at crestal, mid and apical level.

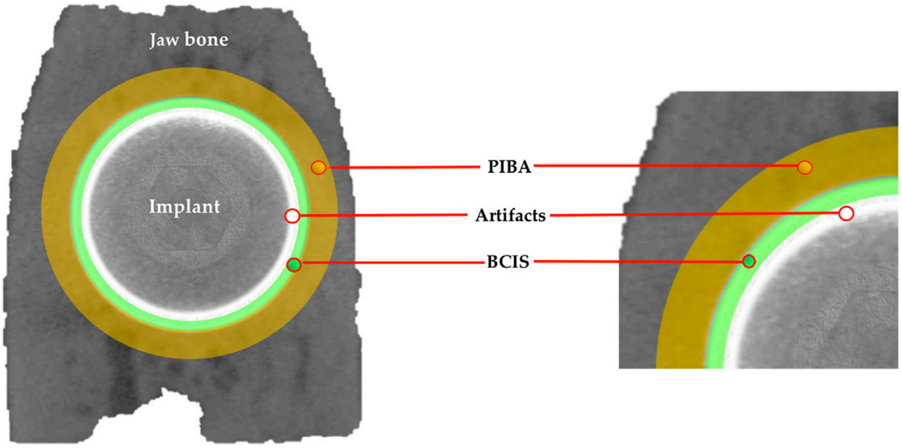

FIGURE 4 | Artifact area in white color; bone in contact with the implant surface (BCIS) in green color and peri-implant bone area (PIBA) in yellow color.

RESULTS

All the implants used in the 5 dogs achieved osseointegration. Two parameters, Bone in Contact to the Implant Surface (BCIS) and Peri-Implant Bone Area (PIBA) were measured in crestal, mid and apical, resulting in a total of 120 sites for each measurement parameter, in the experimental group (ChtG) and in the control group (CG).

The mean value and standard deviation of the trends for each group are shown in **Tables 1**, **2**. For BCIS the values in crestal, mid and apical, in the experimental group (ChtG), were 3,770.11 ± 245.60, 3,245.25 ± 1,477.08 and 4,196.82 ± 453.03, respectively and 3,829.29 ± 249.08, 3,958.75 ± 1,477.08 and 4,112.13 ± 112.6, respectively, in the control group (CG). Trend analysis in the experimental group showed a higher statistical significance ($p = 0.005$) with respect to the control group ($p = 0.014$). For PIBA the values in crestal, mid and apical, in the experimental group, were 3,613.00 ± 1,109.12, 3,905.75 ± 809.65 and 3,759.17 ± 944.73, respectively and 4,162.50 ± 618.02, 3,705.20 ± 1,045.86 and 3,832.71 ± 1,201.43, respectively, in the control group. Trend analysis in the experimental group showed considerable statistical significance ($p < 0.001$) versus the control group ($p = 0.02$). **Figures 6**, **7** represents the boxplots of the results.

DISCUSSION

Since Brånemark published his first study on the osseointegration of Ti implants in 1969, there have been numerous variations of

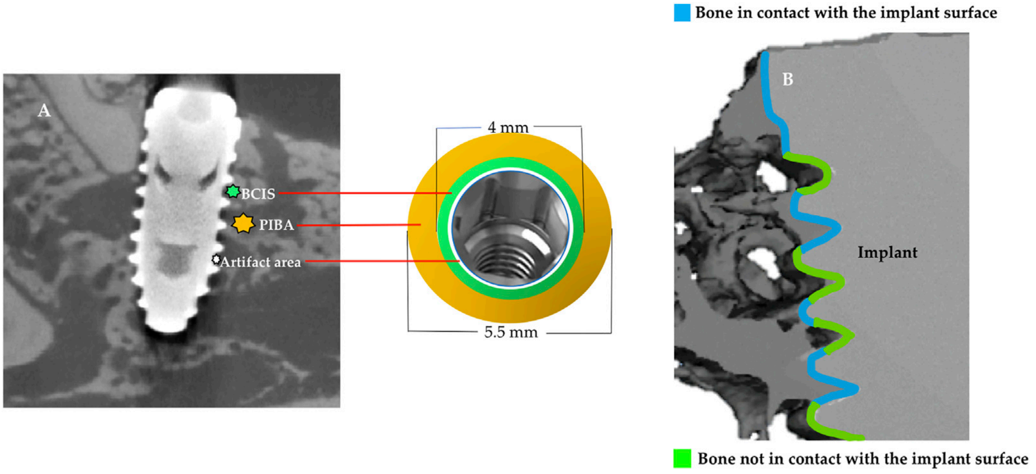

FIGURE 5 | (A), Micro-CT image in sagittal plane and graph to represent the artifact area, bone in contact with the implant surface (BCIS) (4 mm Ø) and peri-implant bone area (PIBA) (5.5 mm Ø); **(B)**, 3D image with the contact and non-contact surfaces of the bone with the implant.

TABLE 1 | Specific crestal, mid and apical trends in the experimental and control groups for BCIS (mean ± deviation).

BCIS	Crestal	Mid	Apical	*p*-values
ChtG	3,770.11 ± 245.60	3,245.25 ± 1,477.08	4,196.82 ± 453.03	0.005 *
CG	3,829.29 ± 249.08	3,958.75 ± 1,477.08	4,112.13 ± 112.6	0.014

*BCIS, bone in contact to the implant surface; ChtG, chitosan group; CG, Control Group. General linear model (p ≤ 0.05). * Statistical significance.*

TABLE 2 | Specific crestal, mid and apical trends in the experimental and control groups for PIBA (mean ± deviation).

PIBA	Crestal	Mid	Apical	*p*-values
ChtG	3,613.00 ± 1,109.12	3,905.75 ± 809.65	3,759.17 ± 944.73	<0.001 *
CG	4,162.50 ± 618.02	3,705.20 ± 1,045.86	3,832.71 ± 1,201.43	0.02

*PIBA, Peri-Implant Bone Area; ChtG, chitosan group; CG, control group. General linear model (p ≤ 0.05). * Statistical significance.*

their surfaces, all with the aim of achieving early and more durable osseointegration. The topography and roughness of the surfaces have been questioned in terms of osteoblastic cell differentiation and it has been shown that the attachment of this type of cells is greater on smooth surfaces, although rougher surfaces have been associated with greater cell differentiation (Bachle and Kohal, 2004; Esposito et al., 2005). Apart from surface characteristics, it is also known that osseointegration is affected by factors such as the biological compatibility of an implant (Annunziata and Guida, 2015). Therefore, to improve the bioactivity of implants, the surface can be modified by incorporating organic and inorganic phases either within or on the Ti oxide layer, using ions, inorganic molecules or organic molecules (Jiang et al., 2014; Anitua et al., 2015).

The evaluation of bone-implant contact provides evidence of an implant anchored in the bone and has traditionally been established as the most common method of evaluation, however, the concept of osseointegration has undergone variations and is now considered as "a reaction to a foreign body in which interfacial bone is formed as a defensive reaction to protect the implant from the tissues" (Albrektsson et al., 2017; Albrektsson and Wennerberg, 2019). The amount of bone in contact with the implant, as well as the frictional properties at the contact interface, are important parameters influencing bone-implant mechanics. However, the stability of implants in trabecular bone has been little studied and considering the reduced contact surface between trabecular bone and implant, it has been suggested that macroscopic phenomena such as trabeculae-implant mechanical fixation would dominate over the microscopic aspects such as friction (Huang et al., 2008; Wirth et al., 2010).

In the present study, a model was designed in the canine mandible, where 2 bone parameters were measured in the area surrounding the implant, Bone in Contact with the Implant Surface (BCIS) and Peri-implant Bone Area (PIBA), at crestal, mid and apical levels, both in the Cht-coated implant group (ChtG) and in the control group (CG), with conventional etched surface, and the results were analyzed by means of micro-CT.

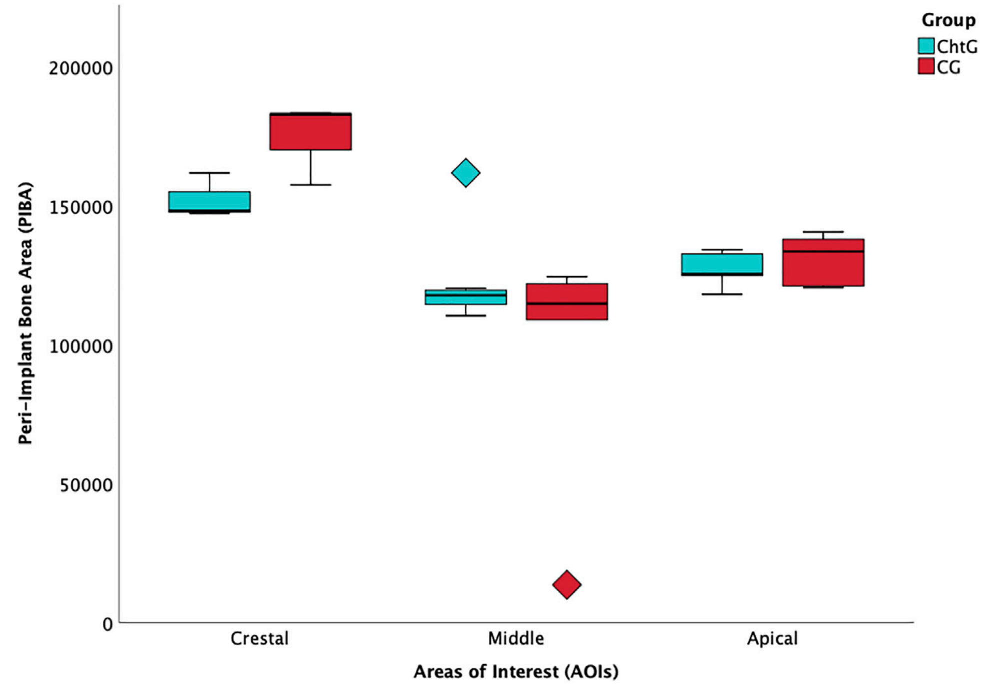

FIGURE 6 | Boxplot of peri-implant bone area (PIBA) values at crestal, mid and apical levels.

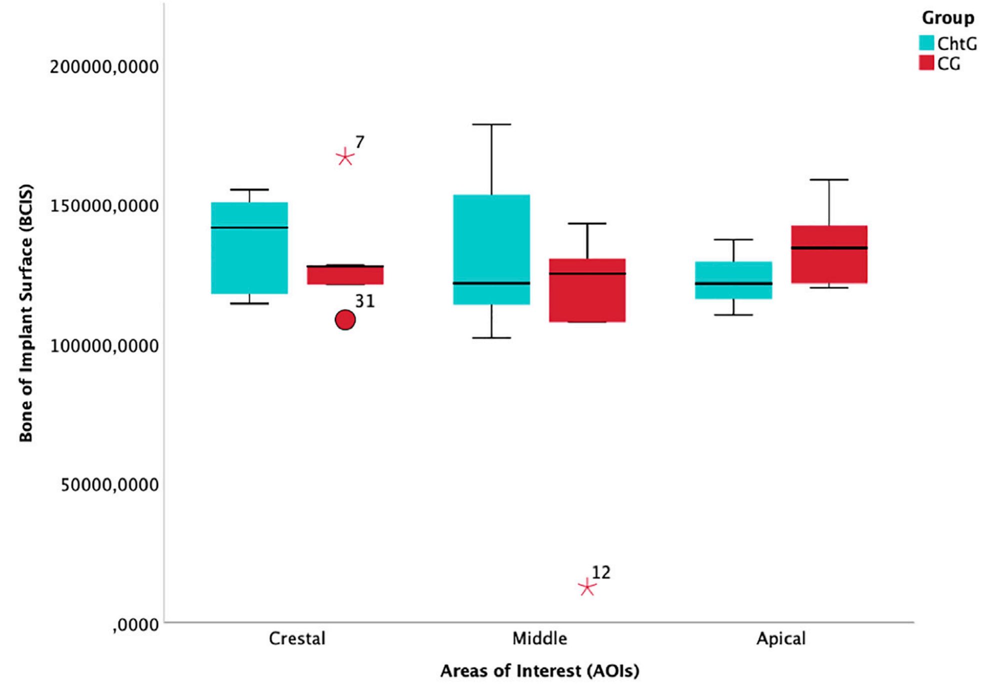

FIGURE 7 | Boxplot of bone in contact with the implant surface (BCIS) values at crestal, mid and apical levels.

Although no single animal species meets all the requirements of an ideal model, an understanding of the differences in bone architecture and remodeling between different species of experimental animals could help to select a suitable species. Most studies resort to modified and inadequate experimental models, both the experimental animal (rabbit rat...) and the implantation site, with extraoral surgical approaches (tibia, femur...), so that the results cannot be extrapolated to humans, among other reasons, because of the lack of cortical remodeling and the fact that the cessation of growth occurs much later in these species than in other mammals (Ferguson et al., 2018). On the other hand, *in vitro* cultures maintain tissues or organs without vascularization, limiting the supply of nutrients, oxygen and waste elimination and, therefore, the extrapolation of the results to the *in vivo* situation limits the model. All this, without taking into account the reduced lifespan of the cultured cells (Pizzoferrato et al., 1994). Our preclinical study used the mandible of a canine model, with greater similarity to the human in terms of bone architecture and remodeling. The dog, along with the pig, are considered valuable models for the study of tissues adjacent to dental implants, and large-breed dogs can support human dental implants (Pearce et al., 2007). To our knowledge, this is the first time that this experimental model has been used for the study of the effectiveness of Cht as a coating for dental implants.

Cht is a macromolecule that has achieved great attention in the biomedical industry, arousing great interest in bone regeneration (De Jonge et al., 2008; Ebhodaghe, 2021). It has the ability to stimulate the recruitment and adhesion of osteogenic progenitor cells, facilitating bone formation. In addition, it has been shown that no inflammatory or allergic reactions occur after topical application (Kim et al., 2003; Waibel et al., 2011; Azuma et al., 2015; Sukpaita et al., 2021).

Typically, toxic reagents, such as 3-isocyanatopropyltriethoxysilane and glutaraldehyde, are used to form Cht coatings for silanization and attachment to the Ti substrate but these techniques involve complex processing that hinders coating deposition and limits clinical applicability (Yuan et al., 2008). However, although efforts have been made to increase the bond strength of hydroxyapatite coatings on implant alloys, as they are brittle materials, it is unclear whether these high bond strengths would be necessary for the polymeric Cht material (Bumgardner et al., 2007).

The dip coating used in our study (Vakili and Asefnejad, 2020), in addition to resisting the forces used during implantation, because of the surgical technique employed, is an inexpensive way of depositing thin layers from chemical solutions, with relatively fair control over the thickness of the layer and offers the possibility of fine-tuning the amount of material that can be deposited and, therefore, the thickness of the final film. For these reasons, it is becoming increasingly popular not only in research and development laboratories, but also in industrial production. Grosso have proposed the immersion technique as a very suitable method to impregnate porosities, make nanocomposites or perform nanofusion. (Grosso, 2011); Brinker et al. (Brinker et al., 1992) pointed out wet methods, as suitable, since they are homogeneously organized in the final film, with adequate thickness control.

The amount of Cht can be adjusted by controlling the concentration of the Cht solution and certain authors have indicated that, as the amount of loaded Cht increases, its antibacterial properties increase; therefore, controlling the amount of loaded Cht would endow the Ti implant with better biological and anti-bacterial properties. Cht loading in 0.5% acidic solution, was considered adequate (Vakili and Asefnejad, 2020), although the optimization of the amount of loaded Cht, degradation rate and antibacterial effect still need to be further investigated (Li et al., 2019b). Most of the existing studies on the efficacy of Cht as a Ti coating, as we have noted above, are *in vitro* studies or *in vivo* studies on inadequate models, or that resort to complicated coating methods, or toxic products, which hinder or impair their clinical applicability (Bumgardner et al., 2007; Kung et al., 2011; Takanche et al., 2018a; Zhang et al., 2020).

Sukpaita et al. (Sukpaita et al., 2019) demonstrated the ability of Cht scaffolds to self-promote bone tissue and repair calvarial bone defects in mice. Tian et al. (Tian et al., 2014), in an *in vitro* study, indicated that Cht film loaded on a Ti surface would promote osteoblast proliferation and differentiation in a dose-dependent manner, which could represent a new approach in the treatment of Ti implants. Zhang et al. (Li et al., 2019b) showed that porous Ti with a Cht/Hydroxyapatite coating could promote osteoblast-like cell proliferation and differentiation and osseointegration *in vivo*. Bumgardner et al. (Bumgardner et al., 2007) evaluated the ability of Cht coatings on Ti to promote bone formation and osseointegration compared to calcium phosphate coatings and uncoated Ti, in a 12-weeks rabbit model, maintaining the hypothesis that it may not be important that the Cht coating persists long-term, once a good bone-implant interface has been established, in the same way that some investigators have speculated with calcium phosphate coatings (Yang et al., 2005).

Even heterotopic (extraskeletal) bone formation induced by Cht-collagen-coated Ti implants has been demonstrated *in vivo* (Kung et al., 2011). Overall, researchers conclude that Cht significantly accelerates the bone regeneration process and, therefore, in terms of its biocompatibility and osteoinductivity, it can be considered as a biomaterial of great relevance in human bone healing (Ge et al., 2004; Pang et al., 2005; Guzmán-Morales et al., 2009; Muzzarelli, 2009; Ezoddini-Ardakani et al., 2012; Mututuvari et al., 2013), which is consistent with the results obtained in our research.

The good film-forming ability of Cht allows its use in the coating of dental or orthopedic implants, and the coated surfaces have been shown to possess good cellular compatibility with fibroblast cells. Klokkevold et al. (Klokkevold et al., 1996) reported that chitosan films enhanced osteoprogenitor cell differentiation, facilitated bone formation, and inhibited fibroblast proliferation. Moreover, the activity of Cht against bacteria such as *Escherichia coli*, *Streptococcus* mutans, *Staphylococcus aureus*, *Bacillus* subtilis and *Actinomyces* naeslundii (Renoud et al., 2012; Lin et al., 2021) and to prevent oxidative damage caused by free radicals (Ngo et al., 2011) has also been demonstrated. Takanche et al. in an *in vivo* study on osteoporotic rat jaws demonstrated, by micro-CT, that Cht-coated Ti implants increased the volume and density of newly formed bone and implant osseointegration, as well as the upregulation of bone morphogenetic protein, by inhibiting osteoclastogenesis. All these and other demonstrated properties make this biopolymer a good biocompatible and bioactive osteoconductor and a useful coating for orthopedic and craniofacial implant devices.

However, in the future, it will be necessary to determine the bond strength of the coatings and changes in bond strength over time and to evaluate the degradation of the coating in lysozyme solutions in the oral environment, as degradation rates may be different in the presence of this enzyme and changes in degradation would be important for the development of the implant-tissue interface (Yuan et al., 2008). It will also be necessary to determine whether changes in initial cell growth, or differences in Cht degradation, result in less cell mineralization. In addition, it will need to be determined whether surface morphology, roughness, and coating chemistry could be related to cell and tissue responses.

In our study, two bone parameters in the vicinity of the implant (BCIS and PIBA) were measured by micro-CT. The best statistical significance was obtained for PIBA, in the experimental group (ChtG) ($p < 0.001$), despite the fact that all the inserted implants obtained optimal osseointegration. The maximum value was obtained for PIBA at the crestal level of M1 in ChG (6,347.05 ± 413.2) and the minimum for BCIS at the mid-level of P2 in CG (1765.03 ± 358.01).

Micro-CT currently allows observation of bone tissue in a three-dimensional manner, as well as quantitative analysis in several sections, which is not possible by histomorphometric analysis. It detects only mineralized tissue and is therefore suitable for analyzing the bony annulus and assessing bone formation around implants during healing periods; moreover, histological studies could not be performed in clinical trials (Vandeweghe et al., 2013b; Nakahara et al., 2019). Rebaudi et al. (Rebaudi et al., 2004), have proposed it as a suitable technique for the analysis of peri-implant bone tissues, proposing it as a non-destructive evaluation, which allows the analysis of the bone-implant interface. Lyu and Lee (Lyu and Lee, 2021), in a study on rabbit tibiae, reported that the measurement of bone in contact with the implant by micro-CT is feasible to evaluate implant osseointegration, obtaining results similar to histomorphometric ones, although they recognize that the method needs further optimization. Likewise, they recognize that, in most cases, they can only use one or two histological sections per implant for histomorphometric evaluation, which could lead to an over- or underestimation of the peri-implant bone.

Nevertheless, we are aware of our limitations, in terms of small sample size and difficulty in accurately detecting the bone in close contact with the implant surface, due to the thin layer of noise in the surrounding area and the microtomography settings. and the difficulty of accurately detecting the bone in close contact with the implant surface, due to the thin layer of noise in the surrounding area and the microtomography settings. These drawbacks should be taken into account when interpreting the results. In future ongoing studies, the samples will be studied by histomorphometric analysis to compare the results.

CONCLUSION

The results of this preliminary study demonstrated the usefulness of Cht coatings on Ti surfaces to improve the osseointegration of dental implants. In addition, within the limitations, the use of nondestructive micro-CT analysis, seems to be useful to evaluate bone healing in the surroundings of the implant surfaces.

Since the design of the present study allowed only a preliminary analysis, the data obtained could serve as a basis for the design of future studies.

DATA AVAILABILITY STATEMENT

The original contributions presented in the study are included in the article/Supplementary Material, further inquiries can be directed to the corresponding author.

ETHICS STATEMENT

The animal study was reviewed and approved by Ethics Committee of the Catholic University of Murcia (Spain) with code CE072004.

AUTHOR CONTRIBUTIONS

Conceptualization, NL-V and AL-V; methodology, NL-V; formal analysis, AL-V; investigation, NL-V and BMS; writing-original draft preparation AL-V; data curation, JMA, MPC, and CR; supervision, JMA and AL-V. All authors have read and agreed to the published version of the manuscript. All authors have read and agreed to the published version of the manuscript.

REFERENCES

Ahn, S.-I., Cho, S., and Choi, N.-J. (2021). Effectiveness of Chitosan as a Dietary Supplement in Lowering Cholesterol in Murine Models: A Meta-Analysis. *Mar. Drugs* 19, 26. doi:10.3390/md19010026

Ahsan, S. M., Thomas, M., Reddy, K. K., Sooraparaju, S. G., Asthana, A., and Bhatnagar, I. (2018). Chitosan as Biomaterial in Drug Delivery and Tissue Engineering. *Int. J. Biol. Macromolecules* 110, 97–109. doi:10.1016/j.ijbiomac.2017.08.140

Albrektsson, T., Chrcanovic, B., Jacobsson, M., and Wennerberg, A. (2017). Osseointegration of Implants-A Biological and Clinical Overview. *JSM Dent Surg.* 2, 1–6.

Albrektsson, T., and Wennerberg, A. (2019). On Osseointegration in Relation to Implant Surfaces. *Clin. Implant Dent Relat. Res.* 21 (Suppl. 1), 4–7. doi:10.1111/cid.12742

Alfarsi, M. A., Hamlet, S. M., and Ivanovski, S. (2014). Titanium Surface Hydrophilicity Modulates the Human Macrophage Inflammatory Cytokine Response. *J. Biomed. Mater. Res.* 102, 60–67. doi:10.1002/jbm.a.34666

Anitua, E., Prado, R., Orive, G., and Tejero, R. (2015). Effects of Calcium-Modified Titanium Implant Surfaces on Platelet Activation, Clot Formation, and Osseointegration. *J. Biomed. Mater. Res.* 103, 969–980. doi:10.1002/jbm.a.35240

Annunziata, M., and Guida, L. (2015). The Effect of Titanium Surface Modifications on Dental Implant Osseointegration. *Front. Oral Biol.* 17, 62–77. doi:10.1159/000381694

Azuma, K., Osaki, T., Minami, S., and Okamoto, Y. (2015). Anticancer and Anti-inflammatory Properties of Chitin and Chitosan Oligosacchrides. *J. Funct. Biomater.* 6, 33–49. doi:10.3390/jfb6010033

Bachle, M., and Kohal, R. J. (2004). A Systematic Review of the Influence of Different Titanium Surfaces on Proliferation, Differentiation and Protein Synthesis of Osteoblast-like MG63 Cells. *Clin. Oral Implants Res.* 15, 683–692. doi:10.1111/j.1600-0501.2004.01054.x

Becker, K., Klitzsch, I., Stauber, M., and Schwarz, F. (2017). Three-dimensional Assessment of Crestal Bone Levels at Titanium Implants with Different Abutment Microstructures and Insertion Depths Using Micro-computed Tomography. *Clin. Oral Impl. Res.* 28, 671–676. doi:10.1111/clr.12860

Boyd, S. K., Moser, S., Kuhn, M., Klinck, R. J., Krauze, P. L., Müller, R., et al. (2006). Evaluation of Three-Dimensional Image Registration Methodologies for *In Vivo* Micro-computed Tomography. *Ann. Biomed. Eng.* 34, 1587–1599. doi:10.1007/s10439-006-9168-7

Brinker, C. J., Hurd, A. J., Schunk, P. R., Frye, G. C., and Ashley, C. S. (1992). Review of Sol-Gel Thin Film Formation. *J. Non-Crystalline Sol.* 147–148, 424–436. doi:10.1016/S0022-3093(05)80653-2

Bumgardner, J. D., Chesnutt, B. M., Yuan, Y., Yang, Y., Appleford, M., Oh, S., et al. (2007). The Integration of Chitosan-Coated Titanium in Bone: an *In Vivo* Study in Rabbits. *Implant Dent* 16, 66–79. doi:10.1097/ID.0b013e3180312011

Bumgardner, J. D., Wiser, R., Elder, S. H., Jouett, R., Yang, Y., and Ong, J. L. (2003). Contact Angle, Protein Adsorption and Osteoblast Precursor Cell Attachment to Chitosan Coatings Bonded to Titanium. *J. Biomater. Sci. Polym. Edition* 14, 1401–1409. doi:10.1163/156856203322599734

Bumgardner, J. D., Wiser, R., Gerard, P. D., Bergin, P., Chestnutt, B., Marini, M., et al. (20032003). Chitosan: Potential Use as a Bioactive Coating for Orthopaedic and Craniofacial/dental Implants. *J. Biomater. Sci. Polym. Edition* 14 (5), 423–438. doi:10.1163/156856203766652048

Chen, R., Cai, X., Ma, K., Zhou, Y., Wang, Y., and Jiang, T. (2017). The Fabrication of Double-Layered Chitosan/gelatin/genipin Nanosphere Coating for Sequential and Controlled Release of Therapeutic Proteins. *Biofabrication* 9 (2), 025028. doi:10.1088/1758-5090/aa70c3

De Jonge, L. T., Leeuwenburgh, S. C. G., Wolke, J. G. A., and Jansen, J. A. (2008). Organic-inorganic Surface Modifications for Titanium Implant Surfaces. *Pharm. Res.* 25, 2357–2369. doi:10.1007/s11095-008-9617-0

Ebhodaghe, S. O. (2021). Natural Polymeric Scaffolds for Tissue Engineering Applications. *J. Biomater. Sci. Polym. Ed.* 32, 2144–2194. doi:10.1080/09205063.2021.1958185

Esposito, M., Coulthard, P., Thomsen, P., and Worthington, H. V. (2005). The Role of Implant Surface Modifications, Shape and Material on the success of Osseointegrated Dental Implants. A Cochrane Systematic Review. *Eur. J. Prosthodont. Restor Dent* 13, 15–31.

Ezoddini-Ardakani, F., Navabazam, A., Fatehi, F., Danesh-Ardekani, M., Khadem, S., and Rouhi, G. (2012). Histologic Evaluation of Chitosan as an Accelerator of Bone Regeneration in Microdrilled Rat Tibias. *Dental Res. J.* 9, 694–699.

Ferguson, J. C., Tangl, S., Barnewitz, D., Genzel, A., Heimel, P., Hruschka, V., et al. (2018). A Large Animal Model for Standardized Testing of Bone Regeneration Strategies. *BMC Vet. Res.* 14, 330. doi:10.1186/s12917-018-1648-0

Ge, Z., Baguenard, S., Lim, L. Y., Wee, A., and Khor, E. (2004). Hydroxyapatite–chitin Materials as Potential Tissue Engineered Bone Substitutes. *Biomaterials* 25, 1049–1058. doi:10.1016/s0142-9612(03)00612-4

Grosso, D. (2011). How to Exploit the Full Potential of the Dip-Coating Process to Better Control Film Formation. *J. Mater. Chem.* 21, 17033–17038. doi:10.1039/c1jm12837j

Guzmán-Morales, J., El-Gabalawy, H., Pham, M. H., Tran-Khanh, N., Marc, D., McKee, W. W., et al. (2009). Effect of Chitosan Particles and Dexamethasone on Human Bone Marrow Stromal Cell Osteogenesis and Angiogenic Factor Secretion. *Bone* 45, 617–626. doi:10.1016/j.bone.2009.06.014

He, T., Cao, C., Xu, Z., Li, G., Cao, H., Liu, X., et al. (2017). A Comparison of Micro-CT and Histomorphometry for Evaluation of Osseointegration of PEO-Coated Titanium Implants in a Rat Model. *Sci. Rep.* 7, 16270. doi:10.1038/s41598-017-16465-4

Höhlinger, M., Heise, S., Wagener, V., Boccaccini, A. R., and Virtanen, S. (2017). Developing Surface Pre-treatments for Electrophoretic Deposition of Biofunctional Chitosan-Bioactive Glass Coatings on a WE43 Magnesium alloy. *Appl. Surf. Sci.* 405, 441–448. doi:10.1016/j.apsusc.2017.02.049

Hotchkiss, K. M., Sowers, K. T., and Olivares-Navarrete, R. (2019). Novel *In Vitro* Comparative Model of Osteogenic and Inflammatory Cell Response to Dental Implants. *Dental Mater.* 35, 176–184. doi:10.1016/j.dental.2018.11.011

Hu, Y., Cai, K., Luo, Z., Zhang, R., Yang, L., Deng, L., et al. (2009). Surface Mediated *In Situ* Differentiation of Mesenchymal Stem Cells on Gene-Functionalized Titanium Films Fabricated by Layer-By-Layer Technique. *Biomaterials* 30, 3626–3635. doi:10.1016/j.biomaterials.2009.03.037

Hu, Z., Zhang, D.-Y., Lu, S.-T., Li, P.-W., and Li, S.-D. (2018). Chitosan-Based Composite Materials for Prospective Hemostatic Applications. *Mar. Drugs* 16, 273. doi:10.3390/md16080273

Huang, H.-L., Hsu, J.-T., Fuh, L.-J., Tu, M.-G., Ko, C.-C., and Shen, Y.-W. (2008). Bone Stress and Interfacial Sliding Analysis of Implant Designs on an Immediately Loaded Maxillary Implant: a Non-linear Finite Element Study. *J. Dentistry* 36, 409–417. doi:10.1016/j.jdent.2008.02.015

Jemat, A., Ghazali, M. J., Razali, M., and Otsuka, Y. (2015). Surface Modifications and Their Effects on Titanium Dental Implants. *Biomed. Res. Int.* 2015, 1, 11. doi:10.1155/2015/791725

Jiang, X., Wang, G., Li, J., Zhang, W., Xu, L., Pan, H., et al. (2014). Magnesium Ion Implantation on a Micro/nanostructured Titanium Surface Promotes its Bioactivity and Osteogenic Differentiation Function. *Ijn* 9, 2387–2398. doi:10.2147/IJN.S58357

Kampschulte, M., Langheinirch, A., Sender, J., Litzlbauer, H., Althöhn, U., Schwab, J., et al. (2016). Nano-Computed Tomography: Technique and Applications. *Fortschr Röntgenstr* 188, 146–154. doi:10.1055/s-0041-106541

Kim, I.-Y., Seo, S.-J., Moon, H.-S., Yoo, M.-K., Park, I.-Y., Kim, B.-C., et al. (2008). Chitosan and its Derivatives for Tissue Engineering Applications. *Biotechnol. Adv.* 26, 1–21. doi:10.1016/j.biotechadv.2007.07.009

Kim, S. E., Park, J. H., Cho, Y. W., Chung, H., Jeong, S. Y., Lee, E. B., et al. (2003). Porous Chitosan Scaffold Containing Microspheres Loaded with Transforming Growth Factor-Beta1: Implications for Cartilage Tissue Engineering. *J. Controlled Release* 91, 365–374. doi:10.1016/s0168-3659(03)00274-8

Klokkevold, P. R., Vandemark, L., Kenney, E. B., and Bernard, G. W. (1996). Osteogenesis Enhanced by Chitosan (Poly-N-Acetyl Glucosaminoglycan) *In Vitro*. *J. Periodontol.* 67, 170–175. doi:10.1902/jop.1996.67.11.1170

Kung, S., Devlin, H., Fu, E., Ho, K. Y., Liang, S. Y., and Hsieh, Y. D. (2011). The Osteoinductive Effect of Chitosan-Collagen Composites Around Pure Titanium Implant Surfaces in Rats. *J. Periodontal Res.* 46, 126–133. doi:10.1111/j.1600-0765.2010.01322.x

Le Guéhennec, L., Soueidan, A., Layrolle, P., and Amouriq, Y. (2007). Surface Treatments of Titanium Dental Implants for Rapid Osseointegration. *Dental Mater.* 23, 844–854. doi:10.1016/j.dental.2006.06.025

Li, B., Xia, X., Guo, M., Jiang, Y., Li, Y., Zhang, Z., et al. (2019). Biological and Antibacterial Properties of the Micro-nanostructured Hydroxyapatite/chitosan Coating on Titanium. *Sci. Rep.* 9 (1), 14052. doi:10.1038/s41598-019-49941-0

Li, X., Qi, M., Sun, X., Weir, M. D., Tay, F. R., Oates, T. W., et al. (2019). Surface Treatments on Titanium Implants via Nanostructured Ceria for Antibacterial and Anti-inflammatory Capabilities. *Acta Biomater.* 94, 627–643. doi:10.1016/j.actbio.2019.06.023

Lin, M. H., Wang, Y. H., Kuo, C. H., Ou, S. F., Huang, P. Z., Song, T. Y., et al. (2021). Hybrid ZnO/chitosan Antimicrobial Coatings with Enhanced Mechanical and Bioactive Properties for Titanium Implants. *Carbohydr. Polym.* 257, 117639. doi:10.1016/j.carbpol.2021.117639

López-Valverde, N., López-Valverde, A., and Ramírez, J. M. (2021). Systematic Review of Effectiveness of Chitosan as a Biofunctionalizer of Titanium Implants. *Biology* 10, 102. doi:10.3390/biology10020102

Lyu, H. Z., and Lee, J. H. (2021). Correlation between Two-Dimensional Micro-CT and Histomorphometry for Assessment of the Implant Osseointegration in Rabbit Tibia Model. *Biomater. Res.* 2511. doi:10.1186/s40824-021-00213-x

Matica, M. A., Aachmann, F. L., Tøndervik, A., Sletta, H., and Ostafe, V. (2019). Chitosan as a Wound Dressing Starting Material: Antimicrobial Properties and Mode of Action. *Ijms* 20, 5889. doi:10.3390/ijms20235889

Mututuvari, T. M., Harkins, A. L., and Tran, C. D. (2013). Facile Synthesis, Characterization, and Antimicrobial Activity of Cellulose–Chitosan–Hydroxyapatite Composite Material: A Potential Material for Bone Tissue Engineering. *J. Bio-medical Mater. Res. A* 101A, 3266–3277. doi:10.1002/jbm.a.34636

Muzzarelli, R. A. A. (2009). Chitins and Chitosans for the Repair of Wounded Skin, Nerve, Cartilage and Bone. *Carbohydr. Polym.* 76, 167–182. doi:10.1016/j.carbpol.2008.11.002

Muzzarelli, R. A. A., Mattioli-Belmonte, M., Tietz, C., Biagini, R., Ferioli, G., Brunelli, M. A., et al. (1994). Stimulatory Effect on Bone Formation Exerted by a Modified Chitosan. *Biomaterials* 15, 1075–1081. doi:10.1016/0142-9612(94)90093-0

Nakahara, K., Haga-Tsujimura, M., Igarashi, K., Kobayashi, E., Schaller, B., Lang, N. P., et al. (2019). Single-staged Implant Placement Using the Bone Ring Technique with and without Membrane Placement: Micro-CT Analysis in a Preclinical *In Vivo* Study. *Clin. Oral Impl Res.* 31, 29-36. doi:10.1111/clr.13543

Ngo, D. H., Qian, Z. J., Ngo, D. N., Vo, T. S., Wijesekara, I., and Kim, S. K. (2011). Gallyl Chitooligosaccharides Inhibit Intracellular Free Radical-Mediated Oxidation. *Food Chem.* 128, 974e981. doi:10.1016/j.foodchem.2011.03.128

Palla-Rubio, B., Araújo-Gomes, N., Fernández-Gutiérrez, M., Rojo, L., Suay, J., Gurruchaga, M., et al. (2019). Synthesis and Characterization of Silica-Chitosan Hybrid Materials as Antibacterial Coatings for Titanium Implants. *Carbohydr. Polym.* 203, 331–341. doi:10.1016/j.carbpol.2018.09.064

Pang, E.-K., Paik, J.-W., Kim, S.-K., Jung, U.-W., Kim, C.-S., Cho, K.-S., et al. (2005). Effects of Chitosan on Human Periodontal Ligament Fibroblasts *In Vitro* and on Bone Formation in Rat Calvarial Defects. *J. Periodontol.* 76, 1526–1533. doi:10.1902/jop.2005.76.9.1526

Pearce, A., Richards, R. G., Richards, R., Milz, S., Schneider, E., and Pearce, S. G. (2007). Animal Models for Implant Biomaterial Research in Bone: a Review. *Eur. Cell Mater* 13, 1–10. doi:10.1016/0267-6605(94)90081-710.22203/ecm.v013a01

Peyrin, F., Dong, P., Pacureanu, A., and Langer, M. (2014). Micro- and Nano-CT for the Study of Bone Ultrastructure. *Curr. Osteoporos. Rep.* 12, 465–474. doi:10.1007/s11914-014-0233-0

Pizzoferrato, A., Ciapetti, G., Stea, S., Cenni, E., Arciola, C. R., Granchi, D., et al. (1994). Cell Culture Methods for Testing Biocompatibility. *Clin. Mater.* 15, 173–190. doi:10.1016/0267-6605(94)90081-7

Rabea, E. I., Badawy, M. E.-T., Stevens, C. V., Smagghe, G., and Steurbaut, W. (2003). Chitosan as Antimicrobial Agent: Applications and Mode of Action. *Biomacromolecules* 4, 1457–1465. doi:10.3390/ijms2023588910.1021/bm034130m

Rebaudi, A., Koller, B., Laib, A., and Trisi, P. (2004). Microcomputed Tomographic Analysis of the Peri-Implant Bone. *Int. J. Periodontics Restorative Dent* 24, 316–325.

Reddy Tiyyagura, H., Rudolf, R., Gorgieva, S., Fuchs-Godec, R., Boyapati, V. R., Mantravadi, K. M., et al. (2016). The Chitosan Coating and Processing Effect on the Physiological Corrosion Behaviour of Porous Magnesium Monoliths. *Prog. Org. Coat.* 99, 147–156. doi:10.1016/j.porgcoat.2016.05.019

Renoud, P., Toury, B., Benayoun, S., Attik, G., and Grosgogeat, B. (2012). Functionalization of Titanium with Chitosan via Silanation: Evaluation of Biological and Mechanical Performances. *PLoS One* 7 (7), e39367. doi:10.1371/journal.pone.0039367

Rojo, L., and Deb, S. (2015). Polymer Therapeutics in Relation to Dentistry. *Front. Oral Biol.* 17, 13–21. doi:10.1159/000381688

Sakka, S., Baroudi, K., and Nassani, M. Z. (2012). Factors Associated with Early and Late Failure of Dental Implants. *J. Invest. Clin. Dent* 3, 258–261. doi:10.1111/j.2041-1626.2012.00162.x

Scriven, L. E. (1988). Physics and Applications of DIP Coating and Spin Coating. *MRS Proc.* 121, 717. doi:10.1557/PROC-121-717

Shukla, S. K., Mishra, A. K., Arotiba, O. A., and Mamba, B. B. (2013). Chitosan-based Nanomaterials: a State-Of-The-Art Review. *Int. J. Biol. Macromolecules* 59, 46–58. doi:10.1016/j.ijbiomac.2013.04.043

Simonis, P., Dufour, T., and Tenenbaum, H. (2010). Long-term Implant Survival and success: a 10-16-year Follow-Up of Non-submerged Dental Implants. *Clin. Oral Implants Res.* 21, 772–777. doi:10.1111/j.1600-0501.2010.01912.x

Singla, A. K., and Chawla, M. (2001). Chitosan: Some Pharmaceutical and Biological Aspects-Aan Update. *J. Pharm. Pharmacol.* 53, 1047–1067. doi:10.1211/0022357011776441

Sukpaita, T., Chirachanchai, S., Pimkhaokham, A., and Ampornaramveth, R. S. (2021). Chitosan-Based Scaffold for Mineralized Tissues Regeneration. *Mar. Drugs* 19 (10), 551. doi:10.3390/md19100551

Sukpaita, T., Chirachanchai, S., Suwattanachai, P., Everts, V., Pimkhaokham, A., and Ampornaramveth, R. S. (2019). *In Vivo* Bone Regeneration Induced by a Scaffold of Chitosan/Dicarboxylic Acid Seeded with Human Periodontal Ligament Cells. *Int. J. Mol. Sci.* 20 (19), 4883. doi:10.3390/ijms20194883

Szmukler-Moncler, S., Testori, T., and Bernard, J. P. (2004). Etched Implants: a Comparative Surface Analysis of Four Implant Systems. *J. Biomed. Mater. Res.* 69B, 46–57. doi:10.1002/jbm.b.20021

Tajdini, F., Amini, M. A., Nafissi-Varcheh, N., and Faramarzi, M. A. (2010). Production, Physiochemical and Antimicrobial Properties of Fungal Chitosan from Rhizomucor Miehei and Mucor Racemosus. *Int. J. Biol. Macromolecules* 47, 180–183. doi:10.1016/j.ijbiomac.2010.05.002

Takanche, J. S., Kim, J. E., Kim, J. S., Lee, M. H., Jeon, J. G., Park, I. S., et al. (2018). Chitosan-gold Nanoparticles Mediated Gene Delivery of C-Myb Facilitates Osseointegration of Dental Implants in Ovariectomized Rat. *Artif. Cell Nanomed Bio-technol* 46 (Suppl. 3), S807–S817. doi:10.1080/21691401.2018.1513940

Tian, A., Zhai, J. J., Peng, Y., Zhang, L., Teng, M. H., Liao, J., et al. (2014). Osteoblast Response to Titanium Surfaces Coated with Strontium Ranelate-Loaded Chitosan Film. *Int. J. Oral Maxillofac. Implants* 29, 1446–1453. doi:10.11607/jomi.3806

Türker, N. S., Özer, A. Y., Kutlu, B., Nohutcu, R., Sungur, A., Bilgili, H., et al. (2014). The Effect of Gamma Radiation Sterilization on Dental Biomaterials. *Tissue Eng. Regen. Med.* 11, 341–349. doi:10.1007/s13770-014-0016-9

Ueno, T., Takeuchi, M., Hori, N., Iwasa, F., Minamikawa, H., Igarashi, Y., et al. (2012). Gamma ray Treatment Enhances Bioactivity and Osseointegration Capability of Titanium. *J. Biomed. Mater. Res.* 100B, 2279–2287. doi:10.1002/jbm.b.32799

Vakili, N., and Asefnejad, A. (2020). Titanium Coating: Introducing an Antibacterial and Bioactive Chitosan-Alginate Film on Titanium by Spin Coating. *Biomed. Tech. (Berl)* 65, 621–630. doi:10.1515/bmt-2018-0108

Vandeweghe, S., Coelho, P. G., Vanhove, C., Wennerberg, A., and Jimbo, R. (2013). Utilizing Micro-computed Tomography to Evaluate Bone Structure Surrounding Dental Implants: A Comparison with Histomorphometry. *J. Biomed. Mater. Res.* 101, 1259–1266. doi:10.1002/jbm.b.32938

Vandeweghe, S., Coelho, P. G., Vanhove, C., Wennerberg, A., and Jimbo, R. (2013). Utilizing Micro-computed Tomography to Evaluate Bone Structure Surrounding Dental Implants: A Comparison with Histomorphometry. *J. Biomed. Mater. Res. B, Appl. Biomater.* 101, 1259–1266. doi:10.1002/jbm.b.32938

von Wilmowsky, C., Moest, T., Nkenke, E., Stelzle, F., and Schlegel, K. A. (2014). Implants in Bone: Part I. A Current Overview about Tissue Response, Surface Modifications and Future Perspectives. *Oral Maxillofac. Surg.* 18, 243–257. doi:10.1007/s10006-013-0398-1

Waibel, K. H., Haney, B., Moore, M., Whisman, B., and Gomez, R. (2011). Safety of Chitosan Bandages in Shellfish Allergic Patients. *Mil. Med.* 176, 1153–1156. doi:10.7205/milmed-d-11-00150

Wirth, A., Müller, R., Müller, R., and van Lenthe, G. (2010). Computational Analyses of Small Endosseous Implants in Osteoporotic Bone. *eCM* 20, 58–71. doi:10.22203/ecm.v020a06

Yang, Y., Kim, K. H., and Ong, J. L. (2005). A Review on Calcium Phosphate Coatings Produced Using Sputtering Process–An Alternative to Plasma Spraying. *Biomaterials* 26, 327–337. doi:10.1016/j.biomaterials.2004.02.029

Ylitalo, R., Lehtinen, S., Wuolijoki, E., Ylitalo, P., and Lehtimäki, T. (2002). Cholesterol-lowering Properties and Safety of Chitosan. *Arzneimittelforschung* 52, 1–7. doi:10.1055/s-0031-1299848

Yu, D., Feng, J., You, H., Zhou, S., Bai, Y., He, J., et al. (2022). The Microstructure, Antibacterial and Antitumor Activities of Chitosan Oligosaccharides and Derivatives. *Mar. Drugs* 20, 69. doi:10.3390/md20010069

Yuan, Y., Chesnutt, B. M., Wright, L., Haggard, W. O., and Bumgardner, J. D. (2008). Mechanical Property, Degradation Rate, and Bone Cell Growth of Chitosan

Coated Titanium Influenced by Degree of Deacetylation of Chitosan. *J. Biomed. Mater. Res. B Appl. Biomater.* 86B, 245–252. doi:10.1002/jbm.b.31012

Zhang, C., Wang, Z., Li, Y., Yang, Y., Ju, X., and He, R. (2019). The Preparation and Physiochemical Characterization of Rapeseed Protein Hydrolysate-Chitosan Composite Films. *Food Chem.* 272, 694–701. doi:10.1016/j.foodchem.2018.08.097

Zhang, T., Zhang, X., Mao, M., Li, J., Wei, T., and Sun, H. (2020). Chitosan/hydroxyapatite Composite Coatings on Porous Ti6Al4V Titanium Implants: *In Vitro* and *In Vivo* Studies. *J. Periodontal Implant Sci.* 50, 392–405. doi:10.5051/jpis.1905680284

Conflict of Interest: The authors declare that the research was conducted in the absence of any commercial or financial relationships that could be construed as a potential conflict of interest.

frontiers | Frontiers in Bioengineering and Biotechnology

ORIGINAL RESEARCH
published: 11 April 2022
doi: 10.3389/fbioe.2022.882308

pH/Redox/Lysozyme-Sensitive Hybrid Nanocarriers With Transformable Size for Multistage Drug Delivery

Zhe Liu[1,2,3], *Dong Zhou*[4] *and Lan Liao*[1,2,3]*

[1]*The Affiliated Stomatological Hospital, Nanchang University, Nanchang, China,* [2]*The Key Laboratory of Oral Biomedicine, Nanchang, China,* [3]*Jiangxi Province Clinical Research Center for Oral Diseases, Nanchang, China,* [4]*College of Chemistry, Nanchang University, Nanchang, China*

The majority of current nanocarriers in cancer treatment fail to deliver encapsulated cargos to their final targets at therapeutic levels, which decreases the ultimate efficacy. In this work, a novel core–shell nanocarrier with a biodegradable property was synthesized for efficient drug release and subcellular organelle delivery. Initially, silver nanoparticles (AgNPs) were grafted with terminal double bonds originating from N, N′-bisacrylamide cystamine (BAC). Then, the outer coatings consisting of chitosan (CTS) and polyvinyl alcohol (PVA) were deposited on the surface of modified AgNPs using an emulsion method. To improve the stability, disulfide-containing BAC was simultaneously reintroduced to cross-link CTS. The as-prepared nanoparticles (CAB) possessed the desired colloidal stability and exhibited a high drug loading efficiency of cationic anticancer agent doxorubicin (DOX). Furthermore, CAB was tailored to transform their size into ultrasmall nanovehicles responding to weak acidity, high glutathione (GSH) levels, and overexpressed enzymes. The process of transformation was accompanied by sufficient DOX release from CAB. Due to the triple sensitivity, CAB enabled DOX to accumulate in the nucleus, leading to a great effect against malignant cells. *In vivo* assays demonstrated CAB loading DOX held excellent biosafety and superior antitumor capacity. Incorporating all the benefits, this proposed nanoplatform may provide valuable strategies for efficient drug delivery.

Keywords: nanocarrier, transformable size, multistage drug delivery, triple sensitivity, antitumor

Edited by:
Yuangang Liu,
Huaqiao University, China

Reviewed by:
Maobin Yang,
Temple University Health System, Inc.,
United States
Hai Zhang,
University of Washington,
United States

***Correspondence:**
Lan Liao
Liaolan5106@ncu.edu.cn

Specialty section:
This article was submitted to Biomaterials,
a section of the journal
Frontiers in Bioengineering and Biotechnology

Received: *23 February 2022*
Accepted: *14 March 2022*
Published: *11 April 2022*

Citation:
Liu Z, Zhou D and Liao L (2022) pH/Redox/Lysozyme-Sensitive Hybrid Nanocarriers With Transformable Size for Multistage Drug Delivery.
Front. Bioeng. Biotechnol. 10:882308.
doi: 10.3389/fbioe.2022.882308

INTRODUCTION

The advances of nanotechnology provide significant promise to reconcile the difficulties of conventional drug delivery (Mitchell et al., 2021). Until now, there have been several nanomaterials used for cancer treatment, such as liposomal doxorubicin and albumin-bound paclitaxel (Penson et al., 2020; Hama et al., 2021). However, a series of defects including poor stability, premature drug leakage, and intracellular unsatisfactory trafficking limit their application (Tan et al., 2019; Chen et al., 2020; Liu et al., 2021). Therefore, considerable therapeutic nanodevices of broad perspective are continually under development, which are generally categorized as organic nanoparticles, inorganic nanoparticles, and inorganic/organic hybrid nanosystems (Huang et al., 2020). Among these designs, the AgNP-based materials have appealed increasing attention. The popularity of AgNPs is intensively related to their unique properties, especially stable nanoscale structures, ease of synthesis, and facile surface chemistry (Rai et al., 2016; Xu et al., 2020; Yang et al., 2021).

To meet the stringent requirement for cellular delivery, AgNPs are typically subjected to surface modifications with organic polymers or biological macromolecules, allowing them for obtaining hybrid nanoparticles of several types (Sharma et al., 2014; Azizi et al., 2017; Austin et al., 2011; Schubert et al., 2018; Pedziwiatr et al., 2020). In this composite structure, AgNPs as the core take charge of size, shape, and traceability, while outer coatings determine colloidal stability, drug encapsulation efficiency, and particle elasticity. Due to the high surface energy, bare AgNPs possess poor colloidal stability, which readily aggregate or agglomerate in the blood circulation, probably causing adverse cytotoxicity (Gutierrez et al., 2020). Consequently, using coating agent for resisting the aggregation of AgNPs merits thorough consideration (Badawy et al., 2010; Hotze et al., 2010). Screening all the materials, PVA, polyethylene glycol (PEG), and poly(N-isopropylacrylamide) (PNIPAM) are excellent candidates (Stolnik et al., 2012; Jiang et al., 2016; Tzounis et al., 2019), and their appropriate compatibility, flexibility, hydrophilicity, and surface charge are highly responsible for the coating usage.

The larger size of such hybrid nanodevices, ranging from 50 to 200 nm in diameter, is beneficial for high drug loading, long circulation, enhanced permeability, and retention (EPR) effect (Duan et al., 2013). However, particles with the aforementioned size preclude subcellular organelle drug delivery because of several biological barriers (Pan et al., 2018). To overcome these limitations, a favorable drug release system (DDS) should be relatively larger in its initial size to achieve the extended circulation half-life and selective accumulation in tumor, but once entered into cells, the outer layer should detach to smaller sized particles (about 30–50 nm) to facilitate effective deep penetration, which is denoted as the “peeling onions” strategy (Ruan et al., 2015; Li et al., 2016; Niu et al., 2018). Such a requirement has promoted the recent advancement of size-transformable nanodevices. While delivering drugs to subcellular organelles, these nanodevices are capable of realizing the degradation and release smaller nanoblocks responding to the internal stimuli of cancerous cells (Tang et al., 2016; Zhou et al., 2020).

Boosting the drug release efficiency is another challenging task. Limited drug release efficiency might result in low drug levels at sites of action and thus compromise the ultimate therapeutic outcome. Therefore, more efforts should be focused on sufficient drug release. In the past few years, a multitude of individual stimulus-responsive DDSs have been developed to control drug release (Qiu et al., 2017; Xiu et al., 2020). However, single-responsive mechanisms undergo incomplete drug release and poor drug bioavailability, maximizing the administrated dosage and minimizing the treatment efficacy. Fortunately, multi-responsive DDSs are promising refinements that can promote sufficient and rapid intracellular drug release, reduce resistance in cancer cells, and garner robust therapeutic efficacy (Cheng et al., 2015; Karimi et al., 2016). It has been demonstrated that the most spectacular attributes of the intracellular milieu are hypoxia, acidic pH, high GSH levels, and overexpressed tumor-associated enzymes, which have been used as important responsive stimuli for on-demand drug release (Mi et al., 2020). Dual or triple combination of these stimuli into one nanoplatform is expected to achieve better controlled drug delivery.

CTS is naturally a kind of polysaccharide consisting of randomly distributed repeating units of both N-acetyl-D-glucosamine and N-D-glucosamine, linked through β-(1-4)-glycosidic bonds (Ravi Kumar et al., 2000). These structural characteristics grant CTS degradability, pH sensitivity, and enzyme sensitivity. Due to these extra properties, CTS is an extraordinary alternative for intelligent and multistage drug release (Ravi Kumar et al., 2000; Zhou et al., 2020).

In this work, novel nanocarriers based on CTS layers surrounding AgNPs were developed (**Figure 1**). For immobilizing CTS, a double-cross-linking approach was used with functionalized AgNPs (forming a core–shell structure) and disulfide-containing BAC (offering redox sensitivity). PVA assembling with CTS layers during synthesis, referring to the double emulsion route, provided the engineered nanoparticles improved colloidal stability. Moreover, these nanocarriers were employed to load DOX (CAB@DOX) for cancer therapy. In the current study, CAB@DOX could respond to acidic pH, GSH, and lysozyme, causing a satisfactory drug release. In parallel, the triple responsive character also allowed CAB@DOX to shrink their size, enabling DOX preferential accumulation in the nucleus. Coupling the aforementioned properties, CAB@DOX harvested superior anticancer performance compared with free DOX.

MATERIALS AND METHODS

Materials

Chitosan (CTS) and silver nitrate ($AgNO_3$) were purchased from Sinopharm Chemical Reagent Co., Ltd. (Shanghai, China). Trisodium citrate (TSC), polyvinyl alcohol (PVA), bis(2-ethylhexyl) sulfosuccinate sodium salt (AOT), and sodium borohydride ($NaBH_4$) were purchased from Aladdin Chemical Reagent Co., Ltd., (Shanghai, China). N, N′-bisacrylamide cystamine (BAC) was purchased from Alfa Aesar Chemical Co., Ltd. (Shanghai, China). Doxorubicin (DOX) was purchased from Dalian Meilun Biotechnology Co., Ltd. (Dalian, China). CAL27 cells (human oral squamous cell carcinoma cell line, OSCC) were derived from the First Affiliated Hospital of Nanchang University (Nanchang, China). Dulbecco-modified eagle medium (DMEM) and fetal bovine serum (FBS) were obtained from GIBCO Co., Ltd. (California, United States). Unless otherwise stated, the other chemical reagents were purchased from the Chinese Pharmaceutical Chemical Reagent Co., Ltd. (Shanghai, China), and the biological reagents were bought from Sigma-Aldrich (MO, United States). The abbreviations used in this article are summarized as follows: Ag-BAC (bAG), CTS/Ag-BAC (CAB), and CTS/Ag-BAC@DOX (CAB@DOX).

Preparation of Nanoparticles

AgNPs were prepared according to the approach reported in the literature (Wang et al., 2020). In brief, TSC (29.41 mg) was mixed

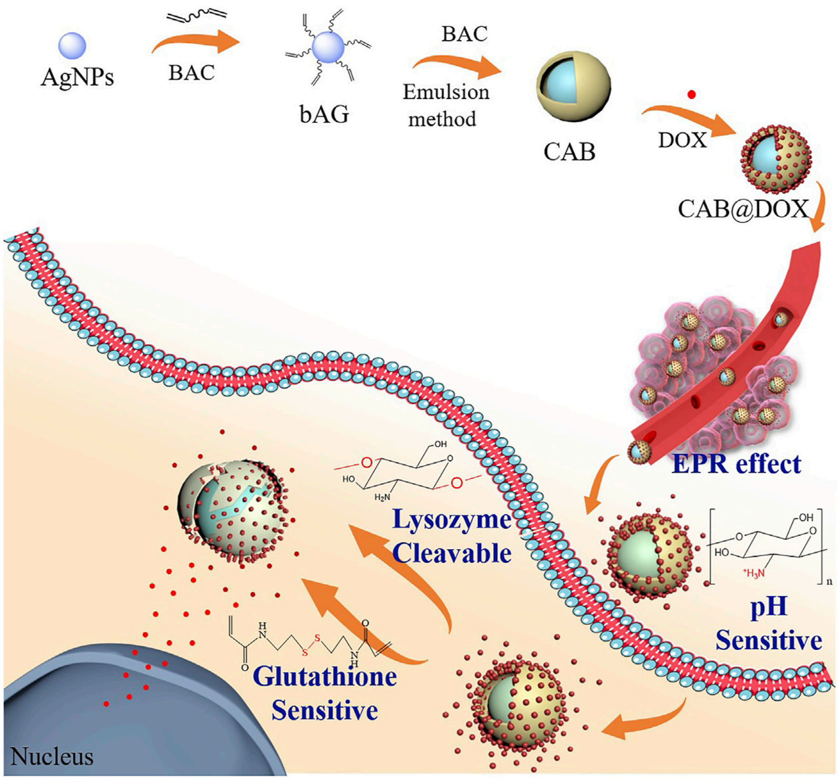

FIGURE 1 | Synthesis scheme of CTS/Ag-BAC@DOX (CAB@DOX) based on chitosan and PVA coating on the AgNP surface by the emulsion method and schematic illustration of its enhanced anticancer mechanisms involving transformable size and multi-responsive drug release.

with $NaBH_4$ (1 mg) in 40 ml of ultrapure water, and the reaction solution was stirred for 30 min at 60°C. Then, after the temperature was raised to 90°C, silver nitrate (10 mg) was added dropwise into the mixture at a pH of 10.5 and stirred for another 20 min, followed by cooling at room temperature. The spherical AgNPs were thus obtained by centrifugation at 12,000 rpm for 20 min and washed with distilled water. Next, the AgNPs and BAC (n (Ag): n (BAC) = 1:2) were mixed in the presence of sodium dodecyl sulfate (SDS) and stirred for 2 h to obtain bAG. After dialysis for 3 days using a dialysis bag (MW: 8000-14000), the obtained nanoparticle solution was preserved at 4°C.

CAB was synthesized using the emulsion method. Specifically, CTS was dissolved in acetic acid solutions (1% v/v) under continuous stirring to prepare a clear solution of chitosan (1 mg/ml). The solution is then mixed with an equal volume of bAG solution, followed by dropwise addition into the 8 ml of dioctyl sulfosuccinate sodium salt (AOT) solution in dichloromethane (2.5 wt%) and kept on stirring for 10 min. Subsequently, the mixture was added dropwise into PVA (30 ml, 2 wt%) with vigorous stirring for the second emulsification. To further cross-link CTS, 1 ml of BAC (5 mg/ml) was added into the mixture and stirred overnight. Last, the CAB solution was obtained by centrifugation at 10,000 rpm and washed 3 times, followed by preservation at 4°C. Additionally, 3 ml of the obtained nanoparticle solutions were lyophilized, respectively, to settle the amounts of nanoparticles for further experiments.

Characterization

The morphology of different samples was detected using a transmission electron microscopy (TEM, JEM-210003040700, Japan). The hydrodynamic diameter and surface charge of different samples were tested using a particle analyzer (Nano ZS 90, Malvern). A UV–Vis spectrophotometer (V-670, Japan) was used to collect the absorbance spectra of different samples. The chemical structure of analyzed samples was studied using a Fourier Transform Infrared (FTIR) spectrometer (Bruker, Germany).

Loading and Release of Doxorubicin

One milliliter of DOX aqueous solution at a concentration of 2 mg/ml was added to 5 ml of CAB nanoparticles solution and allowed to stir for 24 h. Then, the mixture was dialyzed against PBS with a dialysis bag (MW: 8000-14000), and the dialysate was collected 9 times. The drug amount in the dialysate was calculated based on the absorbance values. The encapsulation efficiency (EE %) of DOX was calculated according to the following formula:

$$EE\% = \frac{w_T - w_D}{w_T} \times 100\%$$

where W_T is the total content of the used DOX during the preparation and W_D is the amount remaining in the dialysate.

To test the breakability of these nanocarriers, CAB@DOX was suspended in a PBS solution (pH 5) of 5 mM of reduced GSH and lysozyme with a concentration of 5 μg/ml for 2 and 24 h. Next, the solution was initially sonicated for 10 minutes and then allowed for TEM analysis.

To evaluate the drug release, 1 ml of CAB loading DOX inside a dialysis bag was placed into 30 ml of PBS solutions with different pH (5.0, 6.5, and 7.4), respectively. At defined time points, 3-ml aliquots were withdrawn from the outside solution to measure its absorbance and replaced with 0.5 ml of fresh PBS solution to keep the overall volume of the solution unchanged. The percentage of DOX released from CAB@DOX (Cr %) was evaluated according to the following formula:

$$C_r = \frac{w_d}{w_T} \times 100\%$$

where W_d is the cumulative amount of DOX released at defined time points and W_T is denoted as total DOX amount contained in CAB. For assessing the release kinetics of CAB@DOX in the absence or presence of lysozyme (5 μg/ml) and GSH (5 mM, 10 mM), the same approach was performed.

In Vitro Cytotoxicity and Cellular Uptake

CAL27 cells and MTT assays were employed to evaluate the biocompatibility and toxicity of the drug. Briefly, the cells were seeded into a 96-well plate at a cell density of 5×10^5 per well for 24 h incubation. Then, culture medium in each well was removed and replaced with 100 μL of fresh DMEM containing CAB, DOX, and CAB@DOX. The concentration of DOX (2.0 μM) in the DOX group and CAB@DOX group were adjusted to equalization before being fed into the well. After incubation for another 24 h, the cells were washed 3 times, and 10 μL of MTT (5 mg/ml) was added to each well for further 4 h incubation. Finally, the cells without any medium were incubated with 150 μL of DMSO for 10 min. The corresponding absorbance per well was detected using a microplate reader at 490 nm. The relative viability (CV %) was calculated by the following formula:

$$CV\% = \frac{OD_{eg}}{OD_{cg}} \times 100\%,$$

where OD_{eg} is the OD value for the experimental group and OD_{cg} is the OD value for the untreated control group.

To evaluate the cell survival and death, CAL27 cells were seeded into the 20-mm CLSM cell culture dish. After the cell confluence reached approximately 70%, the initial medium was replaced by fresh PBS solution containing DOX and CAB@DOX for 24-h incubation, respectively, in which the concentration of DOX was maintained at 2 μM. Then, these treated cells were stained with AO/EB for 15 min and imaged under a confocal microscope (CLSM, Nikon C2, Japan).

To demonstrate the superiority of CAB in aiding DOX to enter cells, the efficiency of cellular uptake in the free group and CAB@DOX group was evaluated. CAL27 cells were seeded into the 20-mm CLSM cell culture dish at a density of 1×10^6 cells. After incubation for 24 h, DOX and CAB@DOX solutions with an equivalent DOX concentration (2 μM) were fed into the dish for further incubation. Later, the solutions were removed at the time points of 4 and 24 h, followed by washing 3 times, and fixing with 4% paraformaldehyde for 30 min. Next, the cells were washed 3 times again and fixed with DAPI for 5 min, followed by washing 3 times. Finally, the samples were subjected to observations with CLSM.

In Vivo Antitumor Studies

Nude mice were brought from Charles River Experimental Animal Co., Ltd. (Beijing, China). All animals were used and handled in accordance with the Guidelines for the Care and Use of Laboratory Animals of Nanchang University. The xenograft OSCC model was established by injecting 100 μL of PBS containing 1×10^7 CAL27 cells subcutaneously in the right side of the oxter of the nude mice. After the tumor volume reached 150 mm^3, the experimental nude mice were randomly allocated into three groups. Each group was injected intraperitoneally with 1 ml of three kinds of solution (PBS, DOX, CAB@DOX). The dosage of DOX was 4 mg kg^{-1} for each mouse. The tumor volume and body weight were determined daily. After 21 days, the heart, liver, spleen, lung, and kidney together with tumor were harvested, followed by fixing with 4% paraformaldehyde solution and sectioning. Next, the tissue slides were stained with hematoxylin and eosin (H&E) in accordance with the standard procedure (Liu et al., 2018). Furthermore, the tissue slides were analyzed using terminal deoxynucleotidyl transferase-mediated dUTP-biotin nick-end labeling (TUNEL) assays (Sharma et al., 2021) to evaluate the antitumor efficacy. Furthermore, blood samples of nude mice with different treatment were collected for biochemical analyses on the 21st day.

Statistical Analysis

Data were presented as mean ± standard deviation. The differences among the independent groups were evaluated by using a two-tailed unpaired Student's t-test, and the differences between multiple groups were evaluated by the one-way analysis of variance (ANOVA). $^*p < 0.05$, $^{**}p < 0.01$, and $^{***}p < 0.001$ were used to express the level of significance.

RESULTS AND DISCUSSION

Preparation and Characterization of Nanoparticles

In contrast to gold nanoparticles, AgNP perhaps is a more valuable nanomaterial on account of lower cost and higher reactivity, which widens the accessibility of surface functionalization (Desireddy et al., 2013). Recently, great efforts were spent to utilize the AgNPs as vehicles for cancer treatment (Zeng et al., 2018; Gomes et al., 2021). To optimize colloidal stability and drug loading, AgNPs are commonly subjected to surface modification with natural macromolecules which embrace outstanding biocompatibility (Akter et al., 2018; Gutierrez et al., 2020). As a representative material of natural polysaccharides, CTS has been approved by the U.S. Food and Drug Administration (FDA) employed in a variety of foods. Of note, CTS possessing the properties of intelligence and biodegradability makes them available for drug delivery,

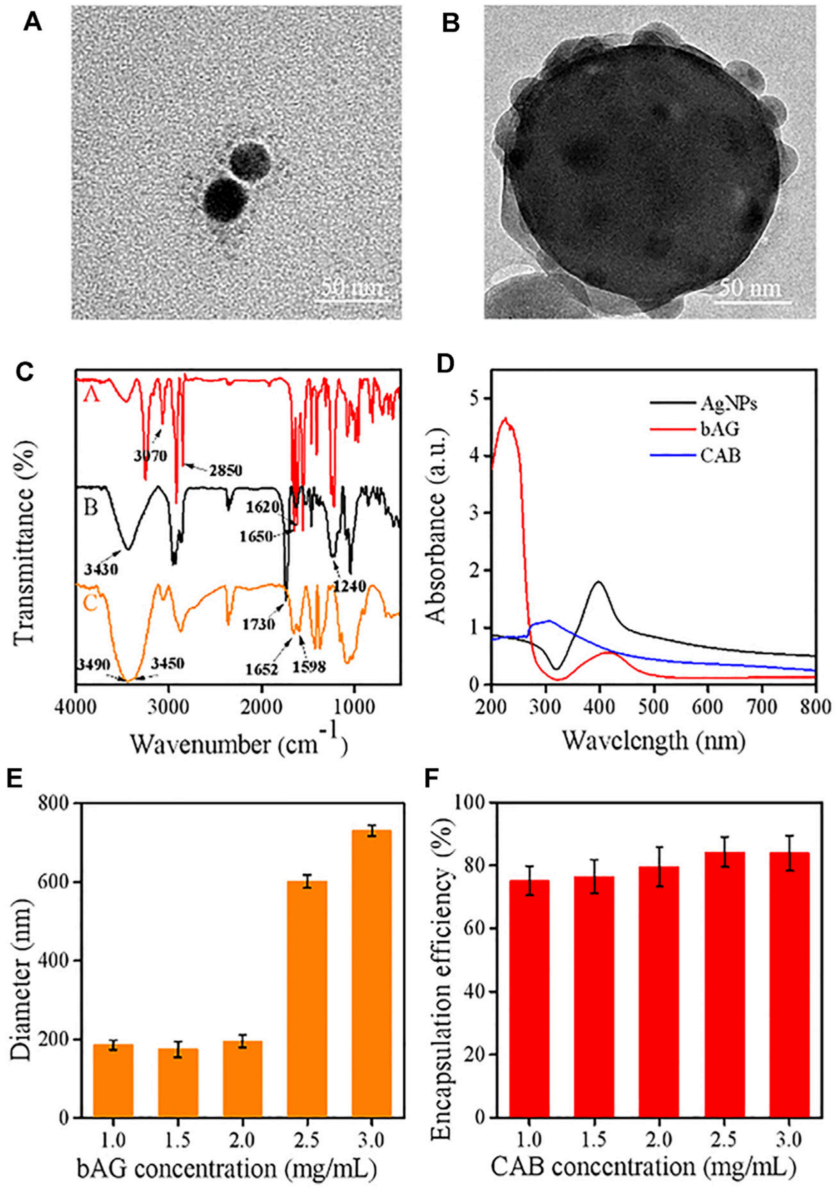

FIGURE 2 | TEM images of **(A)** bAG and **(B)** CAB; **(C)** FT-IR spectra of various samples [bAG **(A)**, CAB **(B)**, and CTS **(C)**]; **(D)** UV–visible absorption spectra of AgNPs, bAG, and CAB; **(E)** effect of bAG concentration on the CAB size; **(F)** effect of CAB concentration on the DOX encapsulation efficiency.

especially in the form of nanogel (Divya et al., 2017; Jafari et al., 2021).

In this work, a type of hybrid AgNPs was prepared by coating the CTS shell containing PVA. Bare AgNPs were initially synthesized which exhibited homogeneous dispersion and size distribution around 36 ± 3 nm (**Supplementary Figure S1**). Subsequently, with the cleavage of the disulfide linkage of BAC, the cystamine units containing terminal carbon–carbon double bonds were anchored onto the surface of AgNP through the Ag-S covalent bond (Huang et al., 2021). The TEM image showed that the size of bAG was slightly larger than AgNPs (**Figure 2A**), supporting the successful modification. Then, the modified AgNPs allowed for cross-linking CTS through the Michael addition reaction between -C=C and -NH_2 of CTS. To enhance the structural stability, BAC was reintroduced to react with CTS, resulting in the formulation of double-cross-linked nanoparticles (CAB). Due to the existence of disulfide bonds, CAB were sensitive to the reductive environment. The TEM analysis of the CAB showed that AgNPs were densely encapsulated by CTS (**Figure 2B**). Furthermore, the preparation process followed a double emulsion method. The emulsifier, PVA, used in this process was able to self-assemble with chitosan through electrostatic interactions. **Figure 2B** provides visual evidence of successful introduction of PVA as contrast could be observed in the outmost layer.

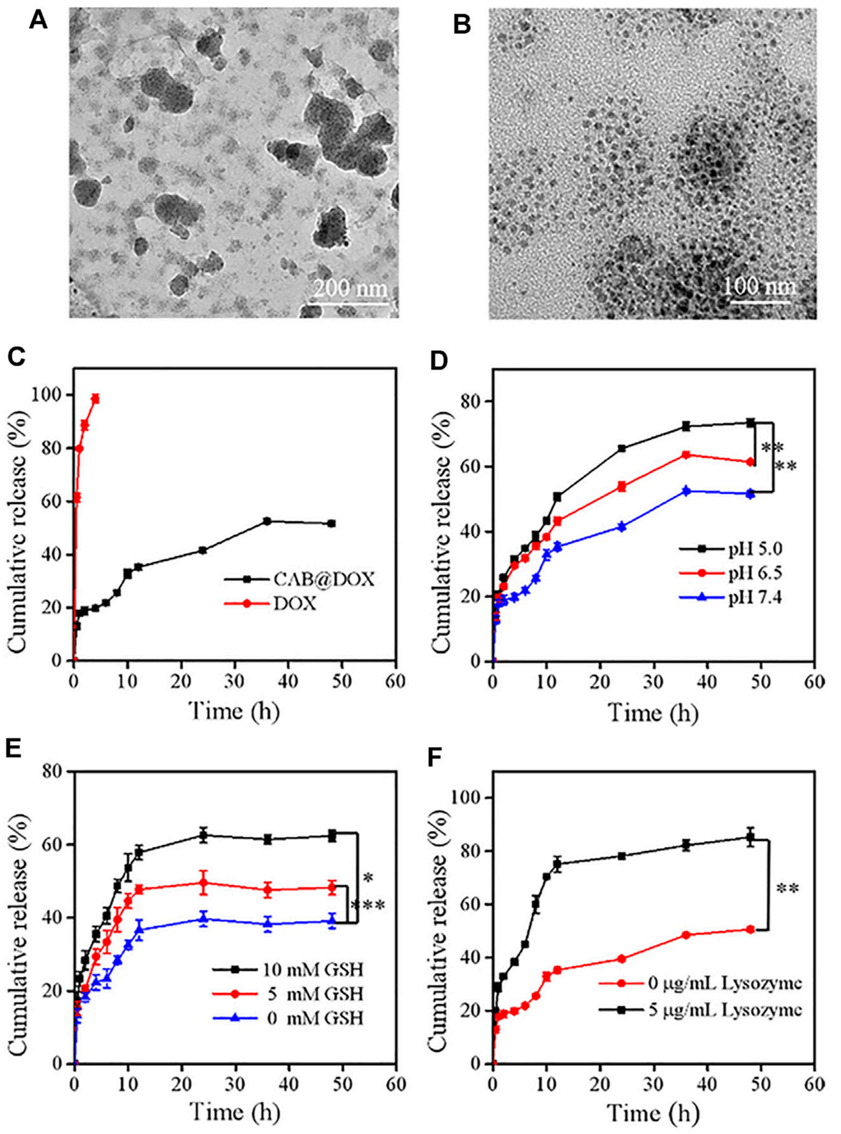

FIGURE 3 | Degradation and release behaviors of CAB@DOX in a stimulation environment *in vitro*. The degradation TEM of CAB@DOX in pH 5, 5 mM GSH, and 5 μg/ml lysozyme of PBS solution for **(A)** 2 h and **(B)** 24 h. **(C)** Release profiles of DOX, CAB@DOX in PBS buffer (pH 7.4) at 37°C; **(D)** profiles of DOX release from CAB at pH values of 5.0, 6.5, and 7.4; **(E)** release profiles of DOX in the presence of different concentrations of GSH (0 mM, 5.0, and 10.0 mM); **(F)** release profiles of DOX in the absence or presence of 5 μg/ml of lysozyme.

The colloidal stability of metallic nanoparticles is a concerning factor, which affects their application potential in the biomedical field. In case of noble metals, AgNPs are the most likely to aggregate. While used in organisms, the aggregates might not only lead to accelerated elimination by the reticuloendothelial system but also cause severe toxicity. Therefore, the colloidal stability of CAB was investigated by using the dispersion test in Ultra-water, DMEM, and PBS, respectively. During the 7-day observation, there was no obvious precipitation for the three groups (**Supplementary Figure S2**), demonstrating the coating agent could well alter the surface attributes of AgNPs and help remove a key obstacle of AgNPs for clinical translation.

FTIR measurements were used to manifest the successful modification of AgNPs. In the spectrum of bAG, two characteristic peaks appeared at 1,650 cm^{-1} and 1,620 cm^{-1}, which were attributed to -C=C- stretch vibration and -C(=O)-NH_2 stretch vibration, respectively. These results suggested successful modification of AgNPs with cystamine unit (Wang et al., 2020; Jafari et al., 2021). Moreover, the FTIR spectrum of CTS exhibited peaks located at 3,490 cm^{-1} and 3,450 cm^{-1}, while a new peak presented at 3,430 cm^{-1} in CAB, indicating primary amines transformed into secondary amines. Meanwhile, the peak at 1,420 cm^{-1} in the spectrum of CAB was assigned to the formation of -C-N- bonds, which

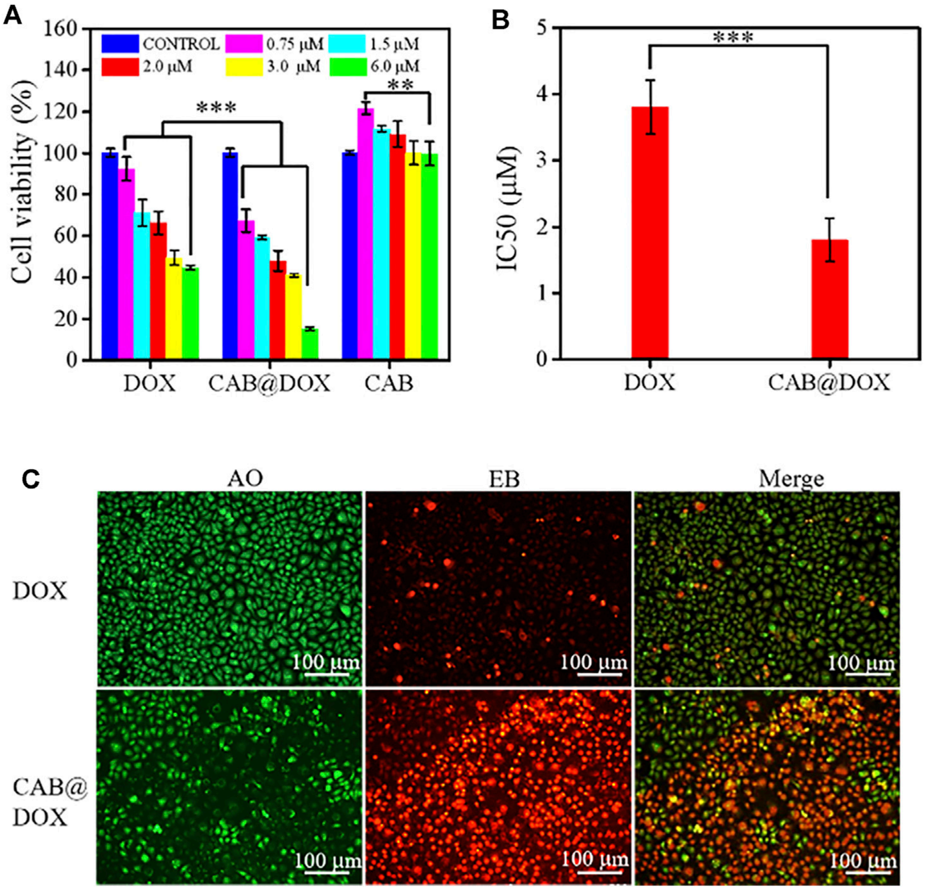

FIGURE 4 | *In vitro* biocompatibility and growth inhibition in CAL27 cells. **(A)** Cell viability of CAL27 cells cultured with different concentration of DOX, CAB@DOX, and CAB for 24 h; **(B)** IC50 value of DOX and CAB@DOX; **(C)** AO/EB staining fluorescence images of CAL27 cells treated with DOX and CAB@DOX for 24 h.

implied the occurrence of Michael's addition reaction (**Figure 2C**). In UV/Vis absorption spectrum, the maximum absorption wavelength in AgNPs and bAG were, respectively, at 400 and 426 nm. The red shift of peak was related to the increase in diameter and thus confirmed successful conjunction of the cystamine unit (**Figure 2D**).

The circulation time determines the ultimate fates of nanoscale drugs, in which particle size and surface charge play a vital role (Patra et al., 2018). In the research setting, a suitable diameter for extending the circulation and targeting tumor accumulation should be less than 200 nm. Therefore, the effects of CTS and bAG at different concentrations on diameters were tested by DLS. It could be observed that the higher was the concentration of CTS, the smaller was the particle size (**Supplementary Figure S3A**). This result might be ascribed to the higher concentration of CTS that made the nanoparticles more compact. As shown in **Figure 2E**, the size of CAB significantly increased in pace with the rise of bAG concentration restricted to 1.0 ~ 3.0 mg/ml. Specifically, adjusting the bAG concentration to 1.0 mg/ml resulted in a diameter of 175 ± 3 nm. Furthermore, the surface charge of nanoparticles affects the adsorption of opsonin and subsequent elimination by macrophages. In pharmacokinetics, the negatively charged nanoparticles reduce the likelihood of phagocytic uptake, facilitating circulation time elongation. Although coated with cationic CTS, CAB showed a negative surface charge. The relationship between CAB potential and bAG concentration is shown in **Supplementary Figure S3B**. At a high bAG concentration, the value of potential was low, which might be attributed to the additional introduction of negatively charged bAG. More importantly, the shell layer accomplished a high loading of cationic DOX at up to 80% encapsulation efficiency, which is favorable for the therapeutic effect. As positively charged CTS possesses poor cationic drug absorption, this nanoplatform might broaden the range of loaded drugs for CTS (**Figure 2F**).

Drug Release and Degradation Assays *In Vitro*

The initial size of AgNPs was 36 nm and increased to around 175 nm after being decorated with CTS. To evaluate the shrinkable capacity, CAB@DOX was incubated in PBS (pH 5.0) with GSH (5 mM) along with lysozyme (5 μg/ml) analog to cancerous cells. After being treated for 2 h, the particles showed decreased size and inhomogeneous distribution (**Figure 3A**), suggesting that nanoparticles could disassemble. This result was

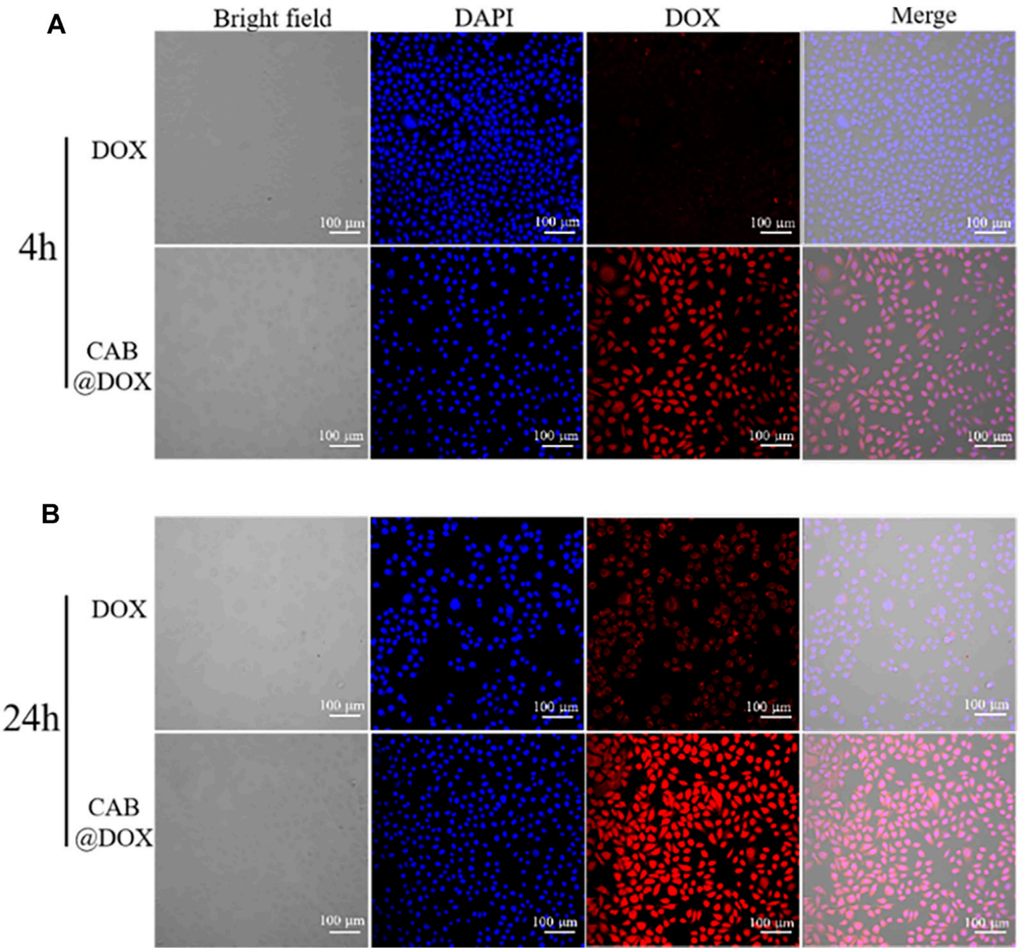

FIGURE 5 | Confocal images of CAL27 cells after incubation with free DOX and CAB@DOX for **(A)** 4 h and **(B)** 24 h.

presumably due to the cleavage of intramolecular β-(1-4)-glycosidic bonds and disulfide bonds in CTS and BAC, while encountering such a microenvironment. At a time interval of 24 h, the variation of CAB@DOX was extremely marked, and many smaller particles were obtained ranging at 10–20 nm (**Figure 3B**). It has been reported that smaller CTS nanoparticles (<39 nm) had a greater chance of localizing in the nucleus (Tammam et al., 2015). CAB@DOX with such size-variable characteristics was consequently beneficial for targeting nucleic delivery of DOX.

The release behavior of DOX, which significantly affects its therapeutic bioactivity, was investigated. Generally, ideal nanodevices should recognize especially the tumor microenvironment, speeding up drug release selectively. Also, they should avoid premature drug leakage under physiological conditions which may lead to off-target effects. Detected by the dialysis approach, free DOX molecules could permeate through the dialysis membrane easily and CAB could heavily suppress the release of DOX as a diffusion barrier (**Figure 3C**). Considering the breakability of CAB@DOX, the unique conditions of tumor tissue could readily trigger the release of DOX. Compared with neutral conditions (pH 7.4), DOX release tended to be much faster during the first 12 h responding to a weakly acidic environment, representing neoplastic interstitial microenvironment (pH 6.5) and endo/lysosomes (pH 5.0) (**Figure 3D**) (Bazban et al., 2017). This difference was profoundly related to ionization of amino groups and the swelling up of CTS (Ahmed et al., 2016). Furthermore, the concentration of GSH in tumor cells (2–10 mM) is 10 times more than that of normal tissue (2–20 μM) (Tu et al., 2017), causing a high redox state. Clearly, upon facing the high level of GSH, the drug release was boosted, reaching about 60% for 15 h (**Figure 3E**). The introduction of disulfide bonds might contribute to accelerated drug release in a reductive environment. Additionally, the enzymes (e.g., lysozyme, phospholipase, and glycosidase) are a fascinating element to design smart DDSs as they are often overexpressed in tumor tissues for cell growth, invasion, and metastasis (Li et al., 2017; Zhou et al., 2020). The cumulative release ratio of DOX in the presence of lysozyme was 80% after 12 h which was 2-fold as high as that in the absence of lysozyme (**Figure 3F**). Nearly all the loaded drug released might be a consequence of the degradation of CAB. By lysozyme, CAB could vary to one hundred smaller

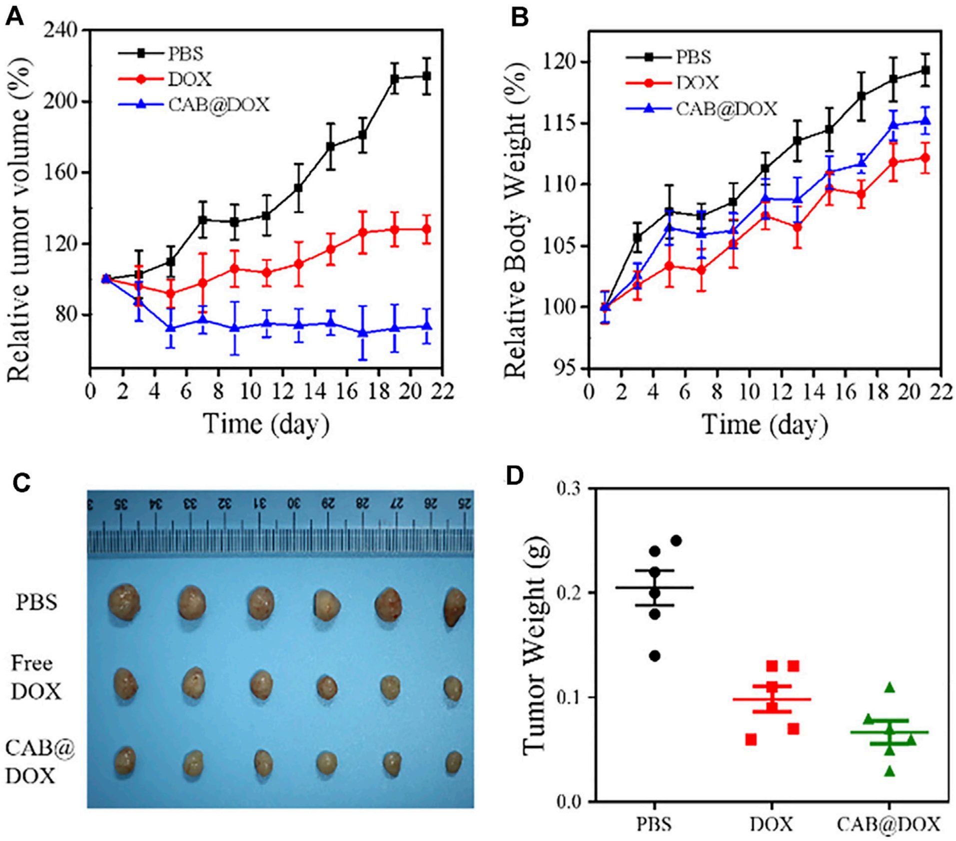

FIGURE 6 | *In vivo* antitumor activity of CAB@DOX in OSCC-bearing mice. **(A)** Relative tumor volume in tumor-bearing mice; **(B)** Relative body weight of the tumor-bearing mice; **(C)** representative images of resected tumors after 21 days of various treatment; **(D)** tumor weight of nude mice.

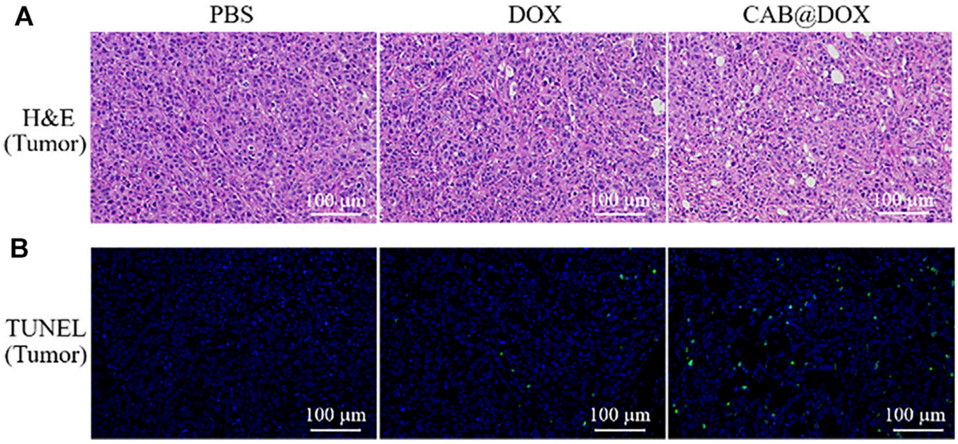

FIGURE 7 | (A) H&E staining of tumors; **(B)** apoptotic cell detection by TUNEL immunofluorescence staining.

sized nanocarriers through the cleavage of β-(1-4)-glycosidic bonds, accompanied with massive drug release. The aforementioned experimental results fully demonstrated CAB@DOX embraced good stability under physiological conditions, lowering unwanted side effects. Furthermore, CAB@DOX experienced sufficient drug release responding to stimulated malignant cell conditions featuring weak acidity, high glutathione (GSH) levels, and overexpressed lysozyme. It was

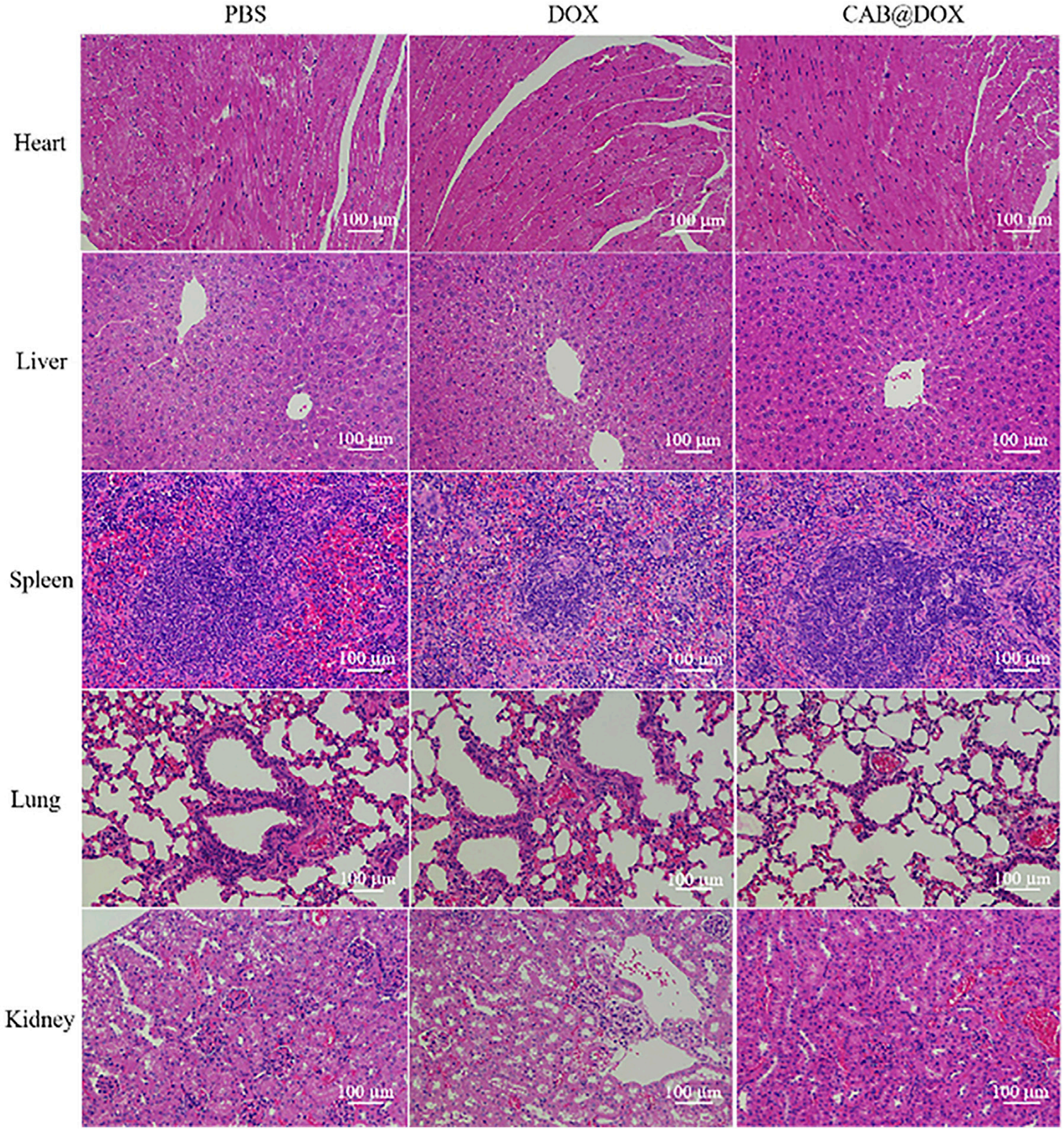

FIGURE 8 | Histological analysis of the vital organs (heart, liver, spleen, lung, and kidney) of mice treated with PBS, DOX, and CAB@DOX, respectively.

expected the triple responsive nature would give rise to a high intracellular drug level.

In Vitro Cytotoxicity and Growth Inhibition in CAL27 Cells

The capability of CAB@DOX to induce cellular apoptosis was evaluated. CAL27 cells were incubated with free DOX and CAB@DOX at different DOX concentrations. In the assays, the concentration of CAB@DOX was expressed based on the DOX content. As shown in both groups, an apparent trend of reduced cell viability was observed at an increasing DOX concentration from 0.75 to 6 μM (**Figure 4A**). Furthermore, in contrast, the proportion of non-viable cells treated with CAB@DOX was larger in all studied concentrations. These results were likely related to high drug loading efficiency and on-demand drug release of CAB@DOX, which caused a corresponding increase in the availability of DOX to targets of action. The grand challenge in AgNP design for drug delivery lies in toxicity (Caballero et al., 2013). For clinical adoption, it is critical to develop many safety AgNP-based vectors. Since CTS and PVA are fascinating biocompatible materials and could render AgNPs a hydrophilic surface to resist aggregation, this nanohybrid might have reduced toxicity. As anticipated, CAL27 cells

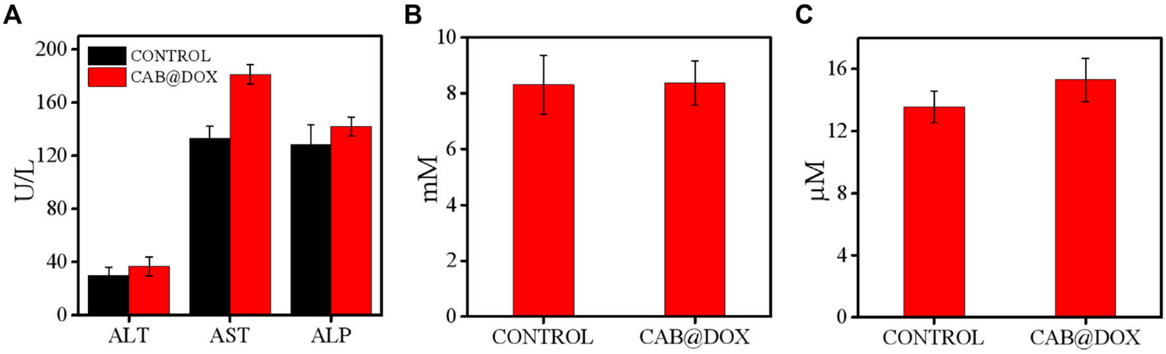

FIGURE 9 | Blood biochemistry indicators including **(A)** ALT, AST, ALP, **(B)** BUN, and **(C)** CRE with or without CAB@DOX, respectively (*n* = 6).

showed no signs of loss in cell viability after incubation with empty CAB even at a high concentration (**Figure 4A**), suggesting that CAB alone was biocompatible and itself did not contribute to the anticancer effect of this transporter–drug conjugate. Furthermore, IC50 of CAB@DOX in the CAL27 cell line at 24 h was 1.9 μM, which was 2-fold less than that of free DOX (~3.8 μM) (**Figure 4B**). Next, more intuitive cytotoxicity assays were conducted by using an AO/EB double staining experiment. Remarkably, most cancerous cells were killed (orange fluorescence) in the CAB@DOX group, while large amounts of cells remained alive (green fluorescence) treated with free DOX (**Figure 4C**). The IC50 value and AO/EB assays further confirmed the great potential of CAB aiding in DOX to implement potent anticancer activity.

In Vitro Cellular Uptake

The potential mechanism of antitumor activity was further elucidated by CLSM. As the nucleus is the main interaction site of DOX, the capability of reaching the nucleus was highlighted. In the first 4-h incubation, DOX alone entered cells slowly as red fluorescence signals were drastically weak. However, strong red fluorescence was observed and overlapped extensively with nuclei in the CAB@DOX group (**Figure 5A**). The rapid cellular uptake of CAB@DOX putatively resulted from CAB@DOX passing through the cell membrane in a manner of endocytosis, which was more efficient than passive diffusion of free DOX (Wang et al., 2012). When increasing the incubation time to 24 h, more DOX entered the cells and enriched the nuclei in the CAB@DOX group, indicating the cellular uptake was in a time-dependent pattern. In sharp contrast, few DOXs were seen in the cytoplasm. Although intracellular DOX in the free DOX group increased, it is mainly located at the peri-nucleus (**Figure 5B**). DOX are internalized into nuclei as soon as they enter the cells in the CAB@DOX group, which might be due to the transformable capability of CAB. In nucleus-targeting nanotherapeutics, creating a transformable vector is the most prevalent resolution as the needs for long circulation time and subcellular drug trafficking are contrary design elements. Specifically, the large particle size avoids excretion by the kidney, while the small size allows for intercellular deep drug delivery. It has been demonstrated nanoparticles of 40 nm diameter enable faster diffusion into the nucleus (Pan et al., 2018). In light of degradation assay, in the cytoplasm, CAB@DOX is capable of responding to the pathological environment, emits smaller sized carriers (less than 40 nm), and consequently concentrates DOX in the nucleus. Therefore, CAB@DOX can exhibit a better inhibitory effect on tumor cells than most DOX-loaded carriers (e.g., mesoporous silica (MSN), carbon nanotubes (CNTs), and hydroxyapatite (HAp)) as the latter could not transport DOX to the site of action (Dong et al., 2017; Llinas et al., 2018; Ghosh et al., 2020).

In Vivo Antitumor Activity

The antitumor efficacy of CAB@DOX *in vivo* was evaluated during the 21-day treatment process. These mice were allocated into three groups randomly (*n* = 6): PBS, DOX, and CAB@DOX. As expected, the tumor volume of the PBS-treated mice increased rapidly, whereas the tumor growth of the nude mice in the free DOX group and CAB@DOX group was markedly inhibited (**Figure 6A**). In particular, the treatment efficacy in the CAB@DOX group was much more apparent than that of the DOX group, and the difference between the two groups could reach 3 times. On day 21, all the mice were killed for tumor collection. It was found that CAB@DOX displayed much higher inhibition efficiency against tumor growth than free DOX (**Figures 6C**,D). Based on the results, it could be demonstrated the great potential of CAB@DOX against OSCC which resulted from enhanced cellular uptake, stimulus-responsive drug release, and higher drug accumulation in nuclei. Furthermore, the fluctuation in body weight is a direct indicator of drug toxicity. Compared with the control, no meaningful difference of body weight change was observed in the CAB@DOX-treated mice over the course of treatment, which might be related to the fact that CAB@DOX effectively reduced side effects caused by DOX (**Figure 6B**).

To further confirm the therapeutic outcome *in vivo*, H&E staining and TUNEL assays were performed. As displayed in **Figure 7A**, severe cancerous cell damage (pyknosis, fragmentation, and lysis) was observed by H&E staining in the CAB@DOX group, which was consistent with the results of the relative tumor volume study. Similarly, TUNEL assays were carried out on the resected tumors, which is a general method to assess apoptotic cells in tumors. **Figure 7B** shows that CAB@DOX induced significant apoptosis in the tumors, while DOX-treated tumors showed an obvious low rate of apoptosis. Therefore, it could be confirmed that DOX loaded in the CAB was more likely to eliminate cancerous cells than systemic direct administration.

The potential toxicity of DOX, also displayed by the change of body weight, impedes its clinical use. Under the results of assays *in vitro*, good parameters for colloidal stability, and selective drug release, CAB@DOX might imply a low biotoxicity. Herein, the biosafety of CAB@DOX was further investigated. All mice were killed at day 21 posttreatment, followed by capturing photographs (**Supplementary Figure S4**), and the H&E staining exhibited no off-target damage to vital organs (liver, heart, lung, kidney, and spleen) (**Figure 8**). Additionally, the blood of the killed mice was collected for blood biochemistry analysis. Eventually, no significant differences were found between CAB@DOX-treated groups and the control group in the blood biochemistry indicators (i.e., alanine transaminase (ALT), aspartate aminotransferase (AST), alkaline phosphatase (ALP), blood urea nitrogen (BUN), and creatinine (CRE)) (**Figure 9**). These outcomes indicated CAB@DOX had negligible side effects and could effectively lower the heart and kidney damage induced by DOX. Although the current work revealed the potential of CAB in improving drug safety, there was still needed more assays to systematically study long-term toxicity.

CONCLUSION

In summary, we rationally developed a core–shell nanocarrier. AgNPs were used as the core, with a well-defined size of around 175 nm. The coatings consisting of CTS and PVA stabilized particles against agglomerates, offering a novel way for developing AgNP-based materials in biomedicine. Moreover, the final nanoparticles, CAB, exhibited high DOX encapsulation efficiency for 80%, which is favorable for antitumor efficacy. While encountering the environment analogous to a cancerous cell, CAB disassembled and emitted smaller sized nanoblocks (10–20 nm). Meanwhile, shrunk nanoparticles allowed for accelerated DOX release and thus help achieve desired drug bioavailability. Due to these properties, DOX loaded in CAB is easily enriched in the nucleus, leading to an obvious inhibitory effect toward CAL27 cells. Using a human oral squamous cell carcinoma-bearing mouse model, CAB@DOX exhibited an enhanced antitumor efficacy than free DOX while showing a negligible influence on normal cells and tissues. Taken together, the nanohybrid is a promising vehicle for cancer therapy which can deliver other types of drugs in the future.

DATA AVAILABILITY STATEMENT

The original contributions presented in the study are included in the article/**Supplementary Material**, further inquiries can be directed to the corresponding author.

ETHICS STATEMENT

The animal study was reviewed and approved by the Animal Ethics Committee of Nanchang University.

AUTHOR CONTRIBUTIONS

LL proposed the study, designed the experiments, and administrated the whole project. ZL and DZ carried out the experiments together, and ZL drafted the original manuscript. All authors have read and agreed to the published version of the manuscript.

FUNDING

This work was supported by the National Natural Science Foundation of China (Nos 82160194 and 81960492), the Natural Science Foundation of Jiangxi Province (20181ACB20022), and the Key Research and Development Program of Jiangxi Province (20212BBG73022).

SUPPLEMENTARY MATERIAL

The Supplementary Material for this article can be found online at: https://www.frontiersin.org/articles/10.3389/fbioe.2022.882308/full#supplementary-material

REFERENCES

Ahmed, T., and Aljaeid, B. (2016). Preparation, Characterization, and Potential Application of Chitosan, Chitosan Derivatives, and Chitosan Metal Nanoparticles in Pharmaceutical Drug Delivery. *Dddt* 10, 483–507. doi:10.2147/dddt.s99651

Akter, M., Sikder, M. T., Rahman, M. M., Ullah, A. K. M. A., Hossain, K. F. B., Banik, S., et al. (2018). A Systematic Review on Silver Nanoparticles-Induced Cytotoxicity: Physicochemical Properties and Perspectives. *J. Adv. Res.* 9, 1–16. doi:10.1016/j.jare.2017.10.008

Austin, L. A., Kang, B., Yen, C.-W., and El-Sayed, M. A. (2011). Plasmonic Imaging of Human Oral Cancer Cell Communities during Programmed Cell Death by Nuclear-Targeting Silver Nanoparticles. *J. Am. Chem. Soc.* 133, 17594–17597. doi:10.1021/ja207807t

Azizi, M., Ghourchian, H., Yazdian, F., Bagherifam, S., Bekhradnia, S., and Nyström, B. (2017). Anti-cancerous Effect of Albumin Coated Silver Nanoparticles on MDA-MB 231 Human Breast Cancer Cell Line. *Sci. Rep.* 7, 5178. doi:10.1038/s41598-017-05461-3

Badawy, A. M. E., Luxton, T. P., Silva, R. G., Scheckel, K. G., Suidan, M. T., and Tolaymat, T. M. (2010). Impact of Environmental Conditions (pH, Ionic Strength, and Electrolyte Type) on the Surface Charge and Aggregation of Silver Nanoparticles Suspensions. *Environ. Sci. Technol.* 44, 1260–1266. doi:10.1021/es902240k

Bazban-Shotorbani, S., Hasani-Sadrabadi, M. M., Karkhaneh, A., Serpooshan, V., Jacob, K. I., Moshaverinia, A., et al. (2017). Revisiting Structure-Property Relationship of pH-Responsive Polymers for Drug Delivery Applications. *J. Controlled Release* 253, 46–63. doi:10.1016/j.jconrel.2017.02.021

Caballero-Díaz, E., Pfeiffer, C., Kastl, L., Rivera-Gil, P., Simonet, B., Valcárcel, M., et al. (2013). The Toxicity of Silver Nanoparticles Depends on Their Uptake by Cells and Thus on Their Surface Chemistry. *Part. Part. Syst. Charact.* 30, 1079–1085. doi:10.1002/ppsc.201300215

Chen, E., Chen, B.-M., Su, Y.-C., Chang, Y.-C., Cheng, T.-L., Barenholz, Y., et al. (2020). Premature Drug Release from Polyethylene Glycol (PEG)-coated Liposomal Doxorubicin *via* Formation of the Membrane Attack Complex. *ACS Nano* 14, 7808–7822. doi:10.1021/acsnano.9b07218

Cheng, R., Meng, F., Deng, C., and Zhong, Z. (2015). Bioresponsive Polymeric Nanotherapeutics for Targeted Cancer Chemotherapy. *Nano Today* 10, 656–670. doi:10.1016/j.nantod.2015.09.005

Desireddy, A., Conn, B. E., Guo, J., Yoon, B., Barnett, R. N., Monahan, B. M., et al. (2013). Ultrastable Silver Nanoparticles. *Nature* 501, 399–402. doi:10.1038/nature12523

Divya, K., and Jisha, M. S. (20172017). Chitosan Nanoparticles Preparation and Applications. *Environ. Chem. Lett.* 16, 101–112. doi:10.1007/s10311-017-0670-y

Dong, X., Sun, Z., Wang, X., Zhu, D., Liu, L., and Leng, X. (2017). Simultaneous Monitoring of the Drug Release and Antitumor Effect of a Novel Drug Delivery system-MWCNTs/DOX/TC. *Drug Deliv.* 24, 143–151. doi:10.1080/10717544.2016.1233592

Duan, X., and Li, Y. (2013). Physicochemical Characteristics of Nanoparticles Affect Circulation, Biodistribution, Cellular Internalization, and Trafficking. *Small* 9, 1521–1532. doi:10.1002/smll.201201390

Ghosh, S., Ghosh, S., and Pramanik, N. (2020). Bio-evaluation of Doxorubicin (DOX)-incorporated Hydroxyapatite (HAp)-Chitosan (CS) Nanocomposite Triggered on Osteosarcoma Cells. *Adv. Compos. Hybrid Mater.* 3, 303–314. doi:10.1007/s42114-020-00154-4

Gomes, H. I. O., Martins, C. S. M., and Prior, J. A. V. (2021). Silver Nanoparticles as Carriers of Anticancer Drugs for Efficient Target Treatment of Cancer Cells. *Nanomaterials* 11, 964. doi:10.3390/nano11040964

Gutierrez, L., Schmid, A., Zaouri, N., Garces, D., and Croue, J.-P., (2020). Colloidal Stability of Capped Silver Nanoparticles in Natural Organic Matter-Containing Electrolyte Solutions. *NanoImpact* 19, 100242. doi:10.1016/j.impact.2020.100242

Hama, M., Ishima, Y., Chuang, V. T. G., Ando, H., Shimizu, T., and Ishida, T. (2021). Evidence for Delivery of Abraxane *via* a Denatured-Albumin Transport System. *ACS Appl. Mater. Inter.* 13, 19736–19744. doi:10.1021/acsami.1c03065

Hotze, E. M., Phenrat, T., and Lowry, G. V. (2010). Nanoparticle Aggregation: Challenges to Understanding Transport and Reactivity in the Environment. *J. Environ. Qual.* 39, 1909–1924. doi:10.2134/jeq2009.0462

Huang, B., Liu, X., Li, Z., Zheng, Y., Wai Kwok Yeung, K., Cui, Z., et al. (2021). Rapid Bacteria Capturing and Killing by AgNPs/N-CD@ZnO Hybrids Strengthened Photo-Responsive Xerogel for Rapid Healing of Bacteria-Infected Wounds. *Chem. Eng. J.* 414, 128805. doi:10.1016/j.cej.2021.128805

Huang, H., Feng, W., Chen, Y., and Shi, J. (2020). Inorganic Nanoparticles in Clinical Trials and Translations. *Nano Today* 35, 100972. doi:10.1016/j.nantod.2020.100972

Jafari, H., Mahdavinia, G. R., Kazemi, B., Ehrlich, H., Joseph, Y., and Rahimi-Nasrabadi, M. (2021). Highly Efficient Sunitinib Release from pH-Responsive mHPMC@chitosan Core-Shell Nanoparticles. *Carbohydr. Polym.* 258, 117719. doi:10.1016/j.carbpol.2021.117719

Jiang, Y., Meng, X., Wu, Z., and Qi, X. (2016). Modified Chitosan Thermosensitive Hydrogel Enables Sustained and Efficient Anti-tumor Therapy *via* Intratumoral Injection. *Carbohydr. Polym.* 144, 245–253. doi:10.1016/j.carbpol.2016.02.059

Karimi, M., Ghasemi, A., Sahandi Zangabad, P., Rahighi, R., Moosavi Basri, S. M., Mirshekari, H., et al. (2016). Smart Micro/nanoparticles in Stimulus-Responsive Drug/gene Delivery Systems. *Chem. Soc. Rev.* 45, 1457–1501. doi:10.1039/c5cs00798d

Li, H.-J., Du, J.-Z., Du, X.-J., Xu, C.-F., Sun, C.-Y., Wang, H.-X., et al. (2016). Stimuli-responsive Clustered Nanoparticles for Improved Tumor Penetration and Therapeutic Efficacy. *Proc. Natl. Acad. Sci. U.S.A.* 113, 4164–4169. doi:10.1073/pnas.1522080113

Li, N., Cai, H., Jiang, L., Hu, J., Bains, A., Hu, J., et al. (2017). Enzyme-sensitive and Amphiphilic PEGylated Dendrimer-Paclitaxel Prodrug-Based Nanoparticles for Enhanced Stability and Anticancer Efficacy. *ACS Appl. Mater. Inter.* 9, 6865–6877. doi:10.1021/acsami.6b15505

Liu, J., Zhang, L., Ren, Y., Gao, Y., Kang, L., and Qiao, Q. (2014). Anticancer and Immunoregulatory Activity of Gynostemma Pentaphyllum Polysaccharides in H22 Tumor-Bearing Mice. *Int. J. Biol. Macromolecules* 69, 1–4. doi:10.1016/j.ijbiomac.2014.05.014

Liu, S., Khan, A. R., Yang, X., Dong, B., Ji, J., and Zhai, G. (2021). The Reversal of Chemotherapy-Induced Multidrug Resistance by Nanomedicine for Cancer Therapy. *J. Controlled Release* 335, 1–20. doi:10.1016/j.jconrel.2021.05.012

Llinàs, M. C., Martínez-Edo, G., Cascante, A., Porcar, I., Borrós, S., and Sánchez-García, D. (2018). Preparation of a Mesoporous Silica-Based Nano-Vehicle for Dual DOX/CPT pH-Triggered Delivery. *Drug Deliv.* 25, 1137–1146. doi:10.1080/10717544.2018.1472678

Mi, P. (2020). Stimuli-responsive Nanocarriers for Drug Delivery, Tumor Imaging, Therapy and Theranostics. *Theranostics* 10, 4557–4588. doi:10.7150/thno.38069

Mitchell, M. J., Billingsley, M. M., Haley, R. M., Wechsler, M. E., Peppas, N. A., Langer, R., et al. (2021). Engineering Precision Nanoparticles for Drug Delivery. *Nat. Rev. Drug Discov.* 20, 101–124. doi:10.1038/s41573-020-0090-8

Niu, Y., Zhu, J., Li, Y., Shi, H., Gong, Y., Li, R., et al. (2018). Size Shrinkable Drug Delivery Nanosystems and Priming the Tumor Microenvironment for Deep Intratumoral Penetration of Nanoparticles. *J. Controlled Release* 277, 35–47. doi:10.1016/j.jconrel.2018.03.012

Pan, L., Liu, J., and Shi, J. (2018). Cancer Cell Nucleus-Targeting Nanocomposites for Advanced Tumor Therapeutics. *Chem. Soc. Rev.* 47, 6930–6946. doi:10.1039/C8CS00081F

Patra, J. K., Das, G., Fraceto, L. F., Campos, E. V. R., Rodriguez-Torres, M. D. P., Acosta-Torres, L. S., et al. (2018). Nano Based Drug Delivery Systems: Recent Developments and Future Prospects. *J. Nanobiotechnol* 16, 71. doi:10.1186/s12951-018-0392-8

Pędziwiatr-Werbicka, E., Gorzkiewicz, M., Horodecka, K., Abashkin, V., Klajnert-Maculewicz, B., Peña-González, C. E., et al. (2020). Silver Nanoparticles Surface-Modified with Carbosilane Dendrons as Carriers of Anticancer siRNA. *Ijms* 21, 4647. doi:10.3390/ijms21134647

Penson, R. T., Valencia, R. V., Cibula, D., Colombo, N., Leath, C. A., Bidziński, M., et al. (2020). Olaparib versus Nonplatinum Chemotherapy in Patients with Platinum-Sensitive Relapsed Ovarian Cancer and a Germline BRCA1/2 Mutation (SOLO3): a Randomized Phase III Trial. *Jco* 38, 1164–1174. doi:10.1200/JCO.19.02745

Qiu, L., Li, J.-W., Hong, C.-Y., and Pan, C.-Y. (2017). Silver Nanoparticles Covered with pH-Sensitive Camptothecin-Loaded Polymer Prodrugs: Switchable Fluorescence "off" or "on" and Drug Delivery Dynamics in Living Cells. *ACS Appl. Mater. Inter.* 9, 40887–40897. doi:10.1021/acsami.7b14070

Rai, M., Ingle, A. P., Birla, S., Yadav, A., and Santos, C. A. D. (2016). Strategic Role of Selected noble Metal Nanoparticles in Medicine. *Crit. Rev. Microbiol.* 42, 1–24. doi:10.3109/1040841X.2015.1018131

Ravi Kumar, M. N. V. (2000). A Review of Chitin and Chitosan Applications. *Reactive Funct. Polym.* 46, 1–27. doi:10.1016/S1381-5148(00)00038-9

Ruan, S., Cao, X., Cun, X., Hu, G., Zhou, Y., Zhang, Y., et al. (2015). Matrix Metalloproteinase-Sensitive Size-Shrinkable Nanoparticles for Deep Tumor Penetration and pH Triggered Doxorubicin Release. *Biomaterials* 60, 100–110. doi:10.1016/j.biomaterials.2015.05.006

Schubert, J., and Chanana, M. (2018). Coating Matters: Review on Colloidal Stability of Nanoparticles with Biocompatible Coatings in Biological media, Living Cells and Organisms. *Cmc* 25, 4553–4586. doi:10.2174/0929867325666180601101859

Sharma, R., Iovine, C., Agarwal, A., and Henkel, R. (2021). TUNEL Assay-Standardized Method for Testing Sperm DNA Fragmentation. *Andrologia* 53 (2), e13738. doi:10.1111/and.13738

Sharma, V. K., Siskova, K. M., Zboril, R., and Gardea-Torresdey, J. L. (2014). Organic-coated Silver Nanoparticles in Biological and Environmental Conditions: Fate, Stability and Toxicity. *Adv. Colloid Interf. Sci.* 204, 15–34. doi:10.1016/j.cis.2013.12.002

Stolnik, S., Illum, L., and Davis, S. S. (2012). Long Circulating Microparticulate Drug Carriers. *Adv. Drug Deliv. Rev.* 64, 290–301. doi:10.1016/j.addr.2012.09.029

Tammam, S. N., Azzazy, H. M., Breitinger, H. G., and Lamprecht, A. (2015). Chitosan Nanoparticles for Nuclear Targeting: the Effect of Nanoparticle Size and Nuclear Localization Sequence Density. *Mol. Pharmaceutics* 12, 4277–4289. doi:10.1021/acs.molpharmaceut.5b00478

Tan, M., Liu, W., Liu, F., Zhang, W., Gao, H., Cheng, J., et al. (2019). Silk Fibroin-Coated Nanoagents for Acidic Lysosome Targeting by a Functional Preservation Strategy in Cancer Chemotherapy. *Theranostics* 9, 961–973. doi:10.7150/thno.30765

Tang, S., Meng, Q., Sun, H., Su, J., Yin, Q., Zhang, Z., et al. (2016). Tumor-microenvironment-adaptive Nanoparticles Codeliver Paclitaxel and siRNA to Inhibit Growth and Lung Metastasis of Breast Cancer. *Adv. Funct. Mater.* 26, 6033–6046. doi:10.1002/adfm.201601703

Tu, Y., Peng, F., White, P. B., and Wilson, D. A. (2017). Redox-sensitive Stomatocyte Nanomotors: Destruction and Drug Release in the Presence of Glutathione. *Angew. Chem. Int. Ed.* 56, 7620–7624. doi:10.1002/anie.201703276

Tzounis, L., Doña, M., Lopez-Romero, J. M., Fery, A., and Contreras-Caceres, R. (2019). Temperature-controlled Catalysis by Core-Shell-Satellite AuAg@pNIPAM@Ag Hybrid Microgels: a Highly Efficient Catalytic Thermoresponsive Nanoreactor. *ACS Appl. Mater. Inter.* 11, 29360–29372. doi:10.1021/acsami.9b10773

Wang, S., Wu, X., Tan, M., Gong, J., Tan, W., Bian, B., et al. (2012). Fighting Fire with Fire: Poisonous Chinese Herbal Medicine for Cancer Therapy. *J. Ethnopharmacology* 140, 33–45. doi:10.1016/j.jep.2011.12.041

Wang, Y., Gao, D., Zhou, D., Li, Y., Wang, X., He, P., et al. (2020). Multifunctional Ag/polymer Composite Nanospheres for Drug Delivery and Cell Imaging. *J. Mater. Sci.* 55, 13995–14007. doi:10.1007/s10853-020-04912-z

Xie, P., and Liu, P. (2020). pH-Responsive Surface Charge Reversal Carboxymethyl Chitosan-Based Drug Delivery System for pH and Reduction Dual-Responsive Triggered DOX Release. *Carbohydr. Polym.* 236, 116093. doi:10.1016/j.carbpol.2020.116093

Xu, L., Wang, Y.-Y., Huang, J., Chen, C.-Y., Wang, Z.-X., and Xie, H. (2020). Silver Nanoparticles: Synthesis, Medical Applications and Biosafety. *Theranostics* 10, 8996–9031. doi:10.7150/thno.45413

Yang, Y., Guo, L., Wang, Z., Liu, P., Liu, X., Ding, J., et al. (2021). Targeted Silver Nanoparticles for Rheumatoid Arthritis Therapy *via* Macrophage Apoptosis and Re-polarization. *Biomaterials* 264, 120390. doi:10.1016/j.biomaterials.2020.120390

Zeng, F., Xu, D., Zhan, C., Liang, C., Zhao, W., Zhang, J., et al. (2018). Surfactant-free Synthesis of Graphene Oxide Coated Silver Nanoparticles for SERS Biosensing and Intracellular Drug Delivery. *ACS Appl. Nano Mater.* 1, 2748–2753. doi:10.1021/acsanm.8b00444

Zhou, D., Liu, S., Hu, Y., Yang, S., Zhao, B., Zheng, K., et al. (2020). Tumor-mediated Shape-Transformable Nanogels with pH/redox/enzymatic-Sensitivity for Anticancer Therapy. *J. Mater. Chem. B* 8, 3801–3813. doi:10.1039/D0TB00143K

Conflict of Interest: The authors declare that the research was conducted in the absence of any commercial or financial relationships that could be construed as a potential conflict of interest.

ORIGINAL RESEARCH
published: 12 April 2022
doi: 10.3389/fbioe.2022.873125

Peptide-Grafted Microspheres for Mesenchymal Stem Cell Sorting and Expansion by Selective Adhesion

Shuo Wu[1], Zongliang Wang[2], Yu Wang[2], Min Guo[2], Mengyang Zhou[1], Liqiang Wang[3], Jie Ma[1]* and Peibiao Zhang[2]*

[1]School of Pharmaceutical Sciences, Jilin University, Changchun, China, [2]Key Laboratory of Polymer Ecomaterials, Changchun Institute of Applied Chemistry, Chinese Academy of Sciences, Changchun, China, [3]Department of Ophthalmology, Third Medical Center, Chinese PLA General Hospital, Beijing, China

Mesenchymal stem cells (MSCs) have considerable value in regenerative medicine because of their unique properties such as pluripotency, self-renewal ability, and low immunogenicity. Isolation and purification are prerequisites for various biomedical applications of MSCs, and traditional sorting methods are often expensive, complicated, and difficult to apply on a large scale. In addition to purification, the requirement for expansion of cells also limits the further application of MSCs. The purpose of this study was to develop a unique magnetic sorting microsphere to obtain relatively pure and high-yield MSCs in an economical and effective way, that can also be used for the expansion of MSCs. Poly (ethylene glycol) (PEG)-based anti-adhesive treatment of the prepared oleic acid grafted Fe_3O_4-poly (lactic-co-glycolic acid) magnetic microspheres was performed, and then E7 peptide was covalently grafted onto the treated microspheres. Upon a series of characterization, the magnetic microspheres were of uniform size, and cells were unable to adhere to the PEG-treated surface. E7 grafting significantly improved cell adhesion and proliferation. The results obtained from separate culture of various cell types as well as static or dynamic co-culture showed that selective adhesion of MSCs was observed on the magnetic sorting microspheres. Furthermore, the cells expanded on the microspheres maintained their phenotype and typical differentiation potentials. The magnetic properties of the microspheres enabled sampling, distribution, and transfer of cells without the usage of trypsin digestion. And it facilitated the separation of cells and microspheres for harvesting of MSCs after digestion. These findings have promising prospects for MSC research and clinical applications.

Keywords: surface modification, mesenchymal stem cells, peptide, cell sorting, magnetic microspheres

Edited by:
Yuangang Liu,
Huaqiao University, China

Reviewed by:
Zhengwei Mao,
Zhejiang University, China
Zhongkui Hong,
University of South Dakota,
United States

***Correspondence:**
Jie Ma
ma_jie@jlu.edu.cn
Peibiao Zhang
zhangpb@ciac.ac.cn

Specialty section:
This article was submitted to Biomaterials, a section of the journal Frontiers in Bioengineering and Biotechnology

Received: *10 February 2022*
Accepted: *09 March 2022*
Published: *12 April 2022*

Citation:
Wu S, Wang Z, Wang Y, Guo M, Zhou M, Wang L, Ma J and Zhang P (2022) Peptide-Grafted Microspheres for Mesenchymal Stem Cell Sorting and Expansion by Selective Adhesion. Front. Bioeng. Biotechnol. 10:873125. doi: 10.3389/fbioe.2022.873125

1 INTRODUCTION

Mesenchymal stem cells (MSCs) are fibroblast-like, multipotent, self-renewing adult cells that have been found in various adult tissues, including adipose tissue (Zuk et al., 2001), bone marrow (Pittenger et al., 1999), and umbilical cords (Wang et al., 2004). These cells possess immunomodulatory effects (Yagi et al., 2010), regenerative potential (Zipori, 2004; Picinich et al., 2007), tendency to migrate to site of injury (Sohni and Verfaillie, 2013), and low immunogenicity (Yagi et al., 2010). Because of these inherent properties, MSCs are being researched globally in the context of cell and tissue therapies (including *in vitro* and animal models) to make them therapeutically available for various diseases such as myocardial infarction (Blocki et al., 2015), diabetes (Urban et al., 2008), rheumatoid arthritis (Papadopoulou et al., 2012), acute graft-versus-host disease (Sanchez-Guijo et al., 2014), osteogenesis imperfecta (Gotherstrom et al., 2021), Parkinson's disease (Meligy et al., 2019), and Alzheimer's disease (Zhao et al., 2021). Initially, Friedenstein and others developed cultures of MSCs based on their intrinsic physical characteristics that allowed them to attach to the surface of plastic flasks or dishes (Friedenstein et al., 1970). Although this method is time-consuming and only heterogeneous cell populations (Xu et al., 1983; Alhadlaq and Mao, 2004) can be obtained, many laboratories continue to use plastic adhesion methods to isolate MSCs because of the lack of credible purification protocols.

Many techniques have been developed, such as density gradient centrifugation, fluorescent-activated cell sorter (FACS) (Herzenberg et al., 2002), and magnetic-activated cell sorter (MACS) (Schmitz et al., 1994). Although the density gradient centrifugation method enables extraction of cells with a high degree of purity, the first fusion of primary cells takes a long time (Li et al., 2013). FACS and MACS, which are affinity-based methods, also have some limitations such as limited sample throughput and processing speed as well as high operating pressure, which may lead to loss of cell function or vitality; bulky instruments occupying a large number of workbenches; and the requirement for technical expertise to operate complex machinery (Nicodemou et al., 2017). Antibodies, at present, are the mainstay of affinity-based cell purification because of their high capture strength and selectivity. However, antibodies are expensive and generally have low biochemical stability (Ruigrok et al., 2011). In addition, their strong binding ability often makes cell elution challenging (Bacon et al., 2020), and only specific MSCs can be obtained by this method (Nadri and Soleimani, 2007). In recent years, peptides have become a cost-effective and robust substitute for protein ligands (Ruigrok et al., 2011). The E7 peptide (EPLQLKM) has been discovered and used to specifically capture MSCs *in vitro* and *in vivo* due to its strong and specific affinity with MSCs. E7 can bind to human (Shao et al., 2012), rabbit (Meng et al., 2017), and rat (Wu et al., 2019) bone marrow MSCs without species-specificity. The use of poly (ethylene glycol) (PEG) molecules to bind protein ligands and thereby enhance the specificity of the target cells is also coming into view (Yu et al., 2018). Because of its hydrophilic and bioinert properties (Chien et al., 2012; Raos et al., 2018), PEG is considered one of the most widely used and effective antifouling polymers. It also works as an "interlayer" to improve the pliability of the immobilized biomolecules, thus increasing their biological activity (Yu et al., 2011).

The application of MSCs not only requires purity but also raises the need for efficient cell production techniques. Obtaining a sufficient number of cells from source cells requires a large *in vitro* expansion scheme (Kabat et al., 2020). For effective expansion of cells *in vitro*, the method of cultivating cells under a three-dimensional (3D) environment has received increasing attention (Antoni et al., 2015). It can supply a proper spatial environment for cell distribution and provide a natural extracellular matrix (ECM)-simulation environment to enhance the biological activity of cells (Flemming et al., 1999). As carriers for cell multiplication on 3D surfaces, microspheres have proven ideal for cell expansion (Gao et al., 2015; Leong and Wang, 2015), with the following remarkable advantages: 1) simple preparation process; and 2) high specific surface area for maximizing space efficiency and promoting cell attachment and proliferation (Leong and Wang, 2015). Compared with planar culture, microsphere-based culture poses a challenge for harvesting cells. After cell separation, it is necessary to remove the microspheres to obtain a pure cell suspension. Regardless of the method used, the harvesting process involves several complicated steps, which must be carried out in time. A protein-coated microcarrier GEM™ (Global Eukaryotic Microcarrier™, Hamilton, Sweden) (Lin et al., 2014) incorporated with internal magnetic particles has been developed, allowing easy recovery of the beads using magnets. This provides a new method for the preparation and application of microcarriers.

In summary, the most critical challenges in the biological application of MSCs are their isolation and culture. To solve these problems, we doped superparamagnetic nanoparticles (NPs) in polymeric matrix to prepare magnetic microspheres. Moreover, by grafting E7 on the surface of the PEGylated microspheres, selective adhesion of MSCs was achieved, and the proliferation of MSCs on the surface of microspheres was promoted. A range of properties such as specific adhesion efficiency, proliferation, and retention of stemness of MSCs on the magnetic sorting microspheres were also explored (**Scheme 1**).

2 MATERIALS AND METHODS

2.1 Materials and Reagents

All reagents were from Aladdin (Aladdin, China), if not otherwise noted. Poly (lactic-co-glycolic acid) (PLGA, LA:GA = 80:20, *M*w = 200,000) was prepared via ring-opening co-polymerization of L-lactide (LA) and glycolide (GA) in our laboratory (Yan et al., 2019).

2.2 Magnetic NP Synthesis

The synthesis of oleic acid grafted Fe_3O_4 (Fe_3O_4-OA) NPs was slightly modified according to the method previously published by our laboratory (Hao et al., 2019). In brief, iron (III) chloride (10.8 g, 40 mM) and sodium oleate (36.5 g, 120 mM) were blended in a mixture of 60 ml distilled water, 80 ml ethanol, and 140 ml n-hexane, in a round bottom flask. Then, the reaction solution was heated to 70°C for a 4 h reflux with violent magnetic stirring. The brown hexane phase was separated from the solution by cooling and washed three times with 30 ml distilled water.

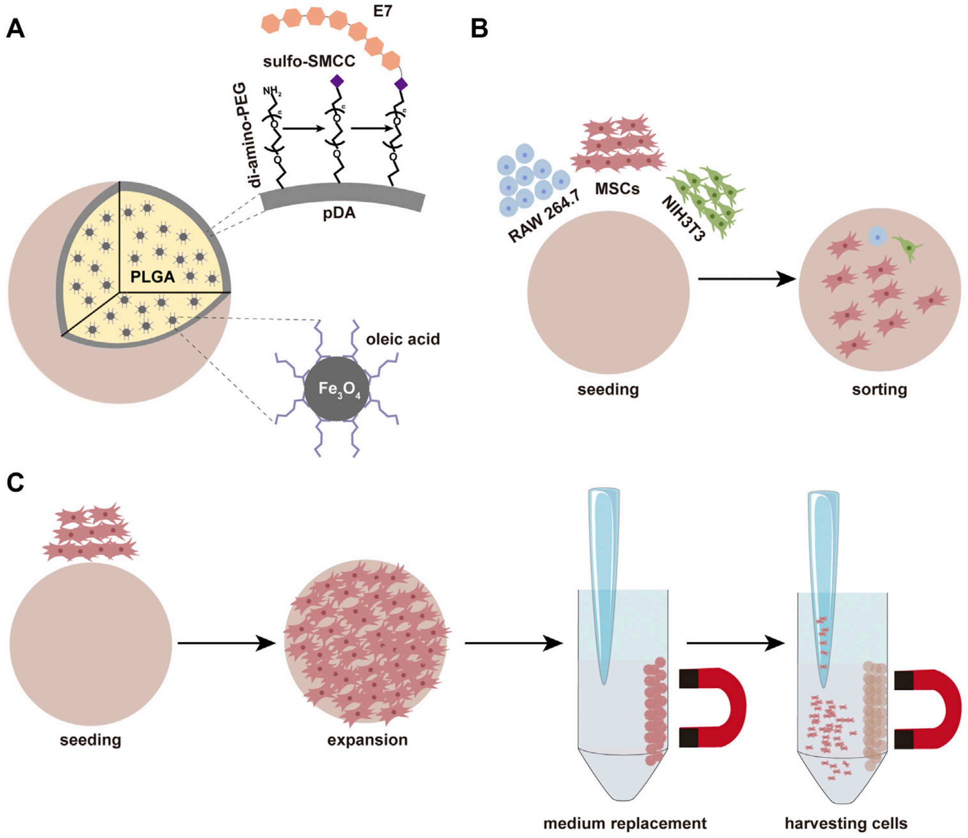

SCHEME 1 | (A) The composition of microspheres and the simple process of modification. **(B)** The microspheres can be used for sorting MSCs. **(C)** The microspheres can be used for the expansion of MSCs.

Then, the hexane phase was transferred to a clean round-bottomed flask and dried in a rotary vacuum evaporator with water bath heating. Subsequently, 6.4 ml oleic acid and 253 ml 1-octadecene were added to the red-brown viscous product. The mixing solution was then ultrasonicated for 30 min to complete dissolution. Finally, a glass capillary was added, and slender branch pipes were connected to the mouth of the flask. After holding at 100°C for 1 h, the reaction mixture was heated to 320°C and held again for 1 h. After cooling down to room temperature, the black products were collected using a magnet, washed three times with 100 ml of petroleum ether, and precipitated with 300 ml of ethanol. The obtained product was dried at room temperature for standby application.

2.3 Fabrication of Fe_3O_4-OA-PLGA Microspheres

Preparation of Fe_3O_4-OA-PLGA microspheres was performed using the high-voltage electrostatic (HVE) technique (Yan et al., 2021). Briefly, PLGA (1 g) and Fe_3O_4-OA NPs (50 mg) were fully dissolved in dichloromethane (DCM, 10 ml). The solution was loaded into a 2 ml syringe with a 27 G needle. The needle tip and the ethanol replacement solution were linked to the positive and negative electrodes of the HVE droplet generator, respectively. The syringe was advanced at a uniform speed. Microspheres were collected through filtration via sieves and washed successively with ethanol solution and distilled water to remove the excess residual organic solvent.

2.4 Modification of Microspheres

To prepare pDA/Fe_3O_4-OA-PLGA microspheres, the obtained Fe_3O_4-OA-PLGA microspheres were immersed in dopamine solution (2 mg ml^{-1}, 10 mM tris, pH = 8.5) for 2 h at room temperature. Then, the pDA/Fe_3O_4-OA-PLGA microspheres were incubated in di-amino-PEG (Mw = 2,000, ToYongbio, China) solution (200 mg ml^{-1}, 10 mM tris, pH = 8.5) at 40°C for 4 h. The modified microspheres were washed with distilled water and termed PEG/pDA/Fe_3O_4-OA-PLGA. In order to enhance the selective adhesion of MSCs, the surface of the microspheres was functionalized with the E7 peptide (GLBiochem, China). The modification of peptide was conducted in the following two ways. 1) The heterobifunctional crosslinker 4-(N-Maleimidomethyl) cyclohexane-1-carboxylic acid 3-sulpho-N-hydroxysuccinimide ester sodium salt (sulfo-SMCC) was used to bind the peptide to the di-amino-PEG molecule on the surface of the microspheres. Sulfo-SMCC was dissolved in distilled water and diluted to

1 mg ml^{-1} with phosphate buffered saline-ethylene diamine tetraacetic acid (PBS-EDTA) coupling buffer. The sulfo-SMCC solution was pipetted into the PEG/pDA/Fe_3O_4-OA-PLGA microspheres, followed by incubation for 1 h at room temperature. The microspheres were then covered with E7 peptide solution (2 mg ml^{-1}, coupling buffer) and incubated overnight at 4°C to obtain E7/PEG/pDA/Fe_3O_4-OA-PLGA. 2) For E7/pDA/Fe_3O_4-OA-PLGA microspheres, pDA/Fe_3O_4-OA-PLGA microspheres were incubated with E7 peptide solution (2 mg ml^{-1}, 10 mM tris, pH = 8.5) overnight at 4°C. If used for cell experiments, the above processes were completed under sterile conditions after the alcohol disinfection of Fe_3O_4-OA-PLGA microspheres. Partial microspheres were dried under vacuum for further characterization.

2.5 Characterization

The chemical structure of Fe_3O_4-OA NPs and PEG-modified microspheres was determined by a Perkin Elmer 2000 FTIR instrument (Perkin Elmer, Germany). A Tecnai G2S-Twin transmission electron microscope (FEI, United States) was used to record the size and shape of the Fe_3O_4-OA NPs. The magnetic properties were determined in a Quantum Design-MPMS-XL7 vibrating sample magnetometer (VSM) system (United States) at 300 K. A Philips XL30 ESEM-FEG instrument (Philips, Japan) was used to observe the surface morphology of microspheres. Elemental mapping was carried out by an XL-30W/TMP scanning electron microscope (Philips, Japan). Static water contact angles were measured using a VCA 2000 contact angle system (AST, United States). The percentage of grafting was measured using a TGA500 thermogravimetry analyzer (TA Instruments, United States). Each sample was heated from room temperature to 600°C at 10°C min^{-1}.

2.6 Cell Isolation and Culture

MSCs were isolated from bone marrow of the tibias and femurs of Sprague-Dawley (SD) rats (100 g, male), as reported previously (Soleimani and Nadri, 2009). The experimental protocol was approved by the Institutional Animal Care and Use Committee of Jilin University School of Pharmaceutical Science. The extracted cells were seeded in a 100-mm cell culture dish (Nest, China) and placed in a humidified incubator at 37°C with 5% CO_2. The culture medium was changed every 3 days until the cells reached 80% confluency for subculture. All experiments were carried out during passages 3–5. NIH3T3 and RAW 264.7 cell lines were purchased from ATCC and cultured under standard conditions.

2.7 Proliferation and Morphology of MSCs on Microspheres

MSCs were seeded at a density of 2 × 10^4 cells well^{-1} in 48-well (containing 30 μl microspheres) for 1, 3, and 7 days. At each predetermined time point, 500 μl of fresh medium containing 30 μl of CCK-8 (Solarbio, China) was used to replace the medium, and the plate was incubated for 2 h at 37°C. After incubation, the solution (100 μl) in each well was pipetted into a new 96-well plate and measured the absorbance at 450 nm using an Infinite M 200 microplate reader (Tecan, Switzerland). For observing the morphology of cells seeded on each microsphere, double staining of 1,1′-dioctadecyl-3,3,3′,3′tetramethylindocarbocyanine perchlorate (DiI) (Meilun Biological, China) and 4′,6-diamidino-2-phenylindole dihydrochloride (DAPI) (Invitrogen, United States) was performed after 3 days. In order to assess the cell area fraction on various microspheres, the image analysis software ImageJ was used.

2.8 Anti-Cell Adhesion Properties of PEG-Modified Microspheres

In order to evaluate the cell-adhesion-resistant effect of PEG/pDA/Fe_3O_4-OA-PLGA microspheres, NIH3T3 cells at a density of 2 × 10^4 cells well^{-1} were seeded on microspheres in a 48-well plate and cultured for 12 h. Cell adhesion was observed by fluorescence microscopy with DAPI staining.

2.9 Selective Adhesion of Separately Cultured Multiple Cells

MSCs, NIH3T3, and RAW 264.7 cells were seeded on the different microspheres in 48-well plates at a density of 2 × 10^4 cells per well. After incubation for 6 h, the microspheres were washed with PBS, respectively stained with DiI, Calcein-AM (Sigma, Germany), and Hoechst 33342 (Beyotime, China), and viewed under a fluorescent microscope.

2.10 Selective Adhesion of Co-Cultured Multiple Cells

2.10.1 Static Culture

According to the manufacturer's instructions, MSCs, NIH3T3, and RAW 264.7 cells were stained with DiI, Calcein-AM and Hoechst 33342, respectively, and co-incubated with a seeding density of 2 × 10^4 in wells for 6 h. Non-adherent cells were washed away with PBS, and the proportion of each cell type was determined by fluorescence microscopy.

All other experimental conditions remained unchanged, except that RAW 264.7 cells were subjected to Calcein-AM staining, and the cells were co-cultured for 12 h to observe their morphology on the microspheres.

2.10.2 Dynamic Culture

Then, 1.5 ml of the same mixed cell suspension was added to a 5 ml-EP (containing 250 μl microspheres) tube at the same density as described above. The EP tube was placed in home-made equipment (**Supplementary Figure S1**) by our laboratory. After blending, the tube was allowed to stand for 40 min and rotated for 10 min at 50 rpm with direction changing every second for 4 h, at 37°C. The proportions of different cells were observed and calculated.

2.11 Stemness of the Adherent MSCs

MSCs cultured on E7/PEG/pDA/Fe_3O_4-OA-PLGA microspheres for 7 days were digested by trypsin digestion for subsequent experiments. An appropriate amount of cells was used to prepare a single-cell suspension, and monoclonal antibodies CD29, CD90, and CD34 (Invitrogen, United States) were added separately to each tube. After incubation at room temperature for 30 min in the dark, the cells were washed with PBS three times to remove the unbound antibodies and detected by flow cytometry. Osteogenic, adipogenic (Puhebio, China), and chondrogenic (Cyagen, China) induction mediums were used instead of basic medium for culture, respectively, to evaluate the differentiation potential of the expanded MSCs. To confirm osteogenesis, cells were stained with the alkaline phosphatase (ALP) assay kit on day 3 of culture and alizarin red on day 14 of culture. Adipogenic differentiation was detected by Oil Red O staining on the 21st day. Alcian blue staining was used to detect the formation of cartilage following 28 days.

2.12 Statistical Analysis

Statistical analysis was conducted using analysis of variance (ANOVA, one-way, Origin 8.0, United States). The data were presented as means ± standard deviations (SD). In each experiment, triplicate samples were evaluated. Significant differences were defined at $p < 0.05$.

3 RESULTS AND DISCUSSION

3.1 Characterization of Magnetic NPs

The dispersion stability of Fe_3O_4-OA NPs was first examined in chloroform. After standing for 50 h, Fe_3O_4 NPs (**Supplementary Figure S2A**) were precipitated, while Fe_3O_4-OA NPs (**Supplementary Figure S2B**) remained well dispersed: given that Fe_3O_4 NPs are poorly dispersed in organic solvents, this was probably due to magnetostatic (magnet dipole-dipole) interactions between magnetic particles (Maity and Agrawal, 2007). However, the mutual repulsion of OA groups on the surface of Fe_3O_4-OA NPs can weaken this phenomenon. This facilitated the preparation of homogeneous magnetic composites. When a magnet was applied, Fe_3O_4-OA NPs were gathered to the side close to the magnet (**Supplementary Figure S2C**), indicating that they had good magnetic responsiveness. Based on these findings, it could be preliminarily concluded that Fe_3O_4-OA NPs were successfully synthesized. Fe_3O_4-OA NPs were characterized using TEM. **Figure 1A** shows TEM images of Fe_3O_4-OA NPs, where it can be seen that the NPs were polygonal and homogeneous in size. TEM images were further analyzed by ImageJ, in which at least 100 NPs were measured (**Figure 1B**). The average size of the NPs was about 15.03 ± 2.47 nm. The size of the individual iron oxide NPs was typical of single domain superparamagnetic iron oxides (Teja et al., 2009), as verified in subsequent magnetic measurements. The magnetization versus the applied field curves was shown in **Figure 1C**. At T = 300 K, neither remanence nor coercivity could be detected for the sample with saturation magnetization of 51.4 emu g^{-1}, indicating that superparamagnetic behavior existed. Superparamagnetic iron oxide nanoparticles are of increasing interest in the biomedical field due to their unique small size, physical properties, low toxicity, and biocompatibility (Neuberger et al., 2005; Hao et al., 2021). As shown in **Figure 1D**, stretching vibration of the Fe-O bonds located at about 578 cm^{-1} was observed in the spectra. In the spectrum of Fe_3O_4-OA NPs, the peak at 2,849 cm^{-1} was due to the symmetrical stretching vibration of methylene groups, while the peak at 2,920 cm^{-1} was attributed to the asymmetric stretching vibration of methylene groups. These bands are a trait of unsaturated hydrocarbon chains of OA. It was found that the two peaks of the sample were concentrated at 1,512 cm^{-1} and 1,417 cm^{-1}, which corresponded to the vibration modes of asymmetric and symmetric carboxylate groups. The stretching vibration of the carbon-carbon double bond in sodium oleate was responsible for the peak at 1,656 cm^{-1}. This indicated that the carboxyl group of oleic acid was chemisorbed on the surface. The weight loss shown by the TGA curve indicated that the grafting of OA on Fe_3O_4-OA NPs was 21.247 wt.%. The peak of the DTA curve for oleic acid in **Figure 1E** was at 270.66°C, while the peak of the DTA curve for Fe_3O_4-OA was at 349.91°C. This weight loss was related to the decomposition of OA covalently bonded to the surface of the NPs (Mahdavi et al., 2013).

3.2 Characterization of Microspheres

Macroscopic observation showed that the Fe_3O_4-OA-PLGA microspheres (right) were darker in color than the Fe_3O_4-PLGA microspheres (left) (**Supplementary Figure S3A**). This was caused by the presence of oleic acid on the surface of Fe_3O_4-OA NPs. The alkane chains on the surface of Fe_3O_4-OA NPs improved the interfacial compatibility with the hydrophobic polymer matrix (Okassa et al., 2007; Hao et al., 2019). Therefore, the dispersion of Fe_3O_4-OA NPs in PLGA solution was more uniform than that of Fe_3O_4 NPs, and the NPs were not easy to precipitate and clog the needle. As seen from the optical microscope, these microspheres were round and regular (**Figure 2A**), with a diameter of about 273.07 ± 19.09 μm (**Figure 2B**). The surface morphology of different microspheres was observed by SEM (**Figure 2C**). Because they were formed by solvent extraction, the microspheres had well-formed sphericity and a porous surface. After pDA modification, the microspheres acquired a rough surface, although their spherical shape was preserved. The saturation magnetization was 2.5 emu g^{-1} for microspheres (**Figure 2D**). The magnetic field had a significant effect on the distribution of microspheres: in the absence of a magnet (**Supplementary Figure S3B**), the microspheres in the water gradually sank because of gravity. After applying the magnet (**Supplementary Figure S3C**), the microspheres were quickly attracted to the vial wall near the magnet.

3.3 Characterization of PEGylated Microspheres

PEG is a versatile polymer that is non-toxic and FDA-approved for use in biomedical research applications, including tissue engineering and drug discovery (Raina et al., 2021). Because of

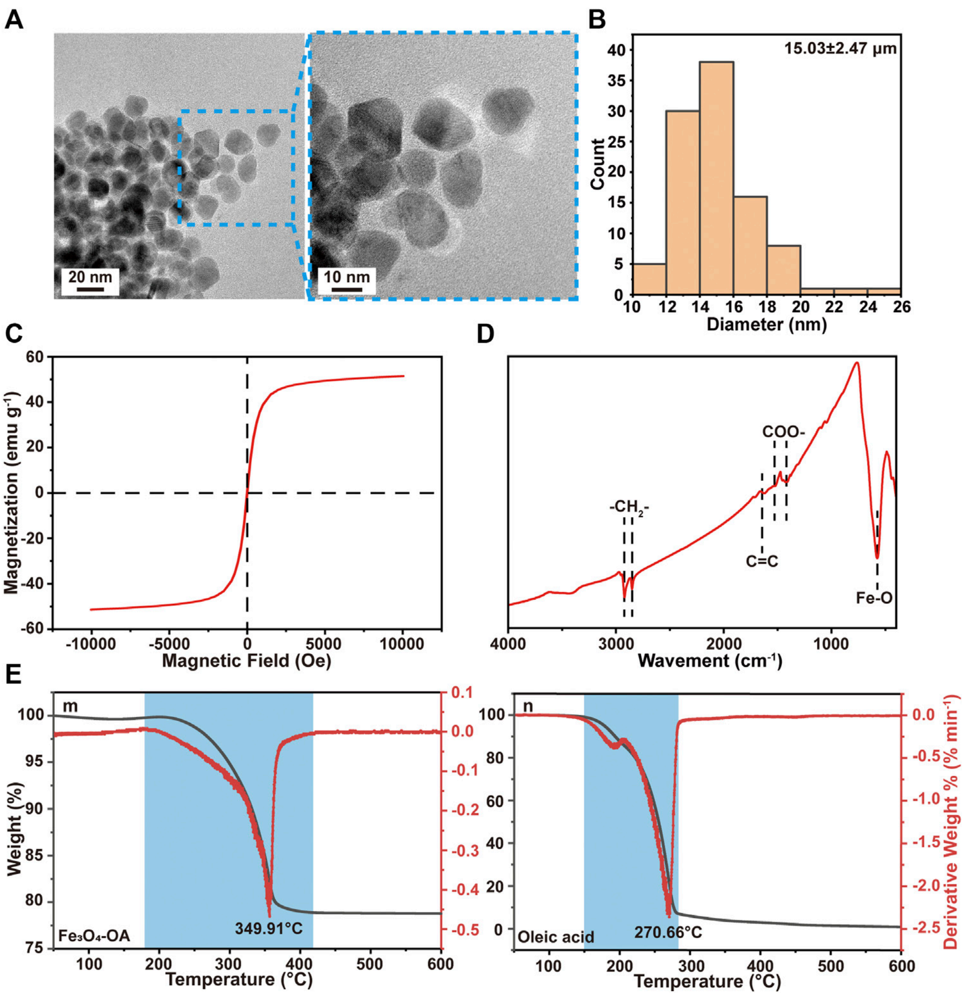

FIGURE 1 | TEM images **(A)** of Fe_3O_4-OA NPs at different magnifications and particle size distribution **(B)** of Fe_3O_4-OA NPs. VSM curve **(C)** of Fe_3O_4-OA NPs. The FTIR spectra **(D)** of Fe_3O_4-OA NPs. TGA and DTA curves **(E)** of Fe_3O_4-OA NPs (m) and oleic acid (n).

the cell-repulsive and non-adhesive properties of PEG, di-amino-PEG is used here as a microsphere surface modifier for facile conjugation and subsequent activation of PEG molecules on the microsphere surface. PEG can act as an anti-adhesive barrier or binding to peptide to promote cell adhesion. Cells cannot adhere to PEG, which helps facilitate contact between the cells and the peptide.

Figure 3A shows the FTIR spectra of the microspheres after dopamine coating and PEG grafting modification. The strong signal at 1760 cm^{-1} that appeared in all spectra could be attributed to the presence of carbonyl groups in the PLGA. The N-H bending vibration peak at 1,613 cm^{-1} after dopamine coating, which might be associated with the amino group contained in polydopamine (pDA), could be seen in the spectra. This indicated the polymerization reaction of dopamine on the surface of the microspheres to form the pDA coating layer. From the spectra, it could be observed that the peak of 2,923 cm^{-1} appeared after grafting PEG on the surface of pDA coated microspheres, suggesting that the tensile vibration of C-H was enhanced. The signal at 1,340 cm^{-1} revealed the strengthening of the C-H bending vibration. This implied that PEG had been grafted on the surface of pDA-coated microspheres.

The NIH3T3 cells were inoculated on the surface of the Fe_3O_4-OA-PLGA, pDA/Fe_3O_4-OA-PLGA, and PEG/pDA/Fe_3O_4-OA-PLGA microspheres. After incubation for 12 h, the adherent cells were fixed and stained with DAPI nuclear dye, then observed and statistically analyzed. Fluorescence photographs (**Figure 3B**) showed that NIH3T3 cells could adhere to the pDA/Fe_3O_4-OA-PLGA and Fe_3O_4-OA-PLGA microspheres, but they could not adhere well on the PEG/pDA/Fe_3O_4-OA-PLGA microspheres. Statistical analysis (**Figure 3C**) showed that cell adhesion on the PEG/pDA/Fe_3O_4-OA-PLGA microspheres was significantly lower than that on the pDA-modified and control

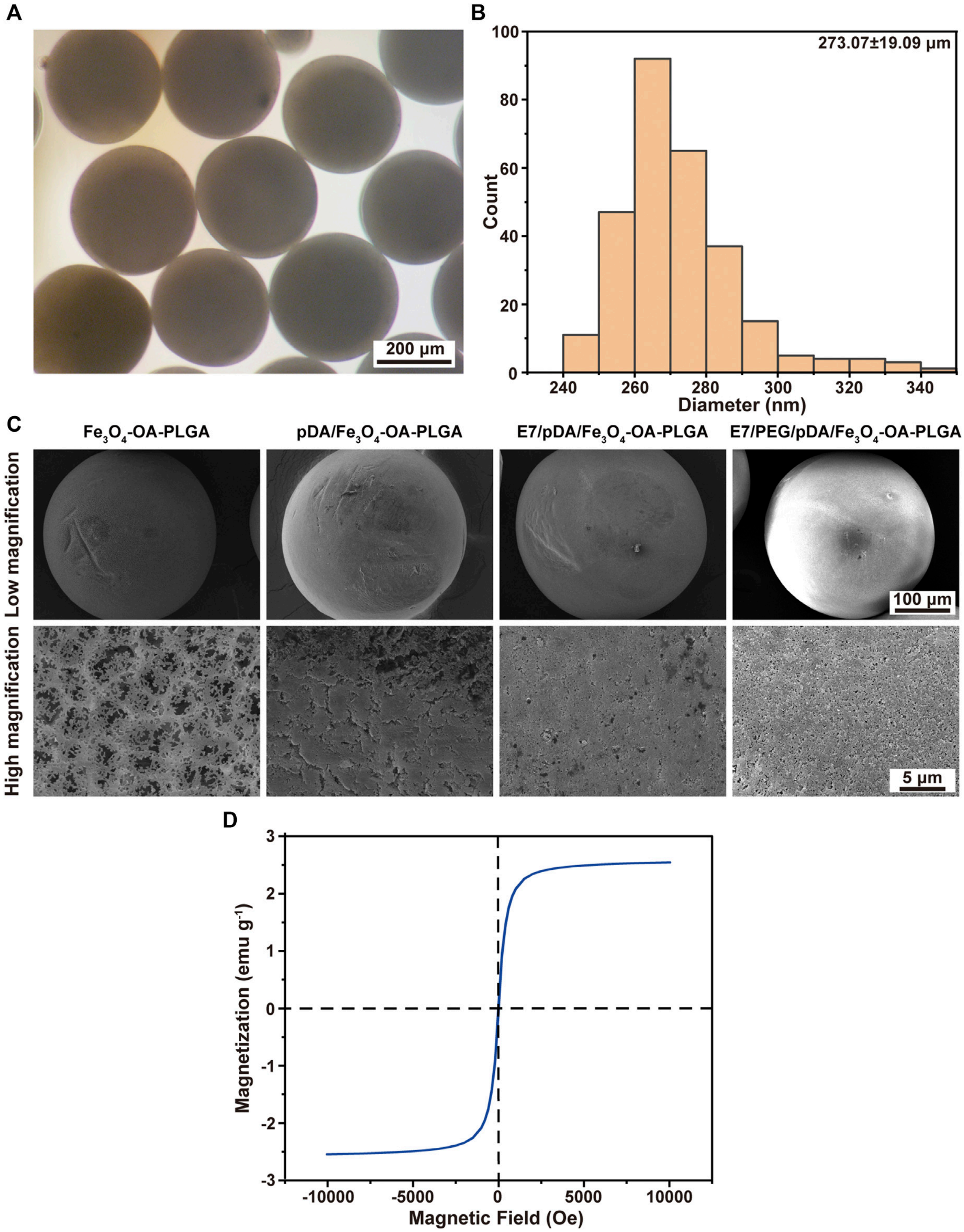

FIGURE 2 | Micrographs **(A)** and size distribution **(B)** of Fe_3O_4-OA-PLGA microspheres. SEM images **(C)** of microspheres under low (above) and high (below) magnification. VSM curve **(D)** of Fe_3O_4-OA-PLGA microspheres.

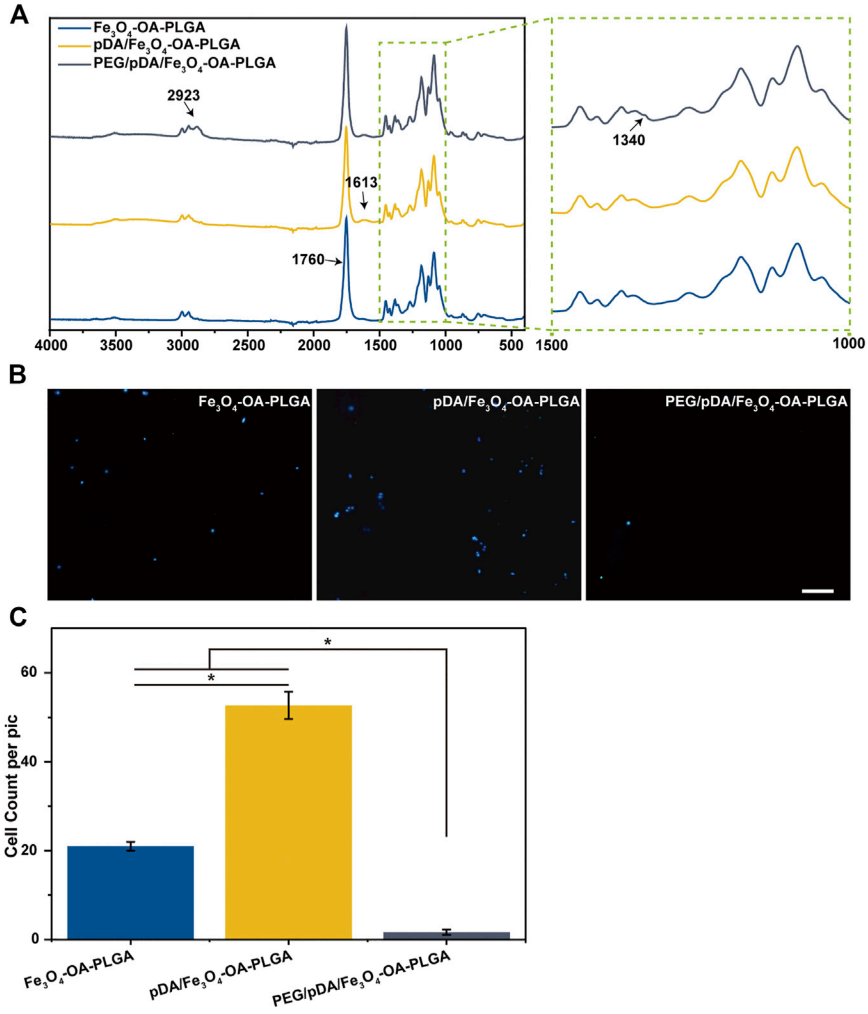

FIGURE 3 | FTIR spectrum **(A)**. Fluorescent images **(B)** of NIH3T3 cells cultured on microspheres for 12 h, and cell count data **(C)**. The cells were stained with DAPI (nucleus, blue). Scale bar = 100 μm. $p < 0.05$, $n = 3$.

surfaces. These results suggest that PEG molecules grafted on the microspheres formed a surface that was more resistant to cell adhesion than the untreated microspheres.

3.4 Characterization of Peptide-Modified Microspheres

In this study, selective adhesion to MSCs was achieved by grafting E7 peptide on PEGylated magnetic microspheres. The activation of grafted di-amino-PEG molecules on the microsphere surface depended on their free terminal amine groups. First, we attached sulfo-SMCC to the di-amino-PEG molecule on the surface of the microspheres. Then, the E7 peptide was ligated to the sulfo-SMCC molecule on the surface of the PEG/pDA/Fe_3O_4-OA-PLGA microspheres via the Cys residue at the C-terminal end of the peptide. The E7/pDA/Fe_3O_4-OA-PLGA microspheres were modified with E7 by pDA coating. Since only the peptide contained sulfur elements, the mapping of sulfur elements was used to characterize the grafting of the peptide. As seen in **Figure 4A**, the surfaces of E7/pDA/Fe_3O_4-OA-PLGA microspheres and E7/PEG/pDA/Fe_3O_4-OA-PLGA microspheres were uniformly covered with elemental sulfur. This result indicated that the E7 peptide was successfully immobilized on the magnetic microspheres.

The water contact angle was 79.76 ± 1.52° for Fe_3O_4-OA-PLGA microspheres, 57.46 ± 1.27° for pDA/Fe_3O_4-OA-PLGA microspheres, and 45.79 ± 0.81° for E7/pDA/Fe_3O_4-OA-PLGA microspheres (**Figure 4B**). Applying pDA and E7 to the microsphere surface decreased the water contact angle, indicating that they improved the hydrophilicity. This was also expected, because pDA and E7 comprise many hydrophilic functional groups, such as amino and hydroxyl groups. The surface of PEG/pDA/Fe_3O_4-OA-PLGA and E7/PEG/pDA/Fe_3O_4-OA-PLGA microspheres became more hydrophilic, with a contact angle of only about 39.13 ± 0.74° and 39.26 ± 0.87°, possibly due to the presence of PEG with excellent hydrophilicity on the modified surface (Lee et al., 1995).

The organic coating content on the prepared microsphere surface was calculated using the TGA method (**Figure 4C**). The mass loss values for Fe_3O_4-OA-PLGA, pDA/Fe_3O_4-OA-PLGA, PEG/pDA/

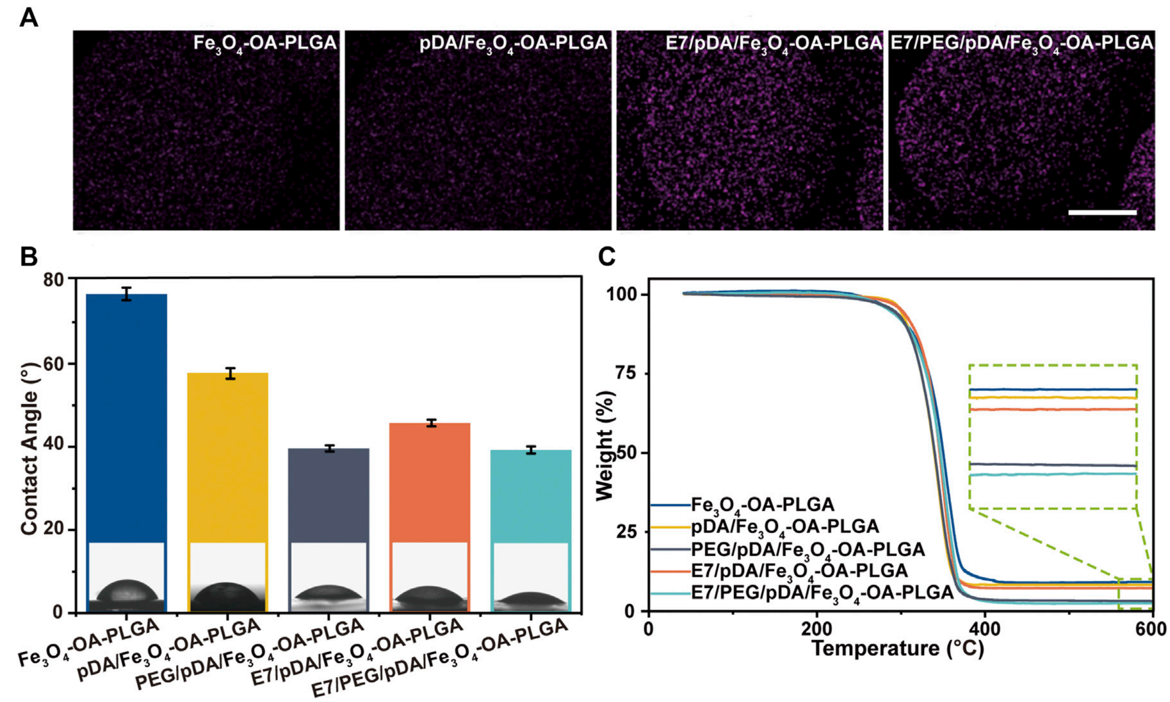

FIGURE 4 | Elemental mapping of sulfur **(A)**. Scale bar = 100 μm. Water contact angle of various microspheres **(B)**. TGA curves of different microspheres **(C)**. $p < 0.05$, $n = 3$.

Fe_3O_4-OA-PLGA, E7/pDA/Fe_3O_4-OA-PLGA, and E7/PEG/pDA/Fe_3O_4-OA-PLGA were at 91.038, 91.858, 97.021, 92.957, and 97.725 wt.%, respectively. E7 grafting of E7/pDA/Fe_3O_4-OA-PLGA and E7/PEG/pDA/Fe_3O_4-OA-PLGA was calculated to be 1.099 wt.% and 0.704 wt.%, respectively, which might be related to the coupling efficiency of sulfo-SMCC.

3.5 Evaluation of the Cytocompatibility of Microspheres

Because cells could not adhere to the PEG/pDA/Fe_3O_4-OA-PLGA microspheres, the PEG/pDA/Fe_3O_4-OA-PLGA microspheres were not evaluated in subsequent experiments.

3.5.1 Cytotoxicity

The toxicity of the microsphere extracts was assessed first (**Supplementary Figure S4**). For the 100% extract, the cell viability ranged from 87.64 ± 2.14% to 94.33 ± 2.96%. For the 50% extract, the cell viability ranged from 91.36 ± 2.033% to 97.32 ± 2.99%. Indirect cytotoxicity assays indicated that these microspheres were safe for *in vivo* application. Although nanoparticles were used, the effect on cell viability was negligible. The binding ability between Fe_3O_4-OA NPs and PLGA matrix might have been strengthened by the oleic acid modification layer on the magnetic nanoparticles, thus reducing their leaching from the microspheres (Hao et al., 2019). In addition, after washing, reagents harmful to the cells were reduced to a reasonable level.

3.5.2 Cell Proliferation

Microspheres should support cell attachment and proliferation. To assess cell behavior, MSCs were seeded and cultured on the microspheres. Cell proliferation was detected on days 1, 3, and 7 with the CCK-8 kit (**Figure 5A**). According to the results, the cell viability of the three groups of microspheres was similar on the first day except for the Fe_3O_4-OA-PLGA microspheres. After 3 and 7 days, E7/pDA/Fe_3O_4-OA-PLGA and E7/PEG/pDA/Fe_3O_4-OA-PLGA exhibited higher cell viability. These results corresponded to those for TGA. E7 grafting affected cell adhesion and proliferation, thus showing better biocompatibility of the microspheres, because E7 is an MSC-specific affinity peptide with a superior affinity for MSCs.

3.5.3 Cell Morphology

Fluorescence microscopy was used after 3 days to assess the distribution of MSCs on the microspheres (**Figure 5B**). In the presence of E7 peptide, the number of cells adhering to the surface of E7/pDA/Fe_3O_4-OA-PLGA and E7/PEG/pDA/Fe_3O_4-OA-PLGA microspheres was increased, and the area fraction (**Figure 5C**) was significantly higher compared with that of the pDA/Fe_3O_4-OA-PLGA and Fe_3O_4-OA-PLGA groups. Cells were uniformly and densely distributed on the E7/pDA/Fe_3O_4-OA-PLGA and E7/PEG/pDA/Fe_3O_4-OA-PLGA microspheres, showing excellent cell adhesion and spreading. These results indicate that the functionalization of grafted di-amino-PEG

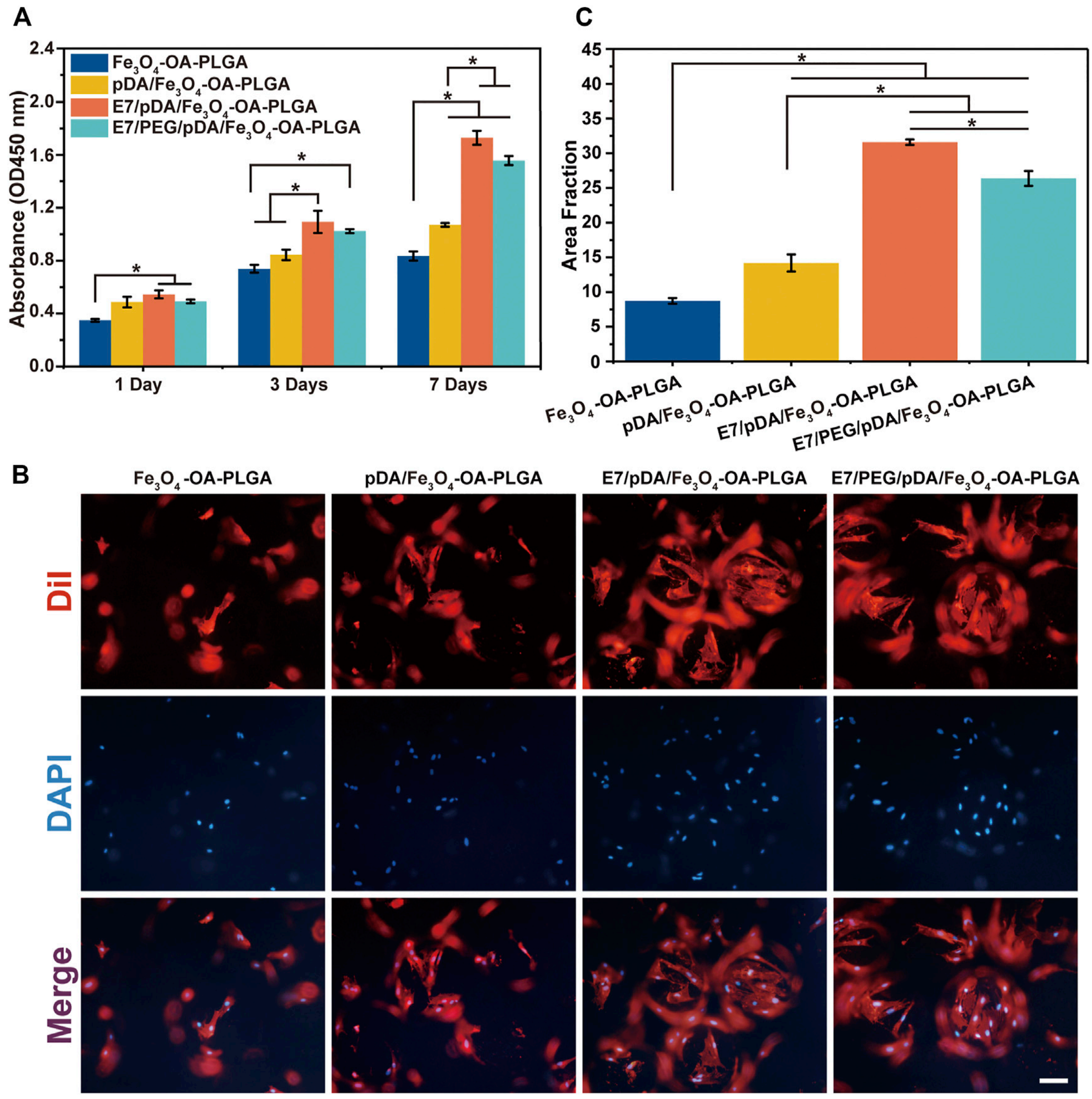

FIGURE 5 | Proliferation of MSCs on microspheres at 1, 3, and 7 days post-seeding evaluated by CCK-8 assay **(A)**. The cellular morphology **(B)** and statistical area fraction **(C)** of MSCs cultured for 3 days on the different microspheres, which were stained by Dil (cytoplasm, red)/DAPI (nuclei, blue). Scale bar = 100 μm. $p < 0.05$, $n = 3$.

molecules with E7 peptide not only restored cell adhesion to the surface but also enhanced it relative to the Fe_3O_4-OA-PLGA and pDA/Fe_3O_4-OA-PLGA.

3.6 Selective Adhesion of Separately Cultured Multiple Cells

The E7 peptide, which was bound on the surface of the microspheres, was initially shown to have a specific affinity for MSCs relative to NIH3T3 (fibroblasts) and RAW 264.7 cells (macrophages). Cell adhesion was detected 6 h after inoculation, as shown in **Figure 6**. The images revealed that the number of cells adhering to the Fe_3O_4-OA-PLGA surface was lower than that on the pDA/Fe_3O_4-OA-PLGA surface, regardless of cell type. The addition of dopamine coating on the microspheres increased non-specific cell adhesion, but the cell proportions did not change (**Figure 6A**). As previously reported (Madhurakkat Perikamana et al., 2015), pDA imparts a positive charge to the material surface, allowing the material to bind more readily to integral protein receptors of the cell membrane, thus improving cell adhesion. On the surface of E7/pDA/

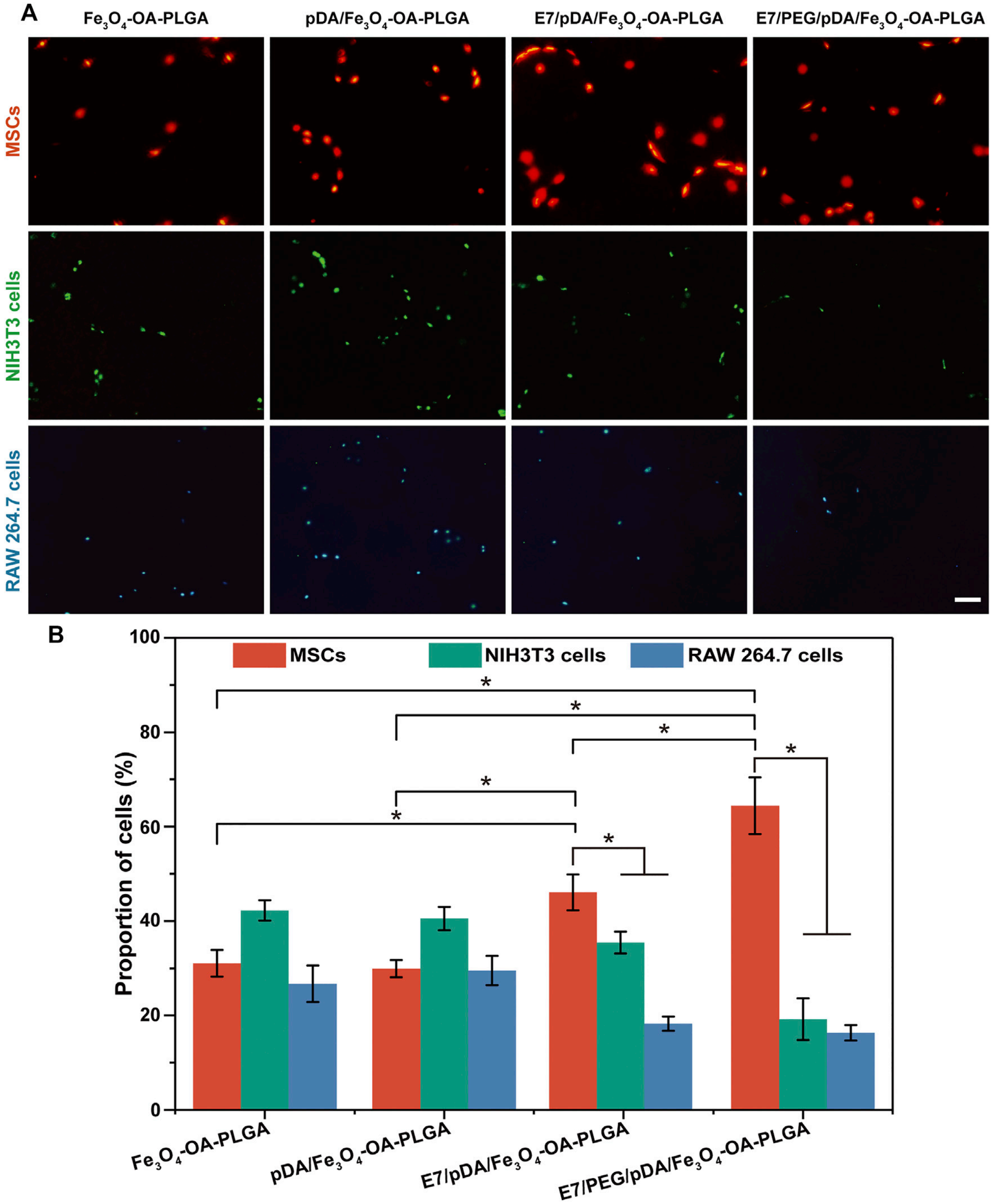

FIGURE 6 | Representative fluorescent images **(A)** of MSCs (DiI, red), NIH3T3 (Calcein-AM, green), and RAW 264.7 cells (Hoechst 33342, blue) adhering to various microspheres after 6 h of separate culture. The proportions **(B)** of adherent MSCs, NIH3T3, and RAW 264.7 cells on the same type of microsphere. Scale bar = 100 μm. At least five fields of view were randomly taken for each group of microspheres. $p < 0.05$, $n = 3$.

Fe_3O_4-OA-PLGA, the adhesion of NIH3T3 and RAW 264.7 cells was not higher than that for pDA/Fe_3O_4-OA-PLGA, whereas the number of adherent MSCs was increased. On E7/PEG/pDA/Fe_3O_4-OA-PLGA microspheres, the cells of MSCs were further increased, while that of NIH3T3 and RAW 264.7 cells were further reduced. Statistical analysis showed that at 6 h post-inoculation (**Figure 6B**), the proportion of adherent MSCs on the surface of E7/PEG/pDA/Fe_3O_4-OA-PLGA was more than two-fold higher than that of NIH3T3 and RAW 264.7 cells. These results indicated that the grafted PEG molecules and E7 peptide effectively resisted the non-specific adhesion of cells.

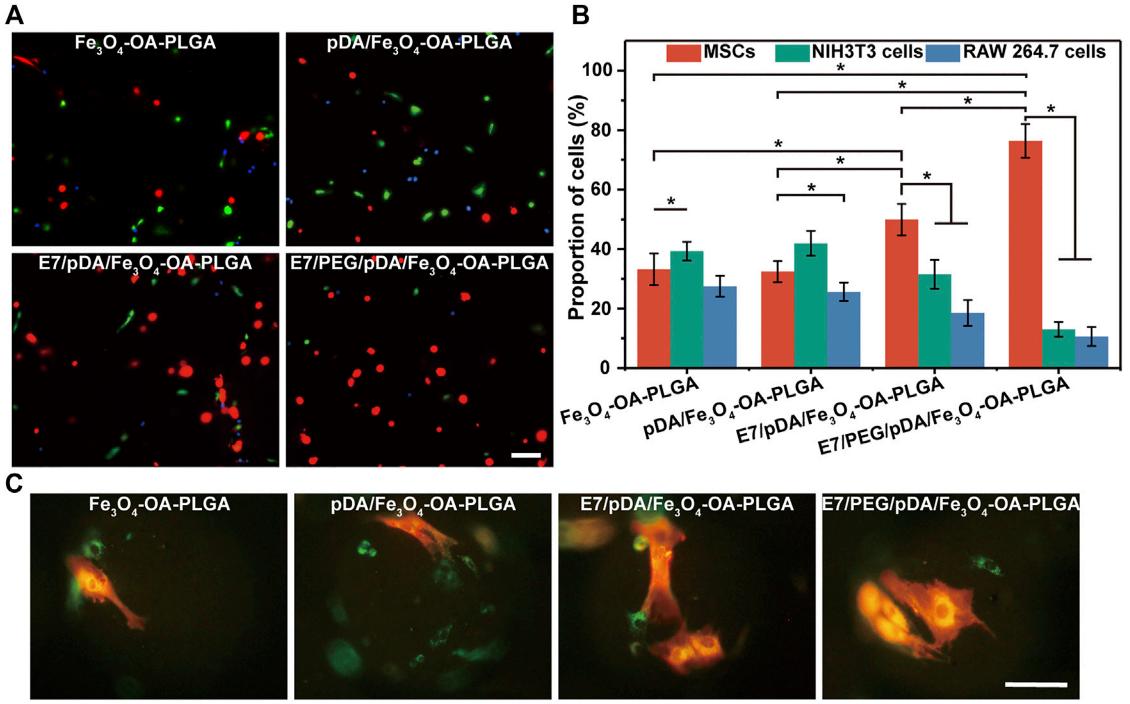

FIGURE 7 | Representative fluorescent images **(A)** of MSCs (DiI, red), NIH3T3 (Calcein-AM, green), and RAW 264.7 cells (Hoechst 33342, blue) co-cultured on different microspheres for 6 h under static conditions. Statistical analysis of the proportions **(B)** of MSCs, NIH3T3, and RAW 264.7 cells per view. The morphology **(C)** of the three types of cells on the microspheres. The red cells were MSCs, and the green cells were NIH3T3 or RAW 264.7 cells. Scale bar = 100 μm. At least five fields of view were randomly taken for each group of microspheres. $p < 0.05$, $n = 3$.

3.7 Selective Adhesion of Co-Cultured Multiple Cells (Static Culture)

The selective adhesion of MSCs to the E7/PEG/pDA/Fe_3O_4-OA-PLGA microspheres was further verified through co-culturing MSCs with NIH3T3 and RAW 264.7 cells under static conditions (**Figure 7A**). The results showed that the total number of cells on the surface of Fe_3O_4-OA-PLGA microspheres was low, and the proportions of the three types of cells were comparable. A large number of adherent MSCs (red), NIH3T3 (green), and RAW 264.7 cells (blue) could be observed on pDA/Fe_3O_4-OA-PLGA microspheres. With the addition of E7 peptide, more red cells were observed on the E7/pDA/Fe_3O_4-OA-PLGA microspheres, indicating enhanced selectivity for MSCs adhesion. However, E7/PEG/pDA/Fe_3O_4-OA-PLGA microspheres exhibited more red cells and fewer green and blue cells than unmodified Fe_3O_4-OA-PLGA microspheres. This suggested that the PEG antifouling layer effectively blocked the non-specific adhesion of cells. Accordingly, the proportions of cells on the different microspheres were statistically analyzed (**Figure 7B**). The percentages of MSCs, NIH3T3, and RAW 264.7 cells cultured on Fe_3O_4-OA-PLGA were 33.19 ± 5.32, 39.32 ± 3.11, and 27.49 ± 3.51%, respectively. Similar to separate culture, when cells were co-cultured on the pDA/Fe_3O_4-OA-PLGA microspheres, there was no significant change in the proportion of each cell type, although there was an increase in the number of each cell type. With respect to E7/pDA/Fe_3O_4-OA-PLGA microspheres, the percentage of MSCs increased from 32.4 ± 3.58% to 49.9 ± 5.27%. Furthermore, on E7/PEG/pDA/Fe_3O_4-OA-PLGA microspheres, the percentage of MSCs was increased to 76.39 ± 5.67%. The above results led us to conclude that the selective adhesion of MSCs to E7/PEG/pDA/Fe_3O_4-OA-PLGA microspheres was significantly enhanced under static culture conditions. Compared with the situation when the 3 cells were inoculated separately, on the surface of E7/pDA/Fe_3O_4-OA-PLGA and E7/PEG/pDA/Fe_3O_4-OA-PLGA microspheres grafted with E7 peptide, the proportions of NIH3T3 and RAW 264.7 cells were decreased, which might be due to the increasing selective affinity of microspheres for MSCs, which caused more adherence of MSCs, and competitively reduced the adherence of NIH3T3 and RAW 264.7 cells.

Observing the morphology of the three types of cells on the microspheres (**Figure 7C**), corresponding to **Figure 7A**, the E7-grafted microspheres exhibited more adhered MSCs. This also suggests that E7 might influence the subsequent proliferation of MSCs by affecting their early adhesion (**Figure 5A**).

3.8 Selective Adhesion of Co-Cultured Multiple Cells (Dynamic Culture)

Because microspheres are often cultured in a dynamic environment as cell microcarriers, the selective capture of MSCs by the obtained microspheres under dynamic conditions was further investigated

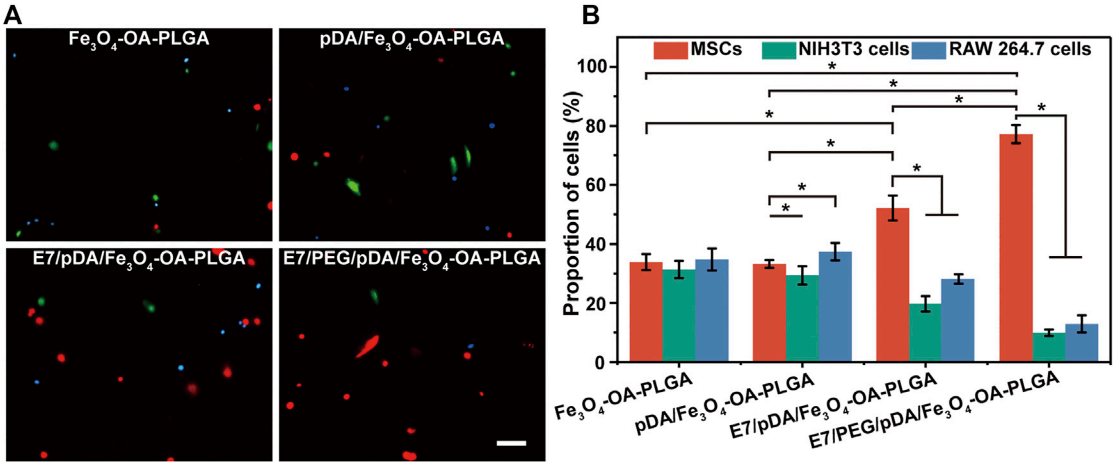

FIGURE 8 | Representative fluorescent images **(A)** of MSCs (DiI, red), NIH3T3 (Calcein-AM, green), and RAW 264.7 cells (Hoechst 33342, blue) co-cultured on different microspheres for 6 h under dynamic conditions. Scale bar = 100 μm. Statistical analysis of the proportions **(B)** of MSCs, NIH3T3, and RAW 264.7 cells per view. At least five fields of view were randomly taken for each group of microspheres. $p < 0.05$, $n = 3$.

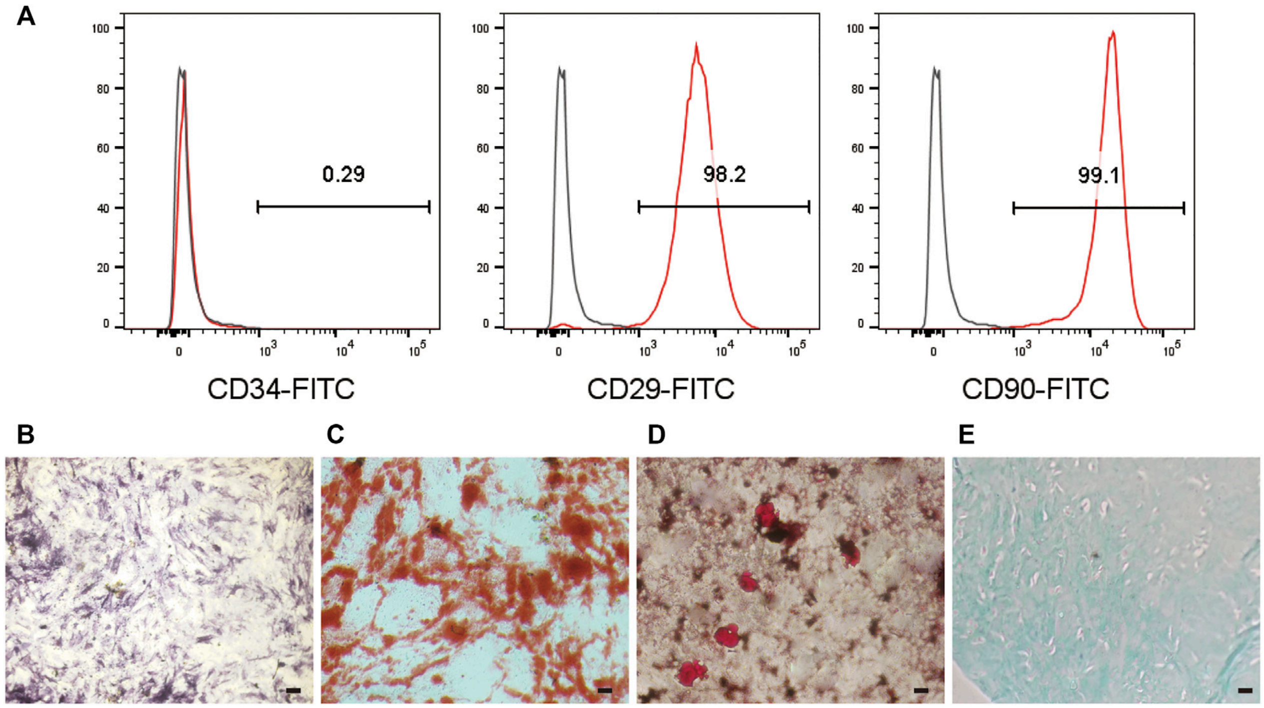

FIGURE 9 | Flow cytometric analysis **(A)** of MSCs cultured on the E7/PEG/pDA/Fe$_3$O$_4$-OA-PLGA microspheres for 7 days. ALP **(B)** and ARS staining **(C)** after osteogenesis induction for 7 or 14 days in MSCs pre-seeded on the E7/PEG/pDA/Fe$_3$O$_4$-OA-PLGA microspheres. Oil red O staining **(D)** after lipogenesis induction for 21 days in MSCs that were pre-seeded on the E7/PEG/pDA/Fe$_3$O$_4$-OA-PLGA microspheres. Alcian blue staining **(E)** after chondrogenic induction for 28 days in MSCs pre-seeded on the E7/PEG/pDA/Fe$_3$O$_4$-OA-PLGA microspheres. Scale bar = 100 μm.

(**Figure 8A**). The total number of adherent cells on the surface of each microsphere decreased compared with that in static culture. Presumably, shear forces in the system may cause adhesion to take longer to achieve (Ning et al., 2013). After modification with dopamine, the number of cells on the pDA/Fe$_3$O$_4$-OA-PLGA microspheres increased (versus the Fe$_3$O$_4$-OA-PLGA microspheres group). Unsurprisingly, modification of the E7 peptide resulted in more MSC adhesion, as under static culture conditions. On the E7/PEG/pDA/Fe$_3$O$_4$-OA-PLGA microspheres, the adherent numbers of NIH3T3 and RAW 264.7 cells were also decreased. These results showed that the PEG antifouling layer could also inhibit non-specific cell adhesion under dynamic conditions. Accordingly, statistical analysis of cell proportions was performed (**Figure 8B**). The percentages of MSCs, NIH3T3, and RAW 264.7 cells cultured on Fe_3O_4-OA-PLGA microspheres were 34.76 ± 3.77, 31.35 ± 2.94, and 33.893 ± 2.71%, respectively. On pDA/Fe_3O_4-OA-PLGA microspheres, the proportions of cells were 37.37 ± 2.94, 29.36 ± 3.10, and 33.27 ± 1.29%. For E7/pDA/Fe_3O_4-OA-PLGA microspheres, MSCs increased to 52.16 ± 4.22%, while NIH3T3 and RAW 264.7 decreased to 19.75 ± 2.59% and 28.09 ± 1.58%. The proportion of MSCs on E7/PEG/pDA/Fe_3O_4-OA-PLGA microspheres further increased to 77.19 ± 3.05%. The results showed that the E7/PEG/pDA/Fe_3O_4-OA-PLGA microspheres were equally selective for MSCs under dynamic conditions compared with that in static culture.

3.9 Stemness of the Adhered MSCs

MSCs can offer promising therapeutic potential for many diseases (Patel et al., 2013). Because of the limited fraction of MSCs collected from tissues, *in vitro* expansion of MSCs is required; nevertheless, loss of stemness and undesired differentiation of MSCs during *in vitro* culture can diminish their efficiency (Saei Arezoumand et al., 2017). Therefore, their stemness qualities must be preserved *in vitro* (McKee et al., 2017). To investigate the stemness retention and differentiation potential of MSCs expanded on the surface of E7/PEG/pDA/Fe_3O_4-OA-PLGA microspheres, the cells were inoculated for an additional 7 days and harvested; then, flow cytometric analysis and induced differentiation were carried out (**Figure 9**). The positive expression indicators CD29 and CD90 and the negative expression indicator CD34 by MSCs were taken as identification reference indicators. Flow cytometry (**Figure 9A**) showed that the cells did not express CD34, but did express CD29 and CD90. This was consistent with the surface marker characteristics of MSCs (Harting et al., 2008). ALP activity was a sign of early osteogenic differentiation in MSCs (Weinreb et al., 1990). **Figure 9B** showed positive ALP staining. Mineral deposition has been shown to be a late marker of osteogenesis, and calcium deposition can be measured using alizarin red staining (Liu et al., 2016). Significant calcium deposition (**Figure 9C**) was found in MSCs inoculated on E7/PEG/pDA/Fe_3O_4-OA-PLGA microspheres. With regard to lipogenic differentiation, oil red O staining (**Figure 9D**) showed the existence of lipid vacuoles. Alcian blue staining (**Figure 9E**) confirmed chondrogenic morphogenesis. The results demonstrated that cells growing on the microspheres still retained the ability to differentiate. Furthermore, we found that the number of MSCs captured on E7/PEG/pDA/Fe_3O_4-OA-PLGA under dynamic conditions was statistically significantly lower than the number of MSCs captured under static conditions (**Supplementary Table S1**). Consistent with the preceding results, it is possible that shear forces affected early cell adhesion (Ning et al., 2013), and such shear forces might, to some extent, also mimic the actual stress environment *in vivo* (Zhang et al., 2010).

Additionally, microspheres can be used not only *in vitro*, but also *in vivo* as supporting material and carriers for cell growth and delivery (Hiraoka et al., 2006; Kang et al., 2009; Kamali et al., 2019). Nevertheless, the non-specific capture of fibrocytes and inflammation-related cells may lead to fibrosis because of the complexity and diversity of the cells participating in the tissue repair procedure (Tabata, 2009). Hence, in order to achieve tissue regeneration without fibrosis, selective capture of MSCs by the E7-modified microspheres in the presence of fibrocytes and inflammatory cells is crucial. MSCs can selectively adhere to such microspheres, reducing the potential for fibrosis and inflammation caused by fibroblasts and inflammatory cells.

4 CONCLUSION

In this study, E7 peptide was grafted onto the surface of PLGA magnetic microspheres via PEG for MSC sorting by selective adhesion. The superparamagnetism of Fe_3O_4-OA NPs was verified by TGA/DTA, VSM, and TEM characterization. Observations from light microscopy and electron microscopy demonstrated that the microspheres had uniform size and satisfied surface morphology requirements. Grafting of PEG exhibited anti-cell adhesion ability, and the subsequent E7 peptide modification fulfilled cell adhesion requirements. The separate culture and co-culture of multiple types of cells on the peptide-modified microspheres, both in static and dynamic conditions, revealed efficient cell sorting ability. Therefore, we demonstrate here that the PLGA magnetic microspheres grafted with E7 peptide via PEG represent a promising platform for MSC sorting and expansion. The method of preparation of microspheres in this study is simple, and the microspheres are easy to use at a low cost. It is noteworthy that, at near 80%, the sorting efficiency of the microspheres is not as high as that of classical sorting methods using antibodies. This might be related to the grafting amount of the peptide, which is also to be improved in our subsequent work.

DATA AVAILABILITY STATEMENT

The original contributions presented in the study are included in the article/**Supplementary Material**, further inquiries can be directed to the corresponding authors.

ETHICS STATEMENT

The animal study was reviewed and approved by the Institutional Animal Care and Use Committee of Jilin University School of Pharmaceutical Science.

AUTHOR CONTRIBUTIONS

JM and PZ proposed the inspiration and design of the experiment. SW conducted the experiment and wrote the article. ZW participated in the experimental guidance and key revision of the manuscript. YW provided some home-made equipment. MG helped to synthesize superparamagnetic nanoparticles. MZ and LW participated in the discussion and provided suggestions. All authors approved the submitted version of the manuscript.

FUNDING

This research was financially supported by the Department of Science and Technology of Jilin Province (No. 20200403043SF), the Dengfeng Projects of Foshan Hospital of Traditional Chinese Medicine (No. 202100046), National Natural Science Foundation of China (No. 52173146), Key Projects of Military Logistics Opening Research (No. BLB20J011) and National Key R&D Program of China (No. 2017YFA0103204).

ACKNOWLEDGMENTS

The authors are also grateful to all the faculty members of the Changchun Institute of Applied Chemistry who were involved in the testing and characterization of the materials.

SUPPLEMENTARY MATERIAL

The Supplementary Material for this article can be found online at: https://www.frontiersin.org/articles/10.3389/fbioe.2022.873125/full#supplementary-material

REFERENCES

Alhadlaq, A., and Mao, J. J. (2004). Mesenchymal Stem Cells: Isolation and Therapeutics. *Stem Cell Develop.* 13 (4), 436–448. doi:10.1089/scd.2004.13.436

Antoni, D., Burckel, H., Josset, E., and Noel, G. (2015). Three-Dimensional Cell Culture: A Breakthrough *In Vivo*. *Int. J. Mol. Sci.* 16 (3), 5517–5527. doi:10.3390/ijms16035517

Bacon, K., Lavoie, A., Rao, B. M., Daniele, M., and Menegatti, S. (2020). Past, Present, and Future of Affinity-Based Cell Separation Technologies. *Acta Biomater.* 112, 29–51. doi:10.1016/j.actbio.2020.05.004

Blocki, A., Beyer, S., Dewavrin, J.-Y., Goralczyk, A., Wang, Y., Peh, P., et al. (2015). Microcapsules Engineered to Support Mesenchymal Stem Cell (MSC) Survival and Proliferation Enable Long-Term Retention of MSCs in Infarcted Myocardium. *Biomaterials* 53, 12–24. doi:10.1016/j.biomaterials.2015.02.075

Chien, H.-W., Kuo, W.-H., Wang, M.-J., Tsai, S.-W., and Tsai, W.-B. (2012). Tunable Micropatterned Substrates Based on Poly(dopamine) Deposition via Microcontact Printing. *Langmuir* 28 (13), 5775–5782. doi:10.1021/la300147p

Flemming, R. G., Murphy, C. J., Abrams, G. A., Goodman, S. L., and Nealey, P. F. (1999). Effects of Synthetic Micro- and Nano-Structured Surfaces on Cell Behavior. *Biomaterials* 20 (6), 573–588. doi:10.1016/s0142-9612(98)00209-9

Friedenstein, A. J., Chailakhjan, R. K., and Lalykina, K. S. (1970). The Development of Fibroblast Colonies in Monolayer Cultures of guinea-pig Bone Marrow and Spleen Cells. *Cell Prolif* 3 (4), 393–403. doi:10.1111/j.1365-2184.1970.tb00347.x

Gao, T., Zhang, N., Wang, Z., Wang, Y., Liu, Y., Ito, Y., et al. (2015). Biodegradable Microcarriers of Poly(Lactide-Co-Glycolide) and Nano-Hydroxyapatite Decorated with IGF-1 via Polydopamine Coating for Enhancing Cell Proliferation and Osteogenic Differentiation. *Macromol. Biosci.* 15 (8), 1070–1080. doi:10.1002/mabi.201500069

Gotherstrom, C., David, A. L., Walther-Jallow, L., Åström, E., and Westgren, M. (2021). Mesenchymal Stem Cell Therapy for Osteogenesis Imperfecta. *Clin. Obstet. Gynecol.* 64 (4), 898–903. doi:10.1097/grf.0000000000000656

Hao, L., Li, L., Wang, P., Wang, Z., Shi, X., Guo, M., et al. (2019). Synergistic Osteogenesis Promoted by Magnetically Actuated Nano-Mechanical Stimuli. *Nanoscale* 11 (48), 23423–23437. doi:10.1039/c9nr07170a

Hao, L., Li, J., Wang, P., Wang, Z., Wu, Z., Wang, Y., et al. (2021). Spatiotemporal Magnetocaloric Microenvironment for Guiding the Fate of Biodegradable Polymer Implants. *Adv. Funct. Mater.* 31 (15), 2009661. doi:10.1002/adfm.202009661

Harting, M. T., Jimenez, F., Pati, S., Baumgartner, J., and Cox, C. S., Jr (2008). Immunophenotype Characterization of Rat Mesenchymal Stromal Cells. *Cytotherapy* 10 (3), 243–253. doi:10.1080/14653240801950000

Herzenberg, L. A., Parks, D., Sahaf, B., Perez, O., Roederer, M., and Herzenberg, L. A. (2002). The History and Future of the Fluorescence Activated Cell Sorter and Flow Cytometry: a View from Stanford. *Clin. Chem.* 48 (10), 1819–1827. doi:10.1093/clinchem/48.10.1819

Hiraoka, Y., Yamashiro, H., Yasuda, K., Kimura, Y., Inamoto, T., and Tabata, Y. (2006). *In Situ* regeneration of Adipose Tissue in Rat Fat Pad by Combining a Collagen Scaffold with Gelatin Microspheres Containing Basic Fibroblast Growth Factor. *Tissue Eng.* 12 (6), 1475–1487. doi:10.1089/ten.2006.12.1475

Kabat, M., Bobkov, I., Kumar, S., and Grumet, M. (2020). Trends in Mesenchymal Stem Cell Clinical Trials 2004-2018: Is Efficacy Optimal in a Narrow Dose Range? *Stem Cell Transl. Med.* 9 (1), 17–27. doi:10.1002/sctm.19-0202

Kamali, A., Oryan, A., Hosseini, S., Ghanian, M. H., Alizadeh, M., Baghaban Eslaminejad, M., et al. (2019). Cannabidiol-loaded Microspheres Incorporated into Osteoconductive Scaffold Enhance Mesenchymal Stem Cell Recruitment and Regeneration of Critical-Sized Bone Defects. *Mater. Sci. Eng. C* 101, 64–75. doi:10.1016/j.msec.2019.03.070

Kang, S.-W., La, W.-G., and Kim, B.-S. (2009). Open Macroporous Poly(lactic-Co-Glycolic Acid) Microspheres as an Injectable Scaffold for Cartilage Tissue Engineering. *J. Biomater. Sci. Polym. Ed.* 20 (3), 399–409. doi:10.1163/156856209x412236

Lee, J., Lee, H., and Andrade, J. (1995). Blood Compatibility of Polyethylene Oxide Surfaces. *Prog. Polym. Sci.* 20 (6), 1043–1079. doi:10.1016/0079-6700(95)00011-4

Leong, W., and Wang, D.-A. (2015). Cell-laden Polymeric Microspheres for Biomedical Applications. *Trends Biotechnol.* 33 (11), 653–666. doi:10.1016/j.tibtech.2015.09.003

Li, X. Y., Zhang, Y., and Qi, G. X. (2013). Evaluation of Isolation Methods and Culture Conditions for Rat Bone Marrow Mesenchymal Stem Cells. *Cytotechnology* 65 (3), 323–334. doi:10.1007/s10616-012-9497-3

Lin, C.-Y., Huang, C.-H., Wu, Y.-K., Cheng, N.-C., and Yu, J. (2014). Maintenance of Human Adipose Derived Stem Cell (hASC) Differentiation Capabilities Using a 3D Culture. *Biotechnol. Lett.* 36 (7), 1529–1537. doi:10.1007/s10529-014-1500-y

Liu, Y., Lin, Z., Guo, J., Xu, G., Li, Y., Xu, T., et al. (2016). Notoginsenoside R1 Significantly Promotes *In Vitro* Osteoblastogenesis. *Int. J. Mol. Med.* 38 (2), 537–544. doi:10.3892/ijmm.2016.2652

Madhurakkat Perikamana, S. K., Lee, J., Lee, Y. B., Shin, Y. M., Lee, E. J., Mikos, A. G., et al. (2015). Materials from Mussel-Inspired Chemistry for Cell and Tissue Engineering Applications. *Biomacromolecules* 16 (9), 2541–2555. doi:10.1021/acs.biomac.5b00852

Mahdavi, M., Ahmad, M., Haron, M., Namvar, F., Nadi, B., Rahman, M., et al. (2013). Synthesis, Surface Modification and Characterisation of Biocompatible Magnetic Iron Oxide Nanoparticles for Biomedical Applications. *Molecules* 18 (7), 7533–7548. doi:10.3390/molecules18077533

Maity, D., and Agrawal, D. C. (2007). Synthesis of Iron Oxide Nanoparticles under Oxidizing Environment and Their Stabilization in Aqueous and Non-aqueous media. *J. Magnetism Magn. Mater.* 308 (1), 46–55. doi:10.1016/j.jmmm.2006.05.001

McKee, C., Chaudhry, G. R., and Biointerfaces, s. B. (2017). Advances and Challenges in Stem Cell Culture. *Colloids Surf. B: Biointerfaces* 159, 62–77. doi:10.1016/j.colsurfb.2017.07.051

Meligy, F. Y., Elgamal, D. A., Abd Allah, E. S. H., Idriss, N. K., Ghandour, N. M., Bayoumy, E. M. R., et al. (2019). Testing Alternatives: the Use of Adipose-Derived Mesenchymal Stem Cells to Slow Neurodegeneration in a Rat Model of Parkinson's Disease. *Mol. Biol. Rep.* 46 (6), 5841–5858. doi:10.1007/s11033-019-05018-9

Meng, Q., Hu, X., Huang, H., Liu, Z., Yuan, L., Shao, Z., et al. (2017). Microfracture Combined with Functional Pig Peritoneum-Derived Acellular Matrix for Cartilage Repair in Rabbit Models. *Acta Biomater.* 53, 279–292. doi:10.1016/j.actbio.2017.01.055

Nadri, S., and Soleimani, M. (2007). Isolation Murine Mesenchymal Stem Cells by Positive Selection. In Vitro *Cell Dev. Biol. Anim.* 43 (8-9), 276–282. doi:10.1007/s11626-007-9041-5

Neuberger, T., Schöpf, B., Hofmann, H., Hofmann, M., Von Rechenberg, B., and materials, M. (2005). Superparamagnetic Nanoparticles for Biomedical Applications: Possibilities and Limitations of a New Drug Delivery System. *J. Magnetism Magn. Mater.* 293 (1), 483–496. doi:10.1016/j.jmmm.2005.01.064

Nicodemou, A., Danisovic, L., and banking, t. (2017). Mesenchymal Stromal/stem Cell Separation Methods: Concise Review. *Cell Tissue Bank* 18 (4), 443–460. doi:10.1007/s10561-017-9658-x

Ning, B., Liu, H., Gong, W., Jiang, J., Hu, Y., and Yang, S.-Y. (2013). Biological Characteristics of Adult Degenerative Nucleus Pulposus Cells in a Three-Dimensional Microcarrier Stirring Culture System. *J. Orthop. Res.* 31 (6), 858–863. doi:10.1002/jor.22306

Okassa, L. N., Marchais, H., Douziech-Eyrolles, L., Hervé, K., Cohen-Jonathan, S., Munnier, E., et al. (2007). Optimization of Iron Oxide Nanoparticles Encapsulation within poly(D,L-lactide-co-glycolide) Sub-micron Particles. *Eur. J. Pharm. Biopharm.* 67 (1), 31–38. doi:10.1016/j.ejpb.2006.12.020

Papadopoulou, A., Yiangou, M., Athanasiou, E., Zogas, N., Kaloyannidis, P., Batsis, I., et al. (2012). Mesenchymal Stem Cells Are Conditionally Therapeutic in Preclinical Models of Rheumatoid Arthritis. *Ann. Rheum. Dis.* 71 (10), 1733–1740. doi:10.1136/annrheumdis-2011-200985

Patel, D. M., Shah, J., and Srivastava, A. S. (2013). Therapeutic Potential of Mesenchymal Stem Cells in Regenerative Medicine. *Stem Cell Int.* 2013, 496218. doi:10.1155/2013/496218

Picinich, S. C., Mishra, P. J., Mishra, P. J., Glod, J., and Banerjee, D. (2007). The Therapeutic Potential of Mesenchymal Stem Cells. *Expert Opin. Biol. Ther.* 7 (7), 965–973. doi:10.1517/14712598.7.7.965

Pittenger, M. F., Mackay, A. M., Beck, S. C., Jaiswal, R. K., Douglas, R., Mosca, J. D., et al. (1999). Multilineage Potential of Adult Human Mesenchymal Stem Cells. *Science* 284 (5411), 143–147. doi:10.1126/science.284.5411.143

Raina, N., Singh, A. K., and Islam, A. (2021). "Biological Implications of Polyethylene Glycol and PEGylation: Therapeutic Approaches Based on Biophysical Studies and Protein Structure-Based Drug Design Tools," in *Innovations and Implementations of Computer Aided Drug Discovery Strategies in Rational Drug Design* (Singapore: Springer), 273–294. doi:10.1007/978-981-15-8936-2_11

Raos, B. J., Doyle, C. S., Simpson, M. C., Graham, E. S., and Unsworth, C. P. (2018). Selective PEGylation of Parylene-C/SiO2 Substrates for Improved Astrocyte Cell Patterning. *Sci. Rep.* 8, 11. doi:10.1038/s41598-018-21135-0

Ruigrok, V. J. B., Levisson, M., Eppink, M. H. M., Smidt, H., and van der Oost, J. (2011). Alternative Affinity Tools: More Attractive Than Antibodies? *Biochem. J.* 436 (1), 1–13. doi:10.1042/bj20101860

Saei Arezoumand, K., Alizadeh, E., Pilehvar-Soltanahmadi, Y., Esmaeillou, M., and Zarghami, N. (2017). An Overview on Different Strategies for the Stemness Maintenance of MSCs. *Artif. Cell Nanomedicine Biotechnol.* 45 (7), 1255–1271. doi:10.1080/21691401.2016.1246452

Sanchez-Guijo, F., Caballero-Velázquez, T., López-Villar, O., Redondo, A., Parody, R., Martínez, C., et al. (2014). Sequential Third-Party Mesenchymal Stromal Cell Therapy for Refractory Acute Graft-Versus-Host Disease. *Biol. Blood Marrow Transplant.* 20 (10), 1580–1585. doi:10.1016/j.bbmt.2014.06.015

Schmitz, B., Radbruch, A., Kümmel, T., Wickenhauser, C., Korb, H., Hansmann, M. L., et al. (1994). Magnetic Activated Cell Sorting (MACS)--a New Immunomagnetic Method for Megakaryocytic Cell Isolation: Comparison of Different Separation Techniques. *Eur. J. Haematol.* 52 (5), 267–275. doi:10.1111/j.1600-0609.1994.tb00095.x

Shao, Z., Zhang, X., Pi, Y., Wang, X., Jia, Z., Zhu, J., et al. (2012). Polycaprolactone Electrospun Mesh Conjugated with an MSC Affinity Peptide for MSC Homing *In Vivo*. *Biomaterials* 33 (12), 3375–3387. doi:10.1016/j.biomaterials.2012.01.033

Sohni, A., and Verfaillie, C. M. (2013). Mesenchymal Stem Cells Migration Homing and Tracking. *Stem Cell Int.* 2013, 1–8. doi:10.1155/2013/130763

Soleimani, M., and Nadri, S. (2009). A Protocol for Isolation and Culture of Mesenchymal Stem Cells from Mouse Bone Marrow. *Nat. Protoc.* 4 (1), 102–106. doi:10.1038/nprot.2008.221

Tabata, Y. (2009). Biomaterial Technology for Tissue Engineering Applications. *J. R. Soc. Interf.* 6, S311–S324. doi:10.1098/rsif.2008.0448.focus

Teja, A. S., and Koh, P. Y. (2009). Synthesis, Properties, and Applications of Magnetic Iron Oxide Nanoparticles. *Prog. Cryst. Growth Charact. Mater.* 55 (1-2), 22–45. doi:10.1016/j.pcrysgrow.2008.08.003

Urban, V. S., Kiss, J., Kovács, J., Gócza, E., Vas, V., Monostori, É., et al. (2008). Mesenchymal Stem Cells Cooperate with Bone Marrow Cells in Therapy of Diabetes. *Stem Cells* 26 (1), 244–253. doi:10.1634/stemcells.2007-0267

Wang, H. S., Hung, S. C., Peng, S. T., Huang, C. C., Wei, H. M., Guo, Y. J., et al. (2004). Mesenchymal Stem Cells in the Wharton's Jelly of the Human Umbilical Cord. *Stem Cells* 22 (7), 1330–1337. doi:10.1634/stemcells.2004-0013

Weinreb, M., Shinar, D., and Rodan, G. A. (1990). Different Pattern of Alkaline Phosphatase, Osteopontin, and Osteocalcin Expression in Developing Rat Bone Visualized by *In Situ* Hybridization. *J. Bone Miner Res.* 5 (8), 831–842. doi:10.1002/jbmr.5650050806

Wu, J., Cao, L., Liu, Y., Zheng, A., Jiao, D., Zeng, D., et al. (2019). Functionalization of Silk Fibroin Electrospun Scaffolds via BMSC Affinity Peptide Grafting through Oxidative Self-Polymerization of Dopamine for Bone Regeneration. *ACS Appl. Mater. Inter.* 11 (9), 8878–8895. doi:10.1021/acsami.8b22123

Xu, C. X., Hendry, J. H., Testa, N. G., and Allen, T. D. (1983). Stromal Colonies from Mouse Marrow: Characterization of Cell Types, Optimization of Plating Efficiency and its Effect on Radiosensitivity. *J. Cel Sci.* 61, 453–466. doi:10.1242/jcs.61.1.453

Yagi, H., Soto-Gutierrez, A., Parekkadan, B., Kitagawa, Y., Tompkins, R. G., Kobayashi, N., et al. (2010). Mesenchymal Stem Cells: Mechanisms of Immunomodulation and Homing. *Cel Transpl.* 19 (6), 667–679. doi:10.3727/096368910x508762

Yan, H., Li, L., Wang, Y., Huang, J., Wang, Z., Shi, X., et al. (2019). An Electrically and Magnetically Responsive Nanocomposite of GdPO4·H2O/P3HT/PLGA with Electrical Stimulation for Synergistically Enhancing the Proliferation and Differentiation of Pre-osteoblasts. *New J. Chem.* 43 (44), 17315–17326. doi:10.1039/c9nj04167b

Yan, H., Wang, Z., Li, L., Shi, X., Jia, E., Ji, Q., et al. (2021). DOPA-derived Electroactive Copolymer and IGF-1 Immobilized Poly(lactic-Co-Glycolic Acid)/hydroxyapatite Biodegradable Microspheres for Synergistic Bone Repair. *Chem. Eng. J.* 416, 129129. doi:10.1016/j.cej.2021.129129

Yu, Q., Zhang, Y., Wang, H., Brash, J., and Chen, H. (2011). Anti-fouling Bioactive Surfaces. *Acta Biomater.* 7 (4), 1550–1557. doi:10.1016/j.actbio.2010.12.021

Yu, D., Tang, L., Dong, Z., Loftis, K. A., Ding, Z., Cheng, J., et al. (2018). Effective Reduction of Non-specific Binding of Blood Cells in a Microfluidic Chip for Isolation of Rare Cancer Cells. *Biomater. Sci.* 6 (11), 2871–2880. doi:10.1039/c8bm00864g

Zhang, L., Ning, B., Jia, T., Gong, W., Cong, M., Chen, J.-F., et al. (2010). Microcarrier Bioreactor Culture System Promotes Propagation of Human Intervertebral Disc Cells. *Ir J. Med. Sci.* 179 (4), 529–534. doi:10.1007/s11845-010-0537-8

Zhao, X., Li, D., Zhang, L., Niu, Y., Wang, W., and Niu, B. (2021). Mesenchymal Stem Cell Therapies for Alzheimer's Disease: Preclinical Studies. *Metab. Brain Dis.* 36 (7), 1687–1695. doi:10.1007/s11011-021-00777-6

Zipori, D. (2004). Mesenchymal Stem Cells: Harnessing Cell Plasticity to Tissue and Organ Repair. *Blood Cell Mol. Dis.* 33 (3), 211–215. doi:10.1016/j.bcmd.2004.08.019

Zuk, P. A., Zhu, M., Mizuno, H., Huang, J., Futrell, J. W., Katz, A. J., et al. (2001). Multilineage Cells from Human Adipose Tissue: Implications for Cell-Based Therapies. *Tissue Eng.* 7 (2), 211–228. doi:10.1089/107632701300062859

Conflict of Interest: The authors declare that the research was conducted in the absence of any commercial or financial relationships that could be construed as a potential conflict of interest.

ORIGINAL RESEARCH
published: 13 April 2022
doi: 10.3389/fbioe.2022.845821

Fucoidan-Mediated Anisotropic Calcium Carbonate Nanorods of pH-Responsive Drug Release for Antitumor Therapy

Pei Wang[1,2,3], Fei Tong[1,2,3], Jun Luo[1,2,3], Zhihua Li[1,2,3], Junchao Wei[1,2,3]* and Yuangang Liu[4]*

[1]School of Stomatology, Nanchang University, Nanchang, China, [2]Jiangxi Province Key Laboratory of Oral Biomedicine, Nanchang, China, [3]Jiangxi Province Clinical Research Center for Oral Diseases, Nanchang, China, [4]Institute of Pharmaceutical Engineering, Huaqiao University, Xiamen, China

The shape of nanoparticles can determine their physical properties and then greatly impact the physiological reactions on cells or tissues during treatment. Traditionally spherical nanoparticles are more widely applied in biomedicine but are not necessarily the best. The superiority of anisotropic nanoparticles has been realized in recent years. The synthesis of the distinct-shaped metal/metal oxide nanoparticles is easily controlled. However, their biotoxicity is still up for debate. Hence, we designed $CaCO_3$ nanorods for drug delivery prepared at mild condition by polysaccharide-regulated biomineralization in the presence of fucoidan with sulfate groups. The $CaCO_3$ nanorods with a pH sensitivity–loaded antitumor drug mitoxantrone hydrochloride (MTO) showed excellent antitumor efficacy for the HeLa cells and MCF-7 cells *in vitro*. We believe that anisotropic nanoparticles will bring forth an emblematic shift in nanotechnology for application in biomedicine.

Keywords: anisotropic nanorods, biocompatibility, control release, chemotherapy, polysaccharide

Edited by:
João Conde,
New University of Lisbon, Portugal

Reviewed by:
Tsung-Rong Kuo,
Taipei Medical University, Taiwan
Ramar Thangam,
Korea University, South Korea

Correspondence:
Junchao Wei
weijunchao@ncu.edu.cn
Yuangang Liu
ygliu@hqu.edu.cn

Specialty section:
This article was submitted to Biomaterials, a section of the journal Frontiers in Bioengineering and Biotechnology

Received: *30 December 2021*
Accepted: *18 March 2022*
Published: *13 April 2022*

Citation:
Wang P, Tong F, Luo J, Li Z, Wei J and Liu Y (2022) Fucoidan-Mediated Anisotropic Calcium Carbonate Nanorods of pH-Responsive Drug Release for Antitumor Therapy. Front. Bioeng. Biotechnol. 10:845821. doi: 10.3389/fbioe.2022.845821

1 INTRODUCTION

Control over the structure, shape, size, and morphology of nanomaterials is an important fundamental goal of bioscience owing to their important roles in determining the properties. In particular, spherical nanoparticles such as nanospheres and liposomes are most broad and widely applied as drug carriers due to easy accessibility (Yang et al., 2018). Nevertheless, spherical nanoparticles are not necessarily in optimal shape for nanocarriers. For instance, Banerjee et al. found that the order of cellular uptake efficiency for the nanoparticles was rod > disc > sphere (Banerjee et al., 2016). Agarwal et al. found maximal accumulation of nanoparticles with disc shape rather than nanospheres in an *in vitro* tumor tissue model (Agarwal et al., 2015). Actually, red blood cells and many representative pathogens in human bodies have distinct shapes. Nowadays, the superiority of nonspherical nanoparticles attracts more and more attention from researchers due to their distinctive physicochemical properties and promising applications in biomedicine (Xie et al., 2017; Ding et al., 2018). The distinct-shaped nanoparticles exhibit different properties affecting their behavior *in vivo* during the delivery and reaction with cells. In addition to impacting the internalization of nanoparticles, blood circulation time and biodistribution also are discrepant for nanomedicine because macrophage uptake during the blood circulation is usually clear circulating nanoparticles (Copp et al., 2014; Liu et al., 2018). In contrast to spherical nanoparticles dependent on clathrin- and caveolin-mediated endocytosis, uptake of rod-shaped nanoparticles mainly based on clathrin-mediated endocytosis by macrophages has been found to be lower (Li et al., 2016). Special-shaped nanoparticles may improve the target for tumor tissues (Agarwal et al., 2015), but there is no report showing only targeting tumor cells or normal cells due to the shape of the nanoparticle.

Over the past years, the nanoparticle shapes of rod (Nakayama et al., 2015), belt (Talloj et al., 2020), wire (Hu et al., 2021), sheet (Mutalik et al., 2022), bipyramid (Yougbaré et al., 2021), triangle (Kuwahara et al., 2020), hexagon (Yong et al., 2021), disc (Chen et al., 2020), cube (Wang et al., 2021), octahedron (Park et al., 2018), tripod (Feng et al., 2020), star (Spedalieri et al., 2021), thorn (Li et al., 2020a), and tetrapod (Qiu and Yang, 2007) have been synthesized for different applications. For example, gold nanorods have been widely used in photothermal therapy because of their surface plasmon peaks in the near-infrared laser in comparison to nanospheres (Darwish et al., 2020). In particular, the shape-effect research studies are mainly dependent on metal or metal oxide nanoparticles such as gold and silver because they are easily controlled (Zhu et al., 2016; Chakraborty and Parak, 2019). However, the cytotoxicity of metallic nanoparticles has to be considered. In addition, the biodegradable organic nanoparticles with anisotropy are usually difficult to synthesize (Yang et al., 2018). Hence, the biocompatible nanoparticles such as mesoporous silica nanoparticles (Kankala et al., 2020), hydroxyapatite nanoparticles (Li et al., 2019; Tan et al., 2020), and calcium carbonate ($CaCO_3$) nanoparticles (Chaudhary and Maiti, 2019) were considered for application in biomedicine.

Calcium carbonate ($CaCO_3$), one of the most abundant minerals, has attracted widespread attention in the biomedicine field owing to its low cost, biocompatibility, biodegradability, and pH-sensitivity (Maleki Dizaj et al., 2015; Dong et al., 2016; Zheng et al., 2021). Hence, the $CaCO_3$ nanoparticles were used as drug/gene delivery vehicles. Lu et al. designed $CaCO_3$/pneumolysin antigen delivery systems by physical absorption to induce cellular immunity for immunotherapy (Lu et al., 2021a). Chen et al. successfully synthesized polyethyleneimine-modified $CaCO_3$ nanoparticles delivering p53 gene for gene therapy (Lu et al., 2021a). In particular, the $CaCO_3$ nanoparticles keep steady under a neutral environment and would be decomposed into Ca^{2+} and CO_2 in acidic pH. In another work, we constructed poly-L-ornithine/fucoidan-coated $CaCO_3$ particles with pH-controlled doxorubicin release for cancer therapy (Wang et al., 2018a). At present, the synthesis process of $CaCO_3$ nanoparticles is carried out mainly through ammonium bicarbonate (NH_4HCO_3) continuously diffusing into the calcium chloride ($CaCl_2$) solution. Moreover, the biomineralization method due to environmental friendliness and wide availability received tremendous attention in recent years (Sugawara-Narutaki, 2013; Lu et al., 2021b; Yang et al., 2021). Therein, the cooperative involvement of macromolecules during the crystallization of $CaCO_3$ nanoparticles is a benign strategy, such as polyacrylic acid (Nakayama et al., 2015), polyacrylamide (Yu et al., 2006), chitin (Ehrlich, 2010), and silk fibroin (Cao, 2008). Therein, fucoidan, as a natural polysaccharide, is a dramatic candidate for biomedical applications due to its unique properties such as biocompatibility and less immunogenicity (Lu et al., 2017; Hsu et al., 2018).

In this work, inspired by biomineralization, we develop anisotropic calcium carbonate nanoparticles having a rod structure through the coprecipitation method mediated by fucoidan (**Figure 1**). Importantly, the mechanism of $CaCO_3$ nanorods (NRs) with different aspect ratios was tested by changing the concentration of fucoidan. Moreover, we applied $CaCO_3$ nanorods in the field of biomedicine after loading with an antitumor drug MTO owing to its degradability in the acidic tumor environment, which can release the drugs quickly and achieve the pH-response drug release. As a result, efficient tumor regression was achieved, suggesting a new avenue for the exploitation of safe and effective therapeutic nanorods.

2 MATERIALS AND METHODS

2.1 Materials

All the reagents and chemicals were acquired commercially. Sodium carbonate and calcium chloride were purchased from Sinopharm Chemical Reagent Co., Ltd. (Shanghai, China). Fucoidan (Mw = 200–400 kDa) was purchased from Jiejing Group (Shandong, China). Mitoxantrone hydrochloride (MTO) was obtained from Meilun Biotech Co., Ltd., (Dalian, China). Penicillin, streptomycin, fetal bovine serum (FBS), and Dulbecco's modified Eagle medium (DMEM) were obtained from Biological Industries Ltd., (Hertzliya Pituach, Israel). The HeLa cells, MCF-7 cells, L929 cells, and C2C12 cells were acquired from the Type Culture Collection of Chinese Academy of Sciences (CAS) (Shanghai, China). MTT Cell Proliferation, acridine orange (AO)/ethidium bromide (EB) Cell Live/dead Kit, and DAPI Staining Solution were obtained from KeyGen Biotech Co., Ltd. (Nanjing, China).

2.2 Synthesis of Calcium Carbonate NRs

The $CaCO_3$ NRs were synthesized by utilizing a biomimetic method at room temperature. Briefly, calcium chloride (0.21 g) and sodium carbonate (0.22 g) were dissolved in 100 ml of water (0.02 M). Then, fucoidan was also dissolved in water at diverse concentrations (5, 10, 20, 30, 40, and 50 mg/ml). Furthermore, fucoidan (10 ml) was added to the calcium chloride solution (10 ml) and stirred for 1 h. Subsequently, sodium carbonate solution (10 ml) was added dropwise to the mixed solution of fucoidan and sodium carbonate to synthesize $CaCO_3$ NRs. Eventually, the products were collected, washed, and suspended in water.

2.3 Characterization of Calcium Carbonate NRs

We used the dynamic light scattering (DLS) instrument (ZetaPALS; Malvern Instruments Co., Ltd.) to measure the nanoparticle size distribution and zeta potential of the designed $CaCO_3$ NRs. The surface morphology was observed by using the scanning electron microscope (SEM, Hitachi S-4800) and transmission electron microscope (TEM, Hitachi H-7650).

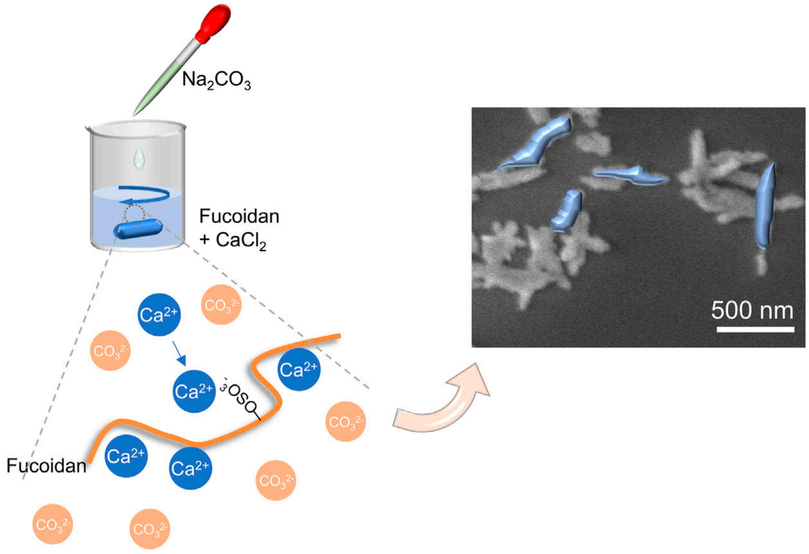

FIGURE 1 | Schematic diagram of the synthesis of $CaCO_3$ nanorods.

The powder X-ray diffraction (PXRD, Bruker AXS D8 Advance) analysis of the copper-impregnated and naked $CaCO_3$ NRs was carried out from 10° to 80° using Cu–Kα radiation. The characteristic groups on the $CaCO_3$ nanorods were analyzed by using Fourier transform infrared spectroscopy (FT-IR, Thermo Scientific Nicolet iS 50). The sample was prepared using a KBr pellet method.

2.4 Drug Loading and Encapsulation Efficiency Measurement

Mitoxantrone hydrochloride (MTO) was loaded with the $CaCO_3$ NRs using the following procedure. First, 5 mg of $CaCO_3$ NRs were dispersed in 25 ml phosphate-buffered solution (PBS) and then 5 mg of MTO was added for loading. After stirring overnight, the product defined as the MC NRs was centrifuged and washed twice with water. Furthermore, the supernatant concentration of MTO was detected by UV–Vis spectroscopy (TU-1810, PERSEE) at 663 nm and calculated with the calibration curve of MTO. Finally, the loading amount and encapsulation efficiency of MTO were calculated according to the following formulas:

$$\text{Loading amount}\,(\%) = (\mathrm{MTO_t} - \mathrm{MTO_s})/\mathrm{MC\ NRs} \times 100$$

$$\text{Encapsulation efficiency}\,(\%) = (\mathrm{MTO_t} - \mathrm{MTO_s}) \times / (\mathrm{MTO_t}) \times 100$$

where MTO_t is the total weight of MTO, MTO_s is the supernatant weight free MTO, and MC NRs is the weight of MC NRs.

2.5 Mitoxantrone Hydrochloride Release From MC NRs *in vitro*

MC NRs (5 mg) were moved into the dialysis bag, and then 20 ml of PBS was added for MTO release. Then, PBS was moved in a shaker kept at 37°C and 100 rpm for 72 h. PBS (2 ml) was removed for the measure at various periods using UV–Vis spectroscopy according to the calibration curve of MTO, and then 2 ml of fresh PBS was supplemented. All the measurements were carried out in triplicate.

2.6 Biocompatibility Assay of Calcium Carbonate NRs

2.6.1 Cytotoxicity Assay

The cytotoxicity assay of the $CaCO_3$ NRs was determined by methyl thiazolyl tetrazolium (MTT) for the L929 cells. First, L929 cells and C2C12 cells with 6×10^3 cells were seeded into a 96-well plate. After 24 h, DMEM was removed and 100 µl of fresh medium containing $CaCO_3$ NRs at different concentrations was added for coincubating for 24 h. Subsequently, the MTT reagent (10 µl) was added to each well for coincubating for 4 h. Finally, DMEM was removed and 150 µl of DMSO was added into a 96-well plate for measuring the absorbance by using a microplate reader (Varioskan Flash 1,510, Thermo Fisher Scientific). The cell viability rate was calculated by the following formula:

$$\text{Cell viability rate}\,(\%) = (\mathrm{OD_{treated}} - \mathrm{OD_{free}})/(\mathrm{OD_{control}} - \mathrm{OD_{free}}) \times 100$$

where $OD_{treated}$ is the absorbance of $CaCO_3$ NRs, OD_{free} is the absorbance of only DMSO, and $OD_{control}$ is the control group.

2.6.2 Hemolysis Test

To evaluate the hemolysis of $CaCO_3$ NRs, $CaCO_3$ NRs were incubated with normal saline and then added 0.2 ml diluted rabbit blood for 60 min at 37°C. Furthermore, we measured

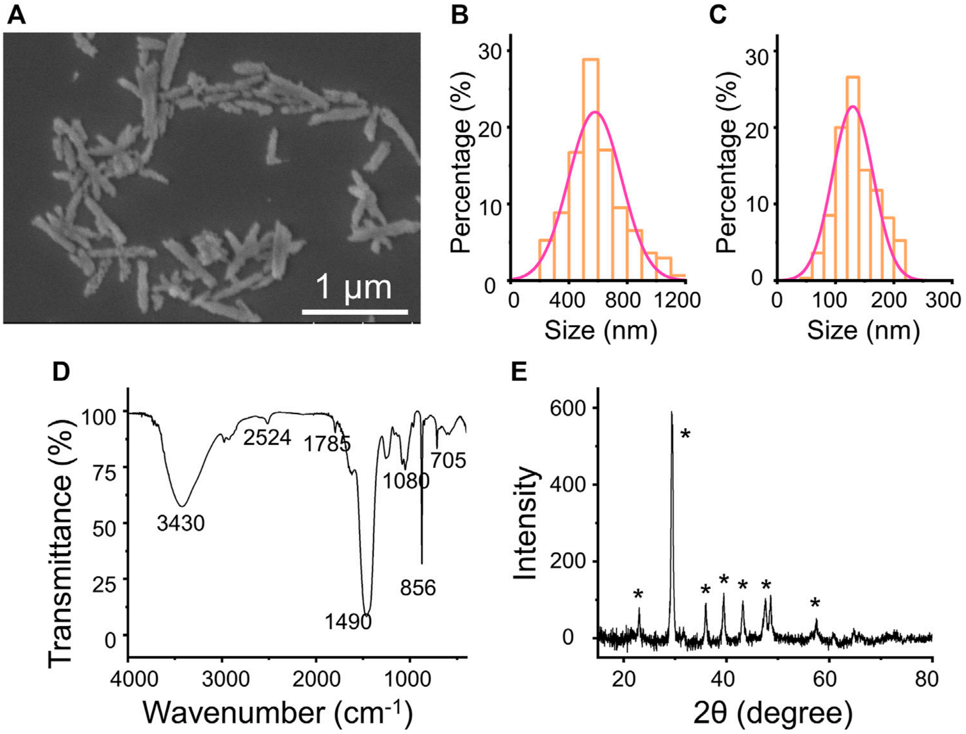

FIGURE 2 | (A) SEM images of the $CaCO_3$ NRs. **(B)** length and **(C)** width statistical chart of the $CaCO_3$ NRs. **(D)** FT-IR spectrum **(E)** XRD of $CaCO_3$ NRs.

TABLE 1 | Average length and width of the calcium carbonate nanorods prepared with different fucoidan concentrations.

Fucoidan (μg/ml)	5	10	20	30	40	50
Length (nm)	1,104 ± 340	792 ± 259	790 ± 226	570 ± 151	725 ± 223	855 ± 349
Width (nm)	462 ± 102	252 ± 45	204 ± 31	130 ± 35	170 ± 42	314 ± 71
Aspect ratio	2.4	3.1	3.9	4.5	4.3	2.7

the supernatant absorbance at 545 nm after centrifugation. The absorption of positive and negative control experiments was incubated with H_2O and normal saline, respectively. The hemolysis rate was calculated by the following formula:

$$\text{Hemolysis rate}\,(\%) = \left(\mathrm{OD}_{\mathrm{treated}} - \mathrm{OD}_{\mathrm{negative}}\right) \Big/ \left(\mathrm{OD}_{\mathrm{positive}} - \mathrm{OD}_{\mathrm{free}}\right) \times 100$$

where $\mathrm{OD}_{\mathrm{treated}}$ is the absorbance of $CaCO_3$ NRs, $\mathrm{OD}_{\mathrm{negative}}$ is the absorbance of normal saline, and $\mathrm{OD}_{\mathrm{positive}}$ is the absorbance of H_2O.

2.7 Cellular Uptake Study

The MCF-7 cells and HeLa cells were seeded at the cover glass in the 24-well plate for 24 h. Then, after coincubation with MC NRs for 2 and 4 h, the cover glass was washed three times with PBS. After staining with 4′,6-diamidino-2-phenylindole (DAPI), the cellular uptake images were observed by using a confocal laser scanning microscope (CLSM, Leica TCS SP5).

2.8 Antitumor Assay *in vitro*

For the antitumor assay *in vitro*, HeLa cells and MCF-7 cells were seeded into 96-well plates. Then, DMEM was removed and 100 μl of fresh DMEM containing MTO and MC NRs at diverse concentrations of 1, 2, 3, 5, and 10 μg/ml was added. Other details were the same as described in **Section 2.6.1**.

Apoptosis of the cancer cells was observed using the AO/EB Kit. The HeLa cells and MCF-7 cells were seeded into a 6-well plate and incubated for 24 h. The media were replaced with 1, 2, 3, 5, and 10 μg/ml of samples (MTO and MC NRs). After 24 h of incubation, the HeLa cells and MCF-7 cells were washed with PBS. Then, AO and EB were added and observed using a fluorescence microscope (Zeiss AXIO Observer Z1).

2.9 Statistical Analysis

All the data were expressed as the mean ± standard deviation (SD, $n \geq 3$). The statistical significance was calculated *via* one-way analysis of variance (ANOVA) followed by Tukey's test. A p-value of <0.05 was considered statistically significant ($^{*}p < 0.05$, $^{**}p < 0.01$, $^{***}p < 0.001$).

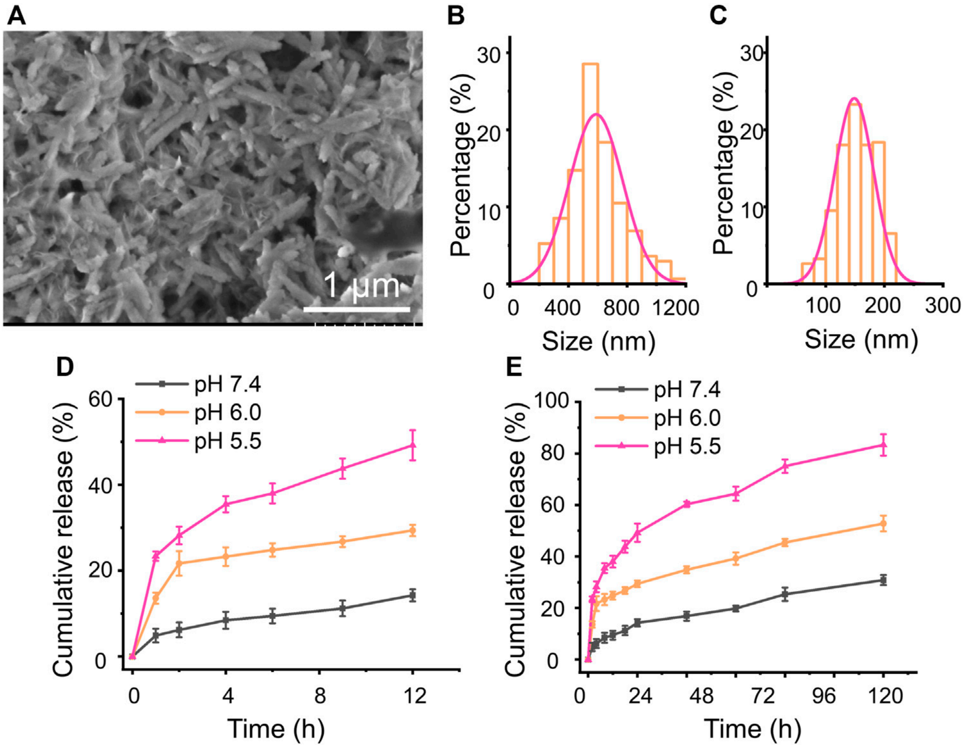

FIGURE 3 | (A) SEM images of the MC NRs. **(B)** length and **(C)** width statistical chart of the MC NRs. *In vitro* MTO cumulative release from the MC NRs in pH 7.4 and 6.0 and pH 5.5 PBS for **(D)** 12 h and **(E)** 72 h.

3 RESULTS AND DISCUSSION

3.1 Physicochemical Characterizations

The rod anisotropic $CaCO_3$ nanoparticles have been successfully prepared by utilizing a kind of natural polysaccharide, fucoidan, as a crystal mediator determined by the crystallographic growth direction and stabilizing agent prevented agglomeration of particles. The procedure for the preparation of $CaCO_3$ NRs is shown in **Figure 1**. Initially, Ca^{2+} was concentrated to fucoidan due to electrostatic attraction and the reaction between the sulfuric ester group and Ca^{2+} in the mixed solution at room temperature. Then, Na_2CO_3 aqueous solution was added dropwise for the crystallization of $CaCO_3$ NRs. During the process, the turbidity of the solution increased, which suggested the synthesis of crystalline $CaCO_3$ nanoparticles. The resultant $CaCO_3$ particles revealed a rod-shaped morphology at a submicrometer scale as observed by the SEM (**Figure 2A**). It should be noted that the monodisperse $CaCO_3$ nanorods were mediated with a relatively narrow distribution in size as shown in **Figure 2B** and **Figure 2C**. The histograms of length and width of the $CaCO_3$ NRs were measured by counting more than 300 samples pictured in the SEM. The average length and width of the $CaCO_3$ NRs were 579 ± 151 nm and 130 ± 35 nm, respectively, suggesting that the aspect ratio was 4.5. In addition, the quality content of S, Ca, and C from the $CaCO_3$ NRs was 0.4, 55.3, and 44.3% (**Supplementary Figure S2**), respectively. Moreover, the effects of fucoidan concentration on the size and morphology of $CaCO_3$ NRs were examined. The morphologies of the $CaCO_3$ nanorods are analogous with the distinct concentration of fucoidan (**Supplementary Figure S1**). The size of the nanorods was decreased with increasing the concentration of fucoidan from 5 to 30 μg/ml and then increasing from 40 to 50 μg/ml (**Table 1**). On the basis of these results, it is suggested that fucoidan not only stabilizes the anisotropic $CaCO_3$ nanorods but the size of nanorods is also sensitive to the fucoidan concentration.

Furthermore, the crystalline phase of the nanocrystals was identified as aragonite by FT-IR spectroscopy (**Figure 2D**) and XRD measurement (**Figure 2E**). The transmittance peaks in the FT-IR spectrum at 705, 856, and 1,080 cm^{-1} are attributed to the $CaCO_3$ aragonite form (Yu et al., 2006). In addition, the peaks at 856 cm^{-1} and 705 cm^{-1} are ascribed to the vibration of the out-of-plane bending and in-plane bending of CO_3^{2-} in aragonite, respectively. In addition, all the peaks in the XRD pattern (**Figure 2E**) are characteristic of aragonite. The diffraction peaks of the $CaCO_3$ nanorods from the XRD (labeled with the symbol ∗) could be indicated to the aragonite $CaCO_3$ accordingly (JCPDS Card no. 05-0453).

3.2 *In vitro* Mitoxantrone Hydrochloride Release From MC NRs

MTO, as a broad anticancer drug, can intercalate into the DNA or RNA through hydrogen bonding to induce cross-links and

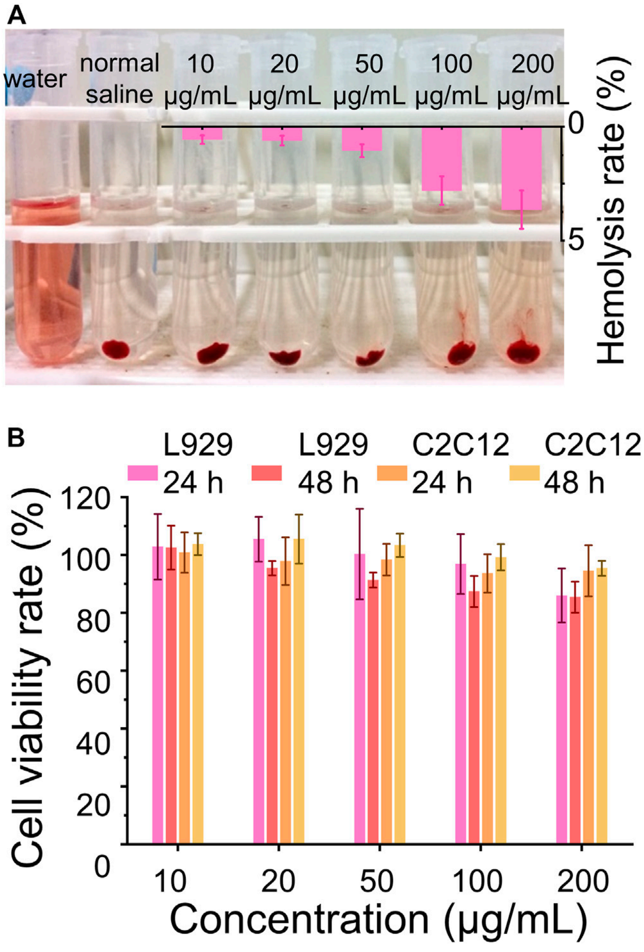

FIGURE 4 | Biocompatibility assay. **(A)** Hemolysis assay after the treatment with different concentrations of the MC NRs. **(B)** Cell viability rate of the L929 cells and C2C12 cells treated with $CaCO_3$ NRs for 24 and 48 h.

strand breaks and interfere with the stabilization of DNA topoisomerase II cleavable complex (Duan et al., 2013; Wang et al., 2019). Herein, the MTO was used to appraise the loading amount of the previously prepared $CaCO_3$ NRs and observed the pH-sensitive release behavior. To prepare the MTO-loaded $CaCO_3$ NRs (MC NRs), MTO was quickly added into the prepared PBS containing $CaCO_3$ NRs and after stirring overnight, the unloaded MTO was removed by centrifugation. In terms of the calibration curves of MTO (**Supplementary Figure S3**), the loading amount and entrapment efficiencies of the MC NRs were calculated as 34.5 ± 2.8% and 52.7 ± 1.9%, respectively. After loading the drug, the characteristics of the MC NRs were observed from the SEM (**Figure 3A**), which intuitively presented a smoother surface. Moreover, the histograms of length (**Figure 3B**) and width (**Figure 3C**) of the MC NRs were measured by counting 300 samples pictured in the SEM, which showed that the MTO-loaded nanoparticles are larger than those of the unloaded ones, suggesting that MTO was loaded into the $CaCO_3$ NRs. The average length and width of the MC NRs were 590 ± 182 nm and 149 ± 33 nm, respectively, suggesting that the aspect ratio of the nanorods was 4.0.

As we all know, $CaCO_3$ can be disintegrated and release Ca^{2+} and CO_2 at low pH. Afterward, a release assay using PBS with pH 7.4, 6.0, and 5.5 simulating the intracorporeal conditions was carried out, drawing the MTO cumulative release profile from the MC NRs. The classic dialysis method with time intervals was used for 72 h. Initially, burst MTO release from the MC NRs within 12 h was observed at neutral and acidic pH (**Figure 3D**), which might be attributed to the water-induced dissolution. In addition, the cumulative release rate dramatically increased with a decrease of pH from 7.4 to 5.5, as PBS with pH 5.5 presented the most drastic MTO release (**Figure 3D**). In particular, merely 17% of the drug was released over 12 h in PBS of pH 7.4, suggesting that the MTO stably loading with the $CaCO_3$ NRs was well-realized. In addition, diminishing the pH value to 5.5 increased the drug release in the MC NRs to approximately 50% at 12 h, proving the pH-responsive property of the $CaCO_3$ NRs (Ferreira et al., 2020). It is an advantage for the MC NRs to serve as a multifunctional drug delivery system in biomedical applications. Notably, the $CaCO_3$ NRs with the nature of acid-triggered decomposition could be appropriate for long blood circulation under the physiological pH and quick release within the acid tumor microenvironment and lysosomes.

3.3 Biocompatibility Study

Biocompatibility is one of the important requirements for biomaterials, which should neither adversely affect normal cells nor destruct their normal balance in clinical applications (Janeesh et al., 2014; Li et al., 2020b; Lin et al., 2021). Furthermore, the biomaterials utilized *in vivo* ineluctably contact and interact with the red blood cells which play important physiological functions and are also the most abundant blood cells. Herein, the interaction between the red blood cells and $CaCO_3$ NRs and the cytotoxicity were used to evaluate the biocompatibility. The results showed that the hemolysis rates of the $CaCO_3$ NRs were less than 5% (**Figure 4A**) within the concentration range from 10 to 200 μg/ml, demonstrating excellent hemocompatibility. In addition, the cytotoxicity of $CaCO_3$ NRs was evaluated with the C2C12 cells and L929 cells. The results showed that all the concentrations had cell viability rates of more than 80% (**Figure 4B**) after coincubating for 24 and 48 h. Therefore, all the results demonstrated that the prepared nanocarriers of the $CaCO_3$ NRs had shown no obvious toxicity.

3.4 Cellular Internalization Efficiency

Based on these rod anisotropic nanoplatforms, next, we studied the interactions of MC nanoparticles *in vitro* with tumor cells. The MCF-7 cells and HeLa cells were incubated with the MC NRs for 2 and 4 h, respectively, at 37°C for observing the cellular uptake ability of our nanoparticles and then imaged by a CLSM (**Figure 5**). The nucleus of the HeLa cells and MCF-7 cells were stained with DAPI dye with

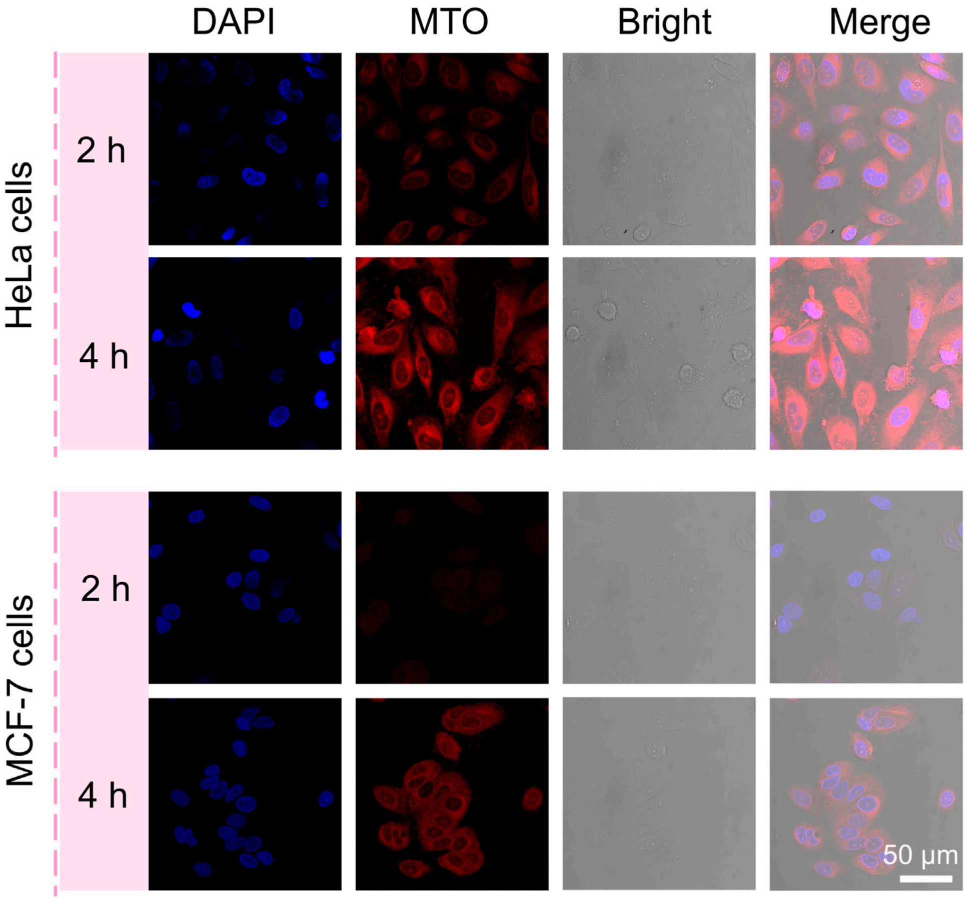

FIGURE 5 | CLSM images of the HeLa cells and MCF-7 cells incubated with MC NRs for 2 or 4 h showing the internalization efficiency of the MC NRs, where the nuclei were counterstained with DAPI.

blue fluorescence. Then, red MTO fluorescence emerged inside the HeLa and MCF-7 cells after incubation with the MC NRs, describing the efficient cellular uptake of our nanoparticles. Especially, while MTO fluorescence was observed only in HeLa cell cytoplasm after 2 h, MTO fluorescence appeared in nuclei after 4 h, indicating the dissociation of MC NRs (lysosomes with acid pH). Moreover, the red fluorescence of the MCF-7 cells was weaker than that of the HeLa cells, suggesting that there was a difference in the cellular uptake of the MC NRs, maybe due to the difference in cellular growth. In addition, the design of the nanocarriers requires a good understanding of the mechanisms of cellular uptake which is related to the improvement of therapeutic efficiency (Ding et al., 2018). The cellular uptake of the MC NRs may mainly be mediated through the clathrin-mediated endocytosis pathway according to other reports (Xie et al., 2017; Ding et al., 2018; Yang et al., 2018). We will further research the endocytosis mechanism of the MC NRs in our future study. In brief, these results indicated that the MC nanoparticles were capable of pH-sensitive manner for drug release specifically responding to the acid microenvironment.

3.5 *In vitro* Antitumor Performance

To observe the antitumor performance of the MC NRs *in vitro*, herein, the HeLa human cervical carcinoma cells and MCF-7 human breast cancer cells were set as model cells. Comparing the antitumor effects, the free MTO and MC NRs were treated with the cancer cells in terms of cell viability over 24 and 48 h. First, the HeLa cells and MCF-7 cells were incubated with free MTO or MC NRs at the equivalent MTO concentrations. After coincubating for 24 h or 48 h, the relative cell viabilities were observed by MTT assay (**Figures 6A–D**). The results show that the MC NRs present a comparable antitumor efficiency to that of free MTO. The cell viability rates of the HeLa cells treated with MC NRs were 30.3 ± 4.2% and 24.7 ± 6.3% with the concentration of 5 μg/ml after 24 and 48 h, comparing 62.6 ± 5.3% and 52.7 ± 4.1% with the free MTO. The cell viability rates of the MCF-7 cells treated with the MC NRs were 29.1 ± 7.1% and 21.8 ± 5.7% with the concentration of 10 μg/ml after 24 and 48 h, comparing 40.6 ± 3.1% and 36.5 ± 3.1% with the free MTO. In addition, the antitumor efficacy of the MC NRs presented a concentration-dependent manner. As expected, the pH sensitivity of the MC NRs after uptake by the tumor cells

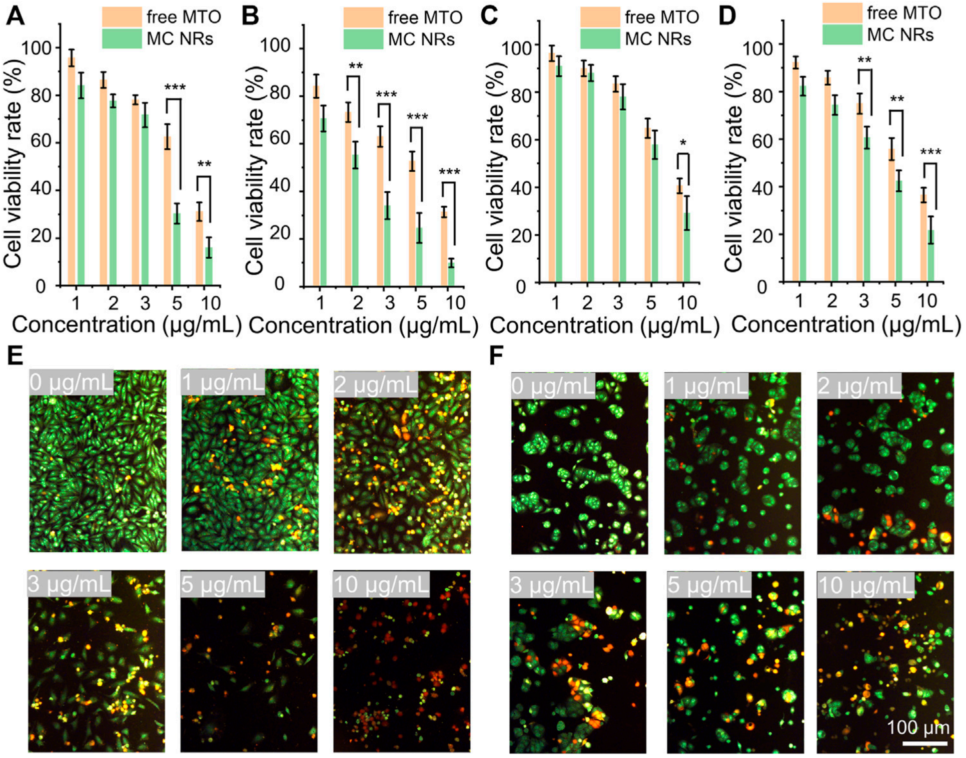

FIGURE 6 | *In vitro* antitumor performance. The cell viability rate of the HeLa cells treated with free MTO and MC NRs for **(A)** 24 h and **(B)** 48 h. The cell viability rate of the MCF-7 cells treated with free MTO and MC NRs for **(C)** 24 h and **(D)** 48 h. Fluorescence images showing **(E)** HeLa cells and **(F)** MCF-7 cells stained with AO (live cells, green fluorescence) and EB (dead cells, red fluorescence) after culturing with different concentration of MTO-CaCO3 NRs (in terms of MTO 0, 1, 2, 3, 5, and 10 μg/ml) for 24 h.

determines the prominent antitumor effects in the intracellular acid lysosomal environment (Wang et al., 2018b). Then, the abundance of the MTO released from the MC nanoparticles slowly permeates into the nuclei (**Figure 5**). Meanwhile, the dysfunctional tumor nuclei were induced by the cytotoxicity of the released MTO. With the accumulated cytotoxicity of the MTO, significant tumor cell death was observed at the concentration of 5 and 10 μg/ml for 24 and 48 h.

To further intuitively observe the anti-tumor efficacy of MC NRs, HeLa and MCF-7 cells were stained using the AO/EB kit after treatment with MC NRs for 24 h. Then, the live cells were stained with green fluorescence, early-apoptosis cells were stained with orange fluorescence, and late-apoptosis cells were stained with red fluorescence (**Figures 6E,F**). Notably, many apoptotic HeLa cells and MCF-7 cells were detected above 3 μg/ml MTO, and the cellular density of both cells significantly decreased with the increase of the concentration of the MC NRs. In addition, the MC NRs exhibit concentration-dependent anticancer activity corresponding to the MTT assay results. Importantly, the MCF-7 cells had fewer late apoptotic cells than HeLa cells, possibly because the MCF-7 cells have a habit of growing into a mass, which is difficult for the MC NRs to penetrate (Hattangadi et al., 2004; Ziegler et al., 2014).

4 CONCLUSION

In summary, the rod anisotropic $CaCO_3$ nanoparticles with different aspect ratios were successfully synthesized using fucoidan as a crystal mediator, which adsorbed the calcium ions through sulfate groups. The $CaCO_3$ NRs present good biocompatibility, which was suitable for drug delivery. Furthermore, the $CaCO_3$ NRs possessed precise pH responsiveness for anticancer-drug release at the tumor microenvironment. In *in vitro* antitumor performance, the MC NRs showed good antitumor effect and cellular uptake for the MCF-7 cells and HeLa cells. Our work provides a new design for forming rod $CaCO_3$ nanocarriers. Our findings open the new possibility to prepare calcium carbonate nanoparticles of different shapes with well-tuned structures using other biomacromolecules or polymers.

DATA AVAILABILITY STATEMENT

The original contributions presented in the study are included in the article/**Supplementary Material**, further inquiries can be directed to the corresponding authors.

AUTHOR CONTRIBUTIONS

PW, JW, and YL contributed to the conception of the study; PW performed the experiment and wrote the manuscript; FT, JL, and ZL helped perform the analysis with constructive discussions.

ACKNOWLEDGMENTS

We sincerely acknowledge for the financial support from the Technological Plan of Health Commission of Jiangxi Province of China (SKJP520204072), the National Natural Science Foundation of China (52163016, 32171337, and 82060198), and the Natural Science Foundation of Jiangxi Province of China (20192BAB205055).

SUPPLEMENTARY MATERIAL

The Supplementary Material for this article can be found online at: https://www.frontiersin.org/articles/10.3389/fbioe.2022.845821/full#supplementary-material

REFERENCES

Agarwal, R., Jurney, P., Raythatha, M., Singh, V., Sreenivasan, S. V., Shi, L., et al. (2015). Effect of Shape, Size, and Aspect Ratio on Nanoparticle Penetration and Distribution inside Solid Tissues Using 3D Spheroid Models. *Adv. Healthc. Mater.* 4 (15), 2269–2280. doi:10.1002/adhm.201500441

Banerjee, A., Qi, J., Gogoi, R., Wong, J., and Mitragotri, S. (2016). Role of Nanoparticle Size, Shape and Surface Chemistry in Oral Drug Delivery. *J. Controlled Release* 238, 176–185. doi:10.1016/j.jconrel.2016.07.051

Cao, X. A. C. (2008). Coeffect of Silk Fibroin and Self-Assembly Monolayers on the Biomineralization of Calcium Carbonate. *The J. Phys. Chem. C* 112 (40), 15844–15849. doi:10.1021/jp804848q

Chakraborty, I., and Parak, W. J. (2019). Protein-Induced Shape Control of Noble Metal Nanoparticles. *Adv. Mater. Inter.* 6 (6), 1801407s. doi:10.1002/admi.201801407

Chaudhary, M., and Maiti, A. (2019). Defluoridation by Highly Efficient Calcium Hydroxide Nanorods from Synthetic and Industrial Wastewater. *Colloids Surf. A: Physicochemical Eng. Aspects* 561, 79–88. doi:10.1016/j.colsurfa.2018.10.052

Chen, A., Majdinasab, E. J., Fiori, M. C., Liang, H., and Altenberg, G. A. (2020). Polymer-Encased Nanodiscs and Polymer Nanodiscs: New Platforms for Membrane Protein Research and Applications. *Front. Bioeng. Biotechnol.* 8, 598450. doi:10.3389/fbioe.2020.598450

Copp, J. A., Fang, R. H., Luk, B. T., Hu, C.-M. J., Gao, W., Zhang, K., et al. (2014). Clearance of Pathological Antibodies Using Biomimetic Nanoparticles. *Proc. Natl. Acad. Sci. U.S.A.* 111 (37), 13481–13486. doi:10.1073/pnas.1412420111

Darwish, W. M., Abdoon, A. S., Shata, M. S., and Elmansy, M. (2020). Vincristine-loaded Polymeric corona Around Gold Nanorods for Combination (Chemo-photothermal) Therapy of Oral Squamous Carcinoma. *Reactive Funct. Polym.* 151, 104575. doi:10.1016/j.reactfunctpolym.2020.104575

Ding, L., Yao, C., Yin, X., Li, C., Huang, Y., Wu, M., et al. (2018). Size, Shape, and Protein Corona Determine Cellular Uptake and Removal Mechanisms of Gold Nanoparticles. *Small* 14 (42), e1801451. doi:10.1002/smll.201801451

Dong, Z., Feng, L., Zhu, W., Sun, X., Gao, M., Zhao, H., et al. (2016). CaCO3 Nanoparticles as an Ultra-sensitive Tumor-pH-Responsive Nanoplatform Enabling Real-Time Drug Release Monitoring and Cancer Combination Therapy. *Biomaterials* 110, 60–70. doi:10.1016/j.biomaterials.2016.09.025

Duan, Q., Cao, Y., Li, Y., Hu, X., Xiao, T., Lin, C., et al. (2013). pH-Responsive Supramolecular Vesicles Based on Water-Soluble Pillar[6]arene and Ferrocene Derivative for Drug Delivery. *J. Am. Chem. Soc.* 135, 10542–10549. doi:10.1021/ja405014r

Ehrlich, H. (2010). Chitin and Collagen as Universal and Alternative Templates in Biomineralization. *Int. Geology. Rev.* 52 (7-8), 661–699. doi:10.1080/00206811003679521

Feng, Y.-G., Niu, H.-J., Mei, L.-P., Feng, J.-J., Fang, K.-M., and Wang, A.-J. (2020). Engineering 3D Hierarchical Thorn-like PtPdNiCu Alloyed Nanotripods with Enhanced Performances for Methanol and Ethanol Electrooxidation. *J. Colloid Interf. Sci.* 575, 425–432. doi:10.1016/j.jcis.2020.04.120

Ferreira, A. M., Vikulina, A. S., and Volodkin, D. (2020). CaCO3 Crystals as Versatile Carriers for Controlled Delivery of Antimicrobials. *J. Controlled Release* 328, 470–489. doi:10.1016/j.jconrel.2020.08.061

Hattangadi, D. K., DeMasters, G. A., Walker, T. D., Jones, K. R., Di, X., Newsham, I. F., et al. (2004). Influence of P53 and Caspase 3 Activity on Cell Death and Senescence in Response to Methotrexate in the Breast Tumor Cell. *Biochem. Pharmacol.* 68 (9), 1699–1708. doi:10.1016/j.bcp.2004.06.033

Hsu, H.-Y., Lin, T.-Y., Hu, C.-H., Shu, D. T. F., and Lu, M.-K. (2018). Fucoidan Upregulates TLR4/CHOP-Mediated Caspase-3 and PARP Activation to Enhance Cisplatin-Induced Cytotoxicity in Human Lung Cancer Cells. *Cancer Lett.* 432, 112–120. doi:10.1016/j.canlet.2018.05.006

Hu, H., Sekar, S., Wu, W., Battie, Y., Lemaire, V., Arteaga, O., et al. (2021). Nanoscale Bouligand Multilayers: Giant Circular Dichroism of Helical Assemblies of Plasmonic 1D Nano-Objects. *ACS nano* 15, 13653–13661. doi:10.1021/acsnano.1c04804

Janeesh, P. A., Sami, H., Dhanya, C. R., Sivakumar, S., and Abraham, A. (2014). Biocompatibility and Genotoxicity Studies of Polyallylamine Hydrochloride Nanocapsules in Rats. *RSC Adv.* 4 (47), 24484–24497. doi:10.1039/c4ra02418d

Kankala, R. K., Han, Y. H., Na, J., Lee, C. H., Sun, Z., Wang, S. B., et al. (2020). Nanoarchitectured Structure and Surface Biofunctionality of Mesoporous Silica Nanoparticles. *Adv. Mater.* 32 (23), e1907035. doi:10.1002/adma.201907035

Kuwahara, S., Narita, Y., Mizuno, L., Kurotsu, H., Yoshino, H., and Kuwahara, M. (2020). Localized Surface Plasmon Resonance-Induced Welding of Gold Nanotriangles and the Local Plasmonic Properties for Multicolor Sensing and Light-Harvesting Applications. *ACS Appl. Nano Mater.* 3 (6), 5172–5177. doi:10.1021/acsanm.0c00608

Li, J., Zhu, D., Ma, W., Yang, Y., Wang, G., Wu, X., et al. (2020). Rapid Synthesis of a Bi@ZIF-8 Composite Nanomaterial as a Near-Infrared-II (NIR-II) Photothermal Agent for the Low-Temperature Photothermal Therapy of Hepatocellular Carcinoma. *Nanoscale* 12 (32), 17064–17073. doi:10.1039/d0nr03907a

Li, X., Wang, N., He, J., Yang, Z., Zhao, F., Wang, K., et al. (2020). One-Step Preparation of Highly Durable Superhydrophobic Carbon Nanothorn Arrays. *Small* 16 (26), e1907013. doi:10.1002/smll.201907013

Li, Y., Hao, H., Zhong, Z., Li, M., Li, J., Du, Y., et al. (2019). Assembly Mechanism of Highly Crystalline Selenium-Doped Hydroxyapatite Nanorods via Particle Attachment and Their Effect on the Fate of Stem Cells. *ACS Biomater. Sci. Eng.* 5 (12), 6703–6714. doi:10.1021/acsbiomaterials.9b01029

Li, Z., Sun, L., Zhang, Y., Dove, A. P., O'Reilly, R. K., and Chen, G. (2016). Shape Effect of Glyco-Nanoparticles on Macrophage Cellular Uptake and Immune Response. *ACS Macro Lett.* 5 (9), 1059–1064. doi:10.1021/acsmacrolett.6b00419

Lin, J., Huang, L., Xiang, R., Ou, H., Li, X., Chen, A., et al. (2021). Blood Compatibility Evaluations of CaCO3 Particles. *Biomed. Mater.* 16 (5), 055010. doi:10.1088/1748-605x/ac19bf

Liu, J.-M., Zhang, D.-D., Fang, G.-Z., and Wang, S. (2018). Erythrocyte Membrane Bioinspired Near-Infrared Persistent Luminescence Nanocarriers for *In Vivo* Long-Circulating Bioimaging and Drug Delivery. *Biomaterials* 165, 39–47. doi:10.1016/j.biomaterials.2018.02.042

Lu, H., Huang, Y.-C., Hunger, J., Gebauer, D., Cölfen, H., and Bonn, M. (2021). Role of Water in CaCO3 Biomineralization. *J. Am. Chem. Soc.* 143 (4), 1758–1762. doi:10.1021/jacs.0c11976

Lu, J., Jiao, Y., Cao, G., and Liu, Z. (2021). Multimode CaCO3/pneumolysin Antigen Delivery Systems for Inducing Efficient Cellular Immunity for Antitumor Immunotherapy. *Chem. Eng. J.* 420, 129746. doi:10.1016/j.cej.2021.129746

Lu, K.-Y., Li, R., Hsu, C.-H., Lin, C.-W., Chou, S.-C., Tsai, M.-L., et al. (2017). Development of a New Type of Multifunctional Fucoidan-Based Nanoparticles for Anticancer Drug Delivery. *Carbohydr. Polym.* 165, 410–420. doi:10.1016/j.carbpol.2017.02.065

Maleki Dizaj, S., Barzegar-Jalali, M., Adibkia, M. H., and Lotfipour, F. (2015). Calcium Carbonate Nanoparticles as Cancer Drug Delivery System. *Expert Opin. Drug Deliv.* 12 (10), 1649–1660. doi:10.1517/17425247.2015.1049530

Mutalik, C., Okoro, G., Krisnawati, D. I., Jazidie, A., Rahmawati, E. Q., Rahayu, D., et al. (2022). Copper Sulfide with Morphology-dependent Photodynamic and Photothermal Antibacterial Activities. *J. Colloid Interf. Sci.* 607, 1825–1835. doi:10.1016/j.jcis.2021.10.019

Nakayama, M., Kajiyama, S., Nishimura, T., and Kato, T. (2015). Liquid-crystalline Calcium Carbonate: Biomimetic Synthesis and Alignment of Nanorod Calcite. *Chem. Sci.* 6 (11), 6230–6234. doi:10.1039/c5sc01820j

Park, S.-K., Choi, J. H., and Kang, Y. C. (2018). Unique Hollow NiO Nanooctahedrons Fabricated through the Kirkendall Effect as Anodes for Enhanced Lithium-Ion Storage. *Chem. Eng. J.* 354, 327–334. doi:10.1016/j.cej.2018.08.018

Qiu, Y., and Yang, S. (2007). ZnO Nanotetrapods: Controlled Vapor-phase Synthesis and Application for Humidity Sensing. *Adv. Funct. Mater.* 17 (8), 1345–1352. doi:10.1002/adfm.200601128

Spedalieri, C., Szekeres, G. P., Werner, S., Guttmann, P., and Kneipp, J. (2021). Intracellular Optical Probing with Gold Nanostars. *Nanoscale* 13 (2), 968–979. doi:10.1039/d0nr07031a

Sugawara-Narutaki, A. (2013). Bio-inspired Synthesis of Polymer-Inorganic Nanocomposite Materials in Mild Aqueous Systems. *Polym. J.* 45, 269–276. doi:10.1038/pj.2012.171

Talloj, S. K., Mohammed, M., and Lin, H.-C. (2020). Construction of Self-Assembled Nanostructure-Based Tetraphenylethylene Dipeptides: Supramolecular Nanobelts as Biomimetic Hydrogels for Cell Adhesion and Proliferation. *J. Mater. Chem. B* 8 (33), 7483–7493. doi:10.1039/d0tb01147a

Tan, J., Liu, Y., Gong, J., Jin, X., Cheng, C., Zhang, R., et al. (2020). Non-aqueous Liquid Crystals of Hydroxyapatite Nanorods. *Acta Biomater.* 116, 383–390. doi:10.1016/j.actbio.2020.09.002

Wang, C., Chen, S., Wang, Y., Liu, X., Hu, F., Sun, J., et al. (2018). Lipase-Triggered Water-Responsive "Pandora's Box" for Cancer Therapy: Toward Induced Neighboring Effect and Enhanced Drug Penetration. *Adv. Mater.* 30 (14), e1706407. doi:10.1002/adma.201706407

Wang, C., Han, M., Liu, X., Chen, S., Hu, F., Sun, J., et al. (2019). Mitoxantrone-preloaded Water-Responsive Phospholipid-Amorphous Calcium Carbonate Hybrid Nanoparticles for Targeted and Effective Cancer Therapy. *Ijn* 14, 1503–1517. doi:10.2147/ijn.s193976

Wang, P., Kankala, R. K., Chen, B., Zhang, Y., Zhu, M., Li, X., et al. (2021). Cancer Cytomembrane-Cloaked Prussian Blue Nanoparticles Enhance the Efficacy of Mild-Temperature Photothermal Therapy by Disrupting Mitochondrial Functions of Cancer Cells. *ACS Appl. Mater. Inter.* 13 (31), 37563–37577. doi:10.1021/acsami.1c11138

Wang, P., Kankala, R. K., Fan, J., Long, R., Liu, Y., and Wang, S. (2018). Poly-L-ornithine/fucoidan-coated Calcium Carbonate Microparticles by Layer-By-Layer Self-Assembly Technique for Cancer Theranostics. *J. Mater. Sci. Mater. Med.* 29 (5), 68–78. doi:10.1007/s10856-018-6075-z

Xie, X., Liao, J., Shao, X., Li, Q., and Lin, Y. (2017). The Effect of Shape on Cellular Uptake of Gold Nanoparticles in the Forms of Stars, Rods, and Triangles. *Sci. Rep.* 7 (1), 3827. doi:10.1038/s41598-017-04229-z

Yang, T., Ao, Y., Feng, J., Wang, C., and Zhang, J. (2021). Biomineralization Inspired Synthesis of CaCO3-Based DDS for pH-Responsive Release of Anticancer Drug. *Mater. Today Commun.* 27, 102256. doi:10.1016/j.mtcomm.2021.102256

Yang, Y., Nie, D., Liu, Y., Yu, M., and Gan, Y. (2018). Advances in Particle Shape Engineering for Improved Drug Delivery. *Drug Discov. Today* 24 (2), 575–583. doi:10.1016/j.drudis.2018.10.006

Yong, Z., Yap, L. W., Fu, R., Shi, Q., Guo, Z., and Cheng, W. (2021). Seagrass-inspired Design of Soft Photocatalytic Sheets Based on Hydrogel-Integrated Free-Standing 2D Nanoassemblies of Multifunctional Nanohexagons. *Mater. Horiz.* 8 (9), 2533–2540. doi:10.1039/d1mh00753j

Yougbaré, S., Chou, H.-L., Yang, C.-H., Krisnawati, D. I., Jazidie, A., Nuh, M., et al. (2021). Facet-dependent Gold Nanocrystals for Effective Photothermal Killing of Bacteria. *J. Hazard. Mater.* 407, 124617. doi:10.1016/j.jhazmat.2020.124617

Yu, Q., Ou, H.-D., Song, R.-Q., and Xu, A.-W. (2006). The Effect of Polyacrylamide on the Crystallization of Calcium Carbonate: Synthesis of Aragonite Single-crystal Nanorods and Hollow Vatarite Hexagons. *J. Cryst. Growth* 286 (1), 178–183. doi:10.1016/j.jcrysgro.2005.09.046

Zheng, P., Ding, B., Shi, R., Jiang, Z., Xu, W., Li, G., et al. (2021). A Multichannel Ca2+ Nanomodulator for Multilevel Mitochondrial Destruction-Mediated Cancer Therapy. *Adv. Mater.* 33 (15), e2007426. doi:10.1002/adma.202007426

Zhu, B., Xu, Z., Wang, C., and Gao, Y. (2016). Shape Evolution of Metal Nanoparticles in Water Vapor Environment. *Nano Lett.* 16 (4), 2628–2632. doi:10.1021/acs.nanolett.6b00254

Ziegler, E., Hansen, M.-T., Haase, M., Emons, G., and Gründker, C. (2014). Generation of MCF-7 Cells with Aggressive Metastatic Potential *In Vitro* and *In Vivo*. *Breast Cancer Res. Treat.* 148 (2), 269–277. doi:10.1007/s10549-014-3159-4

Conflict of Interest: The authors declare that the research was conducted in the absence of any commercial or financial relationships that could be construed as a potential conflict of interest.

frontiers | Frontiers in Materials

ORIGINAL RESEARCH
published: 19 May 2022
doi: 10.3389/fmats.2022.914853

Bone Response to Osteopontin-Functionalized Carboxyethylphosphonic Acid-Modified Implants. Experimental Study in a Minipig Model

Javier Aragoneses[1†], Nansi López-Valverde[1†], Antonio López-Valverde[2]*, Cinthia Rodríguez[3], Bruno Macedo De Sousa[4] and Juan Manuel Aragoneses[5]

[1]Department of Medicine and Medical Specialties, Faculty of Health Sciences, Universidad Alcalá de Henares, Madrid, Spain, [2]Department of Surgery, Instituto de Investigación Biomédica de Salamanca (IB-SAL), University of Salamanca, Salamanca, Spain, [3]Department of Dentistry, Universidad Federico Henríquez y Carvajal, Santo Domingo, Dominican Republic, [4]Institute for Occlusion and Orofacial Pain Faculty of Medicine, Polo I-Edifício Cen-tral Rua Larga, University of Coimbra, Coimbra, Portugal, [5]Faculty of Dentistry, Universidad Alfonso X El Sabio, Madrid, Spain

OPEN ACCESS

Edited by:
Min Jiang,
Nanjing Tech University, China

Reviewed by:
Fei Tan,
Tongji University, China
Juan Carlos Ibanez,
Catholic University of Córdoba,
Argentina

***Correspondence:**
Antonio López-Valverde
alopezvalverde@usal.es

[†]These authors have contributed equally to this work

Specialty section:
This article was submitted to Biomaterials,
a section of the journal
Frontiers in Materials

Received: 07 April 2022
Accepted: 05 May 2022
Published: 19 May 2022

Citation:
Aragoneses J, López-Valverde N, López-Valverde A, Rodríguez C, Macedo De Sousa B and Aragoneses JM (2022) Bone Response to Osteopontin-Functionalized Carboxyethylphosphonic Acid-Modified Implants. Experimental Study in a Minipig Model.
Front. Mater. 9:914853.
doi: 10.3389/fmats.2022.914853

Currently, dental implants have become a common and reliable treatment for restoring masticatory function in edentulous patients. Their surface topography is of great importance for the adhesion and remodeling of bone cells, both in the initial phases and over time, and different strategies have been proposed to improve the biological performance of conventional sandblasted, large-grit, acid-etched implant surfaces. Corrosion has been identified as one of the causes of implant failure due to contact with oral fluids. Carboxyethylphosphonic acid is a potent anticorrosive that would form stable bonds with titanium oxide, generating an organic layer on which modifications could be made to improve cell adhesion. Osteopontin is considered a molecule capable of improving the osseointegration of titanium. Our study evaluated the osseointegration capacity of titanium implants modified with carboxyethylphosphonic acid and functionalized with osteopontin in a minipig model. A total of 16 implants were inserted in the tibial diaphysis of two minipigs, 8 implants modified with carboxyethylphosphonic acid and functionalized with osteopontin from the experimental group and 8 from the control group with sandblasted, large-grit, acid-etched surface treatment. After 4 weeks, the animals were sacrificed and the samples were analyzed by histomorphometric analysis, assessing bone-implant contact, cortical bone-implant contact, percentage of new bone, peri-implant bone density and interthread bone area interthread. Statistical analysis was performed using SPSS v.18. Statistical significance was found between groups for the percentage of new bone ($p = 0.04$) and for interthread bone area interthread ($p = 0.01$). Functionalization of titanium surfaces by osteopontin may be of interest for conditioning bone remodeling in the early stages of osseointegration, although more *in vivo* studies are needed to determine its real influence in this aspect.

Keywords: titanium dental implants, carboxyethylphosphonic acid, osteopontin, surface bioactivation, mini-pig model

INTRODUCTION

Dental implants represent, nowadays, a reliable treatment for the rehabilitation of masticatory and esthetic function in totally or partially edentulous patients.

There are currently more than 1,300 different implant systems in terms of dimensions, design, thread, implant-abutment connections, surface topography and chemistry, wettability and surface modification (Junker et al., 2009). Surface topography, wettability and coatings contribute to the biological processes during osseointegration, as they are in close relationship with host osteoblasts during the osseointegration process (Smeets et al., 2016).

Despite the high long-term survival rate of dental implants, there is a low failure rate (1%), due to insufficient osseointegration during the first months of implant placement, although this rate is increased (5%) throughout implant survival, due to peri-implantitis (Chrcanovic et al., 2014; Smeets et al., 2014).

During implant osseointegration, in the contact osteogenesis phase, osteoblasts migrate towards the implant surface, differentiating and leading to the formation of new bone (Junker et al., 2009; Yuan et al., 2018).

The surface topography of dental implants is of great importance for adhesion, differentiation and bone remodeling, both during the initial phase of osseointegration and in the long term (Pellegrini et al., 2018). It is now considered that implant topography together with adequate implant bed preparation are the fundamental basis for clinical success (Le Guéhennec et al., 2007; Coelho et al., 2015; Ogle, 2015; Ren et al., 2021). Titanium (Ti) implants with a Sandblasted, Large-grit, Acid-etched (SLA) surface show superior bone-to-implant contact (50–60%) compared to other surface modifications, and the suitability of this type of surface in terms of overall osteogenic performance has been demonstrated *in vivo* (Mendonça et al., 2008; Zhang et al., 2020); however, there are techniques aimed at depositing hydroxyapatite and fluorapatite on the surface of Ti, which use a coating and blasting method at room temperature (CoBlast) that have reported excellent *in vitro* results (Dunne et al., 2015). In order to improve the biological performance of implant surfaces, biochemical and/or biophysical signals can be introduced by mechanical, physical or chemical methods (Mendonça et al., 2008; Dunne et al., 2015). Current research considers that the most representative hierarchical Ti surface is the SLA surface, which consists of micrometer-scale (20–40 μm) concavities produced by large-grain sandblasting and smaller submicrometer-scale (0.5–3 μm) concavities produced by acid etching. This type of surface has been shown to promote osseointegration and achieve satisfactory clinical results (Zhao et al., 2007).

Saliva contact corrosion has been pointed out as one of the failure mechanisms in dental implants (Corne et al., 2019), despite the fact that Titanium-Aluminum-Vanadium (Ti-6Al4V) alloys, nowadays employed in dental implantology, present additional advantages in terms of corrosion resistance, such as rupture potential, corrosion rate, pitting degradation and crevice corrosion (Klekotka et al., 2020). Carboxyethylphosphonic acid, (HO2C-CR1H-CR2H-PO3H2) (CEPA), is characterized as a potent corrosion inhibitor. CEPA molecules can form stable bonds with passivated metal oxides, such as aluminum oxide (Al_2O_3) or Ti oxide (TiO_2), producing an organic monolayer on which modifications could be made to improve cell adhesion and biocompatibility of dental implant surfaces (Aresti et al., 2021).

Surface bioactivation, on the other hand, is a biochemical method of surface modification based on the immobilization of proteins, enzymes or peptides that induce a specific cellular response at the bone-implant interface. Coating implant surfaces with bioactive molecules can modulate the biological response (Meng et al., 2016).

It has been shown that certain adhesion molecules, such as fibronectin, hyaluronic acid and osteopontin (OPN), are able to enhance osseointegration of Ti surfaces *in vitro*; moreover, OPN, from the extracellular matrix, would play an important role as a mediator in bone cell adhesion and bone mineralization (Icer and Gezmen-Karadag, 2018).

Therefore, the purpose of this research was to evaluate whether the application of OPN on CEPA-modified Ti implants would improve the osseointegration of dental implants by histomorphometric study of five parameters: bone-to-implant contact (BIC), cortical bone-to-implant contact (BICc), bone volume/total volume BV/TV, bone density inside the implant threads (BDIT) and perimplant bone density PBD, in comparison with implants with conventional surface treatment (SLA-type).

MATERIAL AND METHODS

Animal Model

The research was carried out on 2 Landrace (large white) minipigs, 18–2 weeks old at the beginning of the research and weighing between 20 and 25 kg (Distrizoo Animals SL, Madrid, Spain) and was approved by the Ethical Committee for Animal Experimentation of the Hospital Universitario Puerta de Hierro Majadahonda, Madrid, Spain, on 31 January 2013, Code CEEA: 017/2013.

Groups

Two groups were created: experimental group (G1) of implants modified with carboxyethylphosphonic acid and functionalized with OPN and control group (G2), with SLA surface treatment. A total of 16 implants were inserted (8 implants for each group). All G1 implants were inserted in the left tibiae and all G2 implants were inserted in the right tibiae. The randomization was carried out so that the operator was unaware of the difference between the experimental and control groups and thus did not affect their placement.

Implants and Surface Treatment

Self-tapping conical implants of Ti alloy grade 5 (Titanium 90%, Aluminum 6% and Vanadium 4%) of 4 mm in diameter and 10 mm in length, with internal conical connection (Galimplant$^{®}$, Sarria, Lugo, Galicia, Spain) were used. The surface treatment using carboxyethylphosphonic acid was described in a previous investigation (Aragoneses et al., 2021). The OPN incubation procedure, at a dose of 0.06 μg per implant (Osteopontin human recombinant, expressed in HEX 293 Cells. Sigma-Aldrich Laboratory), was performed once the necessary carboxyl groups had been activated so that they were able to

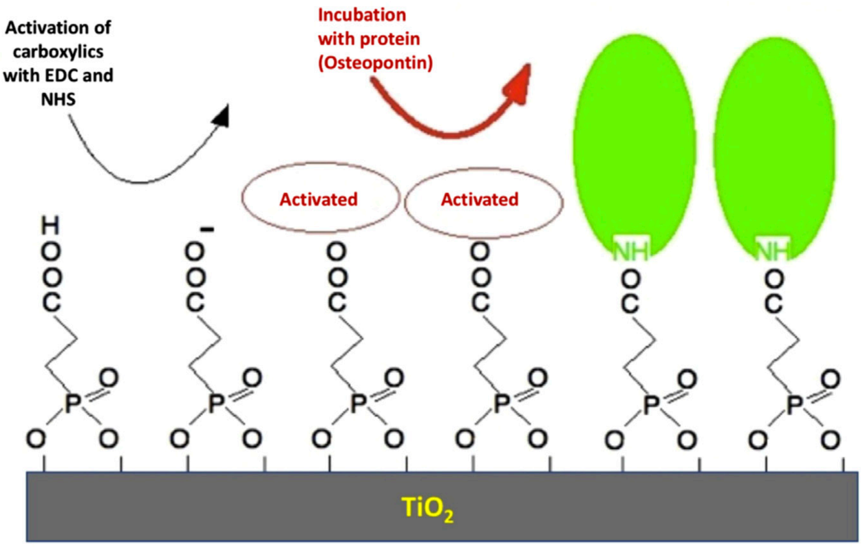

FIGURE 1 | Activation of the carboxyl groups and immobilization of the protein between the carboxyl group and the protein amine. EDC (Ethyl-3-[3-dimethylaminopropyl] carboxyamide). NHS (N-hydroxysulfamide).

react with the amino groups of the protein (**Figure 1**). Sterilization was performed by gamma radiation at a dose of 25 KGy. The implants were sealed under the manufacturer's quality guarantee (Galimplant®, Sarria, Lugo, Galicia, Spain). The entire handling process was performed in a sterile environment and field. This sterilization method was preferred for the experimental group to avoid sterilization biases with the control group. Other methods, such as ethylene oxide, in addition to leaving residues detrimental to health, could damage the molecular structure of the coating and its susceptibility to degradation, although the effects of sterilization on the stability of the molecular structure and the mechanical properties of the coating itself are unclear. Some *in vitro* studies have shown that the early stages of mineralization are essentially independent of the sterilization method (Ueno et al., 2012; Türker et al., 2014).

Surgery

The surgical procedure was performed on the same day and by a single oral surgeon. During the 18 h prior to surgery, the animals were fasted from solid food, with free access to water consumption until 6 h before the start of surgery, to ensure the smallest possible volume of gastric contents and to avoid possible complications during the procedure, such as regurgitation of gastric contents. Premedication was performed intramuscularly in the lateral part of the neck (at the level of the trapezius and cleido-occipital muscles), using a combination of medetomidine at a dose of 0.01 mg/kg and ketamine (Ketolar®, Pfizer SL, Madrid, Spain) at a dose of 5 mg/kg, plus midazolam (Dormicum®, Roche SA., Basel, Switzerland) at a dose of 0.2 mg/kg and atropine (atropine Braun® BRAUN MEDICAL, SA Jaen, Spain) at a dose of 0.02 mg/kg. For anesthetic induction and endotracheal intubation, propofol (Diprivan®, AstraZeneca, Cambridge,United Kingdom) was administered intravenously. Once endotracheal intubation was performed, an adequate anesthetic plane was maintained with propofol at a dose of 0.2–0.4 mg/kg/min. During the entire surgical procedure, the animal was monitored by means of electrocardiogram evaluation, capnography and temperature control; in addition, mechanical ventilation was established. Subsequently, epidural anesthesia was performed with bupivacaine (Bupivacaina®, Braun Medical, SA, Barcelona, Spain) and fentanyl (Fentanest®, Barcelona, Spain); in addition, local anesthesia was used infiltrated in the dermis where the incision would be made to access the tibia, in order to control hemorrhage through the vasoconstrictor of the anesthetic, in addition to enhance anesthesia and prevent animal suffering (Articaine 4% and adrenaline 1:100.000, Ultracain®, Normon, Madrid, Spain).

The location chosen in the tibia to insert the implants was the medial aspect of the diaphysis, away from the path of large blood vessels. The site chosen was away from the joints and muscle insertions. This ensured proper mobility and health of the animals from the time of surgery until the date of euthanasia. An Implantmed W&H® implant motor and a 20:1 contra-angle reducer (W&HWI-75E/KM) were used, with the surgical specifications indicated by the surgical sequence protocol for performing the osteotomy. The drilling of the bone beds was cooled with cold physiological serum (Vitulia Sol® Physiological Serum. 0.9%, ERN SA, Barcelona, Spain). Once the 4 osteotomies were performed in the tibia of the pig's leg, 4 implants (10 mm length x 4 mm Ø) were placed in each of the chosen tibias of the animal. Prior to implant insertion, a 4.1 mm Ø thread former was used on the bone cortex to prevent the insertion force from acting negatively on the coating. The implants in the left tibiae were from the experimental group (G1) and those in the right tibiae from the control group (G2). The suture was made by planes, the deepest one, using fast resorbable polyglactin of 5/0 thickness (VICRYL®, Johnson and Johnson SA, Madrid, Spain) and dermis and epidermis using non-resorbable braided silk of 3/0 thickness (Laboratorios Aragó, Barcelona, Spain) (**Figure 2**). After surgery, each animal was given

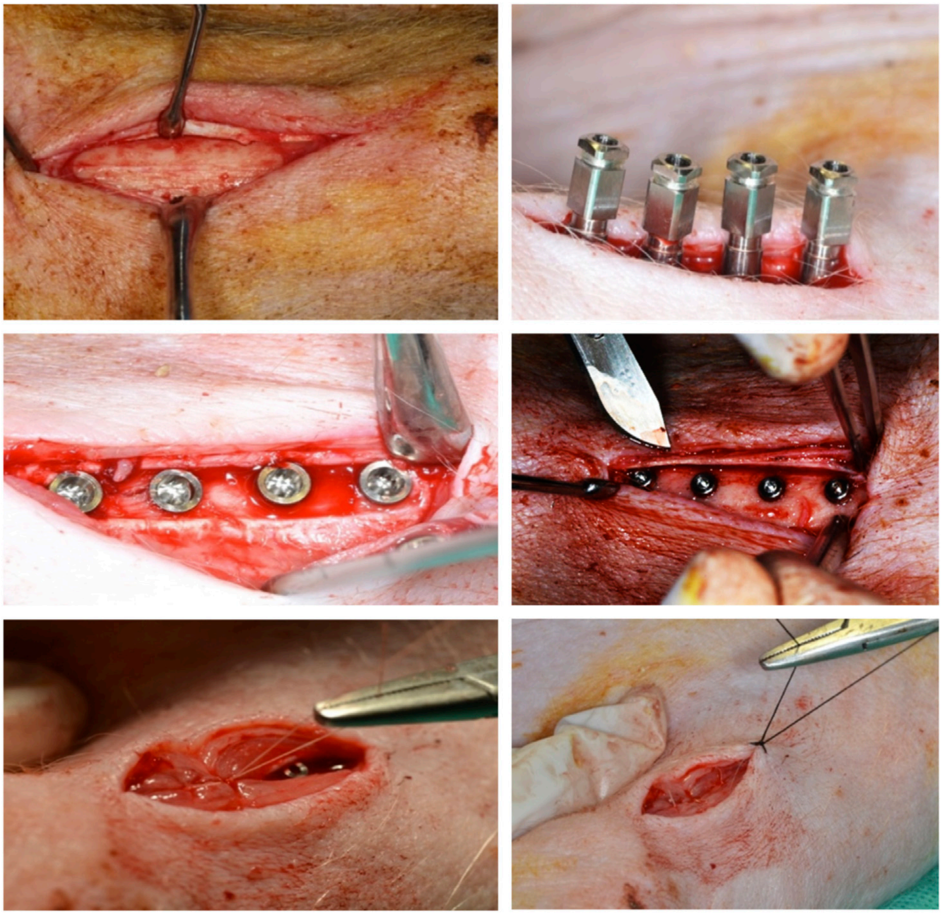

FIGURE 2 | Surgery.

antibiotic coverage to prevent surgical wound infection with amoxicillin (Clamoxyl®, Pfizer, New York, NY, United States) at a dose of 1.5 g, prepared as an injectable solution, intramuscularly for 5 days. The opioid analgesic used was intramuscular buprenorphine at a rate of 0.01–0.04 mg/kg, every 6–8 h (Buprex®, Quintiles, Danbury, CT, United States).

Preparation and Analysis of the Samples

Four weeks after implant placement, all the animals were sacrificed. The tibiae were extracted and kept in 10% formalin for at least 15 days before study. Subsequently, they were further processed following the protocol proposed by Donath and Breuer (Donath and Breuner, 1982). All samples and specimens were radiographed using a Schick Tecnologies® (Long Island City, NY 11101, United States) digital X-ray device. The cut and dehydrated specimens were embedded in methacrylate (Technovit 7,200®, VLC-Heraus Kulzer GMBH, Werheim, Germany). All samples with polished and treated surface were subjected to a staining process with the method of Lévai Laczkó (Jenö and Géza, 1975) for subsequent microscopic analysis.

An optical microscope (BX51, Olympus Corporation, Japan) connected to a camera and digital image analysis equipment (DP71, Cell-Sens Dimension 1.5, Olympus Corporation, Japan) was used for histomorphometric analysis of the samples. The stained samples were photographed with the digital camera at 40x magnification. The digitized images were processed at high resolution with the Cell Sens Dimensions computer system, Olympus, Japan. The digitized images were processed using software (Adobe Photoshop CS3, San Jose, CA, United States) and a digitizer tablet (Intuos 4 large, Wacom, Saitama, Japan).

The analysis of the measurements was performed according to the studies of Nkenke et al. and Kuchler et al. (Nkenke et al., 2005; Kuchler et al., 2013) with the following measurement protocol:

- Bone-to-implant contact (BIC).
- Bone-implant cortical contact (BICc).
- Percentage of new bone (BV/TV).
- Peri-implant bone density (Peri-implant Bone Area, Tissue Area, PBA/TA) and interthread bone density (Interthread Bone Area, Tissue Area, IBA/TA).

To generate homogeneous measurements, a 5 × 5 mm square around the coronal portion of the implants was assumed as the working area. The BIC was defined as the amount of implant perimeter surface in direct contact with the bone tissue; the bone density inside the threads (IBA/TA) was defined as the area of bone grown inside the threads, in relation to the total interthread space

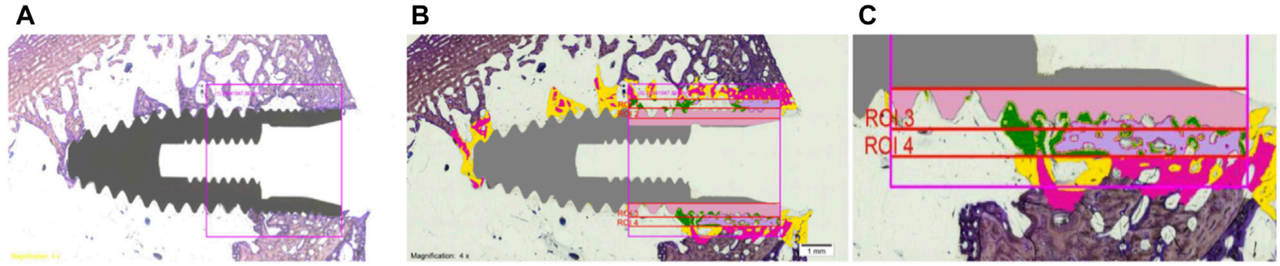

FIGURE 3 | Image processing with Adobe Photoshop CS3 (San Jose, CA, United States). **(A)**, Area of interest; **(B)** and **(C)**, areas of new bone and interrosseous bone.

TABLE 1 | Mean, standard deviation and *p* value in the groups for the different parameters.

Group	BIC	BICc	BV/TV	IBA/TA	PBA/TA
G1	19 ± 47.81	24.81 ± 55.37	13.28 ± 39.47	14.52 ± 34.39	32.98 ± 58.57
G2	34 ± 36.97	41.10 ± 63.86	16.38 ± 40.22	22.52 ± 45.28	29.36 ± 57.30
p value G1 vs. G2	0.527	0.345	0.046[a]	0.012[a]	0.293

BIC, bone implant contact; BICc, Bone-implant cortical contact; BV/TV, percentage of new bone; IBA/TA, interthread bone area; PBA/TA, Peri-implant Bone Area, Tissue Area.
[a]Statistical significance.

available; perimplant bone density (PBA/TA) was defined as the amount of bone generated in relation to the total implant surface at a distance of 0.3 mm from the implant and the percentage of new bone (BV/TV) was defined as the new bone present inside the threads, up to a distance of 0.3 mm away from the implant (**Figure 3**).

Statistical Analysis

The SPSS v.18 program was used. IBM (Chicago: SPSS Inc. United States). The statistical analysis was carried out in two distinct phases: the first using descriptive statistics to calculate the arithmetic mean, median, standard deviation, variance, range and standard error, expressing the values using a 95% confidence interval; the second, using inferential statistics with a significance level of $p < 0.05$. Heterogeneity was calculated using the Kolmogorov-Smirnov test, Shapiro-Wilk test and Q-Q normality plots.

RESULTS

Statistical Results

Using a 95% confidence interval, with a significance level <0.05, statistical significance was found between G1 and G2 for BV/TV ($p = 0.04$) and IBA/TA ($p = 0.01$); for BIC, BICc and PBA/TA the differences between groups were not significant (**Table 1**).

Figures 4, **5** show boxplots and Q-Q (quantile-quantile) plots for BV-TV and IBA/TA for the experimental and control groups, respectively. The graph in **Figure 6** shows the difference in means between the experimental and control groups.

Histomorphometric Analysis

Histological analysis by light microscopy of longitudinal sections of the specimens revealed bone-to-implant contact with interrupted medullary spaces at the bone-to-implant interface. No signs of fibrous tissue formation were found. **Figure 7** shows a total of 32 frames (16 for each experimental animal, 8 for each tibia). The first image of each frame shows the longitudinal section of the specimen before being processed by the software for data extraction. The second image of each frame shows the implants in gray color, in order to distinguish, by means of the software, the areas of old bone (in pink color), the areas of new bone (in yellow color) and the areas of soft tissue (in white color) (**Figure 7**). The highest values for BIC and BICc were obtained in the implants placed closer to the abdomen, in the right and left tibiae of G2 (46.47 and 63.83% respectively). The highest values for BV/TV and IBA/TA were obtained in the implants placed closer to the abdomen in the left tibiae of G1 (45.28 and 52.11% respectively).

DISCUSSION

The objective of our research was to determine the effect on osseointegration and early bone tissue formation of CEPA-treated and OPN-functionalized Ti implant surfaces compared to conventional etched surface implants in a minipig model.

The use of phosphonic acids for the purpose of bonding specific molecules, or simply to modify the microscopic properties of the implant surface, has been extensively studied. Esposito et al. (Esposito et al., 2013) evaluated, by means of a randomized clinical study, the clinical efficacy of a surface treatment of Ti dental implants using a monolayer of permanently bonded multiphosphonic acid molecules, mimicking the surface of natural hydroxyapatite, obtaining no

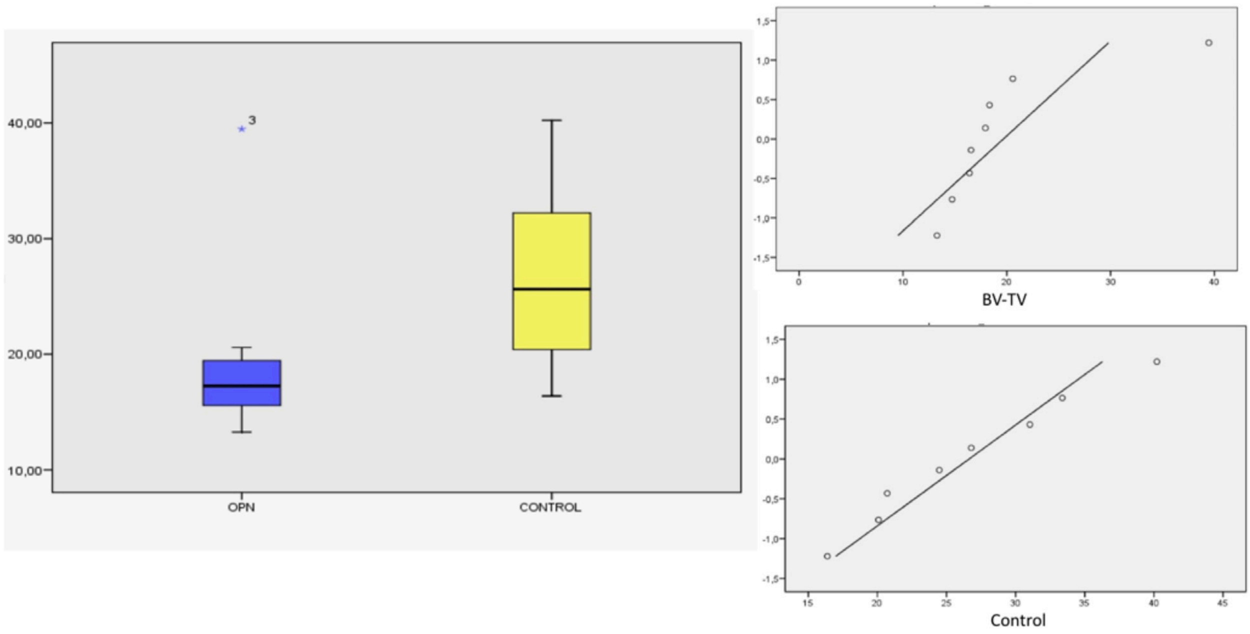

FIGURE 4 | Boxplot and Q-Q plot for BV-TV.

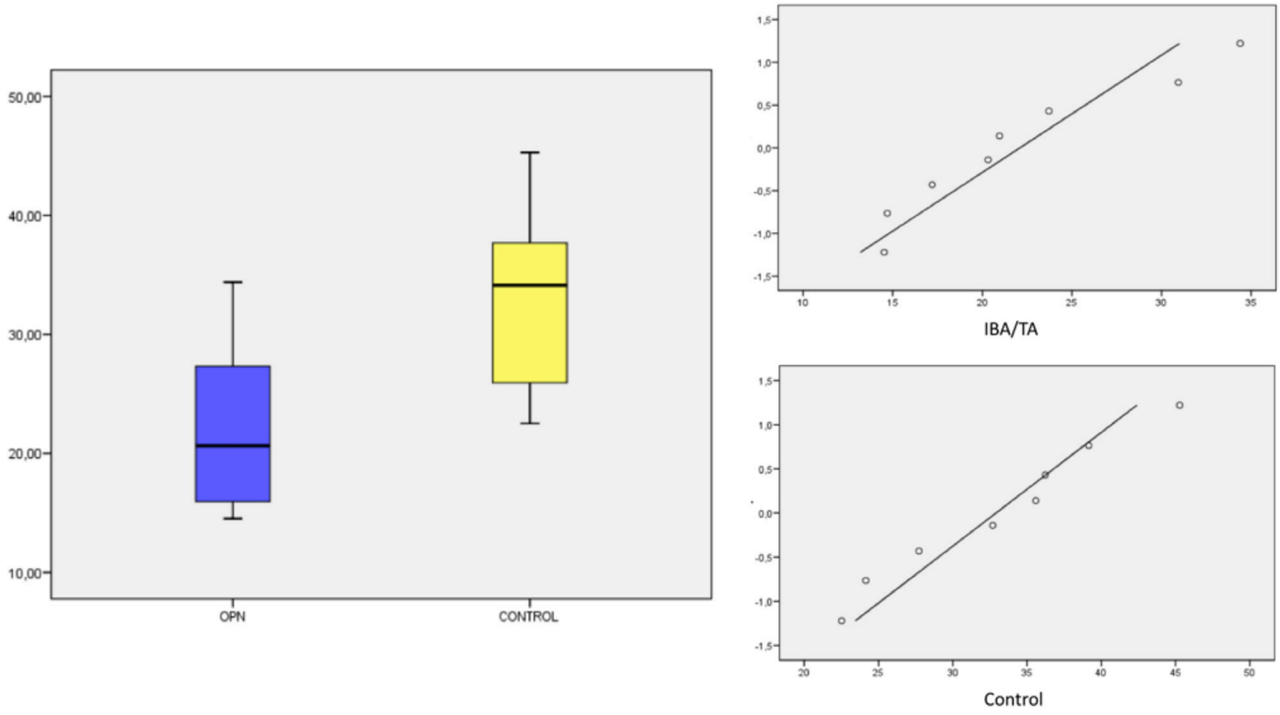

FIGURE 5 | Boxplot and Q-Q plot for IBA/TA.

significant differences in terms of clinical healing with respect to the SLA surface control group. Maho et al. (Maho et al., 2013) studied the primary bone bioactivity of phosphonic acid functionalized Ti substrates. Viornery et al. (Viornery et al., 2002) assessed the proliferation, differentiation and protein production of rat osteoblastic cells on phosphonic acid-

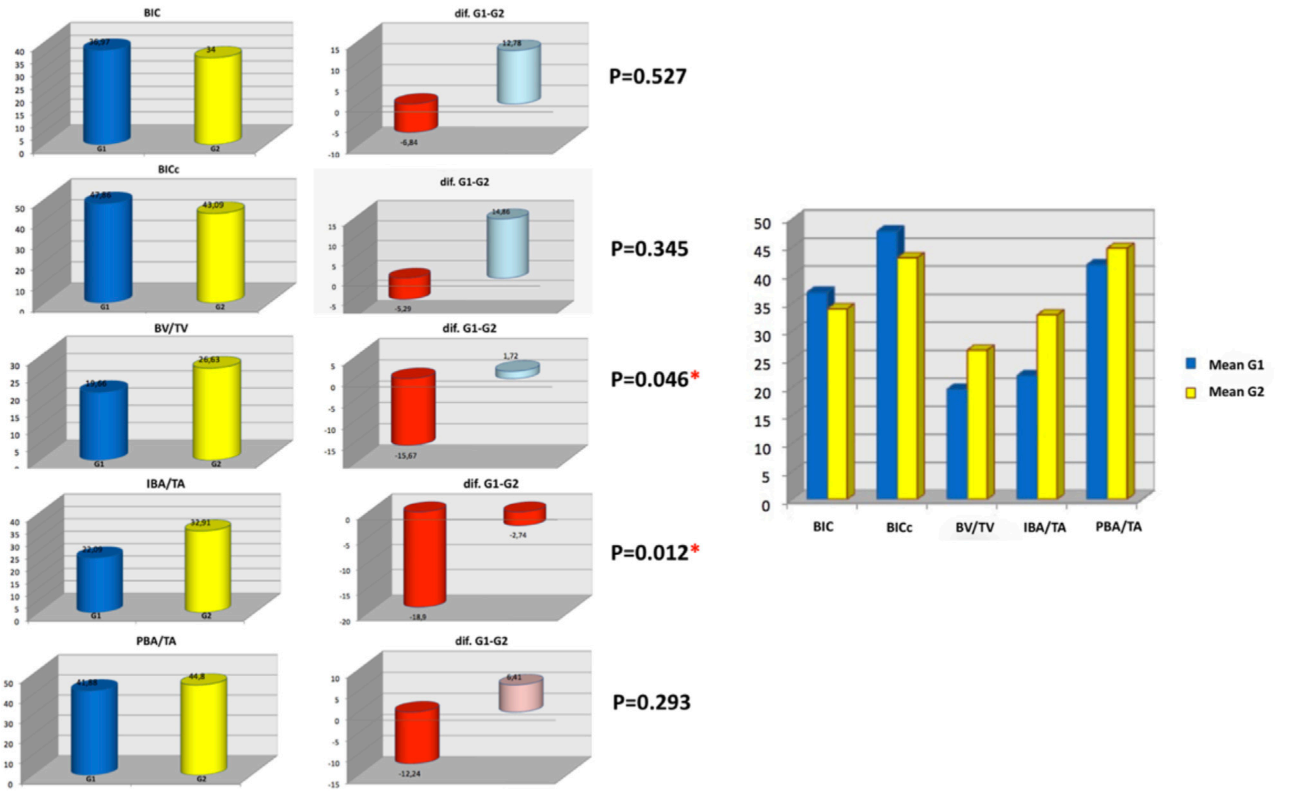

FIGURE 6 | Difference in means between experimental and control groups.

modified titanium surfaces *in vitro*, finding no statistical difference in osteoblast proliferation between phosphonic acid-modified titanium and unmodified titanium, which would indicate the absence of toxicity of phosphonic acids for the osteoblasts used in the study, however, they found that the synthesis of type I collagen was sensitive to surface modification and the total amount of protein synthesized was significantly higher than on unmodified titanium surfaces.

The ideal surface of dental implants should be one that is capable of inducing osseointegration, regardless of the implantation site and the quantity and quality of available bone (Fiorellini et al., 2016). Nowadays, research on distant osteogenesis has become a discovery of great importance, for the development of dental implant surfaces and therefore, different molecules have been proposed for the biochemical modification of surfaces, such as peptides, extracellular matrix proteins, growth factors and pharmacological agents (Meng et al., 2016; Tan and Al-Rubeai, 2019). Germanier et al. (Germanier et al., 2006) investigated on a minipig model, peptide-modified implant surfaces, finding a significant increase in BIC at 2 weeks compared to controls. Other studies have demonstrated the positive effect on peri-implant bone formation and osseointegration of Ti surfaces biochemically modified with collagen (Morra et al., 2006; Schliephake et al., 2006).

It should be noted that during the proliferative phase of osseointegration, fibroblasts are stimulated by growth factors to secrete extracellular matrix proteins such as collagen, chondroitin, fibronectin, vitronectin and other proteoglycans. The extracellular matrix provides a guide for osteoprogenitor cells, which migrate to the implant surface through integrin interaction (Terheyden et al., 2012). It has been proposed that osteoblasts originate from a subset of mesenchymal stem cells that line the minor vessels, called pericytes, and that after the release of bone morphogenetic protein (BMP), these cells differentiate into osteoblasts (Murray et al., 2014). Stadlinger et al. (Stadlinger et al., 2008) studied the osseointegration in pigs of implants coated with extracellular matrix components, suggesting that implants coated with chondroitinsulfate could lead to a higher degree of bone formation compared to control implants.

OPN has been shown to play a role in bone mineralization, wound healing, angiogenesis, cell adhesion, cell differentiation and foreign body response (Ishijima et al., 2007; Carvalho et al., 2018). Certain studies have found that some adhesion molecules, such as hyaluronic acid, fibronectin and OPN, together with OPN-derived synthetic adhesion peptides, are able to enhance the osseointegration of titanium surfaces *in vitro* (Lasa et al., 1997). Other *in vitro* investigations have studied different synthetic materials coated with OPN, with the purpose of exploring whether it could influence the functionality of biomaterial surfaces (Lee et al., 2003; Gordjestani et al., 2006; Liu et al., 2007; Bernards et al., 2008). Jensen et al. demonstrated *in vitro* that the bone mass density around OPN-coated hydroxyapatite surfaces were superior to uncoated surfaces, which would mean a great potential for OPN-coated biomaterials such as functional protein coatings, drug delivery systems in orthopedic implants, or scaffolds for tissue engineering (Jensen et al., 2010).

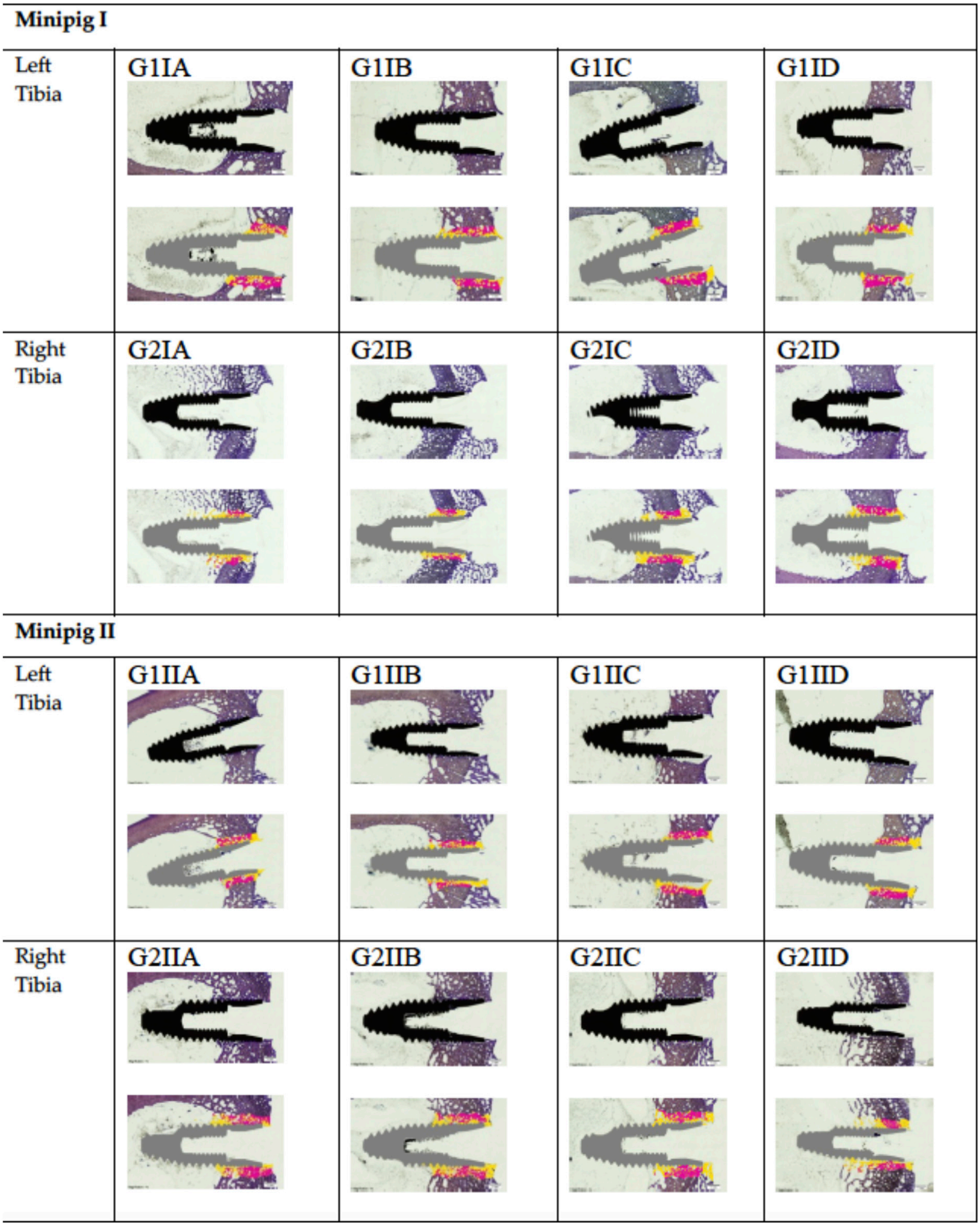

FIGURE 7 | Images of histomorphometric sections of all implants in the study in groups G1 and G2. **(A)** and **(B)** represent the osteotomies with the least and most proximity to the abdomen, respectively, and **(C)** and **(D)** the osteotomies with the least and most proximity to the hoof, respectively. The first image shows the longitudinal section of the specimen, before computer processing; the second image shows the photoshop-processed longitudinal section with the implants in gray and the areas of old bone (pink), areas of new bone (yellow) and areas of soft tissue (white).

OPN is naturally present on the non-organic surfaces of mineralized tissues, and several *in vivo* studies have examined the influence of OPN on the formation and remodeling of mineralized tissue (McKee and Nanci, 1996). Changes in mineralized tissue hardness, bone remodeling rate and vascularization have also been reported. In a rabbit cranial bone substitute model, OTP-coated coral HA granules were used (McKee and Nanci, 1996; McKee et al., 2011), and a positive effect of OPN on bone growth was observed; in addition, an inhibitory effect on the adverse foreign body reaction to implants has also been reported (Tsai et al., 2005; Liu et al., 2008). Asou et al. (Asou et al., 2001) used ectopically implanted bone discs in muscle in wild-type mice and compared them with OTP knockout mice; histological analysis indicated that the number of osteoclasts associated with the implanted discs was reduced in OPN knockout mice. In addition, they examined vascularization immunohistologically, and found that the number of vessels containing endothelial cells around the bone discs implanted in the muscle was reduced in the OTP knockout mice. This would indicate the link between OPN-dependent vascularization and osteoclast accumulation and that OPN is necessary for efficient vascularization by hemangiogenic endothelial cells and subsequent osteoclastic bone resorption.

Some *in vivo* studies have shown that differences in apoptosis rates would not explain the effects of OPN on vascularization, highlighting the possibility that vitronectin or other molecules may compensate for the absence of OPN in preventing apoptosis (McHugh et al., 2000; Lee et al., 2019).

The functional and structural characteristics of OPN predict a capacity of this protein to regulate calcification in the matrix of mineralized tissues and to participate, more specifically, in cell-matrix and matrix-matrix/mineral adhesion; it has been shown that OPN production is one of the first and last secretory activities of the osteoblast lineage and that this activity manifests, morphologically, as a limiting line at the interface of mineralized tissues at the bone matrix interface, implicating this protein in osteoclast adhesion and possibly in haptotaxis; it has even been suggested that it could act as a promoter of interfacial adhesion between opposing substrates, maintaining overall bone integrity during the bone remodeling sequence and resulting in an adherent between different dissimilar tissues or biocompatible materials such as osseointegrated implants (Wai and Kuo, 2004; Carvalho et al., 2021). Certain studies have reported that several types of bone tissue-related cells, such as osteoblasts and osteoclasts, are forced to mediate by OPN induction (Chellaiah and Hruska, 2003; Shin et al., 2004). However, some studies have recognized that OPN may have negative effects on the mineralization process, probably through inhibition of nucleation and growth of hydroxyapatite crystals (Pampena et al., 2004; Azzopardi et al., 2010).

Our study did not find statistical significance for BIC, BICc and PBA/TA values, in the OPN-functionalized implants, versus the control group, however, statistically significant values were found for BV/TV (p = 0.04) and IBA/TA (p = 0.01), results consistent with other recent studies, such as Makishi et al. who in a study in knockout mice, suggested that OPN-coated implants would enhance direct osteogenesis during osseointegration (Makishi et al., 2022). Implant healing time shows a large variation in the time of evaluation, ranging from 1 week to 6 months. Some studies evaluate a single reading, while others have evaluated up to four readings. Our research established 4 weeks of waiting until euthanasia of the animals, although the tendency to healing over time was not analyzed, something that we consider to be one of the limitations of the study and that, if it had been extended (12 weeks, for example), different BIC results would have been obtained (Ramazanzadeh et al., 2014). On the other hand, another factor that seems to influence peri-implant bone formation is the anatomic location of the implant, since the dynamics of bone formation differ among the different locations (Jenny et al., 2016). In the same way, implants with wider diameters are associated with less bone formation (Jimbo et al., 2014). All this could have contributed to the poor results obtained in the experimental group for some of the parameters studied.

Finally, all research suggests that chemically nanostructured Ti surfaces can enhance endogenous extracellular OPN deposition by osteogenic cells *in vitro* as a function of etching time, a finding that should be taken into account in strategies for biofunctionalization of implant surfaces with cell-binding molecules (Bueno et al., 2011).

CONCLUSION

Based on the results obtained, it could be verified that the biofunctionalization of the Ti surface can be a good option to condition the biological processes that take place in the bone remodeling around dental implants. However, OPN should be carefully studied in different concentrations and at different times of bone remodeling, in extensive *in vivo* studies that allow us to perceive its real influence on the formation of a greater quantity and quality of peri-implant bone.

DATA AVAILABILITY STATEMENT

The original contributions presented in the study are included in the article/supplementary material, further inquiries can be directed to the corresponding author.

ETHICS STATEMENT

The animal study was reviewed and approved by Ethical Committee for Animal Experimentation of the Hospital Universitario Puerta de Hierro Majadahonda, Madrid, Spain. CEEA: 017/2013.

AUTHOR CONTRIBUTIONS

Conceptualization, JA and NL-V; methodology, JA and NL-V; software, CR; validation, JMA and AL-V; investigation, JA and NL-V; data curation, BM; writing—original draft preparation, AL-V; writing—review and editing, JMA; supervision, JMA All authors have read and agreed to the published version of the manuscript.

REFERENCES

Aragoneses, J., Suárez, A., López-Valverde, N., Martínez-Martínez, F., and Aragoneses, J. M. (2021). Assessment of the Tissue Response to Modification of the Surface of Dental Implants with Carboxyethylphosphonic Acid and Basic Fibroblastic Growth Factor Immobilization (Fgf-2): An Experimental Study on Minipigs. *Biology* 10 (5), 358. doi:10.3390/biology10050358

Aresti, A., Aragoneses, J., López-Valverde, N., Suárez, A., and Aragoneses, J. M. (2021). Effectiveness of Biofunctionalization of Titanium Surfaces with Phosphonic Acid. *Biomedicines* 9 (11), 1663. doi:10.3390/biomedicines9111663

Asou, Y., Rittling, S. R., Yoshitake, H., Tsuji, K., Shinomiya, K., Nifuji, A., et al. (2001). Osteopontin Facilitates Angiogenesis, Accumulation of Osteoclasts, and Resorption in Ectopic Bone*. *Endocrinology* 142, 1325–1332. doi:10.1210/endo.142.3.8006

Azzopardi, P. V., O'Young, J., Lajoie, G., Karttunen, M., Goldberg, H. A., and Hunter, G. K. (2010). Roles of Electrostatics and Conformation in Protein-Crystal Interactions. *PLoS ONE* 5, e9330. doi:10.1371/journal.pone.0009330

Bernards, M. T., Qin, C., and Jiang, S. (2008). MC3T3-E1 Cell Adhesion to Hydroxyapatite with Adsorbed Bone Sialoprotein, Bone Osteopontin, and Bovine Serum Albumin. *Colloids Surfaces B Biointerfaces* 64, 236–247. doi:10.1016/j.colsurfb.2008.01.025

Bueno, R. d. B. e. L., Adachi, P., Castro-Raucci, L. M. S. d., Rosa, A. L., Nanci, A., and Oliveira, P. T. d. (2011). Oxidative Nanopatterning of Titanium Surfaces Promotes Production and Extracellular Accumulation of Osteopontin. *Braz. Dent. J.* 22, 179–184. doi:10.1590/s0103-64402011000300001

Carvalho, M. S., Poundarik, A. A., Cabral, J. M. S., da Silva, C. L., and Vashishth, D. (2018). Biomimetic Matrices for Rapidly Forming Mineralized Bone Tissue Based on Stem Cell-Mediated Osteogenesis. *Sci. Rep.* 8, 14388. doi:10.1038/s41598-018-32794-4

Carvalho, M. S., Cabral, J. M. S., da Silva, C. L., and Vashishth, D. (2021). Bone Matrix Non-collagenous Proteins in Tissue Engineering: Creating New Bone by Mimicking the Extracellular Matrix. *Polymers* 13, 1095. doi:10.3390/polym13071095

Chellaiah, M. A., and Hruska, K. A. (2003). The Integrin {alpha} V {beta} 3 and CD44 Regulate the Actions of Osteopontin on Osteoclast Motility. *Calcif. Tissue Int.* 72, 197–205. doi:10.1007/s00223-002-1025-6

Chrcanovic, B. R., Albrektsson, T., and Wennerberg, A. (2014). Reasons for Failures of Oral Implants. *J. Oral Rehabil.* 41, 443–476. doi:10.1111/joor.12157

Coelho, P. G., Jimbo, R., Tovar, N., and Bonfante, E. A. (2015). Osseointegration: Hierarchical Designing Encompassing the Macrometer, Micrometer, and Nanometer Length Scales. *Dent. Mater.* 31, 37–52. doi:10.1016/j.dental.2014.10.007

Corne, P., De March, P., Cleymand, F., and Geringer, J. (2019). Fretting-corrosion Behavior on Dental Implant Connection in Human Saliva. *J. Mech. Behav. Biomed. Mater.* 94, 86–92. doi:10.1016/j.jmbbm.2019.02.025

Donath, K., and Breuner, G. (1982). A Method for the Study of Undecalcified Bones and Teeth with Attached Soft Tissues*. The Sage-Schliff (Sawing and Grinding) Technique. *J. Oral Pathol. Med.* 11, 318–326. doi:10.1111/j.1600-0714.1982.tb00172.x

Dunne, C. F., Twomey, B., Kelly, C., Simpson, J. C., and Stanton, K. T. (2015). Hydroxyapatite and Fluorapatite Coatings on Dental Screws: Effects of Blast Coating Process and Biological Response. *J. Mater Sci. Mater Med.* 26, 5347. doi:10.1007/s10856-014-5347-5

Esposito, M., Dojcinovic, I., Germon, L., Lévy, N., Curno, R., Buchini, S., et al. (2013). Safety and Efficacy of a Biomimetic Monolayer of Permanently Bound Multi-Phosphonic Acid Molecules on Dental Implants: 1 Year Post-loading Results from a Pilot Quadruple-Blinded Randomised Controlled Trial. *Eur. J. Oral Implantol.* 6, 227–236. PMID: 24179977.

Fiorellini, J., Glindmann, S., Salcedo, J., Weber, H.-P., Park, C.-J., and Sarmiento, H. (2016). The Effect of Osteopontin and an Osteopontin-Derived Synthetic Peptide Coating on Osseointegration of Implants in a Canine Model. *Int. J. Periodontics Restor. Dent.* 36, e88–e94. doi:10.11607/prd.2830

Germanier, Y., Tosatti, S., Broggini, N., Textor, M., and Buser, D. (2006). Enhanced Bone Apposition Around Biofunctionalized Sandblasted and Acid-Etched Titanium Implant Surfaces. A Histomorphometric Study in Miniature Pigs. *Clin. Oral Implants Res.* 17, 251–257. doi:10.1111/j.1600-0501.2005.01222.x

Gordjestani, M., Dermaut, L., De Ridder, L., De Waele, P., De Leersnijder, W., and Bosman, F. (2006). Osteopontin and Bone Metabolism in Healing Cranial Defects in Rabbits. *Int. J. Oral Maxillofac. Surg.* 35, 1127–1132. doi:10.1016/j.ijom.2006.07.002

Icer, M. A., and Gezmen-Karadag, M. (2018). The Multiple Functions and Mechanisms of Osteopontin. *Clin. Biochem.* 59, 17–24. doi:10.1016/j.clinbiochem.2018.07.003

Ishijima, M., Tsuji, K., Rittling, S. R., Yamashita, T., Kurosawa, H., Denhardt, D. T., et al. (2007). Osteopontin Is Required for Mechanical Stress-dependent Signals to Bone Marrow Cells. *J. Endocrinol.* 193, 235–243. doi:10.1677/joe.1.06704

Jenny, G., Jauernik, J., Bierbaum, S., Bigler, M., Grätz, K. W., Rücker, M., et al. (2016). A Systematic Review and Meta-Analysis on the Influence of Biological Implant Surface Coatings on Periimplant Bone Formation. *J. Biomed. Mat. Res.* 104, 2898–2910. doi:10.1002/jbm.a.35805

Jenö, L., and Géza, L. (1975). A Simple Differential Staining Method for Semi-thin Sections of Ossifying Cartilage and Bone Tissues Embedded in Epoxy Resin. *Mikroskopie* 31, 1–4. PMID: 51484.

Jensen, T., Dolatshahi-Pirouz, A., Foss, M., Baas, J., Lovmand, J., Duch, M., et al. (2010). Interaction of Human Mesenchymal Stem Cells with Osteopontin Coated Hydroxyapatite Surfaces. *Colloids Surfaces B Biointerfaces* 75, 186–193. doi:10.1016/j.colsurfb.2009.08.029

Jimbo, R., Janal, M. N., Marin, C., Giro, G., Tovar, N., and Coelho, P. G. (2014). The Effect of Implant Diameter on Osseointegration Utilizing Simplified Drilling Protocols. *Clin. Oral Impl. Res.* 25, 1295–1300. Epub 2013 Oct 8. doi:10.1111/clr.12268

Junker, R., Dimakis, A., Thoneick, M., and Jansen, J. A. (2009). Effects of Implant Surface Coatings and Composition on Bone Integration: a Systematic Review. *Clin. Oral Implants Res.* 20, 185–206. doi:10.1111/j.1600-0501.2009.01777.x

Klekotka, M., Dąbrowski, J. R., and Rećko, K. (2020). Fretting and Fretting Corrosion Processes of Ti6Al4V Implant Alloy in Simulated Oral Cavity Environment. *Materials* 13 (7), 1561. doi:10.3390/ma13071561

Kuchler, U., Pfingstner, G., Busenlechner, D., Dobsak, T., Reich, K., Heimel, P., et al. (2013). Osteocyte Lacunar Density and Area in Newly Formed Bone of the Augmented Sinus. *Clin. Oral Impl. Res.* 24, 285–289. doi:10.1111/j.1600-0501.2012.02533.x

Lasa, M., Chang, P.-L., Prince, C. W., and Pinna, L. A. (1997). Phosphorylation of Osteopontin by Golgi Apparatus Casein Kinase. *Biochem. Biophysical Res. Commun.* 240, 602–605. doi:10.1006/bbrc.1997.7702

Le Guéhennec, L., Soueidan, A., Layrolle, P., and Amouriq, Y. (2007). Surface Treatments of Titanium Dental Implants for Rapid Osseointegration. *Dent. Mater.* 23, 844–854. doi:10.1016/j.dental.2006.06.025

Lee, Y.-J., Park, S.-J., Lee, W.-K., Ko, J. S., and Kim, H.-M. (2003). MG63 Osteoblastic Cell Adhesion to the Hydrophobic Surface Precoated with Recombinant Osteopontin Fragments. *Biomaterials* 24, 1059–1066. doi:10.1016/s0142-9612(02)00439-8

Lee, G. S., Salazar, H. F., Joseph, G., Lok, Z. S. Y., Caroti, C. M., Weiss, D., et al. (2019). Osteopontin Isoforms Differentially Promote Arteriogenesis in Response to Ischemia via Macrophage Accumulation and Survival. *Lab. Invest.* 99, 331–345. doi:10.1038/s41374-018-0094-8

Liu, L., Qin, C., Butler, W. T., Ratner, B. D., and Jiang, S. (2007). Controlling the Orientation of Bone Osteopontin via its Specific Binding with Collagen I to Modulate Osteoblast Adhesion. *J. Biomed. Mat. Res.* 80A, 102–110. doi:10.1002/jbm.a.30858

Liu, L., Chen, G., Chao, T., Ratner, B. D., Sage, E. H., and Jiang, S. (2008). Reduced Foreign Body Reaction to Implanted Biomaterials by Surface Treatment with Oriented Osteopontin. *J. Biomaterials Sci. Polym. Ed.* 19, 821–835. doi:10.1163/156856208784522083

Maho, A., Detriche, S., Delhalle, J., and Mekhalif, Z. (2013). Sol-gel Synthesis of Tantalum Oxide and Phosphonic Acid-Modified Carbon Nanotubes Composite Coatings on Titanium Surfaces. *Mater. Sci. Eng. C* 33, 2686–2697. doi:10.1016/j.msec.2013.02.025

Makishi, S., Yamazaki, T., and Ohshima, H. (2022). Osteopontin on the Dental Implant Surface Promotes Direct Osteogenesis in Osseointegration. *Int. J. Mol. Sci.* 23, 1039. doi:10.3390/ijms23031039

McHugh, K. P., Hodivala-Dilke, K., Zheng, M.-H., Namba, N., Lam, J., Novack, D., et al. (2000). Mice Lacking β3 Integrins Are Osteosclerotic Because of Dysfunctional Osteoclasts. *J. Clin. Invest.* 105, 433–440. doi:10.1172/JCI8905

McKee, M. D., and Nanci, A. (1996). Osteopontin at Mineralized Tissue Interfaces in Bone, Teeth, and Osseointegrated Implants: Ultrastructural Distribution and

Implications for Mineralized Tissue Formation, Turnover, and Repair. *Microsc. Res. Tech.* 33, 141–164. doi:10.1002/(sici)1097-0029(19960201)33:2<141::aid-jemt5>3.0.co;2-w

McKee, M. D., Pedraza, C. E., and Kaartinen, M. T. (2011). Osteopontin and Wound Healing in Bone. *Cells Tissues Organs* 194, 313–319. doi:10.1159/000324244

Mendonça, G., Mendonça, D. B. S., Aragão, F. J. L., and Cooper, L. F. (2008). Advancing Dental Implant Surface Technology - from Micron- to Nanotopography. *Biomaterials* 29, 3822–3835. doi:10.1016/j.biomaterials.2008.05.012

Meng, H.-W., Chien, E. Y., and Chien, H.-H. (2016). Dental Implant Bioactive Surface Modifications and Their Effects on Osseointegration: a Review. *Biomark. Res.* 4, 24. doi:10.1186/s40364-016-0078-z

Morra, M., Cassinelli, C., Cascardo, G., Mazzucco, L., Borzini, P., Fini, M., et al. (2006). Collagen I-Coated Titanium Surfaces: Mesenchymal Cell Adhesion Andin Vivo Evaluation in Trabecular Bone Implants. *J. Biomed. Mat. Res.* 78A, 449–458. doi:10.1002/jbm.a.30783

Murray, I. R., West, C. C., Hardy, W. R., James, A. W., Park, T. S., Nguyen, A., et al. (2014). Natural History of Mesenchymal Stem Cells, from Vessel Walls to Culture Vessels. *Cell. Mol. Life Sci.* 71, 1353–1374. doi:10.1007/s00018-013-1462-6

Nkenke, E., Fenner, M., Vairaktaris, E. G., Neukam, F. W., and Radespiel-Tröger, M. (2005). Immediate versus Delayed Loading of Dental Implants in the Maxillae of Minipigs. Part II: Histomorphometric Analysis. *Int. J. Oral Maxillofac. Implants* 20, 540–546. PMID: 16161738.

Ogle, O. E. (2015). Implant Surface Material, Design, and Osseointegration. *Dent. Clin. N. Am.* 59, 505–520. doi:10.1016/j.cden.2014.12.003

Pampena, D. A., Robertson, K. A., Litvinova, O., Lajoie, G., Goldberg, H. A., and Hunter, G. K. (2004). Inhibition of Hydroxyapatite Formation by Osteopontin Phosphopeptides. *Biochem. J.* 378, 1083–1087. doi:10.1042/BJ20031150

Pellegrini, G., Francetti, L., Barbaro, B., and Del Fabbro, M. (2018). Novel Surfaces and Osseointegration in Implant Dentistry. *J. Invest. Clin. Dent.* 9, e12349. doi:10.1111/jicd.12349

Ramazanzadeh, B. A., Fatemi, K., Dehghani, M., Mohtasham, N., Jahanbin, A., and Sadeghian, H. (2014). Effect of Healing Time on Bone-Implant Contact of Orthodontic Micro-implants: a Histologic Study. *ISRN Dent.* 2014, 1–7. doi:10.1155/2014/179037

Ren, B., Wan, Y., Liu, C., Wang, H., Yu, M., Zhang, X., et al. (2021). Improved Osseointegration of 3D Printed Ti-6Al-4V Implant with a Hierarchical Micro/nano Surface Topography: An *In Vitro* and *In Vivo* Study. *Mater. Sci. Eng. C* 118, 111505. doi:10.1016/j.msec.2020.111505

Schliephake, H., Scharnweber, D., Roesseler, S., Dard, M., Sewing, A., and Aref, A. (2006). Biomimetic Calcium Phosphate Composite Coating of Dental Implants. *Int. J. Oral Maxillofac. Implants* 21, 738–746. PMID: 17066635.

Shin, H., Zygourakis, K., Farach-Carson, M. C., Yaszemski, M. J., and Mikos, A. G. (2004). Attachment, Proliferation, and Migration of Marrow Stromal Osteoblasts Cultured on Biomimetic Hydrogels Modified with an Osteopontin-Derived Peptide. *Biomaterials* 25, 895–906. doi:10.1016/s0142-9612(03)00602-1

Smeets, R., Henningsen, A., Jung, O., Heiland, M., Hammächer, C., and Stein, J. M. (2014). Definition, Etiology, Prevention and Treatment of Peri-Implantitis - a Review. *Head. Face Med.* 10, 34. doi:10.1186/1746-160X-10-34

Smeets, R., Stadlinger, B., Schwarz, F., Beck-Broichsitter, B., Jung, O., Precht, C., et al. (2016). Impact of Dental Implant Surface Modifications on Osseointegration. *BioMed Res. Int.* 2016, 1–16. doi:10.1155/2016/6285620

Stadlinger, B., Pilling, E., Huhle, M., Mai, R., Bierbaum, S., Scharnweber, D., et al. (2008). Evaluation of Osseointegration of Dental Implants Coated with Collagen, Chondroitin Sulphate and BMP-4: an Animal Study. *Int. J. Oral Maxillofac. Surg.* 37, 54–59. doi:10.1016/j.ijom.2007.05.024

Tan, F., and Al-Rubeai, M. (2019). Customizable Implant-specific and Tissue-specific Extracellular Matrix Protein Coatings Fabricated Using Atmospheric Plasma. *Front. Bioeng. Biotechnol.* 7, 247. doi:10.3389/fbioe.2019.00247

Terheyden, H., Lang, N. P., Bierbaum, S., and Stadlinger, B. (2012). Osseointegration - Communication of Cells. *Clin. Oral Impl. Res.* 23, 1127–1135. doi:10.1111/j.1600-0501.2011.02327.x

Tsai, A. T., Rice, J., Scatena, M., Liaw, L., Ratner, B. D., and Giachelli, C. M. (2005). The Role of Osteopontin in Foreign Body Giant Cell Formation. *Biomaterials* 26, 5835–5843. doi:10.1016/j.biomaterials.2005.03.003

Türker, N. S., Özer, A. Y., Kutlu, B., Nohutcu, R., Sungur, A., Bilgili, H., et al. (2014). The Effect of Gamma Radiation Sterilization on Dental Biomaterials. *Tissue Eng. Regen. Med.* 11, 341–349. doi:10.1007/s13770-014-0016-9

Ueno, T., Takeuchi, M., Hori, N., Iwasa, F., Minamikawa, H., Igarashi, Y., et al. (2012). Gamma Ray Treatment Enhances Bioactivity and Osseointegration Capability of Titanium. *J. Biomed. Mat. Res.* 100B, 2279–2287. doi:10.1002/jbm.b.32799

Viornery, C., Guenther, H. L., Aronsson, B.-O., Péchy, P., Descouts, P., and Grätzel, M. (2002). Osteoblast Culture on Polished Titanium Disks Modified with Phosphonic Acids. *J. Biomed. Mat. Res.* 62, 149–155. doi:10.1002/jbm.10205

Wai, P. Y., and Kuo, P. C. (2004). The Role of Osteopontin in Tumor Metastasis. *J. Surg. Res.* 121, 228–241. doi:10.1016/j.jss.2004.03.028

Yuan, X., Pei, X., Zhao, Y., Li, Z., Chen, C. H., Tulu, U. S., et al. (2018). Biomechanics of Immediate Postextraction Implant Osseointegration. *J. Dent. Res.* 97, 987–994. doi:10.1177/0022034518765757

Zhang, J., Liu, J., Wang, C., Chen, F., Wang, X., and Lin, K. (2020). A Comparative Study of the Osteogenic Performance between the Hierarchical Micro/submicro-Textured 3D-Printed Ti6Al4V Surface and the SLA Surface. *Bioact. Mater.* 5, 9–16. doi:10.1016/j.bioactmat.2019.12.008

Zhao, G., Raines, A., Wieland, M., Schwartz, Z., and Boyan, B. (2007). Requirement for Both Micron- and Submicron Scale Structure for Synergistic Responses of Osteoblasts to Substrate Surface Energy and Topography. *Biomaterials* 28, 2821–2829. doi:10.1016/j.biomaterials.2007.02.024

Conflict of Interest: The authors declare that the research was conducted in the absence of any commercial or financial relationships that could be construed as a potential conflict of interest.

ORIGINAL RESEARCH
published: 27 May 2022
doi: 10.3389/fbioe.2022.894636

Gold Nanoparticle-Functionalized Diatom Biosilica as Label-Free Biosensor for Biomolecule Detection

Tongtong Chen[1], Feifei Wu[1], Yang Li[2], Hussein E. Rozan[1,3], Xiguang Chen[1,4] and Chao Feng[1]*

[1]College of Marine Life Science, Ocean University of China, Qingdao, China, [2]College of Life Sciences, Qingdao University, Qingdao, China, [3]Department of Biochemistry, Faculty of Agriculture, Al-Azhar University, Cairo, Egypt, [4]Qingdao National Laboratory for Marine Science and Technology, Qingdao, China

Diatom biosilica (DBs) is the cell wall of natural diatom called frustule, which is made of porous hydrogenated amorphous silica possessing periodic micro- to nanoscale features. In this study, a simple, sensitive, and label-free photoluminescence (PL) immune-detection platform based on functionalized diatom frustules was developed. Gold nanoparticles (AuNPs) deposited on poly-dopamine-coated diatom frustules *via in situ* deposition which considerably decreased the intrinsic blue PL intensity of diatom biosilica. Then, goat anti-rabbit immunoglobulin G (IgG) was added to functionalize diatom biosilica-poly-dopamine-AuNPs (DBs-PDA-AuNPs). PL studies revealed that the specific binding with antigen rabbit IgG increased the peak intensity of PL in comparison with the non-complimentary antigen (human IgG). The enhancement in PL intensity of DBs-PDA had a linear correlation with antigen (rabbit IgG) concentration, whose limit of detection (LOD) reached 8×10^{-6} mg/ml. Furthermore, PL detection based on DBs-PDA-AuNPs showed a high detection sensitivity with the LOD as low as 8×10^{-9} mg/ml and spread over almost eight orders of magnitude, making it suitable for the sensitive quantitative analysis of immune complex compared with traditional fluorescence immunoassay. Hence, the study proves that the AuNP-functionalized diatom frustules can serve as an effective biosensor platform for label-free PL-based immunoassay.

Keywords: antibody, biosensor, diatom, biosilica, photoluminescence, gold nanoparticles

Edited by:
Junchao Wei,
Nanchang University, China

Reviewed by:
Jichang Han,
Ningbo University, China
Piwu Li,
Qilu University of Technology, China

***Correspondence:**
Chao Feng
fengchao@ouc.edu.cn

Specialty section:
This article was submitted to Biomaterials,
a section of the journal
Frontiers in Bioengineering and Biotechnology

Received: *12 March 2022*
Accepted: *21 April 2022*
Published: *27 May 2022*

Citation:
Chen T, Wu F, Li Y, Rozan HE, Chen X and Feng C (2022) Gold Nanoparticle-Functionalized Diatom Biosilica as Label-Free Biosensor for Biomolecule Detection.
Front. Bioeng. Biotechnol. 10:894636.
doi: 10.3389/fbioe.2022.894636

1 INTRODUCTION

Immuno-detection *via* special recognition with antibody–antigen is an essential tool for clinical detection and diagnosis of diseases rapidly and reliably (Uram et al., 2006; Lin et al., 2013). Compared to electrical and mass measurement methods, optical biosensors have attracted much attention because of their high sensitivity, specificity, and convenience (Dong et al., 2015; Peltomaa et al., 2018; Wang et al., 2019). Label-based optical biosensor such as fluorescence bio-sensing has been widely used in immunoassay, but the photo-bleaching and the limitation of multiplex detection are normally along with the contamination of the sample matrix due to the introduction of labels, which restricts its application in clinic (Gale et al., 2009). Label-free optical bio-sensing platforms can offer real-time monitoring of immune-complex and avoid these drawbacks mentioned earlier (Viji et al., 2014). Surface plasmon resonance (SPR) is one of the most used label-free optical biosensors whose plasmon mode will change when biomolecules bind to the surface of a metal film (Meyer et al., 2011). However, there is a challenge for SPR sensor to detect small biomolecules, such as antibodies, since the binding of small size molecules changes little the refractive index, which reduces the sensitivity of the measurement. On the other hand, the signal uniformity and reproducibility of surface-enhanced Raman spectroscopy (SERS) for small molecules detection, for example, aptamers and antibodies, also confine its uses in the laboratory (Kashif et al., 2020).

Diatoms are mono-cellular eukaryotic phytoplankton widely distributed in oceans and lakes. Diatoms take up soluble silicon to form the cell wall of amorphous silica, which possesses three-dimensional micro- to nano-porous structures (Gordon et al., 2009; De Tommasi et al., 2013). Several studies found that DBs possessed unique photoluminescence (PL) properties which changed upon different biomolecules depositing on its surface, which revealed their promising applications in optical bio-sensing without labeling (Qin et al., 2008; De Tommasi, 2016; LeDuff et al., 2016; Mishra et al., 2020). The PL property of DBs was induced by various surface groups on DBs including Si-OH, Si-H groups, non-bridging oxygen hole centers, and self-trapped excitons (He et al., 2004). Nucleophilic biomolecules such as antibodies enhanced the PL peak intensity by donating electrons to non-radiative defect sites on DBs (Gale et al., 2009; Viji et al., 2014). Within the past few years, DBs has been developed as label-free bio-sensing platforms of PL-based gas sensors for detecting small biomolecules, such as antibodies and explosive derivatives (Viji et al., 2014; Rea et al., 2016; Zhen et al., 2016).

Considering the definite limitations of DBs in immunoassay due to its unreactive nature of the surface, Gregory and his colleagues introduced $-NH_2$ on DBs by reaction with 3-aminopropyltrimethoxysilane (APS) and then covalently attached with rabbit immunoglobulin G (IgG) (Gale et al., 2009). The special binding between rabbit IgG with the complimentary antigen goat anti-rabbit IgG increased the PL peak intensity by at least three times in comparison with bare DBs. Furthermore, the enhancement in PL intensity with antigen (goat anti-rabbit IgG) concentration was displayed by a Langmuir model for immune-complex formation. De Stefano et al. (2009) also utilized APTS to modify DBs, using the PL of *Coscinodiscus concinnus* for quantitative analysis and detection of proteins. Zhen et al. (2016) found that the PL emission was partially quenched when TNT binding to the anti-TNT ScFv-functionalized DBs. These results validate that DBs can be used as an optical biosensor platform for PL-based immunoassay. Aforementioned strategies are all based on chemical modification. Poly-dopamine (PDA) can coat the surface of DBs in virtue of its great adhesive properties which is considered an environmentally friendly method for the surface modification of DBs (Uthappa et al., 2019). PDA coating can promote antibody functionalization by virtue of its adhesion properties. In addition, PDA coating can improve the sensitivity of diatoms PL detection by reducing the defect concentration of DBs. Therefore, we used PDA to modify DBs to make it a better optical biosensor based on PL detection.

Noble metal nanoparticles such as gold nanoparticles (AuNPs) and silver nanoparticles (AgNPs) exhibit unique optical properties. They can display the localized surface plasmon resonance (LSPR) phenomenon, whose absorbance will be light very intense when excited at certain wavelengths (Ren et al., 2013; Liu et al., 2018; Petzold and Zollfrank, 2019). According to the surface state luminescence model proposed by Xie et al. (1992), the deposition of metal nanoparticles on the surface of DBs change its surface state and cause its PL intensity to decay. Thus, AuNPs may have the potential to be used in optical biosensors based on PL. In addition, AuNPs possess advantages of being easy to synthesize and modify, good stability, and biocompatibility (Leng et al., 2010). On the other hand, AuNPs possessing ultra-small sizes bound and assemble on the surface of DBs, increasing the available surface area of binding biomolecules and enhancing optical signal sensitivity. Therefore, the deposition of AuNPs on DBs can serve as substrates for optical biosensors.

In this study, we utilized PDA and AuNP-functionalized DBs (**Scheme 1**). Then, the antibody goat anti-rabbit IgG was attached to PDA coated on DBs (DBs-PDA) and AuNPs deposited on DBs-PDA (DBs-PDA-AuNPs). We examined the correlation of antibody goat anti-rabbit IgG-functionalized DBs-PDA and DBs-PDA-AuNPs with antigen rabbit IgG concentrations in the range from 8×10^{-9} to 8×10^{-2} mg/ml. DyLight 488-labeled rabbit IgG was employed for immunoassay to compare with the PL and fluorescence detection. Furthermore, in order to validate the universality of DBs as a photo-luminescent immune-sensor, we detected the correlation between the PL peak intensity of rabbit anti-human IgG-functionalized DBs-PDA and DBs-PDA-AuNPs and different concentrations of human IgG (from 8×10^{-9} to 8×10^{-2} mg/ml). In conclusion, PL detection based on DBs-PDA-AuNPs can be applied to the selectivity, high sensitivity, and label-free immunoassay.

2 MATERIALS AND METHODS

2.1 Reagents and Materials

NaOH, bovine serum albumin (BSA), and dopamine hydrochloride (DA) were all purchased from Sigma-Aldrich (United States), and 0.2 M phosphate-buffered saline (PBS) (pH 7.4) was prepared by mixing the stock solutions of KH_2PO_4 and K_2HPO_4. $HAuCl_4{\cdot}3H_2O$ was purchased from Shanghai Aladdin Biochemical Technology Co., Ltd. Rabbit IgG (RIgG), human IgG (HIgG), goat anti-rabbit IgG (GaR), DyLight 488-rabbit IgG (DyLight 488-RIgG), and rabbit anti-human IgG (RaH) were all purchased from Wuhan Boster Biological Technology Ltd. *C. cryptica* (GY-H32) was obtained from the Key Laboratory of Marine Genetics and Breeding, Ocean University of China.

2.2 Preparation of Diatom Biosilica

2.2.1 Cultivation of Diatom

C. cryptica was cultured in F/2 medium at 20°C with an alternating light/night cycle of 12:12 h for 2 weeks. The diatom cells were obtained *via* filtration and washed three times using deionized water.

2.2.2 Treatment of Diatom Frustules

C. cryptica of 25 g was mixed with 50 ml lye (potassium hydroxide: urea: water = 16:8:66) and stirred evenly, repeated

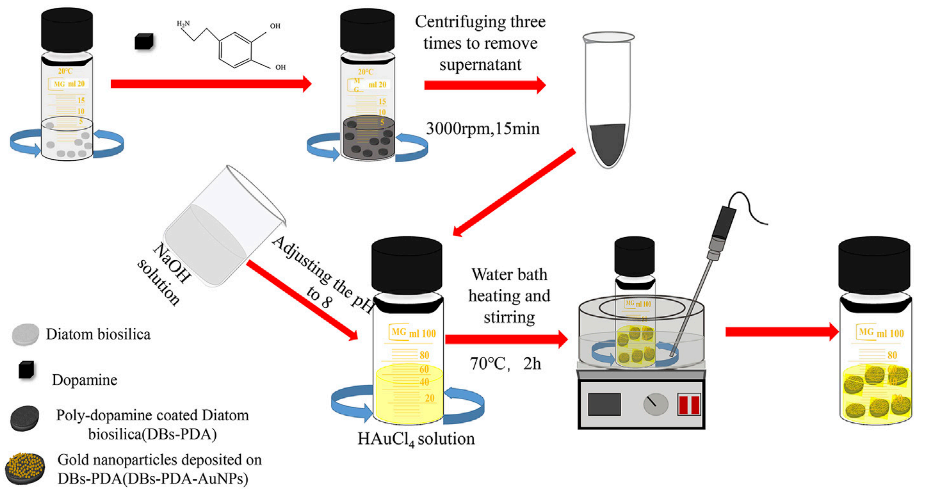

SCHEME 1 | Schematic diagram illustration of the synthesis of DBs-PDA and DBs-PDA-AuNPs.

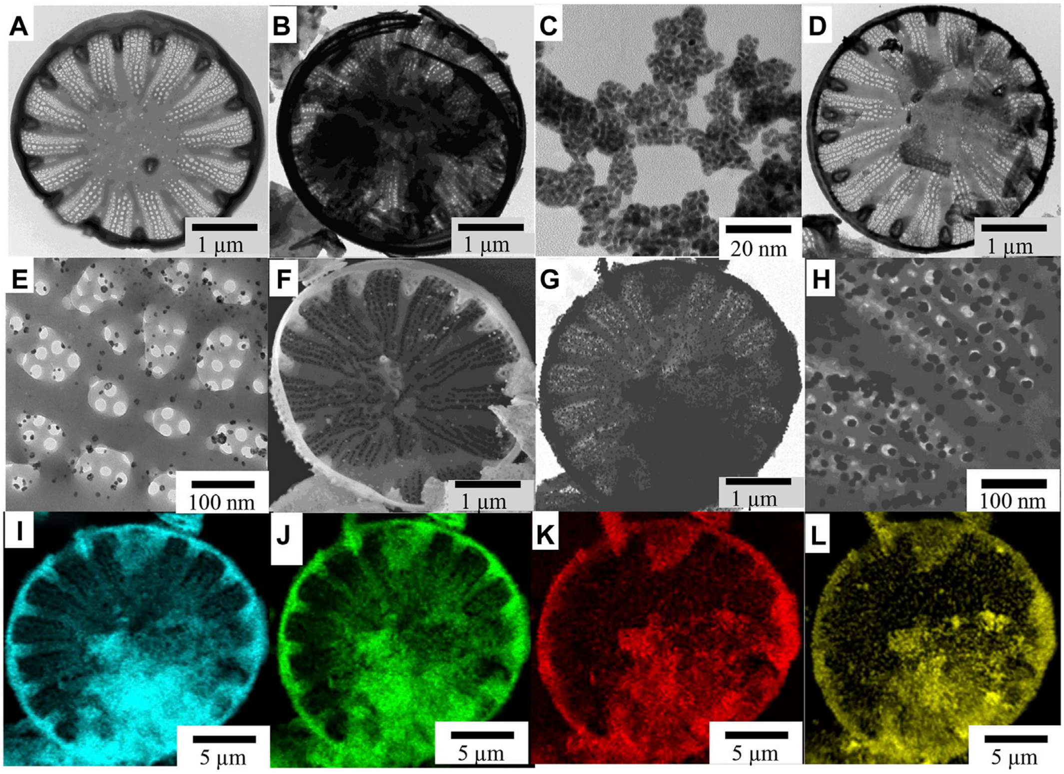

FIGURE 1 | TEM images of **(A)** frustule of C. cryptica, **(B)** PDA-coated diatoms, **(C)** free AuNPs, **(D)** 172 AuNP-deposited DBs-PDA, and **(E)** details of AuNPs on the surface of DBs-PDA. SEM images of 173 **(F)** DBs-PDA-AuNPs, **(G)** DBs-PDA-AuNPs, and **(H)** details of AuNPs on the DBs-PDA. **(I–L)** In total, 174 EDS images of **(I)** Si, **(J)** O, **(K)** C, and (m) Au in DBs-PDA-AuNPs.

freezing (under−25°C for 5~6 h each time) and thawing twice frozen twice, and rinsed several times. Then, the pre-cooled treated sample was added to 50 ml of chilled piranha solution (sulfuric acid: hydrogen peroxide = 7:3), which was subsequently heated in a water bath of 75°C for 30 min and stirred constantly, followed by cooling, diluting once, washing by centrifugation several times, and drying in the oven to obtain DBs with the hierarchical porous structure (**Figure 1A**).

2.3 Dopamine Coating on DBs

DBs of 10 mg was dissolved in 10 ml deionized water and stirred continuously for 40 min. Then, 40 mg dopamine hydrochloride (DA) and 200 µl NaOH solution (0.1 M, 50 ml) were added into the diatom solution and stirred evenly. Dopamine hydrochloride (DA) is self-polymerized to poly-dopamine (PDA) in a weak alkaline environment. Then, the sample was centrifuged (3,000 rpm, 15 min) three times, and the supernatant was removed. DBs coated by PDA (DBs-PDA) could be observed using the transmission electron microscope (**Figure 1B**).

2.4 Synthesis of AuNP-Functionalized DBs-PDA

AuNPs were fabricated by the modified method reported previously (Jia et al., 2005). Chloroauric acid ($HAuCl_4 \cdot 3H_2O$) of 85 mg was dispersed in 50 ml ultrapure water and adjusted the pH to 8.0 with 0.1 M NaOH solution. Next, the obtained DBs-PDA was added, heated to 70°C, and continuously stirred for 2 h. Afterward, the resulting solution mixture was centrifuged (3,000 rpm, 15 min) until the absence of Cl^- ion and removed the supernatant. Finally, the precipitates were dried completely in the oven.

2.5 Preparation of Immuno-Sensors

2.5.1 Immobilization of Antibody on DBs-PDA-AuNPs

DBs functionalized with antibody was prepared by following the methods reported previously (Lai et al., 2013). First, DBs-PDA-AuNP (1.5 mg/ml) suspension was adjusted to the pH 9.0 with 0.1 M K_2CO_3. Then, 30 µl goat anti-rabbit IgG was added to 50 µl suspension, by gently mixing at room temperature for 2 h. The sample was then centrifuged for 15 min, followed by mixing with 5% BSA for 1 h for blocking, and washing with PBS twice successively. After centrifugation, antibody-conjugated diatom frustules were collected and re-dissolved in 0.5 ml PBS containing 0.1% BSA. The resulting product was then stored at 4°C for further use.

2.5.2 Immunological Reactions

Stocked antigens were prepared by mixing 10 µl RIgG (with the concentration of 10 mg/ml) with 990 µl PBS. Then, 100 µl DBs-PDA-AuNPs-GaR and RIgG with the concentrations ranging from 8×10^{-9} to 8×10^{-2} mg/ml were dissolved in a polystyrene 12-well plate containing 2 ml PBS, which was then gently mixed for 2 h at room temperature.

3 RESULTS AND DISCUSSION

3.1 Synthesis and Characterization of DBs-PDA-AuNPs

DBs was isolated from cultured *C. cryptica* using chilled piranha solution to remove the organic matter in cells. The purified DBs was drum-shaped with a diameter of 10~30 µm and possessed a hierarchical pore structure (**Figure 1A**). After mixing DBs and DA under weak alkaline conditions (**Scheme 1**), DA could be oxidized spontaneously, and PDA coating was formed (**Figure 1B**) *via* the self-polymerization-crosslinking reaction on the surface of DBs. AuNPs were likely to self-assemble with regular size and shape on the surface of DBs-PDA via in situ deposition (**Figures 1D, F, G**). The free AuNPs were 3~5 nm diameter and aggregated to form clusters (**Figure 1C**). In contrast, the AuNPs on DBs-PDA-AuNPs were agglomerated for a larger size with a diameter of 15~20 nm and distributed evenly on the surface of DBs (**Figure 1G**). This might be explained by the higher agglomeration tendency of AuNPs when depositing on DBs. EDS images validated that elements of Si (**Figure 1I**), O (**Figure 1J**), C (**Figure 1K**), and Au (**Figure 1L**) could be found on DBs-PDA-AuNPs which also confirmed the successful immobilization of AuNPs on DBs.

The UV-Vis spectra of DBs, DBs-PDA, AuNPs, and DBs-PDA-AuNPs showed that there were no characteristic absorption peaks in the spectra of DBs and DBs-PDA at the wavelength range of 400–600 nm, and their spectral shapes were very similar (**Figure 2A,B**). The noticeable characteristic absorption band peaking at 550 nm, which was an indicative of the formation of AuNPs, was observed in the UV-Vis spectrum (**Figure 2C**). After AuNPs deposited on the surface of DBs-PDA, the absorption peak intensity of DBs-PDA-AuNPs increased in comparison with AuNPs alone. The absorption band of DBs-PDA-AuNPs was red-shifted and the peak appeared at about 580 nm, indicating the aggregation of AuNPs on DBs-PDA (**Figure 2d**), which was consistent with the agglomeration tendency observed in the SEM image (**Figure 1H**). The energy dispersive X-ray spectrum (EDS) of DBs-PDA-AuNPs presented the distribution of elements including C, O, Si, and Au and further validated the existence of AuNPs (**Figure 2B**). The FT-IR spectra clearly showed characteristic peaks for DBs, including Si–O–Si bending at 466 and 806 cm^{-1}, Si–O–Si stretching at 1,090 cm^{-1}, and O–H stretching of surface-bound hydroxyl groups at 3,147 cm^{-1}, which mainly included bound water, H–O–Si, and pyrocatechol of poly-dopamine. After PDA coated on DBs, the strong peaks at 1,615 cm^{-1} shown in the spectrum corresponded to the typical absorption peak of amide bonds on the PDA chain (Yang et al., 2014). However, when AuNPs deposited on DBs-PDA, the amide bonds almost disappeared, which might suggest the formation of Au–N. According to the infrared spectra, the characteristic absorption peak at −3,147 cm^{-1} weakened after AuNPs functionalized DBs, suggesting that the free Si–OH on DBs reacted with AuNPs to form the Si–O–Au group (**Figure 2C**). From the aforementioned results, it could be concluded that AuNPs had been successfully fixed on the surface of DBs-PDA.

The XPS survey spectrum indicated that AuNPs were successfully deposited on the surface of DBs (**Figure 3A**). The functionalization of PDA coating and AuNPs only displays a peak C1s at 284.73 eV (**Figure 3B**). After AuNPs deposited on DBs, the two components of Au $4f_{7/2}$ were at binding energy = 83.9 and 87.6 eV, which indicated the emergence of Au^0 and the ion of Au^{+1} on the surface of DBs-PDA-AuNPs, respectively. This result demonstrated that the chloroauric acid was reduced to AuNPs and successfully immobilized on DBs-PDA (**Figure 3f**). The appearance of the N_{1s} peak of DBs-PDA and DBs-PDA-AuNPs near 399 eV could be attributed to the existence of NSi_2O (**Figure 3d**). The Si_{2p} of DBs located at 103.62 eV was

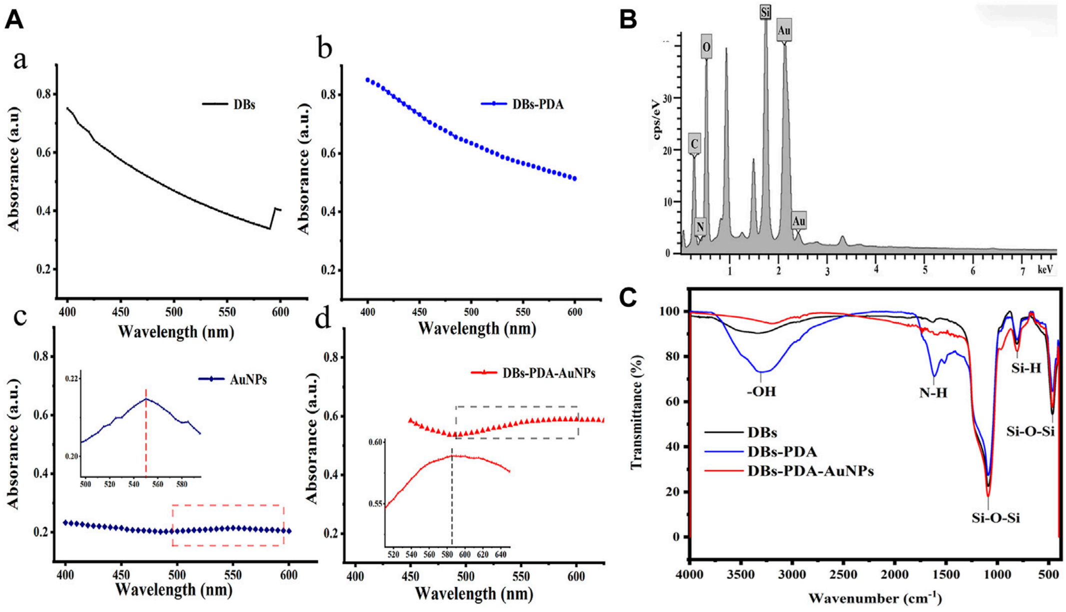

FIGURE 2 | (A) UV-Vis absorption spectra of **(a)** DBs, **(b)** DBs-PDA, **(c)** AuNPs (Inset: the UV-Vis absorption spectrum of AuNPs from 495 to 600 nm), and **(d)** DBs-PDA-AuNPs (Inset: the UV-Vis absorption spectrum of DBs-PDA-AuNPs from 510 to 650 nm). **(B)** EDS spectrum of DBs-PDA-AuNPs. **(C)** FITR spectra of DBs, DBs-PDA, and DBs-PDA-AuNPs.

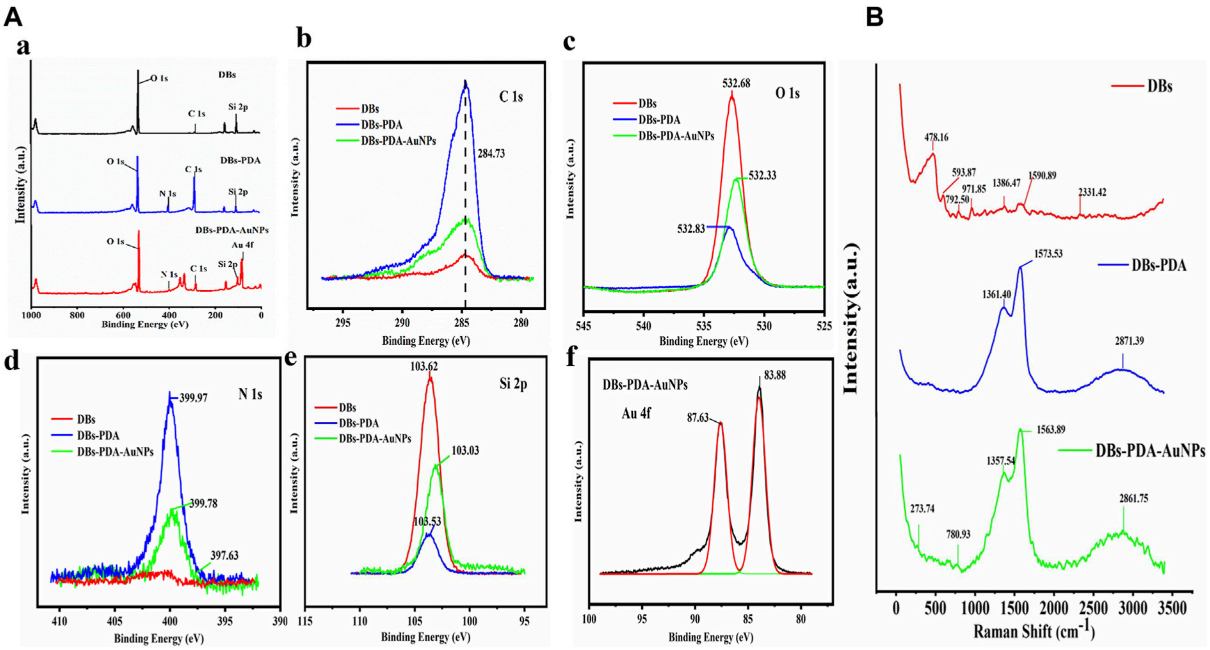

FIGURE 3 | (A) XPS spectra of DBs, DBs-PDA, and DBs-PDA-AuNPs. **(a)** XPS survey spectrum of DBs and PDA-coated DBs as well as AuNP-deposited DBs-PDA. **(b)** C_{1s} scan spectrum, **(c)** O_{1s} scan spectrum, **(d)** N_{1s} scan spectrum, **(e)** Si_{2p} scan spectrum, and **(f)** Au_{4f} scan spectrum. **(B)** SERS spectrum of DBs, DBs-PDA, and DBs-PDA-AuNPs.

attributed to SiO_2, and the peak value of DBs-PDA was shifted toward a lower binding energy around 0.09 eV (from 103.6 to 103.5 eV), implying that part of the Si–OH bond had been transferred into Si–N bond. In addition, the Si_{2p} of DBs-PDA-AuNPs located at 103.0 eV was shifted to lower binding energy by 0.5 eV than that of DBs-PDA, suggesting that part of the Si–N

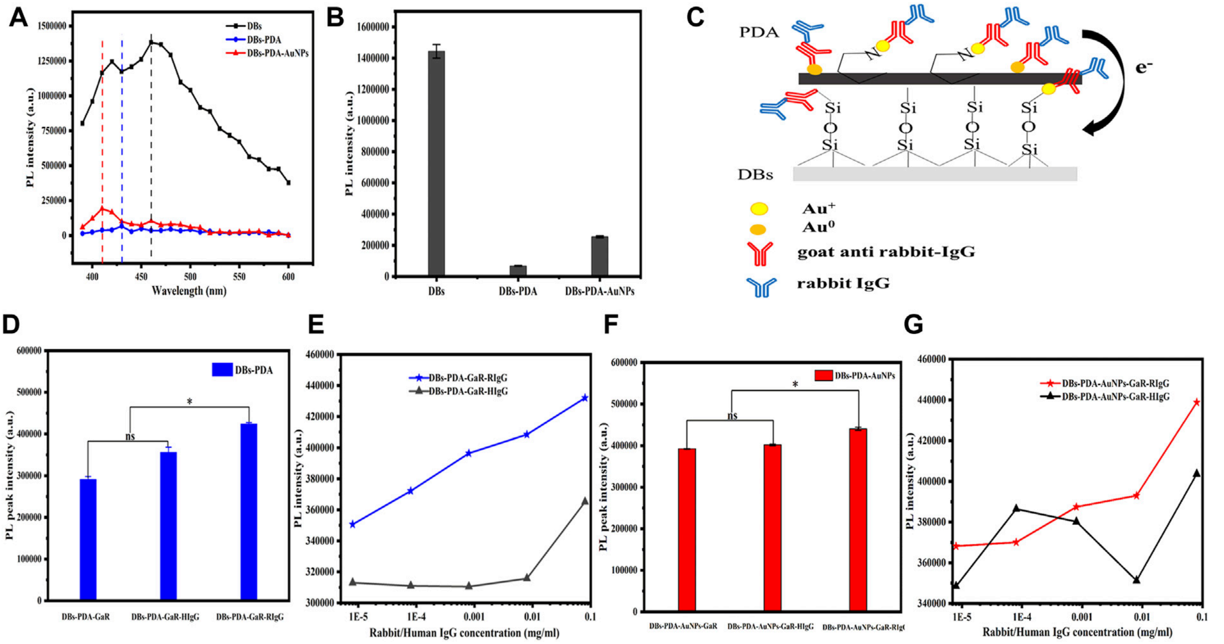

FIGURE 4 | (A) PL spectra of DBs, DBs-PDA, and DBs-PDA-AuNPs. **(B)** Comparison of PL peak intensity of DBs, DBs-PDA, and DBs-PDA-AuNPs. **(C)** Schema of functionalized DBs-PDA-AuNPs with antibody GaR and complimentary antigen RIgG. **(D)** Comparison of the PL peak intensity of DBs-PDA-GaR (DBs-PDA-antibody), DBs-PDA-GaR with RIgG (DBs-PDA-antibody-comp. antigen), and DBs-PDA-GaR with HIgG (DBs-PDA-antibody-non-comp. antigen). **(E)** Comparison of PL peak intensity variation of DBs-PDA-GaR versus RIgG and HIgG (from 8×10^{-6} to 8×10^{-2} mg/ml), respectively. ns represents no significant difference, $p > 0.05$* represents a significant difference, and $p < 0.05$. **(F)** Comparison of PL peak intensity of DBs-PDA-AuNPs-GaR, DBs-PDA-AuNPs-GaR with RIgG, and DBs-PDA-AuNPs-GaR with HIgG. **(G)** Comparison of PL peak intensity variation of DBs-PDA-AuNPs-GaR versus RIgG and HIgG (from 8×10^{-6} to 8×10^{-2} mg/ml), respectively. Excitation wavelength was 360 nm.

bond had changed to Si–Au bond (**Figure 3e**). Thus, AuNPs were more likely to form Si–O–Au bonds with the free Si–OH on the surface of DBs.

The Raman spectrum of DBs had a characteristic peak at 478.2 cm^{-1}, corresponding to Si–O–Si stretching vibration (red curve). Due to the introduction of PDA, peaks of −1,362 and −1,571 cm^{-1} of DBs-PDA and DBs-PDA-AuNPs both appeared in the Raman spectra which were attributed to the presence of aromatic phenyl in PDA (blue and green curves). The characteristic absorption peak at 2,850–2,923 cm^{-1} was attributed to the stretching vibration of -CH. DBs-PDA-AuNPs (green curve) had a weak characteristic peak at −270 cm^{-1} which did not appear in the Raman spectra of DBs and DBs-PDA (red and blue curve) (**Figure 3b**). It was supposed that this characteristic absorption peak was concerned with the formation of N–Au (**Figure 4C**). The aforementioned results showed that when AuNPs were deposited on the surface of DBs-PDA, PDA chelated Au (I) *via* catechol and amino groups. Therefore, AuNPs were immobilized on the surface of DBs-PDA.

3.2 PL Studies

3.2.1 PL Detection of DBs-PDA-AuNPs

The PL properties of DBs, DBs-PDA, and DBs-PDA-AuNPs were evaluated using the multimode microplate reader. Several studies have demonstrated that DBs have intrinsic blue photoluminescence due to the surface defects on the DBs, (Rorrer et al., 2007; Arteaga-Larios et al., 2014; De Tommasi, 2016) which was also confirmed by our studies. It was observed that bare DBs emitted strong blue photoluminescence centered at 450 nm when samples were excited at 360 nm (**Figure 4A**). After being coated by PDA, the PL intensity of DBs-PDA was violently quenched, which displayed 13-fold lower than that of bare DBs (**Figure 4B**). The peak wavelength for DBs-PDA exhibited a blue shift from 450 to 430 nm caused by the interaction of PDA and the surface of DBs (**Figure 4A**). Defect concentration affected the PL properties of DBs. Thus, the decreased PL peak intensity and blue shift of DBs-PDA might be ascribed to the reduction of defect concentration when there is existence of PDA coating on the surface of DBs. Fedorenko et al. (2020) reported the similar results that PDA coating on ZnO nanorods caused the decrease of the defect concentration and the PL peak intensity. The PL emission spectra clearly showed 6-fold weaker PL peak intensity of DBs-PDA-AuNPs than that of bare DBs (**Figure 4B**). AuNPs functionalized DBs by forming Si–O–Au bonds, which induced the emergence of a new non-radiative center on the surface of DBs and decreased the PL peak intensity of DBs-PDA-AuNPs. The PL spectrum of DBs-PDA-AuNPs showed an obvious blue shift (from 450 to 410 nm). This result highlighted that AuNPs deposited on DBs *via in situ* polymerization would lead to the blue shift of the peak position. However, the PL peak intensity of DBs-PDA-AuNPs was one-fold higher than that of DBs-PDA. It was supposed that Au^{+}, which was formed by Au^{3+} reduction, combined with amino functional groups of PDA on the surface of DBs-PDA-

AuNPs to form N–Au bonds. The interaction between AuNPs and PDA induced the enhancement of surface passivation on DBs-PDA-AuNPs, which affected the surface recombination centers, the radiative points responsible for the PL of DBs. This inference could explain the rise of PL peak intensity after AuNPs functionalized DBs-PDA compared with DBs-PDA alone (**Figure 4C**).

3.2.2 Specificity

Our experiments validated the specificity of antibody-functionalized DBs-PDA-AuNPs with its complimentary antigen. First, when GaR-functionalized DBs-PDA (DBs-PDA-GaR) bonds with non-complimentary antigen HIgG, the PL peak intensity of DBs-PDA-GaR-HIgG showed no significant change. However, when the complimentary antigen RIgG bound with DBs-PDA-GaR, the PL peak intensity was significantly different ($p < 0.05$) which increased by more than 45% than that of DBs-PDA-GaR alone. (**Figure 4D**). The PL peak intensity of the formed complex between RIgG and GaR-functionalized DBs-PDA-AuNPs (DBs-PDA-AuNPs-GaR) changed significantly ($p < 0.05$) which increased more than 12% than DBs-PDA-AuNPs-GaR. However, no significant change in the PL peak intensity was observed after DBs-PDA-AuNPs-GaR functionalized with non-complimentary antigen HIgG (**Figure 4F**). The reason behind the peak PL intensity increase of the immune complex was the forming of nucleophilic molecules on the surface of DBs that transferred electrons to non-radiative defect sites on DBs (**Figure 4C**). In immune complex formation, the PL intensity of antibody binding on DBs-PDA-GaR and DBs-PDA-AuNPs-GaR showed a linear increase with the antigen RIgG concentration ranging from 8×10^{-6} to 8×10^{-2} mg/ml whereas non-complimentary antigen HIgG did not (**Figures 4E,G**). These results illustrated the specificity of DBs-PDA and DBs-PDA-AuNPs applied to immune-detection.

3.4 RIgG Detection Based on DBs-PDA-AuNPs

According to PL spectra of DBs-PDA-AuNPs and DBs-PDA-AuNPs-RIgG, when RIgG functionalized DBs-PDA-AuNPs, its peak PL intensity basically did not change compared with DBs-PDA-AuNPs, and the characteristic absorption peak did not change either (**Figure 5A**). As the concentration of RIgG changed (from $8 \times 10{-}^{9}$ to 8×10^{-2} mg/ml), the peak PL intensity of DBs-PDA-AuNPs-RIgG did not show a linear relationship with the concentration change (**Figure 5B**). These results indicated that RIgG did not bind to the surface of DBs through reaction with AuNPs. A minute quantity of RIgG deposited on DBs, which would not affect the PL property of DBs-PDA-AuNPs. However, after GaR functionalized DBs-PDA-AuNPs, the peak PL intensity was 2-fold as that of DBs-PDA-AuNPs. In addition, the enhancement of defect concentration on the surface of DBs-PDA-AuNPs-GaR contributed to a slight blue shift of the PL characteristic peak (from 410 to 415 nm). Furthermore, the specific binding between GaR and its complimentary antigen RIgG induced the PL intensity, with a 10% increase in comparison with DBs-PDA-AuNPs-GaR, and more than one-fold higher than that of DBs-PDA-AuNPs (**Figure 6A**). These results confirmed that the nucleophilic complex attaching to DBs could increase PL intensity. The PL emission spectra of DBs-PDA-AuNPs showed that the peak PL intensity was linearly increased with RIgG concentrations in the range of 8×10^{-9} to 8×10^{-2} mg/ml without any peak shifts (**Figure 6B**). The increase in PL peak intensity with various RIgG concentrations was described by the best-fit equation: $y = 443530.57x + 1.03E04$ and the coefficients of determination (R^2) of 0.9781 (**Figure 6C**). These results illustrated that antigen RIgG molecules were adsorbed on the surface of DBs-PDA-AuNPs-GaR and involved in the formation of immuno-complex (**Figure 6D**). As a platform of immuno-detection, DBs-PDA-AuNPs showed an outstanding PL performance for detecting RIgG with the LOD reaching as low as 8×10^{-9} mg/ml.

For DBs-PDA groups, the PL emission spectra clearly indicated that the PL peak intensity of RIgG-functionalized DBs-PDA (DBs-PDA-RIgG) barely changed and without any peak shift as compared to that of DBs-PDA alone (**Figure 7A**). Furthermore, there was no linear relationship between the PL peak intensity and RIgG concentrations (from 8×10^{-9} to 8×10^{-2} mg/ml) (**Figure 7B**). This indicated that RIgG did not react with the free groups on the surface of DBs-PDA, and only a small amount of RIgG was deposited on DBs-PDA. Thus, the PL performance of DBs-PDA-RIgG was consistent with that before RIgG deposition. When RIgG bonds with DBs-PDA-GaR (**Figure 8D**), the PL peak intensity was enhanced by more than 10%, and a slight blue peak shift could be observed in PL emission spectra which was due to the decrease of defect concentration on the surface of DBs-PDA (**Figure 8A**). In immune-complex formation, the PL peak intensity showed a linear increase with concentrations of the complementary antigen RIgG from the range of 8×10^{-6} to 8×10^{-2} mg/ml (**Figure 8B**). The PL emission spectra clearly showed the increase in PL peak intensity with various RIgG concentrations (from 8×10^{-9} to 8×10^{-2} mg/ml). However, the peak PL intensity of DBs-PDA was found to be increasing linearly with the RIgG concentrations from 8×10^{-6} to 8×10^{-2} mg/ml. The regression equation was $y = 19373.31x + 4.49E05$ with the correlation coefficient of determination (R^2) of 0.99026 (**Figure 8C**). The limit of PL detection for RIgG based on DBs-PDA reached 8×10^{-6} mg/ml, which was three orders of magnitude lower than that of DBs-PDA-AuNP-based detection.

3.5 PL-Detection Compared With Fluorescence Immunoassay

Several studies have demonstrated the potential of the AuNP-based fluorescence-labeling probe technique applied on immunoassay and biosensors. The fluorescence spectra showed that GaR functionalized DBs-PDA and DBs-PDA-AuNPs and challenged with DyLight 488-RIgG concentrations ranging from 8×10^{-9} to 8×10^{-4} mg/ml. The fluorescence peak intensity was not proportional to the change of antigen DyLight 488-RIgG concentrations (**Figures 9A,D**). In addition, after binding with different DyLight 488-RIgG concentrations ranging from 8×10^{-9} to 8×10^{-4} mg/ml,

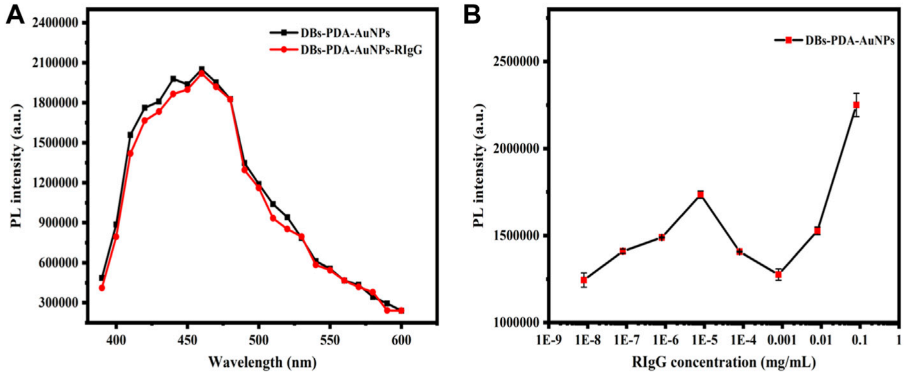

FIGURE 5 | (A) PL spectra of DBs-PDA-AuNPs and DBs-PDA-AuNPs-RIgG. **(B)** PL spectra showed DBs-PDA-AuNPs binding to different concentrations of RIgG (8×10^{-9}~8×10^{-2} mg/ml). Excitation wavelength was 360 nm.

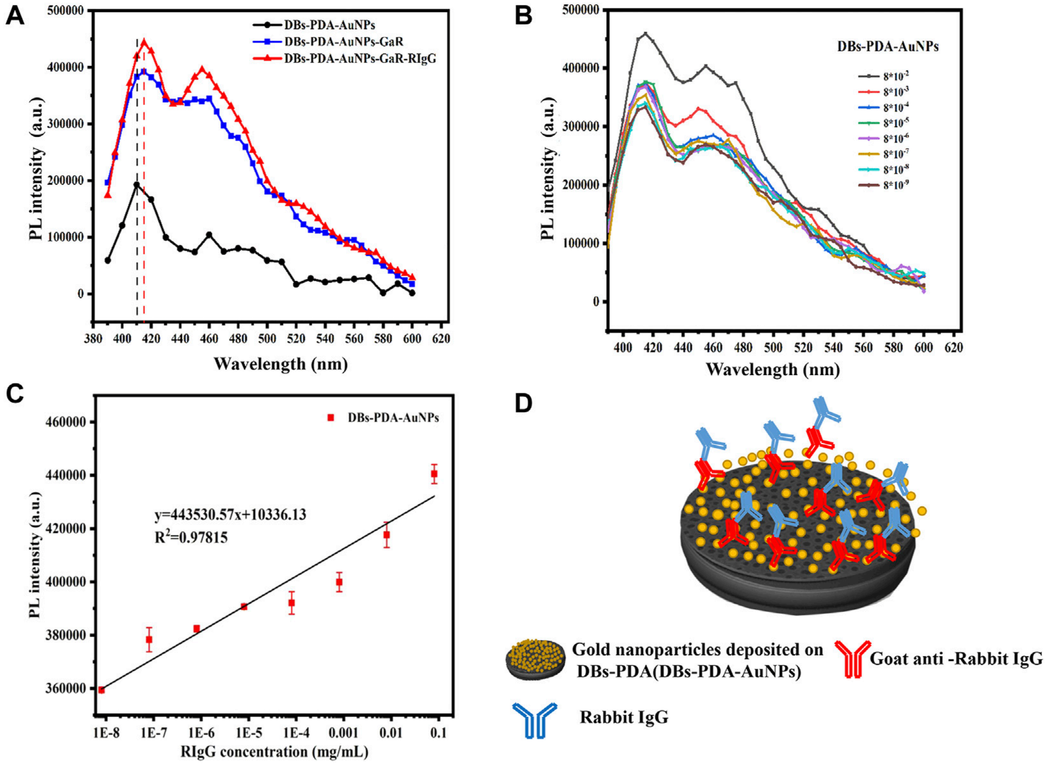

FIGURE 6 | (A) PL spectra of DBs-PDA-AuNPs, DBs-PDA-AuNPs-GaR, and DBs-PDA-AuNPs-GaR with its complimentary antigen (RIgG). **(B)** PL spectra showed DBs-PDA-AuNPs-GaR binding to different concentrations of RIgG (from 8×10^{-9} to 8×10^{-2} mg/ml). **(C)** PL intensity of DBs-PDA-AuNPs-GaR labeled with different concentrations of RIgG (from 8×10^{-9} to 8×10^{-2} mg/ml) with a coefficient of determination (R^2) of 0.97815. Excitation wavelength was 360 nm. **(D)** Schema of RIgG binding with DBs-PDA-AuNPs-GaR.

the fluorescence peak intensity was observed in fluorescence spectra. Two curves showed a similar variation trend and further indicated that there was no linear relation between fluorescence peak intensity and DyLight 488-RIgG concentrations. When challenged with RIgG-labeled DyLight 488, the entire surface of DBs-PDA and DBs-PDA-AuNPs both emitted green light which illustrated the successful binding between DyLight 488-RIgG and GaR-functionalized DBs-PDA and DBs-PDA-AuNPs, respectively (**Figures 9B,E**, Inset). With the increase of DyLight 488-RIgG concentrations from 8×10^{-9} to 8×10^{-4} mg/ml, the PL peak intensity of DBs-PDA was found increasing linearly over a range from 8×10^{-9} to 8×10^{-4} mg/ml. The regression equation was y = 23468.19x + 1.05E06 with the coefficient of determination

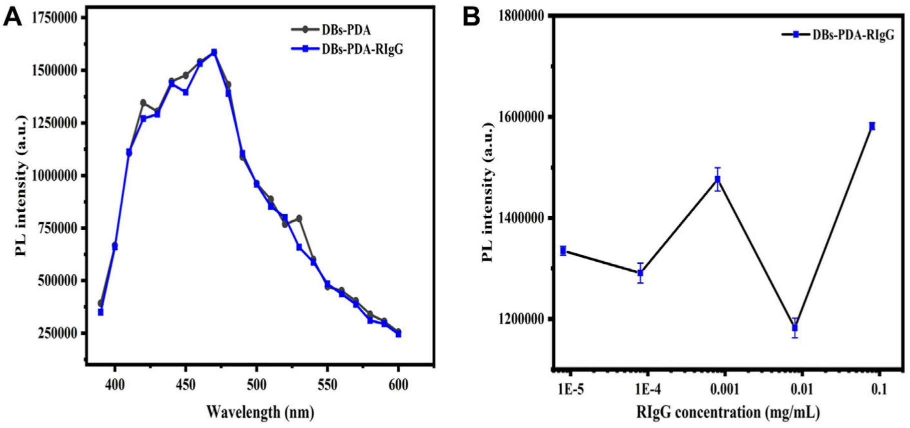

FIGURE 7 | (A) PL spectra of DBs-PDA and DBs-PDA-RIgG. **(B)** PL spectra showed DBs-PDA binding to different concentrations of RIgG (from 8 × 10^{-9} to 8 × 10^{-2} mg/ml). Excitation wavelength was 360 nm.

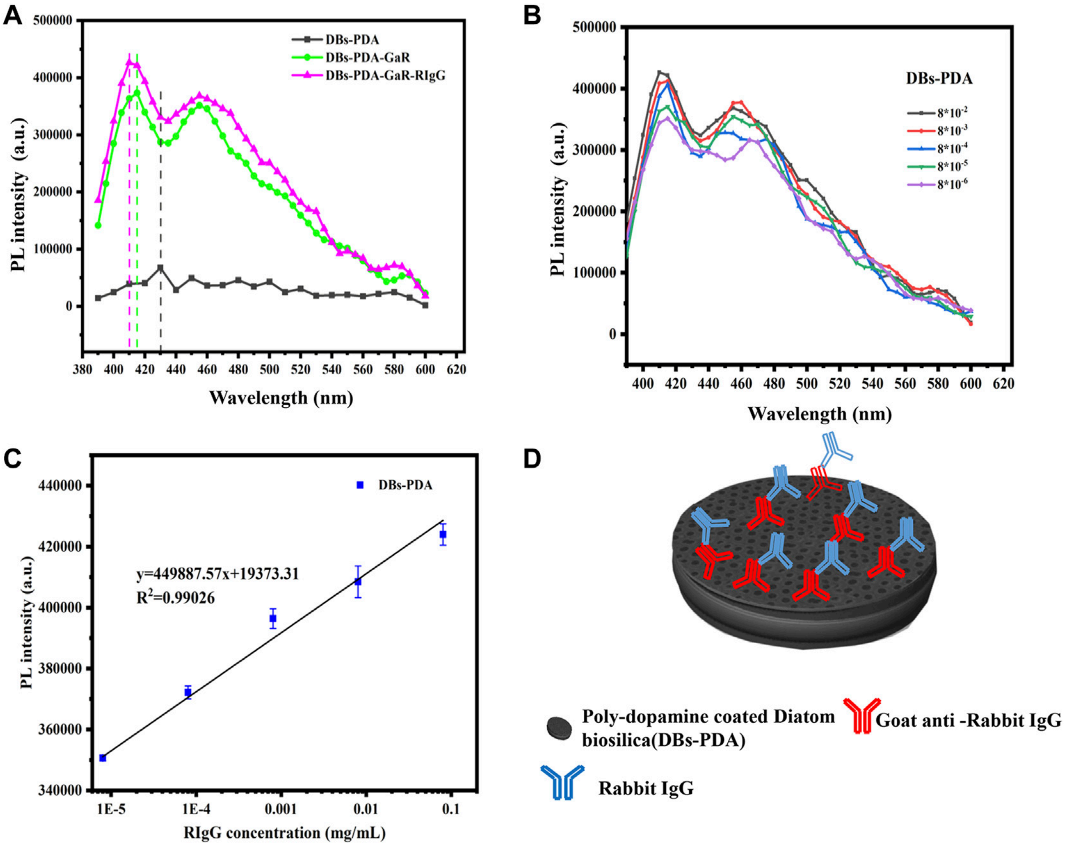

FIGURE 8 | (A) PL spectra of DBs-PDA, DBs-PDA-GaR, and DBs-PDA-GaR against its complimentary antigen (RIgG). **(B)** PL spectra showed DBs-PDA-GaR versus different concentrations of RIgG (from 8 × 10^{-6} to 8 × 10^{-2} mg/ml). **(C)** PL intensity of DBs-PDA-GaR labeled with different concentrations of RIgG (from 8 × 10^{-9} to 8 × 10^{-2} mg/ml) with a coefficient of determination (R^2) of 0.97815. Excitation wavelength was 360 nm. **(D)** Schema of RIgG binding with DBs-PDA-GaR.

(R^2) of 0.98309 (**Figure 9C**). The correlation of DBs-PDA-AuNPs-GaR versus different concentrations of antigen DyLight 488-RIgG could be found in the PL spectrum. The peak intensity of PL was observed increasing linearly with RIgG concentrations over a range from 8 × 10^{-9} to 8 × 10^{-4} mg/ml. The regression equation was y = 66996.69x + 1.25E06 with the

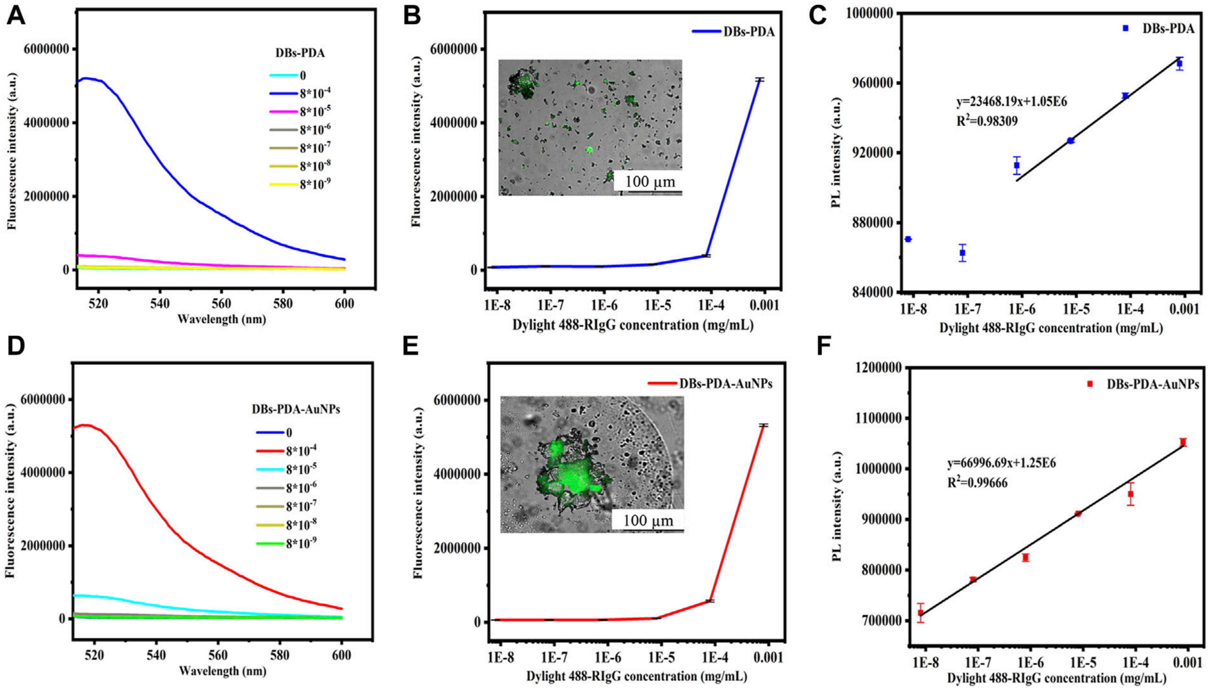

FIGURE 9 | Fluorescence spectra of GaR-functionalized **(A)** DBs-PDA and **(D)** DBs-PDA-AuNPs challenged with DyLight 488-RIgG with concentrations from 8 × 10^{-9} to 8 × 10^{-4} mg/ml. Peak fluorescence intensity variations of GaR-functionalized **(B)** DBs-PDA and **(E)** DBs-PDA-AuNPs versus DayLight 488-RIgG with different concentrations (from 8 × 10^{-9} to 8 × 10^{-4} mg/ml). Inset: fluorescence images of **(B)** GaR-functionalized DBs-PDA and **(E)** DBs-PDA-AuNPs challenged with DyLight 488-RIgG, respectively. Excitation wavelength was 488 nm. PL emission spectra of goat-anti-RIgG-functionalized **(C)** DBs-PDA and **(F)** DBs-PDA-AuNPs binding to different concentrations of DyLight 488-RIgG (from 8 × 10^{-9} to 8 × 10^{-4} mg/ml) with the coefficient of determination (R^2) of 0.98309 and 0.99666, respectively. Excitation wavelength was 360 nm.

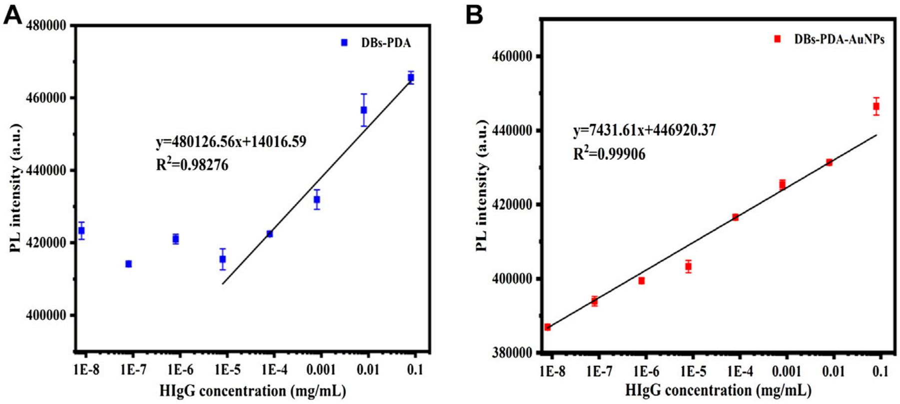

FIGURE 10 | PL peak intensity variations of **(A)** DBs-PDA and **(B)** DBs-PDA-AuNPs versus the HIgG concentration with a coefficient of determination (R^2) of 0.98276 and 0.99906, respectively. Excitation wavelength was 360 nm.

coefficient of determination (R^2) of 0.99666 (**Figure 9F**). The limit of PL detection for DyLight 488-RIgG based on DBs-PDA-AuNPs was three orders of magnitude higher than that based on DBs-PDA. Furthermore, the PL detection was more suitable in selective and quantitative detection of antigen DyLight 488-RIgG than fluorescence immunoassay.

3.6 HIgG Detection Based on DBs-PDA-AuNPs

The PL detection for HIgG was conducted to validate the universality of DBs-PDA and DBs-PDA-AuNPs as label-free optical biosensors for immune-detection. The increase in PL peak intensity of RaH-functionalized DBs-PDA-AuNPs (DBs-

PDA-AuNPs-RaH) with antigen HIgG concentrations ranged from 8×10^{-9} to 8×10^{-2} mg/ml was displayed. The PL peak intensity was found increasing linearly over a wide range from 8×10^{-9} to 8×10^{-2} mg/ml. The regression equation was y = 7,431.61x + 4.47E05 with the correlation coefficient of determination (R^2) of 0.99906 (**Figure 10B**). The LOD of DBs-PDA-AuNPs could reach 8×10^{-9} mg/ml. With the increase of HIgG concentrations, the PL peak intensity was linearly related to the concentration of HIgG concentrations from 8×10^{-6} to 8×10^{-2} mg/ml with the regression equation of y = 480126.56x + 1.40E04 and the correlation coefficient (R^2) of 0.98276 (**Figure 10A**). The LOD for HIgG detection based on DBs-PDA was three orders of magnitude lower than DBs-PDA-AuNPs. This result suggested that DBs-PDA-AuNPs were more suitable for quantitative detection of HIgG concentrations. Furthermore, PL detection based on DBs-PDA-AuNPs had the universality to be applied for immune detection in clinical samples.

4 CONCLUSION

In this present work, DBs obtained from the centric diatom *C. cryptica* were employed to establish a nanostructured immune assay platform coated with PDA and functionalized *via* AuNPs, which induced the decrease of defect concentration and quenched the PL peak intensity of DBs. N–Au formed after AuNPs reacted with PDA and further enhanced the surface passivation of DBs, which amplified the PL peak intensity of DBs-PDA-AuNPs as compared to DBs-PDA. The PL detection for RIgG based on DBs-PDA and DBs-PDA-AuNPs all exhibited high biological specificity. Nucleophilic complex formation increased the PL peak intensity of DBs-PDA and DBs-PDA-AuNPs. Furthermore, physisorption between antibody and DBs-PDA-AuNPs was likely to concentrate plenty of complimentary antigens on the surface, which resulted in high sensitivity and a decrease in the LOD. The LOD of PL detection for RIgG and HIgG based on DBs-PDA-AuNPs could reach 8×10^{-9} mg/ml, which was three orders of magnitude higher than that of DBs-PDA. In addition, PL detection for DyLight 488-RIgG based on DBs-PDA-AuNPs exhibited higher LOD than fluorescence immunoassay. As such, antibody-functionalized DBs-PDA-AuNPs could serve as an efficient optical biosensor platform for the selective, sensitive, and label-free PL-based immunoassay.

DATA AVAILABILITY STATEMENT

The original contributions presented in the study are included in the article/Supplementary Material; further inquiries can be directed to the corresponding author.

AUTHOR CONTRIBUTIONS

All the authors contributed to the research. TC performed research, analyzed data and prepared figures; YL, FW, and HR performed research; XC and CF conceived and designed the study.

FUNDING

The work was supported by the National Natural Science Foundation of China (Nos. 82172095 and 81801846), the Shandong Provincial Natural Science Foundation, China (No. ZR2019QD005), the Qingdao Science and Technology Demonstration and Guidance Project (20-3-4-50-nsh), and the Taishan Scholar Program.

REFERENCES

Arteaga-Larios, N. V., Nahmad, Y., Navarro-Contreras, H. R., Encinas, A., and Viridiana García-Meza, J. (2014). Photoluminescence Shift in Frustules of Two Pennate Diatoms and Nanostructural Changes to Their Pores. *Luminescence* 29 (8), 969–976. doi:10.1002/bio.2646

De Stefano, L., Rotiroti, L., De Stefano, M., Lamberti, A., Lettieri, S., Setaro, A., et al. (2009). Marine Diatoms as Optical Biosensors. *Biosens. Bioelectron.* 24 (6), 1580–1584. doi:10.1016/j.bios.2008.08.016

De Tommasi, E. (2016). Light Manipulation by Single Cells: The Case of Diatoms. *J. Spectrosc.* 2016, 1–13. doi:10.1155/2016/2490128

De Tommasi, E., Rea, I., De Stefano, L., Dardano, P., Di Caprio, G., Ferrara, M., et al. (2013). "Optics With Diatoms: Towards Efficient, Bioinspired Photonic Devices at the Micro-scale," in Spie Optical Metrology, Munich, Germany. 8792, 87920O. doi:10.1117/12.2021613

Dong, Y.-L., Jiang, T., Xia, W., Dong, H.-P., Lu, S.-H., and Cui, L. (2015). Light Harvesting Proteins Regulate Non-photochemical Fluorescence Quenching in the Marine Diatom Thalassiosira Pseudonana. *Algal Res.* 12, 300–307. doi:10.1016/j.algal.2015.09.016

Fedorenko, V., Viter, R., Mrówczyński, R., Damberga, D., Coy, E., and Iatsunskyi, I. (2020). Synthesis and Photoluminescence Properties of Hybrid 1D Core-Shell Structured Nanocomposites Based on ZnO/polydopamine. *RSC Adv.* 10 (50), 29751–29758. doi:10.1039/d0ra04829a

Gale, D. K., Gutu, T., Jiao, J., Chang, C.-H., and Rorrer, G. L. (2009). Photoluminescence Detection of Biomolecules by Antibody-Functionalized Diatom Biosilica. *Adv. Funct. Mat.* 19 (6), 926–933. doi:10.1002/adfm.200801137

Gordon, R., Losic, D., Tiffany, M. A., Nagy, S. S., and Sterrenburg, F. A. S. (2009). The Glass Menagerie: Diatoms for Novel Applications in Nanotechnology. *Trends Biotechnol.* 27 (2), 116–127. doi:10.1016/j.tibtech.2008.11.003

He, N., Ge, S., Yang, C., Hu, C., and Gu, M. (2004). Investigation on the Mechanism of the Photoluminescence of MCM-41. *Mater. Res. Bull.* 39 (12), 1931–1937. doi:10.1016/j.materresbull.2004.05.018

Jia, M., Shen, Y., Li, C., Bao, Z., and Sheng, S. (2005). Effect of Supports on the Gold Catalyst Activity for Catalytic Combustion of CO and HCHO. *Catal. Lett.* 99 (3-4), 235–239. doi:10.1007/s10562-005-2129-1

Kashif, M., Majeed, M. I., Hanif, M. A., and Rehman, A. u. (2020). Surface Enhanced Raman Spectroscopy of the Serum Samples for the Diagnosis of Hepatitis C and Prediction of the Viral Loads. *Spectrochimica Acta Part A Mol. Biomol. Spectrosc.* 242, 118729. doi:10.1016/j.saa.2020.118729

Lai, G., Zhang, H., Yong, J., and Yu, A. (2013). *In Situ* deposition of Gold Nanoparticles on Polydopamine Functionalized Silica Nanosphere for Ultrasensitive Nonenzymatic Electrochemical Immunoassay. *Biosens. Bioelectron.* 47, 178–183. doi:10.1016/j.bios.2013.03.029

LeDuff, P., Roesijadi, G., and Rorrer, G. L. (2016). Micro-photoluminescence of Single Living Diatom Cells. *Luminescence* 31 (7), 1379–1383. doi:10.1002/bio.3118

Leng, C., Lai, G.-S., Yan, F., and Ju, H.-X. (2010). Gold Nanoparticle as an Electrochemical Label for Inherently Crosstalk-free Multiplexed Immunoassay on a Disposable Chip. *Anal. Chim. Acta* 666 (1-2), 97–101. doi:10.1016/j.aca.2010.03.060

Lin, H., Li, L., Lei, C., Xu, X., Nie, Z., Guo, M., et al. (2013). Immune-independent and Label-free Fluorescent Assay for Cystatin C Detection Based on Protein-Stabilized Au Nanoclusters. *Biosens. Bioelectron.* 41, 256–261. doi:10.1016/j.bios.2012.08.030

Liu, Y.-S., Lin, H.-C., and Xu, H.-L. (2018). The Surface Plasmon Resonance Effect on the Defect-Mode Cholesteric Liquid Crystals Doped with Gold Nanoparticles. *IEEE Photonics J.* 10 (5), 1–7. doi:10.1109/jphot.2018.2821560

Meyer, S. A., Le Ru, E. C., and Etchegoin, P. G. (2011). Combining Surface Plasmon Resonance (SPR) Spectroscopy with Surface-Enhanced Raman Scattering (SERS). *Anal. Chem.* 83 (6), 2337–2344. doi:10.1021/ac103273r

Mishra, M., Singh, S. K., Bhardwaj, A., Kumar, L., Singh, M. K., and Sundaram, S. (2020). Development of a Diatom-Based Photoluminescent Immunosensor for the Early Detection of Karnal Bunt Disease of Wheat Crop. *ACS OMEGA* 5 (14), 8251–8257. doi:10.1021/acsomega.0c00551

Peltomaa, R., Glahn-Martínez, B., Benito-Peña, E., and Moreno-Bondi, M. (2018). Optical Biosensors for Label-free Detection of Small Molecules. *Sensors* 18 (12), 4126. doi:10.3390/s18124126

Petzold, A., and Zollfrank, C. (2019). A Facile Route to Diatoms Decorated with Gold Nanoparticles and Their Optical Properties. *Bioinspired, Biomim. Nanobiomaterials* 8 (1), 81–85. doi:10.1680/jbibn.18.00003

Qin, T., Gutu, T., Jiao, J., Chang, C.-H., and Rorrer, G. L. (2008). Photoluminescence of Silica Nanostructures from Bioreactor Culture of Marine Diatom Nitzschia Frustulum. *J. Nanosci. Nanotechnol.* 8 (5), 2392–2398. doi:10.1166/jnn.2008.241

Rea, I., Terracciano, M., Chandrasekaran, S., Voelcker, N. H., Dardano, P., Martucci, N. M., et al. (2016). Bioengineered Silicon Diatoms: Adding Photonic Features to a Nanostructured Semiconductive Material for Biomolecular Sensing. *Nanoscale Res. Lett.* 11 (1), 405. doi:10.1186/s11671-016-1624-1

Ren, F., Campbell, J., Wang, X., Rorrer, G. L., and Wang, A. X. (2013). Enhancing Surface Plasmon Resonances of Metallic Nanoparticles by Diatom Biosilica. *Opt. Express* 21 (13), 15308. doi:10.1364/oe.21.015308

Rorrer, G., Jeffryes, C., Chang, C., Lee, D., Gutu, T., Jiao, J., et al. (2007). "Biological Fabrication of Nanostructured Silicon-Germanium Photonic Crystals Possessing Unique Photoluminescent and Electroluminescent Properties," in Proceedings of Spie the International Society for Optical Engineering, San Diego, CA. 6645, 66450A. doi:10.1117/12.735365

Uram, J. D., Ke, K., Hunt, A. J., and Mayer, M. (2006). Label-Free Affinity Assays by Rapid Detection of Immune Complexes in Submicrometer Pores. *Angew. Chem.* 118 (14), 2339–2343. doi:10.1002/ange.200502862

Uthappa, U. T., Kigga, M., Sriram, G., Ajeya, K. V., Jung, H.-Y., Neelgund, G. M., et al. (2019). Facile Green Synthetic Approach of Bio Inspired Polydopamine Coated Diatoms as a Drug Vehicle for Controlled Drug Release and Active Catalyst for Dye Degradation. *Microporous Mesoporous Mater.* 288, 109572. doi:10.1016/j.micromeso.2019.109572

Viji, S., Anbazhagi, M., Ponpandian, N., Mangalaraj, D., Jeyanthi, S., Santhanam, P., et al. (2014). Diatom-based Label-free Optical Biosensor for Biomolecules. *Appl. Biochem. Biotechnol.* 174 (3), 1166–1173. doi:10.1007/s12010-014-1040-x

Wang, Z., Xianyu, Y., Liu, W., Li, Y., Cai, Z., Fu, X., et al. (2019). Nanoparticles-Enabled Surface-Enhanced Imaging Ellipsometry for Amplified Biosensing. *Anal. Chem.* 91 (10), 6769–6774. doi:10.1021/acs.analchem.9b00846

Xie, Y. H., Wilson, W. L., Ross, F. M., Mucha, J. A., Fitzgerald, E. A., Macaulay, J. M., et al. (1992). Luminescence and Structural Study of Porous Silicon Films. *J. Appl. Phys.* 71 (5), 2403–2407. doi:10.1063/1.351097

Yang, H.-C., Liao, K.-J., Huang, H., Wu, Q.-Y., Wan, L.-S., and Xu, Z.-K. (2014). Mussel-inspired Modification of a Polymer Membrane for Ultra-high Water Permeability and Oil-In-Water Emulsion Separation. *J. Mat. Chem. A* 2 (26), 10225–10230. doi:10.1039/c4ta00143e

Zhen, L., Ford, N., Gale, D. K., Roesijadi, G., and Rorrer, G. L. (2016). Photoluminescence Detection of 2,4,6-trinitrotoluene (TNT) Binding on Diatom Frustule Biosilica Functionalized with an Anti-TNT Monoclonal Antibody Fragment. *Biosens. Bioelectron.* 79, 742–748. doi:10.1016/j.bios.2016.01.002

Conflict of Interest: The authors declare that the research was conducted in the absence of any commercial or financial relationships that could be construed as a potential conflict of interest.

frontiers | Frontiers in Bioengineering and Biotechnology

ORIGINAL RESEARCH
published: 17 June 2022
doi: 10.3389/fbioe.2022.887970

Liquid Crystal Modified Polylactic Acid Improves Cytocompatibility and M2 Polarization of Macrophages to Promote Osteogenesis

Zexiang Zheng[1†], *Renqin Wang*[2†], *Jianjun Lin*[1], *Jinhuan Tian*[1], *Changren Zhou*[1], *Na Li*[3]* and *Lihua Li*[1]*

[1]*Department of Materials Science and Engineering, Engineering Research Center of Artificial Organs and Materials, Jinan University, Guangzhou, China,* [2]*Affiliated Stomatology Hospital of Guangzhou Medical University, Guangzhou Key Laboratory of Basic and Applied Research of Oral Regenerative Medicine, Guangzhou, China,* [3]*Foshan Stomatology Hospital, School of Medicine, Foshan University, Foshan, China*

OPEN ACCESS

Edited by:
Yuangang Liu,
Huaqiao University, China

Reviewed by:
Kirtikumar B. Jadhav,
University of Vienna, Austria
Mingyan Zhao,
Affiliated Hospital of Guangdong Medical College Hospital, China

***Correspondence:**
Na Li
lina1102@fosu.edu.cn
Lihua Li
tlihuali@jnu.edu.cn

[†]*These authors have contributed equally to this work*

Specialty section:
This article was submitted to Biomaterials, a section of the journal Frontiers in Bioengineering and Biotechnology

Received: 02 March 2022
Accepted: 05 May 2022
Published: 17 June 2022

Citation:
Zheng Z, Wang R, Lin J, Tian J, Zhou C, Li N and Li L (2022) Liquid Crystal Modified Polylactic Acid Improves Cytocompatibility and M2 Polarization of Macrophages to Promote Osteogenesis. Front. Bioeng. Biotechnol. 10:887970. doi: 10.3389/fbioe.2022.887970

Liquid crystalline phases (LC phases) are widely present in an organism. The well-aligned domain and liquidity of the LC phases are necessary for various biological functions. How to stabilize the floating LC phases and maintain their superior biology is still under study. In addition, it is unclear whether the exogenous LC state can regulate the immune process and improve osteogenesis. In this work, a series of composite films (PLLA/LC) were prepared using cholesteryl oleyl carbonate (COC), cholesteryl pelargonate (CP), and polylactic acid (PLLA) via a controlled facile one-pot approach. The results showed that the thermo-responsive PLLA/LC films exhibited stable LC phases at human body temperature and the cytocompatibility of the composites was improved significantly after modification by the LC. In addition, the M2 polarization of macrophages (RAW264.7) was enhanced in PLLA/LC films, and the osteogenic differentiation of bone marrow mesenchymal stem cells (BMSCs) was improved as co-cultured with macrophages. The *in vivo* bone regeneration of the materials was verified by calvarial repair, in which the amount of new bone in the PLLA-30% LC group was greater than that in the PLLA group. This work revealed that the liquid crystal-modified PLLA could promote osteogenesis through immunomodulation.

Keywords: liquid crystal, polylactic acid, cytocompatibility, macrophages, bone regeneration

1 INTRODUCTION

Liquid crystal (LC) is a fluid with a micro-structure between an anisotropic crystal and an isotropic liquid, also known as a mesogenic or LC phase which has remarkable viscoelastic characteristics (Lowe and Abbott, 2012; Soon et al., 2013; Du et al., 2017; Chaudhuri et al., 2020). The LC phase exists in different organisms, such as in their bone (Giraud-Guille et al., 2000; Hulmes, 2002; Ghazanfari et al., 2016), chitin (Li et al., 2019; Liu et al., 2020), nucleic acids (Saurabh et al., 2017), lipids (Róg et al., 2009), and so on (Stewart, 2004; Rey, 2010; Hirst and Charras, 2017). Physiological activities such as mass transport, information transmission, cell recognition, and cell fusion and division cannot proceed smoothly without the LC phase of the cell films (Jewell, 2011; Gupta et al., 2015; Wu et al., 2017; Saw et al., 2018; Chen et al., 2020). Different LC elastomers have been studied and showed unique longitudinal and multi-responses for cell attachment, proliferation, and alignment (Prévôt and Hegmann, 2017). For example, LC collagen made by concentrated solution and aligned shearing was proved to possess good guidance for cell attachment and proliferation (Price et al., 2016; Tang et al., 2016). Cholesterol is an important component of cell films and has a large affinity for cells, so it has been widely studied and used in the biomimetic design of biomaterials (Li et al., 2001; Hwang et al., 2002; Chen et al., 2020). However, the mixing of cholesterol with other materials always causes spontaneous phase separation and leads to the rapid aggregation of cholesterol. This will result in high cholesterol concentration and cytotoxicity. Previous studies showed that cholesteryl ester ramification was a new class of bio-related materials with good thermal stability and low toxicity (Soon et al., 2009; Soon et al., 2014). In the literatures, cholesteryl ester ramification is usually applied solely to modify polymeric biomaterials to get higher cellular affinity (Li et al., 2001; Du et al., 2017). However, most biocompatible cholesteryl substances such as COC and CP with good blood compatibility are not in the LC state at the range of human physiological temperatures, which block the biological function of the LC phase in the human body (Li et al., 2001; Xie et al., 2020). According to the well-known van't Hoff equation, the transition temperature (clean point) of the composite liquid crystals is lower than that of each component. But in most of the cases, the measured clean point sits between that of each component (Tai and Lee, 1990). Hence, the clean point of the CP/COC mixture could be near 37°C by controlling their concentrations, because the clean point for CP and COC is 90 and 35°C, respectively.

PLLA has multiple distinguished features, including easy processing, good thermal stability, excellent mechanical and physical properties, and biodegradability in the human body of which degradation products have no side effects (Agrawal and Ray, 2001; da Silva et al., 2018; Dhandapani et al., 2020). Therefore, PLLA is approved by the FDA as the type III medical material and has been widely used in the field of medicine (Madhavan Nampoothiri et al., 2010; Yao et al., 2017; Wei and Dai, 2021). However, PLLA lacks active functional groups for cell adhesion, spreading, and proliferation, which leads to unsatisfactory cytocompatibility. In addition, the acidic degradation products will cause inflammation and then hinder the regeneration of tissues when the PLLA is used as bone repair material (Bergsma et al., 1993; Critchley et al., 2020).

It is well known that bone repair is, in fact, involved in the process of immune regulation (Schlundt et al., 2015; Chen et al., 2016; Lee et al., 2019). Macrophages are one of the cells that play important roles in regulating the inflammatory response (Browne and Pandit, 2015), which can be polarized into pro-inflammatory M1 macrophages or anti-inflammatory M2 macrophages under the stimulation of the inflammatory environment (Freytes et al., 2013; Spiller et al., 2015; Zhang et al., 2017; Huang et al., 2020; Mahon et al., 2020; Qiu et al., 2020). Once the biomaterials are implanted into the body, a series of inflammatory responses will be activated. To date, researchers have been trying to improve cell compatibility and immunogenicity of PLLA through bulk or surface modification, to introduce specific biological functional ligands (Lutolf and Hubbell, 2005; Liu et al., 2017; Pellegrino et al., 2017; Liu et al., 2019) or biologically active molecules (Ding et al., 2016; Li X et al., 2021).

In view of the good biocompatibility and suitable LC state temperature of CP and COC, PLLA was modified by blending the LC state to enhance its functionality, and to study the immunoregularity of the composite materials for bone regeneration. Since CP, COC, and PLLA are easily dissolved in organic reagents and form uniform composite by solution casting, a series of functional PLLA/LC films were obtained by a one-pot but controlled blending approach. We expected that the bionic liquid crystal composite materials would better simulate the microenvironment of tissue culture *in vivo*, including the compatibility of PLLA materials and regulation of inflammatory response for tissue regeneration. Many exciting anti-inflammatory results of the liquid crystal materials were observed in our preliminary experiments.

2 MATERIALS AND METHODS

2.1 Materials

Polylactic acid (PLLA, Mw = 200000, PDI = 1.5, CAS: 33135-50-1) was provided by Jinan Daigang Biomaterials Co., Ltd. Cholesteryl oleyl carbonate (COC, CAS: 17110-51-9) was purchased from Tokyo Chemical Industry. Cholesteryl pelargonat (CP, CAS: 1182-66-7) was purchased from Sigma-Aldrich. Dulbecco's Modified Eagle Medium (DMEM), fetal bovine serum (FBS), and penicillin–streptomycin solution were purchased from Gibco BRL. The Cell Counting Kit-8 (CCK-8) was purchased from Dojindo Molecular Technologies Inc. The AO-EB Double Staining Kit was purchased from Beijing Solarbio Science and Technology Co., Ltd. Rhodamine phalloidin and 4′, 6-dimidyl-2-phenylindole (DAP, CAS:28718-90-3) were purchased from Molecular Probes, United States. Osteoblastic induction medium and Alizarin Red solution were purchased from Cyagen Biosciences Inc. Fluorescein isothiocyanate conjugated anti-mouse CD206 (FITC-CD206) and Allophycocyanin conjugated anti-mouse CD80 (APC-CD80) were purchased from Dakewe Biotech Co., Ltd. The BCIP/NBT alkaline phosphatase color reagent kit was purchased from Beyotime Biotechnology Co., Ltd. ALP and the BCA protein assay kit was purchased from Nanjing Jiancheng Bioengineering Institute. All cells were obtained from the American Type Culture Collection (ATCC). All other reagents were purchased from Guangzhou Reagent Co., Ltd., analytical grade.

2.2 Preparation of COC/CP Composite LC

A series of COC/CP composite liquid-crystal were prepared by the melting method. In brief, a certain amount of COC and CP was added into a 5 ml centrifuge tube at room temperature. The tube was transferred to an oven at 90 °C. The liquid COC and CP were then mixed by stirring. The COC weight fraction in the composite LC was 0–100% with a gradient of 10%.

2.3 Preparation of PLLA/LC Composite Film

Three different PLLA/LC composite films were prepared by the solution casting method. According to our previous work (Li N et al., 2021), PLLA and LC (70%COC-30%CP) were stirred in dichloromethane at room temperature for 6 h to produce a clear and uniform PLLA/LC solution. The solution was then cast on a clean Teflon plate and the solvent was evaporated in a clean environment for 48 h. Then the film was placed in a vacuum oven for 12 h to remove the residual solvent. The weight fractions of the LC in the composite films were 10%, 30%, and 50%, which were labeled as PLLA-10% LC, PLLA-30% LC, and PLLA-50% LC, respectively. The thickness of the film and the aggregation state of the LC in the composite film could be controlled by the properties of the solvent, the concentration of the solution, and the temperature.

2.4 Thermal Analysis

A differential scanning calorimeter (DSC) (TA, Netzsch, Germany) was used to measure the clean point and the liquid-crystal phase transition temperature of COC/CP LC and PLLA/LC composite films. The heating and cooling rate was 10°C min^{-1} while the scanning ranges were −20–100°C and 0–200°C for COC/CP LC and PLLA/LC, respectively. The secondary temperature rise curve was taken for analysis.

The LC phase texture of the COC/CP LC and PLLA/LC composite film was observed by using polar optical microscope (POM, OLYMPUS, Japan). The slide was placed on the hot platform, a small amount of sample was placed on the slide, and the cover glass was pressed. The heating and cooling rates were set as 10°C·min^{-1} by a heating and cooling program.

2.5 Cytocompatibility Analysis

2.5.1 Cell Culture

In this experiment, mouse pre-osteoblasts (MC3T3-E1) were selected as seeded cells to evaluate the cytocompatibility of the materials *in vitro*. The cell culture medium was a complete medium containing 10% fetal bovine serum, 1% antibiotics, and 89% DMEM. The cells were cultured in a T25 culture flask in a CO_2 incubator at 37°C, 5% CO_2 concentration, and 95% relative humidity. The cell culture medium was replaced every other day.

The LC-10% CP, LC-30% CP, LC-50% CP, PLLA, PLLA-10% LC, PLLA-30% LC, and PLLA-50% LC composite films were immersed in 75% ethanol for 1 h and sterilized under UV for 2 h. The cells were seeded on different films at a density of 1×10^4 cells·well^{-1} in three parallel samples per group after sterilizing.

2.5.2 Cell Activity and Toxicity Analysis

A CCK-8 kit was used to evaluate MC3T3-E1 cell activity at 1, 3, 5, and 7 days, the medium in the wells was aspirated and the cells were washed once with PBS. A CCK-8 reaction solution was used right after it was prepared from the CCK-8 solution and fresh complete medium at a volume ratio of 1:10. A total of 500 μL reaction liquid was added to the 24-well plate and placed in a CO2 incubator and incubated in the dark for 2 h. From each sample well, 100 μL of the reaction solution was aspirated into a 96-well plate. The OD value of each well was measured by enzyme-linked immunoassay at $\lambda_{\max} = 450$ nm.

The cells were stained with AO-EB solution to evaluate the toxicity of the material. At 1 and 3 days, the cells were washed twice with PBS, followed by AO-EB staining (AO: EB: PBS = 1: 1: 100) for 5 min at 37°C. After staining, the cells were washed again with PBS and observed under a fluorescent microscope. Living cells were stained green by acridine orange (AO) and dead cells were stained red by ethidium bromide (EB).

2.5.3 Cell Morphology and Microstructure

When the cells were cultured on the material for 3 days, the medium in the well was aspirated, the cells were washed twice with PBS, and a 4% paraformaldehyde solution was added to fix the cells for 30 min. Then, the materials were soaked in a series of gradient concentration ethanol solutions (volume ratio: 50%, 60%, 70%, 80%, 90%, 95%, 100%) for 15 min. The samples were air-dried at room temperature and sprayed with gold, and then were observed and photographed under SEM (ULTRA55, Carl Zeiss Jena Ltd, German) with 5 kV acceleration voltage under a scanning electron microscope.

The samples were washed with PBS and fixed with 4% paraformaldehyde for 20 min. Then they were washed with PBS three times and permeabilized with 0.1% Triton X-100 for 5 min. The cells were blocked by adding 3% BCA solution for 30 min, washed three times with PBS, and incubated with rhodamine phalloidin for 1 h. They were washed twice with PBS after incubating with DAPI for 15 min at room temperature. Cytoskeleton analysis was then performed following the steps described previously.

2.5.4 Cell Migration Experiment

LC-30% CP was coated on 50% of the 14-mm diameter cell slide. The samples were then placed in a confocal Petri dish and sterilized by UV for 3 h. The cells were seeded on the materials at a density of 5×10^3 cells·well^{-1} in three parallel samples per group on 24-well culture plates.

The films were transferred into 24-well plates with a 600 μL culture medium. With transwell chambers (pore size = 8 μm), 100 μL of cell suspension was added to each sample with 5×10^3 cells. The cells were stained with crystal violet after culturing for 24 and 72 h. Then the chambers were observed under a microscope and pictures were taken, and randomly selected three visual fields under the appropriate magnification microscope to observe the cell number and count. The stained cells on the chambers after 72 h were decolorized with 33% acetic acid. The decolorization solution was transferred into a 96-well plate with 100 μL per well. The OD values were measured at 570 nm.

2.6 Osteogenic Immunomodulation

2.6.1 Polarization of Macrophages

A mouse macrophage cell, RAW264.7, was selected in this experiment. The cells were seeded into 24-well plates with

TABLE 1 | Osteogenic primer sequences for RT-PCR.

Gene	Forward sequence (5′-3′)	Reverse sequence (3′-5′)
GAPDH	GGCCTCCAAGGAGTAAGAAA	GCCCCTCCTGTTATTATGG
OCN	AGGGCAATAAGGTAGTGAA	CGTAGATGCGTCTGTAGGC
COL-I	CTTCACCTACAGCACCCTTGT	AAGGGAGCCACATCGATGAT
OPN	ACCATTCGGATGAGTCTGAT	TCAGTCCATAAGCCAAGCTA
Runx-2	TGCCCAGTGAGTAACAGAAAGAC	CTCCTCCCTTCTCAACCTCTAA

different prepared films at a density of 1×10^4 cells·well^{-1}. The cells were collected after culturing for 24 and 48 h. After adding FITC-CD206 and APC-CD80 (FITC-CD206:APC-CD80: PBS = 1:1:100), the cells were incubated for 30 min at 4°C in the dark. The polarization of RAW264.7 was analyzed by using an analytical flow cytometer (BD FACSCanto, America).

2.6.2 Alkaline Phosphatase (ALP) Staining and Quantitative Analysis

RAW264.7 and bone marrow mesenchymal stem cells (BMSCs) were co-cultured with an osteoblastic induction medium in this experiment. A total of 600 μL of BMSCs was seeded into 24-well plates with different prepared films at a density of 1×10^4 cells·well^{-1}. The transwell chambers (pore size = 0.4 μm) were put into plates. A total of 100 μL of RAW264.7 suspension was added to each chamber at a density of 1×10^4 cells·well^{-1}. The plates were put into the incubator and culture for 2 days, and then the chambers were taken out. After 7 days of culture, the BMSCs were stained with a BCIP/NBT alkaline phosphatase color reagent kit. After 7 and 14 days of culture, an alkaline phosphatase kit and BCA protein kit were used to detect the alkaline phosphatase activity of the BMSCs.

2.6.3 Alizarin Red Staining and Quantitative Analysis

RAW264.7 and bone marrow mesenchymal stem cells (BMSCs) were co-cultured with an osteoblastic induction medium following the procedure 2.6.2. After 21 days of incubation, the samples were washed with PBS and fixed with 4% paraformaldehyde for 20 min. After washing with PBS three times, the samples were stained with Alizarin Red solution and observed under an optical microscope. After imaging, 500 μL of 10% hexadecylpyridinium chloride monohydrate was added to each well. After 30 min, 100 μL of the reaction solution from each well was aspirated into a 96-well plate. The OD value of each well was measured by an enzyme-linked immunoassay at λmax = 540 nm. The control group in **Figures 5**, **6** means that the cells were growing on the 24-well plates.

2.6.4 Polymerase Chain Reaction CR Analysis

RAW264.7 and bone marrow mesenchymal stem cells (BMSCs) were co-cultured with an osteoblastic induction medium using the procedures presented in 2.6.2. After 7 and 14 days of culture, the cells were collected. The gene expression of the osteogenic related genes OCN, COL-1, OPN, and Runx-2 of the BMSCs cultured on different films were detected by RT-PCR technology, using β-actin as an internal control. The PCR primer series is shown in **Table 1**.

2.7 Rat Skull Defect Repair Experiment

Female Sprague–Dawley (SD) rats were selected to construct a skull defect model as control, PLLA, and PLLA-30% LC groups. Each group had three rats with a weight of 220–280 g. All the rats were purchased from the Experimental Animal Center of Southern Medical University. The rats were anesthetized with 1% pentobarbital sodium (30 mg/kg). After anesthetizing, the heads of the rats were disinfected with 75% alcohol and iodophor. A 2.5-cm incision was made vertically in the center of the rat's head. A 5-mm diameter ring drill was used to make a 5-mm hole on both sides of the center of the parietal bone with full thickness. PLLA-30% LC films were filled into the bone defect. The periosteum, subcutaneous tissue, and skin were then sutured in layers. After 4 weeks, the rats were sacrificed by cervical dislocation. The collected skulls were fixed with 4% paraformaldehyde for subsequent micro-CT detection and H&E staining.

2.8 Statistic Analysis

All results are reported as mean ± standard deviation and statistically analyzed using Graphpad Prism 7.0 software. At least three parallel samples (n = 3) of each group were used for all experiments. This value is considered statistically significant only when $p < 0.05$.

3 RESULT AND DISCUSSION

3.1 Thermal Properties of COC/CP Liquid-Crystal and PLLA/LC Composite Films

According to DSC thermal analysis, no LC phase was detected in pure COC or CP (**Figure 1A**) at 37°C. However, by blending COC and CP, the cholesteric ester LC phase was obtained at 37°C (**Figure 1A**). It was worth mentioning that the mixture (LC-30% CP) indicated good stability and 37°C was the middle point of the phase transition temperature range. The liquid-crystal phase transition temperature of the COC/CP liquid-crystal measured by DSC matched the measurement in POM. At 37°C, an obvious LC phase flow could be seen (**Figure 1C**). With the increase in the CP concentration, the liquid-crystal phase transition temperature of COC/CP also increased. The LC phase transition temperature became higher than 37°C when the CP concentration exceeded 50%. The increase in

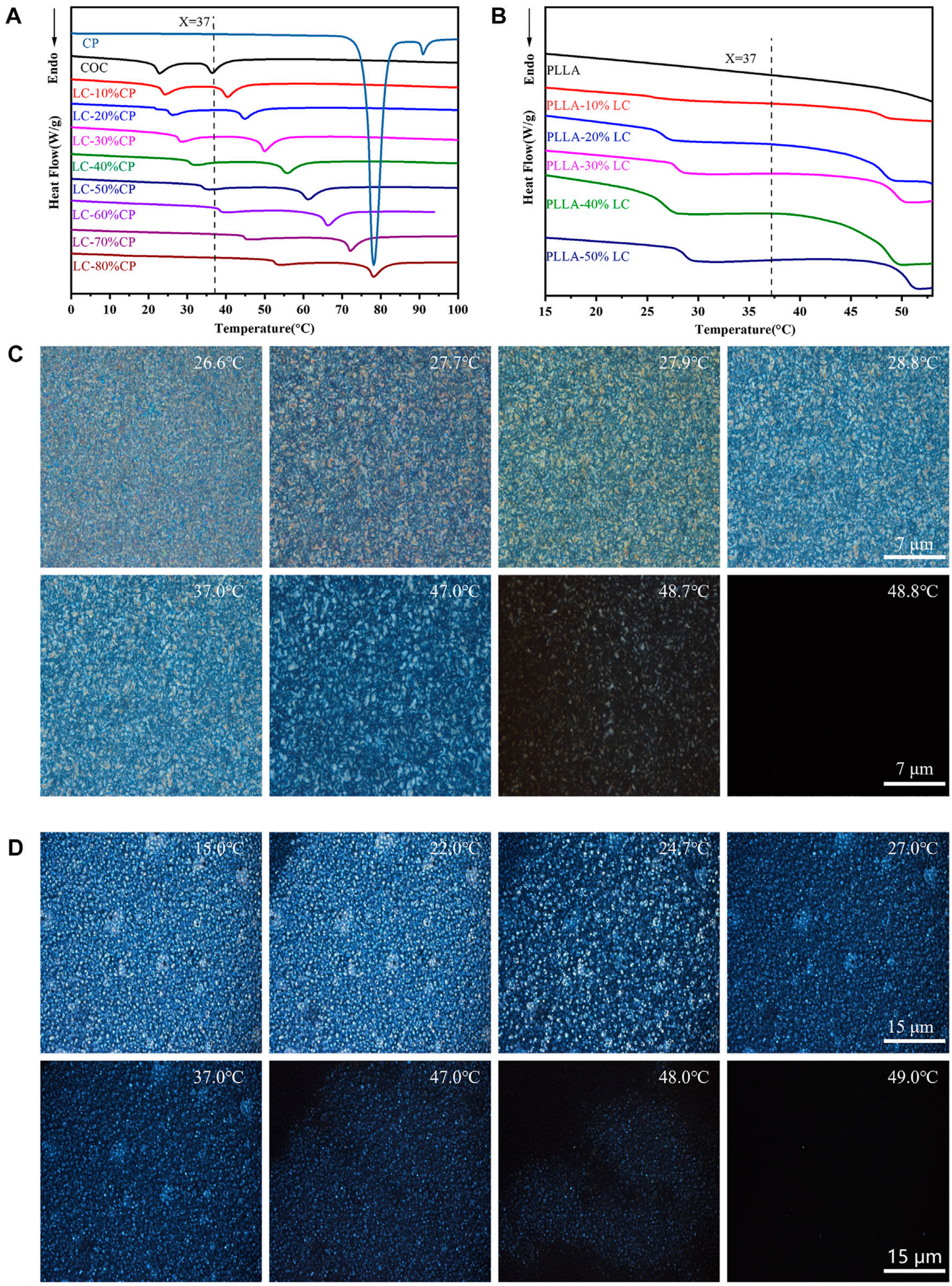

FIGURE 1 | Thermal properties of the composite LC. **(A)** DSC curve of COC/CP LC; **(B)** DSC curve of PLLA/LC composite films; **(C)** blended LC LC-30% CP LC texture observed under POM; and **(D)** LC texture of the PLLA-30% LC composite films observed under POM.

the LC phase transition temperature of the blend is because the increase in CP (decrease of molecular dimensions) caused the increase in the phase-transition temperature of the COC/CP binary system (Li N et al., 2021). The clearing point of the mixed LC followed the empirical formula (Tai and Lee, 1990):

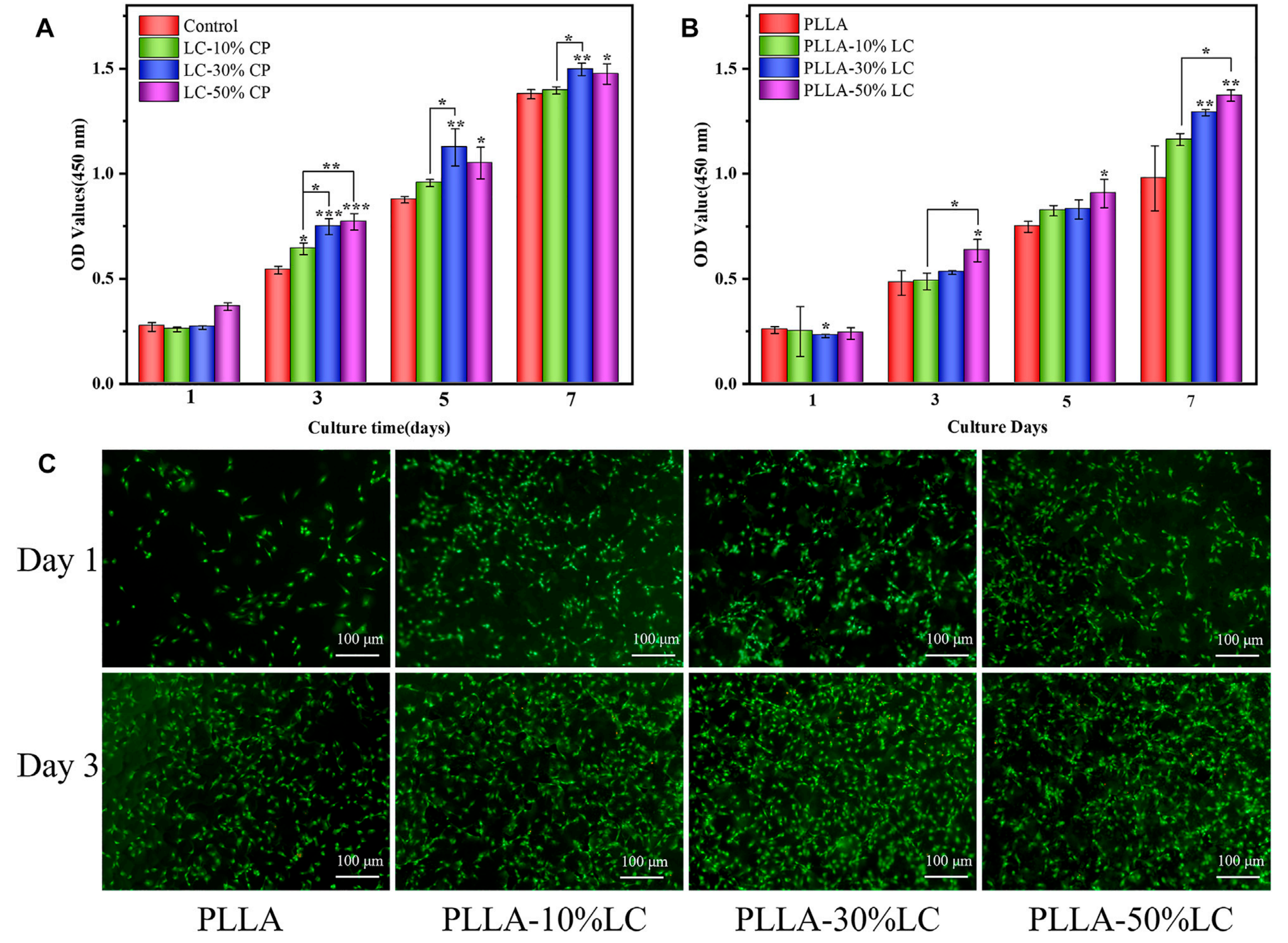

FIGURE 2 | (A) Cell proliferation in COC/CP LC and **(B)** PLLA-LC composites for 7 days * refer to statistically significant proliferation $p < 0.05$. **(C)** AO-EB staining of MC3T3-E1 cells seeded on pure PLLA, PLLA-10% LC, PLLA-30% LC, and PLLA-50% LC films.

$$\frac{1}{T_i} = \frac{W_{cp}}{T_{cp}} + \frac{W_{coc}}{T_{coc}}, \tag{1}$$

T_i is the clear point of the mixture, W_{cp} is the weight fraction of CP in the mixture, T_{cp} is the clearness of CP, W_{coc} is the weight fraction of COC in the mixture, and T_{coc} is the clearness of COC in the formula.

By adding COC/CP LC, an LC phase could be formed within PLLA. The LC phase was uniformly distributed in the composite film at 37°C (**Figure 1B, D**). This liquid crystal phase domain could promote the transport of materials and the transmission of signals. It also enabled the response to external temperature stimuli which successfully simulated the flow mosaic model of biofilms (Wu et al., 2017; Chen et al., 2020).

3.2 Cell Viability

CCK-8 and live/dead assays were carried out to evaluate the cytocompatibility of the LC materials using MC3T3-E1. Compared with the control group, COC/CP LC had better cytocompatibility while LC-30% CP showed the best compatibility (**Figure 2A**). This was also why LC-30% CP was chosen to modify PLLA in subsequent studies. The MC3T3-E1 cell proliferation rate was significantly higher than the controlled group when the concentration of LC in the PLLA/LC composite film was 30% (wt) and 50% (wt) (**Figure 2B**). The cell density on the PLLA/LC composite films was greater than that on the PLLA film (**Figure 2C**) indicating that the LC materials were non-cytotoxic, and the addition of the LC facilitated cell proliferation. This was because many life processes associated with cell proliferation such as mass transport, information transmission, cell recognition, and cell fusion and division can proceed smoothly because of the flowing LC state (Wu et al., 2017; Saw et al., 2018; Chen et al., 2020).

3.3 Cell Morphology

Compared with pure PLLA, MC3T3-E1 cells could adhere tighter to the PLLA/LC composite films and yield more ECM which was confirmed by SEM (**Figure 3A**). The cells connected to each other through ECM suggesting that cells showed better viability on the surface of PLLA/LC composite films. From the laser confocal microscope (CLSM) photo

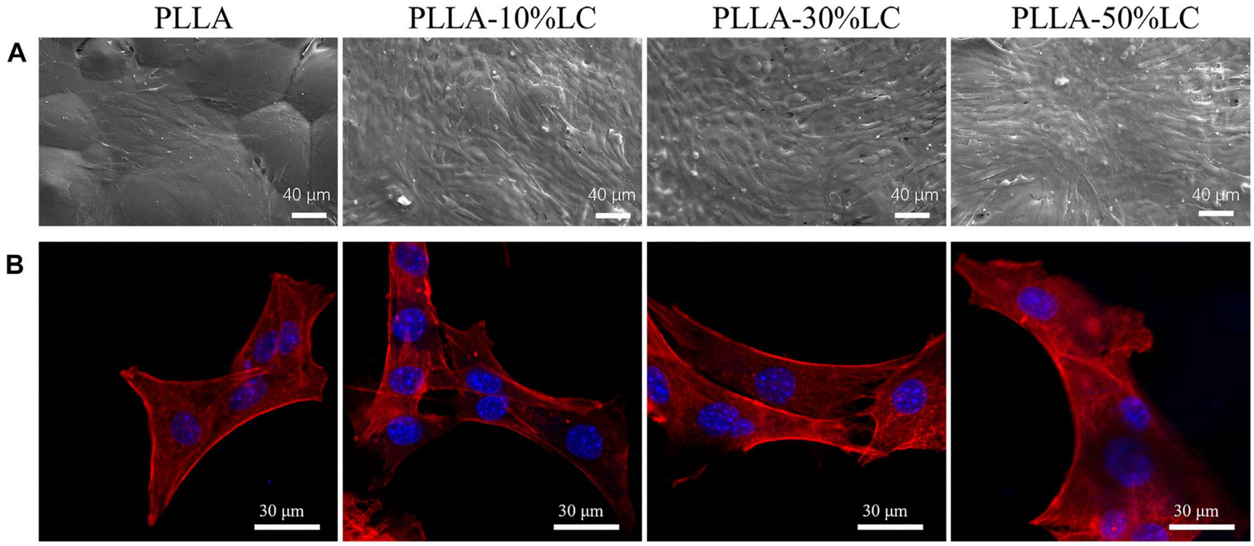

FIGURE 3 | (A)SEM images of morphologies of MC3T3-E1 cells culturing on pure PLLA, PLLA-10% LC, PLLA-30% LC, and PLLA-50% LC films for 3 days; **(B)** CLSM images of morphologies of MC3T3-E1 cell culturing on pure PLLA, PLLA-10% LC, PLLA-30% LC, and PLLA-50% LC films for 1 day.

(**Figure 3B**), compared with pure PLLA, MC3T3-E1 cells fully covered the surface of PLLA/LC composite films with well-extended actin fiber bundles and filamentous pseudopods. Moreover, the nucleus structure was complete, and the cytoplasm was stained uniformly. Some cells were in contact with each other, reflecting an irregular or polygonal shape. We speculated that it was the LC environment that helped the cell to guide and guided the flow and order of the LC to guide the extension of the cell's pseudopods. According to SEM and CLSM, MC3T3-E1 cells exhibited better early adhesion and growth on the surface of PLLA/LC than pure PLLA. This observation implied that the cholesteric LC in the PLLA matrix can still exert its bioactive effect. It was further confirmed that LC concentrations of 30% (wt) and 50% (wt) improved cell adhesion of PLLA.

3.4 Cell Migration

The cell migration experiment (**Figure 4A–C**) showed that MC3T3-E1 cells had a higher migration rate in PLLA/LC than in the cell slide and pure PLLA. Especially in the PLLA/LC (30% wt) composite film, the numbers and spreading effect of MC3T3-E1 cells were much higher than pure PLLA at 24 and 72 h. This confirmed that COC/CP cholesterol esters could significantly increase the cell affinity of PLLA.

From the POM images, the boundary between the liquid crystal and the non-liquid crystal area (the black part in the picture) was obvious. **Figure 4D** indicates that the cells were likely to spread out within the liquid crystal domains rather than the glass matrix. The cell density of different areas was different, and there were obvious boundaries (**Figure 4D**). This boundary just coincided with the distribution boundary of the cells, which may be due to the LC phase domains of the LC mimicking the movable morphology of the natural biomembrane surface which probably provided active sites for cell attachment to the substrate and then promote cell adhesion.

3.5 Osteogenic Immunomodulation

The results of the macrophage polarization experiment (**Figure 5**) indicated that the macrophages highly expressed CD80 which is mainly pro-inflammatory M1 macrophages after being cultured for 24 h on both PLLA and PLLA/LC films. However, the expression of CD206 of macrophages was increased with the increase of LC-30% CP content after being cultured 48 h with PLLA-30% LC and PLLA-50% LC films. This indicated that the PLLA/LC films can significantly promote M2 polarization of RAW264.7 while the liquid crystal content reaches a certain height. It is worth mentioning that the biological effect caused by LC domains could reduce the inflammatory response of the material implanted in the organism during bone tissue repair, which was beneficial to the reparation of bone tissue (Schlundt et al., 2015; Chen et al., 2016; Lee et al., 2019).

Bone tissue repair involved a series of complicated dynamic immune regulatory processes. To simulate the microenvironment of bone tissue repair in the living body more realistically, the macrophages were co-cultured with BMSCs to observe the osteogenic differentiation of BMSCs under a corresponding immune condition environment. ALP is a specific protein secreted in the early stage of osteogenic differentiation. The ALP staining results (**Figure 6E**) showed that PLLA-10% LC and PLLA-30% LC composite films could significantly promote the ALP expression of BMSCs compared with PLLA on the 7th day, which was consistent with the result of the ALP quantitative analysis (**Figure 6A**). However, the ALP expression of BMSCs cultured in PLLA-50% LC composite films was lower than that of PLLA whether it was

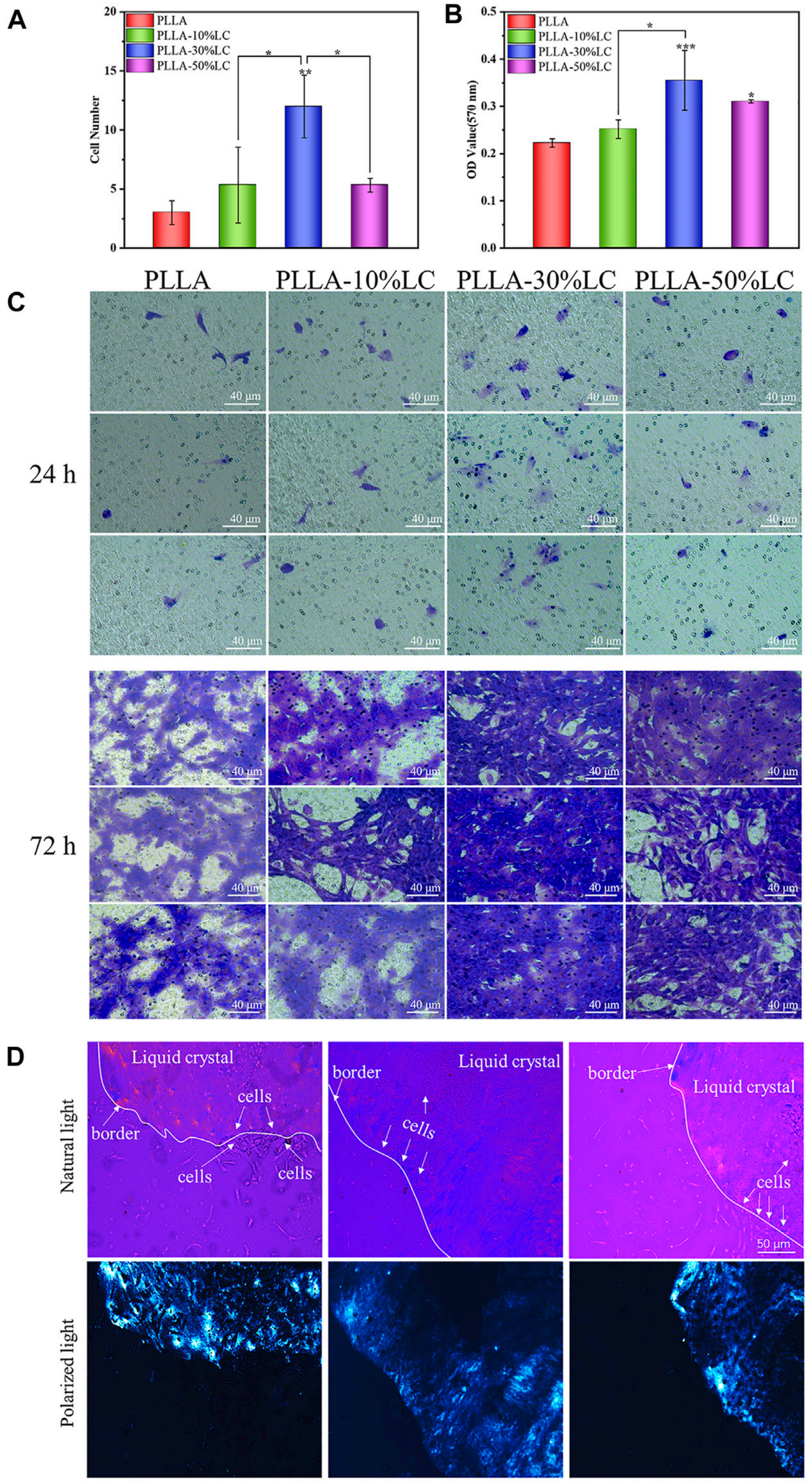

FIGURE 4 | (A) Cell count of osteoblasts migrating in the transwell chamber for 24 h; **(B)** quantitative analysis of osteoblasts migrating in the transwell chamber for 72 h; **(C)** crystal violet staining of osteoblasts migrating in the transwell chamber for 24 and 72 h; and **(D)** distribution of cells on LC-30% CP.

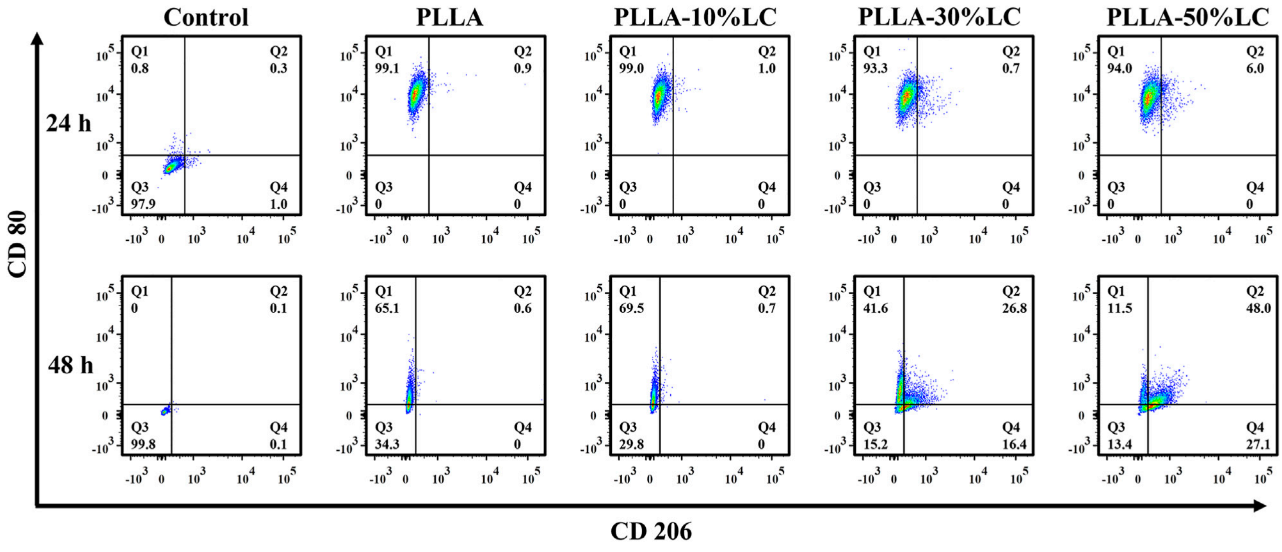

FIGURE 5 | Polarization of macrophages on the material.

on the 7th or 14th day, which also indicated that the liquid crystal proportion would not linearly generate PLLA/LC composite films to promote the osteogenic differentiation of BMSCs.

In the late stage of osteogenic differentiation, BMSCs deposit calcium and phosphate salts forming calcium nodules. Calcium nodules could be used to evaluate the degree of osteogenic differentiation of BMSCs, for they can chelate with Alizarin Red and form red insoluble. Quantitative analysis of calcium nodules was usually used to evaluate the late stage of osteogenic differentiation of BMSCs, since it was considered a benchmark to evaluate the bone induction ability of materials. It could be seen from **Figure 6F** that the calcium nodules on the PLLA-50% LC group were similar to the PLLA group, and the calcium nodules were lighter in red which indicated that the number of calcium nodules on the surface was smaller. The calcium nodules in PLLA-10% LC and PLLA-30% LC groups were significantly darker than those in the PLLA group, which indicated that the number of calcium nodules was significantly higher in PLLA-10% LC and PLLA-30% LC groups. Similarly, the quantitative analysis of calcium nodules (**Figure 6B**) showed that the OD values of PLLA-10% LC and PLLA-30% LC groups were higher than those in the PLLA and PLLA-50% LC groups. The OD value of the PLLA-10% LC group was basically the same as that of the PLLA-30% LC group. The result of the calcium nodule quantitative analysis further proved that the bone formation performance of PLLA-10% LC and PLLA-30% LC groups was significantly better than in the other groups.

The PCR results (**Figure 6C, D**) showed that on the 7th day, the expression of Runx-2 of BMSCs cultured in the PLLA-30% LC film was significantly higher than that of PLLA. On the 14th day, the expression of OCN of BMSCs in PLLA-30% LC films was significantly higher than in PLLA. Runx-2 is a sign of the beginning of osteogenic differentiation of cells, and OCN is a sign of osteogenic differentiation and maturation of cells (Schroeder et al., 2005; Chen et al., 2016). These results further showed that PLLA-30% LC films could better enhance the osteogenic differentiation of cells than PLLA.

3.6 Calvarial Repair *In Vivo*

According to the micro-CT analysis (**Figure 7C**), only a small amount of bone tissue was found at the edge of the defect area in the sham surgery group 4 weeks after surgery. This indicated that SD rats could not repair large-scale calvarial defects without other treatments in 4 weeks. Compared with the sham surgery (control) group, a small amount of new bone tissue could be seen in the PLLA group. This was because PLLA could promote cell proliferation and osteogenic differentiation at a certain level, but its bone repair ability was still weak. Compared with the control and PLLA groups, the PLLA-30% LC (experimental) group demonstrated excellent bone repair ability, with a large amount of new bone tissue generated in the defect area. The data on bone volume (**Figure 7A**) and bone volume density (**Figure 7B**) also showed that the bone repair effect of PLLA-30% LC was better than that of the other two groups. Subsequently, the H&E staining analysis (**Figure 7D**) 4 weeks after surgery showed that a large amount of new bone tissue was formed in the PLLA-30% LC group and a small amount of lamellar bone and woven bone was obvious in the PLLA group. However, the defect area was almost full of fibrous connective tissue, and no obvious new bone tissue formation was found in the control group. This may be when PLLA was modified with LC-30% CP liquid crystal, a liquid crystal layer could be formed on the surface of PLLA. The cholesteric group in the liquid crystal had biological

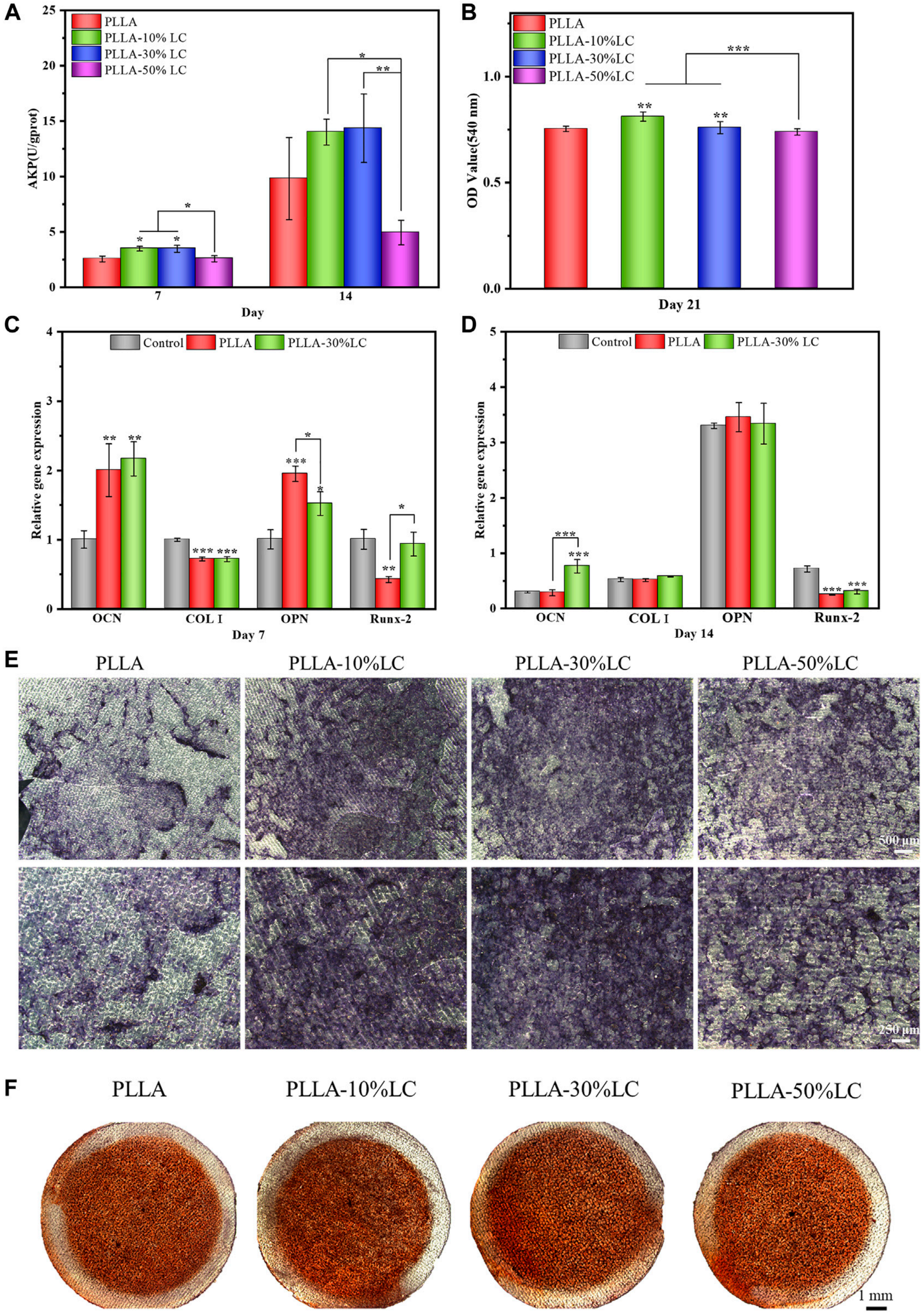

FIGURE 6 | (A) ALP quantitative analysis; **(B)** Alizarin Red staining quantitative analysis; **(C)** and **(D)** BMSC-related osteogenic gene expression on different materials; **(E)** ALP staining; and **(F)** Alizarin Red dyeing.

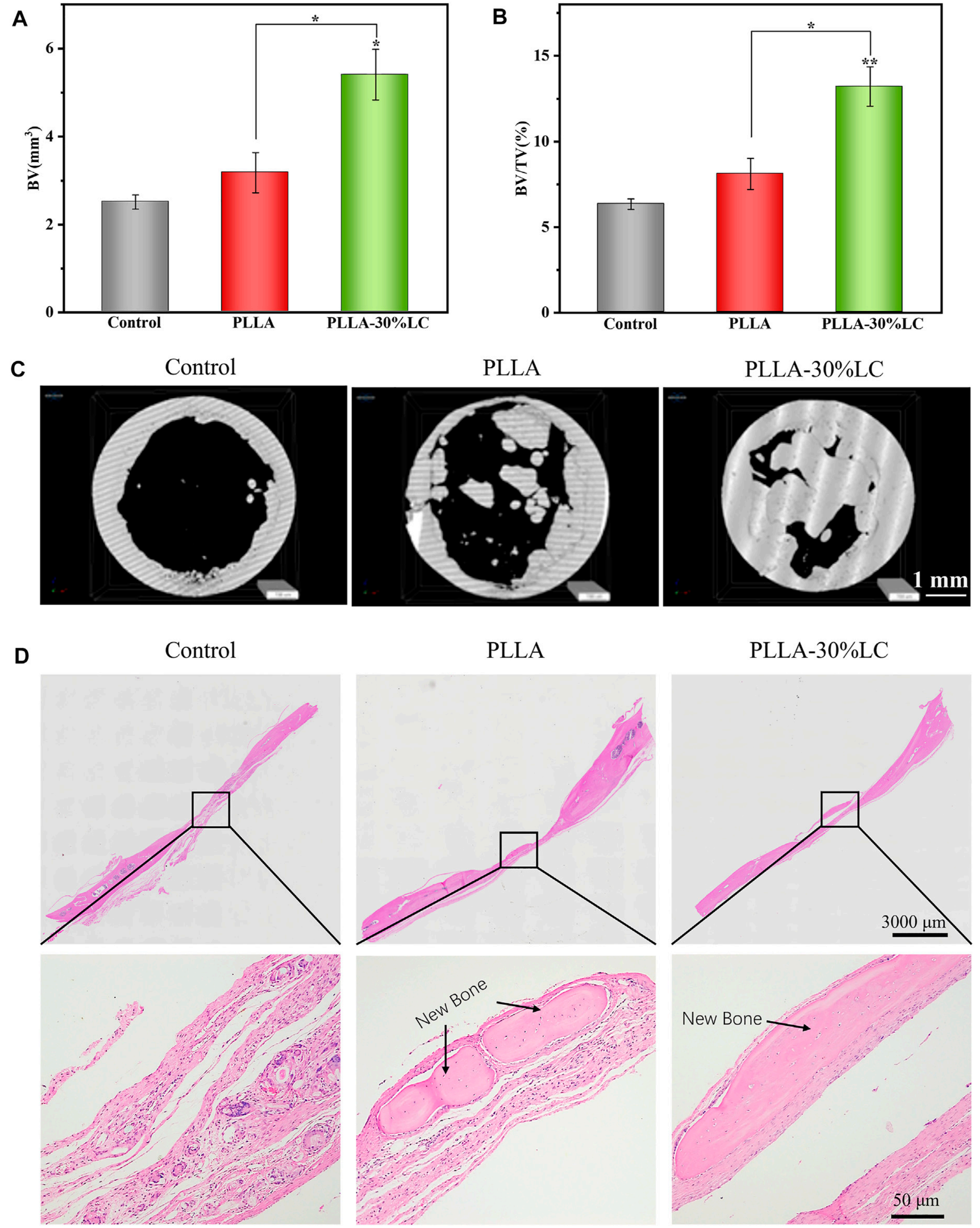

FIGURE 7 | (A) Bone volume analysis; **(B)** bone volume density analysis; **(C)** micro-CT image of an SD rat skull defect 4 weeks after operation; and **(D)** HE staining photograph of an SD rat skull defect.

activity and could promote cell adhesion, proliferation, and osteogenic differentiation, and remarkably improved the cell compatibility of the material. At the same time, it also improved the immunogenicity of PLLA via enhancing the M2 polarization of RAW264.7 which benefited the bone tissue regeneration *in vivo*. In addition, the LC layer was in the LC state at 37°C and could respond to changes in the external temperature, which may be conducive to the transportation of nutrients and the conduction of information *in vivo*. The special surface characteristics of liquid crystal were similar to the structure and function of the extracellular matrix, and more similar to the microenvironment of tissue culture *in vivo*.

4 CONCLUSION

This study showed that the LC phase domain distribution was uniform in the PLLA/LC composite films and the films were in the LC state at a physiological temperature. The LC phase in the PLLA/LC composite films was similar to the flow mosaic model of biological films with the property of flow and order that was conducive to material transportation and signal transmission and could respond to temperature stimuli sensitively. Cytocompatibility experiments showed that COC/CP LCs were beneficial to improve the cytocompatibility of PLLA. When the LC concentration was 30% (wt) and 50% (wt), the PLLA/LC composite films could significantly promote proliferation and adhesion. Compared with other methods of modifying the cell compatibility of PLLA, COC/CP LCs could functionalize the surface of PLLA without providing any specific biological functional ligands, thereby providing affinity for cell attachment. In addition, osteogenic immunomodulation experiments showed that the PLLA/LC composite films promoted the M2 polarization of RAW264.7, improved the inflammatory environment of implants, and promoted the osteogenic differentiation of BMSCs which were beneficial to the repair of bone tissue *in vivo*. Moreover, the PLLA/LC composite films were simpler to prepare, lower in cost, and easier to popularize. Therefore, this novel of LC modified biomaterials is very promising to be used in clinical bone defect treatment in the future.

DATA AVAILABILITY STATEMENT

The original contributions presented in the study are included in the article/supplementary material, further inquiries can be directed to the corresponding authors.

ETHICS STATEMENT

Ethical review and approval was not required for the animal study because Experimental Animal Ethics Committee, Southern Medical University.

AUTHOR CONTRIBUTIONS

ZZ: preparation, methodology, and writing—original draft. RW: software, methodology, data curation and validation. JL: methodology, data curation, software and preparation. NL: conceptualization, methodology, writing—reviewing and editing, and funding acquisition. JT: supervision, methodology software and validation. LL: conceptualization, resources, writing—reviewing and funding acquisition. CZ: conceptualization, reviewing, supervision and methodology.

FUNDING

This work was supported by the National Key Research and Development Project (2019YFD0901905); National Natural Science Foundation of China (32101061); Basic and Applied Basic Research Foundation of Guangdong Province (2019A1515110013); and Medical Scientific Research Foundation of Guangdong Province (A2021148).

REFERENCES

Agrawal, C. M., and Ray, R. B. (2001). Biodegradable Polymeric Scaffolds for Musculoskeletal Tissue Engineering. *J. Biomed. Mat. Res.* 55, 141–150. doi:10.1002/1097-4636(200105)55:2<141::aid-jbm1000>3.0.co;2-j

Bergsma, E. J., Rozema, F. R., Bos, R. R. M., and Bruijn, W. C. D. (1993). Foreign Body Reactions to Resorbable Poly(l-Lactide) Bone Plates and Screws Used for the Fixation of Unstable Zygomatic Fractures. *J. Oral Maxillofac. Surg.* 51, 666–670. doi:10.1016/S0278-2391(10)80267-8

Browne, S., and Pandit, A. (2015). Biomaterial-mediated Modification of the Local Inflammatory Environment. *Front. Bioeng. Biotechnol.* 3, 67. doi:10.3389/fbioe.2015.00067

Chaudhuri, O., Cooper-White, J., Janmey, P. A., Mooney, D. J., and Shenoy, V. B. (2020). Effects of Extracellular Matrix Viscoelasticity on Cellular Behaviour. *Nature* 584, 535–546. doi:10.1038/s41586-020-2612-2

Chen, Z., Klein, T., Murray, R. Z., Crawford, R., Chang, J., Wu, C., et al. (2016). Osteoimmunomodulation for the Development of Advanced Bone Biomaterials. *Mater. Today* 19, 304–321. doi:10.1016/j.mattod.2015.11.004

Chen, J., Yang, Y., Wu, J., Rui, X., Wang, W., Ren, R., et al. (2020). Spatiotemporal Variations of Contact Stress between Liquid-Crystal Films and Fibroblasts Guide Cell Fate and Skin Regeneration. *Colloids Surfaces B Biointerfaces* 188, 110745. doi:10.1016/j.colsurfb.2019.110745

Critchley, S., Sheehy, E. J., Cunniffe, G., Diaz-Payno, P., Carroll, S. F., Jeon, O., et al. (2020). 3D Printing of Fibre-Reinforced Cartilaginous Templates for the Regeneration of Osteochondral Defects. *Acta Biomater.* 113, 130–143. doi:10.1016/j.actbio.2020.05.040

da Silva, D., Kaduri, M., Poley, M., Adir, O., Krinsky, N., Shainsky-Roitman, J., et al. (2018). Biocompatibility, Biodegradation and Excretion of Polylactic Acid (PLA) in Medical Implants and Theranostic Systems. *Chem. Eng. J.* 340, 9–14. doi:10.1016/j.cej.2018.01.010

Dhandapani, R., Krishnan, P. D., Zennifer, A., Kannan, V., Manigandan, A., Arul, M. R., et al. (2020). Additive Manufacturing of Biodegradable Porous Orthopaedic Screw. *Bioact. Mater.* 5, 458–467. doi:10.1016/j.bioactmat.2020.03.009

Ding, J., Chen, B., Lv, T., Liu, X., Fu, X., Wang, Q., et al. (2016). Bone Marrow Mesenchymal Stem Cell-Based Engineered Cartilage Ameliorates Polyglycolic Acid/Polylactic Acid Scaffold-Induced Inflammation through M2 Polarization of Macrophages in a Pig Model. *Stem Cells Transl. Med.* 5, 1079–1089. doi:10.5966/sctm.2015-0263

Du, L., Yang, X., Li, W., Luo, X., Wu, H., Zhang, J., et al. (2017). Construction of Physical Crosslink-Based Chitosan/liquid Crystal Composite Hydrogel and Evaluation on Their Cytocompatibility. *Regen. Biomater.* 4, 39–45. doi:10.1093/rb/rbw035

Freytes, D. O., Kang, J. W., Marcos-Campos, I., and Vunjak-Novakovic, G. (2013). Macrophages Modulate the Viability and Growth of Human Mesenchymal Stem Cells. *J. Cell. Biochem.* 114, 220–229. doi:10.1002/jcb.24357

Ghazanfari, S., Khademhosseini, A., and Smit, T. H. (2016). Mechanisms of Lamellar Collagen Formation in Connective Tissues. *Biomaterials* 97, 74–84. doi:10.1016/j.biomaterials.2016.04.028

Giraud-Guille, M.-M., Besseau, L., Chopin, C., Durand, P., and Herbage, D. (2000). Structural Aspects of Fish Skin Collagen Which Forms Ordered Arrays via Liquid Crystalline States. *Biomaterials* 21, 899–906. doi:10.1016/S0142-9612(99)00244-6

Gupta, M., Sarangi, B. R., Deschamps, J., Nematbakhsh, Y., Callan-Jones, A., Margadant, F., et al. (2015). Adaptive Rheology and Ordering of Cell Cytoskeleton Govern Matrix Rigidity Sensing. *Nat. Commun.* 6, 7275. doi:10.1038/ncomms8525

Hirst, L. S., and Charras, G. (2017). Liquid Crystals in Living Tissue. *Nature* 544, 164–165. doi:10.1038/544164a

Huang, X., Chen, M., Wu, H., Jiao, Y., and Zhou, C. (2020). Macrophage Polarization Mediated by Chitooligosaccharide (COS) and Associated Osteogenic and Angiogenic Activities. *ACS Biomater. Sci. Eng.* 6, 1614–1629. doi:10.1021/acsbiomaterials.9b01550

Hulmes, D. J. S. (2002). Building Collagen Molecules, Fibrils, and Suprafibrillar Structures. *J. Struct. Biol.* 137, 2–10. doi:10.1006/jsbi.2002.4450

Hwang, J. J., Iyer, S. N., Li, L.-S., Claussen, R., Harrington, D. A., and Stupp, S. I. (2002). Self-assembling Biomaterials: Liquid Crystal Phases of Cholesteryl Oligo(L -lactic Acid) and Their Interactions with Cells. *Proc. Natl. Acad. Sci. U.S.A.* 99, 9662–9667. doi:10.1073/pnas.152667399

Jewell, S. A. (2011). Living Systems and Liquid Crystals. *Liq. Cryst.* 38, 1699–1714. doi:10.1080/02678292.2011.603846

Lee, J., Byun, H., Madhurakkat Perikamana, S. K., Lee, S., and Shin, H. (2019). Current Advances in Immunomodulatory Biomaterials for Bone Regeneration. *Adv. Healthc. Mat.* 8, 1801106. doi:10.1002/adhm.201801106

Li, L., Tu, M., Mou, S., and Zhou, C. (2001). Preparation and Blood Compatibility of Polysiloxane/liquid-Crystal Composite Membranes. *Biomaterials* 22, 2595–2599. doi:10.1016/s0142-9612(00)00222-2

Li, W., Liu, W., Wen, W., Liu, H., Liu, M., Zhou, C., et al. (2019). The Liquid Crystalline Order, Rheology and Their Correlation in Chitin Whiskers Suspensions. *Carbohydr. Polym.* 209, 92–100. doi:10.1016/j.carbpol.2019.01.006

Li N, N., Zheng, Z., Cai, X., Liu, Q., Zhang, Y., Zhou, C., et al. (2021). A Novel Thermoresponsive Membrane as Potential Material for Tissue Engineering. *Liq. Cryst.* 48, 653–664. doi:10.1080/02678292.2020.1802672

Li X, X., Wei, L., Li, J., Shao, J., Yi, B., Zhang, C., et al. (2021). Multifunctional SDF-1-Loaded Hydroxyapatite/polylactic Acid Membranes Promote Cell Recruitment, Immunomodulation, Angiogenesis, and Osteogenesis for Biomimetic Bone Regeneration. *Appl. Mater. Today* 22, 100942. doi:10.1016/j.apmt.2021.100942

Liu, H., Li, W., Luo, B., Chen, X., Wen, W., and Zhou, C. (2017). Icariin Immobilized Electrospinning poly(L-Lactide) Fibrous Membranes via Polydopamine Adhesive Coating with Enhanced Cytocompatibility and Osteogenic Activity. *Mater. Sci. Eng. C* 79, 399–409. doi:10.1016/j.msec.2017.05.077

Liu, Y., Xu, C., Gu, Y., Shen, X., Zhang, Y., Li, B., et al. (2019). Polydopamine-modified Poly(l-Lactic Acid) Nanofiber Scaffolds Immobilized with an Osteogenic Growth Peptide for Bone Tissue Regeneration. *RSC Adv.* 9, 11722–11736. doi:10.1039/c8ra08828d

Liu, W., Liu, K., Zhu, L., Li, W., Liu, K., Wen, W., et al. (2020). Liquid Crystalline and Rheological Properties of Chitin Whiskers with Different Chemical Structures and Chargeability. *Int. J. Biol. Macromol.* 157, 24–35. doi:10.1016/j.ijbiomac.2020.04.158

Lowe, A. M., and Abbott, N. L. (2012). Liquid Crystalline Materials for Biological Applications. *Chem. Mat.* 24, 746–758. doi:10.1021/cm202632m

Lutolf, M. P., and Hubbell, J. A. (2005). Synthetic Biomaterials as Instructive Extracellular Microenvironments for Morphogenesis in Tissue Engineering. *Nat. Biotechnol.* 23, 47–55. doi:10.1038/nbt1055

Madhavan Nampoothiri, K., Nair, N. R., and John, R. P. (2010). An Overview of the Recent Developments in Polylactide (PLA) Research. *Bioresour. Technol.* 101, 8493–8501. doi:10.1016/j.biortech.2010.05.092

Mahon, O. R., Browe, D. C., Gonzalez-Fernandez, T., Pitacco, P., Whelan, I. T., Von Euw, S., et al. (2020). Nano-particle Mediated M2 Macrophage Polarization Enhances Bone Formation and MSC Osteogenesis in an IL-10 Dependent Manner. *Biomaterials* 239, 119833. doi:10.1016/j.biomaterials.2020.119833

Pellegrino, L., Cocchiola, R., Francolini, I., Lopreiato, M., Piozzi, A., Zanoni, R., et al. (2017). Taurine Grafting and Collagen Adsorption on PLLA Films Improve Human Primary Chondrocyte Adhesion and Growth. *Colloids Surfaces B Biointerfaces* 158, 643–649. doi:10.1016/j.colsurfb.2017.07.047

Prévôt, M., and Hegmann, E. (2017). From Biomaterial, Biomimetic, and Polymer to Biodegradable and Biocompatible Liquid Crystal Elastomer Cell Scaffolds. *Adv. Bioinspired Biomed. Mater.* 2, 3–45. doi:10.1021/bk-2017-1253.ch001

Price, J. C., Roach, P., and El Haj, A. J. (2016). Liquid Crystalline Ordered Collagen Substrates for Applications in Tissue Engineering. *ACS Biomater. Sci. Eng.* 2, 625–633. doi:10.1021/acsbiomaterials.6b00030

Qiu, P., Li, M., Chen, K., Fang, B., Chen, P., Tang, Z., et al. (2020). Periosteal Matrix-Derived Hydrogel Promotes Bone Repair through an Early Immune Regulation Coupled with Enhanced Angio- and Osteogenesis. *Biomaterials* 227, 119552. doi:10.1016/j.biomaterials.2019.119552

Rey, A. D. (2010). Liquid Crystal Models of Biological Materials and Processes. *Soft Matter* 6, 3402–3429. doi:10.1039/B921576J

Róg, T., Pasenkiewicz-Gierula, M., Vattulainen, I., and Karttunen, M. (2009). Ordering Effects of Cholesterol and its Analogues. *Biochim. Biophys. Acta Biomembr.* 1788, 97–121. doi:10.1016/j.bbamem.2008.08.022

Saurabh, S., Lansac, Y., Jang, Y. H., Glaser, M. A., Clark, N. A., and Maiti, P. K. (2017). Understanding the Origin of Liquid Crystal Ordering of Ultrashort Double-Stranded DNA. *Phys. Rev. E* 95, 032702. doi:10.1103/PhysRevE.95.032702

Saw, T. B., Xi, W., Ladoux, B., and Lim, C. T. (2018). Biological Tissues as Active Nematic Liquid Crystals. *Adv. Mat.* 30, 1802579. doi:10.1002/adma.201802579

Schlundt, C., Schell, H., Goodman, S. B., Vunjak-Novakovic, G., Duda, G. N., and Schmidt-Bleek, K. (2015). Immune Modulation as a Therapeutic Strategy in Bone Regeneration. *J. Exp. Ortop.* 2, 1. doi:10.1186/s40634-014-0017-6

Schroeder, T. M., Jensen, E. D., and Westendorf, J. J. (2005). Runx2: A Master Organizer of Gene Transcription in Developing and Maturing Osteoblasts. *Birth Defect Res. C* 75, 213–225. doi:10.1002/bdrc.20043

Soon, C. F., Youseffi, M., Blagden, N., Berends, R., Lobo, S. B., Javid, F. A., et al. (2009). "Characterization and Biocompatibility Study of Nematic and Cholesteryl Liquid Crystals," in *World Congress on Engineering 2009, Vols I and II*. Editors S. I. Ao, L. Gelman, D. W. L. Hukins, A. Hunter, and A. M. Korsunsky (Hong Kong: Int Assoc Engineers-Iaeng), 1872–1875.

Soon, C. F., Youseffi, M., Berends, R. F., Blagden, N., and Denyer, M. C. T. (2013). Development of a Novel Liquid Crystal Based Cell Traction Force Transducer System. *Biosens. Bioelectron.* 39, 14–20. doi:10.1016/j.bios.2012.06.032

Soon, C. F., Omar, W. I. W., Berends, R. F., Nayan, N., Basri, H., Tee, K. S., et al. (2014). Biophysical Characteristics of Cells Cultured on Cholesteryl Ester Liquid Crystals. *Micron* 56, 73–79. doi:10.1016/j.micron.2013.10.011

Spiller, K. L., Nassiri, S., Witherel, C. E., Anfang, R. R., Ng, J., Nakazawa, K. R., et al. (2015). Sequential Delivery of Immunomodulatory Cytokines to Facilitate the M1-To-M2 Transition of Macrophages and Enhance Vascularization of Bone Scaffolds. *Biomaterials* 37, 194–207. doi:10.1016/j.biomaterials.2014.10.017

Stewart, G. T. (2004). Liquid Crystals in Biology II. Origins and Processes of Life. *Liq. Cryst.* 31, 443–471. doi:10.1080/02678290410001666066

Tai, H. S., and Lee, J. Y. (1990). Phase Transition Behaviors and Selective Optical Properties of a Binary Cholesteric Liquid Crystals System: Mixtures of Oleyl Cholesteryl Carbonate and Cholesteryl Nonanoate. *J. Appl. Phys.* 67, 1001–1006. doi:10.1063/1.345807

Tang, M., Ding, S., Min, X., Jiao, Y., Li, L., Li, H., et al. (2016). Collagen Films with Stabilized Liquid Crystalline Phases and Concerns on Osteoblast Behaviors. *Mater. Sci. Eng. C* 58, 977–985. doi:10.1016/j.msec.2015.09.058

Wei, W., and Dai, H. (2021). Articular Cartilage and Osteochondral Tissue Engineering Techniques: Recent Advances and Challenges. *Bioact. Mater.* 6, 4830–4855. doi:10.1016/j.bioactmat.2021.05.011

Wu, H., Shang, Y., Zhang, J., Cheang, L. H., Zeng, X., and Tu, M. (2017). The Effects of Liquid Crystal-Based Composite Substrates on Cell Functional Responses of Human Umbilical Cord-Derived Mesenchymal Stem Cells by Mechano-Regulatory Process. *J. Biomater. Appl.* 32, 492–503. doi:10.1177/0885328217733378

Xie, W., Ouyang, R., Wang, H., Li, N., and Zhou, C. (2020). Synthesis and Cytotoxicity of Novel Elastomers Based on Cholesteric Liquid Crystals. *Liq. Cryst.* 47, 449–464. doi:10.1080/02678292.2019.1657594

Yao, Q., Cosme, J. G. L., Xu, T., Miszuk, J. M., Picciani, P. H. S., Fong, H., et al. (2017). Three Dimensional Electrospun PCL/PLA Blend Nanofibrous Scaffolds with Significantly Improved Stem Cells Osteogenic Differentiation and Cranial Bone Formation. *Biomaterials* 115, 115–127. doi:10.1016/j.biomaterials.2016.11.018

Zhang, Y., Böse, T., Unger, R. E., Jansen, J. A., Kirkpatrick, C. J., and van den Beucken, J. J. J. P. (2017). Macrophage Type Modulates Osteogenic Differentiation of Adipose Tissue MSCs. *Cell Tissue Res.* 369, 273–286. doi:10.1007/s00441-017-2598-8

Conflict of Interest: The authors declare that the research was conducted in the absence of any commercial or financial relationships that could be construed as a potential conflict of interest.

frontiers | Frontiers in Bioengineering and Biotechnology

ORIGINAL RESEARCH
published: 23 June 2022
doi: 10.3389/fbioe.2022.940634

Development of Biomimetic Hepatic Lobule-Like Constructs on Silk-Collagen Composite Scaffolds for Liver Tissue Engineering

Lina Guo[1], Ziqing Zhu[2], Chuanzhou Gao[1], Kaiwen Chen[3], Shenzhou Lu[2], Hexin Yan[4,5], Wenming Liu[4,5], Mingqi Wang[1], Yanfang Ding[1], Lin Huang[1]* and Xiuli Wang[1,6]*

[1]College of Basic Medical Science, Dalian Medical University, Dalian, China, [2]National Engineering Laboratory for Modern Silk, College of Textile and Clothing Engineering, Soochow University, Suzhou, China, [3]School of Bioengineering, State Key Laboratory of Fine Chemistry, Dalian University of Technology, Dalian, China, [4]Department of Anesthesiology and Critical Care Medicine, Renji Hospital, Shanghai Jiaotong University School of Medicine, Shanghai, China, [5]Shanghai Engineering Research Center of Peri-operative Organ Support and Function Preservation, Shanghai, China, [6]General Surgery Center, Department of Hepatobiliary Surgery II, Zhujiang Hospital, Southern Medical University, Guangzhou, China

Edited by:
Yuangang Liu,
Huaqiao University, China

Reviewed by:
Xiaohui Zhang,
Xi'an Jiaotong University, China
Yubing Xie,
SUNY Polytechnic Institute,
United States

***Correspondence:**
Lin Huang
lhuang@dmu.edu.cn
Xiuli Wang
panpan1210@dicp.ac.cn

Specialty section:
This article was submitted to Biomaterials, a section of the journal Frontiers in Bioengineering and Biotechnology

Received: *10 May 2022*
Accepted: *31 May 2022*
Published: *23 June 2022*

Citation:
Guo L, Zhu Z, Gao C, Chen K, Lu S, Yan H, Liu W, Wang M, Ding Y, Huang L and Wang X (2022) Development of Biomimetic Hepatic Lobule-Like Constructs on Silk-Collagen Composite Scaffolds for Liver Tissue Engineering. Front. Bioeng. Biotechnol. 10:940634. doi: 10.3389/fbioe.2022.940634

Constructing an engineered hepatic lobule-mimetic model is challenging owing to complicated lobular architecture and crucial hepatic functionality. Our previous study has demonstrated the feasibility of using silk fibroin (SF) scaffolds as functional templates for engineering hepatic lobule-like constructs. But the unsatisfactory chemical and physical performances of the SF-only scaffold and the inherent defect in the functional activity of the carcinoma-derived seeding cells remain to be addressed to satisfy the downstream application demand. In this study, SF-collagen I (SFC) composite scaffolds with improved physical and chemical properties were fabricated, and their utilization for bioengineering a more hepatic lobule-like construct was explored using the immortalized human hepatocyte-derived liver progenitor-like cells (iHepLPCs) and endothelial cells incorporated in the dynamic culture system. The SFC scaffolds prepared through the directional lyophilization process showed radially aligned porous structures with increased swelling ratio and porosity, ameliorative mechanical stiffness that resembled the normal liver matrix more closely, and improved biocompatibility. The iHepLPCs displayed a hepatic plate-like distribution and differentiated into matured hepatocytes with improved hepatic function *in vitro* and *in vivo*. Moreover, hepatocyte–endothelial cell interphase arrangement was generated in the co-culture compartment with improved polarity, bile capillary formation, and enhanced liver functions compared with the monocultures. Thus, a more biomimetic hepatic lobule-like model was established and could provide a valuable and robust platform for various applications, including bioartificial liver and drug screening.

Keywords: hepatic lobule, silk fibroin, collagen, liver tissue engineering, dynamic culture, biomimetic, transplantation

INTRODUCTION

Constructing three-dimensional (3D) liver models with biomimetic structure and function is of great interest owing to its promisingly potential applications in clinical treatment, fundamental research, and drug screening. Unfortunately, desirable hepatocyte cultivation *in vitro* is severely hindered by deficiency technology to fully recapitulate the native growth conditions. Co-culture with multiple nonparenchymal cells and/or incorporation with different extracellular matrixes (ECM) has been widely explored to improve the viability, maturation, and function of hepatocytes (Cuvellier et al., 2021; Das et al., 2020; Liu et al., 2021). Nonetheless, few investigations have focused on precisely controlling hepatic tissue architecture at the microscale, although both the complex architecture and specific organization of hepatic lobules play an important role in determining the phenotype and function of the actual liver tissue. It is known that native human hepatocytes organize into hepatic irregular plates that radiate toward a central vein to form polygonal hepatic lobules. This unique architecture provides a foundation for the high integration of hepatocytes and their surrounding microenvironment, which promotes the generation of bile capillaries and enhances its adequate spatial and temporal contact with blood for mass transport.

Motivated by the goal of recreating more histologically and physiologically relevant hepatocyte culture systems *in vitro*, different strategies, such as decellularized liver scaffolds (Uygun et al., 2010; Watanabe et al., 2019), micro-fluidic chips (Ho et al., 2013; Ya et al., 2021), and 3D printing methods (Kang et al., 2020), have been employed to reconstruct a liver biomimetic architecture, and the biomimetic configuration has been confirmed to positively affect hepatocyte morphology, polarity, viability, and maturation. However, most methods are still limited by uncontrollable cell localization, pseudo-3D cultures, or complex construction processes that might lead to cell damage. Recently, our laboratory reported the fabrication of lobule-like silk fibroin (SF) scaffolds using a radially directional freezing strategy (Wang et al., 2022). By co-culturing hepatocytes and endothelial cells on this SF scaffold, a more biomimetic human hepatic lobule-like culture model with improved phenotype and function was developed *in vitro*. This study strongly supports the important role of matrix architecture in determining cell behavior and hepatic tissue reconstruction.

Although our previous study has proven encouraging for the construction of a lobule-mimetic culture model *in vitro*, we are nonetheless faced with certain limitations. On the one hand, due to the lack of integrin-mediated cell-binding sites, cell adhesion to SF scaffolds was less desirable, mainly relying on low-affinity cell-binding domains (carboxy-terminal arginine residues or electrostatic interactions between cells and scaffolds) (Maghdouri-White et al., 2014; Ruoslahti and Pierschbacher, 1987). In addition, SF-only scaffolds possess relatively high mechanical properties. For example, our previous study demonstrated that the modulus of the scaffold prepared with a 6% (w/v) SF solution was 67.3 ± 2.0 kPa, which was significantly higher than that of the normal liver (approximately 2.8 ± 7.4 kPa). On the other hand, the immortalized hepatocarcinoma C3A cells used before were inadequate in replicating the native hepatic phenotype and function due to their insurmountable inherent defects associated with cancerous phenotype and impaired functionality. Their immortalized activity poses a risk of carcinogenesis once implanted *in vivo*, hindering not only the model-based exploration of the complex interactions between hepatocytes and the microenvironment but also the downstream application for *in vivo* implantation.

Studies have demonstrated that mixing SF solutions with natural biomolecular polymers could overcome some drawbacks of SF scaffolds (Buitrago et al., 2018; Goczkowski et al., 2019). Type I collagen, a predominant subtype synthesized in connective tissue, is the most abundant collagen in human liver tissues with rich integrin-mediated cell-binding sites (Martinez-Hernandez and Amenta, 1993; Willemse et al., 2020; Kumaran et al., 2005). Importantly, several precedents for using collagen as a biomaterial either in the hepatocyte culture *in vitro* or the clinical settings have been noted (Rico-Llanos et al., 2021; Serna-Márquez et al., 2020), in which collagen provides biomimetic matrix support for the 3D culture of mammalian cells. Hence, given these apparent advantages of collagen over the existing culture system, its incorporation in the 3D culture compartment may benefit to establish a lobule-mimetic culture model with improved phenotype and function.

Therefore, in the present study, an SF-collagen (SFC) composite scaffold was fabricated by directional lyophilization with an SF-collagen type I mixed solution. Meanwhile, more functional primary human hepatocyte-derived liver progenitor-like cells (iHepLPCs) were employed to replace the immortalized hepatocarcinoma C3A cells before. We hypothesized that the primary iHepLPCs growing in a 3D microenvironment provided by the stromal cells, ECM molecules, and SFC composite scaffold with unique lobule-like architecture not only generate liver tissue-like structures that more closely resemble the *in vivo* hepatic lobule morphology but also contribute to producing an optimized 3D biomimetic lobule-like culture model with improved differentiated functionality. Toward this goal, the reconstructed 3D culture model was characterized by its growth profile, histology, and gene expression. Moreover, its potential capability for transplantation was evaluated through subcutaneous implantation in nude mice.

EXPERIMENTAL METHODS

Cell Maintenance Culture and Differentiation

The human hepatoma cell line C3A (American Type Culture Collection, Manassas, VA, United States) was cultured in Eagle's minimum essential medium (Gibco, Carlsbad, CA, United States). The complete medium contained 10% fetal bovine serum (FBS, ScienCell Research Laboratory, Carlsbad, CA, United States) and 1% penicillin/streptomycin solution (P/S, Solarbio, Peking, China). Professor Hexin Yan of the Shanghai Cancer Institute (Shanghai, China) provided the iHepLPCs, GFP-transfected iHepLPCs, transition and expansion medium (T&EM), and hepatic maturation medium (HMM). The detailed transfection method and components of both mediums can be found in a previous study (Wang et al., 2019). The cells were maintained and expanded in T&EM and passaged at a ratio of 1:3 after dissociation in TrypLE solution (Gibco). Subsequently, the iHepLPCs were maintained in T&EM until they attained 90% confluence for rapid hepatic differentiation. Then, the medium was replaced with HMM, and the cells were cultivated for an additional 7–10 days to allow for complete differentiation into iHepLPC-derived hepatocytes (iHepLPC-Heps). Alternatively, human umbilical vein endothelial cells (HUVECs, ScienCell) were cultured in an endothelial growth medium (EGM, ScienCell) and used between passages three and six. All the cells were incubated in a humidified incubator containing 5% CO_2 at 37°C, and the medium was changed every other day.

For iHepLPCs and HUVECs co-culture experiments, a combined medium composed of T&EM/HMM and EGM at a volume ratio of 2:1 was used, which had previously been tested to ensure the proper growth of each cell type under monolayer culture conditions.

Preparation of SF Solution

Soochow University (Suzhou, China) kindly provided SF aqueous stock solution. Briefly, SF fibers isolated from the cocoons of a *Bombyx mori* silkworm were boiled for 30 min in an aqueous solution of 0.02 M Na_2CO_3 (Solarbio). Subsequently, the fibers were rinsed thoroughly with distilled water to extract the glue-like sericin proteins. After air-drying, the degummed silk fibers were placed in a 9.3 M lithium bromide (Aladdin Bio-Chem Technology, Shanghai, China) solution in a glass beaker at 60°C for 4–5 h. Then, the solution was dialyzed against distilled water in a dialysis bag with a molecular weight cut-off of 3500 Da for 3 days. Finally, the solution was centrifuged, and the concentration was determined by weighing the residual solid of a known solution volume after drying at 60°C.

Fabrication of SFC Composite Hepatic Lobule-like Scaffolds

The composite biomimetic hepatic lobule-like silk scaffolds were fabricated following our previous study with minor modifications (**Supplementary Figure S1**) (Wang et al., 2022). To prepare the SFC composite scaffolds, 6% SF solution (w/v) was mixed with 2 mg/ml rat tail collagen I solution at a ratio of 5:1 and 2:1 to keep the SF concentration at 5 and 4%; 5 and 4% SF solution served as the control (**Supplementary Table S1**). After complete blending, SFC and SF solutions at different concentrations were transferred into 15-ml centrifuge tubes and rapidly immersed in liquid nitrogen for 30 min in an upright position. Next, the frozen solutions were lyophilized for 48 h and then autoclaved to induce SF β-sheet structure formation. Finally, ready-to-use scaffolds with a thickness of 1–2 mm, an outer diameter of 6 mm, and an inner diameter of 1 mm were prepared.

Performance Testing of SFC Composite Hepatic Lobule-like Scaffolds

Swelling Ratio

The scaffolds were immersed in ultrapure water at room temperature for 24 h. After excess water was removed, the wet weight of the scaffolds (Ws) was determined. The samples were then dried overnight in an oven at 60°C under vacuum, after which the dry weight of the scaffolds (W_d) was determined. By running the samples of each group in triplicate, the swelling ratio of the scaffolds was calculated as follows:

$$\text{Swelling ratio} = \left((W_s - W_d)/W_d\right) \times 100\%.$$

Porosity

A scaffold of weight W_1 (in g) and volume V (in cm^3) was immersed in hexane (Sigma-Aldrich, St. Louis, MO, United States) for 10 min at room temperature. After removing excess liquid from the surface, the total weight of the scaffold was recorded as W_2 (g). The density of hexane is 0.66 g/cm^3. Subsequently, by running each sample in triplicate, the porosity of the scaffolds was determined using the following formula:

$$\text{Scaffold porosity} = (W_2 - W_1)/0.66V \times 100\%.$$

In Vitro Degradation

Dried cylindrical scaffolds (8 mm in diameter and 2 mm in height) with a weight of W_0 (g) were incubated and immersed in 1 ml of PBS solution with or without 6 U/ml protease XIV (Sigma-Aldrich) for 2, 4, 6, and 8 days. The samples were incubated at 37°C, after which the medium was changed every 2 days. At each time point, the scaffolds were dried at 60°C and weighed (W_n) (g). By running the samples in triplicate, the remaining mass fraction of the scaffolds *in vitro* was calculated using the following formula:

$$\text{Remaining mass fraction} = (W_n/W_0) \times 100\%.$$

Mechanical Properties

We determined mechanical strength using cylindrical scaffolds (8 mm in diameter and 8 mm in height) immersed in ultrapure water for 12 h at room temperature. The compression properties of the scaffolds were evaluated at room temperature using an Instron 3365 testing frame (Instron, Norwood, MA, United States) with a 100 N loading cell. The load was applied until the scaffold had compressed to 80% of its original height. Subsequently, the pressure was released. The compressive modulus was calculated from the linear elastic region in the stress–strain curve, and all data were analyzed as averages of four to six tests, comprising three parallel scaffolds.

Fourier Transform Infrared Spectroscopy (FTIR)

The secondary structures of the scaffolds were analyzed using a Nicolet FTIR 5700 spectrometer in the attenuated total reflection mode (Thermo Scientific, FL, United States). Briefly, a thin layer of the SF scaffold with a thickness of 1–2 mm was cut and subjected to FTIR analysis. Sixty-four scans were recorded for each measurement, with a resolution of 4 cm^{-1} and wavenumber of 400–4000 cm^{-1}. The samples were run in triplicate in each group.

3D Culture on Silk Scaffolds

Before cell inoculation, the ready-to-use scaffolds were autoclaved for sterilization and then pre-coated with a growth factor reduced-Matrigel™ (0.15 mg/ml; BD Biosciences, SanJose, CA, United States) diluted using a culture medium to facilitate cell attachment. Then, to construct the human-engineered liver lobule-like cultures, iHepLPCs and HUVECs in culture were harvested and mixed at a ratio of 4:1. Next, mixed iHepLPCs–HUVEC pellets were resuspended in a T&EM/EGM co-culture medium and transferred into a 24-well ultra-low attachment culture plate (Corning, Kennebunk, ME, United States) to form 3D cell spheroids for 24 h. Subsequently, after incubation for 24 h in a humidified incubator containing 5% CO_2 at 37°C, the cell spheroids were collected and mixed with the neutralized type I collagen solution (final concentration, 1 mg/ml; BD Biosciences). This cell spheroids–collagen mixture (20–25 μl/scaffold) was later inoculated into pretreated scaffolds, keeping the number of iHepLPCs constant (400,000 cells/scaffolds). After gelation at 37°C for 1 h, the cell-loaded scaffolds were transferred into a 12-well plate. A T&EM/EGM co-culture medium was added gently to avoid disturbing the scaffolds. Monocultures of iHepLPCs (without HUVECs) under the same conditions with the same seeding density or monolayer cultures (2D culture) of iHepLPCs in Petri dishes served as the control.

To promote oxygen, nutrient, and waste exchange among the cells in the scaffolds, Rotary Cell Culture System™ (RCCS, Synthecon Incorporated, Houston, TX, United States) was used for the dynamic culture of the cells–scaffolds complex. First, 24 h after the seeding process of cell spheroids, the resultant cell-loaded scaffolds were gently transferred to culture vessels and filled with an HMM/EGM co-culture medium to initiate hepatic differentiation. The rotational speed was set at 15–20 rpm, and the culture medium was changed every other. The cell-loaded scaffolds were cultured for up to 3 weeks in the RCCS. To distinguish hepatocytes from endothelial cells within the co-cultures, CellTracker™ DiI and CellTracker™ DiO (Invitrogen, Carlsbad, CA, United States) were applied to label iHepLPCs and HUVECs, respectively. Briefly, the adherent cells at 80–90% confluence were incubated in a pre-warmed medium containing 25 μM CellTracker™ dye under growth conditions for 30–40 min. Finally, the dye-containing medium was replaced by a fresh medium, and the cells were incubated for another 30 min at 37°C. After washing with PBS solution, the labeled cells were harvested and inoculated for 7 days on the scaffolds, and then the scaffolds were harvested and captured using confocal laser scanning microscopy (CLSM, Wetzlar, Germany).

Electron Microscopy

The harvested samples were prefixed in 2.5% glutaraldehyde solution (Solarbio) overnight at 4°C. Then, they were washed with PBS solution to remove the glutaraldehyde solution thoroughly and postfixed with 2% osmium tetraoxide solution (Solarbio) for at least 2 h at ambient temperature. For scanning electron microscopy (SEM) detection, the samples were lyophilized and sputter-coated with gold particles, and then images were captured using a JEOL-F200 microscope (Japan). For transmission electron microscopy (TEM) detection, after postfixation, the samples were embedded with Epon 812 to prepare ultrathin sections and visualized under a JEM-2000EX microscope (Japan).

Cell Viability

Cell viability was assessed using a calcein-AM/EthD-1 staining kit (Invitrogen) according to the manufacturer's instructions. First, the samples were collected at the indicated time points and washed with PBS solution. Then, they were incubated with a working solution of calcein-AM/EthD-1 for 2 h at 37°C. After washing with an FBS-free culture medium, they were loaded into a petri-dish with a glass bottom, and their images were captured using CLSM.

Histology and Staining

Hematoxylin and Eosin (H&E) Staining

Before embedding in paraffin, the samples were harvested and fixed overnight in 4% paraformaldehyde (Solarbio). Paraffin sections (5 μm) were prepared at the Pathology Department at Dalian Medical University (Dalian, China). The sections were deparaffinized and stained with H&E solution as described previously (Wang et al., 2010), and images were captured using a Leica TCS microscope (Wetzlar).

Whole-Mount Immunofluorescence (IF) Staining

Whole-mount IF staining of the cell-loaded scaffolds was performed as described previously (Wang et al., 2010). In brief, the samples were collected at the indicated time points and fixed in 4% paraformaldehyde for 12 h. After thoroughly washing with PBS solution, the scaffolds underwent sequential membrane permeabilization and blocking with nonspecific antigens. Subsequently, they were incubated overnight at 4°C using the following primary antibodies: mouse anti-human ALB (dilution, 1:50; Santa Cruz Biotechnology, Santa Cruz, CA, United States), rabbit anti-human CYP3A4 (dilution, 1:100; Proteintech, China), rabbit anti-human MRP_2 (dilution, 1:50; Proteintech), and Alexa Fluor® 647 Mouse anti-Human CD31 (dilution, 1:100; BD Biosciences). Samples not incubated with specific primary antibodies served as negative controls. Next, cell-loaded scaffolds were incubated with FITC-conjugated Goat anti-Rabbit IgG Secondary Antibody or FITC-conjugated Donkey anti-Mouse Secondary Antibody (dilution, 1:200; Invitrogen) for 2 h at room temperature. DAPI (2 μg/ml, Research Organics, Cleveland, OH, United States) was used to counterstain the cell nucleus, and images were captured using CLSM.

Immunohistochemical (IHC) Staining

IHC staining was conducted as described previously (Liu et al., 2018). Briefly, deparaffinized sections were rehydrated and underwent an antigen retrieval process. Then, the samples were treated sequentially with 3% hydrogen peroxide and a nonimmune goat serum, followed by incubation with the same primary antibodies as those used in IF staining overnight at 4°C. Sections not incubated with specific primary antibodies served as negative controls. Following incubation with the primary antibodies, the samples were incubated again with a cocktail of biotinylated goat anti-rabbit or anti-mouse secondary antibodies for 15 min. Next, they were incubated with an avidin/biotin/peroxidase complex for 15 min. Following thorough washing, the sections were colored with a diaminobenzidine chromogenic solution, counterstained with hematoxylin, dehydrated, and mounted. Images were captured using a Leica TCS microscope. For IHC data quantification, six fields from a minimum of three samples were blindly analyzed using the NIH ImageJ plugin IHC Image Analysis Toolbox.

Real-Time Quantitative PCR (RT-qPCR)

The total RNA of 2D cells and 3D cultures were extracted using TRIzol reagent (Ambion Life Technologies, Denmark) according to the manufacturer's protocols. Then, 1 μg of RNA was reverse transcribed using a cDNA synthesis kit (TaKaRa Bio, Shiga, Japan). Real-time PCR was conducted using Agilent Technologies System (Peking, China) and SYBR® Premix Ex Taq™II Kit (Takara Bio). Amplification was conducted for 40 cycles of 3 s each at 95°C, 30 s each at 58°C, and 30 s at 72°C. Gene expression was calculated using the $2^{-\Delta\Delta Ct}$ method and was normalized to that of β-actin. Each sample was analyzed in triplicate. The primer sequences are listed in **Supplementary Table S2**.

Hepatic Function Detection

For the intake of acetylated low-density lipoprotein (ac-LDL), 3D constructs were incubated with 10 μg/ml DiI-ac-LDL (Invitrogen) for 5 h and then 1× Hoechst 33342 (Invitrogen) for another 1 h. After thoroughly rinsing with PBS solution, images were captured using CLSM.

The supernatants of 2D cultures, 3D monocultures, and 3D co-cultures were collected at the indicated time points to assess the secretion of human ALB. The amount of ALB secreted was determined using a Human Albumin ELISA kit (Bethyl Laboratory, Montgomery, TX, United States) according to the manufacturer's instructions. The absorbance was measured using a Synergy NEO Hybrid Multi-Mode Microplate Reader (BioTek, VT, United States). To determine urea production, 2D cultures, 3D monocultures, and co-cultures were incubated in a medium containing 3 mM NH_4Cl (Solarbio) for 24 h, after which the supernatants were collected. The urea concentration was measured using a QuantiChromTM urea assay kit (BioAssy Systems, Hayward, CA, United States) according to the manufacturer's protocols. The total DNA of each group was quantified using the Pico Green DNA assay kit (Gibco), and all data were corrected for culture time and total DNA content.

Subsequently, the 3D constructs were incubated for 1 h with 1× Hoechst 33342 and another 30 min with 10 μg/ml 5(6)-carboxy-2′, 7′-dichlorofluorescein diacetate (CDCFDA, Invitrogen) to determine functional polarization. They were washed with ice-cold PBS containing calcium and magnesium and imaged using CLSM.

Alternatively, 2D differentiated cells and 3D cultures were incubated with 25 μM rifampicin (induction of CYP3A4) or 50 μM omeprazole (induction of CYP1A2) (all from Sigma-Aldrich) dissolved in a culture medium for 72 h to evaluate CYP450 induction. The relative gene expression was quantified using RT-qPCR as described above.

In Vivo Subcutaneous Implantation in Mice

The Animal Care and Use Committee of Dalian Medical University approved all procedures. The experiments were conducted under animal care protocols. All animals used in this study were 6–8-week-old male BALB/C nude mice weighing 22–25 g (Liaoning Changsheng Biotechnology Co., Ltd., China). The mice were randomly assigned to two groups with three time points (7, 14, and 21 days). Then, 24 h after cell spheroid inoculation, cell-loaded scaffolds (diameter: 6 mm; thickness: 2 mm) were preincubated in a serum-free medium for 2 h. The cells were subcutaneously implanted in the lateral subcutaneous pocket of each mouse under general anesthesia using 4% chloral hydrate (10 μl/g of body weight of mice). Acellular scaffolds served as the blank control. The healing process at the incision region was monitored daily, and no deaths were registered during the experiment. Finally, the mice were euthanized at the indicated time points to check for the implantation outcomes, after which the samples were collected along with the surrounding tissue for histological examination.

Statistical Analyses

All quantitative experiments were conducted in triplicate, and the results were expressed as mean ± standard deviation. All statistical analyses were performed using GraphPad Prism 8. First, the two-tailed unpaired *t-test* was performed to compare the statistical significance between the two groups. Then, a two-way analysis of variance was performed with Tukey correction for multiple comparisons of multiple values. A *p*-value of <0.05 was considered statistically significant.

RESULTS

Morphology of the Composite SFC Scaffolds

Biomimetic hepatic lobule-like scaffolds fabricated from various solutions (4–6% SF, and 4–5% SFC) were characterized based on their morphology using SEM (**Figure 1**). Although the scaffolds exhibited radial pores formed by aligned lamellar sheets, the gap distances increased with decreasing SF concentrations. Specifically, the 6 and 5% SF concentrations ensured the formation of well-defined radially aligned lamellar sheets. Locally, a pore collapse could be seen when the concentration of SF was reduced by 4% (**Supplementary Figure S2**). The lamellar sheets of SFC scaffolds were relatively rough, with projections on the wall surface compared with SF scaffolds, which might promote cell adhesion and migration.

Physical Performance of the Composite SFC Scaffolds

Structural and Degradation Properties of the Composite SFC Scaffolds

The prominent SFC scaffold peaks at different concentrations were seen at approximately 1630 cm^{-1}, which were characteristic peaks assigned to β-sheets (1616–1637 cm^{-1} in the amide I region) and were similar to that of the SF scaffolds after

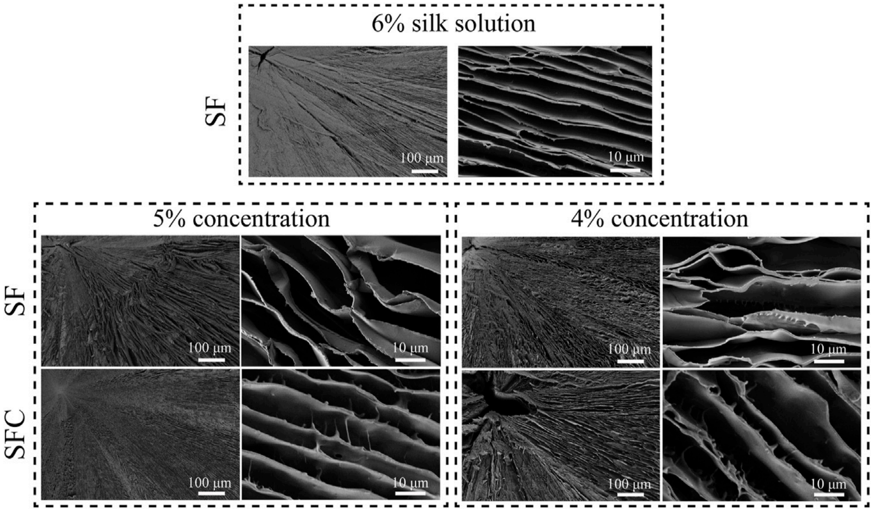

FIGURE 1 | SEM images of SF and SFC scaffolds at different concentrations (w/v).

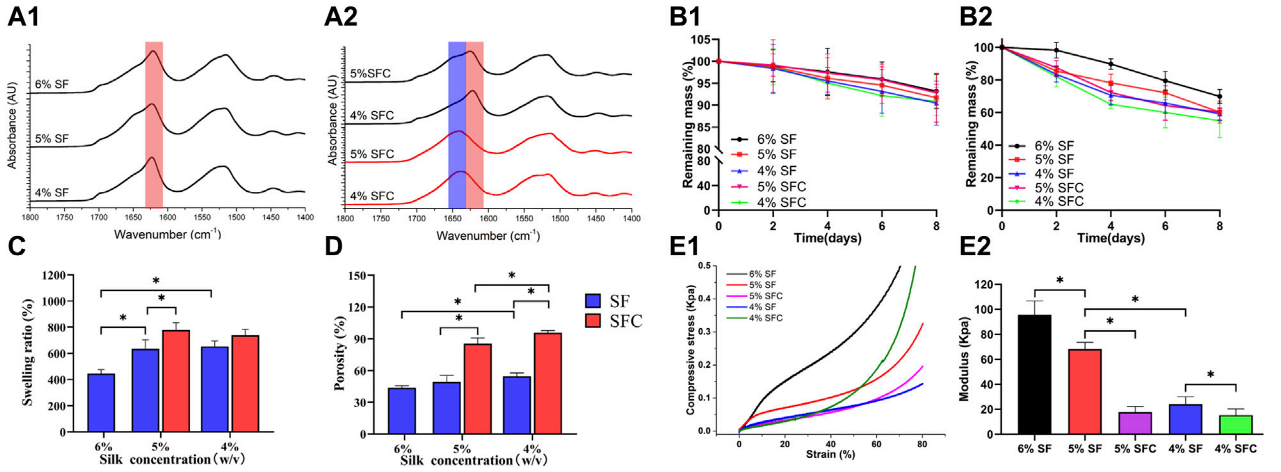

FIGURE 2 | Physical performance of SF and SFC scaffolds at concentrations of 4, 5, and 6% (w/v). FTIR spectra of SF **(A1)** and SFC **(A2)** scaffolds at different concentrations (w/v) before (red line) and after (dark line) autoclaving. Time-dependent weight change of SF and SFC scaffolds in a PBS buffer **(B1)** and protease XIV solution **(B2)** are shown. Adding collagen I increased the swelling ratio **(C)** and porosity **(D)**. A compressive stress–strain curve showing SF and SFC scaffolds in the hydrated state **(E1)** and the summary of the compressive modulus for SF and SFC scaffolds **(E2)**. (*$p < 0.05$).

autoclaving (**Figure 2A**). Therefore, collagen I rarely affected SF structural transitions from random coils to β-sheets, causing water insolubility and stability to the freeze-dried hepatic lobule-like silk scaffolds. Immersing the SF and SFC scaffolds in PBS solution resulted in a slow degradation (**Figure 2** B1). The weight of the scaffolds was reduced faster by immersing them in protease XIV solutions. Furthermore, after 8 days of incubation, 60.3 ± 2.2% and 55.0 ± 10.4% of the original weights remained for the 5 and 4% SFC groups, respectively. In contrast, the original mass of the 5 and 4% SF scaffolds was reduced to 60.2 ± 6.7% and 59.1 ± 3.8% at similar incubation periods (**Figure 2** B2). Thus, adding collagen had little effect on the degradation rate of the scaffolds, which ensures long-term support for the growth and differentiation of *in vitro* cells.

Permeability and Mechanical Properties of the Composite SFC Scaffolds

Swelling ratio and porosity are crucial for the exchange of nutrients and waste throughout the scaffold as they are the main factors that affect permeability (Huang et al., 2019). The swelling ratio of the 5 and 4% SFC scaffolds was 778.1 ± 56.5% and 738.4 ± 44.3% respectively, which were significantly higher than those of the SF scaffolds (5%: 635.0 ± 68.3%; 4%: 653.5 ± 41.4%) ($p < 0.05$, **Figure 2C**). This increase was also related to the increased porosity. Specifically, the scaffold porosity of 5% SFC (85.4 ± 5.4%) and 4% SFC (95.7 ± 2.1%) was higher than that of 5% SF (49.3 ± 6.0%) and 4% SF (54.5 ± 3.1%) ($p < 0.05$, **Figure 2D**). **Figure 2E1** showed the compressive stress–strain curves for the hepatic lobule-like silk scaffolds fabricated from

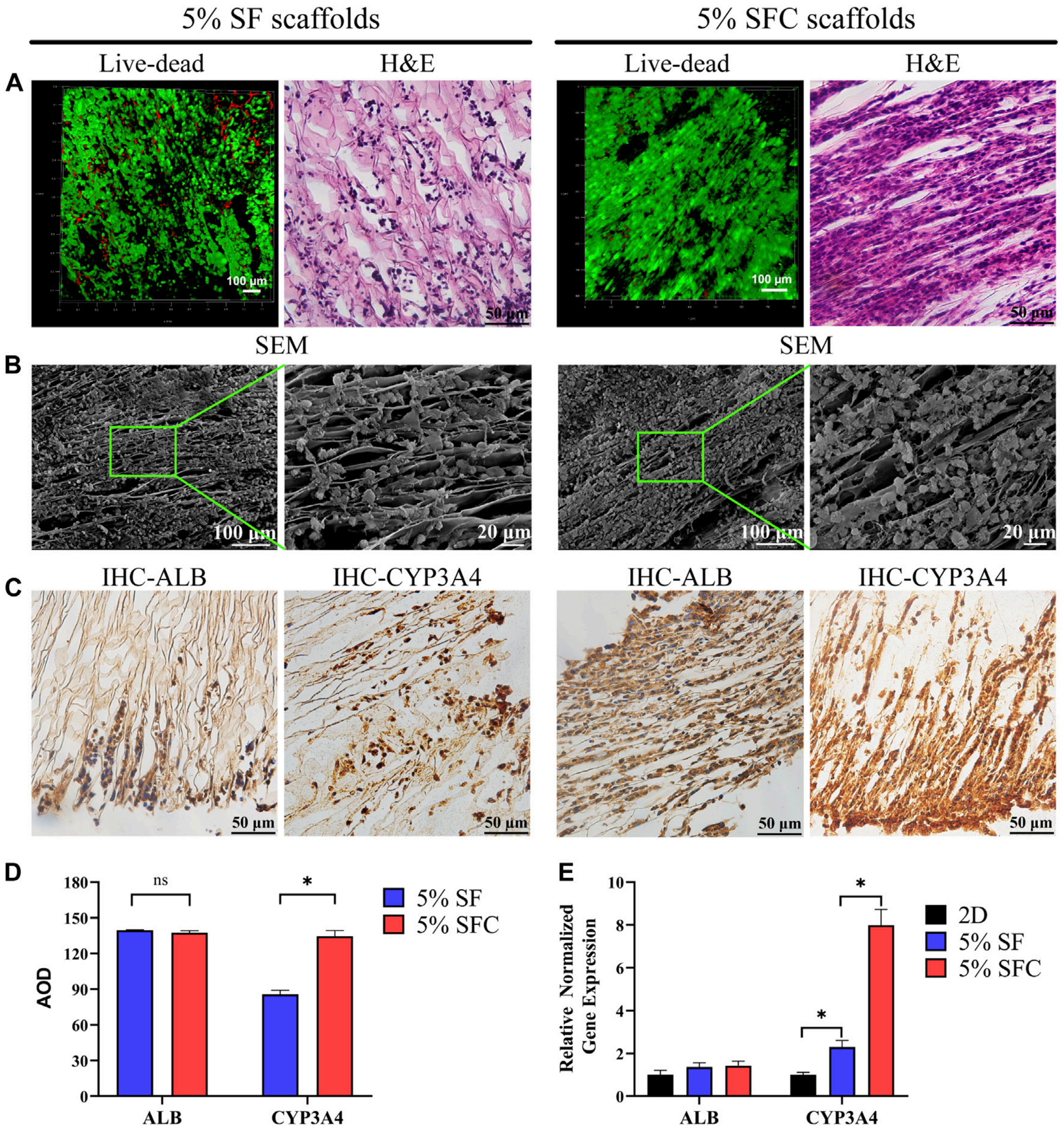

FIGURE 3 | Biocompatibility of 5% composite SFC scaffolds (w/v). The viability staining and H&E staining of cells in both scaffolds **(A)**. SEM images **(B)** showing the cell growth pattern on the surface of both scaffolds. IHC detection **(C)** of ALB and CYP3A4 expression of C3A cells in both scaffolds. Quantitative analysis of IHC staining **(D)** and functional gene expression of C3A cells in both scaffolds **(E)**. ($^*p < 0.05$).

various solutions. The compressive modulus decreased gradually with a lower concentration of SF, which is consistent with the results in our previous experiments (**Figure 2E2**). The compressive modulus of the 5% and 4% SF scaffolds were 68.2 ± 5.5 kPa and 24.2 ± 5.8 kPa, respectively, which were significantly higher than those of the 5% SFC (17.7 ± 4.4 kPa, $p < 0.05$) and 4% SFC (15.3 ± 4.9 kPa, $p < 0.05$) scaffolds. Therefore, while the mechanical properties of the collagen I-modified scaffolds were optimized, the modulus was closer to that of the native liver tissue (approximately 2.8–7.4 kPa).

Taking into account the scaffold integrity, improvement in physical properties (swelling ratio, porosity, and mechanical properties), and long-term hepatic culture (degradation properties) *in vitro* and *in vivo*, 5% SFC scaffolds were adopted in the following experiments, and 5% SF scaffolds served as the control.

C3A Distribution and Performance on the Composite SFC Scaffolds

The majority of cells in both 5% SFC and 5% SF scaffolds exhibited good viability after 2 weeks of culture (**Figure 3A**). H&E staining revealed a more detailed growth pattern within 5% SF scaffolds, wherein C3A cells migrated to and were

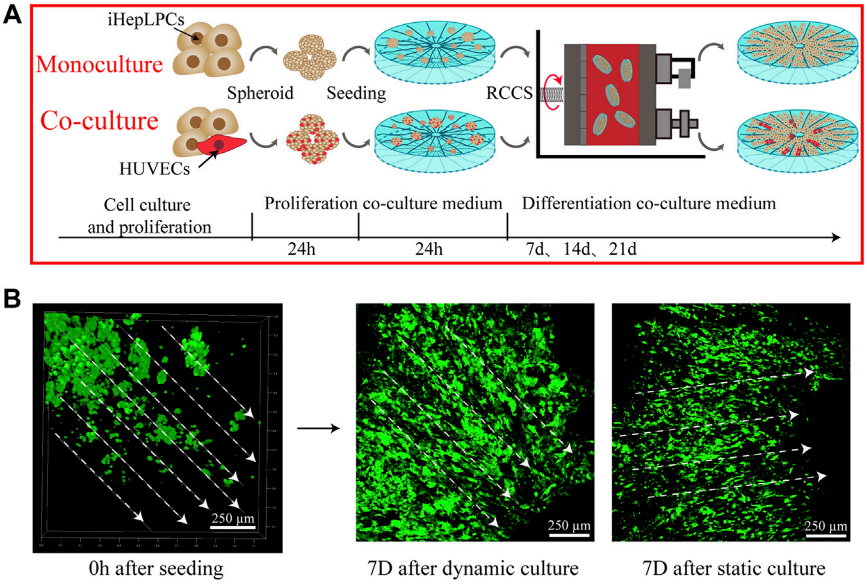

FIGURE 4 | A schematic showing the construction process of hepatic lobule-like cultures **(A)**. Distribution and morphological changes in iHepLPCs (GFP-transfected) after dynamic or static culture conditions **(B)** are shown.

distributed in the margin, while cell migration in 5% SFC scaffolds was significantly promoted and formed a bionic hepatic cord-like configuration (**Figure 3A**). Notably, cells were in closer contact with each other within 5% SFC scaffolds. On the scaffold surface, C3A cells adhered to laminar sheets while some cells resided along with the spacing between both scaffolds as showed by SEM (**Figure 3B**). This finding, combined with H&E results, further indicated that more cells had migrated from the surface into the interior of the 5% SFC scaffold.

No significant differences were detected in the ALB expression between the two groups. However, C3A cells cultured in 5% SFC scaffolds showed significant upregulation in CYP3A4 expression in both the protein and gene levels ($p < 0.05$, **Figures 3C-E**) compared with cells cultured in 5% SF scaffolds. This suggested that the 5% SFC scaffolds were superior to the SF scaffolds in promoting the expressions of mature hepatic markers.

The above results indicated that 5% SFC scaffolds were equipped with not only improved swelling ratio/porosity and ameliorative mechanical properties but also the ability to promote hepatocytes migration and function. Thus, 5% SFC scaffolds were chosen to serve as a more suitable template to construct a biomimetic hepatic lobule-like compartment.

Growth Profile of Cells on the Composite SFC Scaffolds

The construction process of the 3D hepatic lobule-like cultures is briefly shown in **Figure 4A**. Cellular spheroids composed of iHepLPCs and HUVECs with a diameter of 50–200 μm were prepared to improve the inoculation efficiency and cell viability (**Supplementary Figure S3**). After 1 week of cell seeding, we observed that the cells in the SFC scaffolds were distributed evenly throughout the scaffold, primarily as single cells or small aggregates. Most of the iHepLPCs (GFP-transfected) were localized along the radial laminar sheet and channels, displaying a well-organized directional configuration. Compared with the static culture, iHepLPCs (GFP-transfected) cultured in RCCS were considered more stretched and complete in shape (**Figure 4B**).

After 3 weeks of culture in RCCS, iHepLPCs and HUVECs displayed good viability, evidenced by their remarkably bright green fluorescence and inconspicuous red fluorescence under CLSM (**Figure 5A**). This result suggested that the SFC scaffolds provided a suitable microenvironment for the *in vitro* culture of hepatocytes and stromal cells. However, the number of cells barely increased over time, as evidenced by the unvaried green fluorescence. This indicates that iHepLPCs lost their proliferative stem cell properties and initiated hepatic differentiation in the 3D-culture environment.

A locally interphase arrangement pattern of iHepLPCs (labeled with DiI, red) and HUVECs (labeled with DiO, green) was observed in 3D co-cultures (**Figure 5B**). This distribution profile was further confirmed by IF staining after 14 days of dynamic culture (**Figure 5C**). Moreover, attributed to a higher initial inoculation radio (4:1), a larger number of hepatocytes than HUVECs were observed.

Cell Morphology and Organization on the Composite SFC Scaffolds

H&E staining displayed that the cells were located between the spaces of laminar sheets, displaying a compact but radial-

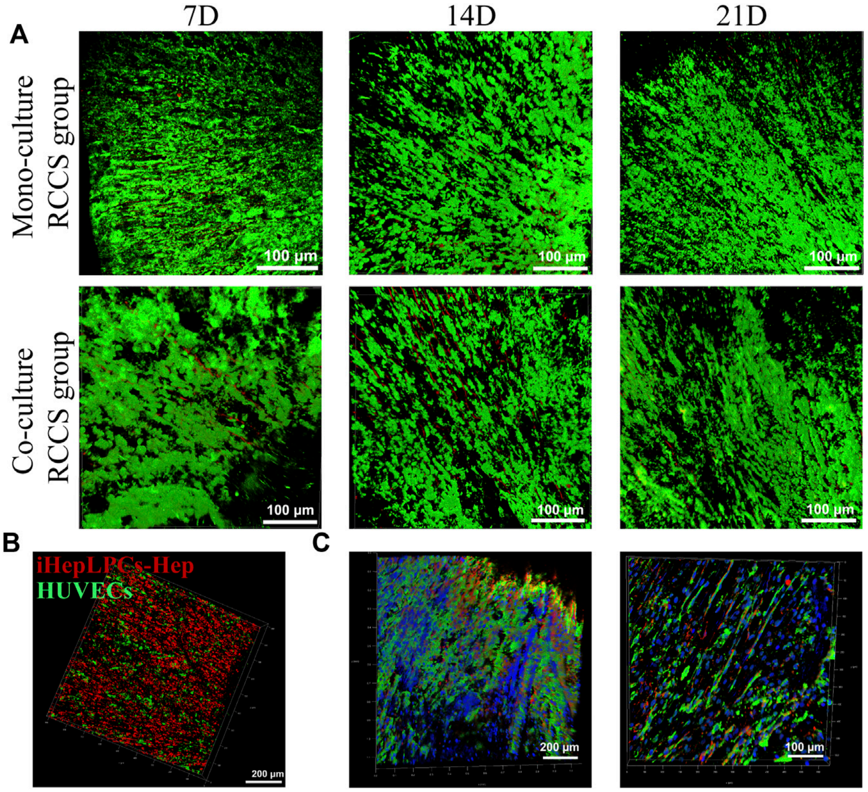

FIGURE 5 | Growth profiles of iHepLPCs on composite SFC scaffolds. The viability staining of both monocultures and co-cultures is shown. Aligned growth pattern of the monocultured or co-cultured cells over time were observed using CLSM **(A)**. Radially aligned hepatocyte and endothelial cell interphase arrangement of 3D co-cultures was revealed using cell-tracker dye staining **(B)** (red, iHepLPC-Heps; green, HUVECs) and IF staining **(C)** (green, ALB-FITC-conjugated secondary antibody-labeled iHepLPC-Heps; red, CD31-Alexa Fluor647-labeled HUVECs; blue, DAPI) under CLSM.

organized morphology after 7 days of culture. Most cells were large, with round nuclei and eosinophilic cytoplasm. After 14 days, local clustering of the cells could be observed, accompanied by disruption of the structural integrity on the scaffold (**Figure 6A**). This indicated that the scaffolds were degrading and replaced by cell-secreted ECM. SEM further revealed the cell distribution on the scaffold surfaces (**Figure 6B**). Although the cells were grown with the directional laminar sheets in a long spindle or polygonal shape with rich ECM secretion, the diverse morphology of the iHepLPCs during maturation led to an indistinguishable morphology of the two cell types.

Subsequently, the ultramicroscopic morphology of the iHepLPC-Heps on SFC scaffolds was characterized using TEM (**Figure 6C**). More ultrastructural characteristics of mature hepatocytes (increased number of mitochondria, endoplasmic reticulum, and appearance of lipid droplets) were displayed in iHepLPC-Heps after 14 days of 3D dynamic culture than in 2D differentiated cells. More importantly, compared with the monoculture RCCS group, co-cultured iHepLPC-Heps exhibited more cell junctions and bile capillary-like structures, indicating improved maturation. This finding suggested that the unique microenvironment, involving both radial scaffold architecture and endothelial cells, promoted the maturation of iHepLPCs.

Functional Gene and Protein Expression Profile of iHepLPC-Heps on the Composite SFC Scaffolds

The transcriptional expression levels of some critical genes for functional hepatocyte differentiation were detected using RT-qPCR, including those encoding secretory proteins (ALB and AAT), multidrug resistance-associated protein 2 (MRP_2) transporters, vital cytochrome P450 (CYP3A4, CYP1A2, CYP2C9, and CYP2D6), some metabolism-related enzymes (CPS-1, UGT1, and G6PC), and HNF4α (**Figure 7A**). Compared with 2D differentiated iHepLPC-Heps, the 3D dynamic cultures exhibited significantly improved transcript expression levels of the genes. Furthermore, a higher expression level with most functional genes was observed in the 3D co-cultured iHepLPC-Heps than in the 3D monocultures. This suggests the importance of endothelial cells in promoting the expression of hepatocyte functional gene *in vitro*. Notably, the expression levels of most genes gradually increased over time, which might benefit their long-

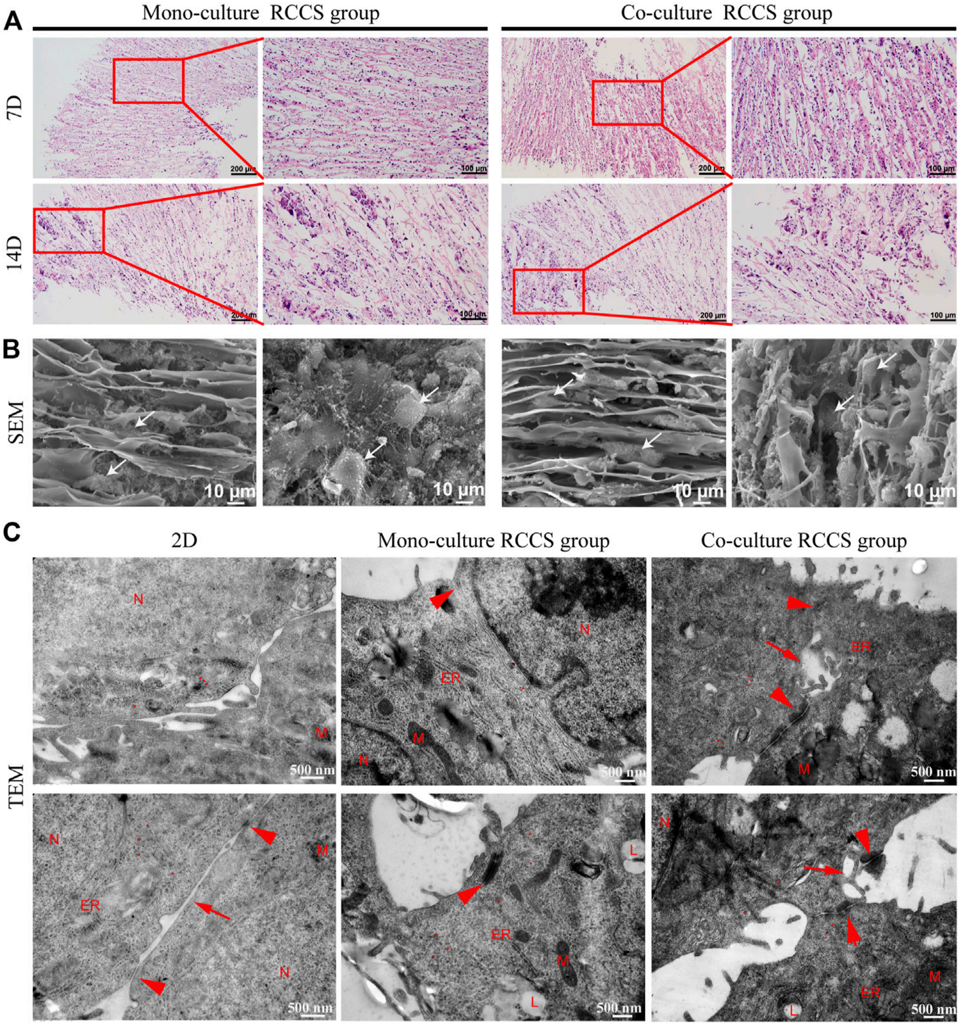

FIGURE 6 | Morphological characteristics of cells on composite SFC scaffolds. H&E staining **(A)** showed that cells displayed a compact but radially organized morphology. Locally clustered cells were observed after 14 days of a dynamic culture. SEM images **(B)** showed the cell growth pattern on the surface of composite SFC scaffolds. Cells (white arrows) exhibited long spindle or polygon shapes and migrated along with the radial pores of scaffolds. Ultramicroscopic TEM images **(C)** indicated the improved maturation of iHepLPC-Heps after 3D dynamic culturing, especially more cell junctions (red arrowheads) and bile canaliculi-like structures (red arrows) were formed in co-cultured iHepLPC-Heps. (Nucleus- N, mitochondria- M, endoplasmic reticulum- ER, lipid droplets- L, red dot-glycogen).

term application in a bioartificial liver support system or drug screening test. IF staining results showed that both groups expressed ALB, CYP3A4, and MRP_2 after 14 days of dynamic culture, although no significant difference was detected, which was consistent with the corresponding gene expression levels (**Figure 7B**).

Functional Evaluation of iHepLPC-Heps on the Composite SFC Scaffolds

The albumin production and urea synthesis in the 3D constructs increased progressively over 3 weeks of culture. Albumin secretion in the co-culture group was significantly higher than that in the 3D monocultures within the first 2 weeks (**Figure 8A**). Compared with the 2D differentiated iHepLPC-Heps, the 3D cultures on the composite SFC scaffolds exhibited elevated levels of urea production, especially co-cultured hepatocytes (**Figure 8B**).

Omeprazole treatment upregulated CYP1A2 expression by 2-fold, 4-fold, and 1-fold in the co-cultures, monocultures, and 2D differentiated cells, respectively (over DMSO-treated controls, $p < 0.05$). Although rifampicin treatment upregulated the expression of CYP3A4 by 1.8-fold in the co-cultures ($p < 0.05$), a small but insignificant upregulation was observed in mono-/2D cultures (over DMSO-treated controls, **Figure 8C**). This finding suggested the role of stromal cells in the enhanced and stable promotion of CYP responses to drugs.

Additionally, more polarized epithelial cells in 3D co-cultures with bile canaliculi-like structures were observed using CDCFDA staining, as evidenced by the increased amount of peri-nuclearly clustered fluorescein instead of

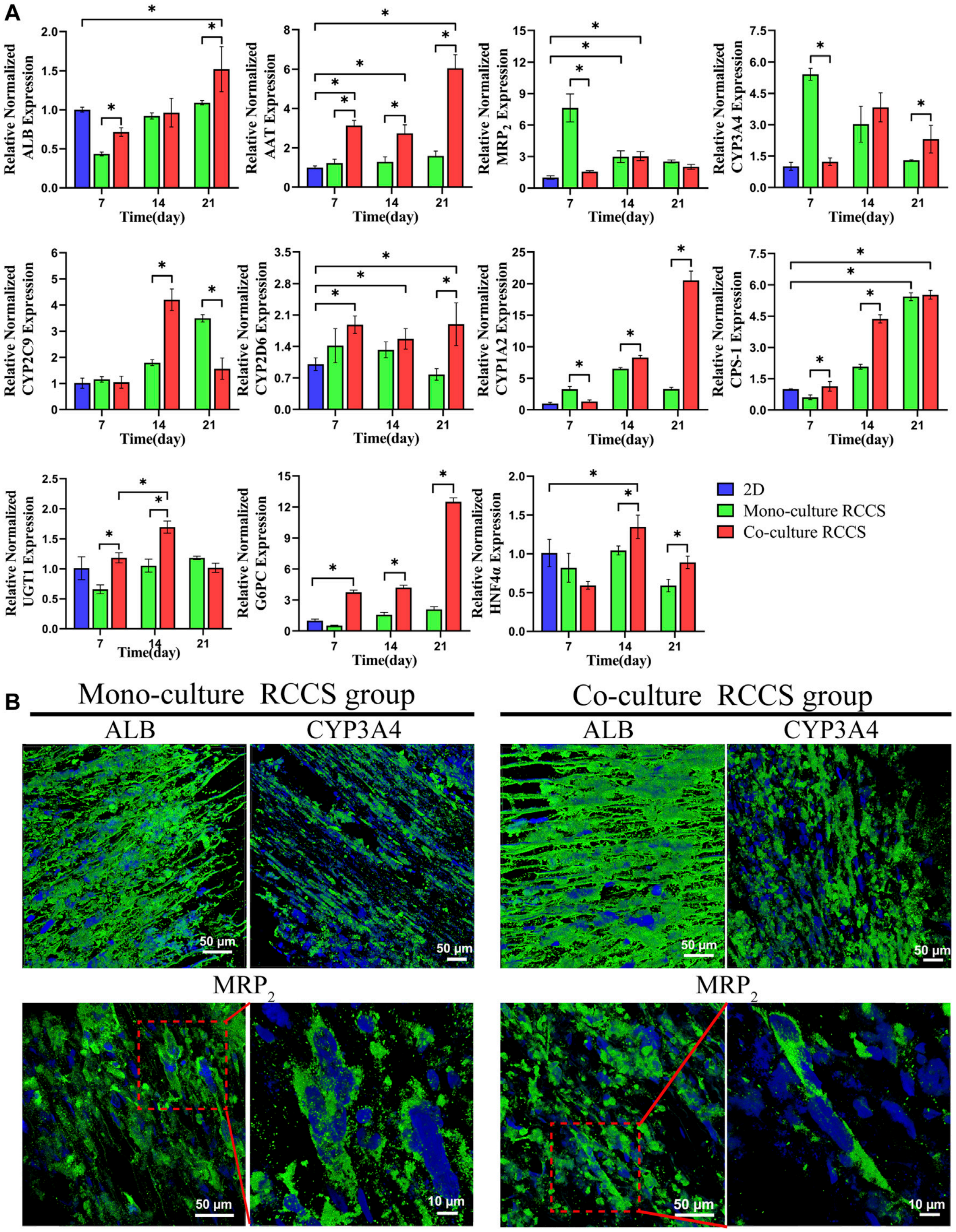

FIGURE 7 | Functional gene and protein expression in different culture conditions using RT-qPCR **(A)** and IF staining **(B)**. Higher functional gene expression was found in the 3D co-cultures than in the 2D cultures and 3D monocultures **(A)**. iHepLPC-Heps in both groups expressed ALB, CYP3A4, and MRP$_2$ after 14 days of culture **(B)**. (*$p < 0.05$).

diffusely distributed fluorescein in the cytoplasm. Although no evident difference was observed, LDL uptake assays showed that 3D cultures could take up LDL (**Figure 8D**). Collectively, these data revealed that iHepLPCs that differentiated in composite SFC scaffolds exhibited functionally mature hepatocyte-like characteristics. Moreover, endothelial cells

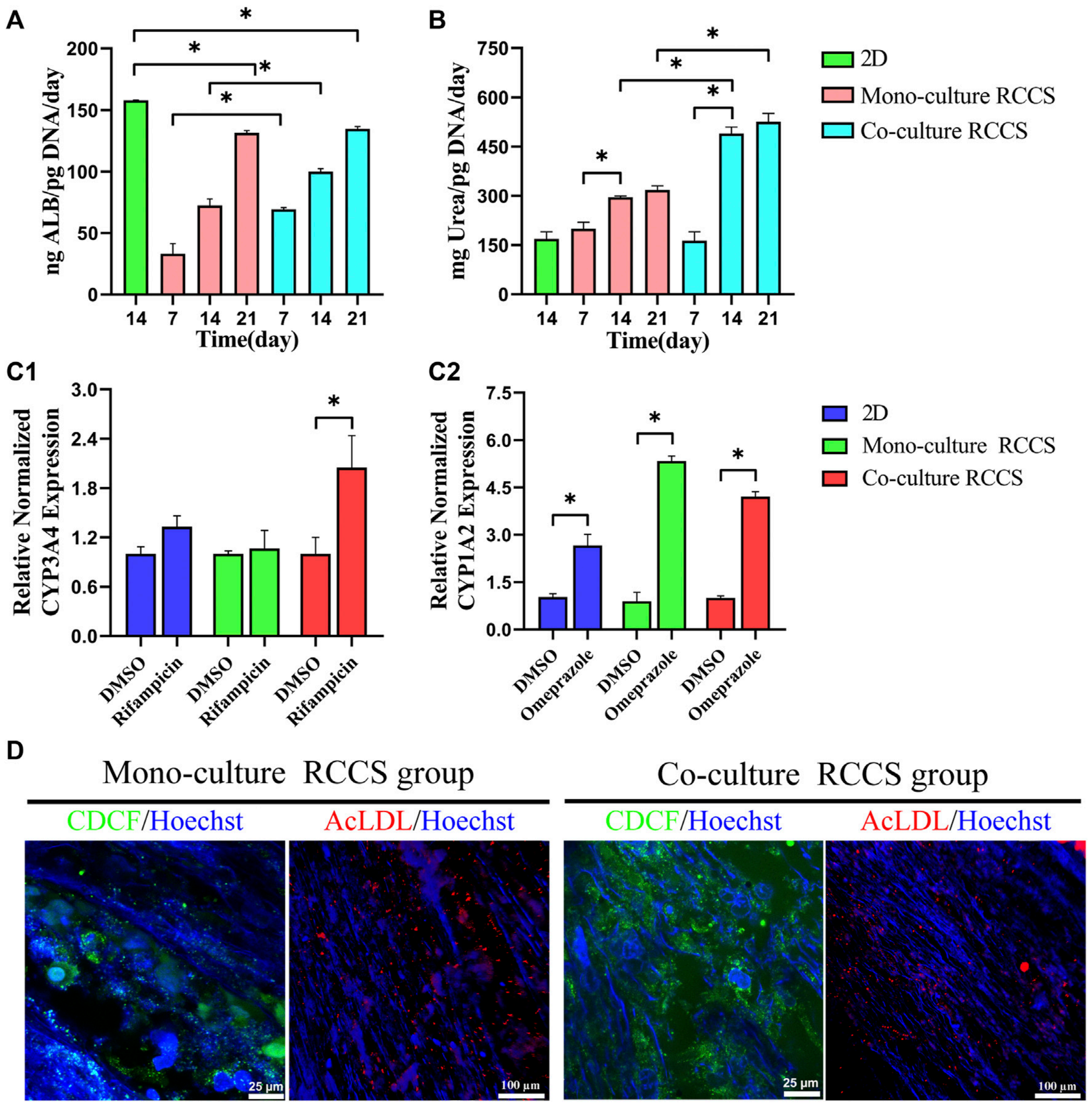

FIGURE 8 | Functional evaluation of iHepLPC-Heps on composite SFC scaffolds. Albumin secretion of different hepatic cultures was assayed using ELISA **(A)**. Urea synthesis of iHepLPC-Heps cultured under different conditions **(B)**. Induction of CYP3A4 **(C1)** and CYP1A2 **(C2)** expression in response to stimulation with omeprazole and rifampicin, assayed using RT-qPCR. Dil-LDL uptake and CDCFDA staining **(D)** of iHepLPC-Heps were examined in both groups. (**p* < 0.05).

could promote and maintain most functions of hepatocytes in direct co-culture.

In Vivo Compatibility of Cell–Scaffold Complex

The morphology and function of the cell–scaffold complex *in vivo* were evaluated. Both monocultures and co-cultures were subcutaneously transplanted into nude mice and acellular SFC scaffolds were used as control. Macroscopically, the incisions healed completely within 1 week without any signs of infection, reddening, or festering. All the implants were complete without degradation and were enveloped by a transparent membrane-like tissue. No evident difference was observed between the cell-loaded and acellular scaffolds. Nevertheless, visible blood vessels extending toward the graft were found, where a dense vascular network was generated after 7 days of implantation. This network is thought to maintain nutrient supply for the epithelial layer of the grafts (**Figure 9A**).

H&E staining results displayed that the cells on the scaffolds were radially organized between the spaces of laminar sheets with large round nuclei and eosinophilic cytoplasm, consistent with the *in vitro* results (**Figure 9B**). Notably, 3D complexes exhibited

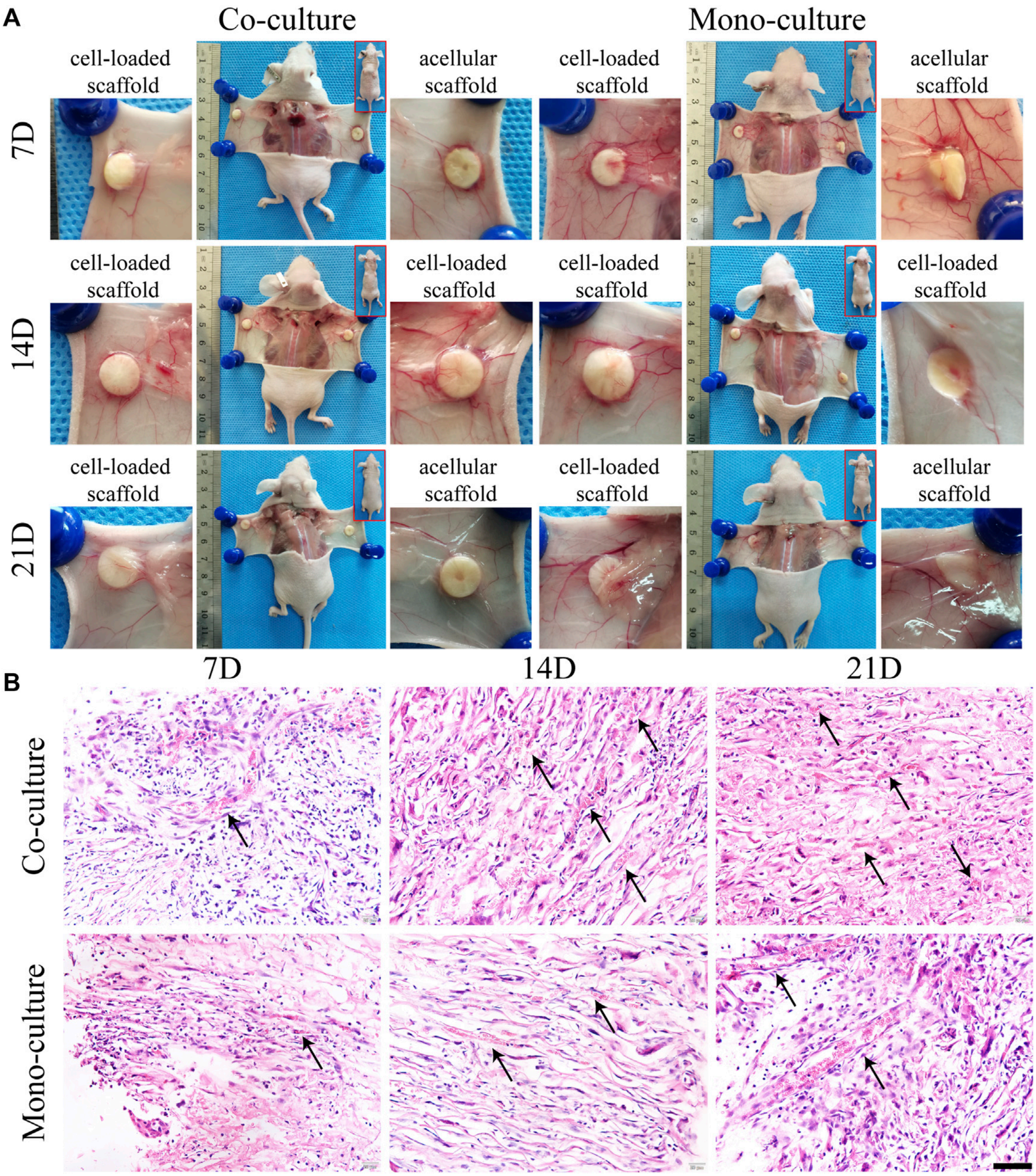

FIGURE 9 | Morphological characterization of cell-loaded cultures after transplantation. General growth morphology of scaffolds in each group was shown at 7, 14, and 21 days after transplantation **(A)**. H&E staining **(B)** showed radially distributed cells in the scaffolds. Host blood vessels (black arrows) grew abundantly within the pores of all cultures, especially the co-cultures. Scale bar, 50 μm.

a biomimetic architecture, with host capillaries radially extending in the pores of SFC scaffolds and aligning to hepatocytes. There were more infiltrated or neovascular capillaries in the co-culture group than that in the monoculture group. However, we failed to detect the integration of human HUVECs in mice capillaries. Nevertheless, our finding showed that endothelial cells were critical in activating angiogenic signaling to promote neovasculogenesis rather than functionally integrating into host capillaries.

Subsequently, the maturity level of the differentiated iHepLPCs was characterized by evaluating the expression of ALB, CYP3A4, and MRP_2 using IHC staining. The expression of ALB, CYP3A4, and MRP_2 increased gradually in both groups with a prolonged transplantation time, showing spontaneous cell differentiation toward iHepLPC-Heps (**Figure 10**). Furthermore, co-cultures had significantly higher ALB, CYP3A4, and MRP_2 expression than the monocultures at all-time points, consistent with the *in vitro* results.

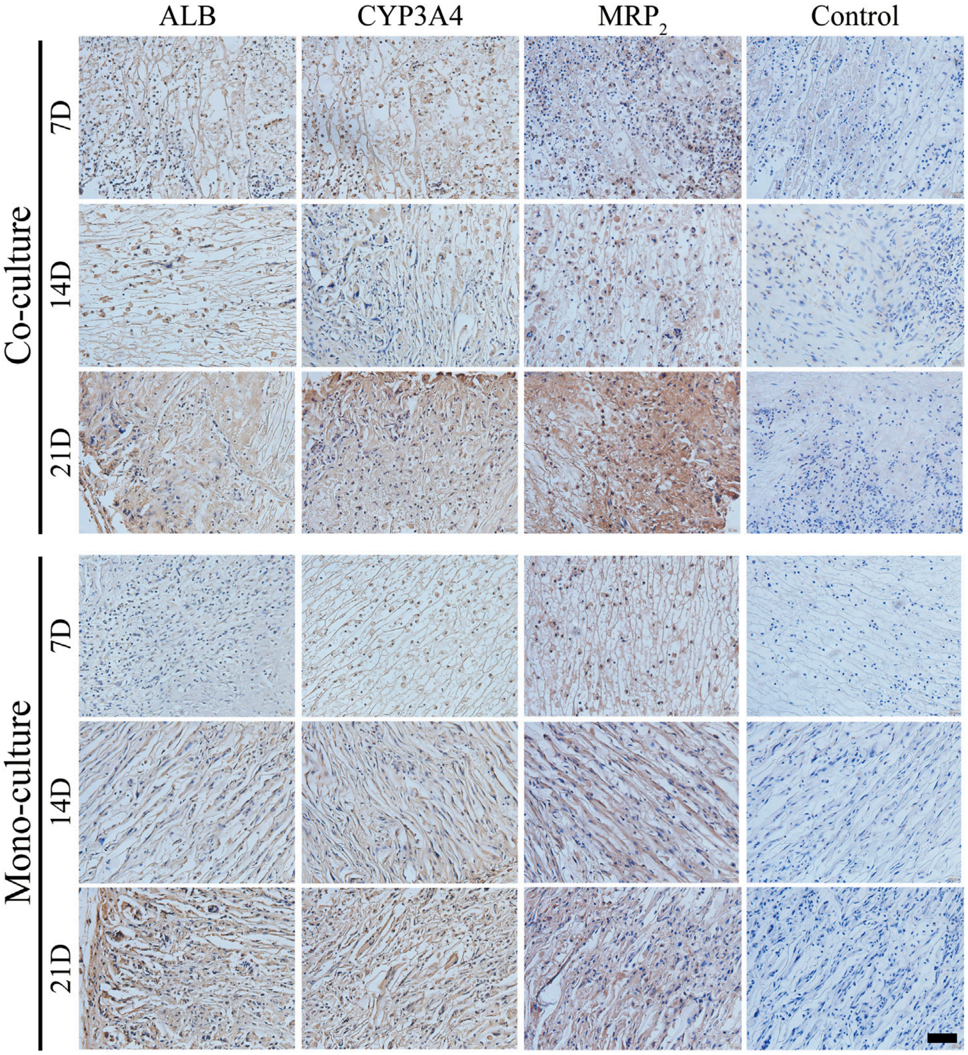

FIGURE 10 | IHC detection of ALB, CYP3A4, and MRP_2 expression in both groups after transplantation. Protein expressions increased gradually over time. Compared with monocultures, the co-culture group showed upregulated expressions at each time point. Scale bar, 50 μm.

DISCUSSION

Recently, increasing evidence pinpoints the importance of matching the performance of biological scaffolds with the *in vivo* parameters of the microenvironment for engineering structural and functionally equivalent hepatic tissue constructs *in vitro* (Luo et al., 2021; Stoppato et al., 2015). Physical properties, such as porosity, water uptake ability, and mechanical properties, are important features of SF porous scaffolds that modulate the biological behavior of cells toward the desired engineered tissue (Kundu et al., 2013), especially the liver, due to its intricate architecture and specific functionality. Previously, we constructed a radially aligned porous SF scaffold and demonstrated its feasibility in the construction of engineered liver lobule-like tissue. However, unsatisfactory physical properties and lack of integrin-mediated cell-binding sites limited its applications. Therefore, we enhanced the physical properties of the scaffold and optimized the construction of 3D-engineered liver models based on the previous model as follows.

First, integrin-mediated cell-binding sites were introduced into the SFC composite hepatic lobule-like scaffolds by incorporating collagen I. Integrin signaling is one of the major factors that regulates cell attachment and initiates downstream signaling for hepatic cellular responses, such as cell survival, proliferation, and cellular functions (Greenhalgh et al., 2019; Weng et al., 2020). Upregulated C3A cell attachment and migration and CYP3A4 expression demonstrated the importance of adding active integrin sites to the scaffold. Moreover, SFC scaffolds displayed better optimized porosity, swelling ratio, and mechanical properties compared to SF scaffolds. Other studies have confirmed the effective improvement of physical performance of SFC hydrogel or electrospun fibers (Buitrago et al., 2018; Maghdouri-White et al., 2014), whereas this is the first study to fabricate SFC porous scaffolds by directional lyophilization. The improvement may be attributed to the increased viscosity of the SF solution when mixed with an unneutralized acidic collagen solution, which altered ice crystal formation (Cho et al., 2012).

Therefore, SFC composite scaffolds provide a new strategy for fabricating a biomimetic liver tissue that structurally and physiologically replicates the human native liver tissue *in vitro*.

Second, primary human hepatocyte (PHH) derived functional liver cells were adopted to facilitate downstream applications for seed cells as they are a prerequisite and key to the success of constructing functional engineered liver tissue. Deficiency in certain liver functions or potential tumorigenicity of hepatocarcinoma cell lines or stem cell-derived hepatocytes is currently one of the major reasons that hinders the application of tissue-engineered livers in drug screening and alternative therapy (Bhatia et al., 2014). However, iHepLPCs converted from PHH could efficiently revert to the mature hepatic state and exhibit enhanced liver-specific functions close to native liver in 3D spheroids culture (Fu et al., 2019; Liu et al., 2021). Moreover, good biocompatibility and the potential for individualized treatment could further be beneficial to the incorporation of functional liver lobule-like tissue we constructed using iHepLPCs into the bioartificial liver to individually benefit patients with liver failure or for the short/long-term hepatotoxicity screening of drugs.

Finally, we used the RCCS bioreactor culture system to dynamically incubate 3D cultures; a more stretched and intact cell morphology was observed and long-term viability was achieved after dynamic culture. Notably, the dynamic nature of the culture system, possessing microgravity, low shear force, and high exchange efficiency of O_2, nutrients, and waste, partly overcomes the shortcomings of a static culture (Li et al., 2009). Studies have demonstrated that long-term culture and promotion of cell viability and proliferation can be achieved using this system (Ferrarini et al., 2013; Zheng et al., 2012). Moreover, especially for hepatocytes cultured *in vitro*, sufficient oxygen supplementation and mass transportation are vital. These results provide the guarantee for applying the hepatic lobule-like tissue as a cell block in biological artificial liver.

Based on the strong influence of endothelial cells on the fate of hepatocytes *in vivo* and *in vitro* (Cuvellier et al., 2021; Ding et al., 2010), we used HUVECs as co-cultured nonparenchymal cells. Compared with the monoculture group, HUVECs promoted maturity of hepatocytes. This finding was consistent with that of our previous work and other studies (Kim et al., 2017; Wang et al., 2022; Ware et al., 2018). However, the mechanisms underlying the positive effect of HUVECs have not been fully elucidated. Besides direct contact, paracrine cytokines secreted by HUVECs have been reported to be involved in hepatocyte function. For example, glial cell line-derived neurotrophic factor was found to activate downstream pathways through the phosphorylation of MET to promote liver functions (Liu et al., 2021). In addition, vascular endothelial growth factor was found to activate PI3K/AKT pathways to promote hepatocyte maturity (Kim et al., 2021; LeCouter, 2003).

A subcutaneous transplantation experiment was performed using nude mice to verify the biocompatibility and biofunctions of hepatic lobule-like cultures *in vivo*. Consistent with the *in vitro* results, the cells migrated within the scaffold. The scaffolds' vascularization occurred rapidly, ensuring the survival of hepatocytes and their further differentiation. The radial pores of the scaffold provided space and guidance for the growth of host blood vessels, forming a highly bionic sinusoid-hepatic plate arrangement with adjacent hepatocytes. Moreover, endothelial cells in the co-culture group resulted in an increased number of host vessels and an expanded distribution range, indicating that HUVECs may play a role in the induction of angiogenesis. Jung, H. R. et al. subcutaneously implanted HUVEC–Huh7 cell spheroids into nude mice. Compared with monocultured 3D Huh7 spheroids, HUVECs induced the formation and maturation of new vessels in Huh7 spheroids (Jung et al., 2017). However, based on our extensive literature search, very few studies have reported the angiogenesis effect of HUVECs *in vivo* based on SF porous scaffolds. Therefore, this study provided a strategy for vascularizing SF porous scaffolds *in vivo* based on 3D-constructed tissue transplantation.

Although the influence of scaffold microarchitecture on cell biological behavior has been demonstrated in various culture models, the exact mechanism is unknown. This is mainly due to the lack of effectively paired scaffolds, wherein one scaffold has highly arranged configurations and the other one does not. Meanwhile, these paired scaffolds should have identical physical properties, such as mechanics or porosity, which are essential because increasing evidence indicates their strong impact on cell behavior. The versatile plasticity and tunable properties of SF favor the fabrication of adaptably matched scaffolds to explore the underlying mechanism. Therefore, SFC composite lobule-like scaffolds with radial configuration and optimized physical performances provide a basis for understanding how the microstructure affects hepatocyte behavior.

CONCLUSION

A bioengineered biomimetic hepatic lobule-like culture was constructed by co-culturing human hepatocytes and endothelial cells on composite SFC scaffolds fabricated by directional freezing and lyophilization. This composite SFC scaffold featured radially aligned lamellar sheets, with physical performances similar to those of the normal liver matrix and with better biocompatibility. The dynamically co-cultured human hepatocytes and endothelial cells in the scaffolds exhibited a biomimetic radially organized interphase arrangement pattern and well-maintained functionality compared with the monoculture *in vitro* and *in vivo*. Thus, this culture system can provide a platform for drug industries or for constructing a functional bioartificial liver unit.

DATA AVAILABILITY STATEMENT

The original contributions presented in the study are included in the article/**Supplementary Files**, further inquiries can be directed to the corresponding author.

ETHICS STATEMENT

The animal study was reviewed and approved by The Animal Care and Use Committee of Dalian Medical University.

AUTHOR CONTRIBUTIONS

LG, LH, and XW contributed to conception and design of the study. LG and YD organized the database. LG and MW performed the statistical analysis. LG wrote the first draft of the manuscript. ZZ, CG, KC, SL, HY, and WL wrote sections of the manuscript. All authors contributed to manuscript revision, read, and approved the submitted version.

FUNDING

This work was supported by the National Key R&D Program of China (2018YFA0108200), the National Natural Science Foundation of China (81173125), and Project of Dalian Ministry of Science and Technology (2022).

ACKNOWLEDGMENTS

The manuscript has been proofread and edited by a professional English editing company- Crimson Interactive (Newark, NJ, United States).

SUPPLEMENTARY MATERIAL

The Supplementary Material for this article can be found online at: https://www.frontiersin.org/articles/10.3389/fbioe.2022.940634/full#supplementary-material

REFERENCES

Bhatia, S. N., Underhill, G. H., Zaret, K. S., and Fox, I. J. (2014). Cell and Tissue Engineering for Liver Disease. *Sci. Transl. Med.* 6 (245), 242s–245s. doi:10.1126/scitranslmed.3005975

Buitrago, J. O., Patel, K. D., El-Fiqi, A., Lee, J.-H., Kundu, B., Lee, H.-H., et al. (2018). Silk Fibroin/collagen Protein Hybrid Cell-Encapsulating Hydrogels with Tunable Gelation and Improved Physical and Biological Properties. *Acta Biomater.* 69, 218–233. doi:10.1016/j.actbio.2017.12.026

Cho, S. Y., Heo, S., and Jin, H.-J. (2012). Controlling Microstructure of Three-Dimensional Scaffolds from Regenerated Silk Fibroin by Adjusting pH. *J. Nanosci. Nanotech.* 12 (1), 806–810. doi:10.1166/jnn.2012.5364

Cuvellier, M., Ezan, F., Oliveira, H., Rose, S., Fricain, J.-C., Langouët, S., et al. (2021). 3D Culture of HepaRG Cells in GelMa and its Application to Bioprinting of a Multicellular Hepatic Model. *Biomaterials* 269, 120611. doi:10.1016/j.biomaterials.2020.120611

Das, P., DiVito, M. D., Wertheim, J. A., and Tan, L. P. (2020). Collagen-I and Fibronectin Modified Three-Dimensional Electrospun PLGA Scaffolds for Long-Term In Vitro Maintenance of Functional Hepatocytes. *Mater. Sci. Eng. C* 111, 110723. doi:10.1016/j.msec.2020.110723

Ding, B.-S., Nolan, D. J., Butler, J. M., James, D., Babazadeh, A. O., Rosenwaks, Z., et al. (2010). Inductive Angiocrine Signals from Sinusoidal Endothelium Are Required for Liver Regeneration. *Nature* 468 (7321), 310–315. doi:10.1038/nature09493

Ferrarini, M., Steimberg, N., Ponzoni, M., Belloni, D., Berenzi, A., Girlanda, S., et al. (2013). Ex-vivo Dynamic 3-D Culture of Human Tissues in the RCCS Bioreactor Allows the Study of Multiple Myeloma Biology and Response to Therapy. *PLoS One* 8 (8), e71613. doi:10.1371/journal.pone.0071613

Fu, G.-B., Huang, W.-J., Zeng, M., Zhou, X., Wu, H.-P., Liu, C.-C., et al. (2019). Expansion and Differentiation of Human Hepatocyte-Derived Liver Progenitor-like Cells and Their Use for the Study of Hepatotropic Pathogens. *Cell Res.* 29 (1), 8–22. doi:10.1038/s41422-018-0103-x

Goczkowski, M., Gobin, M., Hindié, M., Agniel, R., and Larreta-Garde, V. (2019). Properties of Interpenetrating Polymer Networks Associating Fibrin and Silk Fibroin Networks Obtained by a Double Enzymatic Method. *Mater. Sci. Eng. C* 104, 109931. doi:10.1016/j.msec.2019.109931

Greenhalgh, S. N., Matchett, K. P., Taylor, R. S., Huang, K., Li, J. T., Saeteurn, K., et al. (2019). Loss of Integrin αvβ8 in Murine Hepatocytes Accelerates Liver Regeneration. *Am. J. Pathology* 189 (2), 258–271. doi:10.1016/j.ajpath.2018.10.007

Ho, C.-T., Lin, R.-Z., Chen, R.-J., Chin, C.-K., Gong, S.-E., Chang, H.-Y., et al. (2013). Liver-cell Patterning Lab Chip: Mimicking the Morphology of Liver Lobule Tissue. *Lab. Chip* 13 (18), 3578. doi:10.1039/c3lc50402f

Huang, Y., Seitz, D., König, F., Müller, P. E., Jansson, V., and Klar, R. M. (2019). Induction of Articular Chondrogenesis by Chitosan/Hyaluronic-Acid-Based Biomimetic Matrices Using Human Adipose-Derived Stem Cells. *Ijms* 20 (18), 4487. doi:10.3390/ijms20184487

Jung, H.-R., Kang, H. M., Ryu, J.-W., Kim, D.-S., Noh, K. H., Kim, E.-S., et al. (2017). Cell Spheroids with Enhanced Aggressiveness to Mimic Human Liver Cancer In Vitro and In Vivo. *Sci. Rep.* 7 (1), 10499. doi:10.1038/s41598-017-10828-7

Kang, D., Hong, G., An, S., Jang, I., Yun, W. S., Shim, J. H., et al. (2020). Bioprinting of Multiscaled Hepatic Lobules within a Highly Vascularized Construct. *Small* 16 (13), 1905505. doi:10.1002/smll.201905505

Kim, K., Utoh, R., Ohashi, K., Kikuchi, T., and Okano, T. (2017). Fabrication of Functional 3D Hepatic Tissues with Polarized Hepatocytes by Stacking Endothelial Cell Sheets in Vitro. *J. Tissue Eng. Regen. Med.* 11 (7), 2071–2080. doi:10.1002/term.2102

Kim, Y., Kim, Y. W., Lee, S. B., Kang, K., Yoon, S., Choi, D., et al. (2021). Hepatic Patch by Stacking Patient-specific Liver Progenitor Cell Sheets Formed on Multiscale Electrospun Fibers Promotes Regenerative Therapy for Liver Injury. *Biomaterials* 274, 120899. doi:10.1016/j.biomaterials.2021.120899

Kumaran, V., Joseph, B., Benten, D., and Gupta, S. (2005). Integrin and Extracellular Matrix Interactions Regulate Engraftment of Transplanted Hepatocytes in the Rat Liver. *Gastroenterology* 129 (5), 1643–1653. doi:10.1053/j.gastro.2005.08.006

Kundu, B., Rajkhowa, R., Kundu, S. C., and Wang, X. (2013). Silk Fibroin Biomaterials for Tissue Regenerations. *Adv. Drug Deliv. Rev.* 65 (4), 457–470. doi:10.1016/j.addr.2012.09.043

LeCouter, J., Moritz, D. R., Li, B., Phillips, G. L., Liang, X. H., Gerber, H.-P., et al. (2003). Angiogenesis-Independent Endothelial Protection of Liver: Role of VEGFR-1. *Science* 299 (5608), 890–893. doi:10.1126/science.1079562

Li, S., Ma, Z., Niu, Z., Qian, H., Xuan, D., Hou, R., et al. (2009). NASA-approved Rotary Bioreactor Enhances Proliferation and Osteogenesis of Human Periodontal Ligament Stem Cells. *Stem Cells Dev.* 18 (9), 1273–1282. doi:10.1089/scd.2008.0371

Liu, M., Zhang, X., Long, C., Xu, H., Cheng, X., Chang, J., et al. (2018). Collagen-based Three-Dimensional Culture Microenvironment Promotes Epithelial to Mesenchymal Transition and Drug Resistance of Human Ovarian Cancer in Vitro. *RSC Adv.* 8 (16), 8910–8919. doi:10.1039/C7RA13742G

Liu, W.-M., Zhou, X., Chen, C.-Y., Lv, D.-D., Huang, W.-J., Peng, Y., et al. (2021). Establishment of Functional Liver Spheroids from Human Hepatocyte-Derived Liver Progenitor-like Cells for Cell Therapy. *Front. Bioeng. Biotechnol.* 9, 738081. doi:10.3389/fbioe.2021.738081

Luo, Y., Kang, K. B., Sartaj, R., Sun, M. G., Zhou, Q., Guaiquil, V. H., et al. (2021). Silk Films with Nanotopography and Extracellular Proteins Enhance Corneal Epithelial Wound Healing. *Sci. Rep.* 11 (1), 8168. doi:10.1038/s41598-021-87658-1

Maghdouri-White, Y., Bowlin, G. L., Lemmon, C. A., and Dréau, D. (2014). Mammary Epithelial Cell Adhesion, Viability, and Infiltration on Blended or Coated Silk Fibroin-Collagen Type I Electrospun Scaffolds. *Mater. Sci. Eng. C* 43, 37–44. doi:10.1016/j.msec.2014.06.037

Martinez-Hernandez, A., and Amenta, P. S. (1993). The Hepatic Extracellular Matrix. *Vichows Arch. A Pathol. Anat.* 423 (1), 1–11. doi:10.1007/BF01606425

Rico-Llanos, G. A., Borrego-González, S., Moncayo-Donoso, M., Becerra, J., and Visser, R. (2021). Collagen Type I Biomaterials as Scaffolds for Bone Tissue Engineering. *Polymers* 13 (4), 599. doi:10.3390/polym13040599

Ruoslahti, E., and Pierschbacher, M. D. (1987). New Perspectives in Cell Adhesion: RGD and Integrins. *Science* 238 (4826), 491–497. doi:10.1126/science.2821619

Serna-Márquez, N., Rodríguez-Hernández, A., Ayala-Reyes, M., Martínez-Hernández, L. O., Peña-Rico, M. Á., Carretero-Ortega, J., et al. (2020). Fibrillar Collagen Type I Participates in the Survival and Aggregation of

Primary Hepatocytes Cultured on Soft Hydrogels. *Biomimetics* 5 (2), 30. doi:10.3390/biomimetics5020030

Stoppato, M., Stevens, H. Y., Carletti, E., Migliaresi, C., Motta, A., and Guldberg, R. E. (2015). Influence of Scaffold Properties on the Inter-relationship between Human Bone Marrow Derived Stromal Cells and Endothelial Cells in Pro-osteogenic Conditions. *Acta Biomater.* 25, 16–23. doi:10.1016/j.actbio.2015.07.013

Uygun, B. E., Soto-Gutierrez, A., Yagi, H., Izamis, M.-L., Guzzardi, M. A., Shulman, C., et al. (2010). Organ Reengineering through Development of a Transplantable Recellularized Liver Graft Using Decellularized Liver Matrix. *Nat. Med.* 16 (7), 814–820. doi:10.1038/nm.2170

Wang, X., Guo, C., Guo, L., Wang, M., Liu, M., Song, Y., et al. (2022). Radially Aligned Porous Silk Fibroin Scaffolds as Functional Templates for Engineering Human Biomimetic Hepatic Lobules. *ACS Appl. Mat. Interfaces* 14 (1), 201–213. doi:10.1021/acsami.1c18215

Wang, X., Sun, L., Maffini, M. V., Soto, A., Sonnenschein, C., and Kaplan, D. L. (2010). A Complex 3D Human Tissue Culture System Based on Mammary Stromal Cells and Silk Scaffolds for Modeling Breast Morphogenesis and Function. *Biomaterials* 31 (14), 3920–3929. doi:10.1016/j.biomaterials.2010.01.118

Wang, Z., Li, W., Jing, H., Ding, M., Fu, G., Yuan, T., et al. (2019). Generation of Hepatic Spheroids Using Human Hepatocyte-Derived Liver Progenitor-like Cells for Hepatotoxicity Screening. *Theranostics* 9 (22), 6690–6705. doi:10.7150/thno.34520

Ware, B. R., Durham, M. J., Monckton, C. P., and Khetani, S. R. (2018). A Cell Culture Platform to Maintain Long-Term Phenotype of Primary Human Hepatocytes and Endothelial Cells. *Cell. Mol. Gastroenterology Hepatology* 5 (3), 187–207. doi:10.1016/j.jcmgh.2017.11.007

Watanabe, M., Yano, K., Okawa, K., Yamashita, T., Tajima, K., Sawada, K., et al. (2019). Construction of Sinusoid-Scale Microvessels in Perfusion Culture of a Decellularized Liver. *Acta Biomater.* 95, 307–318. doi:10.1016/j.actbio.2018.12.042

Weng, Y., Lieberthal, T. J., Zhou, V. X., Lopez-Ichikawa, M., Armas-Phan, M., Bond, T. K., et al. (2020). Liver Epithelial Focal Adhesion Kinase Modulates Fibrogenesis and Hedgehog Signaling. *JCI Insight* 5 (20), e141217. doi:10.1172/jci.insight.141217

Willemse, J., Verstegen, M. M. A., Vermeulen, A., Schurink, I. J., Roest, H. P., van der Laan, L. J. W., et al. (2020). Fast, Robust and Effective Decellularization of Whole Human Livers Using Mild Detergents and Pressure Controlled Perfusion. *Mater. Sci. Eng. C* 108, 110200. doi:10.1016/j.msec.2019.110200

Ya, S., Ding, W., Li, S., Du, K., Zhang, Y., Li, C., et al. (2021). On-Chip Construction of Liver Lobules with Self-Assembled Perfusable Hepatic Sinusoid Networks. *ACS Appl. Mat. Interfaces* 13 (28), 32640–32652. doi:10.1021/acsami.1c00794

Zheng, H., Tian, W., Yan, H., Yue, L., Zhang, Y., Han, F., et al. (2012). Rotary Culture Promotes the Proliferation of MCF-7 Cells Encapsulated in Three-Dimensional Collagen-Alginate Hydrogels via Activation of the ERK1/2-MAPK Pathway. *Biomed. Mat.* 7 (1), 015003. doi:10.1088/1748-6041/7/1/015003

Conflict of Interest: The authors declare that the research was conducted in the absence of any commercial or financial relationships that could be construed as a potential conflict of interest.

frontiers | Frontiers in Bioengineering and Biotechnology

ORIGINAL RESEARCH
published: 11 July 2022
doi: 10.3389/fbioe.2022.934151

Tumor Cell-Specific and Lipase-Responsive Delivery of Hydrogen Sulfide for Sensitizing Chemotherapy of Pancreatic Cancer

Libing Tian[1], Rui Pei[1], Xiaojun Zhang[1], Kun Li[1], Yuting Zhong[1], Yougen Luo[2], Shu-Feng Zhou[1]* and Lichan Chen[1]**

[1]College of Chemical Engineering, Huaqiao University, Xiamen, China, [2]Department of Basic Medical Science, Jiangsu Vocational College of Medicine, Yancheng, China

The inability of small molecule drugs to diffuse into tumor interstitium is responsible for the relatively low effectiveness of chemotherapy. Herein, a hydrogen sulfide (H_2S) gas–involved chemosensitization strategy is proposed for pancreatic cancer treatment by developing a tumor-specific lipase-responsive nanomedicine based on aptamer-conjugated DATS/Dox co-loaded PCL-*b*-PEO micelle (DA/D@Ms-A). After receptor-mediated endocytosis and subsequent digestion of PCL blocks by intracellular lipase, the nanomedicine releases Dox and DATS, which then react with intracellular glutathione to produce H_2S. The cytotoxicity result indicates that H_2S can enhance Dox chemotherapy efficiency owing to the synergetic therapeutic effect of Dox and H_2S. Moreover, the nanomedicine is featured with well tumor penetration capability benefitting from the targeting ability of aptamers and high *in vivo* biocompatibility due to the high density of PEO and biodegradable PCL. The nanomedicine capable of synergetic gas-chemotherapy holds great potential for pancreatic cancer treatment.

Keywords: synergetic gas-chemotherapy, targeted drug delivery, pancreatic cancer, micelles, H_2S

Edited by:
Junchao Wei,
Nanchang University, China

Reviewed by:
Jinjin Chen,
Tufts University, United States
Dan Shao,
South China University of Technology, China

****Correspondence:***
Lichan Chen
lchen@hqu.edu.cn
Shu-Feng Zhou
szhou@hqu.edu.cn
Yougen Luo
lyougen@163.com

Specialty section:
This article was submitted to Biomaterials,
a section of the journal
Frontiers in Bioengineering and Biotechnology

Received: *02 May 2022*
Accepted: *08 June 2022*
Published: *11 July 2022*

Citation:
Tian L, Pei R, Zhang X, Li K, Zhong Y, Luo Y, Zhou S-F and Chen L (2022) Tumor Cell-Specific and Lipase-Responsive Delivery of Hydrogen Sulfide for Sensitizing Chemotherapy of Pancreatic Cancer.
Front. Bioeng. Biotechnol. 10:934151.
doi: 10.3389/fbioe.2022.934151

INTRODUCTION

Pancreatic cancer is one of the most malignant cancers with high mortality (Sung et al., 2021) since pancreatic malignancies are difficult to diagnose in the early stage and only a few of them are resectable (Kamisawa, Wood, Itoi, & Takaori, 2016; Goess & Friess, 2018). Chemotherapy is one of the treatment choices for pancreatic cancer patients who are not surgical candidates (Kamisawa et al., 2016). Although the chemotherapeutic drugs such as gemcitabine and doxorubicin (Dox) have good anticancer activity towards pancreatic cancer, the overall chemotherapeutic outcome is sometimes not ideal due to the limitations of the small molecular drugs including short circulation half-life and poor water solubility associated nonspecific off-target effects (Lohse & Brothers, 2020). Targeted drug delivery systems provide an excellent solution to these limitations (Su, Yang, Gao, Liu, & Li, 2020; F.; Yang et al., 2011). A targeted drug delivery system usually consists of both a stimuli-responsive drug nanocarrier and a targeting moiety. The targeting moiety allows for selective accumulation of the nanocarrier at target sites, and the stimulus-response enables drug release from the nanocarrier controllable, thus achieving enhanced chemotherapeutic efficacy while reducing side effects. Many efforts have been made to develop various targeted drug delivery systems, but the chemotherapeutic efficacy is still relatively low due to the inability of small molecule drugs to diffuse into tumor interstitium.

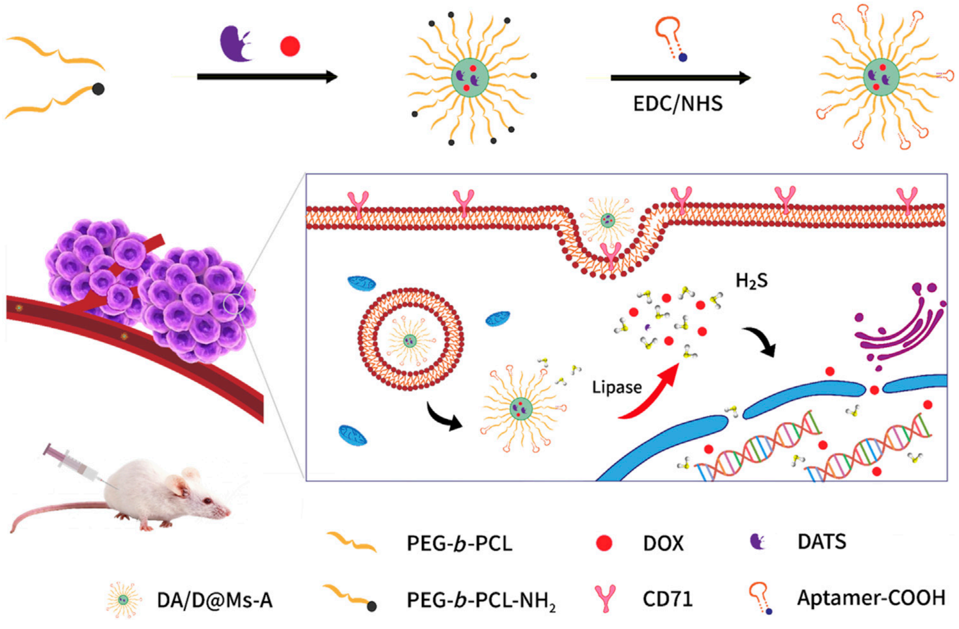

FIGURE 1 | Schematic illustration of the working mechanism of aptamer targeting micelles for synergetic chemo-H_2S gas therapy.

Gas-involved cancer therapy has attracted intense attention in recent years due to its biosafety and capability to sensitize current anticancer modalities such as chemotherapy, radiotherapy, immunotherapy, photodynamic therapy, photothermal therapy, ultrasound therapy, and sonodynamic therapy (L. C. Chen, Zhou, Su, & Song, 2019; Yu, Hu, & Chen, 2018). The sensitization is usually achieved *via* the following mechanisms: 1) the capability of gas molecules to diffuse freely through the cell membrane and into the tumor depth region (Mathai et al., 2009; Riahi & Rowley, 2014), 2) inhibiting the cancer cells survival with appropriate gas concentration by reversing the Warburg effect (Szabo, 2016). Hydrogen sulfide (H_2S), an important gasotransmitter in human health and disease, has been found to exert dose-dependent functions in cancer biology ranging from cytoprotective to cytotoxic effects (Szabó, 2007). The millimolar concentration of H_2S promotes cancer cell apoptosis by inhibition of mitochondrial activity, activation of the endoplasmic reticulum stress response, and elevation of intracellular reactive oxygen species concentration (Szabó, 2007).

In this work, we hypothesize that synergetic H_2S-chemotherapy can promote chemotherapeutic efficacy toward pancreatic cancer. To test the hypothesis, a pancreatic tumor-specific lipase-responsive nanomedicine is firstly prepared based on aptamer-conjugated small molecule chemotherapeutic drug and H_2S prodrug coloaded micelles (**Figure 1A**). The micelles are constructed by self-assembly of amphiphilic diblock copolymers poly(ε-caprolactone)-block-poly(ethylene oxide) (PCL-*b*-PEO) and amino terminal PCL-*b*-PEO (PCL-*b*-PEO-NH_2) for their FDA approval, biocompatibility and biodegradability by endogenous lipase that is highly expressed in pancreatic cancer. The co-loading of drugs for synergetic H_2S-chemotherapy is achieved by simultaneous encapsulation of chemotherapeutic drug Dox and H_2S prodrug diallyl trisulfide (DATS) in micelles during self-assembly of the copolymers *via* hydrophobic interaction between PCL blocks and the drugs. The surface functionalization of the micelles is realized by conjugating the carboxyl terminal XQ-2d ssDNA aptamer against CD71 (Wu et al., 2019), a transferrin receptor highly expressed on the surface of pancreatic cancer cells, onto the amino terminal of PEO blocks *via* amidation reaction. The morphology and drug-loading efficiency of the micelles are investigated followed by their targeting and penetration capability towards pancreatic cancer cells and multicellular spheroids. By treating pancreatic cancer cells with the micelles, the micelles enter into the cells by CD71 receptor-mediated endocytosis, and the PCL blocks in the micelles are digested by intracellular lipase to release Dox and DATS (Li et al., 2002), which then reacts with intracellular glutathione to produce H_2S (Liang, Wu, Wong, & Huang, 2015) (**Figure 1B**). The therapeutic efficacy of the micelles evaluated by the cell counting kit-8 (CCK-8) assay demonstrates that H_2S indeed enhances the chemotherapeutic efficacy of Dox in pancreatic cancer cells. The biocompatibility of the micelles is further analyzed in healthy mice. The nanomedicine capable of synergetic gas-chemotherapy holds a great promising prospect for improving tumor therapeutic efficacy.

MATERIALS AND METHODS

Materials

Dimethyl sulfoxide (DMSO), triethylamine (TEA), N-hydroxy-succinimide (NHS), N-ethyl-N′-(3-dimethyl-aminopropyl) carbodiimide (EDC), and diallyl trisulfide (DATS) were purchased from Alfa Aesar. Lipase from *Pseudomonas cepacia*

(38.6 U/mg) was bought from Sigma. The amphiphilic diblock copolymers poly(ε-caprolactone)-block-poly(ethylene glycol) without and with a functional amino group, PCL_{5k}-*b*-$PEO_{5k,}$ and PCL_{5k}-*b*-PEO_{5k}-NH_2, were obtained from Ruixi Bio-Tech Co., Ltd. (Xi'an, China). Dialysis bags with various molecular weights cut off were from Viskase. Human pancreatic cancer cells (Panc-1) and human liver cancer cells (HepG2) were ordered from Shanghai Institute of Biological Sciences, Chinese Academy of Sciences. Phosphate buffer solution (PBS), cell culture medium (dulbecco's modified eagle medium, DMEM), x100 penicillin-streptomycin solution, Trypsin/EDTA solution, and hematoxylineosin (HE) were purchased from Shanghai Peiyuan Bio-Tech Co., Ltd. Fetal calf serum (FBS) was received from Gibco Company (United States). Doxorubicin (DOX), cell counting kit-8, diaminophenylindole (DAPI), Hoechst 33258, propidium iodide (PI), and annexin V-FITC were procured from Solarbio (Beijing, China). Washington State Probe-1 (WSP-1) for fluorescence imaging of H_2S release in living cells was from Maokang Bio-Tech Co. Ltd. (Shanghai, China). KM mice (SPF grade, 25 g, half male and half female) were ordered from the Fuzhou Wushi laboratory animal center (Fujian, China). All chemicals were used as received. Ultrapure water with a resistivity of 18.2 MΩ (Millipore) was used throughout this work. The carboxyl modified XD-2d aptamer against CD71 was obtained from Sangon Biotech (Shanghai, China), and its base sequence was shown as follows: 5′-COOH-ACT CAT AGG GTT AGG GGC TGC TGG CCA GAT ACT CAG ATG GTA GGG TTA CTA TGA GC-3′.

Characterizations

Transmission electron microscopy (TEM) images of micelles were acquired on a Japan Hitachi HT7700 electronic microscope by negatively staining the micelles with 2.0% phosphotungstic acid. The hydrodynamic diameter and zeta potential of micelles were determined using a dynamical light scattering (DLS) system (NanoBook Omni Instrument, United States). UV-vis spectra were recorded with a UV-2450 UV-vis spectrometer (Shimadzu, Japan). Fluorescent images were captured on a Leica TCS SP8 confocal laser scanning microscopy (CLSM) (Leica, Germany). Cell apoptosis was measured by a BD FACS Melody flow cytometer.

Preparation of Aptamer-Conjugated Drug-Loaded Micelles

1 ml DMSO was subsequently added with 8 mg PCL-*b*-PEO, 2 mg PCL-*b*-PEO-NH_2, 5 mg DOX and/or 5 mg DATS, and 10 μl TEA for neutralization. The solution was stirred at room temperature for 4 h. After complete dissolution, the solution was dropwise added into 10 ml water with gentle stirring for 8 h to allow the formation of drug-loaded micelles. The solution was then dialyzed using cellulose dialysis membranes (MW cut off ~14 kDa) against water for 3 days to remove the residual organic solvent and free doxorubicin and/or DATS. The as-obtained micelles were filtrated against a 0.22 μm filter membrane and stored in a 4°C refrigerator for later use. The blank micelles, DOX-loaded micelles, DATS-loaded micelles, and DOX and DATS co-loaded micelles were designated as BMs, D@Ms, DA@Ms, and DA/D@Ms, respectively.

The micelles were further conjugated with the aptamer *via* an amidation reaction (Tian, Pei, Zhong, Ji, & Zhou, 2020). Briefly, 1 mg EDC, 1 mg NHS, and 10 OD carboxyl modified aptamer were dissolved in 5 ml water and reacted for 2 h to activate the carboxyl group of the aptamer, then added with the micelles above and reacted for 72 h. The aptamer-conjugated micelles were obtained after dialysis using cellulose dialysis membranes (MW cut off ~20 kDa) against water for 3 days. Aptamer-conjugated DOX and DATS co-loaded micelles were designated as DA/D@Ms-A. The stability of the micelles was investigated by measurement of their zeta potentials after suspending in PBS and full medium (DMEM supplemented with 10% FBS and 1% penicillin-streptomycin) for 48 h.

The drug loading efficiency was defined as the weight percentage of the drug in the micelles and quantified by measuring the absorbance of DOX at 480 nm and DATS at 354 nm using a UV-vis spectrophotometer. Typically, the freeze-dried drug-loaded micelles were dissolved in DMSO for UV-vis measurement. The drug content was determined by the calibration curve, which was obtained with various concentrations of DOX or DATS in the DMSO solution.

In Vitro Lipase Responsive Drug Release From the Micelles

The stimuli-responsive release profiles of drugs from the micelles were studied at 37°C in PBS with different concentrations of lipase. Briefly, 2 ml 1 mg/ml D@Ms in 10 mM pH 7.4 PBS with 0.2 mg/ml and 1 mg/ml lipase was transferred into two dialysis bags (MW cut off ~10 kDa), which were then immersed into 4 ml of the release media (10 mM pH 7.4 PBS), respectively. At selected time intervals, the release media was removed for UV-vis analysis and replaced with fresh release media. Dox concentration was calculated based on the absorbance intensity at 480 nm. In the release profiles describing drug-release behavior, the cumulative release percentages of drugs from micelles were plotted against time. The percentage of cumulative release was calculated according to the formula: cumulative release percentage (%) $= 2 \times \frac{\Sigma C_n}{W_0} \times 100\%$, where C_n and W_0 refer to the Dox concentration of the n time collected release media and the total Dox amount in micelles. The release experiments were conducted in triplicate.

Fluorescence Imaging of H_2S Release From the Micelles in Living Cells

Panc-1 cells were seeded in a 35 mm confocal dish at 1.0×10^5 cells per well, and cultured with a full medium in a humidified atmosphere of 5% CO_2 at 37°C. When the cells grew to about 70%, the medium was removed, and a 1.0 ml fresh serum-free medium containing 0.01 mg/ml of DA@Ms and DA@Ms-A were then added and incubated for 2 and 4 h, respectively. After that, the cells were washed with PBS, incubated with a 15 μM WSP-1 probe in PBS for 40 min, then washed with PBS three times and added with 1 ml PBS. The generation of H_2S was observed immediately by CLSM with an excitation wavelength fixed at 488 nm.

Selective Cellular Uptake and Penetration Capability of the Micelles

Panc-1 cells and HepG2 cells were seeded in a 35 mm confocal dish at 1.0×10^5 cells per well, and cultured with a full medium at a humidified atmosphere of 5% CO_2 at 37°C. When the cells grew to about 70%, the medium was removed, and a 1.0 ml fresh serum-free medium containing 0.01 mg/ml of DA@Ms and DA@Ms-A were then added and incubated for 0.5, 1, and 2 h, respectively. After that, the cells were stained with DAPI according to the instructions provided by the manufacturer, washed with PBS three times, and added with 1 ml PBS. The targeting efficiency of the micelles was observed immediately by CLSM with excitation wavelength fixed at 488 nm for the Dox channel and 405 nm for the DAPI channel.

3D cell spheroids were cultured to investigate the penetration capability of the micelles. In brief, 10 ml of 1.5 w/v% hot agarose solution was added to a 25 ml dish. After cooling down, the semisolid agarose coating provided a non-adherent surface preventing cellular adhesion. 1.0×10^6 Panc-1 cells in 15 ml full medium was transferred to the dish, and cultured for 4 days to generate spheroids. The spheroids were collected by centrifugation, washed with PBS, and resuspended in a 1 ml serum-free medium containing 0.01 mg/ml DA/A@Ms and DA/D@Ms-A, respectively. After incubation for 4, 12, and 24 h, the spheroids were washed with PBS three times and then observed by CLSM Z-stack scanning with excitation wavelength fixed at 488 nm.

Cytotoxicity Evaluation

Panc-1 cells were seeded in 96-well plates with 1×10^4 cells per well, and cultured with a full medium for 24 h. Then the cells were treated with DMEM medium containing 0.1 mg/ml BMs, D@Ms, DA@Ms, DA/D@Ms, DA/D@Ms-A and Dox for 72 h, 0.05 mg/ml Dox for 36 h then 0.05 mg/ml DATS for 36 h, and 0.05 mg/ml DATS for 36 h then 0.05 mg/ml Dox for 36 h, respectively. Cell viability was determined with CCK-8 assay according to the instructions provided by the manufacturer. The cell viability was calculated according to the formula: cell viability $= \frac{OD_{450}^{Treat\ group} - OD_{450}^{Blank\ group}}{OD_{450}^{Control\ group} - OD_{450}^{Blank\ group}} \times 100\%$.

To test apoptosis by Hoechst 33258, Panc-1 cells were seeded in a 35 mm confocal dish at 1.0×10^6 cells per well, cultured with a full medium for 24 h, and then cultured with serum-free medium containing 0.1 mg/ml micelles for 24 h. The cells were stained by Hoechst 33258 for 30 min, washed three times with PBS, added with 1 ml PBS, and then observed by CLSM with excitation wavelength fixed at 405 nm.

To quantitate apoptosis, Panc-1 cells were seeded in 12-well plates with 1.0×10^6 cells per well, cultured with a full medium for 24 h, and then treated with serum-free medium containing 0.1 mg/ml micelles for 24 h. The collected cells were washed twice with cold PBS and then resuspended in 0.5 ml PBS. The cells were then co-stained by PI and annexin V-FITC and analyzed by flow cytometry.

Biosafety Evaluation of the Micelles

Forty-eight mice were divided into six groups, including a control, BMs, DA@Ms, D@Ms, DA/D@Ms, and DA/D@Ms-A group. The samples (0.1 ml of 1 mg/ml micelle suspension or sterile PBS as control) were injected into the abdominal cavity of each mouse every other day. The body weight of mice was recorded every other day, and the clinical manifestations and fatalities were observed daily. After 2 weeks, the heart, liver, spleen, lung, and kidney were dissected, rinsed with PBS, fixed in 4% paraformaldehyde, then subjected to paraffin section, HE staining, and histopathological examination.

RESULTS AND DISCUSSION

Preparation and Characterization of Aptamer-Conjugated Drug-Loaded Micelles

The drug-loaded micelles were prepared by simultaneous encapsulation of Dox and DATS in micelles during self-assembly of the diblock copolymers PCL-*b*-PEO and PCL-*b*-PEO-NH_2. The aptamer functionalization of the drug-loaded micelles was realized by the covalent binding of the carboxyl terminal XD-2d aptamer to the amino terminal micelles through an amidation reaction. The hydrodynamic size of the micelles was characterized by DLS measurement. As shown in **Table 1**, the hydrodynamic size of blank micelles (BMs) is ca. 87.68 nm; after drug loading, the sizes of the micelles are increased to 178.83 nm for Dox loaded micelles (D@Ms), 176.68 nm for DATS loaded micelles (DA@Ms), and 195.95 nm for DATS and Dox coloaded micelles (DA/D@Ms). The micelles size increment after drug loading is because the hydrophobic DOX and DATS change the hydrophobic bonds in the micellar core and thus increase the packing density and the size of the hydrophobic micellar core. Notably, after aptamer conjugation to the surface of DA/D@Ms through amidation reaction, the size of the micelles is further increased to 209.80 nm, indicating the successful formation of aptamer modified DA/D@Ms (DA/D@Ms-A). The size distribution and morphology of the micelles were further investigated by TEM. As shown in **Figure 2**, the micelles with and without drug loading are near-spherical in shape and are monodisperse particles with high uniformity; and the particle sizes are gradually increased after drug loading and aptamer conjugation, that is, 76, 75, 146, and 163 nm for D@Ms, DA@Ms, DA/D@Ms, and DA/D@Ms-A, respectively, agreeing well with the results obtained from DLS measurement. The sizes of the micelles obtained from TEM are smaller than those obtained from DLS measurement. This is because the collapse in the hydrophilic layer of the micelles during TEM sample preparation leads to reduced particle sizes of the micelles.

The change in the zeta potential of the micelles was also recorded to monitor the surface decoration. As shown in **Table 1**, the zeta potential of the micelles in ultrapure water shows a slight change after drug loading but significantly increases after aptamer conjugation, indicating that aptamer modification could increase the stability of the micelles. To examine their stability in different

TABLE 1 | Characterization of the micelles.

Micelles	DLS (nm)	Zeta potential (mV)			Drug-loading efficiency (%)
		H_2O[a]	PBS[a]	Full medium[a,b]	
BMs	87.68 ± 3.52	−18.74	−12.90	−13.35	-
D@Ms	178.83 ± 4.07	−20.74	−14.40	−15.91	10.34
DA@Ms	176.68 ± 5.48	−19.19	−14.99	−14.28	9.06
DA/D@Ms	195.95 ± 5.89	−21.88	−15.75	−16.58	16.32
DA/D@Ms-A	209.80 ± 6.07	−23.73	−16.80	−30.48	17.83

[a] *Zeta potential was measured after suspending the micelles in the solvents for 48 h. All data presented were the average of three parallel assays.*

[b] *Full medium: DMEM supplemented with 10% FBS and 1% penicillin-streptomycin.*

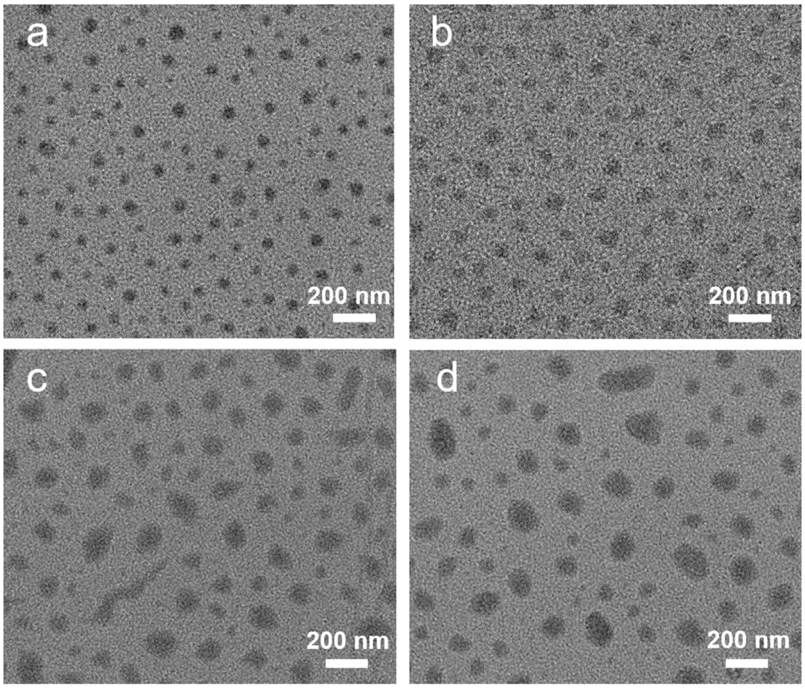

FIGURE 2 | TEM images of **(A)** D@Ms, **(B)** DA@Ms, **(C)** DA/D@Ms, and **(D)** DA/D@Ms-A.

media, the micelles were kept in PBS and full medium for 48 h followed by zeta potential measurement. The slight change indicates good stability of the micelles in PBS and full medium. Furthermore, it can be seen from **Table 1** that simultaneous encapsulation of DATS and Dox in micelles can greatly increase the drug loading efficiency of the micelles, providing the possibility of higher therapeutic efficiency.

Selective Cellular Uptake and the Penetration Capability of the Micelles

Selective cellular uptake of therapeutic drugs is important for cancer therapy to reduce side effects. Specific ligand-mediated targeting is a feasible strategy to realize selective cellular uptake. To examine the selectivity, we compared the internalization of DA/D@Ms-A and DA/D@Ms in Panc-1 cells overexpressing CD71 and HepG2 cells that hardly express CD71. The cells seeded in confocal dishes were incubated with 0.01 mg/ml DA/D@Ms-A and DA/D@Ms for different time, that is, 0.5, 1, and 2 h, and the cellular uptake was monitored by checking the fluorescence intensity of Dox using CLSM. As shown in **Figure 3**, Panc-1 cells incubated with DA/D@Ms-A exhibit bright red fluorescence in the Dox channel, and the fluorescence intensity increases with time, indicating the effective accumulation of the micelles within the cells by aptamer-receptor mediated endocytosis; while Panc-1 cells incubated with DA/D@Ms and HepG2 incubated with both DA/D@Ms-A and DA/D@Ms display weak red fluorescence in Dox channel, suggesting that only a few micelles enter into the cells by pinocytosis. All the results indicate that aptamer modification endows the micelles with high targeting efficiency and good selectivity towards pancreatic cancer cells with CD71 overexpression.

In addition to targeting efficiency, the penetration capability of the micelles was also investigated by CLSM tomography using Panc-1 cell-derived multicellular spheroids (MCSs) as an *in vitro*

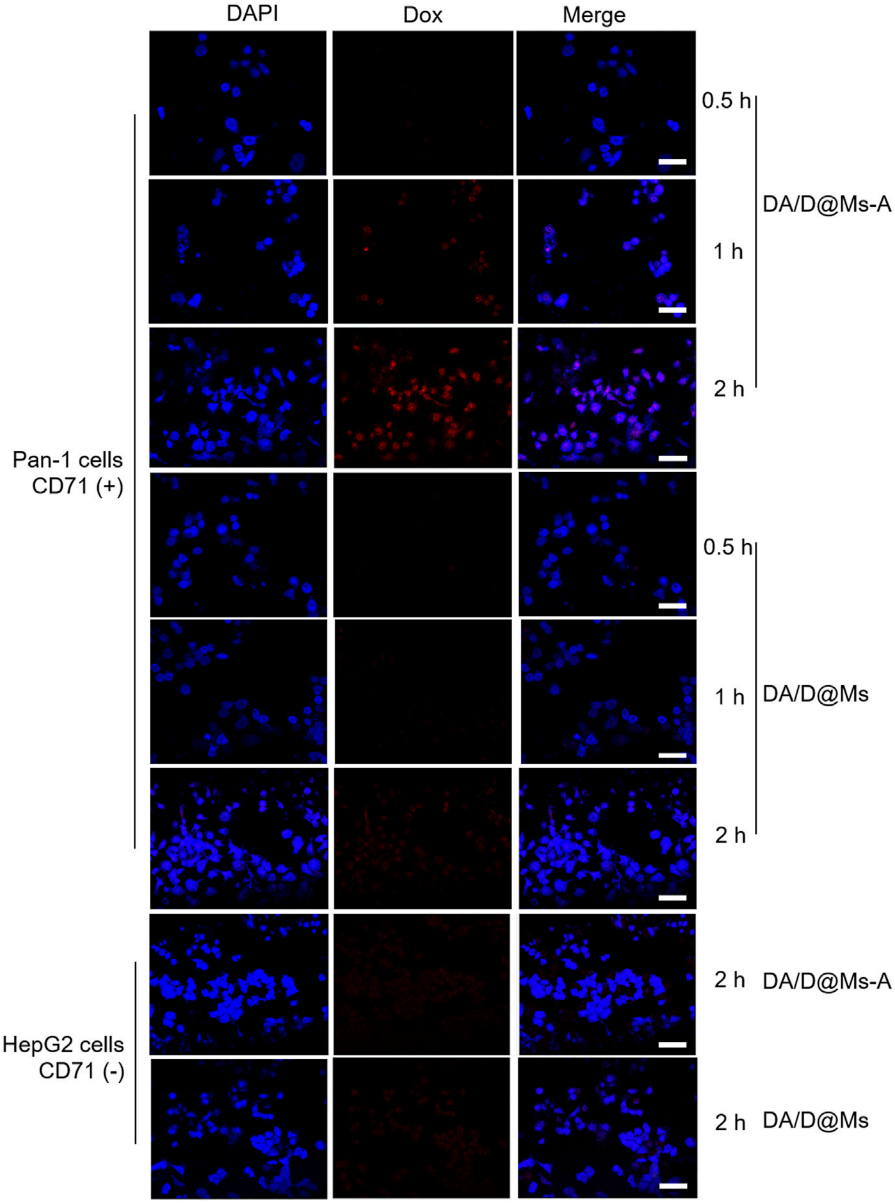

FIGURE 3 | CLSM images of Panc-1 cells and HepG2 cells incubated with 0.01 mg/ml DA/D@Ms-A and DA/D@Ms for 0.5, 1, and 2 h, respectively. DAPI channel with excitation wavelength at 405 nm exhibits blue fluorescence from DAPI stained cell nuclei. Dox channel with excitation wavelength at 488 nm shows red fluorescence from Dox. Scale bar = 50 μm.

model. MCSs are versatile three-dimensional models for cancer theranostics benefiting from their similarity in morphology and biological microenvironment to solid tumors (Abbott, 2003). The penetration activity of DA/D@Ms-A and DA/D@Ms was monitored by CLSM Z-stack scanning after incubation of MCSs with 0.01 mg/ml DA/D@Ms-A and DA/D@Ms for different time, that is, 4, 12, and 24 h. As shown in **Figure 4**, strong red fluorescence from Dox can be observed on the periphery of the MCSs incubated with DA/D@Ms-A for 4 h due to the targeting capability of DA/D@Ms-A towards the Panc-1 MSCs. The red fluorescence in the interior area of the MSCs can clearly be observed even at the scanning depth of 85 μm. In the case of DA/D@Ms for 4 h, red fluorescence can be seen on the periphery of the MCSs due to the enhanced permeation and retention effect mediated passive targeting of DA/D@Ms, however, the red fluorescence in the interior area of the MSCs rapidly attenuates and becomes faint at the scanning depth of 65 μm. The results indicate that the aptamer modification endows DA/D@Ms-A with great tumor penetration capability. It is worth noting that with the increase in incubation time, the red fluorescence brightness increases in both the cells incubated with DA/D@Ms-A and DA/D@Ms,

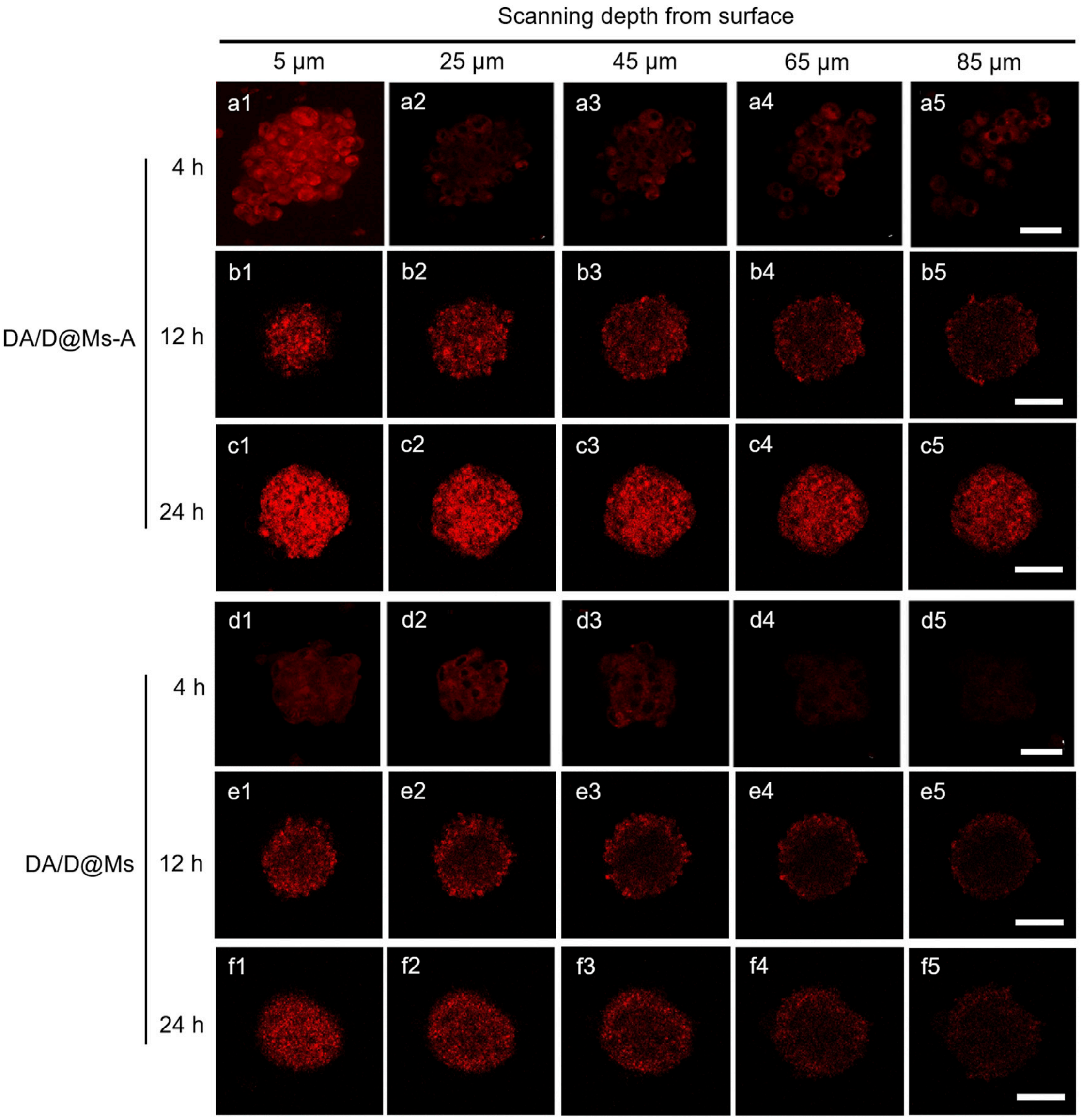

FIGURE 4 | CLSM images showing *in vitro* penetration of DA/D@Ms-A and DA/D@Ms in Panc-1 multicellular spheroids. The spheroids were incubated with 0.01 mg/ml DA/D@Ms-A or DA/D@Ms for 4, 12, and 24 h, respectively, and measured by CLSM Z-stack scanning. The surface of the spheroids was defined as 0 μm. Excitation wavelength = 488 nm, scale bar = 50 μm.

however, the brightness of the red fluorescence enhances greatly even at the scanning depth of 85 μm after incubation of Panc-1 MCSs with DA/D@Ms-A for 24 h. This is probably because that cell apoptosis induced by DA/D@Ms-A causes the enhancement in permeability of cell membrane and MSCs, which in turn facilitates the penetration of DA/D@Ms-A in MSCs.

In Vitro Cytotoxicity of the Micelles

The lipase-responsive drug release profile from the micelles was investigated by taking D@Ms as an example. **Figure 5A** shows the release profile of Dox from D@Ms in PBS containing 0.2 mg/ml and 1 mg/ml lipase at 37°C. In the presence of 0.2 mg/ml lipase, 50.68% of Dox was released in 5 h and 58.96% was released in 20 h. With a higher lipase concentration of 1 mg/ml, 54.31% of Dox was released in 5 h and 90.00% was released in 20 h. The results confirm the possibility of lipase-responsive drug release from micelles by lipase-mediated PCL blocks digestion-induced micelles disassembly.

To verify the intracellular glutathione-triggered H_2S release, a commercially available probe (WSP-1), whose fluorescence can be selectively turned on by H_2S (Liu et al., 2011), was employed for the detection of H_2S in living Panc-1 cells. As shown in **Figure 5B**, Panc-1 cells exhibit weak fluorescence of WSP-1 after incubation with DA@Ms for 2 h, and the fluorescence becomes brighter with the increase of incubation time. Panc-1 cells display much stronger fluorescence of WSP-1 after incubation with DA@

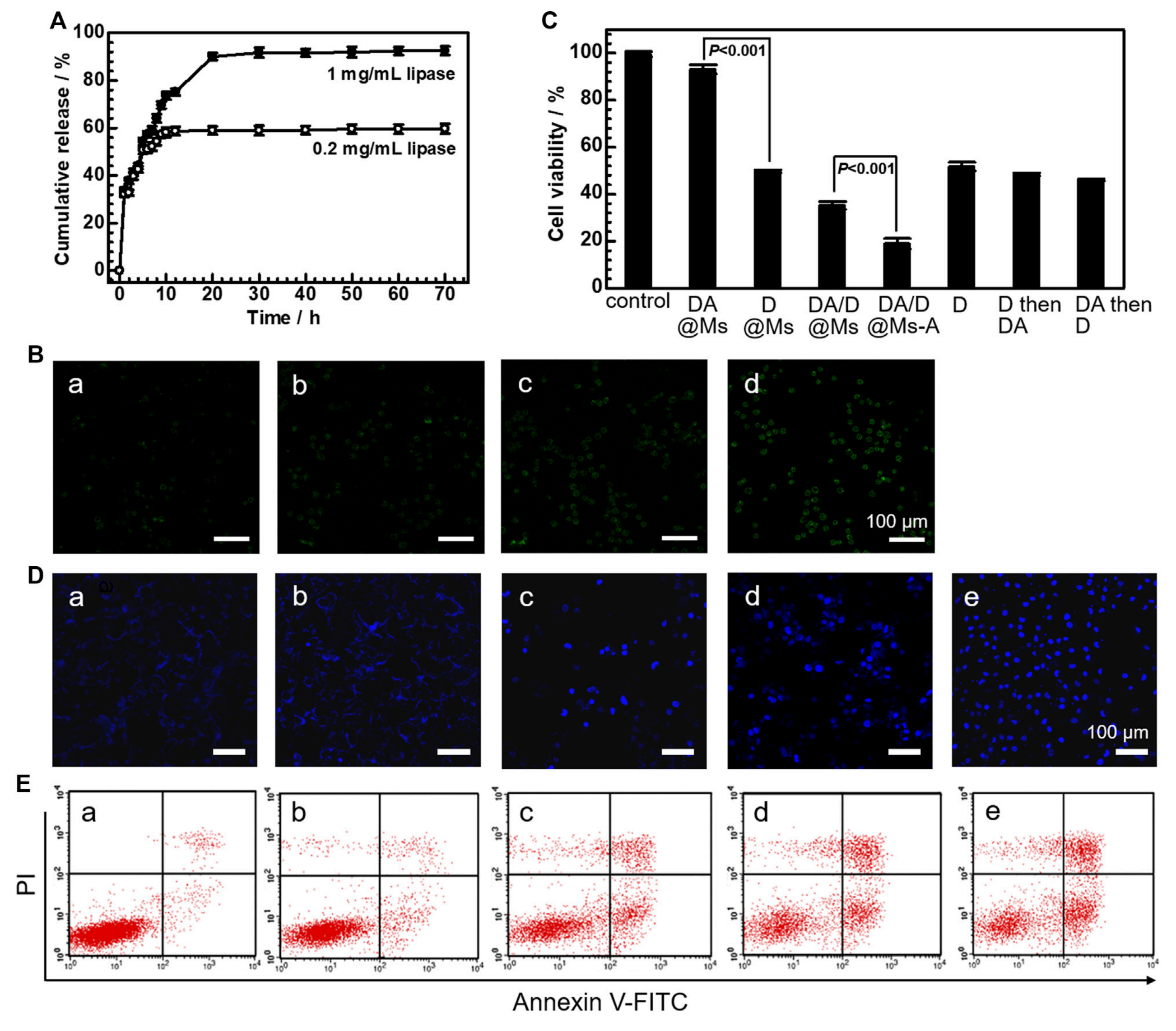

FIGURE 5 | *In vitro* cytotoxicity. **(A)** The release profiles of Dox from D@Ms in the presence of 0.2 mg/ml and 1 mg/ml lipase. **(B)** Fluorescence imaging of H_2S release in Panc-1 living cells after incubation with **(a,b)** DA@Ms and **(c,d)** DA@Ms-A for 2 h **(a,c)** and 4 h **(b,d)**, respectively. **(C)** Cell viability of Panc-1 cells treated with 0.1 mg/ml micelles and Dox for 72 h, 0.05 mg/ml Dox for 36 h then 0.05 mg/ml DATS for 36 h, and 0.05 mg/ml DATS for 36 h then 0.05 mg/ml Dox for 36 h by CCK-8 assay, respectively. **(D)** CLSM images of Panc-1 cells stained with Hoechst 33258 and **(E)** flow cytometry of Panc-1 cells stained with FTIC and PI after treatment with 0.1 mg/ml micelles for 24 h. **(a)** control, **(b)** DA@Ms, **(c)** D@Ms, **(d)** DA/D@Ms, and **(e)** DA/D@Ms-A.

Ms-A, indicating that more H_2S is generated in cells by taking advantage of the targeting capability of DA@Ms-A. The results suggest that after the micelles enter into cells, the digestion of PCL blocks by intracellular lipase leads to the release of the encapsulated DATS from the hydrophobic micellar core into the cytoplasm, and the DATS subsequently reacts with intracellular glutathione to generate H_2S.

To evaluate the therapeutic efficacy of the micelles, the cell viability was monitored by CCK-8 assay after incubation of Panc-1 cells with the micelles for 72 h. As shown in **Figure 5C**, BMs have no obvious cytotoxic effect against Panc-1 cells, indicating the biocompatibility of the micelles assembled by diblock copolymers PCL-*b*-PEO and PCL-*b*-PEO-NH_2. The cell viability of Panc-1 cells treated with DA@Ms, D@Ms, and DA/D@Ms is decreased to 93.11%, 49.73%, and 35.19%, respectively. This suggests that the therapeutic effect of DATS is not significant when it is used alone, but it can act as a sensitizer to enhance the therapeutic effect of Dox by combined DATS and Dox treatment. The micelles such as DA@Ms, D@Ms, and DA/D@Ms enter into cells by pinocytosis and release the encapsulated Dox and DATS, which then reacts with intracellular glutathione to generate H_2S. H_2S with a concentration above a certain value has been reported to exhibit a cytotoxic effect by inducing intense intracellular acidification *via* overdriving cancer glycolysis (Cao et al., 2019), causing apoptosis *via* downregulation of the downstream anti-apoptotic proteins (Kashfi, 2014; Yao, Yang,

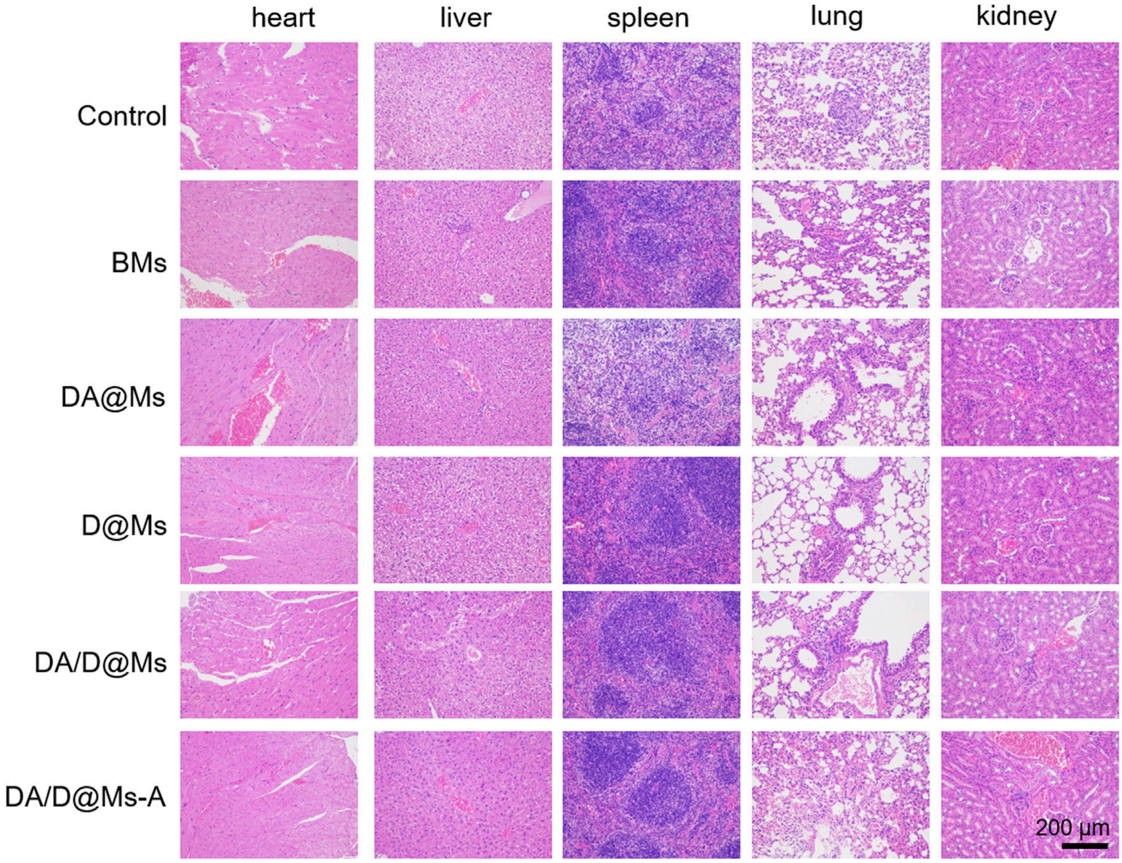

FIGURE 6 | HE stained major organs collected from mice post intraperitoneal administration of micelles every other day for 2 weeks. Scale bar = 200 μm.

Xu, He, & Yang, 2022), inducing mitochondrial dysfunction *via* suppression of the mitochondrial cytochrome c oxidase activity (Hill et al., 1984; Szabó, 2007; Szabo et al., 2014; Z. Yang et al., 2021), and aggravating hypoxia and oxidative stress *via* suppression of catalase expression (Xie et al., 2020). H_2S has also been found to be able to activate hypoxia-responsive prodrugs (Fang et al., 2020), and to upregulate the level of intracellular Dox by decreasing P-gp mediated efflux (Chegaev et al., 2016), thus promoting the chemotherapeutic efficacy. Therefore, it can be deduced that the achieved H_2S-enhanced chemotherapy in this work has resulted from the intrinsic cytotoxicity of H_2S, the facilitation of Dox release from the hydrophobic micellar core into the cytoplasm due to the intense intracellular acidification caused by H_2S and the pH-related release property of Dox, and the accumulation of Dox inside cells owing to the less efflux. The chemosensitization of H_2S is furthered improved by the comparable therapeutic efficacy of Panc-1 cells treated with 0.1 mg/ml Dox only, 0.05 mg/ml Dox then 0.05 mg/ml DATS, and 0.05 mg/ml DATS then 0.05 mg/ml Dox, namely 51.70%, 48.45% and 46.00%, respectively. The cell viability is further down to 18.41% by incubation of Panc-1 cells with DA/D@Ms-A. This suggests that the aptamer-CD71 receptor interaction mediated endocytosis promotes the cancer cell-killing efficacy by increasing the intracellular drug concentration. The higher cytotoxicity reached by the lower drug concentration as compared to the free Dox provides DA/D@Ms-A a promising prospect in raising therapeutic effects and reducing side effects in clinical application.

Apoptosis is the main mechanism accounting for the anticancer action of Dox and H_2S. Apoptotic cell death was confirmed by nucleus chromatin condensation by Hoechst 33258 staining. As shown in **Figure 5D**, the nuclei of Panc-1 cells treated with BMs can only stain an ultraweak and homogeneous blue color since Hoechst 33258 is unable to infiltrate into the living cells, while the nuclei of Panc-1 cells treated with DA@Ms or D@Ms stains bright blue due to the synergetic effect of apoptosis associated cell membrane permeability enhancement and apoptosis induced chromatin condensation. The blue emission light in Panc-1 cells treated with DA/D@Ms is much bright than those treated with DA@Ms and D@Ms only, suggesting that more cells undergo apoptosis by the strong synergetic effects between Dox and H_2S. The brightness of the blue emission light in Panc-1 cells treated with DA/D@Ms-A is further enhanced than those treated with DA/D@Ms, indicating that the targeting strategy promotes the therapeutic efficacy of synergetic gas and chemotherapy. To further examine the apoptotic characteristics in the micelles treated Panc-1 cells, flow cytometry was used to investigate the treated cells co-stained with Annexin V-FTIC and PI. Annexin V-FITC is a phospholipid-binding protein with a high affinity for phosphatidylserine, which can be used as a sensitive probe for phosphatidylserine exposure to the cell membrane (S. Chen, Cheng, Wang, & Peng, 2008). During the early apoptosis, the cells become reactive with annexin V-FITC after the onset of chromatin condensation, but prior to the loss of the plasma membrane's ability to exclude PI. On the basis, non-apoptotic cells, early apoptotic cells, late apoptotic/necrotic cells, and dead cells can be discriminated by co-staining the cells with annexin V-FITC and PI. As shown in **Figure 5E**, after incubation with BMs, DA@Ms, and D@Ms for 24 h, the percentage of apoptotic cells was 3.53%, 9.73%, and 30.35%, respectively. The percentage of apoptotic cells increases to 40.97% by treatment with DA/D@Ms, and further increases to 50.18% by treatment with DA/D@Ms-A, verifying the effectiveness of targeted synergetic gas-chemotherapy.

In Vivo Biocompatibility of the Micelles

The *in vitro* toxicity of the micelles was evaluated by intraperitoneal administration of 0.1 ml 1 mg/ml micelles to healthy mice every other day for 2 weeks. HE staining was used to investigate morphological changes in the major organs such as the heart, liver, spleen, lung, and kidney in mice. The results are shown in **Figure 6**. All the tissue slices display normal cell morphology, well-organized tissue structures, and no significant lesions, indicating that the micelles are biocompatible, and safe for clinical applications.

CONCLUSION

In summary, we have proposed an H_2S gas-involved chemosensitization strategy for improving pancreatic cancer chemotherapeutic efficacy. The nanomedicine for synergetic gas-chemotherapy has been constructed by encapsulation of both Dox and DATS in aptamer conjugated PCL-*b*-PEO micelles. The DA/D@Ms-A nanomedicine with the size of *ca.* 200 nm has shown well colloidal stability, competitive drug loading efficiency, effective targeting efficiency, and well penetration capability towards CD71 overexpressed multicellular spheroids, good *in vitro* and *in vivo* biocompatibility, and endogenous lipase and glutathione responsiveness. The DA/D@Ms-A nanomedicine with a concentration of 0.1 mg/ml was able to kill *ca.* 82% of pancreatic cancer cells after 72 h incubation, and the therapeutic efficiency of synergetic gas-chemotherapy was *ca.* 15% higher than that of individual chemotherapy. The gas-involved chemosensitization strategy and the as-developed targeted stimuli-responsive nanomedicine hold great promise for the improvement of pancreatic cancer treatment.

DATA AVAILABILITY STATEMENT

The original contributions presented in the study are included in the article/supplementary material; further inquiries can be directed to the corresponding authors.

ETHICS STATEMENT

The animal study was reviewed and approved by the Animal ethics committee of Huaqiao University.

AUTHOR CONTRIBUTIONS

LT: data curation, writing-original draft. RP: validation. XZ: methodology. KL: methodology. YZ: software. YL: methodology, funding acquisition. S-FZ: conceptualization. LC: project administration, conceptualization, funding acquisition, writing–review, and editing.

FUNDING

This work was supported by the Natural Science Foundation of Fujian Province (2019J01079), the Scientific Research Funds of Huaqiao University (605-50Y18030), the Jiangsu Innovation and Entrepreneurship Talent Program (JSSCBS20211166), and the Yancheng Innovation and Entrepreneurship Leading Talent Program [Yanwei (2020)40].

REFERENCES

Abbott, A. (2003). Biology's New Dimension. *Nature* 424 (6951), 870–872. doi:10.1038/424870a

Cao, X., Ding, L., Xie, Z.-z., Yang, Y., Whiteman, M., Moore, P. K., et al. (2019). A Review of Hydrogen Sulfide Synthesis, Metabolism, and Measurement: Is Modulation of Hydrogen Sulfide a Novel Therapeutic for Cancer? *Antioxidants Redox Signal.* 31 (1), 1–38. doi:10.1089/ars.2017.7058

Chegaev, K., Rolando, B., Cortese, D., Gazzano, E., Buondonno, I., Lazzarato, L., et al. (2016). H2S-Donating Doxorubicins May Overcome Cardiotoxicity and Multidrug Resistance. *J. Med. Chem.* 59 (10), 4881–4889. doi:10.1021/acs.jmedchem.6b00184

Chen, L., Zhou, S.-F., Su, L., and Song, J. (2019). Gas-mediated Cancer Bioimaging and Therapy. *ACS Nano* 13 (10), 10887–10917. doi:10.1021/acsnano.9b04954

Chen, S., Cheng, A.-C., Wang, M.-S., and Peng, X. (2008). Detection of Apoptosis Induced by New Type Gosling Viral Enteritis Virus *In Vitro* through Fluorescein Annexin V-FITC/PI Double Labeling. *Wjg* 14 (14), 2174. doi:10.3748/wjg.14.2174

Fang, C., Cen, D., Wang, Y., Wu, Y., Cai, X., Li, X., et al. (2020). ZnS@ZIF-8 Core-Shell Nanoparticles Incorporated with ICG and TPZ to Enable H2S-Amplified Synergistic Therapy. *Theranostics* 10 (17), 7671–7682. doi:10.7150/thno.45079

Goess, R., and Friess, H. (2018). A Look at the Progress of Treating Pancreatic Cancer over the Past 20 Years. *Expert Rev. Anticancer Ther.* 18 (3), 295–304. doi:10.1080/14737140.2018.1428093

Hill, B. C., Woon, T. C., Nicholls, P., Peterson, J., Greenwood, C., and Thomson, A. J. (1984). Interactions of Sulphide and Other Ligands with Cytochrome C Oxidase. An Electron-Paramagnetic-Resonance Study. *Biochem. J.* 224 (2), 591–600. doi:10.1042/bj2240591

Kamisawa, T., Wood, L. D., Itoi, T., and Takaori, K. (2016). Pancreatic Cancer. *Lancet* 388 (10039), 73–85. doi:10.1016/S0140-6736(16)00141-0

Kashfi, K. (2014). Anti-cancer Activity of New Designer Hydrogen Sulfide-Donating Hybrids. *Antioxidants Redox Signal.* 20 (5), 831–846. doi:10.1089/ars.2013.5308

Li, S., Garreau, H., Pauvert, B., McGrath, J., Toniolo, A., and Vert, M. (2002). Enzymatic Degradation of Block Copolymers Prepared from ε-Caprolactone and Poly(ethylene Glycol). *Biomacromolecules* 3 (3), 525–530. doi:10.1021/bm010168s

Liang, D., Wu, H., Wong, M. W., and Huang, D. (2015). Diallyl Trisulfide Is a Fast H2S Donor, but Diallyl Disulfide Is a Slow One: The Reaction Pathways and Intermediates of Glutathione with Polysulfides. *Org. Lett.* 17 (17), 4196–4199. doi:10.1021/acs.orglett.5b01962

Liu, C., Pan, J., Li, S., Zhao, Y., Wu, L. Y., Berkman, C. E., et al. (2011). Capture and Visualization of Hydrogen Sulfide by a Fluorescent Probe. *Angew. Chem. Int. Ed.* 50 (44), 10327–10329. doi:10.1002/anie.201104305

Lohse, I., and Brothers, S. P. (2020). Pathogenesis and Treatment of Pancreatic Cancer Related Pain. *Anticancer Res.* 40 (4), 1789–1796. doi:10.21873/anticanres.14133

Mathai, J. C., Missner, A., Kügler, P., Saparov, S. M., Zeidel, M. L., Lee, J. K., et al. (2009). No Facilitator Required for Membrane Transport of Hydrogen Sulfide. *Proc. Natl. Acad. Sci. U.S.A.* 106 (39), 16633–16638. doi:10.1073/pnas.0902952106

Riahi, S., and Rowley, C. N. (2014). Why Can Hydrogen Sulfide Permeate Cell Membranes? *J. Am. Chem. Soc.* 136 (43), 15111–15113. doi:10.1021/ja508063s

Su, T., Yang, B., Gao, T., Liu, T., and Li, J. (2020). Polymer Nanoparticle-Assisted Chemotherapy of Pancreatic Cancer. *Ther. Adv. Med. Oncol.* 12, 175883592091597. doi:10.1177/1758835920915978

Sung, H., Ferlay, J., Siegel, R. L., Laversanne, M., Soerjomataram, I., Jemal, A., et al. (2021). Global Cancer Statistics 2020: GLOBOCAN Estimates of Incidence and Mortality Worldwide for 36 Cancers in 185 Countries. *CA A Cancer J. Clin.* 71 (3), 209–249. doi:10.3322/caac.21660

Szabo, C. (2016). Gasotransmitters in Cancer: from Pathophysiology to Experimental Therapy. *Nat. Rev. Drug Discov.* 15 (3), 185–203. doi:10.1038/nrd.2015.1

Szabó, C. (2007). Hydrogen Sulphide and its Therapeutic Potential. *Nat. Rev. Drug Discov.* 6 (11), 917–935. doi:10.1038/nrd2425

Szabo, C., Ransy, C., Módis, K., Andriamihaja, M., Murghes, B., Coletta, C., et al. (2014). Regulation of Mitochondrial Bioenergetic Function by Hydrogen Sulfide. Part I. Biochemical and Physiological Mechanisms. *Br. J. Pharmacol.* 171 (8), 2099–2122. doi:10.1111/bph.12369

Tian, L., Pei, R., Zhong, L., Ji, Y., Zhou, D., and Zhou, S. (2021). Enhanced Targeting of 3D Pancreatic Cancer Spheroids by Aptamer-Conjugated Polymeric Micelles with Deep Tumor Penetration. *Eur. J. Pharmacol.* 894, 173814. doi:10.1016/j.ejphar.2020.173814

Wu, X., Liu, H., Han, D., Peng, B., Zhang, H., Zhang, L., et al. (2019). Elucidation and Structural Modeling of Cd71 as a Molecular Target for Cell-specific Aptamer Binding. *J. Am. Chem. Soc.* 141 (27), 10760–10769. doi:10.1021/jacs.9b03720

Xie, C., Cen, D., Ren, Z., Wang, Y., Wu, Y., Li, X., et al. (2020). FeS@BSA Nanoclusters to Enable H 2 S-Amplified ROS-Based Therapy with MRI Guidance. *Adv. Sci.* 7 (7), 1903512. doi:10.1002/advs.201903512

Yang, F., Jin, C., Jiang, Y., Li, J., Di, Y., Ni, Q., et al. (2011). Liposome Based Delivery Systems in Pancreatic Cancer Treatment: From Bench to Bedside. *Cancer Treat. Rev.* 37 (8), 633–642. doi:10.1016/j.ctrv.2011.01.006

Yang, Z., Luo, Y., Hu, Y., Liang, K., He, G., Chen, Q., et al. (2021). Photothermo-Promoted Nanocatalysis Combined with H 2 S-Mediated Respiration Inhibition for Efficient Cancer Therapy. *Adv. Funct. Mat.* 31 (8), 2007991. doi:10.1002/adfm.202007991

Yao, X., Yang, B., Xu, J., He, Q., and Yang, W. (2022). Novel Gas-based Nanomedicines for Cancer Therapy. *View* 3 (1), 20200185. doi:10.1002/VIW.20200185

Yu, L., Hu, P., and Chen, Y. (2018). Gas-generating Nanoplatforms: Material Chemistry, Multifunctionality, and Gas Therapy. *Adv. Mat.* 30 (49), 1801964. doi:10.1002/adma.201801964

Conflict of Interest: The authors declare that the research was conducted in the absence of any commercial or financial relationships that could be construed as a potential conflict of interest.

ORIGINAL RESEARCH
published: 22 July 2022
doi: 10.3389/fbioe.2022.960586

Directed Self-Assembly of Heterologously Expressed Hagfish EsTKα and EsTKγ for Functional Hydrogel

*Ruishuang Sun, Ruonan Zheng, Wenlong Zhu, Xiqin Zhou, Luo Liu and Hui Cao**

Beijing Bioprocess Key Laboratory, Beijing University of Chemical Technology, Beijing, China

Hagfish slime proteins have long been considered useful due to their potential applications in novel green, environmental, and functional bionic materials. The two main component proteins in the slime thread of hagfish, (opt)EsTKα and (opt)EsTKγ, were used as raw materials. However, the methods available to assemble these two proteins are time- and labor-intensive. The conditions affecting protein self-assembly, such as the pH of the assembly buffer, protein concentration, and the protein addition ratio, were the subject of the present research. Through a series of tests, the self-assembly results of a variety of assembly conditions were explored. Finally, a simplified protein self-assembly method was identified that allows for simple, direct assembly of the two proteins directly. This method does not require protein purification. Under the optimal assembly conditions obtained by exploration, a new gel material was synthesized from the hagfish protein through self-assembly of the (opt)EsTKα and (opt)EsTKγ. This assembly method has the benefits of being a simple, time-saving, and efficient. The self-assembled protein gel products were verified by SDS polyacrylamide gel electrophoresis (SDS-PAGE) and contained (opt)EsTKα and (opt)EsTKγ proteins. Scanning electron microscopy (SEM) was used to investigate the self-assembled protein gel after freeze-drying, and it was observed that the self-assembled protein formed a dense, three-dimensional porous network structure, meaning that it had good water retention. Evaluation of the gel with atomic force microscopy (AFM) indicated that the surface of the protein fiber skeleton show the network-like structure and relatively smooth. Characterization by circular dichroism (CD) and Fourier transform infrared spectroscopy (FT-IR) demonstrated that the two proteins were successfully assembled, and that the assembled protein had a secondary structure dominated by α-helices. The rheological properties of the self-assembled products were tested to confirm that they were indeed hydrogel property.

Keywords: hagfish slime protein, recombinant protein, self-assembly, phase separation, isolation, purification

Edited by:
Yuangang Liu,
Huaqiao University, China

Reviewed by:
Xin Xiong,
NMI Natural and Medical Sciences Institute, Germany
Xiaoyan Qiu,
Nanjing Tech University, China

****Correspondence:***
Hui Cao
caohui@mail.buct.edu.cn

Specialty section:
This article was submitted to Biomaterials,
a section of the journal
Frontiers in Bioengineering and Biotechnology

Received: *03 June 2022*
Accepted: *24 June 2022*
Published: *22 July 2022*

Citation:
Sun R, Zheng R, Zhu W, Zhou X, Liu L and Cao H (2022) Directed Self-Assembly of Heterologously Expressed Hagfish EsTKα and EsTKγ for Functional Hydrogel.
Front. Bioeng. Biotechnol. 10:960586.
doi: 10.3389/fbioe.2022.960586

INTRODUCTION

Hagfish, an ancient chordate, is a seabed-dwelling fish with a soft eel-like body (Lim et al., 2006). There are many glands on both sides of the hagfish's body for storing slime, and when they are under pressure or attacked, a large amount of defensive slime is secreted from the slime glands (Fudge et al., 2005; Lim et al., 2006). The slime secreted by the slime glands of the hagfish is not affected by benthic high pressure or high salt, and it has high water absorption. Hagfish slime could expand to 10000 times its initial volume within a few milliseconds of contact with seawater (Fudge et al., 2005). The slime has many biological functions, including blocking the parotids of potential predators, which allows the hagfish to escape from danger and survive (Fernholm, 1981; Lim et al., 2006; Zintzen et al., 2011). The slime of hagfish is very unusual. It is composed of both mucin and protein-based fibers, and the protein-based fibers give the slime its strength and toughness (Downing et al., 1981; Fernholm, 1981; Koch et al., 1991).

The protein-based fibers of hagfish slime are mainly composed of axially arranged Intermediate filament (IF) proteins (Fudge et al., 2015). IF proteins comprise an important protein superfamily that plays a crucial-role in cell mechanics. And IF proteins are also critical components of the cytoskeleton in most animal cells (Herrmann and Aebi, 2000). The IF proteins found in hagfish is mainly composed of two types of thread keratins (TKα and TKγ) (Fu et al., 2015). In the present study, we analyzed the Eptatretus stouti thread keratins (EsTKα and EsTKγ). The EsTKα and EsTKγ proteins are homologous to vertebrate type Ⅰ and Ⅱ IF keratins, and the molecular weights of EsTKα and EsTKγ are 66.7 and 62.8 kDa, respectively (Fu et al., 2015).

In a 2015 study, Jing Fu et al. used synthetic biology and other methods to heterologously express two kinds of thread keratins, EsTKα and EsTKγ, in *E. coli*. Subsequently, they obtained EsTKα and EsTKγ artificial hagfish protein through artificial synthesis (Fu et al., 2015). After exploring these proteins under various experimental conditions, they determined the conditions for self-assembly of the two protein coils. Their experiments laid the foundation for engineering biomimetic recombinant artificial hagfish thread keratin materials. In 2017, Jing Fu et al. processed a fiber rich in β-sheet through the artificial slime thread of hagfish generated by recombinant protein expression and then used glutaraldehyde to covalently cross-link the processed fiber to obtain an artificial hagfish protein fiber with high hardness and a modulus value of 20 GPa (Fu et al., 2017). Paula E. Oliveira et al. studied unassembled separate EsTKα and EsTKγ proteins. The highest average tensile strength of fibers spun at a 1:1 ratio of the two proteins reached nearly 200 MPa, with an elastic modulus of 5.7 GPa, which can basically represent the highest tensile strength reported for these proteins in the absence of chemical cross-linking (Oliveira et al., 2021).

The recombinant α-helical structure of hagfish protein is soft, which allows it to be formed into soft composite materials. These materials could be used to make safety helmets and other products that could absorb heavy impacts. However, the intensity of the hagfish protein is higher when it forms the recombinant β-sheet structure. The resulting materials may be used to weave bulletproof vests and other products. Both α-helix and β-sheet hagfish protein materials could improve the performance of protective materials without increasing their weight (Johnson et al., 1994; Pinto et al., 2014). In summary, from the perspective of sustainable development, recombinant hagfish protein materials may become green, environmental, and functional biomimetic materials similar to bioderived materials such as spider silk and silkworm silk, and become an excellent alternative to chemically synthesized materials in the future (Aigner et al., 2018; Ma et al., 2018).

Protein self-assembly technology exists at the convergence of polymer chemistry and supramolecular chemistry. During the assembly process, proteins may be cross-linked through hydrophobic interactions, electrostatic interactions, hydrogen bond interactions, disulfide bonds, or van der Waals forces to form spatial network structures (Cheng et al., 2019). Compared with various polyhydroxy polymers, protein gels have structural advantages and better biodegradability. Phase separation of the protein solution could occur after high-speed centrifugation (Boeynaems et al., 2018). After protein self-assembly, the fully mixed an homogenized assembled protein solution is rearranged so that different concentrations occupy different spatial regions, allowing for separation and purification (Boeynaems et al., 2018). A more convenient and efficient way to achieve purification and separation is by gathering proteins through phase transformation. This process could be achieved based on the various specific interactions between EsTKα and EsTKγ. The two crude, purified proteins obtained by simple washing were directly assembled, and the assembled proteins were subsequently isolated from solutions containing unassembled EsTKα, EsTKγ proteins, and miscellaneous proteins by phase separation. Using this process, we separated and purified the assembly proteins. The existing assembly methods for EsTKα and EsTKγ thread keratins are cumbersome, inefficient, and time-intensive. Therefore, a simplified assembly method is needed. In the present study, we were able to directly assemble the two proteins by altering various conditions to establish a simple, quick, and efficient assembly method without the need for protein purification. Through the principle of phase separation, the assembled protein was concentrated and separated using ultrafiltration centrifugation, and the assembled protein product was obtained. Subsequently, the assembled protein products were characterized by various methods. These findings provide a theoretical basis for further research to improve hagfish protein assembly.

MATERIALS AND METHODS

Experimental Materials

We used the pET-22b (+) expression vector, BL21 (DE3) competent cells, and the specific optimized hagfish protein gene, as well as other materials referred to by Yang et al. (2021). The recombinant plasmids were named pET22b-(opt) EsTKα and pET22b-(opt)EsTKγ.

Acquisition and Crude Purification of (opt) EsTKα and (opt)EsTKγ Proteins

The expression and washing methods for (opt)EsTKα and (opt) EsTKγ have been previously described (Yang et al., 2021). (opt) EsTKα and (opt)EsTKγ proteins were expressed in *E. coli* and then obtained from inclusion bodies. The bacterial pellet was resuspended in lysis buffer (50 mM Tris, 200 mM NaCl, 1 mM PMSF). The bacteria were then lysed by high-pressure homogenization. The resulting liquid was centrifuged at 4°C and 10000 rpm, for 20 min. The precipitate was resuspended and washed in inclusion body washing buffer 1 (100 mM Tris, 5 mM EDTA, 2 M urea, 2% TritonX-100, 5 mM DTT) and then in inclusion body washing buffer 2 (100 mM Tris, 5 mM EDTA, 5 mM DTT). The precipitate was washed twice with each washing buffer, and the supernatant was discarded after each centrifugation (10000 rpm for 15 min at 4°C). Finally, the washed inclusion body protein was dissolved in a high concentration urea solution (8 M urea, 0.02 M NaH_2PO_4, 0.5 M NaCl). SDS-PAGE analysis was then performed to verify the molecular weights of the two proteins.

Self-Assembly of (opt)EsTKα and (opt) EsTKγ Proteins

The self-assembly conditions of (opt)EsTKα and (opt)EsTKγ proteins were designed according to methods known to promote helical folding, coiled-coil formation, and IF assembly of type Ⅰ and type Ⅱ IF *in vitro* (Herrmann et al., 2002). First, the crudely purified (opt)EsTKα and (opt)EsTKγ proteins were diluted to 0.4 mg/ml with high-concentration urea solution (8 M urea, 0.02 M NaH_2PO_4, 0.5 M NaCl). Next, equal volumes of the two protein solutions were mixed. Subsequently, a gradient dialysis of urea concentration (8 M→ 4 M→ 2 M→ 0 M) was performed in Tris buffer (urea concentrations of 4 M, 2 M, and 0 M, respectively, all containing 2 mM Tris, 1 mM DTT, and dialysis bag specifications of MD77, 10 kDa) at pH 7.0, 7.5, 8.0, 8.5, and 9.0. The dialysis temperature was 4°C. A total of 72 h of dialysis were performed. Each urea concentration was dialyzed for 24 h and the dialysate was changed every 12 h. Then, high concentration urea solutions of the two proteins with different protein concentrations (0.2, 0.4, 0.6, 0.8 and 1.0 mg/ml) were prepared. The two protein solutions were mixed in equal volumes and concentrations. A self-assembly experiment of gradient dialysis was carried out in Tris buffer (Urea concentrations of 4 M, 2 M and 0 M, respectively, both containing 2 mM Tris and 1 mM DTT, and the specification of dialysis bag were MD77 and 10 kDa) at 4°C, pH 9. Finally, according to different ratios (1:1, 1: 2, 2:1) a concentration of 1 mg/ml (opt)EsTKα and (opt)EsTKγ two protein were added to the high concentration urea solution. The self-assembly experiment of gradient dialysis was carried out in Tris buffer (Urea concentrations of 4 M, 2 M and 0 M, respectively, both containing 2 mM Tris and 1 mM DTT, and the specification of the dialysis bag was MD77 and 10 kDa) at 4°C, pH 9. The self-assembled solution after dialysis was ultrafiltered and concentrated (the specifications of the ultrafiltration tube were 1.5 ml, 10 kDa). The self-assembled products of the two proteins were obtained by centrifugation and concentration at 4°C and 6000 rpm. Two proteins, (opt)EsTKα and (opt)EsTKγ, with protein concentrations of 1 mg/ml, were subjected to gradient dialysis for 72 h in the dialysis solution at 4°C, pH 9, respectively, as described above. Ultrafiltration concentration was then carried out as previously described.

SDS Polyacrylamide Gel Electrophoresis

The protein products obtained after self-assembly were diluted in different folds. The composition of two proteins, (opt)EsTKα and (opt)EsTKγ, after self-assembly was investigated using SDS-PAGE. The loading volume of the protein marker was 10 μL. The self-assembled protein product was diluted with Tris buffer (2 mM Tris, 1 mM DTT) for different multiples, and the loading volume was 10 μl. Equal concentrations of highly purified (opt) EsTKα and (opt)EsTKγ proteins were mixed in equal volumes, and the total loading volume was 10 μl.

Scanning Electron Microscopy Observation

The (opt)EsTKα proteins, (opt)EsTKγ proteins and the assembled protein products (pH = 9, (opt)EsTKα and (opt) EsTKγ concentrations were 1 mg/ml, the ratio of the two proteins was 1:1, and the next characterized assembly proteins, are also products formed under this condition) were loaded into a centrifuge tube and snap frozen in liquid nitrogen. Snap freezing of proteins in liquid nitrogen was performed to minimize damage to the assembled structure. The snap frozen assembled protein was then freeze-dried using a vacuum freeze-dryer. The microstructure of the freeze-dried assembled protein gel was observed using a SEM (Hitachi SU1510). A small amount of protein gel sample was taken after vacuum freeze-drying, and affixed to the sample bench using a conductive adhesive. After treatment by ion sputtering gold spray, the samples were placed on the SEM platform. The microstructure of the mixed proteins was observed and photographed at a voltage of 5 kV.

Atomic Force Microscopy Observations

A small amount of the gel-like assembled protein product was dropped onto the surface of a double-polished silicon wafer. Then, the silicon wafer and the sample were freeze-dried together. Observation was performed at room temperature using AFM (Nanoscope Systems). Silicon nitride high frequency vibration probes were used and the sample was scanned using intelligent mode, tapping mode, and phase imaging techniques. Image processing software was used to analyze the image (Nova image processing software attached to AFM) (Chromy et al., 2003; Stine et al., 2011).

Water Holding Capacity (WHC) Testing

The assembled protein gel's WHC was measured according to the centrifugation method of Kocher et al. with slight changes (Kocher and Foegeding, 1993). A certain mass of the gel-like assembly protein sample was weighed and transferred to a centrifuge tube with mass of m_0. The total mass of the sample and centrifuge tube is represented by m_1. The sample was centrifuged for 15 min at 4°C for 10000 rpm. After centrifugation, the water in the upper layer of the centrifuge tube was removed and the surface of the protein gel was dried with filter paper. The total mass of the sample and centrifuge tube after centrifugation is represented by m_2. The following formula represents the WHC calculation. Protein gel samples were measured three times in parallel.

$$WHC\% = \frac{(m_1 - m_0) - (m_1 - m_2)}{m_1 - m_0}$$

Circular Dichroism Testing

The individually dialyzed (opt)EsTKα and (opt)EsTKγ proteins and the assembled protein product were each diluted to a concentration of 1.0 mg/ml in buffer containing 2 mM Tris and 1 mM DTT. Triplicate measurement was obtained in the wavelength range from 190 to 260 nm, using the step size of 1 nm and the bandwidth of 1 nm (JASCO J-1500 circular dichroism spectrometer). Average spectra and smoothing were calculated on the CD spectral data using spectra manager software, and the wavenumber range was selected as 190–260 nm. The data were saved and uploaded to http://dichroweb.cryst.bbk.ac.uk. The website performed the calculations to obtain the relative content of the protein secondary structure of the assembled protein.

Fourier Transform Infrared Spectroscopy Testing

The secondary structure of the assembled protein sample was analyzed using the KBr compression method. The compression was performed using the assembled protein samples that had been snap-frozen in liquid nitrogen and freeze-dried. The absorbance of the sample was measured in the range of 400–4000 cm^{-1} (Nicolet IS10 Fourier transform infrared spectrometer). The scanning temperature was 25°C, and 64 scans were performed at a resolution of 4 cm^{-1}. Each protein sample was tested three times. The infrared spectra from 1600 to 1700 cm^{-1} were baseline corrected, Gaussian deconvoluted, and processed for second derivatives using Peakfit software. They were then subjected to peak splitting fitting.

Determination of Rheological Properties

Frequency scanning experiments were performed on the samples using the oscillating mode of the rheometer to measure their dynamic viscoelasticity. The specific parameters were as follows: shear strain (γ) was 1%, the range of frequency (f) was 0.1–10 Hz, and the test temperature was 25°C. The changes of storage modulus (G'), loss modulus (G''), and loss factor ($\tan \delta = G'/G'$) of the assembly products similar to gel were measured.

RESULTS AND ANALYSIS

Protein Assembly and SDS-PAGE

In the process of protein assembly, the pH value of the assembly buffer is crucial. Differently pH-ed buffers affect the ionization of proteins and their net charges. This in turn affects the attraction and repulsion between protein molecules, as well as their interactions with water. Our results showed that (opt)EsTKα and (opt)EsTKγ were correctly expressed. When the pH of the protein self-assembly dialysis solution was 7.0, 7.5, 8.0, or 8.5, and the protein solution assembled by dialysis was concentrated by ultrafiltration centrifugation, the inner tube of the ultrafiltration tube showed a clear liquid state. When the pH of the dialysate was 9.0, a small amount of white flocculent substances were visible in the ultrafiltration tube after the assembly protein solution was concentrated by ultrafiltration centrifugation (**Figure 1A**). Subsequently, the pH of the protein self-assembled dialysate was fixed at 9.0, while the concentrations of (opt)EsTKα and (opt)EsTKγ were changed for the self-assembly experiments. Our findings showed that the concentrations of the two proteins increased during self-assembly, and more white substances were obtained by ultrafiltration concentration by the end of assembly. When the concentration of both (opt)EsTKα and (opt)EsTKγ was 1.0 mg/ml and concentrated by ultrafiltration after assembly, a gel-like assembly protein appeared in the solution in the ultrafiltration tube (**Figure 1B**). This is a physical-process in which supersaturated component solutions spontaneously separate into a dense phase and dilute phase and stably coexist (Boeynaems et al., 2018). The gel-like assembly protein was slowly picked up with a pipette tip to separate it from the precipitated (opt)EsTKα or (opt)EsTKγ proteins and miscellaneous proteins. This process enables the simple, rapid, and efficient assembly of the two proteins. When performing the assembly of (opt)EsTKα and (opt)EsTKγ proteins in different ratios, it was found that the experimental results after changing the ratio were similar to those when the addition ratio was 1:1. The two proteins, EsTKα and EsTKγ, were purified as described by Jing Fu et al. using size exclusion chromatography (Fu et al., 2015). Both proteins were diluted with a high concentration urea solution to concentrations of 0.2 mg/ml. Self-assembly was successfully performed by adding the two proteins in equal proportions at a dialysate pH of 8.4 and a temperature of 4°C. Because the crude purified protein still contains some miscellaneous proteins that could interfere with the interaction between (opt)EsTKα and (opt)EsTKγ, the use of crude purified protein in this method of direct self-assembly requires increasing the concentration of two proteins, (opt)EsTKα and (opt)EsTKγ, during assembly. This allows them to resist the effects of the miscellaneous proteins so that the two proteins could be successfully assembled.

The gel-like assembled proteins were diluted at different concentrations. SDS-PAGE was then performed to validate each component of the gelatinous protein. The process of boiling at high temperature before electrophoresis will denature and disintegrate the assembled gelatinous histones. Using this method, it is possible to induce the formation of depolymers of the two proteins at the target band positions (**Figure 2**). We observed almost no miscellaneous protein on the SDS-PAGE gel. The electrophoretic bands from the assembled sample corresponded identically to the bands observed from the direct mixture of the two proteins. The molecular weight expressed was consistent with the molecular weights of (opt)EsTKα and (opt)EsTKγ proteins (66.7 and 62.8 kDa, respectively). The bands of the two proteins contained essentially the same amount of protein, indicating that the ratio of the two proteins in the assembled protein was approximately 1:1. We calculated that approximately 4 ml of gel-shaped assembled protein would be formed per 10 mg of a mixed (opt)EsTKα and (opt)EsTKγ (where the ratio of (opt)EsTKα and (opt)EsTKγ was 1:1 and the concentration was 1.0 mg/ml for both).

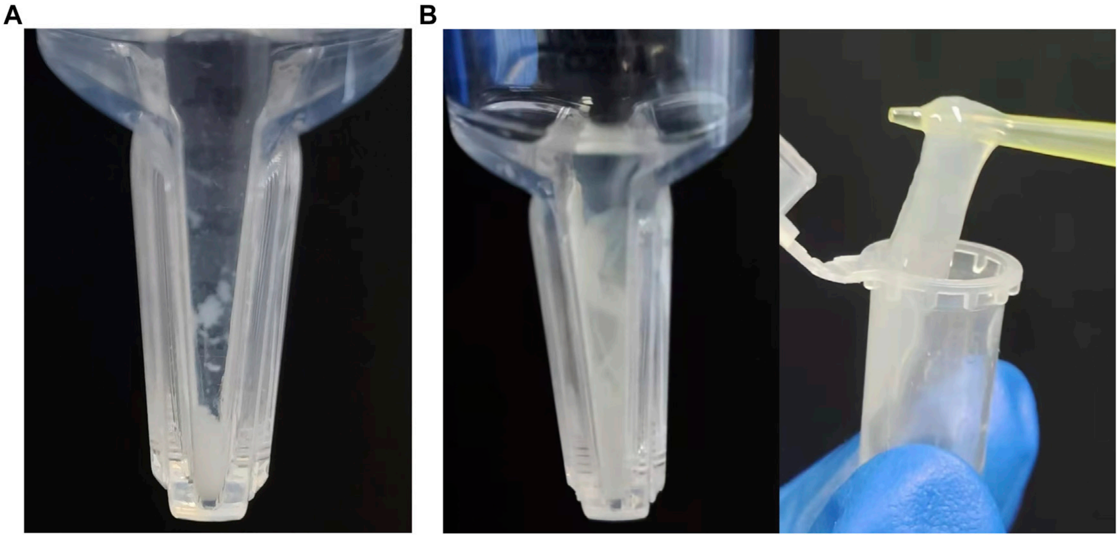

FIGURE 1 | Assembly results at pH 9, 4°C with (opt)EsTKα and (opt)EsTKγ in a 1:1 ratio. **(A)** The concentration of (opt)EsTKα and (opt)EsTKγ were each 0.4 mg/ml. **(B)** The concentration of (opt)EsTKα and (opt)EsTKγ were each 1.0 mg/ml.

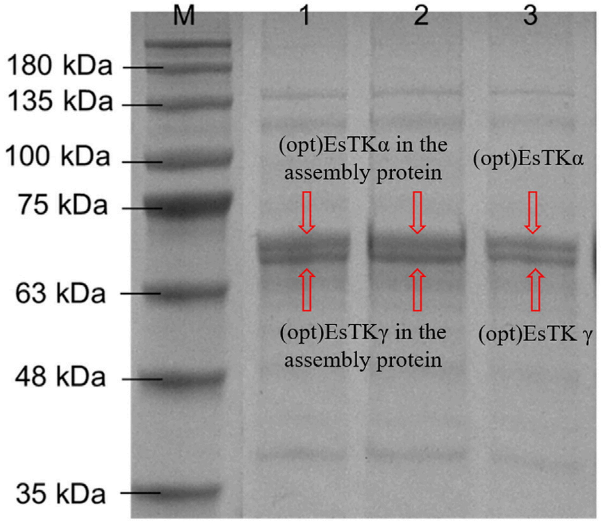

FIGURE 2 | Results of SDS-PAGE. M: Marker. 1, 2: Assembled proteins at different diluted. 3: Direct mixture of (opt)EsTKα and (opt)EsTKγ.

Microstructure of Assembled Proteins

The surface morphologies of the (opt)EsTKα and (opt)EsTKγ proteins and the self-assembled protein samples after liquid nitrogen snap freezing and freeze-drying could be clearly observed by scanning electron microscopy. **Figures 3A–D** shows that the surface microstructure of (opt)EsTKα and (opt) EsTKγ proteins without assembly and treatment was relatively disordered, and there was no mature network structure. Meanwhile **Figures 3E–H** shows that the proteins of the assembled products self-assembled to form fibrous structures through various interactions between protein molecules. Moreover, these protein fibers formed a clear and dense stereoporous network-like structure through mutual cross-linking and various aggregations. The pores in the network were interlaced and connected with each other, and the pore size was uneven, ranging from 5–25 μm. Amplification of the network skeleton revealed that the mesh skeleton was not uniform in thickness, but the surface was relatively smooth. The diameter of the fibrous network skeleton was in the range of 1–10 μm.

These findings show that using our method of direct assembly, two proteins, (opt)EsTKα and (opt)EsTKγ, could achieve self-assembly at a low temperature. After pure silk fibroin is assembled into a gel, its surface also shows a porous structure, and the size of the pores is also heterogeneous, but its pore size is small, roughly in the range of 2–5 μm (Wu, 2012). Both hagfish slime thread protein and silk fibroin protein are animal-derived fibrins, and their surface morphologies are similar after they are assembled into gels.

AFM was used to observe the microscopic morphology of the assembled gel protein products at room temperature. Consistent with the previous SEM observation results, the protein gel skeleton was composed of many assembled protein fibers, and the bright and dark staggered stripes formed by the arrangement of the assembled protein fibers were clearly visible (**Figure 4A**). The surface height could be observed by examining the white, straight part of the protein in **Figure 4A**, focusing in on the section of the protein mentioned above to further clarify the surface height. **Figure 4B** represents the surface fluctuation. These images show that the diameter of this protein fiber was about 3.3 μm, which is consistent with the results of SEM observation. **Figure 4C** shows the amplification of the fiber portion in **Figure 4A**. The surface height could be observed by examining the white, straight part of the protein in **Figure 4C**. **Figure 4D** shows

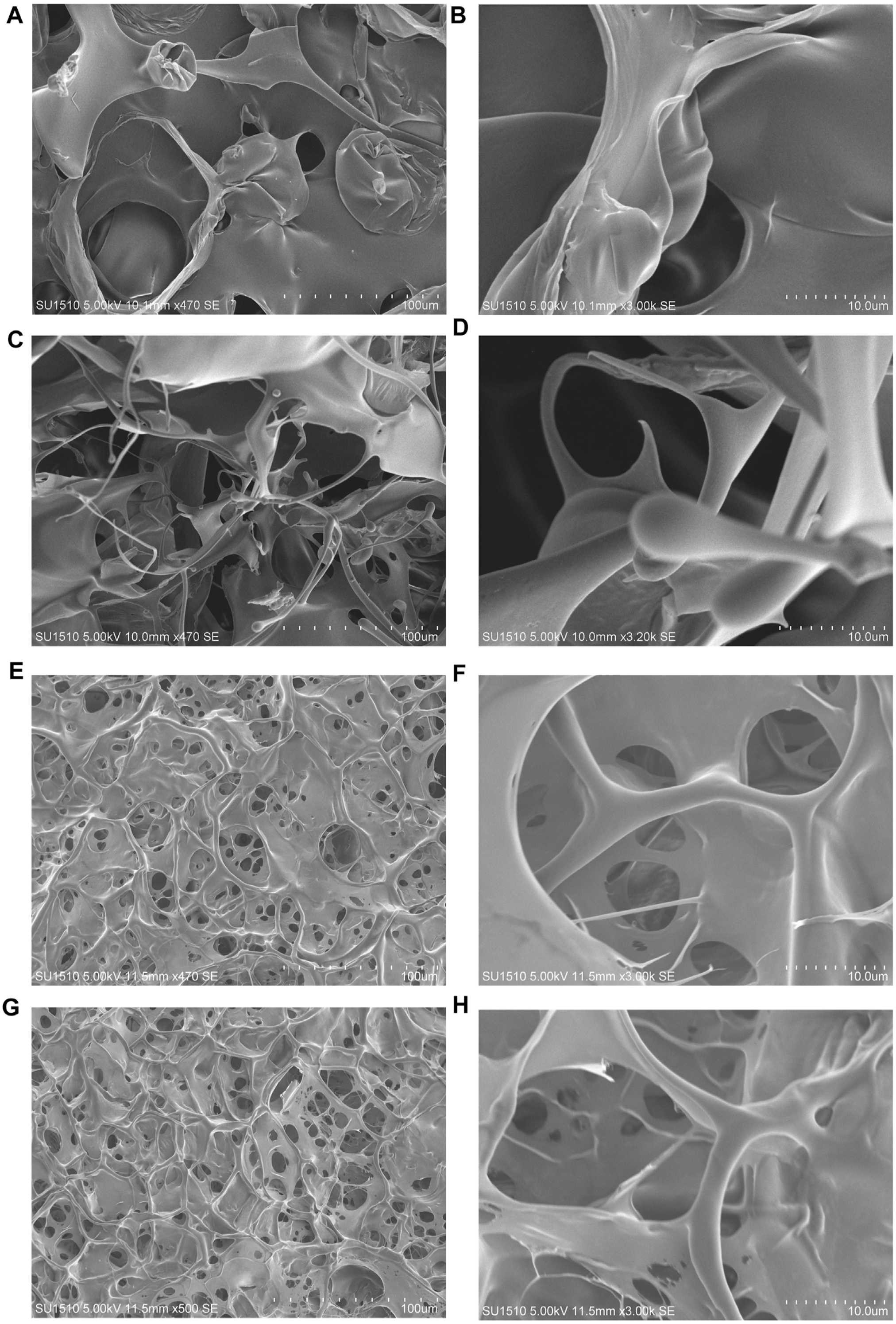

FIGURE 3 | The surface morphology observed by SEM. **(A,B)** The surface morphology of the (opt)EsTKα protein sample. **(C,D)** The surface morphology of the (opt) EsTKγ protein sample. **(E–H)** The surface morphology of the self-assembled protein sample.

the surface undulation of the protein fiber. Based on these images, the height difference of the undulating surface of the assembled protein fiber was less than 2 nm. The diameter of the protein fiber was thousands of times its surface undulation height, indicating that the assembled protein fiber surface was relatively smooth.

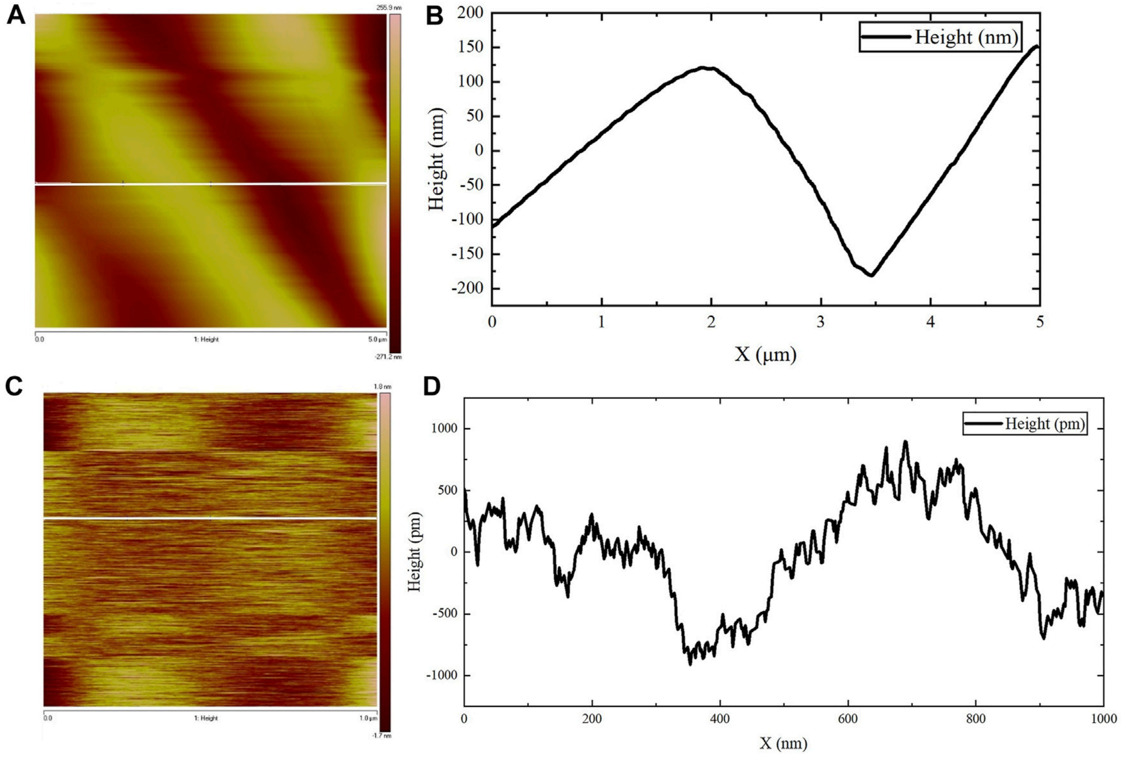

FIGURE 4 | AFM observations. **(A,C)** The surface height map of the protein fiber. **(B)** The surface fluctuation map of the white straight area in **(A)**. **(D)** The surface fluctuation map of the white straight area in **(C)**.

WHC of Assembled Proteins

Results of the WHC tests are shown in **Table 1**. Results of the three parallel determinations were close to each other. The average WHC of the assembled protein products was about 66.14%, indicating a good water holding performance. WHC reflects the ability of the gel-like assembled protein network to hold water after freeze-drying, as observed using SEM. SEM indicated that the assembled protein products formed a network-like, three-dimensional structure with relatively dense pores. This structure enables the protein to envelope water and other components, forming a gel. Salvador et al. studied the correlation between gel's structure and its water holding capacity and found that gels with dense structure were able to hold more water (Salvador et al., 2009). Therefore, the denser porous network structure of the assembled protein product is key to its water holding performance.

TABLE 1 | Results for WHC.

	m_0 (mg)	m_1 (mg)	m_2 (mg)	WHC (%)
1	860.75	1349.29	1181.09	65.57
2	842.50	1322.24	1173.33	68.96
3	861.29	1352.54	1175.10	63.88

Secondary Structure of Assembled Proteins

CD chromatography accurately reflects the secondary structure of proteins. This method was used to study the secondary structure of the two proteins, (opt)EsTKα and (opt)EsTKγ, and the assembled protein [(opt)EsTKs protein]. The CD test was first performed on the single (opt)EsTKα protein and (opt)

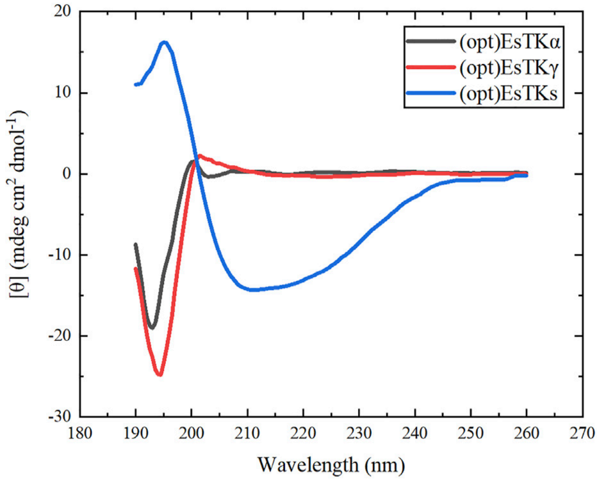

FIGURE 5 | CD spectra of (opt)EsTKα, (opt)EsTKγ and (opt)EsTKs proteins.

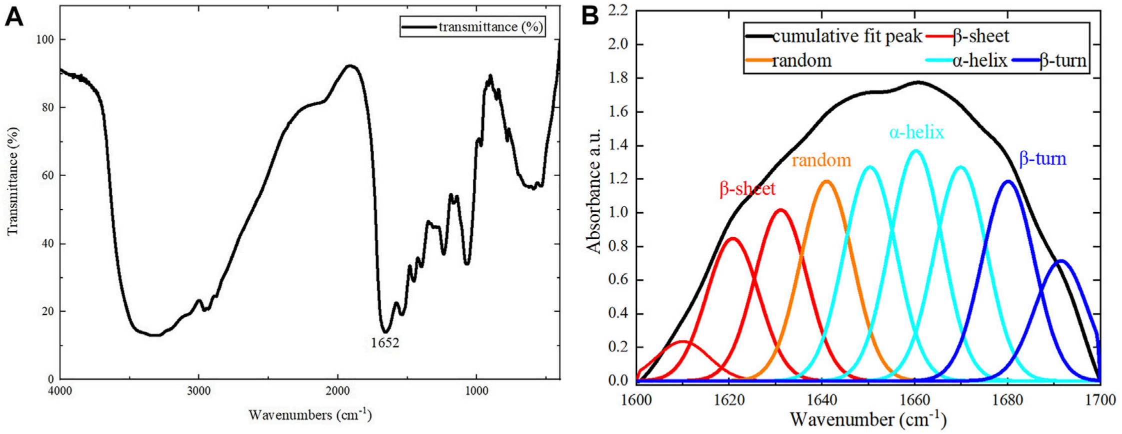

FIGURE 6 | FT-IR results. **(A)** Results for the assembled protein in the range of 400–4000 cm^{-1}. **(B)** The peak separation of the amide I band.

EsTKγ protein. The assembled (opt)EsTKs protein was then subjected to CD testing. As shown in **Figure 5**, the CD spectra of the (opt)EsTKα protein showed a negative peak near 193 nm, and the CD spectra of (opt)EsTKγ protein showed a negative peak near 195 nm. Both of these negative peaks are typical of random coil structures (Li et al., 2008). The CD spectrum of the (opt)EsTKs protein showed a positive peak at near 198 nm, which is characteristic of the β-sheet conformation (Li et al., 2008). The CD spectrum of the assembled (opt)EsTKs protein showed a strong negative peak near 210 nm. The intensity ratio of 222/208 in the CD output of (opt)EsTKs protein was 0.93. Proteins with a 222/208 nm ratio above 1 are considered to exhibit coiled-coil folding (Frère et al., 1995). Data processing was used to calculate the relative content of each secondary structure (α-helix, β-sheet, β-turn, random coil) in the assembled protein product. The assembled product was comprised of 43.0% α-helix, 21.9% β-turn, 11.2% β-sheet, and 23.9% random coil. By comparing the CD test results before and after assembly of the two proteins, we observed that the assembled (opt)EsTKα and (opt)EsTKγ proteins changed dramatically in their secondary structures due to the interactions between the two protein molecules. Specifically, the proteins changed their secondary structures from random coil to α-helix. Jing Fu et al. previously assembled the purified EsTKα and EsTKγ proteins (Fu et al., 2015). Based on their CD analysis, the CD spectra of Jing Fu et al.'s assembled protein products had obvious minimum values at 208 and 222 nm. The 222/208 intensity ratio in the CD results for the assembled proteins was 0.92 (Fu et al., 2015). Jing Fu et al.'s assembled products also consisted primarily of α-helix. Therefore, the assembled proteins obtained by our method and Fu et al.'s method were similar in their secondary structures.

For the assembled protein products, FT-IR tests were performed in addition to CD tests. The FT-IR spectrum is shown in **Figure 6A**. The amide I band (1600–1700 cm^{-1}) in the FT-IR spectrum contains abundant secondary structure information (α-helix, β-sheet, β-turn, random coil, etc.), and was the focus of our analysis. Different sub-peaks were

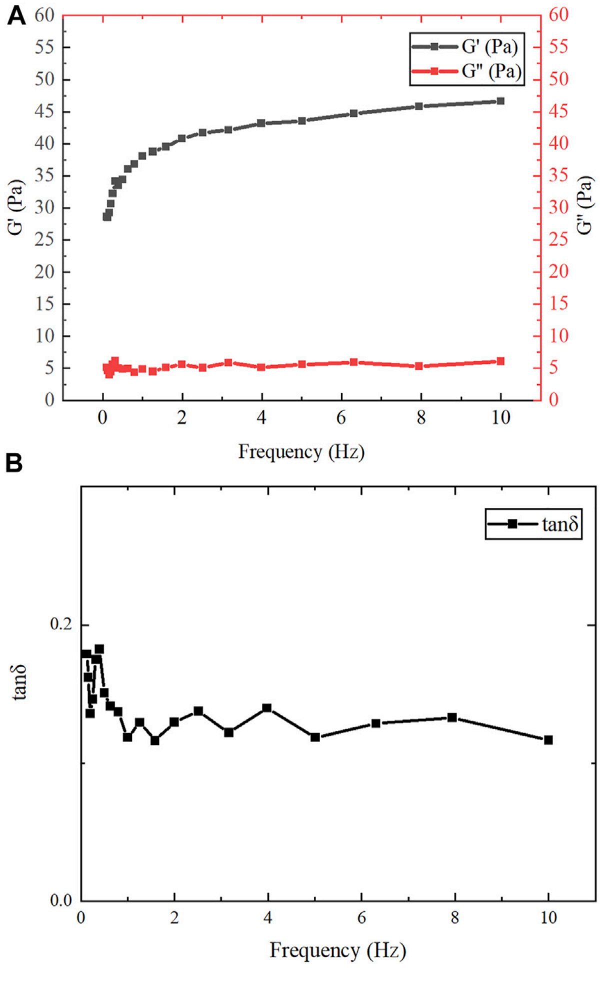

FIGURE 7 | Rheological test results. **(A)** The variation of G′ and G″ of gelatinous products in the range of f (0.1–10 Hz). **(B)** The variation of tan δ in the range of f (0.1–10 Hz).

obtained by deconvolution and Gaussian fitting of the amide I band (**Figure 6B**). By analyzing the amide I band, the α-helix content was 42.8%, the β-turn content was 20.3%, the β-sheet content was 23.9%, and the random coil content was 13.0% (Wu et al., 2017; Dong et al., 2021). There were some differences between CD and FT-IR analyses of the assembled protein products, due to the limitations of each method. Therefore, the exact secondary structure compositions obtained by CD and FT-IR were not identical. However, both methods were consistent in their determination that the secondary structure of the assembled protein consists primarily of α-helix.

Rheology of Assembled Proteins

After assembly at low temperature, the protein product was milky white, transparent, and flowing. The dynamic frequency scanning results of the assembled protein products under the conditions of 1% γ and 0.1–10 Hz f are shown in **Figure 7A**. In the entire measured frequency range, the change of G'' is not obvious, but G' gradually increases with the increase of f. Therefore, compared with G'', G' plays a leading role in the entire f range. This shows that the dependence of the viscoelastic modulus on oscillation frequency is relatively high, which means that the overall chain mobility of the network is relatively high (Lopes-da-Silva et al., 2007). As shown in **Figure 7B**, the change of tan δ was not obvious in the measured frequency range and was always less than 1, indicating that the assembled protein products showed gel-like behavior (Fu et al., 2015). Jing Fu et al. also found through experiments that all 1:1 mixtures of purified proteins at concentrations higher than 0.2 mg/ml showed gel-like behavior ($G''/G' < 1$) (Fu et al., 2015).

CONCLUSION

The present study demonstrates direct self-assembly of (opt)EsTKα and (opt)EsTKγ under the assembly conditions of 4°C, dialysis solution pH 9, and a 1:1 starting ratio of (opt)EsTKα:(opt)EsTKγ both at 1.0 mg/ml. After self-assembly, the two proteins form a new protein gel material. This method of direct assembly omits the need for protein purification, which saves time, allows for rapid and efficient protein assembly. The assembled protein gel was determined by SDS-PAGE analysis to have roughly equal proportions of (opt)EsTKα and (opt)EsTKγ proteins. We calculated that 5 mg each of (opt)EsTKα and (opt) EsTKγ would form approximately 4 ml of gel-like assembled protein. The protein gels after freeze-drying were observed using SEM and AFM. After self-assembly, the protein had many fiber structures with indications of a smooth surface. These protein fibers cross and aggregate to create a three-dimensional porous network structure with dense pores, forming the backbone of the protein gel. This network structure provides the assembled proteins with good water holding capacity. The rheological property test also showed that this new protein material exhibited gel-like behavior. CD analysis of the two proteins before and after assembly showed that the two proteins had random coil structures before self-assembly that changed after self-assembly. These results demonstrate that the method of direct assembly could successfully assemble both proteins. The CD and FT-IR spectra of the assembled protein gels were analyzed to obtain the secondary structure, which was found consist of more than 40% α-helix. The specific interactions between (opt)EsTKα and (opt)EsTKγ and their overall structural characteristics require further study. Due to the excellent biocompatibility and biodegradability of protein-based hydrogel. These properties make it a more widely used potential in the non-food industry field, such as simulating organism tissues, as a carrier for drugs, etc., for biomedical engineering. Moreover, it also has a wide application potential in leather, pharmaceutical, cosmetic, plastic, textile, biochemical and other industries. In addition, protein gels could be applied as water absorbers and retaining agents in a variety of fields due to their water absorption and retainment abilities. However, poor salt tolerance is an insurmountable drawback for most existing hydrogels. The hagfish slime protein used in this study is a potential solution to this challenge because it comes from the ocean and has a unique salt tolerance. In future studies, the hagfish slime assembled protein gel could be complexed with a polyaspartic acid hydrogel to prepare a high-performance biomimetic salt-tolerant hydrogel. It may replace some synthetic substances derived from oil and become a high-performance green and environmentally friendly, sustainable natural material.

DATA AVAILABILITY STATEMENT

The original contributions presented in the study are included in the article/supplementary material, further inquiries can be directed to the corresponding author.

AUTHOR CONTRIBUTIONS

LL and HC contributed to conception and design of the study. RS, RZ, WZ, and XZ performed the experiments and wrote the first draft of the manuscript. RS and RZ performed the data analysis and the production of tables and diagrams. RS, WZ, and XZ wrote sections of the manuscript. All authors contributed to manuscript revision, read, and approved the submitted version.

FUNDING

BUCT received financial support from the National Key Research and Development Program of China (grant number 2021YFF0600703).

REFERENCES

Aigner, T. B., DeSimone, E., and Scheibel, T. (2018). Biomedical Applications of Recombinant Silk-Based Materials. *Adv. Mater.* 30 (19), 1704636. doi:10.1002/adma.201704636

Boeynaems, S., Alberti, S., Fawzi, N. L., Mittag, T., Polymenidou, M., Rousseau, F., et al. (2018). Protein Phase Separation: A New Phase in Cell Biology. *Trends Cell Biol.* 28 (6), 420–435. doi:10.1016/j.tcb.2018.02.004

Cheng, Y., Donkor, P. O., Ren, X., Wu, J., Agyemang, K., Ayim, I., et al. (2019). Effect of Ultrasound Pretreatment with Mono-Frequency and Simultaneous Dual Frequency on the Mechanical Properties and Microstructure of Whey Protein Emulsion Gels. *Food Hydrocoll.* 89, 434–442. doi:10.1016/j.foodhyd.2018.11.007

Chromy, B. A., Nowak, R. J., Lambert, M. P., Viola, K. L., Chang, L., Velasco, P. T., et al. (2003). Self-Assembly of Abeta(1-42) into Globular Neurotoxins. *Biochemistry* 42 (44), 12749–12760. doi:10.1021/bi030029q

Dong, X., Yang, X., Li, H., Che, H., Song, L., Chen, X., et al. (2021). Effects of Oxidation on the Structure of Collagen Fibers of Sea Cucumber (Apostichopus Japonicus) Body Wall during Thermal Processing. *LWT- Food Sci. Technol.* 138, 110528. doi:10.1016/j.lwt.2020.110528

Downing, S. W., Spitzer, R. H., Salo, W. L., Downing, J. S., Saidel, L. J., and Koch, E. A. (1981). Threads in the Hagfish Slime Gland Thread Cells: Organization, Biochemical Features, and Length. *Science* 212 (4492), 326–328. doi:10.1126/science.212.4492.326

Fernholm, B. (1981). Thread Cells from the Slime Glands of Hagfish (Myxinidae). *Acta Zool.* 62 (3), 137–145. doi:10.1111/j.1463-6395.1981.tb00623.x

Frère, V., Sourgen, F., Monnot, M., Troalen, F., and Fermandjian, S. (1995). A Peptide Fragment of Human DNA Topoisomerase II α Forms a Stable Coiled-Coil Structure in Solution. *J. Biol. Chem.* 270 (29), 17502–17507. doi:10.1074/jbc.270.29.17502

Fu, J., Guerette, P. A., and Miserez, A. (2015). Self-Assembly of Recombinant Hagfish Thread Keratins Amenable to a Strain-Induced α-Helix to β-Sheet Transition. *Biomacromolecules* 16 (8), 2327–2339. doi:10.1021/acs.biomac.5b00552

Fu, J., Guerette, P. A., Pavesi, A., Horbelt, N., Lim, C. T., Harrington, M. J., et al. (2017). Artificial Hagfish Protein Fibers with Ultra-high and Tunable Stiffness. *Nanoscale* 9 (35), 12908–12915. doi:10.1039/c7nr02527k

Fudge, D. S., Levy, N., Chiu, S., and Gosline, J. M. (2005). Composition, Morphology and Mechanics of Hagfish Slime. *J. Exp. Biol.* 208 (Pt 24), 4613–4625. doi:10.1242/jeb.01963

Fudge, D. S., Schorno, S., and Ferraro, S. (2015). Physiology, Biomechanics, and Biomimetics of Hagfish Slime. *Annu. Rev. Biochem.* 84 (1), 947–967. doi:10.1146/annurev-biochem-060614-034048

Herrmann, H., and Aebi, U. (2000). Intermediate Filaments and Their Associates: Multi-Talented Structural Elements Specifying Cytoarchitecture and Cytodynamics. *Curr. Opin. Cell Biol.* 12 (1), 79–90. doi:10.1016/S0955-0674(99)00060-5

Herrmann, H., Wedig, T., Porter, R. M., Lane, E. B., and Aebi, U. (2002). Characterization of Early Assembly Intermediates of Recombinant Human Keratins. *J. Struct. Biol.* 137 (1-2), 82–96. doi:10.1006/jsbi.2002.4466

Johnson, G. A., Tramaglini, D. M., Levine, R. E., Ohno, K., Choi, N.-Y., and L-Y. Woo, S. (1994). Tensile and Viscoelastic Properties of Human Patellar Tendon. *J. Orthop. Res.* 12 (6), 796–803. doi:10.1002/jor.1100120607

Koch, E. A., Spitzer, R. H., Pithawalla, R. B., and Downing, S. W. (1991). Keratin-Like Components of Gland Thread Cells Modulate the Properties of Mucus from Hagfish (Eptatretus Stouti). *Cell Tissue Res.* 264 (1), 79–86. doi:10.1007/BF00305724

Kocher, P. N., and Foegeding, E. A. (1993). Microcentrifuge-Based Method for Measuring Water-Holding of Protein Gels. *J Food Sci.* 58 (5), 1040–1046. doi:10.1111/j.1365-2621.1993.tb06107.x

Li, X.-G., Wu, L.-Y., Huang, M.-R., Shao, H.-L., and Hu, X.-C. (2008). Conformational Transition and Liquid Crystalline State of Regenerated Silk Fibroin in Water. *Biopolymers* 89 (6), 497–505. doi:10.1002/bip.20905

Lim, J., Fudge, D. S., Levy, N., and Gosline, J. M. (2006). Hagfish Slime Ecomechanics: Testing the Gill-Clogging Hypothesis. *J. Exp. Biol.* 209 (4), 702–710. doi:10.1242/jeb.02067

Lopes-da-Silva, J. A., Santos, D. M., Freitas, A., Brites, C., and Gil, A. M. (2007). Rheological and Nuclear Magnetic Resonance (NMR) Study of the Hydration and Heating of Undeveloped Wheat Doughs. *J. Agric. Food Chem.* 55 (14), 5636–5644. doi:10.1021/jf070379

Ma, D., Wang, Y., and Dai, W. (2018). Silk Fibroin-Based Biomaterials for Musculoskeletal Tissue Engineering. *Mater. Sci. Eng. C* 89, 456–469. doi:10.1016/j.msec.2018.04.062

Oliveira, P. E., Chen, D., Bell, B. E., Harris, T. I., Walker, C., Zhang, H., et al. (2021). The Next Generation of Protein Super-fibres: Robust Recombinant Production and Recovery of Hagfish Intermediate Filament Proteins with Fibre Spinning and Mechanical-Structural Characterizations. *Microb. Biotechnol.* 14 (5), 1976–1989. doi:10.1111/1751-7915.13869

Pinto, N., Yang, F.-C., Negishi, A., Rheinstädter, M. C., Gillis, T. E., and Fudge, D. S. (2014). Self-Assembly Enhances the Strength of Fibers Made from Vimentin Intermediate Filament Proteins. *Biomacromolecules* 15 (2), 574–581. doi:10.1021/bm401600a

Salvador, P., Toldrà, M., Saguer, E., Carretero, C., and Parés, D. (2009). Microstructure-function Relationships of Heat-Induced Gels of Porcine Haemoglobin. *Food Hydrocoll.* 23 (7), 1654–1659. doi:10.1016/j.foodhyd.2008.12.003

Stine, W. B., Jungbauer, L., Yu, C., and LaDu, M. J. (2011). Preparing Synthetic Aβ in Different Aggregation States. *Methods Mol. Biol.* 670, 13–32. Humana Press. doi:10.1007/978-1-60761-744-0_2

Wu, X., Liu, Y., Liu, A., and Wang, W. (2017). Improved Thermal-Stability and Mechanical Properties of Type I Collagen by Crosslinking with Casein, Keratin and Soy Protein Isolate Using Transglutaminase. *Int. J. Biol. Macromol.* 98, 292–301. doi:10.1016/j.ijbiomac.2017.01.127

Wu, X. (2012). *Preparation and Characterization of Injectable In-Ssitu Regenerated Silk Hydrogels*. Suzhou: Soochow University. master's thesis.

Yang, R., Sun, R., Zhu, W., Zhang, Q., Liu, D., Zheng, R., et al. (2021). Heterologous Expression and Purification of Hagfish Mucus Protein. *J. Biobased Mat. Bioenergy* 15 (1), 20–32. doi:10.1166/jbmb.2021.2031

Zintzen, V., Roberts, C. D., Anderson, M. J., Stewart, A. L., Struthers, C. D., and Harvey, E. S. (2011). Hagfish Predatory Behaviour and Slime Defence Mechanism. *Sci. Rep.* 1, 131. doi:10.1038/srep00131

Conflict of Interest: The authors declare that the research was conducted in the absence of any commercial or financial relationships that could be construed as a potential conflict of interest.

frontiers | Frontiers in Bioengineering and Biotechnology

ORIGINAL RESEARCH
published: 04 August 2022
doi: 10.3389/fbioe.2022.916931

Heparin/Collagen-REDV Modification of Expanded Polytetrafluoroethylene Improves Regional Anti-thrombosis and Reduces Foreign Body Reactions in Local Tissues

Yaping Shan[†], Gang Chen[†], Qiqi Shi[†], Jiaxi Huang, Yaping Mi, Wenbo Zhang, Huifeng Zhang and Bing Jia**

Shanghai Key Laboratory of Cardiovascular Disease, Department of Cardiovascular Center, Children's Hospital of Fudan University, Shanghai, China

Prosthetic implants of expanded polytetrafluoroethylene (ePTFE) in the cardiovascular system have a high failure rate over the long term because of thrombosis and intimal hyperplasia. Although multiple surface modification methods have been applied to improve the anti-thrombotic and *in situ* endothelialization abilities of ePTFE, none have delivered outstanding results *in vivo*. Our previous study combined heparin/collagen multilayers and REDV peptides to modify ePTFE, and the *in-vitro* results showed that modification ePTFE with heparin/collagen-REDV can promote the cytocompatibility and antiplatelet property. This study illustrated the physical change, selective endothelial cells capture ability, and *in vivo* performance in further. The physical test demonstrated that this modification improved the hydrophilicity, flexibility and strength of ePTFE. A competition experiment of co-cultured endothelial cells and vascular smooth muscle cells verified that the heparin/collagen-REDV modification had high specificity for endothelial cell capture. A rabbit animal model was constructed to evaluate the *in vivo* performance of modified ePTFE implanted in the right ventricular outflow tract. The results showed that heparin/collagen-REDV modification was safe, promoted endothelialization, and successfully achieved regional anti-thrombosis without influencing body-wide coagulation function. The pathologic manifestations and mRNA expression pattern in tissues in contact with modified ePTFE indicated that this modification method may reduce M2-type macrophage infiltration and the expression of genes related to immune and inflammatory responses. The heparin/collagen-REDV modification may lower the incidence of complications related to ePTFE implantation and has good prospects for clinical use.

Keywords: expanded polytetrafluoroethylene (ePTFE), surface modification, endothelialization, foreign body reaction, biocompatibility

Edited by:
Rumen Krastev,
Reutlingen University, Germany

Reviewed by:
Katsuhiro Hosoyama,
Iwate Prefectural Central Hospital, Japan
Deirdre Anderson,
Oregon Health and Science University, United States
Xin Xiong,
NMI Natural and Medical Sciences Institute, Germany

****Correspondence:***
Huifeng Zhang
pluckzhang06@163.com
Bing Jia
jiabing2012@hotmail.com

[†]These authors have contributed equally to this work and share first authorship

Specialty section:
This article was submitted to Biomaterials, a section of the journal Frontiers in Bioengineering and Biotechnology

Received: *10 April 2022*
Accepted: *07 June 2022*
Published: *04 August 2022*

Citation:
Shan Y, Chen G, Shi Q, Huang J, Mi Y, Zhang W, Zhang H and Jia B (2022) Heparin/Collagen-REDV Modification of Expanded Polytetrafluoroethylene Improves Regional Anti-thrombosis and Reduces Foreign Body Reactions in Local Tissues. Front. Bioeng. Biotechnol. 10:916931. doi: 10.3389/fbioe.2022.916931

Abbreviations: ePTFE, Expanded Polytetrafluoroethylene; REDV, Arg-Glu-Asp-Val; FBR, Foreign Body Reaction; ECs, Endothelial Cells; WCA, Water Contact Angle; N-ePTFE, Normal ePTFE; M-ePTFE, Modified ePTFE; SMCs, Smooth Muscle CellsSMCs; PT, Prothrombin Time; TT, Thrombin Time; APTT, Activated Partial Thromboplastin Time; Fib, Fibrinogen; DEmRNAs, Differentially Expressed mRNAs.

1 INTRODUCTION

Expanded polytetrafluoroethylene (ePTFE) is a polymer that is widely used in medical devices (Goodson, 1987; Levine and Berman, 1995; Sigurdsson et al., 1995; Redbord and Hanke, 2008). Its durable physical and chemical characteristics have made ePTFE synthetic vascular grafts the cardiovascular surgeon's first choice for the reconstruction of blood flow when lacked the autologous grafts (Cassady et al., 2014; Ambler and Twine, 2018). In Asia, ePTFE valved conduits, which comprise an ePTFE membrane sewn to an ePTFE vascular graft, have become popular in pediatric population for the reconstruction of right ventricular outflow tract (Chang et al., 2021). Although ePTFE offers great advantages for cardiovascular uses, improvements are still needed. The biggest limitation in ePTFE implantation is the high incidence of stenosis, especially for grafts with small diameters (≤6 mm) (Sasikumar et al., 2017; Yamamoto et al., 2019; Shibutani et al., 2020).

In recent years, there have been many efforts to reduce the occurrence of stenosis following ePTFE implantation, with most of the research focused on improving anti-thrombosis using a variety of techniques (Hedayati et al., 2019; Jeong et al., 2020). However, little attention has been paid to another important cause of stenosis: foreign body reaction (FBR), a type of chronic inflammatory response that occurs locally in tissues in contact with foreign materials (Anderson et al., 2008).

Heparin was a common anticoagulant which can exert activity both *in vivo* and *in vitro*, and it was proved that heparin combined with collagen to modify materials can promote the anticoagulant properties and cell proliferation (Lu et al., 2013; Ferreira et al., 2016). Arg-Glu-Asp-Val (REDV) peptides can specific recognize $\alpha 4\beta 1$ integrin receptor expressed on the membrane of endothelial cells (ECs), and it was verified that modification materials of REDV peptides can improve the ECs attachment on materials (Butruk-Raszeja et al., 2016). Our previous study first combined heparin, collagen and REDV peptides to modify ePTFE, and the results showed that this modification method inhibited platelet aggregation and promoted endothelial cells adhesion *in vitro* (Shan et al., 2018). So, we hypothesized that this modification method can also improve the anti-thrombotic and *in situ* endothelization abilities *in vivo* and reduce the stenosis after ePTFE implantation. In this study, we aimed to evaluate the safety of ePTFE modified with heparin/collagen-REDV, and to further examine its anti-thrombotic and *in situ* endothelization abilities in a rabbit model. We also investigated the degree and mechanism of FBR in local tissue implanted with this modification of ePTFE using pathologic and molecular analyses.

2 MATERIALS AND METHODS

2.1 Expanded Polytetrafluoroethylene Modification

The modification of ePTFE (W.L. Gore & Associates, Newark, DE, United States) with heparin, collagen and REDV peptides was carried out according to our previously published method (Shan et al., 2018). Briefly, five bilayers of heparin (4 mg/L, Aladdin Chemistry Co., Ltd., Shanghai, China) and collagen which extracted from rat tail (each at 4 mg/L, Aladdin Chemistry Co., Ltd., Shanghai, China) were fabricated onto ePTFE membranes using a layer-by-layer technique. Successful assembly was verified by Fourier-transform infrared (FTIR) spectroscopy on a Nicolet 6,700 (Thermo Electron Corp, Waltham, MA, United States). GREDVY (Gly-Arg-Glu-Asp-Val-Tyr) peptides which containing REDV (Shanghai Science Peptide Biological Technology Co., Ltd., Shanghai, China) and labeled with fluorescein isothiocyanate were then added using a chemical grafting technique; successful grafting was confirmed by observing the fluorescence density via confocal laser scanning microscopy (Leica, Wetzlar, Germany).

2.2 *In vitro* Study

2.2.1 Water Contact Angle Test

The water contact angle (WCA) of normal (unmodified) ePTFE (N-ePTFE, $n = 3$) and modified ePTFE (M-ePTFE, $n = 3$) was measured at room temperature using a SZ10-JC2000A contact angle goniometer (Beijing Zhongxianda Technology Co., Ltd., Beijing, China). Averaged WCA values were calculated after dropping a 3-μL volume of deionized water onto the surface of each material, tested at three different places.

2.2.2 Tensile Properties

N-ePTFE ($n = 3$) and M-ePTFE ($n = 3$) membranes were cut into uniform strips with a 1.5-cm × 0.4-cm cutter. Tensile tests were carried out by an Instron 5,966 (Instron, Norwood, MA, United States) equipped with a 100-N load cell at 37°C. Samples were stretched at a constant extension speed of 10 mm/min, and tensile force was applied until the materials failed. Concurrently, a stress–strain curve was recorded, and the Young's modulus and percent elongation at break were calculated.

2.2.3 Specificity of Endothelial Cells Adsorption

The vascular endothelial cells and vascular smooth muscle cells (SMCs) were obtained from pulmonary artery of rats (Shanghai Upenol Biological Technology Co., Ltd., Shanghai, China), and cultured in high-glucose Dulbecco's modified Eagle's medium containing 10% fetal bovine serum at 37°C in a humidified 5% CO^2 incubator. ECs and SMCs were labeled with the fluorescent dyes CellTracker Red (CM-Dil) and CellTracker Green (5-chloromethylfluorescein diacetate), respectively (Invitrogen, Carlsbad, CA, United States). M-ePTFE ($n = 3$) and N-ePTFE ($n = 3$) membranes were fixed with circular glass molds to the bottom of Nunc glass-bottom cell culture dishes (Invitrogen); blank wells are normal cell culture dishes without ePTFE coating were set as the Control group ($n = 3$). A mixture of ECs and SMCs in equal proportions were then seeded at a final density of 2×10^5 cells/well. After co-culturing for 8 h, materials adhered to the bottom of the dishes were removed, the materials were washed three times with phosphate-buffered saline and transferred to new dishes, followed by the addition of fresh culture medium for another 24 h of co-culturing. The cell numbers and types on each material were observed at 8 and 24 h via confocal laser scanning microscopy with ×20 objective lens (Leica, Wetzlar, Germany).

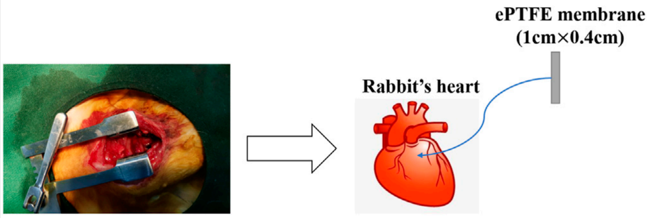

FIGURE 1 | Surgical diagram of expanded polytetrafluoroethylene (ePTFE) implantation site.

2.3 *In vivo* Study

2.3.1 Animal Model

We implanted M-ePTFE (n = 12) and N-ePTFE (n = 12) membranes into the right ventricular outflow tract of 3-month-old New Zealand rabbits (Shanghai Jiagan Inc., Shanghai, China). Prior to the operation, the experimental rabbits were food-fasted for 6 h, anesthetized intramuscularly with 15 mg/kg Zoletil®50 (Virbac S.A, France), and oxygenized with a mask. After being placed on the operating table, skin was shaved and disinfected, and a median sternal incision was made to expose the heart, and the pericardial membrane was cut to locate the right ventricular outflow tract. A purse-string suture was preset, and a 1-cm × 0.4-cm ePTFE membrane was inserted into the right ventricle from the middle of the purse-string, ensuring that the ePTFE membrane was exposed to blood and in contact with myocardium. **Figure 1** showed the general surgical procedure: After fixing the ePTFE membrane in place, the sternum was closed. No anticoagulants or antiplatelet agents were used after the operation, but antibiotics were used for 3 days. Control group rabbits (n = 12) did not receive the operation. Body weight was measured every 2 weeks, and typical blood indexess, including inflammatory response, coagulation function, renal and liver function, and creatine kinase levels were continuously monitored at 1st, 3rd, 7th, 14th, 30th and 90th days post-operation. At 14th and 90th days postoperatively, 6 rabbits from each group were anesthetized by injecting air through an auricular vein to remove the ePTFE membranes and to collect myocardial tissue with a diameter of 0.5 cm around the implanted material. The myocardial tissue from every rabbit was divided into two parts. The first part which fixed by paraformaldehyde was used to pathologic analysis, and the second part was cut up into little pieces and stored in RNAlater (Invitrogen) at -20°C for RNA analysis. The experimental protocol was approved by the Animal Care and Ethical Committee of Children's Hospital of Fudan University, and animal experiments were performed according to their guidelines.

2.3.2 Thrombosis and Endothelialization Assessment

After removing the implanted materials from the heart and washing them with 0.9% NaCl solution, the ePTFE membrane was divided into two equal parts along the long axis; one part was fixed with 2.5% glutaraldehyde solution for observation under scanning electron microscopy (SEM, Hitachi, Tokyo, Japan), and the other was fixed with 4% paraformaldehyde solution for immunofluorescence with CD34 antibody (Cell Signaling Technology, Danvers, MA, United States). to detect ECs on the ePTFE.

2.3.3 Blood Analyses

Whole blood was collected from the rabbits preoperatively, and at first, 3rd, 7th, 14th, 30th and 90th days postoperatively, for routine examinations using a BC-2800 vet automated hematology analyzer (Shenzhen Ledu Life Science and Technology Co., Ltd., Shenzhen, China). After isolating the serum, interleukin (IL)-1β was detected with an enzyme-linked immunosorbent assay kit (Invitrogen) under a BioTek ELx800 automatic microplate reader (Winooski, VT, United States). Kits were used to measure the levels of alanine aminotransferase (ALT), total bilirubin (TBIL), creatinine (Cr), and creatine kinase (CK) were measured by the corresponding kits for each using a Chemray 240 automatic biochemical analyzer (Shenzhen Reidu Life Science and Technology). To evaluate body-wide coagulation function, kits (Shenzhen Reidu Life Science and Technology) and a RAC-030 automatic blood coagulation analyzer (Shenzhen Reidu Life Science and Technology) were used to measure prothrombin time (PT), thrombin time (TT), activated partial thromboplastin time (APTT), and fibrinogen (Fib) in plasma isolated from whole blood.

2.3.4 Pathologic Analysis

The myocardial tissue which fixed with paraformaldehyde were embedded with paraffin and cut into 4 μm-thick myocardial tissue. Then dewaxed it in xylene, rehydrated through decreasing concentration of ethanol. Masson trichrome staining (Wuhan Google Seville Co., Ltd., Wuhan, China) was used to make the fibrosis tissue in blue. A distant view photograph of a stained myocardium section can be obtained by PANNORAMIC scanner. Then ImageJ software (Rawak Software Inc., Stuttgart, Germany) was used to calculate the area of fibrosis by identifying blue color. The degree of inflammation was evaluated by the infiltration of M1 and M2 type macrophages in the myocardium by technique: After dewaxing and antigen recovery of myocardium tissue sections, CD86 and CD206 (Proteintech, Rosemont, IL, United States) antibodies which label M1 and M2 type macrophages respectively were incubated with sections. Then the tissue sections were incubated with secondary antibodies which labeled with purple (Alexa Fluor 647) or green (Alexa Fluor 488) fluorescence and can combined with CD86 (purple) or CD206 (green) antibodies. After that, observe the tissue section under laser scanning confocal microscope with ×20 objective lens and capture 3 pictures of each section at random. The M1 and M2 macrophage infiltration was quantized by calculated area of fluorescence color by ImageJ software.

2.3.5 Transcriptome Analysis

Total RNA was extracted from myocardium surrounding the implants using a mirVana miRNA Isolation Kit (Ambion-1561; Thermo Fisher Scientific, Waltham, MA, United States) following the manufacturer's protocol. RNA integrity was evaluated using an Agilent 2,100 Bioanalyzer (Agilent Technologies, Santa Clara, CA, United States). Samples with an RNA Integrity Number

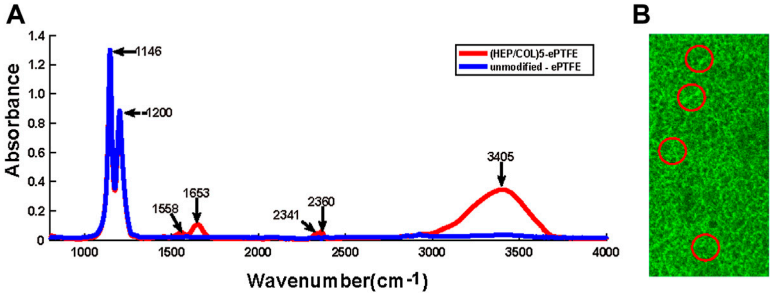

FIGURE 2 | Confirmation of the assembly of heparin, collagen and REDV, Arg-Glu-Asp-Val; peptides on ePTFE, expanded polytetrafluoroethylene membranes. **(A)** Fourier-transform infrared (FTIR) spectroscopy of unmodified ePTFE and ePTFE modified with 5 bilayers of heparin and collagen (HEP/COL)5 **(B)** Confocal laser scanning microscopy illustrating the distribution of REDV peptides on modified ePTFE membranes (areas of green fluorescence circled in red color); scale bar = 75 μm.

(RIN) ≥ 7 were subjected to the subsequent analyses. Libraries were constructed using a TruSeq Stranded mRNA LTSample Prep Kit (Illumina, San Diego, CA, United States) according to the manufacturer's instructions. Transcriptome sequencing and analysis were conducted by OE Biotech Co., Ltd., (Shanghai, China). Differentially expressed mRNAs (DEmRNAs) were identified by a DESeq R package using functions to estimate size factors and run the NbinomTest (Anders and Huber). *p* values <0.05 and fold changes >2 or <0.5 were set as the threshold for significantly differential expression. The distribution of common and specific DEmRNAs in different comparison groups was illustrated by Venna analyses. To analyze the function of DEmRNAs, Gene Ontology (GO) enrichment and Kyoto Encyclopedia of Genes and Genomes (KEGG) enrichment was conducted using R studio based on the hypergeometric distribution. Each GO term can be classified according to three function domains: cellular compartment (CC), biological process (BP), and molecular function (MF); the top 30 GO terms with the smallest *p* values, or all terms if fewer than 30 met the statistical criteria, were selected for graphical display. KEGG enrichment was used to find the signal pathways which contain DEmRNAs.

2.4 Statistical Analysis

Continuous variables are presented as the mean ± standard deviation. The Kolmogorov-Smirnov test was used to confirm the normality of variables of each group. One-way analysis of variance was used to identify the differences between multiple groups, and the *t* test was used to identify the differences between two groups. *p* values <0.05 were considered to be statistically significant.

3 RESULTS

3.1 Modification Expanded Polytetrafluoroethylene With Heparin/ Collagen-Arg-Glu-Asp-Val

The detection of the specific spectra of heparin (2,300–2,400 cm^{-2}) and collagen (1,500–1700 cm^{-2}) by FTIR spectrometry of M-ePTFE membranes indicated the successful assembly of the two substances (**Figure 2A**). Compact, uniform green fluorescence under confocal laser scanning microscopy confirmed the successful grafting of REDV peptides (**Figure 2B**).

3.2 *In vitro* Performance Evaluations

3.2.1 WCA and Hydrophilicity

As shown in **Figure 3A**, the average WCA of unmodified ePTFE (N-ePTFE) was 132 ± 4°, which indicated that N-ePTFE was a hydrophobic material. Upon modification with heparin/collagen-REDV, the average WCA decreased to 42 ± 4° (p = 0.00), demonstrating that the modification improved the hydrophilicity of ePTFE.

3.2.2 Tensile Properties

As shown in **Figure 3B**, the heparin/collagen-REDV modification significantly decreased the Young's modulus from 28.04 ± 0.73 MPa for N-ePTFE to 22.73 ± 0.80 MPa for M-ePTFE (p = 0.01), and the percent elongation increased from 217.78 ± 15.61% for N-ePTFE to 248.42 ± 10.14% for M-ePTFE (p = 0.044). These results indicated that the modification of ePTFE with heparin/collagen-REDV improved the flexibility of ePTFE without reducing its strength.

3.2.3 Specificity of EC Adsorption

The distribution and the number of ECs and SMCs in different group after cultured 8 and 24 h was shown in **Figure 4**. Although there was no significant differences in the numbers of ECs and SMCs in the N-ePTFE (4.13 ± 2.00 vs. 3.26 ± 1.75, p = 0.217) and control group (26.67 ± 2.92 vs. 27.07 ± 3.79, p = 0.748) after 8 h co-culture, there were more ECs than SMCs in the M-ePTFE group at 8 h (21.27 ± 3.61 vs. 4.60 ± 1.64, p = 0.000), and the number of ECs on M-ePTFE group was larger than on N-ePTFE group (p = 0.000), which indicated that the modification improved ECs attachment specifically (**Figure 4B**). After 24 h of co-culture M-ePTFE with EC-SMC mixture, the number of ECs increased significantly (92.87 ± 7.25 vs. 21.27 ± 3.61, p = 0.000) and was the highest among the three groups (p = 0.00), the number of SMCs on M-ePTFE group at 24 h wasn't increased when compared 8 h (4.13 ± 2.36 vs. 4.60 ± 1.64, p = 0.534), and the number of ECs was significantly larger than SMCs (p = 0.00).

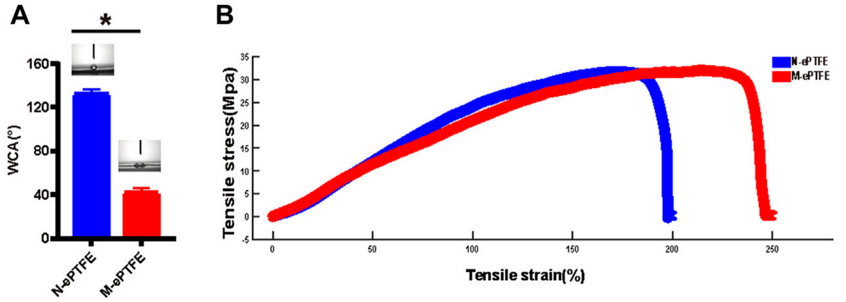

FIGURE 3 | Differences in **(A)** water contact angle (WCA) and **(B)** tensile properties between unmodified N-ePTFE/M-ePTFE, expanded polytetrafluoroethylene and modified ePTFE (M-ePTFE).

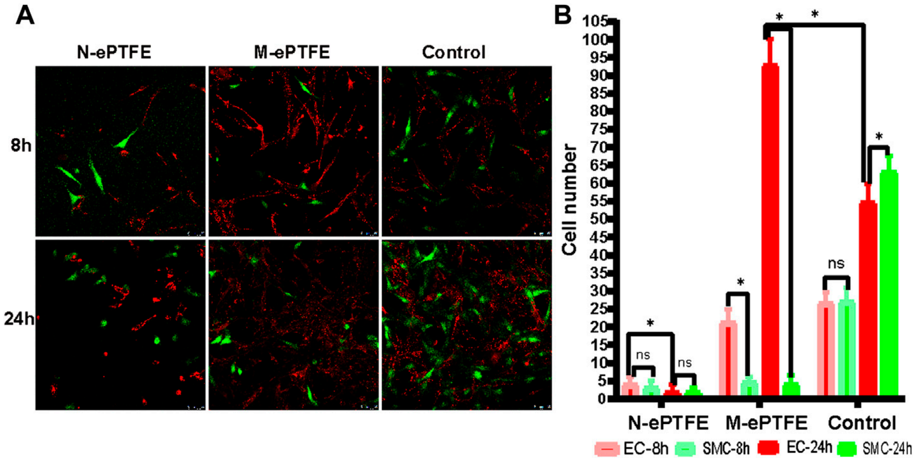

FIGURE 4 | Type and number of EC, endothelial cells; and SMC, smooth muscle cells; co-cultured on unmodified N-ePTFE/M-ePTFE, expanded polytetrafluoroethylene , modified (M-ePTFE) or control plates **(A)** Distribution of EC (labeled with red dye) and SMC (labeled with green dye) in each group (scale bar = 50 μm) **(B)** Numbers of EC and SMC after co-culturing for 8 and 24 h $^*p < 0.05$.

On Control group, both the number of ECs (26.67 ± 2.92 vs. 54.73 ± 5.08, $p = 0.00$) and SMCs (26.07 ± 3.79 vs. 63.13 ± 4.42, $p = 0.00$) increased significantly, but the number of ECs was less than SMCs ($p = 0.00$). However, both the number of ECs (4.13 ± 2.00 vs. 2.00 ± 1.89, $p = 0.006$) and SMCs (3.27 ± 1.75 vs. 1.80 ± 1.37, $p = 0.016$) decreased significantly on N-ePTFE group after 24 h co-culture. All those results indicated that the modification promoted the cytocompatibility of ePTFE and the proliferation of ECs.

3.3 *In vivo* Performance Evaluations

3.3.1 General Information on the Study Animals

In the N-ePTFE group, 17 rabbits received the operation, 3 died from surgical injuries and 2 died from diarrhea. In the M-ePTFE group, 16 rabbits received the operation, 1 died from surgical injuries and 3 died from diarrhea. In the control group, 14 rabbits received anesthesia but not the operation, and 2 rabbits died from diarrhea. All deaths happened within 1 week of the operation, and there was no significant difference in mortality rate between the N-ePTFE and M-ePTFE groups. Ultimately, 12 rabbits were included in each group; those that died were not included in the statistical analysis. The average body weights (kg) on the day of operation and 90th day later were 2.74 ± 0.12 and 3.85 ± 0.17, respectively, in the N-ePTFE group, 2.77 ± 0.95 and 4.04 ± 0.08 in the M-ePTFE group, and 2.79 ± 0.12 and 4.00 ± 0.15 in the Control group. There were no significant differences in weight at any point in time between the groups (Postoperative: $p = 0.547$, Day 90: $p = 0.083$).

3.3.2 Morphologic Change and Thrombosis After Implantation

At postoperative day 14, the N-ePTFE and M-ePTFE membranes that were removed from the right ventricular outflow tract were similar in appearance, with no visible changes compared with their appearance at pre-implantation (**Supplementary Figure S1**). Under SEM, however, there were marked differences between N-ePTFE and M-ePTFE (**Figure 5A,B**). There were multiple thrombi on the surface and micropores of N-ePTFE, but none on the M-ePTFE. At 90 d post-implantation, M-ePTFE membranes removed from the right ventricular

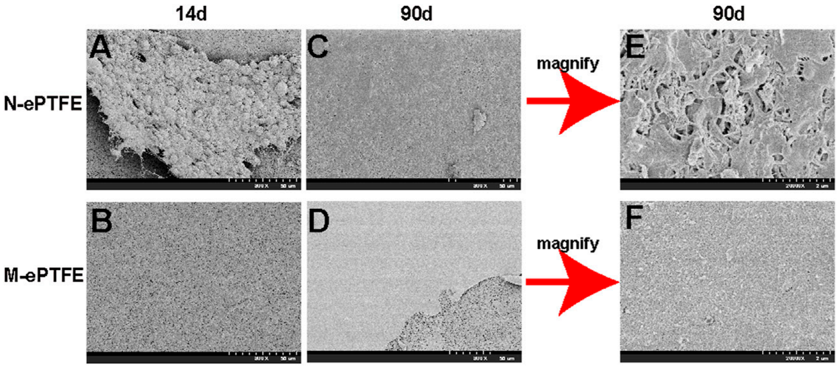

FIGURE 5 | Scanning electron microscopy showing the morphology of unmodified N-ePTFE/M-ePTFE, expanded polytetrafluoroethylene and modified (M-ePTFE) at 14 d and 90 d post-implantation in rabbits. Scale bar of **(A)–(D)** = 50 μm (2000×); Scale bar of **(E,F)** = 2 μm (20000×).

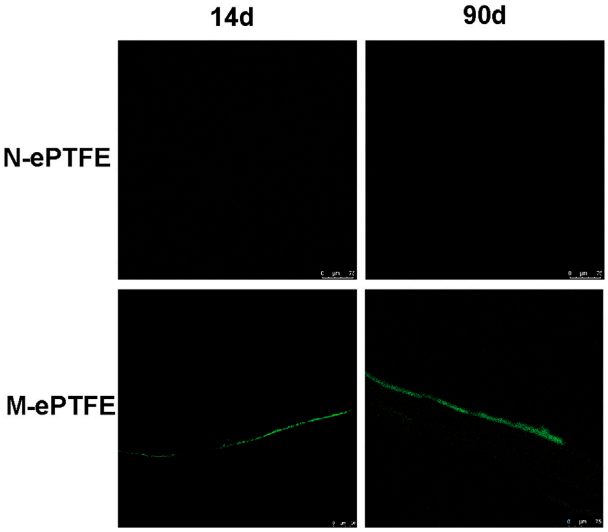

FIGURE 6 | Immunofluorescence of CD34 (green) as a marker for endothelial cells on unmodified N-ePTFE/M-ePTFE, expanded polytetrafluoroethylene and modified (M-ePTFE) at 14 d and 90 d post-implantation in rabbits. Scale bar = 75 μm.

outflow tract had become transparent, while N-ePTFE membranes were still white in color **Supplementary Figure S1**). Additionally, SEM showed that the surface of N-ePTFE was covered with a rough substance (**Figure 5C**) that was verified as thrombi under the higher power lens (**Figure 5E**). By contrast, the surface of M-ePTFE was covered with a smooth, thin film-like substance (**Figure 5D**) that appeared to be extracellular matrix when observed under the higher power lens (**Figure 5F**). There were no thrombi on the surface or micropores of M-ePTFE at 90 d post-implantation, indicating that it had good anticoagulation ability.

3.3.3 Endothelialization *in vivo*

To evaluate the level of endothelialization of ePTFE membranes implanted in the rabbit body, we used immunofluorescence of CD34 antibodies as a marker for the presence of ECs. As shown at **Figure 6**, ECs were found on M-ePTFE both at 14d and 90 d post-implantation, and the degree of endothelization increased over time. In contrast, there was no CD34-positive cells on N-ePTFE at either time period after implantation. These results indicated that the modification of ePTFE with heparin/collagen-REDV promoted the level of endothelialization *in situ*. This endothelial barrier may potentially protect implanted M-ePTFE materials from failure.

3.3.4 Systemic Inflammation Evaluation

Three blood biomarkers were used to evaluate the level of body-wide inflammation: white blood cell (WBC) count, and concentrations of serum IL-1β and plasma fibrinogen. As shown in (**Figures 7A–C**), both the N-ePTFE and M-ePTFE implantation could lead to a significant increase of those inflammatory biomarkers when compared to control group, and the time of peak values and the time which the biomarkers recovered to preoperative level was same between N-ePTFE and M-ePTFE group, which indicated that the heparin/collagen-REDV modification did not aggravate the inflammation caused by implantation of ePTFE materials. Another finding is that the time of IL-1β returned to its preoperative level was at day 30, which was longer than the time of WBC (day 14) and fibrinogen recovered to its preoperative level.

3.3.5 Systemic Coagulation Evaluation

Because the modification of ePTFE included the application of heparin, an anticoagulant, we calculated the body-wide coagulation function in each group. Although there were slight fluctuations in the three coagulation indexes (APTT, PT and TT) over time (**Figures 7D–F**), the there was no significant difference in the values of all those three indexes at any time point when compared to preoperative level. Those results showed that the heparin/collagen-REDV modification did not influence the body-wide coagulation function.

3.3.6 Whole Body Safety Evaluation

To evaluate the safety of the heparin/collagen-REDV modification of ePTFE in rabbits, several blood indexes were

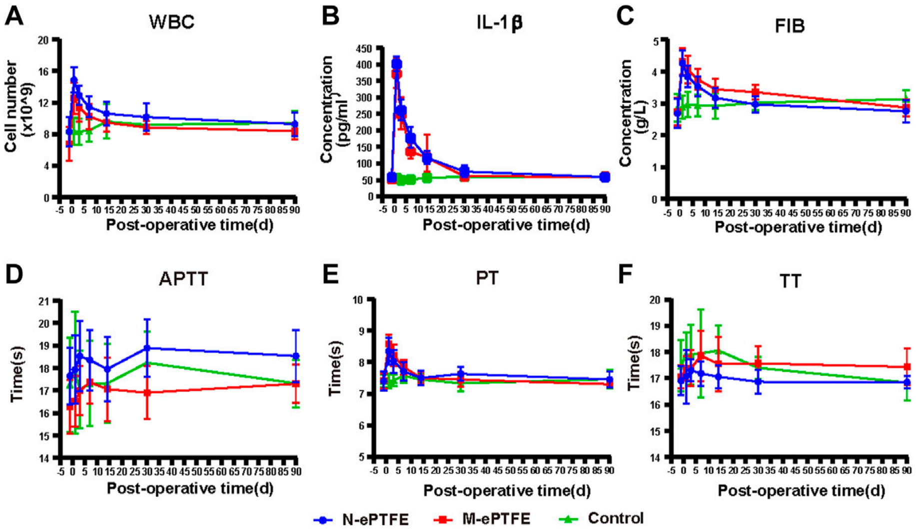

FIGURE 7 | Changes in indexes for inflammation **(A–C)** and coagulation **(C–F)** in the three groups at each time point(perioperative, 1 d,3 d,7 d,14 d,30 d, 90 d after operation). WBC, white blood cells; IL-1β, interleukin-1β; FIB, fibrinogen; PT, prothrombin time; TT, thrombin time; APTT, activated partial thromboplastin time; N-ePTFE/M-ePTFE, unmodified/modified expanded polytetrafluoroethylene; Control: No implantation.

TABLE 1 | Blood indexess in the three study groups.

Index	Time	N-ePTFE	M-ePTFE	Control	*p* Value
RBC ($\times 10^{12}$/L)	preoperative	5.05 ± 0.55	5.23 ± 0.71	5.68 ± 1.71	0.380
	14 d	4.28 ± 0.63	4.28 ± 0.73	5.28 ± 0.88	0.003
	90 d	5.23 ± 0.24	5.10 ± 0.55	4.82 ± 0.81	0.467
WBC ($\times 10^{9}$/L)	preoperative	8.30 ± 1.89	6.76 ± 2.10	8.43 ± 1.72	0.072
	14 d	10.60 ± 1.47	9.46 ± 1.19	9.60 ± 2.20	0.206
	90 d	9.27 ± 1.50	8.37 ± 1.06	9.40 ± 1.58	0.403
PLT ($\times 10^{9}$/L)	preoperative	372.50 ± 200.69	293.92 ± 166.73	363.42 ± 155.80	0.494
	14 d	335.83 ± 185.57	255.48 ± 148.57	363.42 ± 152.23	0.257
	90 d	388.67 ± 188.67	329.50 ± 164.15	333.17 ± 128.46	0.788
ALT (U/L)	preoperative	47.74 ± 13.98	56.83 ± 18.35	52.00 ± 7.71	0.297
	14 d	58.80 ± 9.89	59.45 ± 13.76	54.64 ± 8.58	0.514
	90 d	51.44 ± 12.43	50.07 ± 14.04	57.10 ± 11.30	0.604
TBIL (μmol/L)	preoperative	11.80 ± 3.28	10.20 ± 3.31	10.09 ± 3.07	0.359
	14 d	11.86 ± 3.09	10.68 ± 3.24	10.40 ± 3.32	0.508
	90 d	11.24 ± 3.06	9.72 ± 3.11	9.47 ± 4.48	0.663
CR (μmol/L)	preoperative	57.04 ± 9.08	57.09 ± 8.15	55.23 ± 9.10	0.840
	14 d	60.82 ± 10.83	62.47 ± 7.99	55.88 ± 8.59	0.205
	90 d	52.04 ± 3.17	54.97 ± 7.54	54.23 ± 5.81	0.669

N-ePTFE/M-ePTFE, unmodified/modified expanded polytetrafluoroethylene; RBC, red blood cells; WBC, white blood cells; PLT, platelets; ALT, alanine aminotransferase; TBIL, total bilirubin; CR, creatinine.

continuously monitored to reflect the blood system (WBC, RBC, PLT) and hepatorenal function (ALT, TBIL, Cr). As shown at **Table1**, there was a decrease in the red blood cell (RBC) level in the N-ePTFE and M-ePTFE groups when compared to control group after implantation, which could be attributed to bleeding during the operation, but there was no significant difference between those two groups and it had returned to normal at 30 d postoperatively. Furthermore, there was no significant increase or decrease for other five blood indexes during the 90 d monitor in all three groups, and there were no significant differences between the three groups at every time point. All those results indicated that modification ePTFE with heparin/collagen-Arg-Glu-Asp-Val was safety.

3.3.7 Myocardial Injury Evaluation

3.3.7.1 CK Assessment

CK is a typical marker used to assess the degree of myocardial injury. As shown in **Figure 8A**, there was no significant difference

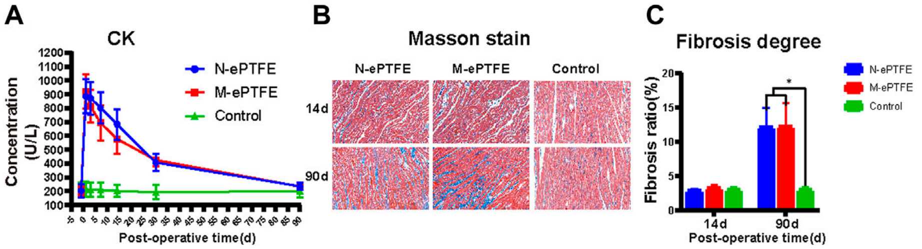

FIGURE 8 | Myocardial injury evaluations **(A)** Creatine kinase (CK) concentrations in whole blood in the three groups at each time point **(B)** Masson staining of normal myocardial tissue (Control) or myocardial tissues in contact with the expanded polytetrafluoroethylene (N-ePTFE) or modified ePTFE (M-ePTFE) membranes at 14 d and 90 d post-implantation (fibrotic tissue stained in blue) **(C)** Quantification of the degree of fibrosis in the three groups at 14 d and 90 d post-implantation (*n* = 6; *$p < 0.05$).

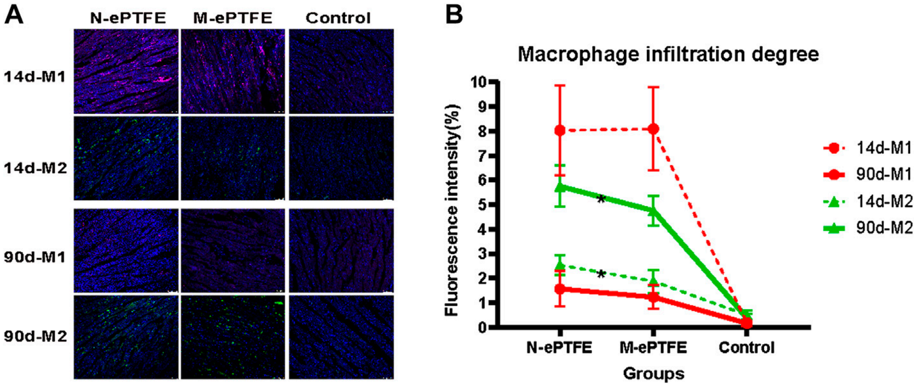

FIGURE 9 | Macrophage infiltration in the myocardium **(A)** Immunofluorescence showing distribution of M1 and M2 type macrophages in the myocardium in the three groups: purple, CD86- labeled M1; green, CD206-labeled M2; blue, nuclei **(B)** Quantification of the degrees of M1 and M2 infiltration at postoperative days 14 and 90 (*n* = 6; *$p < 0.05$). N-ePTFE/M-ePTFE, unmodified/modified expanded polytetrafluoroethylene; Control: No implantation.

in CK before operation between three groups, but this index in N-ePTFE or M-ePTFE groups was higher than in Control groups postoperatively. However, there was no significant difference in CK between the N-ePTFE and M-ePTFE groups at any time point, and the time of CK reached a peak level or down to the perioperative level was same between two ePTFE groups, which indicated that the heparin/collagen-REDV modification did not further aggravate the myocardial injury caused by the operation itself.

3.3.7.2 Degree of Myocardial Fibrosis

As shown at **Figure 8B,C** although fibrosis of myocardial tissue in contact with the M-ePTFE and N-ePTFE membranes did not become obvious when compared to control group at 14 d post-implantation (2.9 ± 0.3 vs. 3.2 ± 0.5 vs. 3.0 ± 0.4, $p = 0.574$)), both the degree of fibrosis in N-ePTFE or M-ePTFE group was higher than control group at 90 d (12.0 ± 2.9 vs. 12.2 ± 3.4 vs. 3.1 ± 0.5, $p = 0.00$). However, there was no significant difference between N-ePTFE and M-ePTFE group both at 14d and 90 d postoperatively. These results indicated that, although the long-term implantation of ePTFE materials in the myocardium did cause myocardial fibrosis, the heparin/collagen-REDV modification did not appear to affect the degree of fibrosis.

3.3.7.3 Inflammation of the Myocardium

Macrophages are an important cell type involved in the inflammatory response. On the 14 d postoperatively (**Figure 9A**), there was increased infiltration of both M1 and M2 type macrophages in the myocardium in the N-ePTFE and M-ePTFE groups compared with that in the Control group, with more severe infiltration of M1. At 90 d after operation (**Figure 9B**), although there was no significant difference in the degree of M1 infiltration between the N-ePTFE and M-ePTFE groups (4.0 ± 1.4 vs. 3.3 ± 0.8, $p = 0.085$), there was a difference in M2 infiltration (2.2 ± 0.3 vs. 1.9 ± 0.5, $p = 0.035$). M1 and M2 infiltration was still apparent at 90 d after operation, but the degree of M1 infiltration in both the M-ePTFE and N-ePTFE groups was decreased compared with that at 14d, while the degree of M2 infiltration was increased in both groups (**Figure 9B**). The degree of M2 infiltration in the N-ePTFE group remained greater than that in the M-ePTFE group at 90 d postoperatively (5.2 ± 0.6 vs. 4.5 ± 0.7, $p = 0.004$).

3.3.7.4 Altered mRNA Expression in the Myocardium

The mRNA sequencing data from myocardial tissues taken at 14 d post-implantation (**Figure 10A,C**) in the three groups

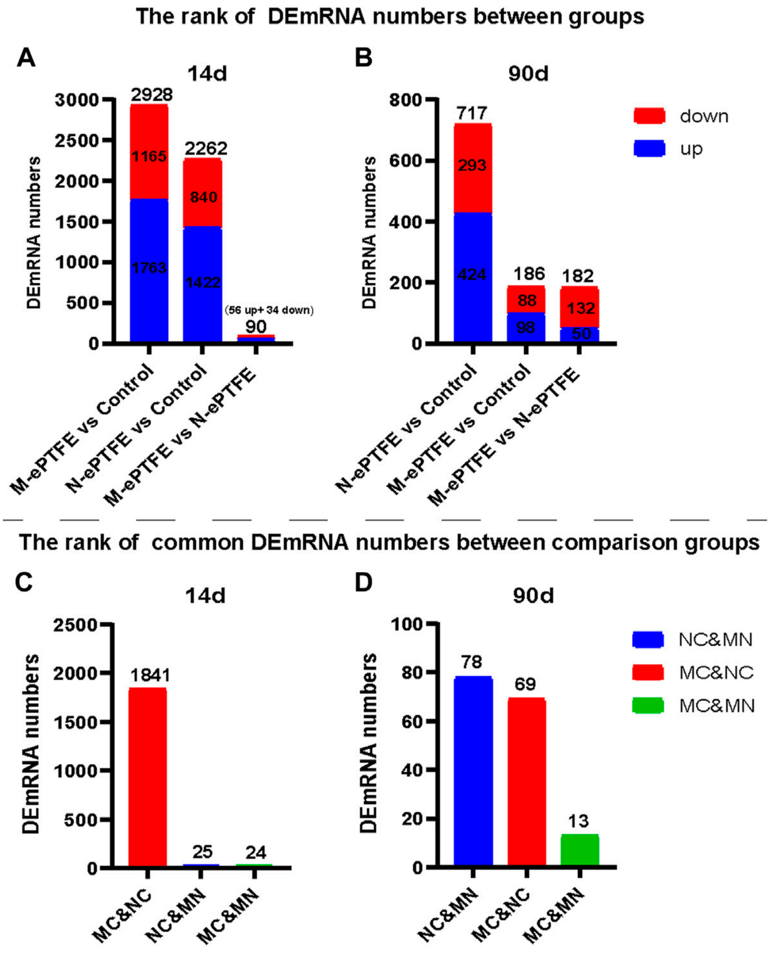

FIGURE 10 | Ranking of differentially expressed mRNA (DEmRNA) in the three groups. Total numbers of DEmRNAs **(A,B)** and numbers of common DEmRNAs **(C,D)** in different group comparisons: NC, unmodified expanded polytetrafluoroethylene (N-ePTFE) vs Control comparison group; MC, modified (M-ePTFE) vs Control comparison group; MN: M-ePTFE vs N-ePTFE comparison group.

revealed the following: the largest difference in the number of DEmRNAs was in the M-ePTFE vs. Control (MC) comparison group (2,928), followed by the N-ePTFE vs. Control (NC) comparison group (2,262); and the number of DEmRNAs in the M-ePTFE vs. N-ePTFE comparison group (MN) was smallest (90). Furthermore, the number of common DEmRNAs between different comparison groups was highest in MC and NC comparison groups. These data indicated a large degree of commonality in gene expression in tissue surrounding the M-ePTFE and N-ePTFE implants at 14 d post-implantation. At 90 d postoperatively, the gene expression patterns had changed dramatically (**Figure 10B,D**): the largest difference in the number of DEmRNAs was not between M-ePTFE vs. Control 186) comparison group but between the N-ePTFE and Control groups (717), which indicated that heparin/collagen-REDV modification can shorten the difference in gene expression between normal myocardium and ePTFE contacted myocardium. In addition, the comparison groups with highest common DEmRNAs were NC and MN comparison groups, which indicated that there was little similarity in gene expression patterns between the NC and MC comparison groups at 90 d when compared to 14 d. Therefore, although the heparin/collagen-REDV modification did not reduce the molecular changes in myocardium caused by ePTFE implantation in rabbits in the short term, it may be expected to reduce such changes over the long term.

Next, we analyzed the function of DEmRNAs in the MN comparison group to predict the molecular mechanisms involved in myocardial changes in response to M-ePTFE implantation. At 14 d post-implantation, GO enrichment analysis showed that DEmRNAs that were downregulated (**Figure 11A**) and upregulated (**Figure 11B**) were enriched in 13 and 19 GO terms, respectively, between the M-ePTFE and N-ePTFE groups. The enriched GO terms indicated that the ePTFE modification downregulated immune or inflammatory response-related genes and upregulated genes related to cell adhesion and the extracellular matrix (**Figure 11A**). At 90 d post-implantation, although the number of enriched GO terms 66) for the downregulated DEmRNAs had increased in the MN comparison groups when compared to 14d, the GO categories were still related to immune and inflammatory responses

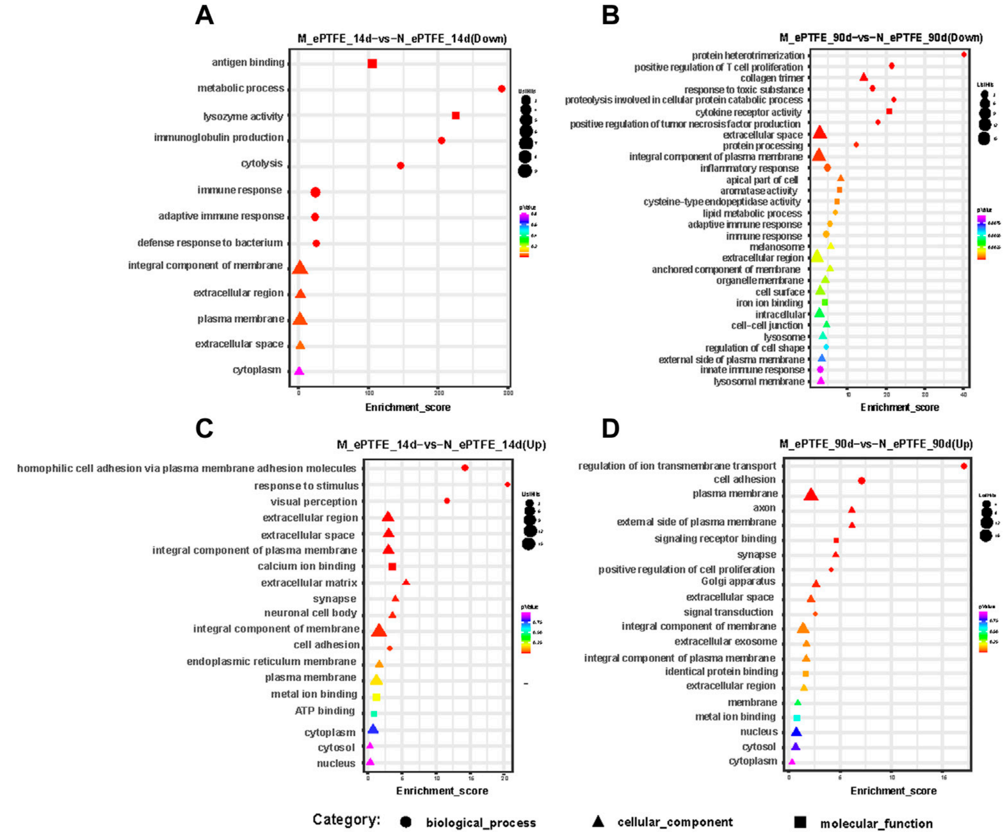

FIGURE 11 | Bubble diagrams of top gene ontology (GO) terms in the modified expanded polytetrafluoroethylene (M-ePTFE) vs unmodified ePFTE (N-ePTFE) comparison group at 14 days **(A)** downregulated; **(C)** upregulated) and 90 days **(B)** downregulated, **(D)** upregulated) post-implantation. The bubble shapes indicate different categories of GO terms, while the color and diameter indicate *p* values and numbers of differentially expressed mRNAs, respectively.

(**Figure 11C**). Otherwise, there were no significant changes in the total number 21) and categories of enriched GO terms among the upregulated DEmRNAs (**Figure 11D**). The KEGG enrichment analysis showed that there was 1 pathway related to inflammatory response with significant different between M-ePTFE and N-ePTFE comparison group at 14 d after operation, and this pathway (Cytokine-cytokine receptor interaction) contains up-regulated DEmRNAs and down-regulated DEmRNAs. At 90 d after operation, there was 3 pathways (PI3K-Akt signaling pathway, Human papillomavirus infection, Human cytomegalovirus infection) related to inflammatory response with significant different between M-ePTFE and N-ePTFE comparison group, and all those 3 pathways just containing down-regulated DEmRNAs. Overall, the result of the GO and KEGG enrichment analysis indicated that modification of ePTFE with heparin/collagen-REDV may reduce the expression of genes related to immune or inflammatory responses in local tissue caused by ePTFE implantation, especially over the long term.

4 DISCUSSION

Although the hydrophobicity of ePTFE has been shown to reduce the adsorption of plasma proteins compared with other biomedical materials (Lu et al., 2013; Gao et al., 2017), the coagulation response is nevertheless induced by ePTFE implantation in the cardiovascular system (Gao et al., 2017), necessitating long-term whole-body anticoagulant therapy to prevent clinical complications (Sasikumar et al., 2017; Zhang et al., 2018). The coagulation cascade occurs immediately in response to the implantation of foreign material in the body, with the degree of response mostly dependent on the surface features of the material (Hedayati et al., 2019). Therefore, improving the surface properties of such materials is one key to increasing their anticoagulant abilities. Surface modification can be used not only to change physical properties, but also to provide regional anticoagulant therapy via coating surface materials with anticoagulant drugs (Hoshi et al., 2013). Indeed, ePTFE modified with heparin has been proven efficacious for clinical use (Samson et al., 2016; Shibutani et al., 2020). The collagen combined with heparin was designed to further stabilize the modification system, improving its anticoagulation ability, cytocompatibility and mechanical properties (Driessen et al., 2003; Ferreira et al., 2016). Surface modification can also be used to achieve endothelialization *in situ*, providing a physical barrier in addition to regulating coagulation, platelet function, and fibrinolysis (Post et al., 2019b). Although there are multiple substances used to attract ECs to implant devices, few have been proven to be effective *in vivo* (Pang et al., 2015). There are two main reasons for this: loss of activity and attraction of cell types other than ECs, such as platelets (Zhao and Feng, 2020). Recently, the REDV peptide, which attracts ECs *via* recognition of the α4β1 integrin receptor expressed on the EC membrane, was reported as having high specificity, stability and efficiency for endothelialization (Chen et al., 2018; Mahara et al., 2020; Liu X. et al., 2021; Liu Y. et al., 2021). Therefore, we designed a modification of ePTFE that combines heparin/collagen multilayers and REDV peptides to simultaneously reduce thrombosis formation and achieve *in situ* endothelialization. Our previous research showed that heparin/collagen-REDV coating on ePTFE demonstrated good anti-platelet activity and endothelial cell compatibility *in vitro* (Shan et al., 2018). This study further confirmed the good anti-thrombosis and *in situ* endothelialization ability of modified ePTFE in a rabbit model. The monitor of blood coagulation indexes showed that this modification method had no influence to endogenous and exogenous coagulation systems of the animal, which indicated that modification of ePTFE with heparin/collagen-REDV can avoid the long-term anticoagulants medication and the complications caused by anticoagulants.

After the implantation of materials, the inflammation storm happened due to stress response, surgical tissue trauma, anesthesia and infection, which can cause the increased level of white blood cells (WBC) activate and inflammation-related protein in blood (Kohl and Deutschman, 2006). This acute inflammatory response often recovered in 1 week if the pathogen related infection didn't exist (Kohl and Deutschman, 2006), so the acute inflammatory biomarkers in our study (WBC and fibrinogen) decreased to perioperative level in 1 week in the N-ePTFE and M-ePTFE group. The IL-1β is secreted by many cells and can increase both in the acute and chronic inflammatory response, so the time of IL-1β recovered to perioperative level was longer than WBC and fibrinogen (Lopez-Castejon and Brough, 2011). As there was no significant difference in the level of inflammatory biomarkers between N-ePTFE and M-ePTFE group, the inflammatory response occurred after M-ePTFE implantation maybe not caused by modification of ePTFE. The inflammatory cascade or immune response in local tissue triggered by implantation of materials reportedly cannot be avoided (Zhou and Groth, 2018; Vasconcelos et al., 2019; Lasola et al., 2020). This immune or inflammatory response is known as a FBR(Anderson et al., 2008; Munday et al., 2014). Regardless of the type of foreign material or where it is placed in the body, the consequence of a FBR is the same: fibrotic hyperplasia, an important factor in the development of stenosis in tissues with implants (Klopfleisch and Jung, 2017; Jeong et al., 2020). This explains why stenosis frequently occurs following ePTFE implantation, even among patients receiving anticoagulant therapy (Che Man et al., 2020). Macrophages are key participants in the FBR caused by biomaterial implantation, and the macrophage phenotype can change in response to alterations of the microenvironment (Chu et al., 2020). M1 macrophages, which secrete inflammatory cytokines such as tumor necrosis factor-α, often appear in the acute inflammatory response stage, while M2 macrophages, which secrete anti-inflammatory cytokines such as IL-10, usually appear in the chronic inflammatory response stage, promoting tissue regeneration and repair (Yunna et al., 2020). Our research showed the same results: The number of M1 macrophages was larger than M2 in the early postoperative period, and the M2 number increased in the late postoperative period. Despite the compared M1 infiltration degree in myocardial tissue between the N-ePTFE group and the M-ePTFE group, the M2 number was significantly lower in M-ePTFE group. We could not conclude whether the decline is good or bad, because appropriate M2 level can promote tissue healing, or tissue regeneration and remodeling, excessive M2 infiltration can also lead to fibrosis caused by FBR (Vasconcelos et al., 2015; Boersema et al., 2016; Araujo-Gomes et al., 2019; Quan et al., 2020). However, the ideal level of M2, or ratio of M1/M2, for tissues in contact with biomaterials has not been determined (Lebre et al., 2016; Taraballi et al., 2018; Vasconcelos et al., 2019; Chu et al., 2020; Lasola et al., 2020). So, we further detect the influence in local tissue caused by ePTFE modification at molecular level. mRNA sequencing combined with bioinformatic analysis not only offers sensitive detection of alterations in total mRNA expression in tissues in contact with biomaterials, but can also predict the meaning of the alterations (Bolger et al., 2014). As reported previously, ePTFE implantation can increase the expression of inflammatory and extracellular matrix-related genes in both blood vessel tissue and cardiac tissue (Willis et al., 2004; Kwon et al., 2018; Shan et al., 2021). Our mRNA sequence data showed that the heparin/collagen-REDV modification reduced the expression levels of immune/inflammatory response-related genes in M-ePTFE implanted rabbit cardiac tissue at both 14d and 90 d after implantation, and the number of down-regulated genes was higher at 90 d after operation, which indicated that this modification method may reduce the inflammatory response in local tissue contacted with ePTFE. 'Cytokine-cytokine receptor interaction' pathway engaged in multiple process including adaptive inflammatory host defenses, cell growth and tissue repair, so the both the up-regulated genes and down-regulated genes in M-ePTFE vs. N-ePTFE comparison group appeared in this pathway. At 90 d after operation, there was no inflammatory response related pathway containing up-regulated genes and 3 inflammatory response related pathways containing down-regulated genes significant enriched in M-ePTFE vs. N-ePTFE comparison group. And among the 3 pathways containing down-regulated genes, PI3K-Akt signaling pathway may play a major role. Because the downstream of many inflammatory pathways and the upstream of cell proliferation or extracellular matrix-related pathways is the PI3K-Akt pathway, and the inhibit of this pathway was reported that reduce inflammatory response (Shan et al., 2021), intimal hyperplasia tumor cell proliferation (Stark et al., 2015; Zhang et al., 2020). Another exciting finding with our modification was that it reduced the gene expression gap between normal cardiac tissue and M-ePTFE–implanted cardiac tissue at 90d, which indicated that this modification method can shorten tissue repair time. On the basis of mRNA analysis, we predicted that the M2 infiltration in myocardial tissue in contact with M-ePTFE was a protective manifestation. Although the degree of fibrosis did not differ between tissues in contact with the N-ePTFE and M-ePTFE in our study, experiments conducted for a longer time period could verify this prediction. In condition that biomaterials used as grafts to connect with vessels, the intimal hyperplasia due to proliferation or migration of vascular smooth muscle cells (VSMCs) increased incidence of stenosis (Jeong et al., 2020). The mechanism of proliferation or migration of VSMCs including disruption of the vascular endothelial cell barrier (Patel et al., 2010), inflammatory response (Che Man et al., 2020) and vascular tone alternation (Post et al., 2019a). Although we didn't evaluate the effect of heparin/collagen-REDV modification to the behavior of VSMCs *in vivo*, the *in vitro* experiment showed the lower attraction of M-ePTFE to SMC when compared to EC, and proliferation ability of SMC on M-ePTFE was lower than the SMC on normal culture dish. And both the lower macrophage infiltration and down regulated of PI3K-Akt pathway has been verified that can inhibit intimal hyperplasia in other study. All those indicated that our modification method may not aggravate the intimal hyperplasia. Further implantation of modified ePTFE grafts in an animal model of vascular transplantation was needed to verify it.

The monitor of index of blood system, hepatorenal function and the inflammation showed the good safety of our modification method, and this medication also improved the elastic modulus and strength of ePTFE according to our mechanical tensile test, which makes ePTFE a better candidate to manufacture cardiac valve (Bernacca et al., 2002).

Considering the low regenerative potential of myocardium (Fu et al., 2020), the irreplaceable function of the heart (Soliman and Rossi, 2020), the lack of research on cardiac tissue injury caused by ePTFE implantation, and duplication of animal models, we chose to use a heart model instead of a vascular graft model in rabbits. Further studies on the implantation of M-ePTFE in small-diameter vessels are needed to evaluate the efficacy of our novel modification method. This research has also provided a novel landscape of mRNA expression in myocardial tissues in contact with ePTFE over time. In future, these data may be analyzed to determine the mechanisms of biomaterial failure in the body, and to design new biomaterial targets and modifications.

5 CONCLUSIONS

We successfully modified ePTFE with heparin, collagen and REDV peptides and created a rabbit model to evaluate the dynamics of its performance *in vivo*. Our research revealed that the heparin/collagen-REDV modification reduced thrombosis formation and promoted endothelization on ePTFE. This novel modification method was not only biologically safe in rabbits, but it also reduced the infiltration of M2 macrophages and the expression levels of genes related to the FBR in myocardial tissues in contact with ePTFE. Taken together, our data indicate that ePTFE modified with heparin/collagen-REDV has good potential for clinical use and may be expected to lower the incidence of complications related to biomaterial implantation.

DATA AVAILABILITY STATEMENT

The original contributions presented in the study are included in the article/**Supplementary Material**, further inquiries can be directed to the corresponding authors.

ETHICS STATEMENT

The animal study was reviewed and approved by Animal Care and Ethical Committee of Children's Hospital of Fudan University.

AUTHOR CONTRIBUTIONS

YS, QS, and JH: conceptualization, methodology, investigation, software, formal analysis, writing–original draft. BJ, GC, and HZ: funding acquisition, methodology, investigation, validation, formal analysis, writing–review and editing. YM and WZ: Resources, Visualization. Funding. All authors have read and agreed to the published version of the manuscript. YS, GC, and QS contributed equally to this work and share first authorship.

FUNDING

This work was supported by the National Natural Science Foundation of China (Grant No: 81873501), National Key Research and Development Program of China (Grant No: 2017YFC1308104) and Shanghai Shenkang New Frontier Project (Grant No: SHDC12019108).

SUPPLEMENTARY MATERIAL

The Supplementary Material for this article can be found online at: https://www.frontiersin.org/articles/10.3389/fbioe.2022.916931/full#supplementary-material

Supplementary Figure S1 | The appearance of unmodified expanded polytetrafluoroethylene (N-ePTFE) and modified ePTFE (M-ePTFE) which taken from animal model after 14 days or 90 days after implantation.

REFERENCES

Ambler, G. K., and Twine, C. P. (2018). Graft Type for Femoro-Popliteal Bypass Surgery. *Cochrane Database Syst. Rev.* 2018 (2), Cd001487. doi:10.1002/14651858.CD001487.pub3

Anderson, J. M., Rodriguez, A., and Chang, D. T. (2008). Foreign Body Reaction to Biomaterials. *Semin. Immunol.* 20 (2), 86–100. doi:10.1016/j.smim.2007.11.004

Araujo-Gomes, N., Romero-Gavilán, F., Zhang, Y., Martinez-Ramos, C., Elortza, F., Azkargorta, M., et al. (2019). Complement Proteins Regulating Macrophage Polarisation on Biomaterials. *Colloids Surfaces B Biointerfaces* 181, 125–133. doi:10.1016/j.colsurfb.2019.05.039

Bernacca, G. M., O'Connor, B., Williams, D. F., and Wheatley, D. J. (2002). Hydrodynamic Function of Polyurethane Prosthetic Heart Valves: Influences of Young's Modulus and Leaflet Thickness. *Biomaterials* 23 (1), 45–50. doi:10.1016/S0142-9612(01)00077-1

Boersema, G. S. A., Grotenhuis, N., Bayon, Y., Lange, J. F., and Bastiaansen-Jenniskens, Y. M. (2016). The Effect of Biomaterials Used for Tissue Regeneration Purposes on Polarization of Macrophages. *BioRes. Open Access* 5 (1), 6–14. doi:10.1089/biores.2015.0041

Bolger, A. M., Lohse, M., and Usadel, B. (2014). Trimmomatic: A Flexible Trimmer for Illumina Sequence Data. *Bioinformatics* 30 (15), 2114–2120. doi:10.1093/bioinformatics/btu170

Butruk-Raszeja, B. A., Dresler, M. S., Kuźmińska, A., and Ciach, T. (2016). Endothelialization of Polyurethanes: Surface Silanization and Immobilization of REDV Peptide. *Colloids Surfaces B Biointerfaces* 144, 335–343. doi:10.1016/j.colsurfb.2016.04.017

Cassady, A. I., Hidzir, N. M., and Grøndahl, L. (2014). Enhancing Expanded Poly(Tetrafluoroethylene) (ePTFE) for Biomaterials Applications. *J. Appl. Polym. Sci.* 131 (15), 1–14. doi:10.1002/app.40533

Chang, T.-I., Hsu, K.-H., Li, S.-J., Chuang, M.-K., Luo, C.-W., Chen, Y.-J., et al. (2021). Evolution of Pulmonary Valve Reconstruction with Focused Review of Expanded Polytetrafluoroethylene Handmade Valves. *Interact. Cardiovasc. Thorac. Surg.* 32 (4), 585–592. doi:10.1093/icvts/ivaa302

Che Man, R., Sulaiman, N., Ishak, M. F., Bt Hj Idrus, R., Abdul Rahman, M. R., and Yazid, M. D. (2020). The Effects of Pro-Inflammatory and Anti-Inflammatory Agents for the Suppression of Intimal Hyperplasia: An Evidence-Based Review. *Int. J. Environ. Res. Public Health* 17 (21), 7825. doi:10.3390/ijerph17217825

Chen, L., Li, J., Wang, S., Zhu, S., Zhu, C., Zheng, B., et al. (2018). Surface Modification of the Biodegradable Cardiovascular Stent Material Mg-Zn-Y-Nd Alloy via Conjugating REDV Peptide for Better Endothelialization. *J. Mater. Res.* 33 (23), 4123–4133. doi:10.1557/jmr.2018.410

Chu, C., Liu, L., Rung, S., Wang, Y., Ma, Y., Hu, C., et al. (2020). Modulation of Foreign Body Reaction and Macrophage Phenotypes Concerning Microenvironment. *J. Biomed. Mater Res.* 108 (1), 127–135. doi:10.1002/jbm.a.36798

Driessen, N. J. B., Boerboom, R. A., Huyghe, J. M., Bouten, C. V. C., and Baaijens, F. P. T. (2003). Computational Analyses of Mechanically Induced Collagen Fiber Remodeling in the Aortic Heart Valve. *J. Biomech. Eng.* 125 (4), 549–557. doi:10.1115/1.1590361

Ferreira, A. M., Gentile, P., Toumpaniari, S., Ciardelli, G., and Birch, M. A. (2016). Impact of Collagen/Heparin Multilayers for Regulating Bone Cellular Functions. *ACS Appl. Mater. Interfaces* 8 (44), 29923–29932. doi:10.1021/acsami.6b09241

Fu, X., Liu, Q., Li, C., Li, Y., and Wang, L. (2020). Cardiac Fibrosis and Cardiac Fibroblast Lineage-Tracing: Recent Advances. *Front. Physiol.* 11, 416. doi:10.3389/fphys.2020.00416

Gao, A., Hang, R., Li, W., Zhang, W., Li, P., Wang, G., et al. (2017). Linker-Free Covalent Immobilization of Heparin, SDF-1alpha, and CD47 on PTFE Surface for Antithrombogenicity, Endothelialization and Anti-Inflammation. *Biomaterials* 140, 201–211. doi:10.1016/j.biomaterials.2017.06.023

Goodson, W. H., 3rd (1987). Application of Expanded Polytetrafluoroethylene (ePTFE) Tubing to the Study of Human Wound Healing. *J. Biomater. Appl.* 2 (1), 101–117. doi:10.1177/088532828700200102

Hedayati, M., Neufeld, M. J., Reynolds, M. M., and Kipper, M. J. (2019). The Quest for Blood-Compatible Materials: Recent Advances and Future Technologies. *Mater. Sci. Eng. R Rep.* 138, 118–152. doi:10.1016/j.mser.2019.06.002

Hoshi, R. A., Van Lith, R., Jen, M. C., Allen, J. B., Lapidos, K. A., and Ameer, G. (2013). The Blood and Vascular Cell Compatibility of Heparin-Modified ePTFE Vascular Grafts. *Biomaterials* 34 (1), 30–41. doi:10.1016/j.biomaterials.2012.09.046

Jeong, Y., Yao, Y., and Yim, E. K. F. (2020). Current Understanding of Intimal Hyperplasia and Effect of Compliance in Synthetic Small Diameter Vascular Grafts. *Biomater. Sci.* 8 (16), 4383–4395. doi:10.1039/d0bm00226g

Klopfleisch, R., and Jung, F. (2017). The Pathology of the Foreign Body Reaction Against Biomaterials. *J. Biomed. Mater. Res.* 105 (3), 927–940. doi:10.1002/jbm.a.35958

Kohl, B. A., and Deutschman, C. S. (2006). The Inflammatory Response to Surgery and Trauma. *Curr. Opin. Crit. Care* 12 (4), 325–332. doi:10.1097/01.ccx.0000235210.85073.fc

Kwon, S. H., Li, L., Terry, C. M., Shiu, Y.-T., Moos, P. J., Milash, B. A., et al. (2018). Differential Gene Expression Patterns in Vein Regions Susceptible versus Resistant to Neointimal Hyperplasia. *Physiol. Genomics* 50 (8), 615–627. doi:10.1152/physiolgenomics.00082.2017

Lasola, J. J. M., Kamdem, H., McDaniel, M. W., and Pearson, R. M. (2020). Biomaterial-Driven Immunomodulation: Cell Biology-Based Strategies to Mitigate Severe Inflammation and Sepsis. *Front. Immunol.* 11, 1726. doi:10.3389/fimmu.2020.01726

Lebre, F., Hearnden, C. H., and Lavelle, E. C. (2016). Modulation of Immune Responses by Particulate Materials. *Adv. Mater.* 28 (27), 5525–5541. doi:10.1002/adma.201505395

Levine, B., and Berman, W. E. (1995). The Current Status of Expanded Polytetrafluoroethylene (Gore-Tex) in Facial Plastic Surgery. *Ear Nose Throat J.* 74 (10), 681–684. doi:10.1177/014556139507401004

Liu, X., Yu, K., Cheng, S., Ren, T., Maitusong, M., Liu, F., et al. (2021). Ulvan Mediated VE Cadherin Antibody and REDV Peptide Co-Modification to Improve Endothelialization Potential of Bioprosthetic Heart Valves. *Mater. Sci. Eng. C* 128, 112337. doi:10.1016/j.msec.2021.112337

Liu, Y., Mahara, A., Kambe, Y., Hsu, Y.-I., and Yamaoka, T. (2021). Endothelial Cell Adhesion and Blood Response to Hemocompatible Peptide 1 (HCP-1), REDV, and RGD Peptide Sequences with Free N-Terminal Amino Groups Immobilized on a Biomedical Expanded Polytetrafluorethylene Surface. *Biomater. Sci.* 9 (3), 1034–1043. doi:10.1039/d0bm01396j

Lopez-Castejon, G., and Brough, D. (2011). Understanding the Mechanism of IL-1β Secretion. *Cytokine & Growth Factor Rev.* 22 (4), 189–195. doi:10.1016/j.cytogfr.2011.10.001

Lu, S., Zhang, P., Sun, X., Gong, F., Yang, S., Shen, L., et al. (2013). Synthetic ePTFE Grafts Coated with an Anti-CD133 Antibody-Functionalized Heparin/Collagen Multilayer with Rapid *In Vivo* Endothelialization Properties. *ACS Appl. Mater. Interfaces* 5 (15), 7360–7369. doi:10.1021/am401706w

Mahara, A., Li, M., Ohya, Y., and Yamaoka, T. (2020). Small-Diameter Synthetic Vascular Graft Immobilized with the REDV Peptide Reduces Early-Stage Fibrin Clot Deposition and Results in Graft Patency in Rats. *Biomacromolecules* 21 (8), 3092–3101. doi:10.1021/acs.biomac.0c00457

Munday, W. R., Klett, Z., McNiff, J. M., and Ko, C. (2014). Foreign Body Giant Cell Reaction to tarSys Xenograft. *J. Cutan. Pathol.* 41 (10), 771–774. doi:10.1111/cup.12374

Pang, J. H., Farhatnia, Y., Godarzi, F., Tan, A., Rajadas, J., Cousins, B. G., et al. (2015). *In Situ* Endothelialization: Bioengineering Considerations to Translation. *Small* 11 (47), 6248–6264. doi:10.1002/smll.201402579

Patel, S. D., Waltham, M., Wadoodi, A., Burnand, K. G., and Smith, A. (2010). The Role of Endothelial Cells and Their Progenitors in Intimal Hyperplasia. *Ther. Adv. Cardiovasc. Dis.* 4 (2), 129–141. doi:10.1177/1753944710362903

Post, A., Diaz-Rodriguez, P., Balouch, B., Paulsen, S., Wu, S., Miller, J., et al. (2019a). Elucidating the Role of Graft Compliance Mismatch on Intimal Hyperplasia Using an *Ex Vivo* Organ Culture Model. *Acta Biomater.* 89, 84–94. doi:10.1016/j.actbio.2019.03.025

Post, A., Wang, E., and Cosgriff-Hernandez, E. (2019b). A Review of Integrin-Mediated Endothelial Cell Phenotype in the Design of Cardiovascular Devices. *Ann. Biomed. Eng.* 47 (2), 366–380. doi:10.1007/s10439-018-02171-3

Quan, H., Kim, Y., Wu, L., Park, H.-C., and Yang, H.-C. (2020). Modulation of Macrophage Polarization by Phospholipids on the Surface of Titanium. *Molecules* 25 (11), 2700. doi:10.3390/molecules25112700

Redbord, K. P., and Hanke, C. W. (2008). Expanded Polytetrafluoroethylene Implants for Soft-Tissue Augmentation: 5-Year Follow-Up and Literature Review. *Dermatol. Surg.* 34 (6), 735–744. doi:10.1111/j.1524-4725.2008.34140.x

Samson, R. H., Morales, R., Showalter, D. P., Lepore, M. R., and Nair, D. G. (2016). Five-Year Patency Rates for Heparin-Bonded Expanded Polytetrafluoroethylene Femoropopliteal Bypass Grafts vs ePTFE Grafts Without Heparin. *J. Vasc. Surg.* 63 (1), 289. doi:10.1016/j.jvs.2015.10.038

Sasikumar, N., Hermuzi, A., Fan, C.-P. S., Lee, K.-J., Chaturvedi, R., Hickey, E., et al. (2017). Outcomes of Blalock-Taussig Shunts in Current Era: A Single Center Experience. *Congenit. Heart Dis.* 12 (6), 808–814. doi:10.1111/chd.12516

Shan, Y., Jia, B., Ye, M., Shen, H., Chen, W., and Zhang, H. (2018). Application of Heparin/Collagen-REDV Selective Active Interface on ePTFE Films to Enhance Endothelialization and Anticoagulation. *Artif. Organs* 42 (8), 824–834. doi:10.1111/aor.13131

Shan, Y., Zhang, W., Chen, G., Shi, Q., Mi, Y., Zhang, H., et al. (2021). Pathological Change and Whole Transcriptome Alternation Caused by ePTFE Implantation in Myocardium. *Biomed. Res. Int.* 2021, 1–17. doi:10.1155/2021/5551207

Shibutani, S., Obara, H., Matsubara, K., Toya, N., Isogai, N., Ogino, H., et al. (2020). Midterm Results of a Japanese Prospective Multicenter Registry of Heparin-Bonded Expanded Polytetrafluoroethylene Grafts for Above-The-Knee Femoropopliteal Bypass. *Circ. J.* 84 (3), 501–508. doi:10.1253/circj.CJ-19-0908

Sigurdsson, T. J., Tatakis, D. N., Lee, M. B., and Wikesjö, U. M. E. (1995). Periodontal Regenerative Potential of Space-Providing Expanded Polytetrafluoroethylene Membranes and Recombinant Human Bone Morphogenetic Proteins. *J. Periodontol.* 66 (6), 511–521. doi:10.1902/jop.1995.66.6.511

Soliman, H., and Rossi, F. M. V. (2020). Cardiac Fibroblast Diversity in Health and Disease. *Matrix Biol.* 91-92, 75–91. doi:10.1016/j.matbio.2020.05.003

Stark, A.-K., Sriskantharajah, S., Hessel, E. M., and Okkenhaug, K. (2015). PI3K Inhibitors in Inflammation, Autoimmunity and Cancer. *Curr. Opin. Pharmacol.* 23, 82–91. doi:10.1016/j.coph.2015.05.017

Taraballi, F., Sushnitha, M., Tsao, C., Bauza, G., Liverani, C., Shi, A., et al. (2018). Biomimetic Tissue Engineering: Tuning the Immune and Inflammatory Response to Implantable Biomaterials. *Adv. Healthc. Mater.* 7 (17), 1800490. doi:10.1002/adhm.201800490

Vasconcelos, D. P., Costa, M., Amaral, I. F., Barbosa, M. A., Águas, A. P., and Barbosa, J. N. (2015). Modulation of the Inflammatory Response to Chitosan Through M2 Macrophage Polarization Using Pro-Resolution Mediators. *Biomaterials* 37, 116–123. doi:10.1016/j.biomaterials.2014.10.035

Vasconcelos, D. P., Águas, A. P., Barbosa, M. A., Pelegrín, P., and Barbosa, J. N. (2019). The Inflammasome in Host Response to Biomaterials: Bridging Inflammation and Tissue Regeneration. *Acta Biomater.* 83, 1–12. doi:10.1016/j.actbio.2018.09.056

Willis, D. J., Kalish, J. A., Li, C., Deutsch, E. R., Contreras, M. A., LoGerfo, F. W., et al. (2004). Temporal Gene Expression Following Prosthetic Arterial Grafting. *J. Surg. Res.* 120 (1), 27–36. doi:10.1016/j.jss.2003.12.014

Yamamoto, Y., Yamagishi, M., Maeda, Y., Asada, S., Hongu, H., Fujita, S., et al. (2019). Histopathologic Analysis of Explanted Polytetrafluoroethylene-Valved Pulmonary Conduits. *Semin. Thorac. Cardiovasc. Surg.* 32 (1019), 990–999. doi:10.1053/j.semtcvs.2019.10.001

Yunna, C., Mengru, H., Lei, W., and Weidong, C. (2020). Macrophage M1/M2 Polarization. *Eur. J. Pharmacol.* 877, 173090. doi:10.1016/j.ejphar.2020.173090

Zhang, H.-F., Ye, M., Yan, X.-G., Chen, G., Tao, Q.-L., and Jia, B. (2018). Application of a Simplified Hand-Sewn Trileaflet Valved Conduit in Right Ventricular Outflow Tract Reconstruction as an Alternative for Bovine Jugular Vein Graft: Single-Center Experience. *Artif. Organs* 42 (1), 41–48. doi:10.1111/aor.12968

Zhang, M., Jang, H., and Nussinov, R. (2020). PI3K Inhibitors: Review and New Strategies. *Chem. Sci.* 11 (23), 5855–5865. doi:10.1039/d0sc01676d

Zhao, J., and Feng, Y. (2020). Surface Engineering of Cardiovascular Devices for Improved Hemocompatibility and Rapid Endothelialization. *Adv. Healthc. Mater.* 9 (18), 2000920. doi:10.1002/adhm.202000920

Zhou, G., and Groth, T. (2018). Host Responses to Biomaterials and Anti-Inflammatory Design-A Brief Review. *Macromol. Biosci.* 18 (8), 1800112. doi:10.1002/mabi.201800112

Conflict of Interest: The authors declare that the research was conducted in the absence of any commercial or financial relationships that could be construed as a potential conflict of interest.

frontiers | Frontiers in Bioengineering and Biotechnology

TYPE Original Research
PUBLISHED 11 August 2022
DOI 10.3389/fbioe.2022.983988

Encapsulated vaterite-calcite $CaCO_3$ particles loaded with Mg^{2+} and Cu^{2+} ions with sustained release promoting osteogenesis and angiogenesis

Lu Fan[1,2], Fabian Körte[1], Alexander Rudt[3], Ole Jung[4], Claus Burkhardt[1], Mike Barbeck[4]* and Xin Xiong[1]*

[1]NMI Natural and Medical Sciences Institute at the University of Tübingen, Reutlingen, Germany, [2]Experimental Medicine, Faculty of Medicine, University of Tübingen, Tübingen, Germany, [3]Faculty of Applied Chemistry, Reutlingen University, Reutlingen, Germany, [4]Medical Center of Rostock University, Rostock, Germany

OPEN ACCESS

EDITED BY
Yuangang Liu,
Huaqiao University, China

REVIEWED BY
Meng Qin,
Beijing University of Chemical Technology, China
Min Jiang,
Nanjing Tech University, China
Klemen Bohinc,
University of Ljubljana, Slovenia

*CORRESPONDENCE
Mike Barbeck,
mike.barbeck@med.uni-rostock.de
Xin Xiong,
xin.xiong@nmi.de

SPECIALTY SECTION
This article was submitted to Biomaterials, a section of the journal Frontiers in Bioengineering and Biotechnology

RECEIVED 01 July 2022
ACCEPTED 18 July 2022
PUBLISHED 11 August 2022

CITATION
Fan L, Körte F, Rudt A, Jung O, Burkhardt C, Barbeck M and Xiong X (2022), Encapsulated vaterite-calcite $CaCO_3$ particles loaded with Mg^{2+} and Cu^{2+} ions with sustained release promoting osteogenesis and angiogenesis.
Front. Bioeng. Biotechnol. 10:983988.
doi: 10.3389/fbioe.2022.983988

Bioactive cations, including calcium, copper and magnesium, have shown the potential to become the alternative to protein growth factor-based therapeutics for bone healing. Ion substitutions are less costly, more stable, and more effective at low concentrations. Although they have been shown to be effective in providing bone grafts with more biological functions, the precise control of ion release kinetics is still a challenge. Moreover, the synergistic effect of three or more metal ions on bone regeneration has rarely been studied. In this study, vaterite-calcite $CaCO_3$ particles were loaded with copper (Cu^{2+}) and magnesium (Mg^{2+}). The polyelectrolyte multilayer (PEM) was deposited on CaCuMg-CO_3 particles *via* layer-by-layer technique to further improve the stability and biocompatibility of the particles and to enable controlled release of multiple metal ions. The PEM coated microcapsules were successfully combined with collagen at the outmost layer, providing a further stimulating microenvironment for bone regeneration. The *in vitro* release studies showed remarkably stable release of Cu^{2+} in 2 months without initial burst release. Mg^{2+} was released in relatively low concentration in the first 7 days. Cell culture studies showed that CaCuMg-PEM-Col microcapsules stimulated cell proliferation, extracellular maturation and mineralization more effectively than blank control and other microcapsules without collagen adsorption (Ca-PEM, CaCu-PEM, CaMg-PEM, CaCuMg-PEM). In addition, the CaCuMg-PEM-Col microcapsules showed positive effects on osteogenesis and angiogenesis in gene expression studies. The results indicate that such a functional and controllable delivery system of multiple bioactive ions might be a safer, simpler and more efficient alternative of protein growth factor-based therapeutics for bone regeneration. It also provides an effective method for functionalizing bone grafts for bone tissue engineering.

KEYWORDS

bioactive cations, vaterite-calcite, polyelectrolyte multilayer, collagen, bone regeneration

1 Introduction

Various materials and functionalization strategies have been developed and extensively investigated in the field of bone regeneration (Lee et al., 2019; O'Neill et al., 2018). Nevertheless, effective vascularization, mineralization and tissue remodeling of regenerating bone tissue remains the main bottleneck for most graft-induced bone healing (Collins et al., 2021; Divband et al., 2021). A major research focus has been the incorporation of protein growth factors into bone implants to improve the efficacy of treatment. Such as the bone morphogenetic protein-2 (BMP-2) has been used clinically to promote bone healing since 2002 due to its diverse functions and osteogenic potential (Halloran et al., 2020; Hettiaratchi et al., 2020). Vascular endothelial growth factor (VEGF) is widely used in bone tissue engineering research for the improvement of tissue vascularization, either alone or in combination with BMP-2 (Liu et al., 2020; Fitzpatrick et al., 2021). However, significant disadvantages are associated with these protein growth factors-based therapeutics, including the sever complications caused by the supraphysiological dose applied, the instability in the fabrication process, and the high cost (Ruehle et al., 2019; Gelebart et al., 2022). Repeated clinical applications of BMP-2 have not been approved as safe and effective by the United States Food and Drug Administration (FDA) (SSED, 2022). Therefore, the alternatives of protein growth factor-based therapeutics are in demand.

Many bioactive metal ions have been shown to modulate osteoblast precursor differentiation *via* growth factor signaling pathways, or other processes to promote bone tissue regeneration (Glenske et al., 2018; O'Neill et al., 2018). Compared to the applications of protein growth factors, the advantages of using metal ions to induce bone tissue repair are manifold, including lower cost, greater simplicity, higher stability, and better efficacy at low concentrations (Glenske et al., 2018; Hurle et al., 2021). One of those efficient bioactive metal ions showed great importance in bone regeneration is calcium ion (Ca^{2+}). The incorporation of Ca^{2+} into bone repair scaffolds has been shown to promote adhesion, proliferation, and differentiation of osteoblasts (Xie et al., 2018; Jeong et al., 2019). Copper ions (Cu^{2+}) show great potential for vascularization, which are critical component of bone formation and tissue engineering (Lin et al., 2020; Kargozar et al., 2021). 50–60% of magnesium ions (Mg^{2+}) are bound in bone and about 40% of Mg^{2+} are sorted in soft tissue (Musso, 2009). Many studies have shown increased bone growth around degradable Mg-alloys (He et al., 2016). Besides, Mg^{2+} showed positive influences to enhance matrix mineralization, osteogenic genes and protein expression of human bone marrow stem cells and osteoblasts (Qiao et al., 2021; Zhao et al., 2021). It should not be underestimated that bioactive cations are able to diffuse through the cellular membrane and regulate the activity of a variety of physiological responses (Mourino et al., 2012; Qiao et al., 2021). Thus, the metal ions induced concentration-dependent cytotoxicity and nonspecific adverse effects might be observed in neurological, cardiological, hematological, and/or endocrine systems (O'Neill et al., 2018). To reduce or avoid these side effects, a stable delivery system is required that can sustain ion release in the bone defect area both temporally and spatially. On this basis, it is of interest to investigate the synergetic therapy of multiple metal ions for bone regeneration.

Calcium carbonate in its vaterite form is widely used as a sacrificial template for efficient drug delivery. $CaCO_3$ vaterite based delivery platforms have exhibited numerous advantages, such as the high loading efficiency, beneficial porosity, high mechanical stability, biodegradability preferential safety profile, simple preparation and low cost (Vikulina et al., 2021; Daria et al., 2022; Feng et al., 2022). However, the application as a platform for the delivery of proteins, and their long term and controlled release are limited, because the high ionic strength and pH changes during vaterite formation and sacrifice process would result in a dramatic loss of protein activity and a burst release of the encapsulated drug (Feoktistova et al., 2020). However, they do not impact $CaCO_3$ being an ideal platform for the delivery of metal ions. Not only as a sacrificial template, $CaCO_3$ is also one of the cargos, because it contains the important bioactive cations, Ca^{2+}. It was reported that the $CaCO_3$ particles could be converted into hydroxyapatite crystals in mild acidic environment (Wei et al., 2015). It enables the steady and continuous release of targets as it biodegrades *in vivo*. The $CaCO_3$ crystals are particularly suitable for loading with multiple active pharmaceutical ingredients by a simple co-precipitation technique. Polyelectrolyte multilayer (PEM) deposited onto the degradable vaterite $CaCO_3$ crystals *via* a layer-by-layer (LbL) process have served as multifunctional and tailored vehicles for advanced drug delivery (Campbell et al., 2020). Due to their tunable and inherent properties, PEMs can further enhance the biodegradability and bioactivity of $CaCO_3$ crystals, and efficiently inhibit the initial burst release of cargos caused by the complex microenvironment *in vivo*.

Collagen is the main organic component in the bone matrix. It plays a crucial role in the bone formation and remodeling process (Toosi & Behravan, 2020). It has been widely reported that the incorporation of collagen can significantly improve the mechanical properties, osteoinductivity and osteogenicity of scaffold materials for bone tissue engineering (Zhang et al., 2018; Yu et al., 2020; Zhong et al., 2022). In many cases, due to the formability, homogeneity and reproducibility, coating is a preferable choice to integrate collagen into different bone matrices and scaffolds as well as inorganic bone substitute materials. Brito Barrera et al. fabricated an osteogenic microenvironment relying on PEMs in combination with multilayers of type I collagen and chondroitin sulfate (Brito Barrera et al., 2020). The LbL technique is a method to fabricate coatings by alternate adsorption of polyanions and polycations, which can neatly combine collagen and PEM (Martin et al., 2021). In this study, the $CaCO_3$ particles were

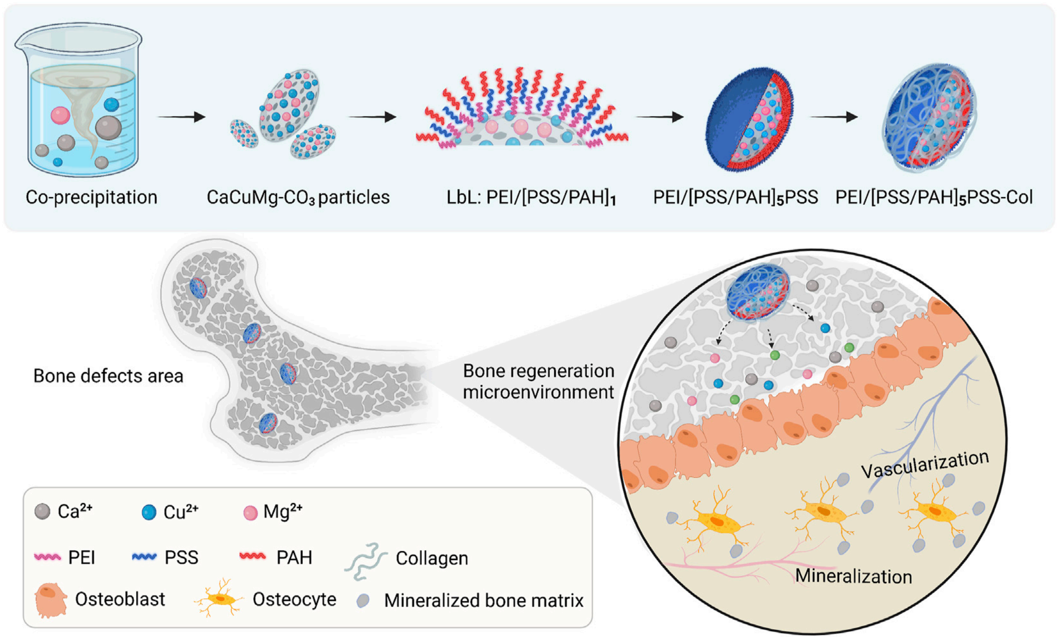

FIGURE 1
Schematic illustration of the fabrication process of CaCuMg-PEM-Col microcapsules [CaCuMg-CO_3 particles + PEI/(PSS/PAH)$_5$PSS + Col], and their effects on bone regeneration.

loaded with Cu^{2+} and Mg^{2+} *via* a co-precipitation process. The co-precipitated particles were further encapsulated with PEMs and collagen, aiming for an elongated and constant release of bioactive cations. Simultaneously, the biofunctionalization of particle surfaces by PEMs and collagen simulated the extracellular microenvironment, together with released bioactive ions promoting bone tissue regeneration. (Figure 1)

2 Materials and methods

2.1 Preparation and characterization of polyelectrolyte multilayers

The polyethyleneimine (PEI, Mw 750 kDa, 50 wt% in water), poly (sodium 4-styrene-sulfonate) (PSS, Mw 70 kDa) were purchased from Sigma-Aldrich, Germany. Poly (allylamine hydrochloride) (PAH, 120–200 kDa) was purchased from Alfa Aesar, Germany. Sodium chloride (NaCl > 99%) was purchased from Sigma-Aldrich, Germany. Collagen from porcine skin (collagen type I content > 90%) was provided by Biotrics bioimplants AG, Germany. Acidic acid (HAc) was purchased from Carl Roth, Germany. All materials were used without further purification. The deionized water (ddH_2O) used in all experiments was prepared in a three stage Milli-Q plus purification system and had a resistivity higher than 18.2 MΩ cm^{-1}.

The polyelectrolytes (PEs) solutions were prepared as follows: PEI was dissolved in ddH_2O at a concentration of 0.01 monomer mol·L^{-1}, pH ~7.0. PSS and PAH were respectively dissolved in 0.5 M of NaCl at a concentration of 2 mg ml^{-1} and adjusted to pH 7.0. Collagen was dissolved in 0.1 M HAc at a concentration of 2 mg ml^{-1} at 4°C overnight under continuous agitation at 60 rpm and thereafter the pH was adjusted to pH 5.0 using NaOH.

The deposition was performed manually using the layer-by-layer (LbL) technique as reported previously (Sun et al., 2017). Gold-crystal sensors (QSX 301 Gold, Biolin scientific, Sweden) were used as a model surface. To characterize the buildup process and the properties of the deposited PEMs, quartz-crystal microbalance with dissipation monitoring (QCM-D) measurement using a Q-Sense E4 instrument (Biolin scientific, Sweden) was employed. Firstly, the QCM sensors were treated with Piranha solution (30% (v/v) H_2O_2, 70% (v/v) H_2SO_4) and washed extensively with ddH_2O. PEI was always applied as precursor layer with a positive charge on the substrate followed by repeated rinsing in ddH_2O (three times for 2 min each). After the deposition of PEI, alternate polyanionic PSS and polycationic PAH layers were deposited up to the desired amount of layers [PEI(PSS/PAH)$_5$ or PEI(PSS/PAH)$_5$PSS] at pH 7.0 with 10 min incubation for each layer. Each adsorption step was followed by three consecutive rinsing steps with ddH_2O for 2 min each. Prior to the collagen deposition, the PEM layers were equilibrated in pH 5.0 ddH_2O. Collagen was deposited as the last layer by incubating the sensors in collagen solution for another 10 min. The PEM and collagen buildup process was performed at 22°C. Finally, sensors were immersed in ddH_2O overnight at 37°C for the stability measurements. In brief, the buildup process for the following systems have been monitored on QCM-D: 1) $PEI[PSS/PAH]_5$ at pH 7.0 switch to pH 5.0 and followed by addition of collagen at pH 5.0; 2) $PEI[PSS/PAH]_5PSS$ at pH 7.0 switch to pH 5.0 and followed by addition of collagen.

The increase in mass adsorbed on the surface of the quartz crystal sensor leads to a decrease in the oscillation frequency.(Marx, 2003) The frequency shift ($-\Delta f$) measured after the deposition of each polyelectrolyte provides direct evidence of adsorption of polyelectrolytes (Aggarwal et al., 2013). The mass of adsorbed polyelectrolyte (Δm) can be calculated from the frequency shift using the Sauerbrey equation:

$$\Delta m = -c\frac{\Delta f}{n}$$

where n (n = 1, 3, and 5... 13) is the overtone number and c is the mass sensitivity constant given by the property of the used quartz crystal (Sauerbrey, 1959). In the present study, f_0 is 5 MHz and c is17.7 ng Hz^{-1} cm^{-2} as stated by the manufacturer. The adsorbed mass and thickness of the PEMs were calculated using the D-Finder program according to the manufacturer's instruction (Biolin scientific, Sweden). All QCM-D measurements were performed using "open module" system.

2.2 Fabrication of Cu^{2+} and Mg^{2+} loaded vaterite $CaCO_3$ ($CaCuMg-CO_3$) particles

Calcium carbonate particles loaded with Cu^{2+} and Mg^{2+} were fabricated on the basis of the previously established co-precipitation approach with some modifications (Sun et al., 2017). Briefly, 0.33 M chloride salt solutions composed of $CaCl_2$, $CuCl_2$ and $MgCl_2$ (Sigma-Aldrich, Germany) at the ratio of *1*) 90%: 5%: 5%, *2*) 80%: 10%: 10%, *3*) 60%: 20%: 20%, *4*) 40%: 30%: *30%* were prepared and stirred at 500 rpm in 50 ml falcon tubes. 0.33 M Na_2CO_3 (Sigma-Aldrich, Germany) solutions with equal volumes were dropped into the respective chloride salt solutions under continuous stirring at 500 rpm with constant speed (0.6 ml/min) using a syringe pump. Stirring was continued for 1 min after the addition of the Na_2CO_3 solution. The obtained slurries were allowed to stand for 10 min and then centrifuged at 2,719 *g* for 2 min. The pellets were quickly resuspended in ddH_2O and centrifuged again for the removal of excessive salts from the carbonates. Afterwards the carbonates were washed three times. The full procedure was performed at 22 ± 1°C.

2.3 Encapsulation with polyelectrolyte multilayers and collagen

To enable the desired sustained release and to improve the biocompatibility, the above-described PEM system with collagen as the most-outer layer was applied for the encapsulation of $CaCuMg-CO_3$ particles. The freshly prepared $CaCuMg-CO_3$ particles were encapsulated with $PEI[PSS/PAH]_5/PSS-Col$ in the same manner as described in 2.1 and 2.2. After each deposition and washing step, the particles were quickly but fully resuspended. The incubation with the respective PEs or collagen were carried out using a tube roller at room temperature. Similarly, each deposition step was followed by centrifugation (2,719 *g*, 2 min) and repeated washing with ddH_2O for three times. The obtained CaCuMg-PEM-Col capsules were lyophilized using a Christ-ε 1-4 LSC plus device (Martin Christ, Osterode am Harz, Germany) and stored at room temperature for subsequent analysis.

For the further investigation of synergistic effects of Cu^{2+}, Mg^{2+} and collagen, *1*) Ca-PEM, *2*) CaCu-PEM, *3*) CaMg-PEM; *4*) CaCuMg-PEM; *5*) CaCuMg-PEM-Col capsules were prepared according to the previously described methods. The ratio of each metal salt was *40%: 30%: 30%*.

2.4 Characterization of CaCuMg-PEM-Col capsules

2.4.1 ζ-potential measurements

The charge and compensation of the charge by alternating adsorption of the polyelectrolytes and collagen are closely related to the properties of the PEM, collagen and the capsules. To monitor the charge compensation and characterize the surface, the ζ-potentials of the surface during the LbL-encapsulation was tracked. The electrophoretic mobility of the microcapsules was measured by photon correlation spectroscopy using a Zetasizer NanoZS (Malvern, Herrenberg, Germany). All measurements were performed at 25°C. The mobility was converted into a ζ-potential using the Smoluchowski relation and the system algorithm provided by Malvern (Salmivirta et al., 1996). Immediately after each layering-washing-resuspension process, surface charge was characterized by the ζ –potential (n = 3). Samples were always fully resuspended in ddH_2O prior to the measurements. The measurements were performed in triplicate at each adsorption step. Samples were always fully dispersed in distilled water in equilibrium with the room atmosphere. 1 mmol L^{-1} KCl solution was applied as the model electrolyte, and 0.1 mol L^{-1} NaOH was used for pH titration from pH 3.0 to 10.0.

2.4.2 Scanning electron microscopy and energy dispersive X-Ray analysis

Scanning electron microscopy (SEM) images and energy dispersive X-Ray analysis (EDS) of capsules were performed with a FIB/SEM microscope (Zeiss crossbeam 550) equipped with an EDS detector (Oxford X-Max). With this set-up we characterized the shape, size, surface morphology and element composition of CaCuMg-PEM-Col capsules. For this observation the lyophilized samples were attached firmly to carbon tape on a SEM stub without sputter coating. SEM images were then taken at accelerating voltages between 1.5 and 3 kV. The EDS analysis was performed with SEM at an acceleration voltage of 8 kV. The EDS analysis clearly show the distribution of Magnesium, Copper and Calcium in the samples.

2.4.3 Fluorescence microscopy

For the visualization of assembled PEM and adsorbed collagen, fluorescence microscopy (Keyence BZ-X800, KEYENCE Deutschland GmbH, Neu-Isenburg, Germany) was applied. FITC-labeled PAH and type I collagen (Biomol GmbH, Germany) were added to the respective unlabeled PAH and type I collagen solutions at a ratio of 4%. The coating procedure was the same as described above under exclusion of light. Two FITC labeled samples were prepared as *1*) CaCuMg-PEM_FITC-Col (FITC labeled PAH at 3rd bilayer) and *2*) CaCuMg-PEM-Col_FITC (FITC labeled collagen at the last layer). The samples were resuspended with ddH$_2$O in a 96-well plate and observed directly under the fluorescence microscope.

2.5 Release kinetics of Ca^{2+}, Cu^{2+} and Mg^{2+}

The Ca^{2+}, Cu^{2+} and Mg^{2+} release profiles were analyzed with a SPECTROBLUE ICP-OES (Inductive coupled plasma-optical emission spectroscopy) analyzer (SPECTRO/AMETEK, Kleve, Germany). Briefly, 0.11 g of each lyophilized sample was immersed in 11 ml Eagle's minimal essential medium (MEM, Gibco) and incubated at 37°C under continuous agitation at 60 rpm. 10 ml supernatant was collected by centrifugation (2,719 *g*, 2 min) at the specified time points (10 min, 1, 3, 7, 14, 21, 28 and 60 days). After sampling, 10 ml of fresh MEM was added to the residual suspension to continue the release kinetics. For measuring the total ion content, the powder was immersed in 11 ml 5% HAc for 24 h (37°C, 60 rpm), then analyzed using ICP-OES. All solutions used were sterile filtrated using a 0.45 μm membrane filter and the samples were handled and kept sterile. After processing of the measurement signals by the instrument, the measured intensities of the elements were evaluated *via* the Smart Analyzer software.

2.6 Cell culture

In this study, the murine fibroblast cell line L929 (ATCC, CCL1) and human derived osteoblast-like MG63 (ATCC, CRL 142) osteosarcoma cells were purchased from ATCC (VA, United States). L929 cells were grown in RPMI medium 1,640 GlutaMAX supplemented with 10% (v/v) fetal bovine serum (FBS) and 1% penicillin/streptomycin (P/S). MG63 cells were cultivated with MEM plus supplemented with 10% FBS, 1% P/S, and 1% sodium pyruvate, 1% nonessential amino acids (NEAA) and 1% L-glutamine. All these materials were purchased from Gibco (Carlsbad, CA, United States). Both cells were grown in a humidified 5% CO$_2$/95% atmosphere and passaged when cell confluence rate was over 80%.

2.7 Cell viability test by cell count kit-8

The cytotoxicity of the CaCuMg-PEM-Col capsules was evaluated by an extraction test and CCK-8 assay of L929 cells according to ISO 10993 part 5 (ISO 10993-5:2009, confirmed in 2017) (ISO, 2009). 10 mg ml^{-1} of CaCuMg-PEM-Col capsules, positive control (PC, polyurethane film containing 0.1% zinc diethyldithiocarbamate (ZDEC), RM-A, HatanoResearch Institute, Japan), negative control (high density polyethylene film, RM-C, HatanoResearch Institute, Japan) in L929 cell culture medium and blank (only cell culture medium) were incubated at 37°C with gentle shaking at 60 rpm for 24 h. The cells were seeded in 96-well plates (10^4 cells/well) and cultured at 37°C for 24 h with 5% CO$_2$. Then, the medium was replaced with the extracts. After culturing for further 24 h, the cell viability of L929 was determined by CCK-8 assay (Sigma-Aldrich, Germany). Briefly, the medium was thoroughly removed, and the cells were then incubated with fresh medium supplemented with 10% CCK-8 reagent. After incubation at 37°C for 2 h, the color change was determined by measuring the absorbance at 450 nm using a microplate reader (TECAN RAINBOW, Germany).

The MG63 cell viability was also evaluated using CCK-8 method. Cells were seeded in 96-well plates (10^4 cells/well) cultured with complete medium for 24 h. Then, the medium was thoroughly aspirated and replaced by fresh culture medium supplemented with the extracts of capsules. After incubation for the designated times, the cell viability was measured using the CCK-8-assay. The medium was replaced every 3 days.

2.8 Alkaline phosphatase activity measurements

As a key osteogenic maker of osteoblastic differentiation, alkaline phosphatase (ALP) activity was determined by conversion of *p*-nitrophenyl phosphate (pNPP) into *p*-nitrophenol (pNP). Incubating MG63 cells with substrate solution (1 mg ml^{-1} pNPP, 50 mM glycine, 1 mM MgCl$_2$, 100 mM TRIS, pH 10.5) at 37°C for 30 min, and then measuring the absorbance at 405 nm using a microplate reader (TECAN RAINBOW, Germany).

2.9 Relative gene expressions

Total RNA extraction, reverse-transcription and real-time PCR were performed by using the Cells-to-CT™ 1-Step TaqMan™ Kit (Thermo Fisher Scientific, Rockford, IL, United States), conducted on

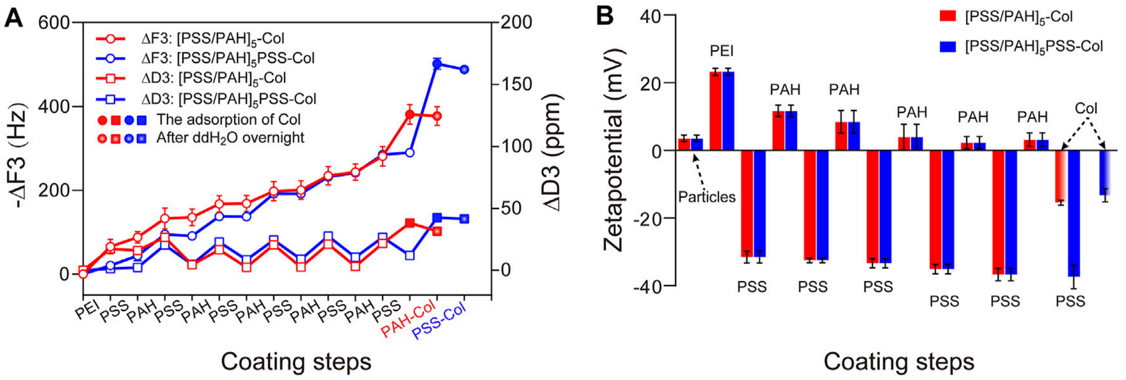

FIGURE 2
(A) QCM-D frequency (ΔF, -o-) and dissipation (ΔD3, -□-) plot for LbL coating process of PEM and collagen. The red broken line represents the buildup process of [PSS/PAH]$_5$, further adsorption of collagen and incubation in ddH$_2$O overnight; the blue broken line represents the coating steps of [PSS/PAH]$_5$PSS-Col and further incubation in ddH$_2$O overnight. **(B)** Zeta-potential measurement of respective surface charges during the PEM and collagen coating process on the basis of CaCuMg-CO$_3$ crystals.

a one-step PCR instrument (Applied Biosystems, Foster City, CA, United States) according to the manufacturer's instruction. For analysis of osteogenic-related genes (COL1A1, MMP1, ALPL, BGLAP, RUNX2) and angiogenic-related genes (VEGFA and HIF1A), the relative expression of mRNAs was calculated using glyceradehyde-3-phosphate dehydrogenase (GAPDH) as an internal reference standard gene by the $2^{-\Delta\Delta Ct}$ method. All primers were purchased from Thermo Fisher Scientific, and more details are listed in Supplementary Table S1, Supporting information.

2.10 Alizarin red staining

The formation of mineralized matrix nodules after 14 days was determined by Alizarin Red staining. Briefly, MG63 cells were fixed with 99% ethanol at −20°C for 2 h, then washed with tape water for three times. After incubating with 0.5% Alizarin Red solution (pH 4.0, Carl Roth) for 30 min at room temperature and another three washing steps, the resulting staining was assessed with optical microscopy. The bound Alizarin Red was resolved with 10% Cetylpyridium chloride solution (Carl Roth) for photometric quantification at the absorbance of 562 nm using a microplate reader (TECAN RAINBOW, Germany).

3 Results and discussion

3.1 Optimization and characterization of PEM and collagen coating

The buildup process of the PEM-systems was monitored by measurements using QCM-D (Figure 2A). The regular frequency shifts confirmed the effective adsorption of each deposited polyelectrolyte-layers and the assembly of the multilayer systems. The collagen was adsorbed on both basic layer-systems [PSS/PAH]$_5$ and [PSS/PAH]$_5$PSS with an average frequency shift of *−380.75 ± 23.45 Hz* and *-501.77 ± 13.33 Hz*. After overnight incubation in ddH$_2$O only a slight increase of the frequency could be observed indicating a stable adsorption as reported previously. (Sun et al., 2017) More (113.23%) collagen could be adsorbed on top of the PSS (*212.06 ± 33.06 Hz*) than PAH (*99.45 ± 13.47 Hz*). At a pH range from 4 to 10, collagen has both positive and negative charges throughout the molecules (Morozova and Muthukumar, 2018). The higher the pH value, the higher the negative charge measured. At a pH of 5, the collagen was predominantly present as positively charged molecules, resulting in greater adsorption on the negatively charged PSS surface compared to the positively charged PAH surface. After overnight incubation in ddH$_2$O, the Δf was 3.48 Hz (3.5% frequency increase) and 13.66 Hz (6.4% frequency increase) for PAH-Col and PSS-Col respectively. Energy dissipation was also monitored and plotted in Figure 2A. ΔD indicated primarily the change of the stiffness of the layers. Both PAH-Col and PSS-Col have reduction of dissipation and the ΔD was −6.6 ± 4.17 ppm and −1.14 ± 2.45 ppm respectively. Taking the results of Δf and ΔD together, it might be concluded that the PAH-Col and PSS-Col coatings retained their integrity after deposition because the negligible changes in frequency and mass. The increase in frequency is most likely due to the rearrangement of the PEM and collagen on the surfaces during the long time incubation in ddH$_2$O. Also, the evaporation of the ddH$_2$O in the used open cells could result in the slight fluctuation of the measurement. In addition, the fitting of the thickness using the QSense_Dfinder software showed a slight reduction of the thickness of the coatings indicating the tightening of the film-structure (Supplementary

Table S1). After deposition and during equilibrium in water, PE molecules could complete the arrangement such as interpenetration due to compensation and stabilization of weak interactions, especially hydrogen-bonding and hydrophobicity-interactions between molecules (Wang et al., 2014). The small Δ*D* suggested a stable system has been formed and kept the stability during further incubation. The slight negative Δ*D* also indicates the increased stiffness and rigidity of the surface. As described in the literature, the lower overtone represents the adsorption and change at the interface between liquid and thin film, and the comparison of other signals recorded for higher overtones indicates the depth integrity of the system. The signals of overtones 3, 5 and 9 did not differ significantly from each other confirming the linearity, rigidity and rather stiffer property of the systems (Wang et al., 2014). As reported previously, molecular water can be pushed out while the structure of the film was rearranged to a much thinner and stable form. This process will also result in a slight frequency increase due to loss of water molecules from the film (Delajon et al., 2009; Kohler et al., 2009).

As mentioned above, collagen has both positively and negatively charged moieties, which allows adsorption to differently charged surfaces. The adsorption determined by QCM might be resulted from the adhesive property of collagen. ς-Potential confirmed the buildup process according to the charge-compensation theory of the PEM-LbL technique (Figure 2B). Moreover, the initial positive charge of the PAH outer layer was reduced to a negative charge (−18.67 mV) after adsorption of collagen, while the strong negative charge of PSS was strongly neutralized to (−24.10 mV) by collagen. This observation was in accordance with the expectation that collagen can be stably adsorbed both on positively and negatively charged surfaces at proper pH value. In one word, the buildup of the designed PEM systems was successfully performed and confirmed by QCM-D analysis. The stability of both systems was proven to be sufficient for further applications. The –PSS showed overall a better adsorption capacity of collagen and stability in comparison to –PAH.

3.2 Characterization of CaCuMg-PEM-Col microcapsules

As mentioned above, the vaterite formation process of $CaCO_3$ is easily influenced by the experimental conditions and the substances introduced during co-precipitation. In order to guarantee stable encapsulation and sustainable release with the desired controllability, different microcapsule formulations were prepared by co-precipitation. The morphology and elemental composition of CaCuMg-PEM-Col particles were investigated *via* SEM combined with EDS-analysis. When the ratio of Ca^{2+}, Cu^{2+} and Mg^{2+} was 90%: 5%: 5%, the formed particles presented three kinds of morphologies: bigger spherical particles (41.38% of total) with an average size around 5.0 ± 0.5 μm (diameter), smaller spherical particles (20.69%) in the size of 2.6 ± 0.3 μm, and oval particles (37.93%, 5.6 ± 0.3 μm × 2.9 ± 0.3 μm) (Figure 3Aa [if subparts are of A]). The SEM image of the 80%: 10%: 10% group showed that most of the particles have an oval shape with relatively uniform size (Length 3.9 ± 0.4 μm Width1.9 ± 0.3 μm) (Figure 3Ab [if subparts are of A]). Interestingly, in the group of *60%: 20%: 20%*, there were no regular shaped vaterite or calcite particles observed. SEM images revealed irregular and porous structures (Figure 3Ac [if subparts are of A]). The particles obtained from the group of *40%: 30%: 30%* showed a similar morphology as the *90%: 5%: 5%* group. The bigger spherical particles in this sample were around 5.5 ± 0.4 μm and account for 12.90%; the smaller ones were in the size of 2.5 ± 0.4 μm (48.39%) and the oval particles were about L 5.474 ± 0.5 μm W 3.0 ± 0.4 μm (29.27%) (Figure 3Ad [if subparts are of A]).

As one of the most effective platforms for drug encapsulation and delivery, the key parameters for size- and shape-controlled synthesis of $CaCO_3$ particles have been well studied. The fast mixing of aqueous calcium chloride and sodium carbonate can immediately result in amorphous calcium carbonate (ACC). Under vigorous stirring, the formed ACC in the precipitation system will dissolve first, and then transform within minutes to produce crystalline forms of vaterite and calcite (Shen et al., 2006). However, when the system is introduced with other divalent cations, the co-precipitation reaction and co-crystallization process will be more complicated, thus rarely being reported. In the co-precipitation system of Ca^{2+}, Cu^{2+}, and Mg^{2+} presented in this work, there are two main factors affecting the morphology of obtained particles: the concentration of Ca^{2+}, and the ionic interactions with Cu^{2+} and Mg^{2+}. It is known that the higher content of Ca^{2+} within a certain range would lead to high yield of vaterite; trace amounts of Cu^{2+}, and Mg^{2+}, which have a smaller ion size than Ca^{2+} could enter and distort the lattice of just formed $CaCO_3$-crystals, and thus influence the size and morphology of the final particles, as shown in Figure 3Aa [if subparts are of A]) (Svenskaya et al., 2018). A certain proportion of Mg^{2+} was reported to promote the formation of vaterite $CaCO_3$ crystals (Kulp and Switzer, 2007). Among the four ratios in this study, 10% of Mg^{2+} might play the optimal role in vaterite formation. Particles obtained at the ratio of *80%: 10%: 10%* showed the most regular oval vaterite morphology (Figure 3Ab [if subparts are of A]). With the increase of Cu^{2+} and Mg^{2+} content, the crystals gradually transformed from vaterite to calcite leading to a reduced uniformity in the particles. The particles from the ratio of 60%: 20%: 20% appeared to stay at the transformation phase of ACC-vaterite, and particles of 40%: 30%: 30% were at vaterite-calcite stage or mixture of different crystallization products (Figures 3Ac,d [if subparts are of A]). Most likely the ions find an equilibrium among vaterite and calcite during particle formation depending on the ratios and precipitation conditions.

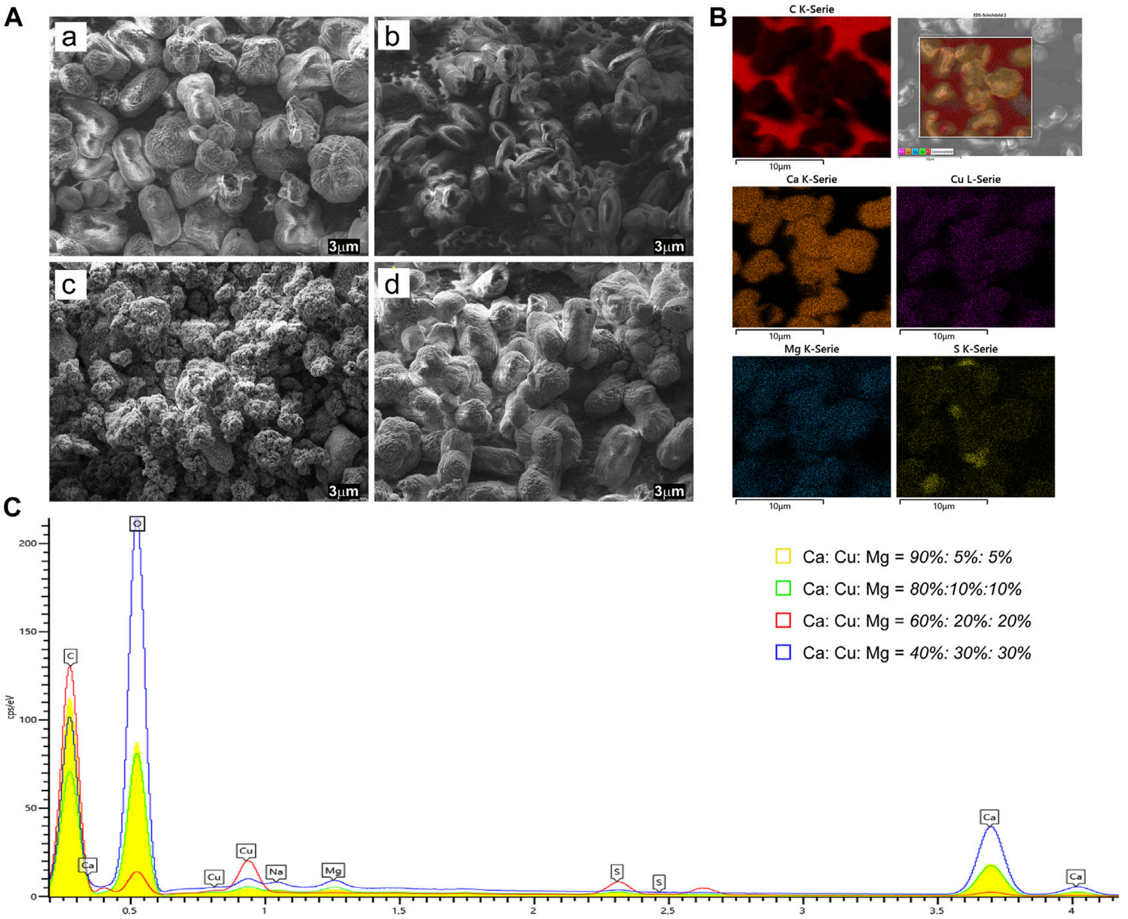

FIGURE 3
(A) SEM images of CaCuMg-PEM-Col microcapsules prepared with different ratios of salts: (a) Ca^{2+}: Cu^{2+}: Mg^{2+} = *90%: 5%: 5%*, (b) Ca^{2+}: Cu^{2+}: Mg^{2+} = *80%: 10%: 10%*, (c) Ca^{2+}: Cu^{2+}: Mg^{2+} = *60%: 20%: 20%*, (d) Ca^{2+}: Cu^{2+}: Mg^{2+} = *40%: 30%: 30%* (scale bar = 3 μm). **(B)** *C, Ca, Cu, Mg, S* element EDS-Mapping of microcapsules (the group of *40%: 30%: 30%*). **(C)** EDS spectra of CaCuMg-PEM-Col microcapsules prepared with four ratios of salts.

This could be due to the excessive electronegativity of Cu^{2+} and Mg^{2+}, which led to a distortion of the crystal plane structure; furthermore, the increasing cocrystallization with $CuCO_3$ ($Cu_2CO_3(OH)_2$) and $MgCO_3$ suppressed the formation and stability of $CaCO_3$ vaterite. Additional influence from the PEM coating should also be considered as a morphology-stabilizing factor. The particles were encapsulated in their precipitated shapes without further modifications as a substrate for coating deposition. $CaCO_3$ has a water solubility of 15 mg L^{-1} and $MgCO_3$ 0.14 g L^{-1}. More complicated, the Cu^{2+} will form so called basic copper carbonate consisting of $Cu_2CO_3(OH)_2$ which has a negligible solubility in water. The basic copper carbonate has a typical monoclinic crystal and spertiniite morphology. Also the formation of dolomite, $CaMg(CO_3)_2$ would further enhance the alternating morphology due to the structural arrangement of the Ca^{2+} and Mg^{2+} ions. These properties derived from basic copper carbonate and dolomite could explain the morphological changes from ACC, to vaterite and calcite in this complex mixture system as shown in Figure 3A. These mixtures of dolomite and basic copper carbonate will also further affect the release kinetics by means of dissolution and degradation.

X-ray energy dispersive spectroscopic (EDS)-mapping images and spectra further revealed the element composition of CaCuMg-PEM-Col capsules. The SEM EDS-mapping images showed that the elements including C, Ca, Cu, Mg, S were uniformly distributed on particles prepared with these four ratios (Figure 3B and Supplementary Figure S1). The EDS spectra exhibited the characteristic peaks for C, Ca, Cu, Mg, and S (Figure 3C) present in the surfaces of the microcapsules. The obtained element composition ratio is shown in Supplementary Table S2. No significant difference in the element composition ratio of the group of 95%: 5%: 5% and 80%: 10%: 10% was observed. The high ratio of Cu and low ratio of Ca in the group of 60%: 20%: 20% suggested a high amount of $CuCO_3$/$Cu_2CO_3(OH)_2$ in the surfaces of microcapsules. The

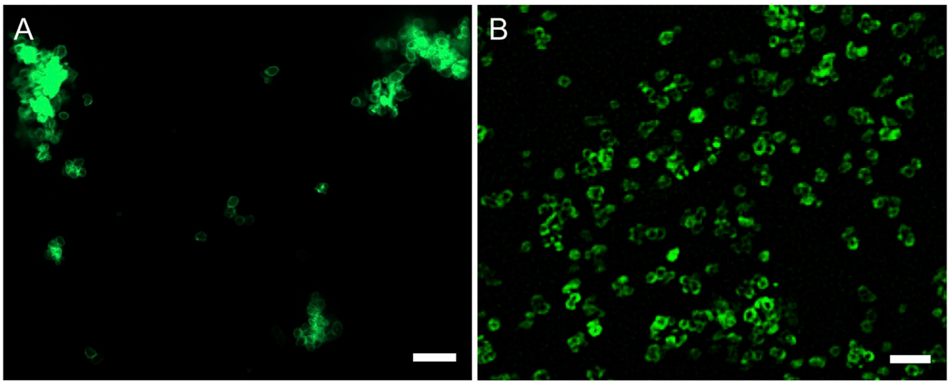

FIGURE 4
Micrographs of **(A)** FITC-labeled PAH coated at 3rd bilayer of CaCuMg-PEM-Col and **(B)** FITC-labeled collagen coated at the outmost layer (scale bar = 50 μm).

group of 40%: 30%: 30% exhibited a relatively more uniform distribution of elements.

Fluorescence microscope imaging was applied to further visualize the adsorbed PEM and collagen on CaCuMg-CO_3 crystals. As shown in Figure 4A, FITC-PAH was uniformly coated on the particles, forming a thin green layer along the particle surfaces. Similarly, the deposition of the FITC-collagen layer was also successfully observed on the surface of the encapsulated particles (Figure 4B). Interestingly, it was found that the CaCuMg-PEM-Col particles exhibited better dispersion than the CaCuMg-PEM particles after further adsorption of collagen. This is consistent with the measurement of the zeta potential. Since the adsorption of collagen leads to a higher negative charge distribution on the surface of the particles, the repulsion between the negatively charged particles is enhanced.

3.3 Ion release behavior of CaCuMg-PEM-Col microcapsules

The release kinetics of the target bioactive cations Cu^{2+} and Mg^{2+} are of particular importance as a sudden increase in concentration due to excessive release of these cations will result in bone loss, irregular crosslinking or excessive cytotoxicity (Wong et al., 2014; Wang et al., 2016). Therefore, the stability and controllability of ion release kinetics during the long-term bone regeneration process is crucial. In this study, we investigated and compared the ion release behavior of the microcapsules prepared with different salt ratios *via* ICP-OES measurements. The two groups with higher Ca^{2+}-content showed a burst release of Cu^{2+} in the first hours and 3 days, then followed by a very slow and incomplete release until day 60 (Figures 5A,B). While the two groups with increased Cu^{2+} and Mg^{2+} content showed stable release throughout the analyzed period without initial burst release (Figures 5C,D). Notably, the Mg^{2+} in the first two groups were below the detection limits of the ICP-OES. But in the groups of 60%: 20%: 20% and 40%: 30%: 30%, trace Mg^{2+} was slowly released in the first 7 days (Figures 5E,F). The amount of target bioactive ions Cu^{2+} and Mg^{2+} released from the capsules differed dramatically between the high and low Ca^{2+}-content groups. The cumulative release profile of Ca^{2+} also showed an initial burst release in groups of 95%: 5%: 5% and 80%: 10%: 10% (Supplementary Figure S2). Interestingly, the concentration of Ca^{2+} decreased as the release process prolonged, whereas the Ca^{2+} release of the other two groups was stable and slow. When the Ca^{2+} content was replaced by increased Cu and Mg content, $CaMgCO_3$ crystallizes in the nucleation region was surrounded by relatively unstable basic Cu and $Mg(OH)_2/MgCO_3$. In particular, the $MgCO_3$ is destabilized by hydration to $Mg(OH)_2$. This reaction cascade dynamically determines the surface morphology of the particles and the release behavior. The higher the Cu content the easier the Cu^{2+} can be released (Figures 5C,D). The unstable surface portion of the Cu/Mg was easily released within the first 7 days. As the dissolution front approaches the calcite core, the release was more limited by the dissolution of the calcite, especially for the Mg. This could explain the relatively short continuous release of Mg measured by ICP (Figures 5E,F). The release curve of Ca^{2+} also confirms the above mentioned mechanisms. After the release of unstable vaterite from the surface, the release rate decreased significantly for a short time, and then rose slowly because of the slow dissolution of calcite core (Supplementary Figure S2). The large amount of Mg^{2+} was increasingly co-crystalized in nucleation region of calcite or dolomite crystals which limited the dissolution process.

3.4 *In vitro* cytotoxicity

In addition to achieve the sustained release function as an encapsulation system, PEM and collagen were also used to mimic

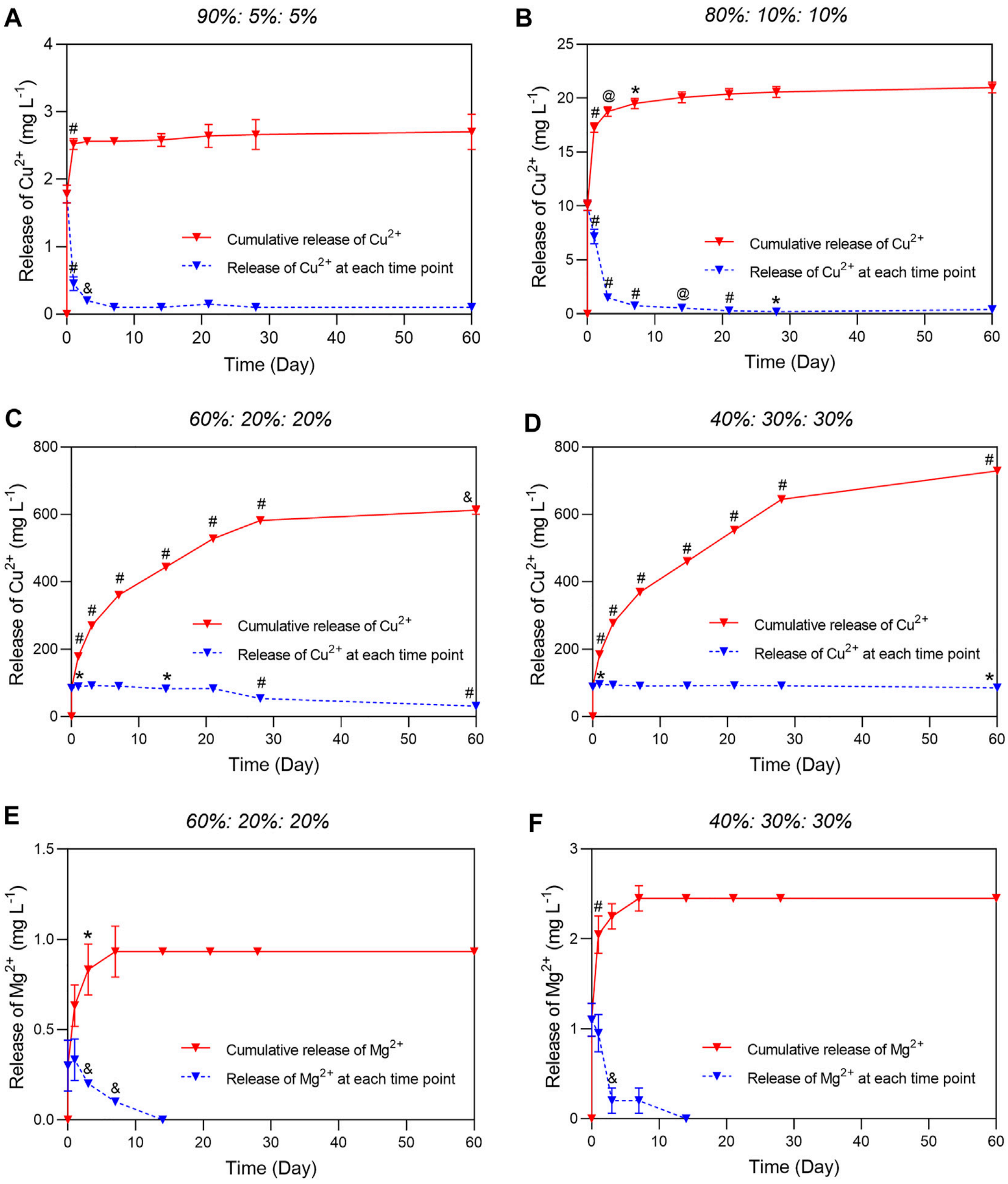

FIGURE 5
Ions release profile of CaCuMg-PEM-Col microcapsules determined by ICP-OES. The concentration of Cu^{2+} released from microcapsules prepared with different ratios of Ca^{2+}, Cu^{2+}, Mg^{2+}: **(A)** *90%: 5%: 5%*, **(B)** *80%: 10%: 10%*, **(C)** *60%: 20%: 20%*, **(D)** *40%: 30%: 30%*. The release behavior of Mg^{2+} in **(E)** group of *60%: 20%: 20%* microcapsules and **(F)** that of *40%: 30%: 30%* microcapsules. (Mean ± SD, $n = 5$; Paired t-test, $^{*}p < 0.05$, $^{\&}p < 0.01$, $^{@}p < 0.001$, $^{\#}p < 0.0001$, indicated that there was a significant difference of released ions content between the two groups).

bone tissue ECM to promote osteogenic differentiation *via* modifying different surface properties which in turn stimulating numerous interfacial interactions with the cells adsorbed to the coated surfaces (Brito Barrera et al., 2020; Sankar et al., 2021). Collagen is an indispensable matrix protein that stimulates various signaling pathways such as cell adhesion, mobility, wound healing, proliferation, and an important process to complete bone regeneration, named ECM remodeling (Zhang et al., 2018). Other physicochemical properties of the surface are also decisive for proper bone regeneration, such as surface roughness, hardness, electrical charge and charge density (Bharadwaz and Jayasuriya, 2020). The PEM provides a highly tunable surface fulfilling these demands. The negative charge of the coated surface attracts

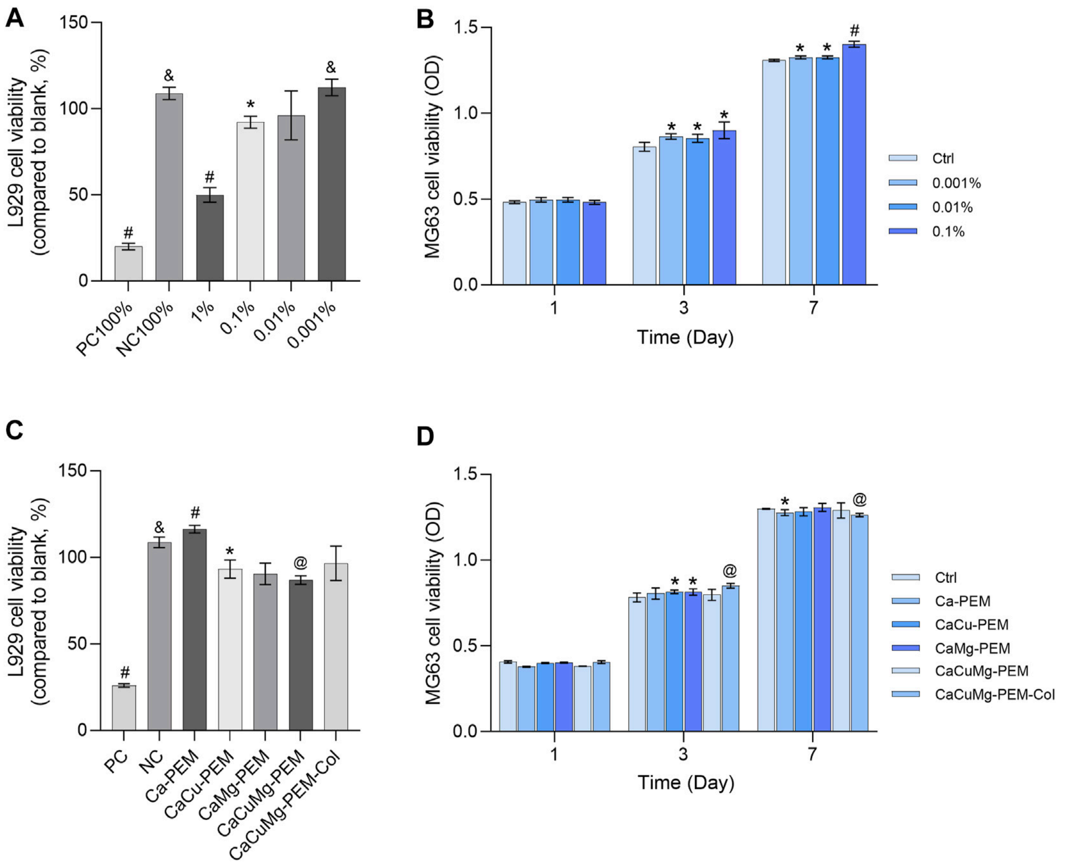

FIGURE 6
In vitro cytotoxicity of control samples (PC, positive control; NC, negative control) and **(A)** extract of CaCuMg-PEM-Col in a series of concentrations, and **(C)** extract of Ca-PEM, CaCu-PEM, CaMg-PEM, CaCuMg-PEM and CaCuMg-PEM-Col microcapsules towards L929 cells. Cell viability of osteoblast-like MG63 cells cultured with extract of microcapsules determined by CCK-8 assay at 1, 3, 7, 10 and 14 days: **(B)** culture medium supplemented with extract of CaCuMg-PEM-Col microcapsules in different concentrations; **(D)** culture medium supplemented with 0.1% extracts of Ca-PEM, CaCu-PEM, CaMg-PEM, CaCuMg-PEM and CaCuMg-PEM-Col microcapsules. (mean ± SD, $n = 6$; Paired t-test, $^{*}p < 0.05$, $^{\&}p < 0.01$, $^{@}p < 0.001$, $^{\#}p < 0.0001$, indicated that there was a significant difference of cell viability in comparison to blank control).

cells and makes them easy to adhere; in addition, cell adhesion and the necessary cell motility are more active on harder surfaces than on softer ones (Sahebalzamani et al., 2022). Therefore, a PEM-Col surface has been chosen for proof of this strategy. In this study, mouse derived L929 fibroblasts were used to evaluate the cytotoxicity of CaCuMg-PEM-Col microcapsules. The cell viability assay has been performed *via* an extraction test on L929 and evaluated by CCK-8 assay. According to the ISO standard, metabolic activity below 70% is considered to be cytotoxic. As shown in Figure 6A, the microcapsules showed a decrease in cytotoxicity with decreasing extract concentration, while the viability of fibroblasts was below 70% only when the extract concentration was higher than 1%. According to the results of ICP measurements as shown in Figure 5, the concentration of Cu^{2+} in 1% extract was 15.63 μM and the concentration of Mg^{2+} is 4.17 μM. These measurements formed the basis for determining a suitable dosage range of the microcapsules. To exclude the bias due to PEM, collagen and their probable degradation products, the extracts of five types of microcapsules have been applied for the cytotoxic evaluation, including Ca-PEM, CaCu-PEM, CaMg-PEM, CaCuMg-PEM and CaCuMg-PEM-Col. All the extracts did not exhibit any significant cytotoxicity on L929 cells (Figure 6C), suggesting good biocompatibility of the microcapsules. It was found that the cells treated with CaCuMg-PEM-Col extract showed higher viability compared to CaCuMg-PEM without a collagen layer, which might be a result of slight desorption of collagen from the surface of the microcapsules. The beneficial effects from the collagen layer might also reduce the toxicity resulting from Mg^{2+} and Cu^{2+} ions within certain concentration threshold (Cu^{2+}: 15.63 μM; Mg^{2+}: 4.17 μM).

Main task of this trimetal microcapsules is to stimulate the bone regeneration *via* controlled release of these bioactive cations. Therefore, cell proliferation of osteoblast-like

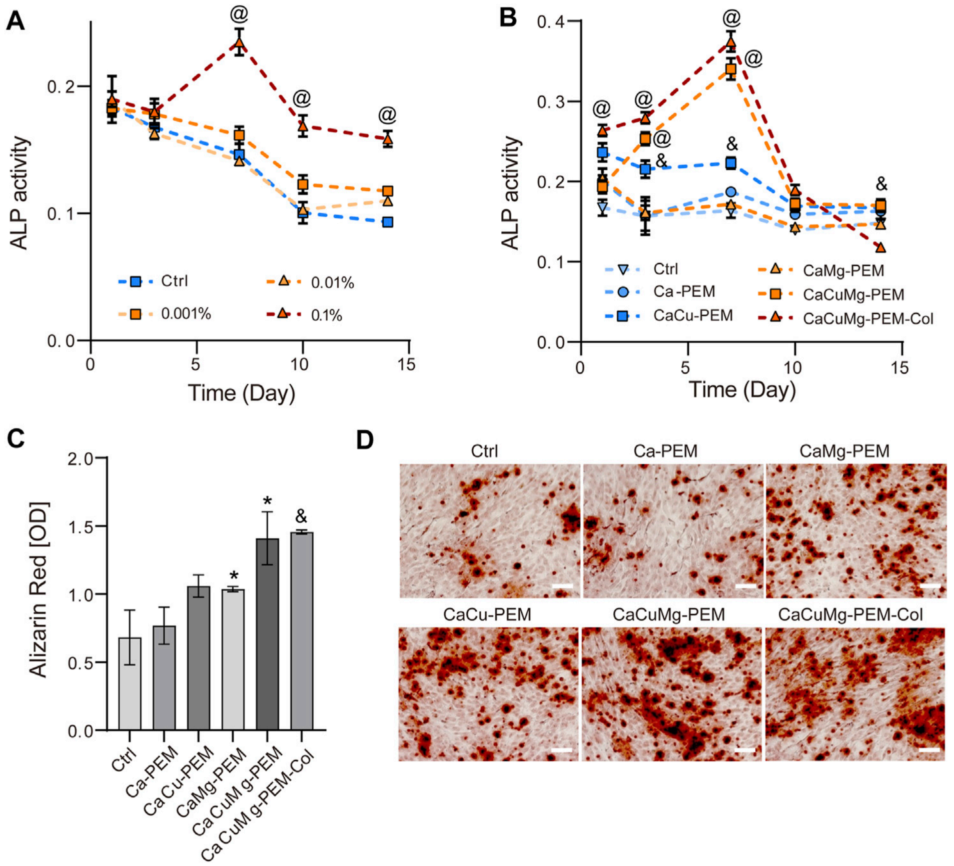

FIGURE 7
ALP activity was evaluated after 1, 3, 7, 10, 14 days with colorimetric method with pNPP as a substrate for ALP: **(A)** MG63 cells cultured with osteogenic medium supplemented with extract of CaCuMg-PEM-Col microcapsules in different concentrations; **(B)** MG63 cells cultured with osteogenic medium supplemented with 1% extracts of Ca-PEM, CaCu-PEM, CaMg-PEM, CaCuMg-PEM and CaCuMg-PEM-Col microcapsules. Osteogenic differentiation was revealed by **(D)** Alizarin Red staining (scale bar = 100 μm) and **(C)** quantification at day 21. ($n = 3$; Paired *t*-test, $^{*}p < 0.05$, $^{\&}p < 0.01$, $^{@}p < 0.001$).

MG63 cells was also carried out by using CCK-8 assay on the cell cultures at 1st, 3rd, and 7th days. Results in Figure 6B showed that cell viability on the 1st day was not markedly affected in any condition of microcapsules extracts (0.001%, 0.01%, and 0.1%) because the cells need sufficient time to recover after the passaging and transfer into the test-cultures. On the 3rd day, cells viability higher than 70% was observed for the groups treated with ionic extracts, all of which were higher than those of the blank controls. The cell viability of the group of 0.1% of microcapsule extract was obviously higher than other groups on the 7th day. A similar trend was observed with cell viability measured by addition of Ca-PEM, CaCu-PEM, CaMg-PEM, CaCuMg-PEM and CaCuMg-PEM-Col capsules (Figure 6D). Results revealed that the cell proliferation ability of the microcapsule groups was similar to or higher than that of blank control. And the cells in the CaCuMg-PEM-Col group showed the highest viability on the 3rd and 7th day. These results indicate that metal ions and CaCuMg-PEM-Col microcapsules did not induce any cytotoxic effect but promoted osteoblast proliferation in conjunction with type I collagen.

3.5 Osteogenic differentiation of osteoblast-like MG63 cells *in vitro*

Bone regeneration mainly includes proliferation and differentiation of osteoblasts. The previous viability measurements confirmed the positive effects of CaCuMg-PEM-Col microcapsules on cell proliferation. Therefore, the impacts on osteogenic differentiation were further investigated. ALP is an early marker of osteoblast differentiation which is an important indicator for bone formation and mineralization as well as for the bone regeneration progress (Hu & Olsen, 2016). The cellular ALP activity of MG63 cells treated with different microcapsule extracts were monitored on the 1st, 3rd, 7th,

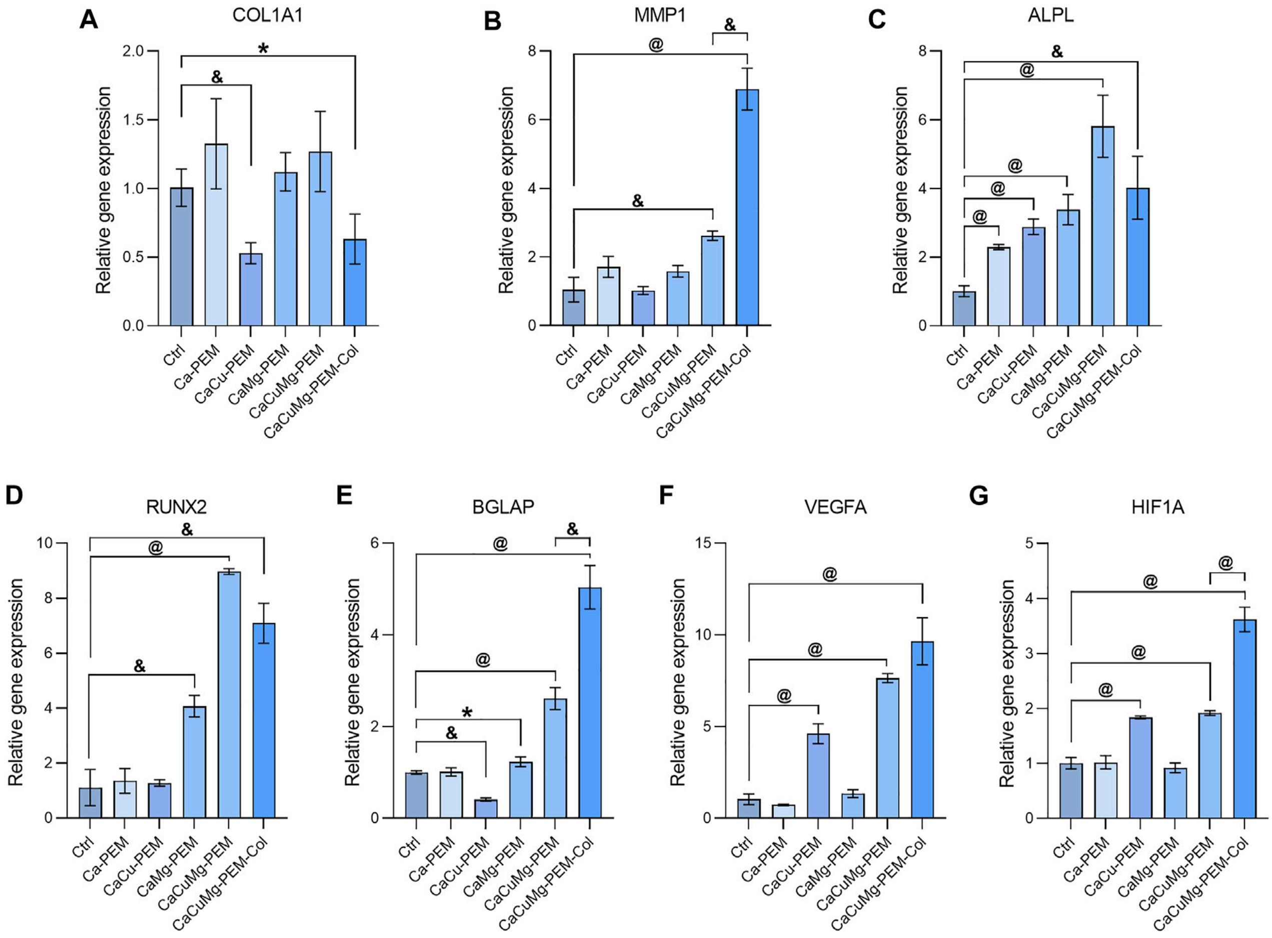

FIGURE 8
Relative gene expression of **(A–E)** osteogenic markers and **(F,G)** angiogenesis markers at 14 days analyzed *via* qRT-PCR (*n* = 3; Paired *t*-test, $*p < 0.05$, $^{\&}p < 0.01$, $^{@}p < 0.001$).

10th and 14th days. As shown in Figure 7A, on the 1st and 3rd day, ALP activity of cells treated with the extract of CaCuMg-PEM-Col microcapsules (0.001%, 0.01%, and 0.1%) were at a similar level as the blank control. Cellular ALP activity of the group of 0.1% reached peak on the 7th day, which was significantly higher than groups of 0.001%, 0.01% and ctrl. From day 7 onwards, decrease in ALP activity was observed under all conditions. Nevertheless, ALP activity of cells treated with 0.1% of microcapsule extracts was still significantly higher than other treated groups and control group. Therefore, 0.1% was adopted as the concentration used for the subsequent investigation (Figure 7B). On the 1st day, cells treated with osteogenic medium supplemented with sample extracts including Ca-PEM, CaCu-PEM, CaMg-PEM, CaCuMg-PEM and CaCuMg-PEM-Col showed higher ALP activity than control group which was only treated with osteogenic medium. On days 3 and 7, the levels and trends of ALP activity in the Ca-PEM and CaMg-PEM groups were the same as those in the blank control group, first increasing and then slowly decreasing. However, there was no significant difference in the expression levels between groups. The group of CaCu-PEM showed a similar trend but significantly higher ALP activity at these time points. Notably, the levels of ALP activity in the CaCuMg-PEM and CaCuMg-PEM-Col groups continued to increase over time, reaching a peak on day 7, in which the ALP activity in these two groups was significantly higher than other groups, and gradually decreased thereafter to levels close to those of the other groups. This indicates the significant synergistic regulation of Cu^{2+} and Mg^{2+} and collagen in osteoblasts differentiation. Interestingly, the ALP activity of the CaCuMg-PEM-Col group also showed the largest decrease among all groups after exhibiting the highest levels on days 1, 3, 7, and 10. It is suggested that CaCuMg-PEM microcapsules further functionalized with collagen could better mimic ECM, thus providing a more suitable microenvironment for bone regeneration and promoting the proliferation and differentiation of osteoblasts. ALP activity downregulated by CaCuMg-PEM-Col at day 14 indicated that the initiation of ECM mineralization completed earlier than other groups.

The effect of CaCuMg-PEM-Col on late differentiation (matrix mineralization) was investigated after 21 days of culture *via* Alizarin Red staining and quantification. As shown in Figure 7D, stronger Alizarin Red staining was observed on CaCuMg-PEM and CaCuMg-PEM-Col as compared to CaCu-PEM, CaMg-PEM, and blank control. Similarly, the result of quantification shows that mineralization on CaCu-PEM ($p < 0.05$), CaCuMg-PEM ($p < 0.05$) and CaCuMg-PEM-Col ($p < 0.01$) were significantly higher than the control group, suggesting that the microcapsules have a positive influence on osteoblast mineralization (Figure 7C).

3.6 Expression of osteogenesis and angiogenesis-related genes

As discussed previously, the bone regeneration process can be briefly divided into three periods: proliferation, ECM maturation and mineralization. Two transition points of gene expression of certain marker genes controlling cell proliferation and differentiation have been reported (Stein et al., 1990). The first transition occurs after completion of proliferation and initiation of ECM, when ALP and collagen are upregulated. The second transition takes place at the initiating of ECM mineralization. In this study, we investigated the gene expression related to osteogenesis and angiogenesis of MG63 at day 14 *via* real-time PCR (Lynch et al., 1995). As shown in Figure 8A, the COL1A1 expression of CaCu-PEM and CaCuMg-PEM-Col were significantly lower than blank control (osteogenic medium). This might result by the ECM-mimicking effect from the PEM and PEM-Col capsules. Reasonably, when compared to the blank control the matrix metalloproteinase-1 (MMP1) gene expression was markedly higher in the CaCuMg-PEM group ($p < 0.01$) and CaCuMg-PEM-Col group ($p < 0.001$) due to the presence of collagen (Figure 8B). All groups of microcapsules (Ca-PEM, CaCu-PEM, CaMg-PEM, CaCuMg-PEM, and CaCuMg-PEM-Col) showed significantly higher expression of ALPL in comparison to the blank control (osteogenic medium), among which the expression in the CaCuMg-PEM group was the highest, followed by the CaCuMg-PEM-Col (Figure 8C). The expression of RUNX2 in groups of CaMg-PEM, CaCuMg-PEM, and CaCuMg-PEM-Col were significantly higher than other groups (Figure 8D). The expression pattern of osteocalcin (BGLAP) was roughly similar to that of MMP1, showed the highest level in the CaCuMg-PEM-Col group, followed by the CaCuMg-PEM group (Figure 8E).

During osteogenic differentiation, (pre-) osteoblasts play a central role in communication with endothelial cells to ensure the temporal and spatial coupling of osteogenesis and angiogenesis *via* the regulation of gene expressions involved in angiogenesis. Interestingly, high expression of VEGFA and HIF1A were found in osteoblasts conditioned with CaCu-PEM, CaCuMg-PEM, and CaCuMg-PEM-Col extracts as shown in Figures 8F,G, suggesting that copper plays a more important role in the promotion of angiogenesis. Notably, we found significant synergistic effects of copper and magnesium, as well as the addition of type I collagen, on angiogenesis.

4 Conclusion

Bioactive metal ions including Ca^{2+}, Cu^{2+} and Mg^{2+} play a predominant role in the process of bone regeneration, which are recognized as an alternative for bone growth factor-based therapeutics. However, a delivery system with high stability and loading capacity of multiple metal ions, and controlled release kinetics is currently highly required. In this study, the vaterite-calcite $CaCO_3$ particles were effectively loaded with Cu^{2+} and Mg^{2+}, then coated with PEM to improve the crystal stability for better sustained release behavior, and further successfully functionalized with collagen to mimic bone tissue ECM. Ca^{2+}, Cu^{2+} and Mg^{2+} could sustainably release from the microcapsules and induce a proper bone regeneration microenvironment, regulating the osteoblasts proliferation and differentiation, promoting the ECM maturation and mineralization. It was shown that both osteogenesis and angiogenesis-related gene expressions were upregulated. Therefore, CaCuMg-PEM-Col microcapsules present a type of bioactive metal ion encapsulation and delivery system for the functionalization of bone graft materials. The presented strategy of combining multi metal ions with biocompatible PEM and collagen provides new inspiration and important prospects for bone tissue engineering.

Data availability statement

The original contributions presented in the study are included in the article/Supplementary Materials, further inquiries can be directed to the corresponding authors.

Author contributions

LF contributed to methodology, investigation, writing the original article, data curation. FK contributed to methodology and validation. AR and OJ contributed to investigation. CB contributed to methodology. MB contributed to methodology, reviewed and edited the manuscript, and funding acquisition. XX contributed to conceptualization, reviewing and editing the article, funding acquisition, investigation, and supervision.

Funding

This work was supported by the Federal Ministry of Education and Research (BMBF, Germany, FKZ: 13GW0400C); and the State Ministry of Baden-Württemberg for Economic Affairs, Labour and Tourism.

Acknowledgments

LF acknowledges the support by the China Scholarship Council (CSC, No. 202008500143). We thank our colleagues Clarissa Geiger, Anastasia Binder for their technique assistance, and Birgit Schröppel for insightful discussions and technique support in SEM and EDX mapping. Schematic figure was created with *BioRender*. The statistical analysis of data was performed with *GraphPad 9*.

Conflict of interest

Publisher's note

Supplementary material

The Supplementary Material for this article can be found online at: https://www.frontiersin.org/articles/10.3389/fbioe.2022.983988/full#supplementary-material

References

Aggarwal, N., Altgarde, N., Svedhem, S., Zhang, K., Fischer, S., and Groth, T. (2013). Effect of molecular composition of heparin and cellulose sulfate on multilayer formation and cell response. *Langmuir* 29 (45), 13853–13864. doi:10.1021/la4028157

Bharadwaz, A., and Jayasuriya, A. C. (2020). Recent trends in the application of widely used natural and synthetic polymer nanocomposites in bone tissue regeneration. *Mater. Sci. Eng. C* 110, 110698. doi:10.1016/j.msec.2020.110698

Brito Barrera, Y. A., Hause, G., Menzel, M., Schmelzer, C. E. H., Lehner, E., Mader, K., et al. (2020). Engineering osteogenic microenvironments by combination of multilayers from collagen type I and chondroitin sulfate with novel cationic liposomes. *Mat. Today Bio* 7, 100071. doi:10.1016/j.mtbio.2020.100071

Campbell, J., Kastania, G., and Volodkin, D. (2020). Encapsulation of low-molecular-weight drugs into polymer multilayer capsules templated on vaterite CaCO3 crystals. *Micromachines (Basel)* 11 (8), 717. doi:10.3390/mi11080717

Collins, M. N., Ren, G., Young, K., Pina, S., Reis, R. L., and Oliveira, J. M. (2021). Scaffold fabrication technologies and structure/function properties in bone tissue engineering. *Adv. Funct. Mat.* 31, 2010609. doi:10.1002/adfm.202010609

Daria, B., Trushina, T. N. B., Belyakov, Sergei, and Antipina, Maria N. (2022). Calcium carbonate vaterite particles for drug delivery: Advances and challenges. *Mater. Today Adv.* 14 (2590-0498), 100214. doi:10.1016/j.mtadv.2022.100214

Delajon, C., Gutberlet, T., Mohwald, H., and Krastev, R. (2009). Absorption of light and heavy water vapours in polyelectrolyte multilayer films. *Colloids Surfaces B Biointerfaces* 74 (2), 462–467. doi:10.1016/j.colsurfb.2009.08.051

Divband, B., Aghazadeh, M., Al-Qaim, Z. H., Samiei, M., Hussein, F. H., Shaabani, A., et al. (2021). Bioactive chitosan biguanidine-based injectable hydrogels as a novel BMP-2 and VEGF carrier for osteogenesis of dental pulp stem cells. *Carbohydr. Polym.* 273, 118589. doi:10.1016/j.carbpol.2021.118589

Feng, Z., Yang, T., Dong, S., Wu, T., Jin, W., Wu, Z., et al. (2022). Industrially synthesized biosafe vaterite hollow CaCO3 for controllable delivery of anticancer drugs. *Mater. Today Chem.* 24, 100917. doi:10.1016/j.mtchem.2022.100917

Feoktistova, N. A., Vikulina, A. S., Balabushevich, N. G., Skirtach, A. G., and Volodkin, D. (2020). Bioactivity of catalase loaded into vaterite CaCO3 crystals via adsorption and co-synthesis. *Mater. Des.* 185, 108223. doi:10.1016/j.matdes.2019.108223

Fitzpatrick, V., Martin-Moldes, Z., Deck, A., Torres-Sanchez, R., Valat, A., Cairns, D., et al. (2021). Functionalized 3D-printed silk-hydroxyapatite scaffolds for enhanced bone regeneration with innervation and vascularization. *Biomaterials* 276, 120995. doi:10.1016/j.biomaterials.2021.120995

Gelebart, P., Cuenot, S., Sinquin, C., Halgand, B., Sourice, S., Le Visage, C., et al. (2022). Microgels based on Infernan, a glycosaminoglycan-mimetic bacterial exopolysaccharide, as BMP-2 delivery systems. *Carbohydr. Polym.* 284, 119191. doi:10.1016/j.carbpol.2022.119191

Glenske, K., Donkiewicz, P., Kowitsch, A., Milosevic-Oljaca, N., Rider, P., Rofall, S., et al. (2018). Applications of metals for bone regeneration. *Int. J. Mol. Sci.* 19 (3), 826. doi:10.3390/ijms19030826

Halloran, D., Vrathasha, V., Durbano, H. W., and Nohe, A. (2020). Bone morphogenetic protein-2 conjugated to quantum Dot®s is biologically functional. *Nanomater. (Basel)* 10 (6), 1208. doi:10.3390/nano10061208

He, L. Y., Zhang, X. M., Liu, B., Tian, Y., and Ma, W. H. (2016). Effect of magnesium ion on human osteoblast activity. *Braz. J. Med. Biol. Res.* 49 (7), 1. doi:10.1590/1414-431X20165257

Hettiaratchi, M. H., Krishnan, L., Rouse, T., Chou, C., McDevitt, T. C., and Guldberg, R. E. (2020). Heparin-mediated delivery of bone morphogenetic protein-2 improves spatial localization of bone regeneration. *Sci. Adv.* 6 (1), eaay1240. doi:10.1126/sciadv.aay1240

Hu, K., and Olsen, B. R. (2016). Osteoblast-derived VEGF regulates osteoblast differentiation and bone formation during bone repair. *J. Clin. Invest.* 126 (2), 509–526. doi:10.1172/JCI82585

Hurle, K., Oliveira, J. M., Reis, R. L., Pina, S., and Goetz-Neunhoeffer, F. (2021). Ion-doped brushite cements for bone regeneration. *Acta Biomater.* 123, 51–71. doi:10.1016/j.actbio.2021.01.004

ISO (2009). *Biological evaluation of medical devices — Part 5: Tests for in vitro cytotoxicity*. Geneva, Switzerland: ISO, 10993–10995. Available at: https://www.iso.org/standard/36406.html.

Jeong, J., Kim, J. H., Shim, J. H., Hwang, N. S., and Heo, C. Y. (2019). Bioactive calcium phosphate materials and applications in bone regeneration. *Biomater. Res.* 23, 4. doi:10.1186/s40824-018-0149-3

Kargozar, S., Mozafari, M., Ghodrat, S., Fiume, E., and Baino, F. (2021). Copper-containing bioactive glasses and glass-ceramics: From tissue regeneration to cancer therapeutic strategies. *Mater. Sci. Eng. C* 121, 111741. doi:10.1016/j.msec.2020.111741

Kohler, R., Donch, I., Ott, P., Laschewsky, A., Fery, A., and Krastev, R. (2009). Neutron reflectometry study of swelling of polyelectrolyte multilayers in water vapors: Influence of charge density of the polycation. *Langmuir* 25 (19), 11576–11585. doi:10.1021/la901508w

Kulp, E. A., and Switzer, J. A. (2007). Electrochemical biomineralization: The deposition of calcite with chiral morphologies. *J. Am. Chem. Soc.* 129 (49), 15120–15121. doi:10.1021/ja076303b

Lee, J., Byun, H., Madhurakkat Perikamana, S. K., Lee, S., and Shin, H. (2019). Current advances in immunomodulatory biomaterials for bone regeneration. *Adv. Healthc. Mat.* 8 (4), e1801106. doi:10.1002/adhm.201801106

Lin, Z., Cao, Y., Zou, J., Zhu, F., Gao, Y., Zheng, X., et al. (2020). Improved osteogenesis and angiogenesis of a novel copper ions doped calcium phosphate cement. *Mater. Sci. Eng. C* 114, 111032. doi:10.1016/j.msec.2020.111032

Liu, H., Du, Y., Yang, G., Hu, X., Wang, L., Liu, B., et al. (2020). Delivering proangiogenic factors from 3D-printed polycaprolactone scaffolds for vascularized bone regeneration. *Adv. Healthc. Mat.* 9, e2000727. doi:10.1002/adhm.202000727

Lynch, M. P., Stein, J. L., Stein, G. S., and Lian, J. B. (1995). The influence of type I collagen on the development and maintenance of the osteoblast phenotype in primary and passaged rat calvarial osteoblasts: Modification of expression of genes supporting cell growth, adhesion, and extracellular matrix mineralization. *Exp. Cell Res.* 216 (1), 35–45. doi:10.1006/excr.1995.1005

Martin, J. R., Howard, M. T., Wang, S., Berger, A. G., and Hammond, P. T. (2021). Oxidation-Responsive, tunable growth factor delivery from polyelectrolyte-coated implants. *Adv. Healthc. Mat.* 10 (9), e2001941. doi:10.1002/adhm.202001941

Marx, K. A. (2003). Quartz crystal microbalance: A useful tool for studying thin polymer films and complex biomolecular systems at the solution-surface interface. *Biomacromolecules* 4 (5), 1099–1120. doi:10.1021/bm020116i

Morozova, S., and Muthukumar, M. (2018). Electrostatic effects in collagen fibril formation. *J. Chem. Phys.* 149 (16), 163333. doi:10.1063/1.5036526

Mourino, V., Cattalini, J. P., and Boccaccini, A. R. (2012). Metallic ions as therapeutic agents in tissue engineering scaffolds: An overview of their biological applications and strategies for new developments. *J. R. Soc. Interface* 9 (68), 401–419. doi:10.1098/rsif.2011.0611

Musso, C. G. (2009). Magnesium metabolism in health and disease. *Int. Urol. Nephrol.* 41 (2), 357–362. doi:10.1007/s11255-009-9548-7

O'Neill, E., Awale, G., Daneshmandi, L., Umerah, O., and Lo, K. W. (2018). The roles of ions on bone regeneration. *Drug Discov. Today* 23 (4), 879–890. doi:10.1016/j.drudis.2018.01.049

Qiao, W., Wong, K. H. M., Shen, J., Wang, W., Wu, J., Li, J., et al. (2021). TRPM7 kinase-mediated immunomodulation in macrophage plays a central role in magnesium ion-induced bone regeneration. *Nat. Commun.* 12 (1), 2885. doi:10.1038/s41467-021-23005-2

Ruehle, M. A., Krishnan, L., Vantucci, C. E., Wang, Y., Stevens, H. Y., Roy, K., et al. (2019). Effects of BMP-2 dose and delivery of microvascular fragments on healing of bone defects with concomitant volumetric muscle loss. *J. Orthop. Res.* 37 (3), 553–561. doi:10.1002/jor.24225

Sahebalzamani, M., Ziminska, M., McCarthy, H. O., Levingstone, T. J., Dunne, N. J., and Hamilton, A. R. (2022). Advancing bone tissue engineering one layer at a time: A layer-by-layer assembly approach to 3D bone scaffold materials. *Biomater. Sci.* 10, 2734–2758. doi:10.1039/d1bm01756j

Salmivirta, M., Lidholt, K., and Lindahl, U. (1996). Heparan sulfate: A piece of information. *FASEB J.* 10 (11), 1270–1279. doi:10.1096/fasebj.10.11.8836040

Sankar, D., Mony, U., and Rangasamy, J. (2021). Combinatorial effect of plasma treatment, fiber alignment and fiber scale of poly (epsilon-caprolactone)/collagen multiscale fibers in inducing tenogenesis in non-tenogenic media. *Mater. Sci. Eng. C* 127, 112206. doi:10.1016/j.msec.2021.112206

Sauerbrey, G. (1959). Verwendung von Schwingquarzen zur Waegung duenner Schichten und zur Mikrowaegung. *Z. Phys.* 155 (2), 206–222. doi:10.1007/bf01337937

Shen, Q., Wei, H., Zhou, Y., Huang, Y., Yang, H., Wang, D., et al. (2006). Properties of amorphous calcium carbonate and the template action of vaterite spheres. *J. Phys. Chem. B* 110 (7), 2994–3000. doi:10.1021/jp055063o

SSED (2022). *Summary of safety and effectiveness data*. Silver Spring, MD, United States: SSED. Available at: https://www.accessdata.fda.gov/cdrh_docs/pdf/P000058B.pdf.

Stein, G. S., Lian, J. B., and Owen, T. A. (1990). Relationship of cell growth to the regulation of tissue-specific gene expression during osteoblast differentiation. *FASEB J.* 4 (13), 3111–3123. doi:10.1096/fasebj.4.13.2210157

Sun, L., Xiong, X., Zou, Q., Ouyang, P., and Krastev, R. (2017). Controlled heparinase-catalyzed degradation of polyelectrolyte multilayer capsules with heparin as responsive layer. *J. Appl. Polym. Sci.* 134 (23), 44916. doi:10.1002/app.44916

Svenskaya, Y. I., InozemtsevaGorin, O. A., Ivanova, A. G., Shtykov, S. N., Gorin, D. A., Parakhonskiy, B. V., et al. (2018). Key parameters for size- and shape-controlled synthesis of vaterite particles. *Cryst. Growth & Des.* 18 (1), 331–337. doi:10.1021/acs.cgd.7b01328

Toosi, S., and Behravan, J. (2020). Osteogenesis and bone remodeling: A focus on growth factors and bioactive peptides. *Biofactors* 46 (3), 326–340. doi:10.1002/biof.1598

Vikulina, A., Webster, J., Voronin, D., Ivanov, E., Fakhrullin, R., Vinokurov, V., et al. (2021). Mesoporous additive-free vaterite CaCO3 crystals of untypical sizes: From submicron to Giant. *Mater. Des.* 197, 109220. doi:10.1016/j.matdes.2020.109220

Wang, H., Zhao, S., Xiao, W., Xue, J., Shen, Y., Zhou, J., et al. (2016). Influence of Cu doping in borosilicate bioactive glass and the properties of its derived scaffolds. *Mater. Sci. Eng. C* 58, 194–203. doi:10.1016/j.msec.2015.08.027

Wang, K. F., Nagarajan, R., and Camesano, T. A. (2014). Antimicrobial peptide alamethicin insertion into lipid bilayer: A QCM-D exploration. *Colloids Surfaces B Biointerfaces* 116, 472–481. doi:10.1016/j.colsurfb.2014.01.036

Wei, Q., Lu, J., Wang, Q., Fan, H., and Zhang, X. (2015). Novel synthesis strategy for composite hydrogel of collagen/hydroxyapatite-microsphere originating from conversion of CaCO3 templates. *Nanotechnology* 26 (11), 115605. doi:10.1088/0957-4484/26/11/115605

Wong, H. M., Chu, P. K., Frankie, K. L., Leung, F. K. L., Cheung, K. M. C., Luk, K. D. K., et al. (2014). Engineered polycaprolactone–magnesium hybrid biodegradable porous scaffold for bone tissue engineering. *Prog. Nat. Sci. Mater. Int.* 24 (5), 561–567. doi:10.1016/j.pnsc.2014.08.013

Xie, H., Gu, Z., He, Y., Xu, J., Xu, C., Li, L., et al. (2018). Microenvironment construction of strontium-calcium-based biomaterials for bone tissue regeneration: The equilibrium effect of calcium to strontium. *J. Mat. Chem. B* 6 (15), 2332–2339. doi:10.1039/c8tb00306h

Yu, L., Rowe, D. W., Perera, I. P., Zhang, J., Suib, S. L., Xin, X., et al. (2020). Intrafibrillar mineralized collagen-hydroxyapatite-based scaffolds for bone regeneration. *ACS Appl. Mat. Interfaces* 12 (16), 18235–18249. doi:10.1021/acsami.0c00275

Zhang, D., Wu, X., Chen, J., and Lin, K. (2018). The development of collagen based composite scaffolds for bone regeneration. *Bioact. Mat.* 3 (1), 129–138. doi:10.1016/j.bioactmat.2017.08.004

Zhao, Z., Li, G., Ruan, H., Chen, K., Cai, Z., Lu, G., et al. (2021). Capturing magnesium ions via microfluidic hydrogel microspheres for promoting cancellous bone regeneration. *ACS Nano* 15, 13041–13054. doi:10.1021/acsnano.1c02147

Zhong, Z., Wu, X., Wang, Y., Li, M., Li, Y., Liu, X., et al. (2022). Zn/Sr dual ions-collagen co-assembly hydroxyapatite enhances bone regeneration through procedural osteo-immunomodulation and osteogenesis. *Bioact. Mat.* 10, 195–206. doi:10.1016/j.bioactmat.2021.09.013

frontiers | Frontiers in Bioengineering and Biotechnology

TYPE Original Research
PUBLISHED 15 August 2022
DOI 10.3389/fbioe.2022.961728

Ultrasound combined with glial cell line-derived neurotrophic factor-loaded microbubbles for the targeted treatment of drug addiction

Feng Wang[1,2], Hongwei Wu[3], Azhen Hu[4], Lei Dong[1], Xiaoxia Lin[1], Menghao Li[1], Yongling Wang[5], Wenjun Li[6], Liansheng Chang[7], Yuqiao Chang[1], Hanqing Liu[8]*, Yu Shi[2]* and Nana Li[1]*

[1]Henan Key Laboratory of Medical Tissue Regeneration, School of Basic Medical Sciences, Xinxiang Medical University, Xinxiang, Henan, China, [2]Department of Ultrasound, Peking University Shenzhen Hospital, Shenzhen, China, [3]Department of Chemistry, Xinxiang Medical University, Xinxiang, Henan, China, [4]Shenzhen PKU-HKUST Medical Center, Shenzhen, China, [5]Department of Physiology and Pathophysiology, School of Basic Medical Sciences, Xinxiang Medical University, Xinxiang, Henan, China, [6]Division of Oral and Craniofacial Biomedicine, University of North Carolina Adams School of Dentistry, Chapel Hill, NC, United States, [7]Department of Human Anatomy Histology and Embryology, School of Basic Medical Sciences, Xinxiang Medical University, Xinxiang, Henan, China, [8]Central Laboratory, Shenzhen Samii Medical Center, Shenzhen, Guangdong, China

Drug addiction is a serious problem globally, recently exacerbated by the COVID-19 pandemic. Glial cell-derived neurotrophic factor (GDNF) is considered a potentially effective strategy for the treatment of addiction. Previous animal experiments have proven that GDNF has a good therapeutic effect on drug addiction, but its clinical application is limited due to its poor blood-brain barrier (BBB) permeability. Low-frequency focused ultrasound, combined with microbubbles, is a non-invasive and reversible technique for locally-targeted BBB opening. In the present study, magnetic resonance imaging-guided low-frequency focused ultrasound, combined with GDNF microbubbles, was used to target BBB opening in the ventral tegmental area (VTA) region. The effects of GDNF on morphine-induced conditioned place preference (CPP) and acute withdrawal symptoms in rats after a partially opened BBB were evaluated by behavioral observation. Western blot was used to detect changes in tyrosine hydroxylase (TH) expression levels in the VTA region after different treatments, and high performance liquid chromatography was used to detect the changes in monoamine neurotransmitter content. The results showed that ultrasound combined with GDNF microbubbles targeted and opened the BBB in the VTA region, and significantly increased GDNF content, destroyed morphine-induced CPP, and reduced the withdrawal symptoms of morphine addiction in rats. Furthermore, the up-regulation of TH expression and the increase of norepinephrine and dopamine content induced by morphine were significantly reversed, and the increase of 5-hydroxytryptamine content was partially reversed. Therefore, ultrasound combined with GDNF microbubbles to target and open the BBB can effectively increase the content of central GDNF, thus playing a therapeutic role in morphine addiction. Our study provides a new approach to locally open

EDITED BY
Yuangang Liu,
Huaqiao University, China

REVIEWED BY
Liujiang Song,
University of North Carolina at Chapel Hill, United States
Yuanyuan Shen,
Shenzhen University, China

*CORRESPONDENCE
Hanqing Liu,
liuhanqing@ssmc-sz.com
Yu Shi,
shiyu@pkuszh.com
Nana Li,
lnndoc@126.com

SPECIALTY SECTION
This article was submitted to Biomaterials,
a section of the journal
Frontiers in Bioengineering and Biotechnology

RECEIVED 05 June 2022
ACCEPTED 18 July 2022
PUBLISHED 15 August 2022

CITATION
Wang F, Wu H, Hu A, Dong L, Lin X, Li M, Wang Y, Li W, Chang L, Chang Y, Liu H, Shi Y and Li N (2022), Ultrasound combined with glial cell line-derived neurotrophic factor-loaded microbubbles for the targeted treatment of drug addiction.
Front. Bioeng. Biotechnol. 10:961728.
doi: 10.3389/fbioe.2022.961728

the BBB and target delivery of neurotrophic factors, such as GDNF, to treat brain diseases like addiction.

KEYWORDS

focused ultrasound, targeted microbubbles, blood-brain barrier, drug addiction, glial cell line-derived neurotrophic factor

Introduction

Drug addiction is a serious problem worldwide (Allen et al., 2013). According to the World Drug Report 2021 (Becker and Fiellin, 2020), published by the United Nations Office on Drugs and Crime, approximately 275 million people used drugs in 2020, an increase of 22% from 2010, and more than 36 million people develop mental disorders as a result of drug abuse. By 2030, demographic factors project the number of people using drugs will increase by 11% worldwide. Drug use killed almost half a million people in 2019, while drug use disorders resulted in 18 million years of healthy life lost, mostly due to opioids. The COVID-19 pandemic has further exacerbated the drug problem by creating conditions that make more people susceptible to drug use and to engaging in illicit crop cultivation. For example, the COVID-19 crisis pushed more than 100 million people into extreme poverty, with 114 million jobs lost globally in 2020. In contrast, drug traffickers have quickly recovered from the initial setback caused by lockdown restrictions and are operating at pre-pandemic levels. Furthermore, access to drugs has become simpler than ever, with an increase in online sales and contactless drug transactions, such as by mail, a trend possibly accelerated by the pandemic.

Opioid drugs are among the most powerful analgesics but also among the most addictive. Opioids are the most widely used addictive substances with the longest history (Belin et al., 2007). According to China’s 2020 drug situation report, by the end of 2020, China had 1.801 million drug users, 734,000 of whom abused opioids, accounting for 40.8% of the total number. In the United States, approximately 50,000 people died from an opioid overdose in 2019, more than double the number of deaths compared to 2010. North America has seen a spike in opioid overdose deaths since the onset of the pandemic. For example, opioid overdose deaths in Canada were 58% higher during the April–June 2020 quarter compared with the same period in 2019. COVID-19 could lead to infection in persons with opioid use disorder, higher opioid overdose rates, reversal of system-level gains in expanding access to medications for opioid use disorder, halt critical research, and prevent exacting legal reparations against opioid manufacturers (Bleier et al., 2016). These could cause an intensification of the opioid crisis.

Understanding the mechanisms of opioid addiction and finding treatment methods have been goals of scientists and doctors for more than a century. Since the mid-1990s, neurotrophic factors, such as brain-derived neurotrophic factor (BDNF) and glial cell line-derived neurotrophic factor (GDNF) have been receiving much attention, especially in drug reward and relapse (Carnicella et al., 2008). GDNF is a neurotrophic factor that promotes the survival of embryonic midbrain dopaminergic neurons. Accumulating evidence suggests that GDNF plays a unique role in negatively regulating the actions of drugs of abuse; thus, the GDNF pathway may be a promising target for the treatment of addiction (Carnicella and Ron, 2009). However, the large molecular weight of GDNF (24 kDa) makes it difficult for it to cross the blood-brain barrier (BBB), which limits its application in disease treatment (Chen et al., 2020). Therefore, how to promote the transmission of GDNF through the BBB and increase the effective drug concentration of GDNF in the central nervous system (CNS) is a key scientific problem for the application of GDNF in the treatment of drug addiction.

In fact, the BBB is one of the major factors restricting the use of many CNS medications (Cheron and Kerchove’Exaerde, 2021). In recent years, scientists have tried many ways to promote the transmission of GDNF through the BBB, such as viruses (Cintrón-Colón et al., 2020), carrier nanoparticles (Everitt and Robbins, 2016), fusion proteins (Fu et al., 2010), and heterotopic mucosal grafts (Gasca-Salas et al., 2021). Focused ultrasound-induced BBB opening is considered a non-viral, non-invasive, and targeted method for drug and gene delivery (Ghitza et al., 2010; Holt, 2021). Focusing ultrasound to open the BBB and increase intracerebral delivery of GDNF has been proven to be safe and effective, and has shown good application prospects in the treatment of a variety of diseases (Kastin et al., 2003; Kilic et al., 2003).

In our previous study, magnetic resonance image (MRI)-guided focused ultrasound was proven to successfully open the BBB and achieve the targeted delivery of GDNF (Lin et al., 2016). Furthermore, we developed GDNF-loaded microbubbles (MBs) and achieved local and precise delivery of GDNF to the CNS through MRI-guided focused ultrasound-induced BBB disruption, and confirmed its therapeutic effects on chronic mild stress rat model of depression (Lin et al., 2015). However, MRI-guided focused ultrasound combined with targeted MBs to open the BBB and deliver GDNF has not been reported for the treatment of drug addiction. Therefore, the present study aimed to use MRI-guided focused ultrasound combined with targeted MBs to open the BBB, promote GDNF crossing the BBB, and target delivery to the VTA region. A morphine addiction model was established, and behavioral observation was used to evaluate the effects of GDNF on acute withdrawal symptoms and psychological craving in rats after partial opening of the BBB. Concurrently, high performance liquid chromatography (HPLC) was used to determine the content of monoamine neurotransmitters in the brain, and to measure the effects of increased brain GDNF levels on central monoamine neurotransmitters after partial opening of the BBB. These results will help determine the target and mechanism of GDNF for detoxification, and provide a scientific basis for the use of GDNF across the BBB for the treatment of drug addiction.

Materials and methods

Preparation and characterization of GDNF-Loaded microbbules

In this study, MBs were biotinylated and lipid coated, which encapsulated a high-molecular-weight gas core of perfluoropropane (C3F8) (Lin et al., 2019). Before preparing the drug-loaded MBs, the MBs were washed three times in a phosphate-buffered sodium (PBS) solution to remove the excess unreacted lipids by centrifugation at 400 *g* for 3 min. A specific amount of avidin (final concentration 3 mg/ml) per 10^9 MBs was then added to the washed MB dispersion. After incubating at room temperature for 15 min, the MBs were washed three times to remove the unreacted avidin further and then incubated with 200 μL biotinylated GDNF. The average diameters of the plain control and GDNF-loaded MBs were determined by an Accusizer (Model 780A; Particle Sizing System, Santa Barbara, CA, United States).

Animals

Male Sprague–Dawley rats (weighing 200–220 g upon arrival) were provided by Guangdong Medical Laboratory Animal Center (Foshan, Guangdong, China) and housed five per cage (before stereotactic nucleus localization surgery) or individually (after stereotactic nucleus localization surgery) under a 12-h light/dark cycle at 22 ± 2°C and relative humidity of 50% ± 10% with *ad libitum* access to food and water. The animals were allowed to acclimatize to a specific pathogen-free environment for 7 days prior to treatment. This animal study was performed in Shenzhen PKU-HKUST Medical Center (animal license number: SYXK 2015-0106) and approved by the Ethics Committee of Peking University Shenzhen Hospital. All of the animal procedures were performed in accordance with the National Institutes of Health Guide for the Care and Use of Laboratory Animals, and the procedures were approved by the Local Animal Use Committee.

Conditioned place preference

The conditioned place preference (CPP) procedure was performed in a three-chamber apparatus using an unbiased, counterbalanced protocol as described previously (Lin et al., 2020). A brief description of the procedure is as follows. Baseline preference was assessed by placing the rats in the center chamber of the CPP apparatus and allowing them to explore all three chambers freely for 15 min. Rats that showed a strong unconditioned preference for either of the side chambers (i.e., >540 s) were excluded from the experiments. The remaining rats were then trained for eight consecutive days with alternating subcutaneous injections of morphine (10 mg/kg) or saline (1 ml/kg) and were confined to the conditioning chambers for 45 min after each injection. The test for the expression of methamphetamine-induced CPP was identical to the initial baseline preference assessment and was performed on the following day after training.

Stereotactic brain surgery

The rats were anesthetized with intraperitoneal (IP) pentobarbital sodium (50 mg/kg) and placed in a stereotaxic apparatus (RWD Life Science Co., LTD., China). The skull was exposed and a cannula was inserted 1 mm above the target brain region (ventral tegmental area, VTA) at the following coordinates (Lin et al., 2019): anterior/posterior (AP), −5.2 mm; medial/lateral (ML), ± 1.8 mm; and dorsal/ventral (DV), −7.5 mm. The cannula was secured to the skull with anchoring screws and dental acrylic cement. A stainless-steel probe was inserted into the cannula to maintain patency, and penicillin (200 k units/day, IP) was injected for seven consecutive days to prevent infection. The rats were housed individually after the surgery and allowed 3–5 days of recovery before behavioral experiments.

Effect of glial cell-derived neurotrophic factor on morphine-induced conditioned place preference in rats

Forty-eight CPP trained rats were randomly divided into six groups ($n = 8$), namely IV-NS group [intravenous (IV), normal saline (NS)], IV-GDNF group (IV, GDNF 3 mg/kg), M group (blank microbubbles, IV), M-GDNF group (GDNF microbubbles, IV), IN-NS group [intranuclear (IN) NS injected into VTA] and IN-GDNF group (IN-GDNF 10 μg/μL injected into VTA). The volume of administration was 0.5 ml in all IV injection groups and 0.5 μL in the IN-injection groups. After drug administration, MRI-guided focused ultrasound was performed in the M and M-GDNF groups. 0.5 ml NS was administered to an additional group of rats during the entire study period as control (Con group). The method used in this study for preparing the GDNF-loaded MBs followed the protocol described in our previously published papers (Lin et al., 2015; Lin et al., 2016). The above treatments were performed on the 2nd and 4th day after completion of the CPP test, and an additional CPP test was performed on the 5th day to observe the changes in each group. The rats were decapitated immediately after the last measurement, and the brain tissue of half the rats in each group was used for Western blot analysis, while the other half was analyzed with HPLC (High-performance liquid chromatography).

Focused ultrasound program

The focused ultrasound system was placed in a 3.0 T MRI chamber for brain tissue imaging and ultrasound localization. The T1-phase scan was used to detect brain tissue in real time and locate brain regions. The right hemisphere of the brain was irradiated by focused ultrasound (frequency, 1 MHz; MB dosage, 0.5 ml; exposure time, 1 min; pressure amplitude, 0.8 MPa; delay time, 60 s). After ultrasound irradiation and MRI image acquisition, Evans blue (EB, 100 mg/kg) was injected through the tail vein to reveal the BBB open area. Rats that did not receive ultrasound were used as controls.

Effects of glial cell-derived neurotrophic factor on withdrawal symptoms

A morphine withdrawal model was established using IP naloxone (Sigma, United States) (4 mg/kg) 4 h after the last injection of morphine in addiction rats to induce withdrawal symptoms. The grouping and administration methods of rats were the same as described above. The treatments were performed 24 and 72 h before naloxone-induced withdrawal. The withdrawal symptoms were observed and scored based on wet dog shaking, abnormal posture, irritability, clenching, vegetative nervous system symptoms, and weight loss. The rats were decapitated immediately after the test, and the brain tissues were analyzed by Western blot and HPLC as described above.

Western blot

The olfactory bulb and cerebellum of rats' brains were removed, and the telencephalon was reserved, placed in n-hexane at −60°C for 20 s, and then placed in a pre-cooled (−20°C) frozen sectioning machine. The brain tissues were embedded with tissue-embedding agent (OCT) and fixed. Continuous 50-μm thickness sectioning was performed until the VTA area was exposed according to the stereotaxic map of the rat brain. Then, the VTA was removed using a syringe needle (size 16) and placed into a cooled Eppendorf tube. RIPA cracking solution containing 1 mM phenylmethyl sulfonyl fluoride (PMSF) was added (150–200 μL/20 mg) and homogenized mechanically three times (15 s each with 5 s apart). After full lysis, centrifugation at 12,000 rpm/min for 5 min was performed, supernatant taken, protein content determined using the BCA method, and sample concentrations in each group adjusted to the same level using lysis solution. All of the operations above were performed on the ice. The 4X protein loading buffer was proportionally added, and the protein was heated in boiling water (3 min) for albuminous degeneration and frozen at −70°C for later use.

A gel caster was successively filled with 10% separated glue and 5% concentrated glue. Marker (2 μL/well) and protein samples (20 μL/well) were successively added, and sodium dodecyl sulfate-polyacrylamide gel electrophoresis (SDS-PAGE) was performed with a constant voltage of 80 V for concentrated glue and 120 V for separated glue. At the end of the electrophoresis, the gel was removed and electro-transferred using a polyvinylidene difluoride (PVDF) at a constant current of 250 mA for 2.5 h. Then, the PVDF membrane was intruded into 5% bovine serum albumin (BSA) and sealed for 2 h. Subsequently, 5% BSA-diluted primary antibody (1:1,000) was added and incubated overnight in the refrigerator at 4°C, and then rinsed three times for 5 min each using TBST. TBST-diluted secondary antibody (1:2,000) was added and incubated at room temperature for 45 min, then rinsed with TBST three times for 5 min each. ECL chemiluminescence solution was used for development to compare the expression level of tyrosine hydroxylase (TH) (Abcam, United Kingdom) in the VTA region of rats in each group.

high performance liquid chromatography test

The rat brain samples were thawed at room temperature, and 500 μL of perchloric acid (0.4 M) were added, mixed, and centrifuged at 15,000 rpm for 3 min. Supernatant (100 μL) was added to 200 μL mobile phase, and 20 μL of the mixture were injected into the chromatography. The peak area was recorded, and was quantified using the standard curve. The standard solution series were determined, and the peak area and concentration were calculated using least square linear regression. The chromatographic conditions were as follows: column, diamond-C18 (250 mm × 4.6 mm, 5 μm); mobile phase, 4.04 g anhydrous sodium acetate, 0.80 g heptane sodium sulfonate, and 0.188 g EDTA dissolved in 1,000 ml water, filtered using 0.25 μm filter membrane, pH adjusted to 4.5 with acetic acid, then to 3.8 with phosphoric acid, and 220 ml methanol added; flow rate, 1.0 ml/min; detector potential, 0.75 V; column temperature, 35°C; and injection volume: 20 μL. Dopamine (DA) hydrochloride (Sigma, United States),

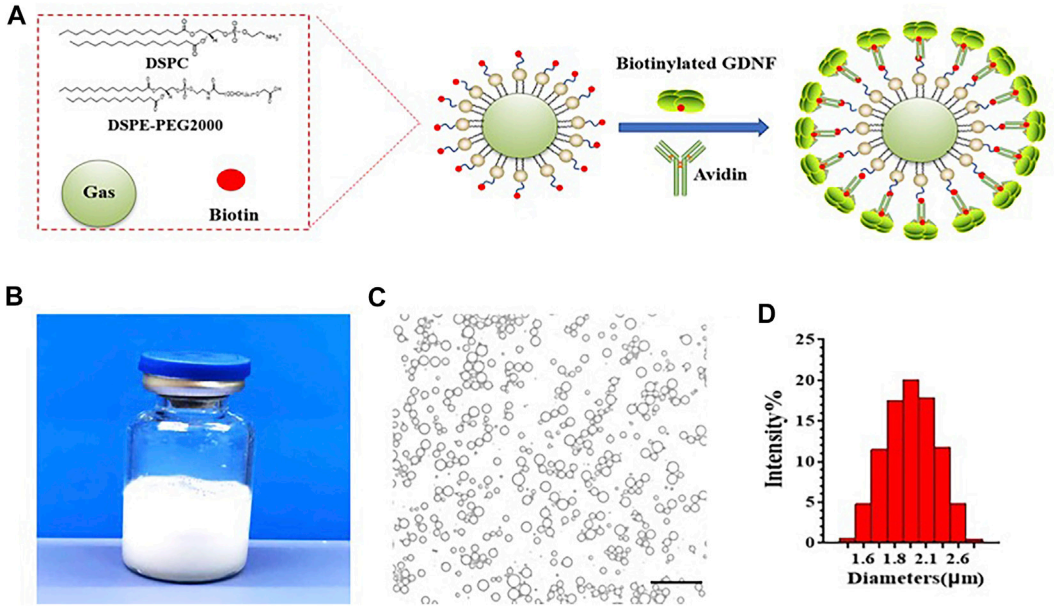

FIGURE 1
GDNF-loaded MBs. **(A)** Diagram of GDNF-loaded MBs. **(B)** Appearance of GDNF-loaded MBs. **(C)** Microscopic examination of GDNF-loaded MBs. **(D)** Particle size detection of GDNF-loaded MBs. GDNF, glial cell-derived neurotrophic factor; MBs, microbubbles. Scale bar = 20 μm.

norepinephrine (NE) (Sigma, United States), and 5-hydroxytryptamine (5-HT) hydrochloride (Sigma, United States) were dissolved in methanol to prepare a standard solution for control. The levels of NE, DA, and 5-HT of NAc were determined.

Statistical analysis

The Western blot strips were analyzed with Quantity One software. The corresponding background box was cut out with the value of the strip box, and the value of the strip was obtained. According to the same sample, the value of each experimental group was compared with the corresponding blank control group, and the ratio was obtained. The measurement data results were expressed as mean ± SEM and analyzed by SPSS 26.0. One-way ANOVA was used for comparison between groups, and $p < 0.05$ was considered statistically significant.

Results

Preparation and characterization of glial cell-derived neurotrophic factor-loaded microbubbles

GDNF-loaded MBs were successfully prepared. A schematic illustration of the structure of M-GDNF is presented in Figure 1A. Figure 1B showed the appearance of the prepared GDNF-loaded MBs in vial. The morphologic appearance of MB-GDNF after conjugating with GDNF was observed through bright-field microscopy (Figure 1C). The mean diameter and concentration of the GDNF-loaded MBs were 1.8 ± 0.5 μm and (2.15 ± 0.4) × 10^{10} MB/ml, respectively (Figure 1D).

Morphine-induced conditioned place preference in rats

Repeated measures ANOVA was used to analyze behavioral data. The results showed that after morphine CPP training, all rats acquired significant CPP, and CPP scores were significantly higher in the CPP training groups (post-C) compared with pre-C ($p < 0.001$). CPP scores in CPP training groups were significantly higher than those in the control group ($p < 0.001$). There was no significant difference in the control group before and after training ($p > 0.05$) (Figure 2).

Effect of focused ultrasound combined with glial cell-derived neurotrophic factor-loaded microbubbles on morphine-induced conditioned place preference in rats

The principle and method of GDNF-targeted delivery to the VTA by focused ultrasound combined with MBs are shown in

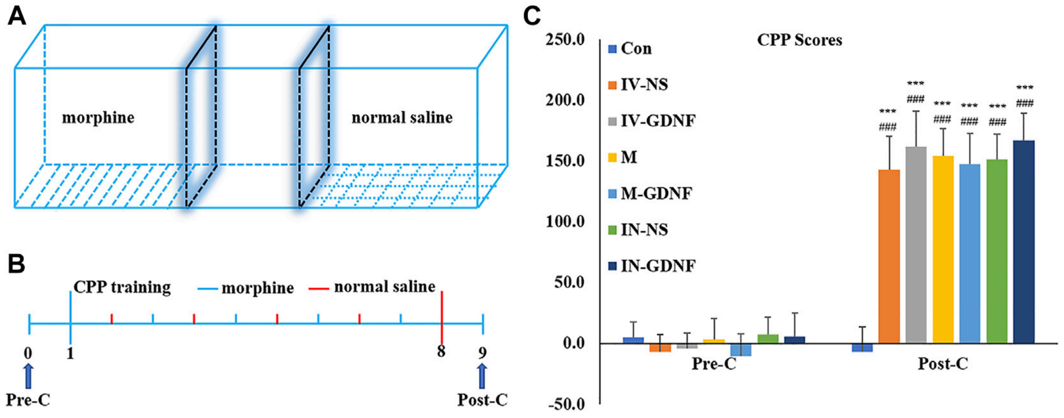

FIGURE 2
Morphine-induced CPP in rats. **(A)** CPP training diagram. **(B)** CPP training protocol. **(C)** CPP scores. Means ± SEM, *n* = 8, $^{***}p < 0.001$ vs. Pre-C; $^{\#\#\#}p < 0.001$ vs. control group. CPP, conditioned place preference.

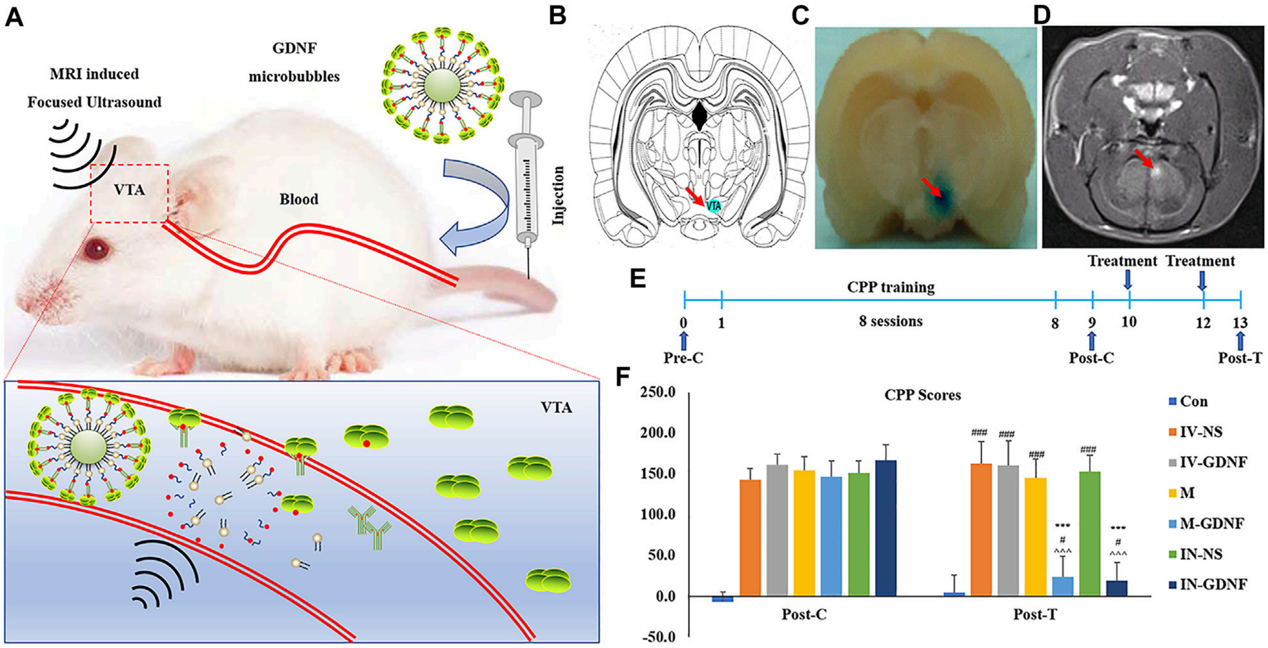

FIGURE 3
Focused ultrasound combined with GDNF-loaded MBs reversed morphine-induced CPP in rats. **(A)** Schematic diagram of targeted delivery of GDNF to VTA via focused ultrasound combined with MBs. **(B)** Schematic representations of VTA. **(C)** The location of the BBB opening was confirmed by EB staining of the affected area (arrows). **(D)** BBB opening was monitored by leakage of the MR contrast agent into the brain parenchyma on coronal (COR) MR images (arrows). **(E)** Schematic diagram of experimental process. **(F)** CPP scores. Means ± SEM, *n* = 8, $^{***}p < 0.001$ vs. Post-C; $^{\#}p < 0.05$, $^{\#\#\#}p < 0.001$ vs. Control group; $^{\wedge\wedge\wedge}p < 0.001$ vs. IV-NS group. BBB, blood-brain barrier; CPP, conditioned place preference; MBs, microbubbles; MR, magnetic resonance; VTA, ventral tegmental area.

Figure 3A. The MRI-guided focused ultrasound irradiation to the VTA can partially open the BBB in this region. The schematic representations showed the location of VTA (Figure 3B). As shown in Figure 3C, EB staining proved that MRI-guided focused ultrasound successfully opened the BBB in the VTA region using the previously measured optimal parameter conditions, which was further confirmed by MRI imaging (Figure 3D). The CPP training and treatment procedures for

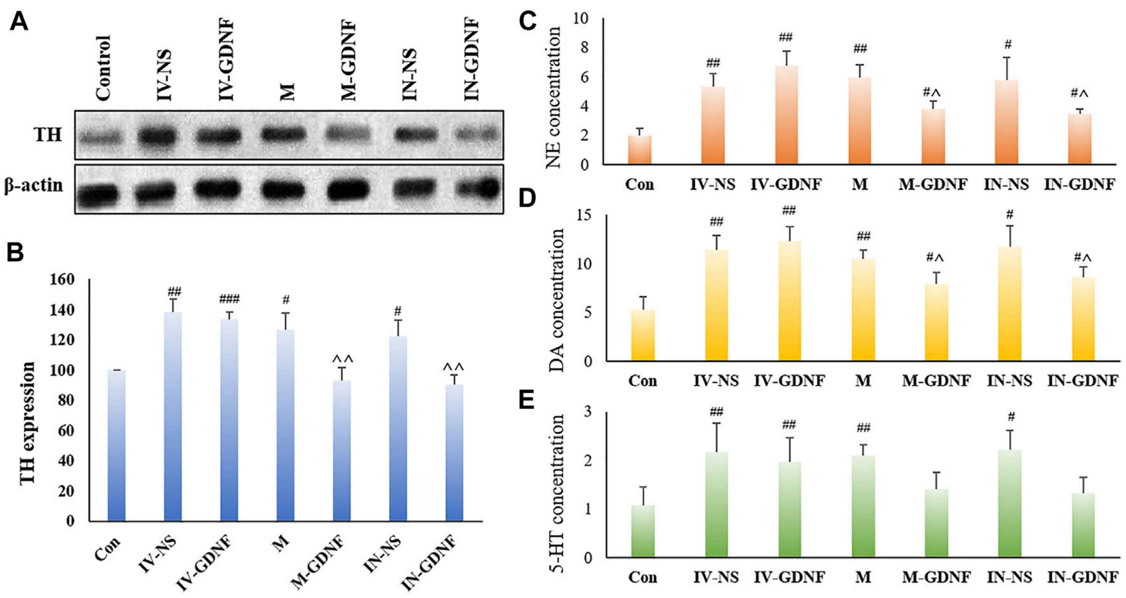

FIGURE 4
Effect of different treatments on morphine neurotransmitters of addiction rats. **(A)** Representative bands of TH expression. **(B)** Analysis of TH expression in different groups. **(C)**. NE concentration measured by HPLC. **(D)** DA concentration measured by HPLC. **(E)**. 5-HT concentration measured by HPLC. Means ± SEM, *n* = 3, $^{\#}p < 0.05$, $^{\#\#}p < 0.01$ vs. control group; $^{\wedge}p < 0.05$ vs. IV-SN group. DA, dopamine; HPLC, high performance liquid chromatography; 5-HT, serotonin; NE, norepinephrine; TH, tyrosine hydroxylase.

rats are shown in Figure 3E. CPP test results showed that the test time had a significant effect on morphine-induced CPP scores [F (2,98) = 719.07, $p < 0.01$], and there was also a significant interaction between each treatment group and the test time [F (12,98) = 54.63, $p < 0.01$]. Post hoc analysis showed that the M-GDNF and IN-GDNF CPP scores were significantly lower than those of the IV-NS group and that test before treatment (post-C), and showed no significant differences compared with the control group. Furthermore, there was no significant difference between the M-GDNF and IV-GDNF groups (Figure 3F). The morphine-induced CPP was not significantly affected by GDNF injection (IV-GDNF) or MBs (M) via caudal vein or NS injected intranuclearly (IN-NS). These results confirm that GDNF can reverse morphine-induced CPP, and targeted delivery of GDNF via focused ultrasound combined with MBs can achieve therapeutic efficacy comparable to that of direct intranuclear injection.

Influences of focused ultrasound combined with glial cell-derived neurotrophic factor-loaded microbubbles on neurotransmitters in addiction rats

One-way ANOVA was used for analysis. Western blot results showed that morphine significantly up-regulated TH expression in the VTA region of rats (Figures 4A,B), TH expression levels of M-GDNF and IN-GDNF groups was significantly down-regulated compared with the IV-NS group, and there was no significant difference between the M-GDNF, IN-GDNF, and control groups (Figure 4B). The contents of NE, DA, and 5-HT in the NAc region were detected by HPLC. The results showed that morphine could significantly induce an increase of NE, DA, and 5-HT in the NAc region of rats, while M-GDNF and IN-GDNF treatment could significantly reverse the increase of NE and DA induced by morphine (Figures 4C,D). For 5-HT, the levels of 5-HT in the M-GDNF and IN-GDNF groups were not significantly different from those in the IV-NS and control groups, suggesting that M-GDNF and IN-GDNF treatments could partially reverse the increase of 5-HT induced by morphine (Figure 4E).

Effect of focused ultrasound combined with glial cell-derived neurotrophic factor-loaded microbubbles on morphine withdrawal symptoms in rats

Naloxone (4 mg/kg, IP) administration 4 h after the last injection of morphine induced obvious withdrawal symptoms in rats. Rats in different groups received corresponding

TABLE 1 Effect of different treatments on naloxone-induced morphine withdrawal symptoms.

Withdrawal sign	Control	IV-NS	IV-GDNF	M	M-GDNF	IN-NS	IN-GDNF
Jumping	0.63 ± 0.52	$2.88 \pm 0.99^{***\wedge\$}$	$2.75 \pm 0.71^{***\$}$	$3.25 \pm 1.28^{***\wedge\wedge\$\$}$	$1.75 \pm 0.71^{*\#}$	$4.13 \pm 1.64^{***\wedge\wedge\wedge\$\$\$}$	1.50 ± 0.93
Teeth Chattering	0.00 ± 0.00	$2.13 \pm 0.99^{***}$	$2.50 \pm 0.93^{***\$}$	$2.00 \pm 0.76^{***}$	$1.75 \pm 0.89^{***}$	$1.88 \pm 0.83^{***}$	$1.63 \pm 0.74^{***}$
Writhing	0.00 ± 0.00	$2.38 \pm 0.92^{***}$	$2.75 \pm 0.89^{***}$	$3.13 \pm 0.83^{***\wedge\$}$	$2.25 \pm 1.04^{***}$	$3.00 \pm 1.07^{***\$}$	$2.00 \pm 0.76^{***}$
Wet-dog Shakes	0.00 ± 0.00	$7.00 \pm 1.60^{***\wedge\wedge\wedge\$\$\$}$	$6.63 \pm 1.06^{***\wedge\wedge\$\$\$}$	$6.13 \pm 1.81^{***\wedge\$\$\$}$	$4.38 \pm 1.41^{***}$	$7.25 \pm 1.28^{***\wedge\wedge\wedge\$\$\$}$	$2.88 \pm 1.25^{***\wedge}$
Exploring	1.13 ± 0.64	$8.50 \pm 1.85^{***\wedge\wedge\$\$\$}$	$9.00 \pm 1.31^{***\wedge\wedge\wedge\$\$\$}$	$9.75 \pm 2.25^{***\wedge\wedge\wedge\$\$\$}$	$5.63 \pm 1.19^{***}$	$10.38 \pm 2.07^{***\wedge\wedge\wedge\$\$\$}$	$4.63 \pm 1.69^{***}$
Ptosis	0.00 ± 0.00	$6.00 \pm 1.77^{***\wedge\$\$}$	$5.00 \pm 1.31^{***}$	$5.38 \pm 1.41^{***}$	$4.38 \pm 1.19^{***}$	$5.88 \pm 1.46^{***\wedge\$\$}$	$4.13 \pm 1.13^{***}$
Piloerection	0.00 ± 0.00	$3.00 \pm 1.41^{***\$\$}$	$2.88 \pm 1.25^{***\$}$	$3.25 \pm 1.04^{***\$\$}$	$2.63 \pm 0.92^{***}$	$3.63 \pm 1.19^{***\$\$\$}$	$1.50 \pm 0.76^{**\wedge}$
Irritability	0.00 ± 0.00	$1.13 \pm 0.64^{***}$	$1.38 \pm 0.74^{***}$	$1.50 \pm 0.53^{***\$}$	$1.00 \pm 0.53^{***}$	$1.63 \pm 0.74^{***\wedge\$}$	$0.88 \pm 0.35^{***}$
Diarrhea	0.00 ± 0.00	$4.25 \pm 1.04^{***\wedge\wedge\$\$\$}$	$5.38 \pm 1.06^{***\wedge\wedge\wedge\$\$\$}$	$4.50 \pm 1.20^{***\wedge\wedge\wedge\$\$\$}$	$2.50 \pm 0.93^{***}$	$5.13 \pm 1.25^{***\wedge\wedge\wedge\$\$\$}$	$2.25 \pm 0.89^{***}$
Weight Loss	1.48 ± 0.49	$5.18 \pm 1.45^{***\wedge\wedge\$\$}$	$4.90 \pm 1.21^{***\wedge\$\$}$	$6.05 \pm 1.44^{***\wedge\wedge\wedge\$\$\$}$	$3.35 \pm 1.28^{**}$	$6.54 \pm 1.61^{***\wedge\wedge\wedge\$\$\$}$	$2.88 \pm 1.11^{*}$

Mean ± SEM. $^{*}p < 0.05$, $^{**}p < 0.01$, $^{***}p < 0.001$ vs. control group; $^{\wedge}p < 0.05$, $^{\wedge\wedge}p < 0.01$, $^{\wedge\wedge\wedge}p < 0.001$ vs. M-GDNF, group; $^{\$}p < 0.05$, $^{\$\$}p < 0.01$, $^{\$\$\$}p < 0.001$ vs. IN-GDNF, group.

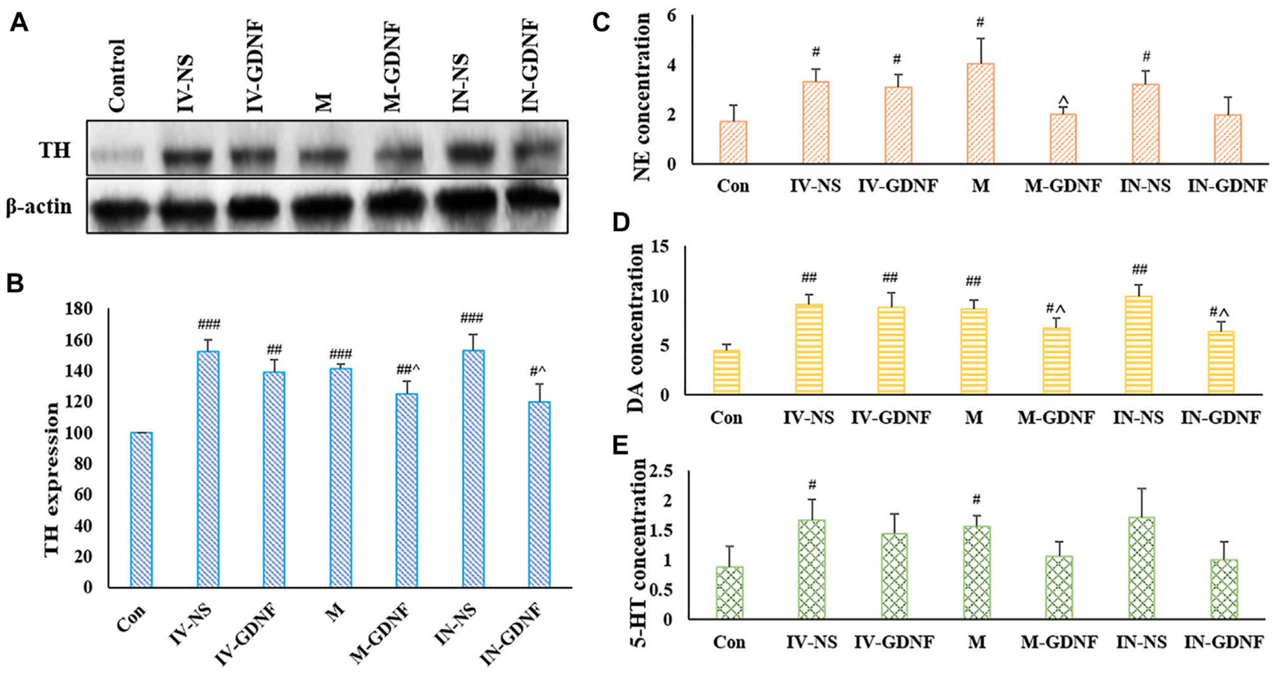

FIGURE 5
Effect of different treatments on neurotransmitters of morphine withdrawal rats. **(A)** Representative bands of TH expression. **(B)** Analysis of TH expression in different groups. **(C)** NE concentration measured by HPLC. **(D)** DA concentration measured by HPLC. **(E)** 5-HT concentration measured by HPLC. Means ± SEM, $n = 3$, $^{\#}p < 0.05$, $^{\#\#}p < 0.01$, $^{\#\#\#}p < 0.001$ vs. Control group; $^{\wedge}p < 0.05$ vs. IV-SN group. DA, dopamine; HPLC, high performance liquid chromatography; 5-HT, serotonin; NE, norepinephrine; TH, tyrosine hydroxylase.

treatments 24 h before naloxone injection to observe the effects on morphine withdrawal symptoms. The results are shown in Table 1. Among the ten withdrawal symptoms observed, the M-GDNF group had five symptoms (jumping, wet dog shakes, exploring, diarrhea, and weight loss) and the IN-GDNF group had six symptoms (jumping, wet dog shakes, exploring, piloerection, diarrhea, and weight loss) scored significantly lower than those in other treatment groups ($p < 0.05$). Compared with the IN-GDNF group, only the scores of wet dog shakes were significantly higher in the M-GDNF group. These results confirm that GDNF can significantly reduce the withdrawal symptoms of morphine, and focused ultrasound combined with MBs-targeted delivery of GDNF can achieve similar therapeutic effects comparable to those of intranuclear injection.

Possible mechanisms of different treatments affecting morphine withdrawal symptoms

The western blot results showed that TH expression in the VTA of morphine withdrawal rats was significantly higher than that of the control group. TH expression levels in the IN-GDNF and M-GDNF groups were significantly lower than in the IV-NS group, and there was no significant difference between the M-GDNF and IN-GDNF groups (Figures 5A,B). The contents of NE, DA and 5-HT in the NAc region were determined by HPLC. The results showed that morphine withdrawal significantly increased the NE, DA, and 5-HT contents in the NAc region of rats, and the up-regulation of NE and DA were significantly reversed by M-GDNF and IN-GDNF treatment (Figures 5C,D). The levels of 5-HT in the M-GDNF and IN-GDNF groups showed no significant difference compared with both the IV-NS and control group, suggesting that M-GDNF and IN-GDNF treatments can partially reverse the increase of 5-HT induced by morphine withdrawal (Figure 5E).

Discussion

The abuse of addictive substances has become a crucial factor affecting world economic development, endangering public health, and threatening social harmony and stability (Maier et al., 2020). Drug abuse can not only cause direct economic losses and increase the probability of crime, but also cause the rapid spread of HIV, HBV, and other infectious diseases (Messer et al., 2000). Therefore, it is of great significance to seek treatment drugs for addiction. The BBB is a vital structure that maintains the stability of the central nervous system. However, the actions of many drugs for addiction treatment, especially macromolecules, are limited due to their inability to cross the BBB and enter the brain. This is a complex problem in the development of drugs for addiction treatment (Nelson, 2006). In recent years, focused ultrasound has been regarded as an effective non-invasive method to open the BBB and achieve targeted drug delivery (United Nation, 2021). This technology may provide new approaches and strategies for the treatment of addiction.

As one of the most representative members of the neurotrophic factor family, GDNF is a large protein with a molecular weight of 24 kDa. GDNF is widely present in the developing central nervous system and mature brain tissue, and can promote the growth, protection, and repair of various neurons, such as glial cells and serotonergic and dopaminergic neurons (Sajadi et al., 2005). GDNF receptors are expressed in many brain regions, including the cerebellum, hypothalamic nucleus, amygdala, and hippocampus, but are mainly found in the SNc and VTA. Furthermore, dopaminergic neurons in the VTA region are closely associated with addiction (Shi et al., 2018). TH is a rate-limiting enzyme of DA synthesis, and the up-regulation of TH levels is considered one of the biomarkers of addiction. Direct injection of GDNF into the VTA region reversed CPP, NR1 subunit of the NMDA receptor, and TH expression in the brain of cocaine-trained rats (Sun et al., 2018). Cocaine increases extracellular DA concentration by blocking synaptic level reuptake, whereas morphine increases DA concentration by stimulating DA neurons in the VTA region (Tosi et al., 2020). It was also found that GDNF could regulate TH activity, and the increase in GDNF levels was closely related to the decrease of TH activity and DA levels in the striatum (Uhl et al., 2019). In addition, injection of GDNF in the VTA region can reverse the elevation of TH protein induced by cocaine and morphine (Sun et al., 2018; Volkow and Boyle, 2018). These studies indicate that GDNF can attenuate the biochemical and behavioral changes of drug abuse, is an effective substance for addiction treatment (Sun et al., 2018; Volkow et al., 2019), and its mechanism may be related to the regulation of TH activity.

Although GDNF has shown potential in the treatment of drug addiction, its difficulty in penetrating the BBB severely limits its use (Wang et al., 2012; Wang et al., 2020). Therefore, a fundamental scientific problem in using GDNF for the treatment of drug addiction is how to promote passage of GDNF through the BBB to achieve effective concentrations in the central nervous system. In this study, we used focused ultrasound combined with GDNF MBs to achieve targeted delivery into the VTA brain region. Our previous study proved that the optimal parameters for ultrasound combined MB opening of the BBB are as follows: 1 MHz frequency, 0.5 ml MB dose, 1 min irradiation time, 0.8 MPa sound pressure, and 60 s delay time (Lin et al., 2015; Lin et al., 2016). These were the parameters used in this study for focused ultrasound-targeted irradiation of the VTA under MRI guidance to open the BBB locally. EB and MRI contrast agent leakage in the local open area were consistent with the VTA positions shown in the model figure, indicating that our study could accurately open the BBB locally and provide a basis for the targeted release of GDNF.

To verify the inhibitory effect of an increased content of GDNF in the brain, achieved through ultrasound combined with GDNF MB opening of the BBB, on morphine addiction, morphine CPP and morphine withdrawal rat models were established. After morphine training, all rats except the control group acquired significant CPP. Compared with the control group, there were significant differences between the M-GDNF and IN-GDNF groups and other groups after the corresponding treatments were given to each. Naloxone can induce significant morphine withdrawal symptoms. In the M-GDNF group, five of ten withdrawal symptoms scores were significantly lower than those of the other treatment groups, while there were no significant differences with the IN-GDNF group except for wet dog shakes. The results showed that ultrasound combined with GDNF MB to open the BBB and increase the content of central GDNF could destroy the CPP and relieve the withdrawal symptoms of morphine addiction in rats and achieve the same effect as brain microinjection of GDNF.

Furthermore, we investigated the effects of increasing the brain content of GDNF via ultrasound combined with GDNF MB on the BBB opening on TH expression and content of mono-ammonia neurotransmitters such as NE, DA, and 5-HT in order to reveal the mechanism of action. The results showed that in both the morphine-induced CPP and naloxone-induced withdrawal models, ultrasound combined with GDNF MB group (M-GDNF) could significantly reverse the increased TH expression and content of NE, DA, and 5-HT, and achieved similar effects to direct injections of GDNF into the brain VTA (IN-GDNF).

Conclusion

This study provides a non-invasive and reversible method to open the BBB, target delivery of GDNF to the VTA region, and treat morphine addiction. This technique can avoid brain tissue damage caused by intracranial microinjection, and further increases the advantages of neurotrophic factors, such as GDNF, in the treatment of brain diseases. It provides a new and effective way to explore the application of peripheral macromolecular drugs in the treatment of neuropsychiatric diseases such as addiction.

Data availability statement

The original contributions presented in the study are included in the article/supplementary materials, further inquiries can be directed to the corresponding authors.

Ethics statement

The animal study was reviewed and approved by the Peking University Shenzhen Hospital. Written informed consent was obtained from the owners for the participation of their animals in this study.

Author contributions

FW and HW conceived and performed the experiments, performed the data analysis, and wrote the manuscript. AH, LD and XL conducted the study. ML, YW, LC and YC collected the samples. WL, HL and YS analyzed the data, drafted and edited the manuscript. NL conceived and designed the experiments, revised the manuscript and approved the final version.

Funding

The study was supported by the grant from the National Natural Science Fund of China (U1804187), the Shenzhen Science and Technology Planning Project (JCYJ20210324105415040 and JYCJ20190808160011529), Guangdong High-level hospital construction fund (No. GD2019260), Shenzhen Municipal Development and Reform Commission (XMHT20190104001), Shenzhen Key Medical Discipline Construction Fund (No. SZXK051), Sanming Project of Medicine in Shenzhen (No. SZSM202111011).

Conflict of interest

The authors declare that the research was conducted in the absence of any commercial or financial relationships that could be construed as a potential conflict of interest.

Publisher's note

References

Allen, S. J., Watson, J. J., Shoemark, D. K., Barua, N. U., and Patel, N. K. (2013). GDNF, NGF and BDNF as Therapeutic Options for Neurodegeneration. *Pharmacol. Ther.* 138 (2), 155–175. doi:10.1016/j.pharmthera.2013.01.004

Becker, W. C., and Fiellin, D. A. (2020). When Epidemics Collide: Coronavirus Disease 2019 (COVID-19) and the Opioid Crisis. *Ann. Intern. Med.* 173 (1), 59–60. doi:10.7326/m20-1210

Belin, D., Deroche-Gamonet, V., and Jaber, M. (2007). Cocaine-induced Sensitization Is Associated with Altered Dynamics of Transcriptional Responses of the Dopamine Transporter, Tyrosine Hydroxylase, and Dopamine D2 Receptors in C57Bl/6J Mice. *Psychopharmacol. Berl.* 193 (4), 567–578. doi:10.1007/s00213-007-0790-3

Bleier, B. S., Kohman, R. E., Guerra, K., Nocera, A. L., Ramanlal, S., Kocharyan, A. H., et al. (2016). Heterotopic Mucosal Grafting Enables the Delivery of Therapeutic Neuropeptides across the Blood Brain Barrier. *Neurosurgery* 78 (3), 448–457. doi:10.1227/neu.0000000000001016

Carnicella, S., Kharazia, V., Jeanblanc, J., Janak, P. H., and Ron, D. (2008). GDNF Is a Fast-Acting Potent Inhibitor of Alcohol Consumption and Relapse. *Proc. Natl. Acad. Sci. U. S. A.* 105 (23), 8114–8119. doi:10.1073/pnas.0711755105

Carnicella, S., and Ron, D. (2009). GDNF--a Potential Target to Treat Addiction. *Pharmacol. Ther.* 122 (1), 9–18. doi:10.1016/j.pharmthera.2008.12.001

Chen, W., Hu, Y., and Ju, D. (2020). Gene Therapy for Neurodegenerative Disorders: Advances, Insights and Prospects. *Acta Pharm. Sin. B* 10 (8), 1347–1359. doi:10.1016/j.apsb.2020.01.015

Cheron, J., and Kerchove d'Exaerde, A. (2021). Drug Addiction: from Bench to Bedside. *Transl. Psychiatry* 11 (1), 424. doi:10.1038/s41398-021-01542-0

Cintrón-Colón, A. F., Almeida-Alves, G., Boynton, A. M., and Spitsbergen, J. M. (2020). GDNF Synthesis, Signaling, and Retrograde Transport in Motor Neurons. *Cell. Tissue Res.* 382 (1), 47–56. doi:10.1007/s00441-020-03287-6

Everitt, B. J., and Robbins, T. W. (2016). Drug Addiction: Updating Actions to Habits to Compulsions Ten Years on. *Annu. Rev. Psychol.* 67, 23–50. doi:10.1146/annurev-psych-122414-033457

Fu, A., Zhou, Q. H., Hui, E. K., Lu, J. Z., Boado, R. J., and Pardridge, W. M. (2010). Intravenous Treatment of Experimental Parkinson's Disease in the Mouse with an IgG-GDNF Fusion Protein that Penetrates the Blood-Brain Barrier. *Brain Res.* 1352, 208–213. doi:10.1016/j.brainres.2010.06.059

Gasca-Salas, C., Fernández-Rodríguez, B., Pineda-Pardo, J. A., Rodríguez-Rojas, R., Obeso, I., Hernández-Fernández, F., et al. (2021). Blood-brain Barrier Opening with Focused Ultrasound in Parkinson's Disease Dementia. *Nat. Commun.* 12 (1), 779. doi:10.1038/s41467-021-21022-9

Ghitza, U. E., Zhai, H., Wu, P., Airavaara, M., Shaham, Y., and Lu, L. (2010). Role of BDNF and GDNF in Drug Reward and Relapse: a Review. *Neurosci. Biobehav. Rev.* 35 (2), 157–171. doi:10.1016/j.neubiorev.2009.11.009

Holt, E. (2021). Drug Legislation May Be Key to Ending HIV Epidemic. *Lancet HIV* 8 (7), e392–e393. doi:10.1016/s2352-3018(21)00131-4

Kastin, A. J., Akerstrom, V., and Pan, W. (2003). Glial Cell Line-Derived Neurotrophic Factor Does Not Enter Normal Mouse Brain. *Neurosci. Lett.* 340 (3), 239–241. doi:10.1016/s0304-3940(03)00007-7

Kilic, U., Kilic, E., Dietz, G. P., and Bähr, M. (2003). Intravenous TAT-GDNF Is Protective after Focal Cerebral Ischemia in Mice. *Stroke* 34 (5), 1304–1310. doi:10.1161/01.Str.0000066869.45310.50

Lin, C. Y., Hsieh, H. Y., Chen, C. M., Wu, S. R., Tsai, C. H., Huang, C. Y., et al. (2016). Non-invasive, Neuron-specific Gene Therapy by Focused Ultrasound-Induced Blood-Brain Barrier Opening in Parkinson's Disease Mouse Model. *J. Control. Release* 235, 72–81. doi:10.1016/j.jconrel.2016.05.052

Lin, C. Y., Hsieh, H. Y., Pitt, W. G., Huang, C. Y., Tseng, I. C., Yeh, C. K., et al. (2015). Focused Ultrasound-Induced Blood-Brain Barrier Opening for Non-viral, Non-invasive, and Targeted Gene Delivery. *J. Control. Release* 212, 1–9. doi:10.1016/j.jconrel.2015.06.010

Lin, C. Y., Lin, Y. C., Huang, C. Y., Wu, S. R., Chen, C. M., and Liu, H. L. (2020). Ultrasound-responsive Neurotrophic Factor-Loaded Microbubble- Liposome Complex: Preclinical Investigation for Parkinson's Disease Treatment. *J. Control. Release* 321, 519–528. doi:10.1016/j.jconrel.2020.02.044

Lin, C. Y., Tsai, C. H., Feng, L. Y., Chai, W. Y., Lin, C. J., Huang, C. Y., et al. (2019). Focused Ultrasound-Induced Blood Brain-Barrier Opening Enhanced Vascular Permeability for GDNF Delivery in Huntington's Disease Mouse Model. *Brain Stimul.* 12 (5), 1143–1150. doi:10.1016/j.brs.2019.04.011

Maier, H. B., Neyazi, M., Neyazi, A., Hillemacher, T., Pathak, H., Rhein, M., et al. (2020). Alcohol Consumption Alters Gdnf Promoter Methylation and Expression in Rats. *J. Psychiatr. Res.* 121, 1–9. doi:10.1016/j.jpsychires.2019.10.020

Messer, C. J., Eisch, A. J., Carlezon, W. A., Jr., Whisler, K., Shen, L., Wolf, D. H., et al. (2000). Role for GDNF in Biochemical and Behavioral Adaptations to Drugs of Abuse. *Neuron* 26 (1), 247–257. doi:10.1016/s0896-6273(00)81154-x

Nelson, R. (2006). Blood-brain Barrier Challenged by New Drug Delivery Vehicle. *Lancet Neurol.* 5 (2), 117. doi:10.1016/s1474-4422(06)70340-4

Sajadi, A., Bauer, M., Thöny, B., and Aebischer, P. (2005). Long-term Glial Cell Line-Derived Neurotrophic Factor Overexpression in the Intact Nigrostriatal System in Rats Leads to a Decrease of Dopamine and Increase of Tetrahydrobiopterin Production. *J. Neurochem.* 93 (6), 1482–1486. doi:10.1111/j.1471-4159.2005.03139.x

Shi, Y., Wang, F., Hu, A.-Z., Wang, Q.-W., Wu, J.-L., Li, M.-H., et al. (2018). Effects and Mechanisms of Jinniu Capsule on Methamphetamine-Induced Conditioned Place Preference in Rats. *Open Chem.* 16 (1), 674–680. doi:10.1515/chem-2018-0074

Sun, Y., Zhang, Y., Zhang, D., Chang, S., Jing, R., Yue, W., et al. (2018). GABRA2 Rs279858-Linked Variants Are Associated with Disrupted Structural Connectome of Reward Circuits in Heroin Abusers. *Transl. Psychiatry* 8 (1), 138. doi:10.1038/s41398-018-0180-0

Tosi, G., Duskey, J. T., and Kreuter, J. (2020). Nanoparticles as Carriers for Drug Delivery of Macromolecules across the Blood-Brain Barrier. *Expert Opin. Drug Deliv.* 17 (1), 23–32. doi:10.1080/17425247.2020.1698544

Uhl, G. R., Koob, G. F., and Cable, J. (2019). The Neurobiology of Addiction. *Ann. N. Y. Acad. Sci.* 1451 (1), 5–28. doi:10.1111/nyas.13989

United Nation (2021). *World Drug Report 2021*.

Volkow, N. D., and Boyle, M. (2018). Neuroscience of Addiction: Relevance to Prevention and Treatment. *Am. J. Psychiatry* 175 (8), 729–740. doi:10.1176/appi.ajp.2018.17101174

Volkow, N. D., Jones, E. B., Einstein, E. B., and Wargo, E. M. (2019). Prevention and Treatment of Opioid Misuse and Addiction: A Review. *JAMA Psychiatry* 76 (2), 208–216. doi:10.1001/jamapsychiatry.2018.3126

Wang, F., Li, N., Wei, X., Jia, X., Liu, H., Wang, Y., et al. (2020). MRI-guided Focused Ultrasound-Induced Blood Brain Barrier Disruption to Deliver Glial Cell Line Derived Neurotropic Factor Proteins into Brain to Treat Rat Depression. *J. Biomed. Nanotechnol.* 16 (5), 626–639. doi:10.1166/jbn.2020.2914

Wang, F., Shi, Y., Lu, L., Liu, L., Cai, Y., Zheng, H., et al. (2012). Targeted Delivery of GDNF through the Blood-Brain Barrier by MRI-Guided Focused Ultrasound. *PLoS One* 7 (12), e52925. doi:10.1371/journal.pone.0052925

frontiers | Frontiers in Bioengineering and Biotechnology

TYPE Mini Review
PUBLISHED 02 September 2022
DOI 10.3389/fbioe.2022.989953

OPEN ACCESS

EDITED BY
Junchao Wei,
Nanchang University, China

REVIEWED BY
Rajesh Baby,
St.Joseph's College of Engineering and Technology, Palai, India
Chengchao Chu,
Xiamen University, China
Xufeng Dong,
Dalian University of Technology, China

*CORRESPONDENCE
Ranjith Kumar Kankala,
ranjithkankala@hqu.edu.cn

SPECIALTY SECTION
This article was submitted to Biomaterials,
a section of the journal
Frontiers in Bioengineering and Biotechnology

RECEIVED 09 July 2022
ACCEPTED 28 July 2022
PUBLISHED 02 September 2022

CITATION
Chen B-Q, Pan Y-J, Zhang D-G, Xia H-Y and Kankala RK (2022), Phase-change materials-based platforms for biomedicine.
Front. Bioeng. Biotechnol. 10:989953.
doi: 10.3389/fbioe.2022.989953

Phase-change materials-based platforms for biomedicine

Biao-Qi Chen[1,2], Yu-Jing Pan[1], Da-Gui Zhang[1], Hong-Ying Xia[1] and Ranjith Kumar Kankala[1,2]*

[1]Institute of Biomaterials and Tissue Engineering, Huaqiao University, Xiamen, China, [2]Fujian Provincial Key Laboratory of Biochemical Technology (Huaqiao University), Xiamen, China

Recently, phase-change materials (PCMs) have gathered enormous attention in diverse fields of medicine, particularly in bioimaging, therapeutic delivery, and tissue engineering. Due to the excellent physicochemical characteristics and morphological characteristics of PCMs, several developments have been demonstrated in the construction of diverse PCMs-based architectures toward providing new burgeoning opportunities in developing innovative technologies and improving the therapeutic benefits of the existing formulations. However, the fabrication of PCM-based materials into colloidally stable particles remains challenging due to their natural hydrophobicity and high crystallinity. This review systematically emphasizes various PCMs-based platforms, such as traditional PCMs (liposomes) and their nanoarchitectured composites, including PCMs as core, shell, and gatekeeper, highlighting the pros and cons of these architectures for delivering bioactives, imaging anatomical features, and engineering tissues. Finally, we summarize the article with an exciting outlook, discussing the current challenges and future prospects for PCM-based platforms as biomaterials.

KEYWORDS

gatekeeper, temperature-controlled release, liposomes, core-shell architectures, phase-change materials

Introduction

In recent times, tremendous advancements have resulted in the development of various advanced nanotechnology-based approaches for targeted delivery to diseased areas precisely with improved biodistribution and appropriate excretion profiles (Fan et al., 2017; Ramasamy et al., 2017). Although the impressive progress in pharmaceutics and materials science has resulted in the diverse nanocarriers with altered sizes and surface properties, the exploration of stimuli-responsive materials has garnered enormous attention, featuring reversible response to a specific stimulus, gating ability to avoid undesired release, highly conducive to load multiple drug payloads, and biodegradability, as well as biocompatibility (Mura et al., 2013). To satisfy these requirements and their subsequent translation, several efforts have been dedicated to using polymeric materials that respond to specific stimuli (receptors, biomarkers, and microenvironments) to formulate smart nanocarriers for precise therapy of the disease (Chen et al., 2018). Nonetheless, several attributes of multi-step preparation and low degradability-induced

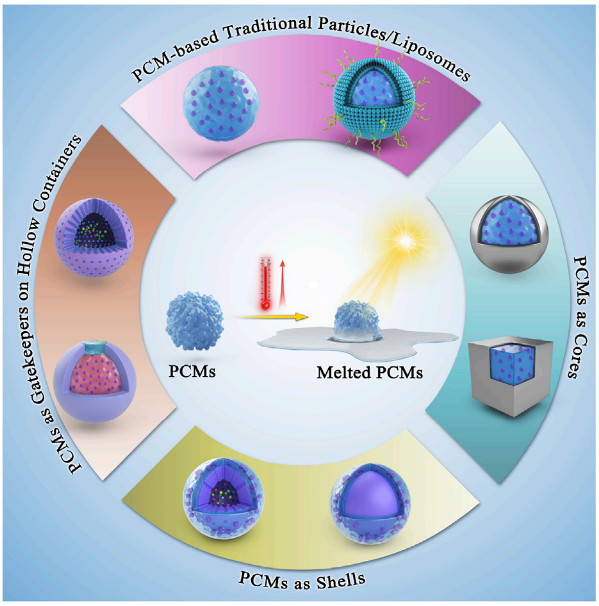

FIGURE 1
Schematic illustrating the conceptual design of various PCMs, in terms of positioning the PCMs and their successive nanoconjugates for biomedicine.

toxicity risks due to chemical modifications may hinder their applicability, limiting the subsequent translation to clinics.

Phase-change materials (PCMs) with unique transition ability between solid and liquid states due to enormous latent fusion heat, have gained particular interest in thermal energy storage and solar energy applications (Dai et al., 2019; Ma et al., 2021). Among various phase transitions (i.e., solid-to-solid, solid-to-liquid, and liquid-to-gas), the solid-to-liquid changeover is often employed due to multiple features of the low transition temperature and high latent energy, as well as excellent thermal conductivity (Sun et al., 2019). These smart matrices encapsulate high drug payloads inside solid PCM and swiftly release them in response to a temperature upon transition from the solid-to-liquid phase (Fu et al., 2021). The classic examples include various thermo-responsive materials, such as natural fatty acids (lauric acid, LA, and stearic acid, SA) or fatty alcohols (1-tetradecanol), as well as their eutectic mixtures due to excellent biocompatibility/biodegradability, suitable melting point, chemical stability, and cost-effectiveness (Zhu et al., 2017a; Qiu et al., 2020). Due to their stable melting points of >37°C and satisfactory release rates, PCMs can be applied as biomaterials for promising therapeutic applications. Typically, photothermal conversion agents (PTCAs) and payloads are co-encapsulated in PCMs-based platforms to trigger light-assisted melting. Upon light irradiation, the platforms would be quickly heated up due to the photothermal effect of the encapsulated PTCAs (Liu Z. et al., 2020; Otaegui et al., 2020). Notably, if the local temperature is increased beyond the melting point, the platforms would melt, leading to the quick and on-demand release of the encapsulated payloads. Although several reviews have been published discussing the PCMs-based platform for biomedicine, the position of PCM in the drug delivery field has received tremendous attention recently. Therefore, a timely review of relevant research progress is of great significance for the continuous development of PCMs-based platforms. From a unique perspective of the PCMs-based platform architecture, in this mini-review, we systematically emphasize various platforms, such as traditional PCMs (liposomes) and their nanoarchitectured composites as thermo-responsive materials, including PCMs as core, shell, and gatekeeper, highlighting the pros and cons of these architectures for delivering bioactives, imaging anatomical features, and engineering tissues (Figure 1). Finally, we summarize the article with an exciting outlook, discussing the current challenges and future opportunities for PCM-based platforms as biomaterials.

Phase-change materials-based platforms

Phase-change materials-based traditional particles/liposomes

Among the classic examples of PCMs, natural fatty acids have gained enormous interest in the generation of traditional PCMs-based particles/liposomes due to their diversity, biocompatibility, biodegradability, abundance, and cost-effectiveness (Cao et al., 2021). For instance, capric acid (CA) and octadecane (OD) are lipophilic PCMs with melting points of 31 and 28°C, respectively, leading to phase change at body temperature and resulting in the leaching of their encapsulated guests. In an attempt to successfully deliver exogenous nitric oxide (NO) donors and address the short half-life of NO, injectable microfluidics-assisted microparticle (MP) systems were fabricated using the PCMs, CA, and OD. These PCM-based MPs as micellar depots successfully encapsulated NONOate, actively trapping and protecting the NO bubbles that are generated *in situ* (Figure 2A) (Lin et al., 2018). These PCMs could prevent the access of hemoglobin to NO bubbles and prolong half-life, resulting in sustained therapeutic function and retreating osteoporosis. In another case, a temperature-regulated system for the controlled release of nerve growth factor (NGF) to promote neurite outgrowth was reported (Xue et al., 2018). The system was based upon microparticles fabricated using a co-axial electrospray approach, with the outer solution containing PCMs (a mixture of LA and SA at a mass ratio of 4:1) and the inner solution encompassing NGF and a near-infrared (NIR) dye, indocyanine green (ICG). The controlled release system was evaluated for potential use in neural tissue engineering by

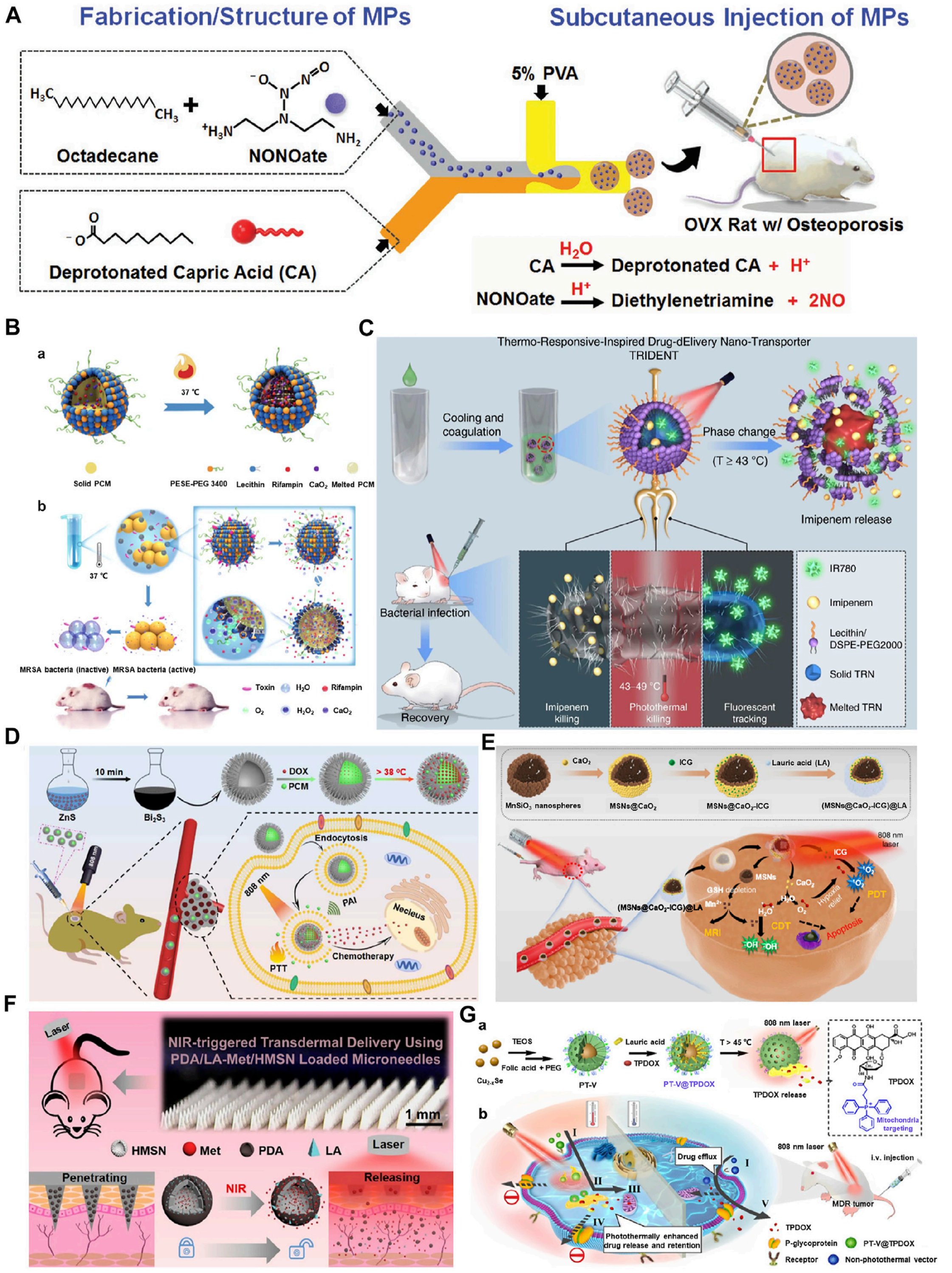

FIGURE 2
(A) Fabrication/structure of injectable microparticles (MPs). The MPs system is developed using a microfluidic device in an oil-in-water (O/W) single emulsion that consists of phase-change materials capric acid and octadecane and encapsulates NONOate. Reproduced with permission from Ref. (Lin et al., 2018). Copyright 2018, John Wiley and Sons. **(B)** Design and characterization of PCM-based liposome nanoreactors. (a) The solid PCM was dissolved in melted PCM at 37°C. (b) The scheme of endogenous stimulus-powered antibiotic release from RFP-CaO_2@PCM@Lec nanoreactors for bacterial infection combination therapy. Reproduced with permission from Ref. (Wu et al., 2019). Copyright 2019, Springer Nature. **(C)** Near infrared-activated nano-transporter (TRIDENT, also named IMP/IR780@TRN) for antibiotic-resistant bacteria killing. The prepared thermo-

(Continued)

FIGURE 2
responsive-inspired drug-delivery nano-transporter is "melted" when the temperature rises above 43°C under the NIR irradiation, leading to the release of imipenem to the infected site. Reproduced with permission from Ref. (Qing et al., 2019). Copyright 2019, Springer Nature. **(D)** Schematic illustration of thermosensitive urchin-like Bi_2S_3 hollow microsphere as a carrier of DOX/PCM for photoacoustic imaging and photothermal-chemo therapy of tumors. Reproduced with permission from Ref. (Zhang C. et al., 2020). Copyright 2020, Elsevier. **(E)** The scheme of the fabrication process and therapeutic mechanism of thermo-responsive (MSNs@CaO_2-ICG)@LA NPs for synergistic CDT/PDT with H_2O_2/O_2 self-supply and GSH depletion. Reproduced with permission from Ref. (Liu C. et al., 2020). Copyright 2020, Springer Nature. **(F)** Schematics for preparation of metformin-loaded and PDA/LA-coated hollow mesoporous SiO_2 nanocomposites and NIR-responsive release of loaded metformin on diabetic rats by the transdermal delivery method. Reproduced with permission from Ref. (Zhang et al., 2018). Copyright 2018, American Chemical Society. **(G)** Schematic illustration of (a) preparation of PT-V@TPDOX and (b) photothermally enhanced drug release and retention towards multidrug resistance cancer cells. I. Receptor-mediated endocytosis. II. Photothermally controlled drug release. III. Mitochondria targeting of TPDOX. IV. Inhibition of P-glycoprotein (P-gp) pathway. V. P-gp mediated drug efflux of TPDOX delivered by non-photothermal vector. Reproduced with permission from Ref. (Ji et al., 2021). Copyright 2020, Elsevier.

sandwiching the microparticles between two layers of electrospun fibers to form a trilayer construct. Upon photothermal heating with a NIR laser, the NGF could be released on demand with well-preserved bioactivity to promote neurite outgrowth. This facile and versatile system could be readily applied to various biomedical applications by switching to different combinations of PCM, biological effector, and scaffolding material (Xue et al., 2020). Notably, the sensing temperature at the subcellular level is of great importance for understanding various biological processes. Recently, a novel organic fluorescent nanothermometer based on aggregation-induced emission (AIE) molecules and natural-derived PCMs was designed, and its application in non-invasive temperature sensing was explored (Xue et al., 2021a). First, a dual-responsive organic luminogen that could respond to the molecular state of aggregation and the environmental polarity was synthesized. Next, the natural saturated fatty acids with sharp melting points, and reversible, as well as rapid phase transitions were employed as the encapsulation matrix to correlate external heat information with the fluorescence properties of the luminogen. To apply the composite materials for biological application, colloidally dispersed nanoparticles were formulated by a technique based on *in situ* surface polymerization and nanoprecipitation. As anticipated, the resultant zwitterionic nanothermometer exhibited sensitive, reversible, reliable, and multiparametric responses to temperature variation within a narrow range around the physiological temperature (i.e., 37°C). Taking spectral position, fluorescence intensity, and fluorescence lifetime as the correlation parameters, the maximum relative thermal sensitivities were determined to be 2.15, 17.06, and 17.72%$^\circ C^{-1}$, respectively, which were much higher than most fluorescent nanothermometers.

Despite the successful encapsulation of the cargo, the particles made of fatty acids suffer from poor aqueous dispersibility, resulting in surface aggregation, which could be considerably addressed by adding amphiphilic molecules, such as phospholipids (Xue et al., 2021b). For instance, calcium peroxide (CaO_2) and antibiotics were encapsulated in a eutectic mixture of fatty acids (4:1, SA, m. p. = 71.8–72.3 °C, and LA, m. p. = 45.7–46.2 °C) and coated with liposome (lecithin and DSPE-PEG3400) against bacterial infections. The release could happen sequentially in a series of steps, in which after bacteria contact the nanoreactors at 37 °C, anchored on the nanoreactor's surface, form pores in the layer, entry of H_2O molecules into the nanoreactors, resulting in the decomposition of formed H_2O_2 and driving antibiotic release (Figure 2B) (Wu et al., 2019). Similarly, versatile architectures referred to as TRIDENT (Thermo-Responsive-Inspired Drug-Delivery Nano-Transporter)-based on PCM using SA and LA were fabricated to address the synergistic effects of fluorescence monitoring and chemo-photothermal-based antimicrobial effectiveness against multidrug-resistant (MDR) bacteria. These hydrophobic TRIDENT PCMs encapsulated with a broad-spectrum antibiotic (imipenem, IMP) and IR780 and subsequently coated with lecithin and DSPE-PEG 2000 not only resulted in the NIR-assisted melting of the nanotransporter but also damaged the membrane facilitating the permeation, as well as interfering in the cell wall biosynthesis and enable bacterial death (Figure 2C) (Qing et al., 2019). In this regard, several PCMs-based on LA and SA, as well as oleic acid, were fabricated for nanotheranostics with the ability of hyperthermia-triggered spatiotemporally tunable drug release (Cai et al., 2021; Lai et al., 2022).

Phase-change materials as cores

Despite the success, the PCMs sometimes may suffer from undesired degradation due to hypersensitivity, resulting in the unwanted leakage of encapsulated therapeutic cargo *in vivo*. To avoid the pre-degradation of fatty acid and subsequent pre-leakage of payload, PCMs and drugs were encapsulated in the micro-/nano-scale carriers as core substances (Zhang et al., 2022). These PCM cores facilitate the protection of therapeutic agents and execute their versatility in the appropriate circumstances. In a case, a eutectic fatty acid mixture of LA and SA with a melting temperature of 39°C and coloaded with doxorubicin (DOX) and ICG was encapsulated in silica-based nanocapsules using the site-selective deposition by templating with Au–PS Janus colloidal particles (Qiu et al., 2019). In another instance, Au nanocages (AuNCs) were encapsulated with the PCM (1-tetradecanol) and either hydrophobic or hydrophilic therapeutics, in which the PCM served as an inner gatekeeper to spatially control the NIR-triggered release in response to raising in temperature beyond the melting point (Moon et al., 2011).

Sonodynamic therapy (SDT), a non-invasive therapeutic strategy, offers enormous potential in treating solid tumors due to its high penetration depth (Bai et al., 2021). Nevertheless, the efficacy is limited due to hypoxia in solid tumors. In an attempt to address this issue, ultrasound-activated nanosystems based on the biodegradable hollow mesoporous organosilica nanoplatforms were developed by encapsulating ferrate (VI) and protoporphyrin IX, followed by PCM, LA deposition (Fu et al., 2019). The hydrogen peroxide and glutathione (GSH)-dependant oxygen production by ferrate (VI) species and subsequent ROS production by protoporphyrin-augmented SDT and intracellular Fenton chemistry, as well as ultrasound-assisted mild hyperthermia leading to phase change of LA, played a synergetic role in SDT-sensitized effects against solid hypoxic tumors. The low melting point of LA (44–46°C) endowed the temperature-sensitive control by the nanosystems over the diffusion of water and release of oxygen. In another instance, Bi_2S_3 hollow urchin-like nanostructures co-loaded with DOX and 1-tetradecanol with a melting point around 38 °C in the hollow cores for photoacoustic imaging and chemo-/photothermal therapy of tumors (Zhang C. et al., 2020). These composites facilitated the conversion of 808 nm NIR-assisted irradiation to heat energy, resulting in the triggered DOX release from the hollow containers after reaching the PCM melting point (Figure 2D). The tumor ablation efficiency, along with photoacoustic imaging and combined therapies, were systematically demonstrated *in vitro* and *in vivo*. Similarly, anticancer drugs and 1-tetradecanol were filled into the hollow magnetic nanoparticles for imaging-guided thermo-chemo combination cancer therapy. The system demonstrated a sensitive thermal response to the alternating current magnetic field for triggering switchable controlled drug delivery with a nearly “zero release” feature. More importantly, the system displays infrared thermal and magnetic resonance imaging properties for the image-guided cancer therapy (Li et al., 2015).

Phase-change materials as shells

Considering the stability of the encapsulated therapeutics in a physiological environment, these PCMs can be employed to coat over highly sensitive molecules as shells. These PCM-based shells not only facilitate the protection of the encapsulated cargo but also enable their precise release through a thermo-responsive manner (Zhang S. C. et al., 2020). In a case, manganese silicate nanospheres (MSNs) supported by calcium peroxide (CaO_2) and ICG were coated with the LA (MSNs@CaO_2-ICG)@LA) for photodynamic (PDT)/chemodynamic (CDT) synergistic cancer therapy (Figure 2E) (Liu C. et al., 2020). The biocompatible and biodegradable LA with a melting point of 44–46°C on the surface was melted due to the NIR-assisted photothermal effect of ICG, in which the exposed CaO_2 would react with water, generating H_2O_2 and O_2, as well as accompanying the exposure of MSNs towards Fenton-like agent Mn^{2+} for H_2O_2-supplementing CDT and MRI-guided synergistic therapy. In an attempt to explore gas therapy with negligible side effects, Zhu and colleagues developed a new type of multi-shell nanoparticles (CuS@SiO_2-l-Arg@PCM-Ce6, CSLPC), in which the PCM wax-sealed profile of the encapsulated Ce6 would be released with the NIR-II-assisted, CuS-triggered photothermal effect in the tumor site (Zhu et al., 2021). In addition, the released l-Arg was oxidized to generate NO for gas therapy, resulting in the synergistic targeted tumor therapy. Similarly, multifunctional nanosystems based on hollow mesoporous organosilica nanoparticles (HMONs) deposited with CuS were generated for the dual stimuli-responsive drug delivery (Chen et al., 2020). These composites coated with 1-tetradecanol substantially facilitated the avoidance of drug leakage and improved CuS-based NIR-assisted temperature-controlled release of encapsulated DOX cargo for chemo- and photothermal therapy. In another similar instance, hollow mesoporous SiO_2 nanoparticles (HMSNs) were coated with PCM (polydopamine (PDA) as photothermal conversion agent/LA, mp ≈ 44–46°C) for the successful delivery of metformin through the NIR-responsive poly (vinylpyrrolidone) microneedle (MN) system (Figure 2F) (Zhang et al., 2018). These MNs for transdermal delivery facilitated the triggering effects of PCM by NIR-responsiveness after being inserted in the skin, leading to the release of the encapsulated cargo from MNs.

Phase-change materials as gatekeepers on hollow containers

Similar to enclosing various therapeutics in the PCM as shells to protect them from pre-leakage, the PCMs can be specifically utilized as gatekeepers on the pores of various inorganic porous architectures. These PCM-based gatekeepers facilitate the protection of enclosed therapeutic cargo and enable their precise release in a specific environment (Hussain and Guo, 2019; Li et al., 2021). It should be noted that the precise selection of PCM depends on the application and the environment that could precisely transform the PCM. Although DOX is the most preferred anticancer molecule in clinics, it is often suffered from MDR efflux, hindering its performance efficacy. In an attempt to address these aspects, TPDOX is encapsulated in the pores of mesoporous silica, please see (Figure 2G). The porous silica was filled with LA (melting point is 45 °C) along with TPDOX in the form of small-sized particles with an average diameter of 40 nm. The NIR (808 nm) laser-assisted melting of LA facilitated the release of TPDOX, significantly inhibiting drug efflux and enabling antitumor therapy (Ji et al., 2021). In another case, You and group fabricated a 1-tetradecanol-based ICG-loaded CuS@mSiO$_2$ nanoplatform (CuS@mSiO$_2$-TD/ICG) (You et al., 2017). The NIR (808 nm)-absorbing ICG in mesopores facilitated the melting of PCM (1-tetradecanol) gatekeepers, resulting in the CuS@mSiO$_2$-assisted PTT and simultaneously ICG-based PDT/PTT effects. The PCM, 1-tetradecanol, offers a reversible change in its physical states at a narrow temperature range, in which it exists as solid in the body temperature but melts at just above it (Tm = 39°C). These observations showcase that the porous cavities are opened rapidly above the body temperature after exposure to the heating source.

In most instances, the PCMs are often based on fatty acids or fatty alcohols, in which the encapsulated drug can be released by substantially melting the PCM by raising the temperature beyond its melting point (Zhu et al., 2017b). However, the release is substantially dependent on the encapsulated PCM species, which could be limited to specific cargo. The precise control over the release kinetics can be altered by regulating the melting point of PCMs, which can be achieved by the composition of different PCM species with a mixture of 1-tetradecanol (at 38°C) and LA (at 44°C) at different ratios (Hyun et al., 2013).

Conclusions and perspectives

In summary, this article has reviewed the recent advances in the development of PCM-based platforms for biomedical applications. Due to their specific physicochemical attributes, these PCMs and their composites (cores, shells, and gatekeepers) have shown excellent prospects in diverse biomedical applications. Despite the success in exploring the characteristics, some unwanted characteristics of PCMs during the phase transition must be altered, for instance, undercooling, volume expansion, low thermal conductivity, and phase separation. In addition, various necessities must be comprehensively considered to meet the application requirements for expanding the scope of PCMs for biomedical applications. Several application principles are required to be addressed according to the application requirements, such as appropriate phase transition temperature and latent heat, suitable chemical stability during the phase change, biosafety, and ease of synthesis using cost-effective precursors, as well as eco-friendly techniques.

Despite the enormous progress, several key features are required to be strictly optimized for their clinical translation. 1) The foremost requirement is the morphological attributes concerning the particle size and pore diameters in the case of mesoporous architectures, as well as shell thickness in the core-shell structures. It should be noted that these morphological features influence the thermal characteristics of PCMs. 2) Efforts to alter the PCM surfaces and regulate the mesoporous characteristics are required further to improve the translation of the PCMs. 3) Similarly, the temperature changes and their effect, along with the mechanistic views, are yet to be resolved. Although several studies have explored the temperature-related PCM conversion and their subsequent synergistic effects on cancer therapy, it is required to investigate the related viewpoints in various other ailments. 4) The biosafety of these PCMs and their composites must be necessary to explore comprehensively, right from the *in vitro* to *in vivo* assessments.

Among the aforementioned challenging tasks, the predominant efficacy-related issue is that realizing the phase transition of PCM materials in deep human tissues remains further studied due to the limited tissue penetration depth of light. To a considerable extent, using ultrasound, X-rays, or magnetic fields to stimulate heat production may help solve these problems. In recent years, catalyzing or *in situ* generations of active substances at the lesion site for treating diseases is an important research direction for precision therapy. Applying PCMs to coat catalysts or substrates, release them quickly after reaching the lesion site, and initiate relevant chemical reactions to treat diseases may be an important research direction for PCMs in the future. In summary, the current review explored the detailed insights of the relevant communities working on PCMs and their composites, which could be applied to biomedical applications.

Author contributions

B-QC and RK conceived the idea. B-QC, Y-JP, D-GZ, and H-YX, wrote the initial draft and supported it in figure illustrations. B-QC and RK supervised the work and fund acquisition. RK revised the article with some meticulous discussions.

Funding

Financial support from the National Key Research Development Program of China (2019YFE0113600), National Natural Science Foundation of China (NSFC, 81971734, and 32071323), the Program for Innovative Research Team in Science and Technology in Fujian

Province University and the Scientific Research Funds of Huaqiao University (20BS104).

Conflict of interest

The authors declare that the research was conducted in the absence of any commercial or financial relationships that could be construed as a potential conflict of interest.

Publisher's note

References

Bai, S., Lu, Z., Jiang, Y., Shi, X., Xu, D., Shi, Y., et al. (2021). Nanotransferrin-based programmable catalysis mediates three-pronged induction of oxidative stress to enhance cancer immunotherapy. *ACS Nano* 16, 997–1012. doi:10.1021/acsnano.1c08619

Cai, B., Hou, M., Zhang, S., Xin, Z., Huang, J., Yang, J., et al. (2021). Dual targeting of endoplasmic reticulum by redox-deubiquitination regulation for cancer therapy. *Int. J. Nanomed.* 16, 5193–5209. doi:10.2147/ijn.s321612

Cao, C., Yang, N., Dai, H., Huang, H., Song, X., Zhang, Q., et al. (2021). Recent advances in phase change material based nanoplatforms for cancer therapy. *Nanoscale Adv.* 3, 106–122. doi:10.1039/d0na00622j

Chen, H., Gu, Z., An, H., Chen, C., Chen, J., Cui, R., et al. (2018). Precise nanomedicine for intelligent therapy of cancer. *Sci. China Chem.* 61, 1503–1552. doi:10.1007/s11426-018-9397-5

Chen, J., Wang, Y., Ma, B., Guan, L., Tian, Z., Lin, K., et al. (2020). Biodegradable hollow mesoporous organosilica-based nanosystems with dual stimuli-responsive drug delivery for efficient tumor inhibition by synergistic chemo- and photothermal therapy. *Appl. Mater. Today* 19, 100655. doi:10.1016/j.apmt.2020.100655

Dai, Y. N., Su, J. Z., Wu, K., Ma, W. K., Wang, B., Li, M. X., et al. (2019). Multifunctional thermosensitive liposomes based on natural phase-change material: near-infrared light-triggered drug release and multimodal imaging-guided cancer combination therapy. *ACS Appl. Mater. Interfaces* 11, 10540–10553. doi:10.1021/acsami.8b22748

Fan, W. P., Yung, B., Huang, P., and Chen, X. Y. (2017). Nanotechnology for multimodal synergistic cancer therapy. *Chem. Rev.* 117, 13566–13638. doi:10.1021/acs.chemrev.7b00258

Fu, J., Li, T., Zhu, Y., and Hao, Y. (2019). Ultrasound-activated oxygen and ROS generation nanosystem systematically modulates tumor microenvironment and sensitizes sonodynamic therapy for hypoxic solid tumors. *Adv. Funct. Mater.* 29, 1906195. doi:10.1002/adfm.201906195

Fu, J., Li, T., Yang, Y., Jiang, L., Wang, W., Fu, L., et al. (2021). Activatable nanomedicine for overcoming hypoxia-induced resistance to chemotherapy and inhibiting tumor growth by inducing collaborative apoptosis and ferroptosis in solid tumors. *Biomaterials* 268, 120537. doi:10.1016/j.biomaterials.2020.120537

Hussain, A., and Guo, S. R. (2019). NIR-triggered release of DOX from sophorolipid-coated mesoporous carbon nanoparticles with the phase-change material 1-tetradecanol to treat MCF-7/ADR cells. *J. Mater. Chem. B* 7, 974–985. doi:10.1039/c8tb02673d

Hyun, D. C., Lu, P., Choi, S.-I., Jeong, U., and Xia, Y. (2013). Microscale polymer bottles corked with a phase-change material for temperature-controlled release. *Angew. Chem. Int. Ed. Engl.* 52, 10662–10665. doi:10.1002/ange.201305006

Ji, C., Cheng, W., Hu, Y., Liu, Y., Liu, F., and Yin, M. (2021). A nano vector with photothermally enhanced drug release and retention to overcome cancer multidrug resistance. *Nano Today* 36, 101020. doi:10.1016/j.nantod.2020.101020

Lai, Y., Dang, Y., Li, F., Ding, C., Yu, H., Zhang, W., et al. (2022). Reactive glycolysis metabolite-activatable nanotheranostics for NIR-II fluorescence imaging-guided phototherapy of cancer. *Adv. Funct. Mater.* 32, 2200016. doi:10.1002/adfm.202200016

Li, J., Hu, Y., Hou, Y., Shen, X., Xu, G., Dai, L., et al. (2015). Phase-change material filled hollow magnetic nanoparticles for cancer therapy and dual modal bioimaging. *Nanoscale* 7, 9004–9012. doi:10.1039/c5nr01744k

Li, M., Gao, X., Lin, C., Shen, A., Luo, J., Ji, Q., et al. (2021). An intelligent responsive macrophage cell membrane-camouflaged mesoporous silicon nanorod drug delivery system for precise targeted therapy of tumors. *J. Nanobiotechnol.* 19, 336. doi:10.1186/s12951-021-01082-1

Lin, Y. J., Chen, C. C., Chi, N. W., Nguyen, T., Lu, H. Y., Nguyen, D., et al. (2018). *In situ* self-assembling micellar depots that can actively trap and passively release NO with long-lasting activity to reverse osteoporosis. *Adv. Mater.* 30, e1705605. doi:10.1002/adma.201705605

Liu, C., Cao, Y., Cheng, Y., Wang, D., Xu, T., Su, L., et al. (2020). An open source and reduce expenditure ROS generation strategy for chemodynamic/photodynamic synergistic therapy. *Nat. Commun.* 11, 1735. doi:10.1038/s41467-020-15591-4

Liu, Z., Wan, P., Liu, Z., Yang, M., Li, S., Wang, Y., et al. (2020). Photothermal generation of oxygen-irrelevant free radicals with simultaneous suppression of glutathione synthesis for an enhanced photonic thermodynamic cancer therapy. *Acs Biomater. Sci. Eng.* 6, 6186–6194. doi:10.1021/acsbiomaterials.0c00889

Ma, K., Zhang, X., Ji, J., Han, L., Ding, X., and Xie, W. (2021). Application and research progress of phase change materials in biomedical field. *Biomater. Sci.* 9, 5762–5780. doi:10.1039/d1bm00719j

Moon, G. D., Choi, S. W., Cai, X., Li, W., Cho, E. C., Jeong, U., et al. (2011). A new theranostic system based on gold nanocages and phase-change materials with unique features for photoacoustic imaging and controlled release. *J. Am. Chem. Soc.* 133, 4762–4765. doi:10.1021/ja200894u

Mura, S., Nicolas, J., and Couvreur, P. (2013). Stimuli-responsive nanocarriers for drug delivery. *Nat. Mater.* 12, 991–1003. doi:10.1038/nmat3776

Otaegui, J. R., Rubirola, P., Ruiz-Molina, D., Hernando, J., and Roscini, C. (2020). Solid materials with near-infrared-induced fluorescence modulation. *Adv. Opt. Mater.* 8, 2001063. doi:10.1002/adom.202001063

Qing, G. C., Zhao, X. X., Gong, N. Q., Chen, J., Li, X. L., Gan, Y. L., et al. (2019). Thermo-responsive triple-function nanotransporter for efficient chemo-photothermal therapy of multidrug-resistant bacterial infection. *Nat. Commun.* 10, 4336. doi:10.1038/s41467-019-12313-3

Qiu, J., Huo, D., Xue, J., Zhu, G., Liu, H., and Xia, Y. (2019). Encapsulation of a phase-change material in nanocapsules with a well-defined hole in the wall for the controlled release of drugs. *Angew. Chem. Int. Ed. Engl.* 58, 10716–10721. doi:10.1002/ange.201904549

Qiu, J., Huo, D., and Xia, Y. (2020). Phase-change materials for controlled release and related applications. *Adv. Mater.* 32, e2000660. doi:10.1002/adma.202000660

Ramasamy, T., Ruttala, H. B., Gupta, B., Poudel, B. K., Choi, H. G., Yong, C. S., et al. (2017). Smart chemistry-based nanosized drug delivery systems for systemic applications: A comprehensive review. *J. Control. Release* 258, 226–253. doi:10.1016/j.jconrel.2017.04.043

Sun, Q., He, F., Bi, H., Wang, Z., Sun, C., Li, C., et al. (2019). An intelligent nanoplatform for simultaneously controlled chemo-photothermal, and photodynamic therapies mediated by a single NIR light. *Chem. Eng. J.* 362, 679–691. doi:10.1016/j.cej.2019.01.095

Wu, Y., Song, Z., Wang, H., and Han, H. (2019). Endogenous stimulus-powered antibiotic release from nanoreactors for a combination therapy of bacterial infections. *Nat. Commun.* 10, 4464. doi:10.1038/s41467-019-12233-2

Xue, J., Zhu, C., Li, J., Li, H., and Xia, Y. (2018). Integration of phase-change materials with electrospun fibers for promoting neurite outgrowth under controlled release. *Adv. Funct. Mater.* 28, 201705563. doi:10.1002/adfm.201705563

Xue, J., Wu, T., Qiu, J., and Xia, Y. (2020). Spatiotemporally controlling the release of biological effectors enhances their effects on cell migration and neurite outgrowth. *Small Methods* 4, 202000125. doi:10.1002/smtd.202000125

Xue, K., Wang, C., Wang, J., Lv, S., Hao, B., Zhu, C., et al. (2021a). A sensitive and reliable organic fluorescent nanothermometer for noninvasive temperature sensing. *J. Am. Chem. Soc.* 143, 14147–14157. doi:10.1021/jacs.1c04597

Xue, K., Lv, S., and Zhu, C. (2021b). Bringing naturally-occurring saturated fatty acids into biomedical research. *J. Mater. Chem. B* 9, 6973–6987. doi:10.1039/d1tb00843a

You, Q., Sun, Q., Wang, J., Tan, X., Pang, X., Liu, L., et al. (2017). A single-light triggered and dual-imaging guided multifunctional platform for combined photothermal and photodynamic therapy based on TD-controlled and ICG-loaded CuS@mSiO$_2$. *Nanoscale* 9, 3784–3796. doi:10.1039/c6nr09042g

Zhang, C., Li, D., Pei, P., Wang, W., Chen, B., Chu, Z., et al. (2020). Rod-based urchin-like hollow microspheres of Bi$_2$S$_3$: Facile synthesis, photo-controlled drug release for photoacoustic imaging and chemo-photothermal therapy of tumor ablation. *Biomaterials* 237, 119835. doi:10.1016/j.biomaterials.2020.119835

Zhang, Y., Jiang, G., Hong, W., Gao, M., Xu, B., Zhu, J., et al. (2018). Polymeric microneedles integrated with metformin-loaded and PDA/LA-Coated hollow mesoporous SiO$_2$ for NIR-triggered transdermal delivery on diabetic rats. *ACS Appl. Bio Mater.* 1, 1906–1917. doi:10.1021/acsabm.8b00470

Zhang, S. Q., Ye, J. W., Liu, X., Wang, G. Y., Qi, Y., Wang, T. L., et al. (2022). Dual stimuli-responsive smart fibrous membranes for efficient photothermal/photodynamic/chemo-therapy of drug-resistant bacterial infection. *Chem. Eng. J.* 432, 134351. doi:10.1016/j.cej.2021.134351

Zhang, S. C., Cao, C. Y., Lv, X. Y., Dai, H. M., Zhong, Z. H., Liang, C., et al. (2020). A H$_2$O$_2$ self-sufficient nanoplatform with domino effects for thermal-responsive enhanced chemodynamic therapy. *Chem. Sci.* 11, 1926–1934. doi:10.1039/c9sc05506a

Zhu, C., Huo, D., Chen, Q., Xue, J., Shen, S., and Xia, Y. (2017a). A eutectic mixture of natural fatty acids can serve as the gating material for near-infrared-triggered drug release. *Adv. Mater.* 29, 1703702. doi:10.1002/adma.201703702

Zhu, C., Pradhan, P., Huo, D., Xue, J., Shen, S., Roy, K., et al. (2017b). Reconstitution of low-density lipoproteins with fatty acids for the targeted delivery of drugs into cancer cells. *Angew. Chem. Int. Ed. Engl.* 56, 10535–10538. doi:10.1002/ange.201704674

Zhu, J., Wang, W., Wang, X., Zhong, L., Song, X., Wang, W., et al. (2021). Multishell nanoparticles with "linkage mechanism" for thermal responsive photodynamic and gas synergistic therapy. *Adv. Healthc. Mater.* 10, e2002038. doi:10.1002/adhm.202002038

frontiers | Frontiers in Bioengineering and Biotechnology

TYPE Systematic Review
PUBLISHED 26 September 2022
DOI 10.3389/fbioe.2022.986112

Effectiveness of biomolecule-based bioactive surfaces, on os-seointegration of titanium dental implants: A systematic review and meta-analysis of *in vivo* studies

Nansi López-Valverde[1†], Javier Aragoneses[1†], Antonio López-Valverde[2,3*], Norberto Quispe-López[2], Cinthia Rodríguez[3] and Juan Manuel Aragoneses[4]

[1]Department of Medicine and Medical Specialties, Faculty of Health Sciences, Universidad Alcalá de Henares, Madrid, Spain, [2]Department of Surgery, Instituto de Investigación Biomédica de Salamanca (IBSAL), University of Salamanca, Salamanca, Spain, [3]Department of Dentistry, Universidad Federico Henríquez y Carvajal, Santo Domingo, Dominican Republic, [4]Faculty of Dentistry, Universidad Alfonso X El Sabio, Madrid, Spain

Titanium and alloy osseointegrated implants are used to replace missing teeth; however, some fail and are removed. Modifications of the implant surface with biologically active substances have been proposed. MEDLINE [via Pubmed], Embase and Web of Science were searched with the terms “titanium dental implants”, “surface properties”, “bioactive surface modifications”, “biomolecules”, “BMP”, “antibacterial agent”, “peptide”, “collagen”, “grown factor”, “osseointegration”, “bone apposition”, “osteogenic”, “osteogenesis”, “new bone formation”, “bone to implant contact”, “bone regeneration” and “*in vivo* studies”, until May 2022. A total of 10,697 references were iden-tified and 26 were included to analyze 1,109 implants, with follow-ups from 2 to 84 weeks. The ARRIVE guidelines and the SYRCLE tool were used to evaluate the methodology and scientific evidence. A meta-analysis was performed (RevMan 2020 software, Cochane Collaboration) with random effects that evaluated BIC at 4 weeks, with subgroups for the different coatings. The heterogeneity of the pooled studies was very high (95% CI, I2 = 99%). The subgroup of BMPs was the most favorable to coating. Surface modification of Ti implants by organic bioactive molecules seems to favor osseointegration in the early stages of healing, but long-term studies are necessary to corroborate the results of the experimental studies.

KEYWORDS

titanium dental implants, bioactive surface modifications, biomolecules, peptides, bone morphogenetic protein, grown factor, components of the extracellular matrix, osteointegration

Check for updates

OPEN ACCESS

EDITED BY
Min Jiang,
Nanjing Tech University, China

REVIEWED BY
Miguel Ángel Garcés-Villalá,
Catholic University San Antonio of Murcia, Spain
Paolo Canepa,
University of Genoa, Italy

*CORRESPONDENCE
Antonio López-Valverde,
alopezvalverde@usal.es

[†]These authors have contributed equally to this work

SPECIALTY SECTION
This article was submitted to Biomaterials,
a section of the journal
Frontiers in Bioengineering and Biotechnology

RECEIVED 04 July 2022
ACCEPTED 12 September 2022
PUBLISHED 26 September 2022

CITATION
López-Valverde N, Aragoneses J, López-Valverde A, Quispe-López N, Rodríguez C and Aragoneses JM (2022), Effectiveness of biomolecule-based bioactive surfaces, on os-seointegration of titanium dental implants: A systematic review and meta-analysis of in vivo studies.
Front. Bioeng. Biotechnol. 10:986112.
doi: 10.3389/fbioe.2022.986112

1 Introduction

Since the introduction of dental implants by Brånemark in the 1960s, titanium (Ti) and some Ti alloys (Ti6Al4V) have been used in edentulous patients to replace missing teeth (Osman and Swain, 2015), their long-term success depending mainly on their osseointegration. However, despite the high success rates recorded, some of them have to be removed due to failure (Moraschini et al., 2015; Alghamdi and Jansen, 2020).

Recently, the attention of researchers has been focused on chemical and topographical modifications of dental implant surfaces and surface coatings with biologically active materials (Le Guéhennec et al., 2007).

These materials, in addition to provoking a response in living tissue, would have the capacity to achieve a faster, higher quality and more durable osseointegration, reducing the waiting time for prosthetic rehabilitations and solving the problems of poor bone quality (Stanford, 2008). Currently, bioceramics, ions and biomolecules are applied for bioactive purposes (Ellingsen et al., 2004; Cooper et al., 2006; Badr and Hadary, 2007; Zagury et al., 2007). The latter include biomacromolecules (lipids, proteins, polynucleic acids and polysaccharides) and biomicromolecules (oligopeptides, deoxyribonucleotides, amino acids, monosaccharides and metabolic products), which are of extraordinary importance for physiological processes and homeostasis (Fischer et al., 2020).

The ability to adhere to bone tissue and the chemical similarity with this tissue have led to great interest in calcium phosphate (CaP) coatings on the surface of implants, precisely because they increase the biochemical anchorage between the bone and the surface materials (Bosco et al., 2013). Similarly, protein coatings have been used in recent years because they accelerate the bone regeneration process at the bone-implant interface and improve osseointegration (Raphel et al., 2016).

Bone morphogenetic protein (BMP) and collagen have been proposed as bone regeneration stimulating materials. Collagen is an important component in bone composition, leading to increased tissue vascularization and decreased inflammation by curbing macrophage and osteoclast activity (Lee et al., 2014). In turn, BMPs play an important role in osteogenesis by regulating the differentiation of bone mesenchymal stem cells (MSCs) and osteogenic cells (Dolanmaz et al., 2015a).

Synthetic peptides have been shown to stimulate bone formation by enhancing the binding of osteoblast cell adhesion receptors (e.g., integrins, selectins, and cadherins). Binding of osteoblast integrin receptors to these bioactive molecules stimulates their interaction with their extracellular matrix (ECM) and promotes cell proliferation and mineralization (Garcia and Reyes, 2005).

Studies have shown that biofunctionalization of implant surfaces with biomimetic peptides would result in a greater increase in the bone-to-implant contact surface (BIC) and an increase in bone density around the implant (Lutz et al., 2010a). However, the process of peptide immobilization on Ti implant surfaces can be a complex process, despite the fact that, in recent years, specific methods have been developed to achieve this goal (Narai and Nagahata, 2003; Russell et al., 2008; Viera-Negron et al., 2008). Also, it has been observed that the biological activity of certain peptides would be reduced by the immobilization process. The surface density, together with the length of the spacers and the orientation, would condition the bactericidal effect of the peptides (Giro et al., 2008). Moussa and Aparicio demonstrated *in vitro* that bacterial abundance on peptide-coated hydroxyapatite (HA) discs was significantly lower than in controls (Andrea et al., 2018a). Makihira et al. tested in edentulous dog mandibles, the osseointegrative capacity of Ti implants coated with a histatin-derived peptide, demonstrating, by histological and micro-CT analysis, increased trabecular bone formation around the coated implants (Riool et al., 2017). Their observations suggest that antimicrobial peptides on Ti implants would decrease bacterial colonization on the implant surface and facilitate osseointegration (Silva et al., 2016; Zhang et al., 2018).

Despite the existence in the literature of reviews to evaluate the effects of different implant surface modifications on peri-implant bone formation and osseointegration (Makihira et al., 2011; Andrea et al., 2018b; Moussa and Aparicio, 2020; Siwakul et al., 2021) and the known benefit on osseointegration of the use of bioactive molecules (Junker et al., 2009), we have not found meta-analyses that investigate the results in depth, so the aim of our study was to evaluate the role and efficacy of bioactive surfaces on osseointegration. Our meta-analysis limited the research interest to titanium dental implants coated with biomolecules, i.e. organic molecules produced by a living organism.

2 Materials and methods

2.1 Registration

This systematic review was registered at INPLASY, registration number INPLASY202260076.

2.2 PICOS and focused question

Supplementary Table S1: PRISMA Checklist]. According to the PRISMA guidelines for Systematic Reviews and Meta-Analyses (Hutton et al., 2016), a specific question was formulated based on the PICOS principle (Participants, Interventions, Control, Outcomes, and Study Design). The focused question was, "Does the bioactive surface of titanium dental implants, based on biomolecules, influence osseointegration?".

P) Participants: Subjects received endosseous implantation.
I) Interventions: Implants with incorporated bioactive surfaces based on biomolecules.

C) Control: Implants with conventional etched surfaces (SLA type).
O) Outcome: Bone to Implant Contact (BIC).
S) Study design: Preclinical studies in unmodified experimental animal models.

2.3 Search strategy

The electronic databases PubMed/MEDLINE, WOS and EMBASE were searched until May 2022, with the terms Medical Subject Headings (MeSH): “titanium dental implants”, “surface properties”, “bioactive surface modifications”, “biomolecules”, “BMP”, “antibacterial agent”, “peptide”, “collagen”, “grown factor”, in combination with “osseointegration”, “bone apposition”, “osteogenic”, “osteogenesis”, “new bone formation”, “bone to implant contact”, “bone regeneration” and “*in vivo* studies”. The Boolean operators AND/OR were used to refine the search. In addition, relevant studies in the gray literature and reference lists of included studies were also examined (cross-referenced). The search strategy and the PICOS strategy are shown in Table 1.

2.4 Inclusion and exclusion criteria

2.4.1 Inclusion criteria

1) Studies regarding Ti implant surfaces coated with biomolecules; b) Studies reporting evaluation of the effect of biomolecular coatings on bone formation or osseointegration; 3) Studies published in English.

2.4.2 Exclusion criteria

1) *In vitro* studies; b) Studies using modified animals; 3) Narrative reviews and systematic reviews; 4) Irrelevant and duplicate studies and those that did not meet the established inclusion criteria.

TABLE 1 Systematic search strategy (PICOS strategy).

Population	**Experimental animals receiving implants with bioactive surfaces based on biomolecules**
Intervention	Intraosseous implant treatments
Comparisons	Intraosseous implants with conventional etched surfaces (SLA type)
Outcomes	Bone to Implant contact (BIC)
Study design	Preclinical studies in unmodified experimental animal models
Search combination	#1 AND #2 OR
Language	English
Electronic databases	PubMed/MEDLINE, WOS and EMBASE

2.5 Data extraction and analysis

Studies that did not refer to the research question were eliminated and only the titles and abstracts of the selected articles were considered and entered into an Excel spreadsheet. Two reviewers (N.L.-V. and A.L.-V.) selected the titles and abstracts independently. Discrepancies between the two reviewers were discussed until a consensus was reached for inclusion of the studies. The full texts of the selected studies were then obtained for inclusion and analysis.

2.6 Risk of bias of included articles

An adapted version of the Cochrane RoB tool with specific biases in animal studies (SYRCLE) was used to assess the scientific evidence in all selected studies (Hooijmans et al., 2014).

2.7 Quality of the reports of the included studies

Two reviewers N.L.-V. and A.L.-V evaluated the included studies according to the ARRIVE (Animal Research: Reporting of *In Vivo* Experiments) guidelines (Stadlinger et al., 2012a), which include a total of 23 items. Each item was scored by 0 (not reported) or 1 (reported), with a complete count of all included studies.

2.8 Statistical analysis

The meta-analysis was performed using RevMan software [Review Manager (RevMan) (Computer program). Version 5.4.1, The Cochrane Collaboration, 2020].

A meta-analysis based on Odds Ratio (OR) with 95% confidence intervals (CI) was performed for adverse event outcomes. Mean difference (MD) and standard deviation (SD) were used to estimate effect size. The random-effects model was selected because of the expected methodological heterogeneity in the included studies; furthermore, heterogeneity was interpreted as significant when the I2 value was >50%. The threshold for statistical significance was defined as $p < 0.05$. A funnel plot was used to assess publication bias.

3 Results

3.1 Selection and description of the studies

Among the available literature, three categories of biomolecular coatings have been evaluated in this review: 1) peptides, 2) BMPs and 3) ECM. The initial electronic search yielded 10,697 references. After eliminating duplicates and irrelevant articles based on their title and abstracts, 84 articles were selected, of which, after eliminating those that did not meet inclusion criteria (*in vitro* studies, systematic reviews, modified animals…), 26 full texts were selected (Anitua, 2006; Germanier et al., 2006; Wikesjö et al., 2008a; Wikesjö et al., 2008b; Wikesjö et al., 2008c; Stadlinger et al., 2008; Anitua et al., 2009; Barros et al., 2009; Ishibe et al., 2009; Yang et al., 2009; Lutz et al., 2010b; Polimeni et al., 2010; Susin et al., 2010; Ramazanoglu et al., 2011; Stadlinger et al., 2012b; Sverzut et al., 2012; Jiang et al., 2013; Cecconi et al., 2014; Korn et al., 2014; Kim et al., 2015; Yoo et al., 2015; Cardoso et al., 2017; Bae et al., 2018; Cho et al., 2019; Cho et al., 2021; Pang et al., 2021). The concordance between reviewers (N.L-V., A.L-V.) was 100% with a Cohen's kappa index of 1 (total concordance). (Figure 1. Flow Diagram).

Table 2 provides the evaluation of the ARRIVE criteria in animal studies, with a mean rating of 16.5 ± 1.5. All studies provided adequate information in terms of title, abstract, introduction, ethical statement, species, surgical procedure, outcome assessment and statistical analysis. Items 5 (Rationale for animal models), 19 (3Rs, Replace, Reduce and Refine), 20 (Adverse events), were not reported in any of the included studies. Item 11 (Accommodation and handling of animals) was reported by only five studies (Anitua, 2006; Anitua et al., 2009; Ishibe et al., 2009; Lutz et al., 2010b; Korn et al., 2014) and item 21 (Study limitations) was reported by six studies (Jiang et al., 2013; Korn et al., 2014; Kim et al., 2015; Yoo et al., 2015; Cardoso et al., 2017; Bae et al., 2018).

3.2 Risk of bias assessment

The Random sequence generation domain was the most frequently mentioned (60%). Blinding of participants and

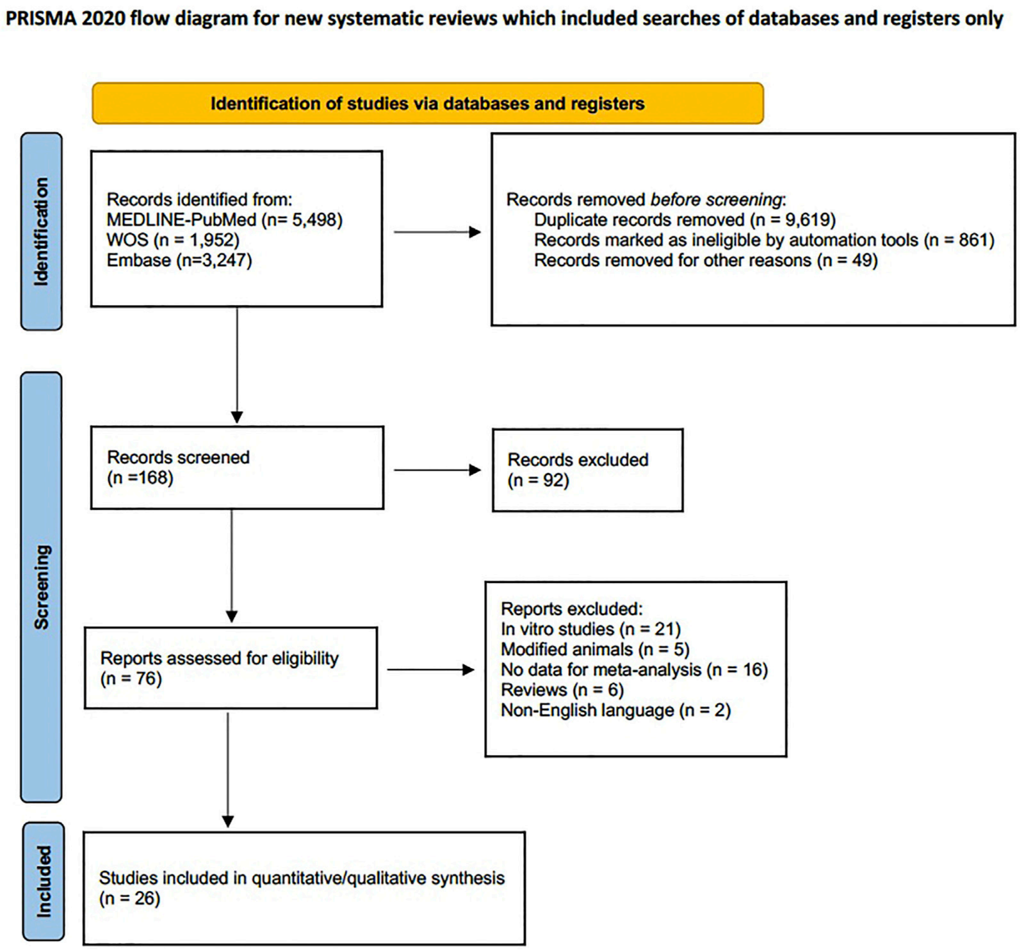

FIGURE 1
Flowchart.

TABLE 2 Checklist of ARRIVE criteria reported by the included studies. Each item was judged as "0" (not reported) or "1" (reported).

Studies	**Germanier et al., 2006 (Germanier et al., 2006)**	**Anitua 2006 (Anitua, 2006)**	**(1) wikesjö et al., 2008 (Wikesjö et al., 2008a)**	**(2) wikesjö et al., 2008 (Wikesjö et al., 2008b)**	**(3) wikesjö et al., 2008 (Wikesjö et al., 2008c)**	**Stadlinger et al., 2008 (Stadlinger et al., 2008)**	**Barros et al., 2009 (Barros et al., 2009)**	**Yang et al., 2009 (Yang et al., 2009)**	**Anitua et al., 2009 (Anitua et al., 2009)**	**Ishibe et al., 2009 (Ishibe et al., 2009)**	**Lutz et al., 2010 (Lutz et al., 2010b)**	**Susin et al., 2010 (Susin et al., 2010)**	**Polimeni et al., 2010 (Polimeni et al., 2010)**
1 Title	1	1	1	1	1	1	1	1	1	1	1	1	1
Abstract													
2 Species	1	1	1	1	1	1	1	1	1	1	1	1	1
3 Key finding	1	1	1	1	1	1	1	1	1	1	1	1	1
Introduction													
4 Background	1	1	1	1	1	1	1	1	1	1	1	1	1
5 Reasons for animal models	0	0	0	0	0	0	0	0	0	0	0	0	0
6 Objectives	1	1	1	1	1	1	1	1	1	1	1	1	1
Methods													
7 Ethical statement	1	1	1	1	1	1	0	1	1	1	1	1	1
8 Study design	1	1	1	1	1	1	1	1	1	1	1	1	1
9 Experimental procedures	1	1	1	1	1	1	1	1	1	1	1	1	1
10 Experimental animals	1	1	1	1	1	1	1	1	1	1	1	1	1
11 Accommodation and handling of animals	0	1	0	0	0	0	0	0	1	1	1	0	0
12 Sample size	1	1	1	1	1	1	1	1	1	1	1	1	1
13 Assignment of animals to experimental groups	1	1	1	1	1	1	0	0	1	1	1	1	1
14 Anaesthesia	1	1	1	1	1	1	1	1	1	1	1	1	1
15 Stadistical methods	1	1	1	1	1	1	1	1	1	1	1	1	1
Results													
16 Experimental results	1	1	1	1	1	1	1	1	1	1	1	1	1
17 Results and estimation	0	1	0	1	1	1	1	1	1	1	1	1	1
Discussion													
	1	1	0	1	0	1	0	1	1	1	0	0	0

(Continued on following page)

TABLE 2 (*Continued*) Checklist of ARRIVE criteria reported by the included studies. Each item was judged as "0" (not reported) or "1" (reported).

Studies	Germanier et al., 2006 (Germanier et al., 2006)	Anitua 2006 (Anitua, 2006)	(1) wikesjö et al., 2008 (Wikesjö et al., 2008a)	(2) wikesjö et al., 2008 (Wikesjö et al., 2008b)	(3) wikesjö et al., 2008 (Wikesjö et al., 2008c)	Stadlinger et al., 2008 (Stadlinger et al., 2008)	Barros et al., 2009 (Barros et al., 2009)	Yang et al., 2009 (Yang et al., 2009)	Anitua et al., 2009 (Anitua et al., 2009)	Ishibe et al., 2009 (Ishibe et al., 2009)	Lutz et al., 2010 (Lutz et al., 2010b)	Susin et al., 2010 (Susin et al., 2010)	Polimeni et al., 2010 (Polimeni et al., 2010)
18 Interpretation and scientific implications													
19 3Rs reported	0	0	0	0	0	0	0	0	0	0	0	0	0
20 Adverse events	0	0	0	0	0	0	0	0	0	0	0	0	0
21 Study limitations	0	0	0	0	0	0	0	0	0	0	0	0	0
22 Generalization/ applicability	0	1	0	0	0	1	0	0	1	0	0	0	0
23 Funding	0	0	1	1	1	1	1	0	0	0	1	1	1
TOTAL SCORE	15	18	15	17	16	18	14	15	18	17	17	16	16

Studies	Ramazanoglu et al., 2011 (Ramazanoglu et al., 2011)	Stadlinger et al., 2012 (Stadlinger et al., 2012b)	Sverzut al. 2012 (Sverzut et al., 2012)	Jiang et al., 2013 (Jiang et al., 2013)	Cecconi et al., 2014 (Cecconi et al., 2014)	Korn et al., 2014 (Korn et al., 2014)	Kim et al., 2015 (Kim et al., 2015)	Yoo et al., 2015 (Yoo et al., 2015)	Cardoso et al., 2017 (Cardoso et al., 2017)	Bae et al., 2018 (Bae et al., 2018)	Cho et al., 2019 (Cho et al., 2019)	Pang et al., 2021 (Pang et al., 2021)	Cho et al., 2021 (Cho et al., 2021)
1. Title	1	1	1	1	1	1	1	1	1	1	1	1	1
Abstract													
2. Species	1	1	1	1	1	1	1	1	1	1	1	1	1
3. Key finding	1	1	1	1	1	1	1	1	1	1	1	1	1
Introduction													
4. Background	1	1	1	1	1	1	1	1	1	1	1	1	1
5. Reasons for animal models	0	0	0	0	0	0	0	0	0	0	0	0	0
6. Objectives	1	1	1	1	1	1	1	1	1	1	1	1	1
Methods													
7. Ethical statement	1	1	1	1	1	1	1	1	1	1	1	1	1
8. Study design	1	1	1	1	1	1	1	1	1	1	1	1	1
9. Experimental procedures	1	1	1	1	1	1	1	1	1	1	1	1	1
10. Experimental animals	1	1	1	1	1	1	1	1	1	1	1	1	1
11. Accommodation and handling of animals	0	0	0	0	0	1	0	0	1	0	0	0	0

(Continued on following page)

TABLE 2 (*Continued*) Checklist of ARRIVE criteria reported by the included studies. Each item was judged as "0" (not reported) or "1" (reported).

Studies	**Ramazanoglu et al., 2011 (Ramazanoglu et al., 2011)**	**Stadlinger et al., 2012 (Stadlinger et al., 2012b)**	**Sverzut al. 2012 (Sverzut et al., 2012)**	**Jiang et al., 2013 (Jiang et al., 2013)**	**Cecconi et al., 2014 (Cecconi et al., 2014)**	**Korn et al., 2014 (Korn et al., 2014)**	**Kim et al., 2015 (Kim et al., 2015)**	**Yoo et al., 2015 (Yoo et al., 2015)**	**Cardoso et al., 2017 (Cardoso et al., 2017)**	**Bae et al., 2018 (Bae et al., 2018)**	**Cho et al., 2019 (Cho et al., 2019)**	**Pang et al., 2021 (Pang et al., 2021)**	**Cho et al., 2021 (Cho et al., 2021)**
12. Sample size	1	1	1	1	1	1	1	1	1	1	1	1	1
13. Assignment of animals to experimental groups	1	1	0	1	0	1	1	1	1	1	0	0	1
14. Anaesthesia	1	1	1	1	1	1	1	1	1	1	1	0	1
15. Stadistical methods	1	1	1	1	1	1	1	1	1	1	1	1	1
Results													
16. Experimental results	1	1	1	1	1	1	1	1	1	1	1	1	1
17. Results and estimation	1	1	1	1	1	1	1	1	1	1	1		
Discussion													
18. Interpretation and scientific implications	1	0	0	1	0	1	1	0	1	0	0	0	1
19. 3Rs reported	0	0	0	0	0	0	0	0	0	0	0	0	0
20. Adverse events	0	0	0	0	0	0	0	0	0	0	0	0	0
21. Study limitations	0	0	0	1	0	1	1	1	1	1	0	0	1
22. Generalization/applicability	0	0	0	0	0	0	0	0	0	0	1	1	0
23. Funding	1	0	1	1	1	1	1	1	1	1	1	0	1
TOTAL SCORE	17	15	15	18	15	19	18	18	19	17	16	13	17

Mean rating: 16.5 ± 1.5.

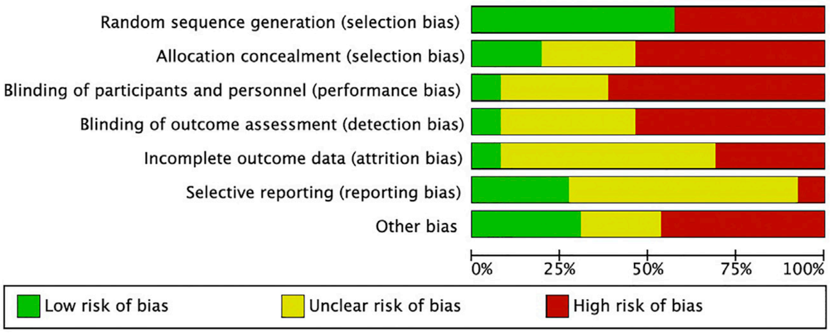

FIGURE 2
SYRCLE's risk of bias tool.

TABLE 3 Surface modification with peptides. Characteristics of the included studies.

Study	Animal model	Biomolecule	Implantation site	Length of study	Implanted device (length and diameter mm)	Material and number of implanted devices	Parameters measured	Findings
Cho et al., 2019 (Cho et al., 2019)	Rabbit	A human vitronectin-derived peptide	Tibiae	2 weeks	11 × 3.5 Ø	Ti, grade 4 (16)	BIC, BA	There were no significant differences in BIC and BA between the groups
Germanier et al. (Germanier et al., 2006)	Pig	RGD-peptide-modified polymer	Maxilla	2 and 4 weeks	6 × 2.7 Ø	Commercially pure Ti (48)	BIC	Bone tissue scaffolding was observed at 2 weeks, increasing bone density at 4 weeks
Lutz et al. (Lutz et al., 2010b)	Pig	Biomimetic active peptide (P-15)	Forehead region	2 and 4 weeks	8 × 3.5 Ø	Commercially pure Ti (54)	BIC, BD	Significant positive effect of the biomimetic peptide group on BIC with high contact rates at both 14 and 30 days. The biomimetic peptide had no significant effect on peri-implant BD
Barros et al. (Barros et al., 2009)	Dog	Bioactive peptide (sequence of aminoacids related to bone formation)	Mandible	8 weeks	9.5 × 4.5 Ø	Commercially pure Ti (48)	BIC, BD	Bone apposition and bone density around Ti implants depended on bioactive peptide concentrations
Yang et al. (Yang et al., 2009)	Rabbit	RGD layer-by-layer	Femur	4, 8, and 12 weeks	10 × 3 Ø	Ti (60)	BIC, BA, RTQ	RGD coating results in increased BIC, peri-implant bone formation and extraction torque values

Ti, Titanium; BIC, bone to implant contact; BA, bone area; BD, bone density; RTQ, removal torque test; RGD, Arginine-glycine-aspartic.

personnel and Blinding of outcome assessment were the least mentioned domains. The domains Incomplete outcome data and Selective reporting were the least clear. The lack of information resulted in a high and unclear risk of bias for most of the included studies (Figure 2).

3.3 Characteristics of the included studies

Qualitative synthesis. A total of 1,109 implants were evaluated. Most of the studies employed commercial Ti and Ti alloy implant models, with the exception of two studies in rat tibias (Ishibe et al.,

TABLE 4 Surface modification with Bone Morphogenetic Proteins (BMPs). Characteristics of the included studies.

Study	Animal model	Biomolecule	Implantation site	Length of study	Implanted device (length and diameter mm)	Material and number of implanted devices	Parameters measured	Findings
Kim et al. (Kim et al., 2015)	Dog	rhBMP-2	Tibiae	8 weeks	7 × 3.5 Ø	Pure Ti (24)	BIC, BV, ISQ	Concentrations of 0.5 and 1 mg/ml rhBMP-2 promote osseointegration and bone regeneration in areas with open bone defects
Pang et al. (Pang et al., 2021)	Rabbit	BMP-2+HA	Tibiae	4 weeks	7 × 3.3 Ø	Pure Ti (8)	BIC, BA, RTQ	The combination of BMP-2 with HAp functions as an activator of osseointegration
Yoo et al. (Yoo et al., 2015)	Rabbit	rhBMP-2/PLGA	Tibiae	3 and 7 weeks	7 × 3.75 Ø	Pure grade IV Ti (32)	BIC, BA	Submicron-sized PLGA/rhBMP-2 Ti coatings showed an increase in BIC during the early stages of healing
Cardoso et al. (Cardoso et al., 2017)	Pig	PPL10BMP	Parietal bone	4, 8 and weeks	6 × 1.1 Ø	Pure Ti (120)	B/T, BIC	The association of PPL10 and BMP-2 did not produce a bone improvement
Ishibe et al. (Ishibe et al., 2009)	Rat	rhBMP-2/heparin	Tibiae	3 weeks	2 × 1 Ø	Pure Ti (70)	BIC	The incorporation of BMP-2 and heparin has the potential to stimulate new bone formation around implants *in vivo*
Jiang et al. (Jiang et al., 2013)	Rabbit	rhBMP-2	Femur	2, 4 and 8 weeks	8 × 4.1 Ø	Pure Ti (30)	BIC	Acid-etched titanium implants coated with BMP-2 slightly accelerated early bone formation around the implant
Susin et al. (Susin et al., 2010)	Dog	rhBMP-7	Jaw	3, 4, 7, and 8 weeks	10 × 4 Ø	Ti (36)	BIC, BD	Porous titanium oxide implants coated with rhBMP-7 stimulated bone formation and osseointegration
Polimeni et al. (Polimeni et al., 2010)	Dog	rhGDF-5	Jaw	3, 4, 7, and 8 weeks	10 × 4 Ø	Ti (72)	BIC, BD	Dental implants coated with rhGDF-5 showed a dose-dependent osteoinductive and/or osteoconductive effect
Ramazanoglu et al. (Ramazanoglu et al., 2011)	Pig	rhBMP-2+rhVEGF1_{65}	Calvaria	1, 2, and 4 weeks	6 × 4.2 Ø	Pure Ti (90)	BIC, BD, BV	The combined administration of rhBMP-2 and rhVEGF165 in biomimetic coating did not result in an improvement of BIC
Wikesjö et al. (Wikesjö et al., 2008a) (1)	Dog	rhBMP-2 (0,75 or 1.5 mg/ml)	Jaw	3, 4, 7 and 8 weeks	10 × 4 Ø	Ti (72)	BIC, BD	The implant surfaces coated with rhBMP-2 induced osseointegration, but BIC values were significantly higher in the control group
Wikesjö et al. (Wikesjö et al., 2008b) (2)	Dog	rhBMP-2 (0.2 or 4.0 mg/ml)	Jaw	4 and 8 weeks	8.5 × 3,75Ø	Ti (32)	BIC, BD	Adsorbed rhBMP-2 on implant surfaces initiates dose-dependent peri-implant bone remodelling

(Continued on following page)

TABLE 4 (*Continued*) Surface modification with Bone Morphogenetic Proteins (BMPs). Characteristics of the included studies.

Study	Animal model	Biomolecule	Implantation site	Length of study	Implanted device (length and diameter mm)	Material and number of implanted devices	Parameters measured	Findings
Wikesjö et al. (Wikesjö et al., 2008c) (3)	Monkey	rhBMP-2 (0,2 or 2 mg/ml)	Maxilla	16 weeks	8.5 × 3,75Ø	Ti (24)	BIC, BD	The rhBMP-2 coated Ti surface enhances/ accelerates local bone formation in type IV bone resulting in significant osseointegration
Anitua (Anitua, 2006) (1)	Goat	PRGF	Tibiae and radii	8 weeks	8.5 x 3Ø	Ti (23)	BIC	Coating dental implants with PRGF immediately before insertion improved osseointegration
Anitua (Anitua et al., 2009) (2)	Goat	PRGF	Tibiae	8 weeks	8.5 x 3Ø	Ti (26)	BIC	Hydration of titanium implants with liquid PRGF improves the integration of oral implants into cortical bone. The potential therapeutic effects of this approach could be extrapolated to other prosthetic devices

Ti, Titanium; BIC, bone to implant contact; BV, bone volume; BA, bone area; ISQ, implant stability quotient; HA, hydroxyapatite; PLGA, poly(D,L-lactide-co-glycolide); PPL10, 10% phosphorylated pullulan; Peri-implant bone formation (B/T); BD, bone density; rhGDF-5, recombinant human GDF-5; rhVEGF1$_{65,}$ recombinant human vascular endothelial growth factor; rhBMP-2, recombinant human bone morphogenetic protein-2; PRGF, plasma rich in growth factors.

TABLE 5 Surface modification with ECM. Characteristics of the included studies.

Study	Animal model	Biomolecule	Implantation site	Length of study	Implanted device (length and diameter) mm	Material and number of implanted devices	Parameters measured	Findings
Sverzut et al. (Sverzut et al., 2012)	Dog	Type I Collagen	Jaw	3 weeks	8.5 × 3.75 Ø	Ti (24)	BIC, BA	The collagen coating of Ti implants improves osteoinduction and tissue vascularization while reducing inflammatory response and macrophage and osteoclast activity
Stadlinger et al. (Stadlinger et al., 2008) (1)	Pig	Type I Collagen/ rhBMP-4	Jaw	3 and 7 weeks	12 × 4.25 Ø	Ti (120)	BIC	The inclusion of chondroitin sulfate in the coating increases the BIC of collagen-coated implants, however, the additional inclusion of a low amount of rhBMP-4 had a detrimental effect

(Continued on following page)

TABLE 5 (*Continued*) Surface modification with ECM. Characteristics of the included studies.

Study	Animal model	Biomolecule	Implantation site	Length of study	Implanted device (length and diameter) mm	Material and number of implanted devices	Parameters measured	Findings
Cho et al. (Cho et al., 2021)	Dog	Type I Collagen/GA	Jaw	8 weeks	8 × 4 Ø	Pure Ti (36)	BIC, BA	Gamma-irradiated collagen crosslinking is as effective as GA crosslinking in terms of bone regeneration efficiency
Bae et al. (Bae et al., 2018)	Rat	Type I Collagen/GA	Tibia	84 weeks	2.5 × 1.5 Ø	Ti (12)	BIC, NBV	Radiation cross-linked collagen-coated Ti implants possess potential osteoinductive qualities without the adverse effects of chemical agents
Korn et al. (Korn et al., 2014)	Pig	Collagen/CS/sHya	Jaw	4 and 8 weeks	15 × 5 Ø	Ti (36)	BIC, BD	Collagen/CS/sHya-coated Ti implants did not show an increase in BIC compared to the acid-etched and blasted References surface. However, they did increase bone density compared to the References surface
Stadlinger et al. (Stadlinger et al., 2012b) (2)	Pig	Collagen/CS	Jaw	4 and 8 weeks	9.5 × 4.5 Ø	Ti (120)	BIC, BD	The coatings did not show a significant effect on BIC or BVD.
Cecconi et al. (Cecconi et al., 2014)	Rabbit	Type I Collagen/Apatite	Femur	7 weeks	8.5 × 4 Ø	Ti (24)	BIC	Coating with bone apatite and type I collagen increased new bone formation and bone attachment around Ti implants

Ti, Titanium; BIC, bone to implant contact; BV, bone volume; BA, bone area; rhBMP-2, recombinant human bone morphogenetic protein-2; GA, glutaraldehyde; NBA, new bone area; ITBD, inter-thread bone densities; NBV, new bone volume; CS, chondroitin sulfate; BVD, bone volume density; sHya, sulfated hyaluronan.

2009; Bae et al., 2018) that used rods and microscrews, respectively. The implants featured either a re-coated or uncoated surface with peptides in five studies (Germanier et al., 2006; Barros et al., 2009; Yang et al., 2009; Lutz et al., 2010b; Cho et al., 2019), BMPs in fourteen studies (Anitua, 2006; Wikesjö et al., 2008a; Wikesjö et al., 2008b; Wikesjö et al., 2008c; Anitua et al., 2009; Ishibe et al., 2009; Polimeni et al., 2010; Susin et al., 2010; Ramazanoglu et al., 2011; Kim et al., 2015; Yoo et al., 2015; Cardoso et al., 2017; Pang et al., 2021), or ECM products in seven studies (Stadlinger et al., 2008; Stadlinger et al., 2012b; Sverzut et al., 2012; Cecconi et al., 2014; Korn et al., 2014; Bae et al., 2018; Cho et al., 2019). Follow-up periods ranged from 2 to 16 weeks, except for the study by Bae et al. (Bae et al., 2018) that the follow-up period was extended to 84 weeks. The most commonly used experimental models were the dog (Wikesjö et al., 2008a; Wikesjö et al., 2008b; Barros et al., 2009; Polimeni et al., 2010; Susin et al., 2010; Sverzut et al., 2012; Kim et al., 2015; Cho et al., 2019) and the pig (Germanier et al., 2006; Stadlinger et al., 2008; Lutz et al., 2010b; Susin et al., 2010; Ramazanoglu et al., 2011; Stadlinger et al., 2012b; Korn et al., 2014; Cardoso et al., 2017). The jaw and tibia were the most commonly used bones for implantation and all included studies evaluated the BIC; six studies evaluated BA (Yang et al., 2009; Sverzut et al., 2012; Yoo et al., 2015; Cho et al., 2019; Cho et al., 2021; Pang et al., 2021) and nine studies evaluated BD (Wikesjö et al., 2008b; Wikesjö et al., 2008c; Stadlinger et al., 2008; Barros et al., 2009; Lutz et al., 2010b; Polimeni et al., 2010; Susin et al., 2010; Ramazanoglu et al., 2011; Korn et al., 2014). The main characteristics of the studies are shown in the tables below (Tables 3–5).

3.4 Quantitative synthesis (meta-analysis)

The same studies included in the qualitative synthesis were used to perform a meta-analysis comparing Ti implants coated with different biomolecules, with Ti implants etched. Meta-analysis of adverse outcomes could not be performed due to

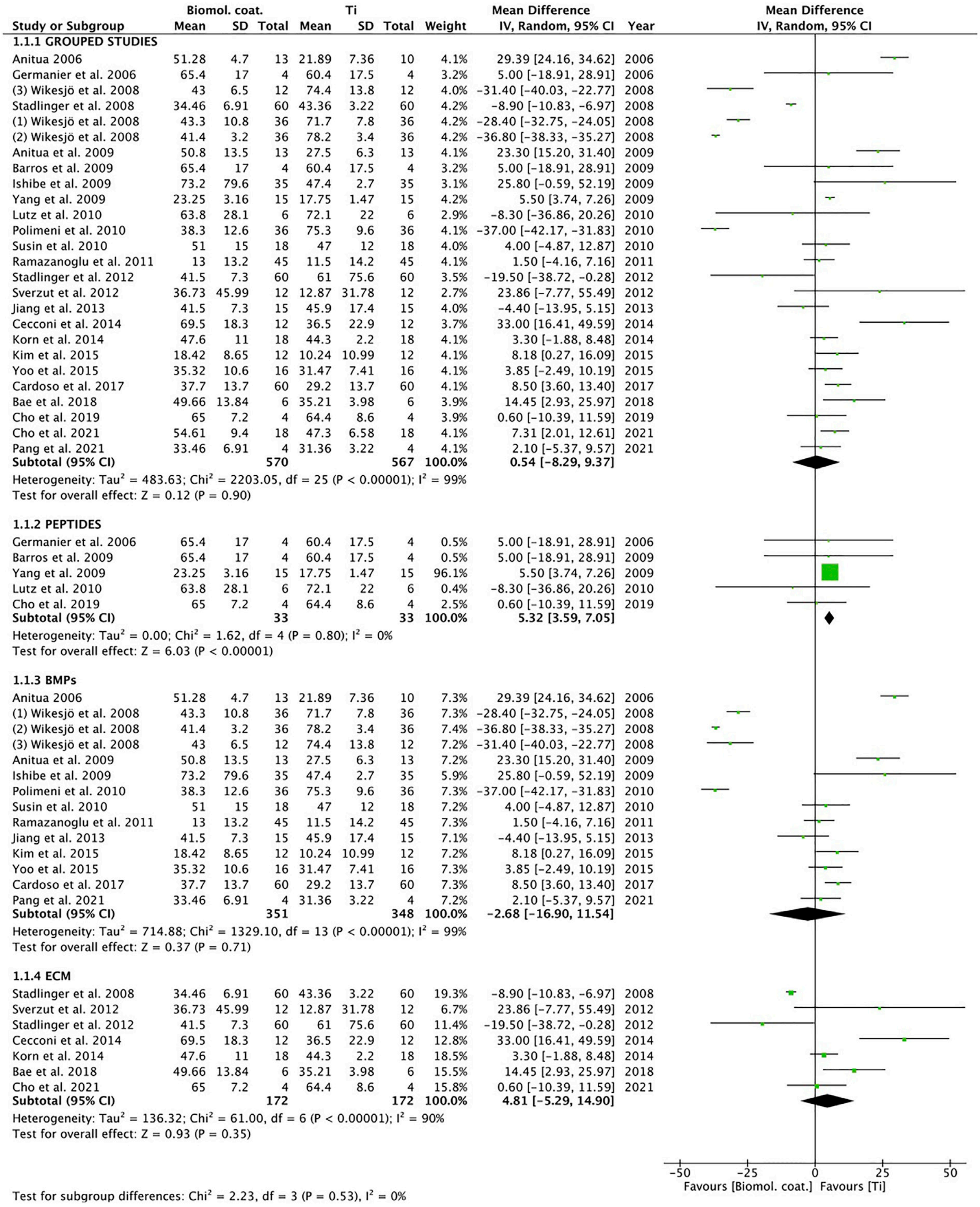

	Biomol. coat.			Ti				Mean Difference	
Study or Subgroup	Mean	SD	Total	Mean	SD	Total	Weight	IV, Random, 95% CI	Year
1.1.1 GROUPED STUDIES									
Anitua 2006	51.28	4.7	13	21.89	7.36	10	4.1%	29.39 [24.16, 34.62]	2006
Germanier et al. 2006	65.4	17	4	60.4	17.5	4	3.2%	5.00 [−18.91, 28.91]	2006
(3) Wikesjö et al. 2008	43	6.5	12	74.4	13.8	12	4.0%	−31.40 [−40.03, −22.77]	2008
Stadlinger et al. 2008	34.46	6.91	60	43.36	3.22	60	4.2%	−8.90 [−10.83, −6.97]	2008
(1) Wikesjö et al. 2008	43.3	10.8	36	71.7	7.8	36	4.2%	−28.40 [−32.75, −24.05]	2008
(2) Wikesjö et al. 2008	41.4	3.2	36	78.2	3.4	36	4.2%	−36.80 [−38.33, −35.27]	2008
Anitua et al. 2009	50.8	13.5	13	27.5	6.3	13	4.1%	23.30 [15.20, 31.40]	2009
Barros et al. 2009	65.4	17	4	60.4	17.5	4	3.2%	5.00 [−18.91, 28.91]	2009
Ishibe et al. 2009	73.2	79.6	35	47.4	2.7	35	3.1%	25.80 [−0.59, 52.19]	2009
Yang et al. 2009	23.25	3.16	15	17.75	1.47	15	4.2%	5.50 [3.74, 7.26]	2009
Lutz et al. 2010	63.8	28.1	6	72.1	22	6	2.9%	−8.30 [−36.86, 20.26]	2010
Polimeni et al. 2010	38.3	12.6	36	75.3	9.6	36	4.1%	−37.00 [−42.17, −31.83]	2010
Susin et al. 2010	51	15	18	47	12	18	4.0%	4.00 [−4.87, 12.87]	2010
Ramazanoglu et al. 2011	13	13.2	45	11.5	14.2	45	4.1%	1.50 [−4.16, 7.16]	2011
Stadlinger et al. 2012	41.5	7.3	60	61	75.6	60	3.5%	−19.50 [−38.72, −0.28]	2012
Sverzut et al. 2012	36.73	45.99	12	12.87	31.78	12	2.7%	23.86 [−7.77, 55.49]	2012
Jiang et al. 2013	41.5	7.3	15	45.9	17.4	15	4.0%	−4.40 [−13.95, 5.15]	2013
Cecconi et al. 2014	69.5	18.3	12	36.5	22.9	12	3.7%	33.00 [16.41, 49.59]	2014
Korn et al. 2014	47.6	11	18	44.3	2.2	18	4.1%	3.30 [−1.88, 8.48]	2014
Kim et al. 2015	18.42	8.65	12	10.24	10.99	12	4.1%	8.18 [0.27, 16.09]	2015
Yoo et al. 2015	35.32	10.6	16	31.47	7.41	16	4.1%	3.85 [−2.49, 10.19]	2015
Cardoso et al. 2017	37.7	13.7	60	29.2	13.7	60	4.1%	8.50 [3.60, 13.40]	2017
Bae et al. 2018	49.66	13.84	6	35.21	3.98	6	3.9%	14.45 [2.93, 25.97]	2018
Cho et al. 2019	65	7.2	4	64.4	8.6	4	3.9%	0.60 [−10.39, 11.59]	2019
Cho et al. 2021	54.61	9.4	18	47.3	6.58	18	4.1%	7.31 [2.01, 12.61]	2021
Pang et al. 2021	33.46	6.91	4	31.36	3.22	4	4.1%	2.10 [−5.37, 9.57]	2021
Subtotal (95% CI)			**570**			**567**	**100.0%**	**0.54 [−8.29, 9.37]**	
Heterogeneity: Tau^2 = 483.63; Chi^2 = 2203.05, df = 25 (P < 0.00001); I^2 = 99%									
Test for overall effect: Z = 0.12 (P = 0.90)									
1.1.2 PEPTIDES									
Germanier et al. 2006	65.4	17	4	60.4	17.5	4	0.5%	5.00 [−18.91, 28.91]	2006
Barros et al. 2009	65.4	17	4	60.4	17.5	4	0.5%	5.00 [−18.91, 28.91]	2009
Yang et al. 2009	23.25	3.16	15	17.75	1.47	15	96.1%	5.50 [3.74, 7.26]	2009
Lutz et al. 2010	63.8	28.1	6	72.1	22	6	0.4%	−8.30 [−36.86, 20.26]	2010
Cho et al. 2019	65	7.2	4	64.4	8.6	4	2.5%	0.60 [−10.39, 11.59]	2019
Subtotal (95% CI)			**33**			**33**	**100.0%**	**5.32 [3.59, 7.05]**	
Heterogeneity: Tau^2 = 0.00; Chi^2 = 1.62, df = 4 (P = 0.80); I^2 = 0%									
Test for overall effect: Z = 6.03 (P < 0.00001)									
1.1.3 BMPs									
Anitua 2006	51.28	4.7	13	21.89	7.36	10	7.3%	29.39 [24.16, 34.62]	2006
(1) Wikesjö et al. 2008	43.3	10.8	36	71.7	7.8	36	7.3%	−28.40 [−32.75, −24.05]	2008
(2) Wikesjö et al. 2008	41.4	3.2	36	78.2	3.4	36	7.4%	−36.80 [−38.33, −35.27]	2008
(3) Wikesjö et al. 2008	43	6.5	12	74.4	13.8	12	7.2%	−31.40 [−40.03, −22.77]	2008
Anitua et al. 2009	50.8	13.5	13	27.5	6.3	13	7.2%	23.30 [15.20, 31.40]	2009
Ishibe et al. 2009	73.2	79.6	35	47.4	2.7	35	5.9%	25.80 [−0.59, 52.19]	2009
Polimeni et al. 2010	38.3	12.6	36	75.3	9.6	36	7.3%	−37.00 [−42.17, −31.83]	2010
Susin et al. 2010	51	15	18	47	12	18	7.2%	4.00 [−4.87, 12.87]	2010
Ramazanoglu et al. 2011	13	13.2	45	11.5	14.2	45	7.3%	1.50 [−4.16, 7.16]	2011
Jiang et al. 2013	41.5	7.3	15	45.9	17.4	15	7.1%	−4.40 [−13.95, 5.15]	2013
Kim et al. 2015	18.42	8.65	12	10.24	10.99	12	7.2%	8.18 [0.27, 16.09]	2015
Yoo et al. 2015	35.32	10.6	16	31.47	7.41	16	7.3%	3.85 [−2.49, 10.19]	2015
Cardoso et al. 2017	37.7	13.7	60	29.2	13.7	60	7.3%	8.50 [3.60, 13.40]	2017
Pang et al. 2021	33.46	6.91	4	31.36	3.22	4	7.2%	2.10 [−5.37, 9.57]	2021
Subtotal (95% CI)			**351**			**348**	**100.0%**	**−2.68 [−16.90, 11.54]**	
Heterogeneity: Tau^2 = 714.88; Chi^2 = 1329.10, df = 13 (P < 0.00001); I^2 = 99%									
Test for overall effect: Z = 0.37 (P = 0.71)									
1.1.4 ECM									
Stadlinger et al. 2008	34.46	6.91	60	43.36	3.22	60	19.3%	−8.90 [−10.83, −6.97]	2008
Sverzut et al. 2012	36.73	45.99	12	12.87	31.78	12	6.7%	23.86 [−7.77, 55.49]	2012
Stadlinger et al. 2012	41.5	7.3	60	61	75.6	60	11.4%	−19.50 [−38.72, −0.28]	2012
Cecconi et al. 2014	69.5	18.3	12	36.5	22.9	12	12.8%	33.00 [16.41, 49.59]	2014
Korn et al. 2014	47.6	11	18	44.3	2.2	18	18.5%	3.30 [−1.88, 8.48]	2014
Bae et al. 2018	49.66	13.84	6	35.21	3.98	6	15.5%	14.45 [2.93, 25.97]	2018
Cho et al. 2021	65	7.2	4	64.4	8.6	4	15.8%	0.60 [−10.39, 11.59]	2021
Subtotal (95% CI)			**172**			**172**	**100.0%**	**4.81 [−5.29, 14.90]**	
Heterogeneity: Tau^2 = 136.32; Chi^2 = 61.00, df = 6 (P < 0.00001); I^2 = 90%									
Test for overall effect: Z = 0.93 (P = 0.35)									

Test for subgroup differences: Chi^2 = 2.23, df = 3 (P = 0.53), I^2 = 0%

FIGURE 3
Forest plot for meta-analysis of studies evaluating BIC at 4 weeks after placement, assuming a random-effects model. SD, standard deviation; CI, confidence interval.

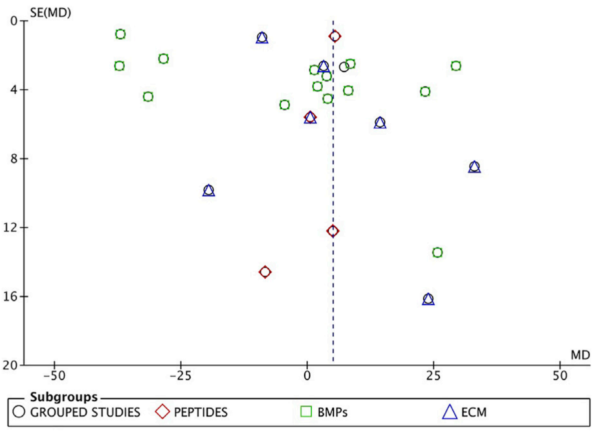

FIGURE 4
Funnel plot of grouped studies. The asymmetry proves publication bias.

lack of data. All included studies (Anitua, 2006; Germanier et al., 2006; Wikesjö et al., 2008a; Wikesjö et al., 2008b; Wikesjö et al., 2008c; Stadlinger et al., 2008; Anitua et al., 2009; Barros et al., 2009; Ishibe et al., 2009; Yang et al., 2009; Lutz et al., 2010b; Polimeni et al., 2010; Susin et al., 2010; Ramazanoglu et al., 2011; Stadlinger et al., 2012b; Sverzut et al., 2012; Jiang et al., 2013; Cecconi et al., 2014; Korn et al., 2014; Kim et al., 2015; Yoo et al., 2015; Cardoso et al., 2017; Bae et al., 2018; Cho et al., 2019; Cho et al., 2021; Pang et al., 2021) evaluated bone-to-implant contact (BIC), using measurement 4 weeks after placement. The heterogeneity of the grouped studies was very high ($I^2 = 99\%$) (Figure 3). Only one result favorable to coating, was found in the BMPs subgroup. Analysis of the grouped studies showed no significant differences between coatings and controls.

3.5 Publication bias and heterogeneity

The grouped studies show graphic signs of publication bias (Figure 4).

4 Discussion

The purpose of the present study was to answer the following clinical question: "Does the bioactive surface of titanium dental implants, based on biomolecules, influence osseointegration?".

Osseointegration is the stable anchorage of an implant through direct bone-to-implant contact (Albrektsson and Johansson, 2001).

The main objective of surface modifications of endosseous implants is to modulate the response of the host bone tissue to achieve better osseointegration.

This review focused on BIC analysis in three categories of biomolecular Ti implant coatings: peptides, BMPs and ECM and identified 26 preclinical research articles that used BIC analysis to assess peri-implant bone formation in different animal models. The included studies found that coatings with bioactive molecules increased bone values around the implant; only the study by Ramazanoglu et al. (2011) found no difference in BIC in the rhBMP-2 coating.

After insertion of an endosseous implant, a series of events occur between the host and the implant surface. During the intercommunication of the implant surface and the blood of the recipient, ligands and proteins are dynamically adsorbed at the implant surface and through a subsequent inflammatory process are released from it, followed by bone formation around the bioactive surface, reaching the maximum degree of organization and biomechanical properties through several remodeling cycles (Lemons, 2004; Goiato et al., 2009). Due to the dynamic nature of the bone-biomaterial interface, biomaterials for endosseous dental implants must have short- and long-term biocompatible and biofunctional properties (Xuereb et al., 2015). It was Puleo and Nanci (Puleo and Nanci, 1999), in 1999, who first indicated that "biochemical surface modification strives to utilize current knowledge of the biology and biochemistry of cell function and differentiation".

Since then, and especially in recent years, surface modifications of Ti and Ti6Al4V implants, using methods based on the immobilization of biologically active organic molecules, have aroused particular interest among researchers, with the aim of increasing cell migration and adhesion to the substrate and avoiding nonspecific addition of proteins, to improve the healing process (Panayotov et al., 2015). (Drexelius and Neundorf, 2021) Antimicrobial peptides have evolved as reliable alternatives to commonly used antibiotics and are positioned as candidates for antimicrobial surface coatings of implants. A review by Drexelius and Neundorf concluded that they have excellent *in vitro* and *in vivo* antimicrobial activity (Drexelius and Neundorf, 2021). Kang et al. (Kang et al., 2013) in a mixed *in vitro* and *in vivo* study used a laminin-2-derived peptide capable of promoting initial cell adhesion and propagation of osteoblast-like cells *in vitro*, acting as an accelerator of osseointegration of implant materials and determining its positive effect, *in vivo*, on BIC values.

Plasma and extracellular matrix proteins (type I collagen, fibronectin, vitronectin, osteopontin, and bone sialoprotein), which contain at binding sites the RGD (Arg-Gly-Asp) sequence, together with receptor integrins, constitute an important recognition system for cell adhesion (Ruoslahti, 1996). Two of the selected studies (Germanier et al., 2006; Yang et al., 2009) investigated the effect of RGD coating by a layered self-assembly technique on porous surface implants, concluding that the peptides possess potential to transmit particular cell adhesion properties to Ti surfaces and are able to enhance cell-material interactions. Kroese-Deutman et al.

(Kroese-Deutman et al., 2005) used a porous Ti fiber mesh implant coated with the RGD peptide in the rabbit skull and compared it with porous Ti fiber mesh disks without the RGD sequence. Histological and histomorphometric examinations after 4 and 8 weeks showed a significant increase in bone growth in the RGD-Ti group compared to the control group.

BMPs belong to the transforming growth factor beta (TGF-β) family and are biological factors with a strong ability to induce bone, cartilage and connective tissue formation through the differentiation of bone mesenchymal stem cells (Dolanmaz et al., 2015b). They have been investigated as one of the growth factors (GF) that stimulate undifferentiated cells to become osteoblasts, with a certain ability to attract undifferentiated mesenchymal cells, regulating angiogenesis, chemotaxis and cell multiplication (Chang et al., 2010; Öncü and Alaaddinoğlu, 2015; Öncü et al., 2016). Numerous studies have reported that the use of BMPs improves the process of osteogenesis, osteoblast activity and osseointegration after dental implantation (Chen et al., 2004; Halloran et al., 2020). Nine of the reviewed studies (Wikesjö et al., 2008a; Wikesjö et al., 2008b; Wikesjö et al., 2008c; Ishibe et al., 2009; Ramazanoglu et al., 2011; Jiang et al., 2013; Kim et al., 2015; Yoo et al., 2015; Pang et al., 2021) used BMP-2 as a Ti implant coating. Wikesjö et al. used recombinant human bone morphogenetic protein-2 (rhBMP-2) in three studies and in different experimental models (Wikesjö et al., 2008a; Wikesjö et al., 2008b; Wikesjö et al., 2008c); in one study with non-human primates (Wikesjö et al., 2008c), they found that Ti surface coated with rhBMP-2 accelerated type IV bone formation; another study, in a canine model (Wikesjö et al., 2008b), based peri-implant bone remodeling on rhBMP-2 doses, reporting that sites receiving implants coated with rhBMP-2 at 3 mg/ml, showed increased formation of immature trabecular bone. On the contrary, the same authors in a third study, also on a canine model (Wikesjö et al., 2008a), demonstrated that rh BMP-2 at doses of 0.75 or 1.5 mg/ml, despite inducing osseointegration, did not increase BIC values, resulting significantly higher in the control group (uncoated Ti). Similarly, Ramazanoglu et al. (Ramazanoglu et al., 2011) found no increase in BIC in Ti implants with rhBMP-2 biomimetic coatings, despite inducing an improvement in peri-implant bone density.

Anitua et al. (Anitua et al., 2007; Anitua et al., 2009) proposed implant wetting with autologous growth factors, obtaining significant improvements in osseointegration. Lee et al. (Lee et al., 2010) reported that Ti porous oxide implants coated with rhBMP-2 significantly induce bone formation and remodeling, although they did not find significant effects according to the application techniques.

The ECM is a three-dimensional network, with an abundance of macromolecules, such as type I collagen, proteoglycans, laminin and fibronectin, which provides biochemical and structural support to surrounding cells (Daley and Yamada, 2013). It has been highlighted that ECM could affect the differentiation, survival and potentiality of mesenchymal stem cells (MSCs) by modulating the activity of growth factors and affecting cell behavior (Assis-Ribas et al., 2018). Feng et al. in a recent investigation (Feng et al., 2020) studied the behavior of MSC laminates, obtained by a decellularization process, on SLA-surfaced implants and demonstrated that they promoted adhesion, proliferation and osteogenic differentiation of bone marrow mesenchymal stem cells (BMSCs) *in vitro*, and improved osseointegration of implants *in vivo*. Shekaran and Garcia in a review study (Shekaran and García, 2011) highlighted the functionalization of implants with ECM peptides or proteins, to modulate host cell responses to the implant material and to enhance osseointegration and bone formation. They also observed that surfaces presenting the peptide Gly-Phe-Hyp-Gly-Glu-Arg (GFOGER), from the α1 chain of type I collagen, promote osteoblastic differentiation of primary bone marrow cells *in vitro*, and that GFOGER-functionalized titanium implants would improve implant integration in a rat cortical model by enhancing peri-implant bone formation and implant attachment to bone. Despite this, studies such as those by Hennessy et al. (Hennessy et al., 2009) disagree with these results, suggesting that collagen mimetic peptides would exclusively stimulate osteoblastic differentiation and that the beneficial effects would be due to the role of these peptides as differentiation rather than adhesion factors. Stadlinger et al. (Stadlinger et al., 2008; Stadlinger et al., 2012b) in two *in vivo* studies did not obtain variations in BIC at 4 and 8 weeks after cycloaddition in collagen-coated implants, finding only a slight increase in bone-to-implant contact around the implants that incorporated CS in the coating and observing that the additional inclusion of a low amount of rhBMP-4 had a detrimental 4meta-analysis had several limitations: first, different experimental models were used, suggesting different bone formation dynamics, especially in early healing times (Pearce et al., 2007; Wancket, 2015). These factors may influence the observed BIC values. Second, this meta-analysis focused only on three biomolecular coatings (peptides, BMPs, and ECMs), leaving out other bioactive coatings; moreover, the coatings in the different studies were not single coatings, but most resorted to combined coatings. Thirdly, the discrepant follow-up periods (2–84 weeks) and differences in the number of animals in the studies, could condition the results. Fourth, the various investigations analyzed several parameters indicative of bone neoformation and in our meta-analysis only BIC was chosen as a measure indicative of osseointegration (Albrektsson and Johansson, 2001; Gehrke et al., 2020).

5 Conclusion

In summary, the present meta-analysis revealed that the use of certain bioactive organic molecules seems to promote peri-implant bone formation, which could influence osseointegration during the early stages of healing; however, different factors make comparison between studies difficult and complicate the interpretation of the results on peri-implant bone formation. Nevertheless, in order to confirm the clinical applicability of these findings, in addition to a greater number of preclinical studies on suitable experimental models, clinical trials with prolonged follow-up periods would be necessary, since the results of preclinical experiments do not necessarily reflect the human clinical reality.

Data availability statement

The original contributions presented in the study are included in the article/Supplementary Material, further inquiries can be directed to the corresponding author.

Author contributions

Conceptualization, NL-V and JA; methodology, NL-V; formal analysis, NQ-L and AL-V; investigation, NL-V and JA; writing—original draft preparation AL-V; data curation, JA and CR; supervision, JA and AL-V. All authors have read and agreed to the published version of the manuscript. All authors have read and agreed to the published version of the manuscript.

Conflict of interest

The authors declare that the research was conducted in the absence of any commercial or financial relationships that could be construed as a potential conflict of interest.

Publisher's note

Supplementary material

The Supplementary Material for this article can be found online at: https://www.frontiersin.org/articles/10.3389/fbioe.2022.986112/full#supplementary-material

References

Albrektsson, T., and Johansson, C. (2001). Osteoinduction, osteoconduction and osseointegration. *Eur. Spine J.* 2 (2), S96–S101. doi:10.1007/s005860100282

Alghamdi, H. S., and Jansen, J. A. (2020). The development and future of dental implants. *Dent. Mat. J.* 39, 167–172. doi:10.4012/dmj.2019-140

Andrea, A., Molchanova, N., and Jenssen, H. (2018). Antibiofilm peptides and peptidomimetics with focus on surface immobilization. *Biomolecules* 8, 27. doi:10.3390/biom8020027

Andrea, A., Molchanova, N., and Jenssen, H. (2018). Antibiofilm peptides and peptidomimetics with focus on surface immobilization. *Biomolecules* 8, 27. doi:10.3390/biom8020027

Anitua, E., Orive, G., Pla, R., Roman, P., Serrano, V., and Andía, I. (2009). The effects of PRGF on bone regeneration and on titanium implant osseointegration in goats: A histologic and histomorphometric study. *J. Biomed. Mat. Res. A* 91, 158–165. doi:10.1002/jbm.a.32217

Anitua, E., Sánchez, M., Orive, G., and Andía, I. (2007). The potential impact of the preparation rich in growth factors (PRGF) in different medical fields. *Biomaterials* 28, 4551–4560. doi:10.1016/j.biomaterials.2007.06.037

Anitua, E. A. (2006). Enhancement of osseointegration by generating a dynamic implant surface. *J. Oral Implantol.* 32, 72–76. doi:10.1563/736.1

Assis-Ribas, T., Forni, M. F., Winnischofer, S. M. B., Sogayar, M. C., and Trombetta-Lima, M. (2018). Extracellular matrix dynamics during mesenchymal stem cells differentiation. *Dev. Biol. N. Y. 1985.* 437, 63–74. doi:10.1016/j.ydbio.2018.03.002

Badr, N., and Hadary, A. (2007). Hydroxyapatite-electroplated cp-titanium implant and its bone integration potentiality: An *in vivo* study. *Implant Dent.* 16, 297–308. doi:10.1097/ID.0b013e31805d7dc4

Bae, E. B., Yoo, J. H., Jeong, S. I., Kim, M. S., Lim, Y. M., Ahn, J. J., et al. (2018). Effect of titanium implants coated with radiation-crosslinked collagen on stability and osseointegration in rat tibia. *Materials* 11 (12), 2520. doi:10.3390/ma11122520

Barros, R. R., Novaes, A. B., Jr, Papalexiou, V., Souza, S. L., Taba, M., Jr, Palioto, D. B., et al. (2009). Effect of biofunctionalized implant surface on osseointegration: A histomorphometric study in dogs. *Braz. Dent. J.* 20, 91–98. doi:10.1590/s0103-64402009000200001

Bosco, R., Edreira, E. R. U., Wolke, J. G., Leeuwenburgh, S. C., van den Beucken, J. J., and Jansen, J. A. (2013). Instructive coatings for biological guidance of bone implants. *Surf. Coat. Technol.* 233, 91–98. doi:10.1016/j.surfcoat.2013.02.039

Cardoso, M. V., de Rycker, J., Chaudhari, A., Coutinho, E., Yoshida, Y., Van Meerbeek, B., et al. (2017). Titanium implant functionalization with phosphate-containing polymers may favour *in vivo* osseointegration. *J. Clin. Periodontol.* 44, 950–960. doi:10.1111/jcpe.12736

Cecconi, S., Mattioli-Belmonte, M., Manzotti, S., Orciani, M., Piccioli, A., and Gigante, A. (2014). Bone-derived titanium coating improves *in vivo* implant osseointegration in an experimental animal model. *J. Biomed. Mat. Res.* 102, 303–310. doi:10.1002/jbm.b.33008

Chang, P. C., Lang, N. P., and Giannobile, W. V. (2010). Evaluation of functional dynamics during osseointegration and regeneration associated with oral implants. *Clin. Oral Implants Res.* 21, 1–12. doi:10.1111/j.1600-0501.2009.01826.x

Chen, D., Zhao, M., and Mundy, G. R. (2004). Bone morphogenetic proteins. *Growth factors.* 22, 233–241. doi:10.1080/08977190412331279890

Cho, C. B., Jung, S. Y., Park, C. Y., Kang, H. K., Yeo, I. L., and Min, B. M. (2019). A vitronectin-derived bioactive peptide improves bone healing capacity of SLA titanium surfaces. *Mater. (Basel)* 12 (20), 3400. doi:10.3390/ma12203400

Cho, W. T., Kim, S. Y., Jung, S. I., Kang, S. S., Kim, S. E., Hwang, S. H., et al. (2021). Effects of gamma radiation-induced crosslinking of collagen type I coated dental titanium implants on osseointegration and bone regeneration. *Mater. (Basel)* 14 (12), 3268. doi:10.3390/ma14123268

Cooper, L., Zhou, Y., Takebe, J., Guo, J., Abron, A., Holmen, A., et al. (2006). Fluoride modification effects on osteoblast behavior and bone formation at TiO grit-blasted c.p. titanium endosseous implants. *Biomaterials* 27, 926–936. doi:10.1016/j.biomaterials.2005.07.009

Daley, W. P., and Yamada, K. M. (2013). ECM-modulated cellular dynamics as a driving force for tissue morphogenesis. *Curr. Opin. Genet. Dev.* 23, 408–414. doi:10.1016/j.gde.2013.05.005

Dolanmaz, D., Saglam, M., Inan, O., Dundar, N., Alniacık, G., Gursoy Trak, B., et al. (2015). Monitoring bone morphogenetic protein-2 and -7, soluble receptor activator of nuclear factor-κB ligand and osteoprotegerin levels in the peri-implant sulcular fluid during the osseointegration of hydrophilic-modified sandblasted acid-etched and sandblaste. *J. Periodontal Res.* 50, 62–73. doi:10.1111/jre.12182

Drexelius, M. G., and Neundorf, I. (2021). Application of antimicrobial peptides on biomedical implants: Three ways to pursue peptide coatings. *Int. J. Mol. Sci.* 22, 13212. doi:10.3390/ijms222413212

Ellingsen, J., Johansson, C., Wennerberg, A., and Holmén, A. (2004). Improved retention and bone-tolmplant contact with fluoride-modified titanium implants. *Int. J. Oral Maxillofac. Implants* 19, 659–666.

Feng, Y., Jiang, Z., Zhang, Y., Miao, X., Yu, Q., Xie, Z., et al. (2020). Stem-cell-derived ECM sheet-implant complexes for enhancing osseointegration. *Biomater. Sci.* 8, 6647–6656. doi:10.1039/d0bm00980f

Fischer, N. G., Münchow, E. A., Tamerler, C., Bottino, M. C., and Aparicio, C. (2020). Harnessing biomolecules for bioinspired dental biomaterials. *J. Mat. Chem. B* 8, 8713–8747. doi:10.1039/d0tb01456g

Garcia, A. J., and Reyes, C. D. (2005). Bio-adhesive surfaces to promote osteoblast differentiation and bone formation. *J. Dent. Res.* 84, 407–413. doi:10.1177/154405910508400502

Gehrke, S. A., AramburúJúnior, J., Pérez-Díaz, L., do Prado, T. D., Dedavid, B. A., Mazon, P., et al. (2020). Can changes in implant macrogeometry accelerate the osseointegration process?: An *in vivo* experimental biomechanical and histological evaluations. *PLoS One* 15 (5), e0233304. doi:10.1371/journal.pone.0233304

Germanier, Y., Tosatti, S., Broggini, N., Textor, M., and Buser, D. (2006). Enhanced bone apposition around biofunctionalized sandblasted and acid-etched titanium implant surfaces. A histomorphometric study in miniature pigs. *Clin. Oral Implants Res.* 17, 251–257. doi:10.1111/j.1600-0501.2005.01222.x

Giro, G., Gonçalves, D., Sakakura, C. E., Pereira, R. M., Marcantonio Júnior, E., and Orrico, S. R. (2008). Influence of estrogen deficiency and its treatment with alendronate and estrogen on bone density around osseointegrated implants: Radiographic study in female rats. *Oral Surg. Oral Med. Oral Pathology Oral Radiology Endodontology* 105, 162–167. doi:10.1016/j.tripleo.2007.06.010

Goiato, M. C., Pellizzer, E. P., dos Santos, D. M., Barão, V. A., de Carvalho, B. M., Magro-Filho, O., et al. (2009). Clinical viability of immediate loading of dental implants: Part I-factors for success. *J. Craniofac. Surg.* 20, 2 139–2142. doi:10.1097/SCS.0b013e3181bec71a

Halloran, D., Durbano, H. W., and Nohe, A. (2020). Bone morphogenetic protein-2 in development and bone homeostasis. *J. Dev. Biol.* 8, 19. doi:10.3390/jdb8030019

Hennessy, K. M., Pollot, B. E., Clem, W. C., Phipps, M. C., Sawyer, A. A., Culpepper, B. K., et al. (2009). The effect of collagen I mimetic peptides on mesenchymal stem cell adhesion and differentiation, and on bone formation at hydroxyapatite surfaces. *Biomaterials* 30, 1898–1909. doi:10.1016/j.biomaterials.2008.12.053

Hooijmans, C. R., Rovers, M. M., de Vries, R. B., Leenaars, M., Ritskes-Hoitinga, M., and Langendam, M. W. (2014). SYRCLE's risk of bias tool for animal studies. *BMC Med. Res. Methodol.* 14, 43. doi:10.1186/1471-2288-14-43

Hubbell, J. A. (1999). Bioactive biomaterials. *Curr. Opin. Biotechnol.* 10, 123–129. doi:10.1016/s0958-1669(99)80021-4

Hutton, B., Catalá-López, F., and Moher, D. (2016). The PRISMA statement extension for systematic reviews incorporating network meta-analysis: PRISMA-NMA. *Med. Clin.* 147 (6), 262–266. doi:10.1016/j.medcli.2016.02.025

Ishibe, T., Goto, T., Kodama, T., Miyazaki, T., Kobayashi, S., and Takahashi, T. (2009). Bone formation on apatite-coated titanium with incorporated BMP-2/heparin *in vivo*. *Oral Surg. Oral Med. Oral Pathology Oral Radiology Endodontology* 108, 867–875. doi:10.1016/j.tripleo.2009.06.039

Jiang, Q. H., Liu, L., Peel, S., Yang, G. L., Zhao, S. F., and He, F. M. (2013). Bone response to the multilayer BMP-2 gene coated porous titanium implant surface. *Clin. Oral Implants Res.* 24, 853–861. doi:10.1111/j.1600-0501.2011.02383.x

Junker, R., Dimakis, A., Thoneick, M., and Jansen, J. A. (2009). Effects of implant surface coatings and composition on bone integration: A systematic review. *Clin. Oral Implants Res.* 20 (4), 185–206. doi:10.1111/j.1600-0501.2009.01777.x

Kang, H. K., Kim, O. B., Min, S. K., Jung, S. Y., Jang, D. H., Kwon, T. K., et al. (2013). The effect of the DLTIDDSYWYRI motif of the human laminin α2 chain on implant osseointegration. *Biomaterials* 34, 4027–4037. doi:10.1016/j.biomaterials.2013.02.023

Kim, N. H., Lee, S. H., Ryu, J. J., Choi, K. H., and Huh, J. B. (2015). Effects of rhBMP-2 on sandblasted and acid etched titanium implant surfaces on bone regeneration and osseointegration: Spilt-mouth designed pilot study. *Biomed. Res. Int.* 2015, 1–11. doi:10.1155/2015/459393

Korn, P., Schulz, M. C., Hintze, V., Range, U., Mai, R., Eckelt, U., et al. (2014). Chondroitin sulfate and sulfated hyaluronan-containing collagen coatings of titanium implants influence peri-implant bone formation in a minipig model. *J. Biomed. Mat. Res. A* 102, 2334–2344. doi:10.1002/jbm.a.34913

Kroese-Deutman, H. C., van den Dolder, J., Spauwen, P. H., and Jansen, J. A. (2005). Influence of RGD-loaded titanium implants on bone formation *in vivo*. *Tissue Eng.* 11 (11-12), 1867–1875. doi:10.1089/ten.2005.11.1867

Le Guéhennec, L., Soueidan, A., Layrolle, P., and Amouriq, Y. (2007). Surface treatments of titanium dental implants for rapid osseointegration. *Dent. Mat.* 23, 844–854. doi:10.1016/j.dental.2006.06.025

Lee, J., Decker, J. F., Polimeni, G., Cortella, C. A., Rohrer, M. D., Wozney, J. M., et al. (2010). Evaluation of implants coated with rhBMP-2 using two different coating strategies: A critical-size supraalveolar peri-implant defect study in dogs. *J. Clin. Periodontol.* 37, 582–590. doi:10.1111/j.1600-051X.2010.01557.x

Lee, S. W., Hahn, B. D., Kang, T. Y., Lee, M. J., Choi, J. Y., Kim, M. K., et al. (2014). Hydroxyapatite and collagen combination-coated dental implants display better bone formation in the peri-implant area than the same combination plus bone morphogenetic protein-2-coated implants, hydroxyapatite only coated implants, and uncoated implants. *J. Oral Maxillofac. Surg.* 72, 53–60. doi:10.1016/j.joms.2013.08.031

Lemons, J. E. (2004). Biomaterials, biomechanics, tissue healing, and immediate-function dental implants. *J. Oral Implantol.* 30, 318–324. doi:10.1563/0712.1

Lutz, R., Srour, S., Nonhoff, J., Weisel, T., Damien, C. J., and Schlegel, K. A. (2010). Biofunctionalization of titanium implants with a biomimetic active peptide (P-15) promotes early osseointegration. *Clin. Oral Implants Res.* 21, 726–734. doi:10.1111/j.1600-0501.2009.01904.x

Lutz, R., Srour, S., Nonhoff, J., Weisel, T., Damien, C. J., and Schlegel, K. A. (2010). Biofunctionalization of titanium implants with a biomimetic active peptide (P-15) promotes early osseointegration. *Clin. Oral Implants Res.* 21, 726–734. doi:10.1111/j.1600-0501.2009.01904.x

Makihira, S., Nikawa, H., Shuto, T., Nishimura, M., Mine, Y., Tsuji, K., et al. (2011). Evaluation of trabecular bone formation in a canine model surrounding a dental implant fixture immobilized with an antimicrobial peptide derived from histatin. *J. Mat. Sci. Mat. Med.* 22, 2765–2772. doi:10.1007/s10856-011-4440-2

Moraschini, V., Poubel, L. A., Ferreira, V. F., and Barboza Edos, S. (2015). Evaluation of survival and success rates of dental implants reported in longitudinal studies with a follow-up period of at least 10 years: A systematic review. *Int. J. Oral Maxillofac. Surg.* 44, 377–388. doi:10.1016/j.ijom.2014.10.023

Moussa, D. G., and Aparicio, C. (2020). Targeting the oral plaque microbiome with immobilized anti-biofilm peptides at tooth-restoration interfaces. *PLoS One* 15 (7), e0235283. doi:10.1371/journal.pone.0235283

Narai, S., and Nagahata, S. (2003). Effects of alendronate on the removal torque of implants in rats with induced osteoporosis. *Int. J. Oral Maxillofac. Implants* 18, 218–223.

Öncü, E., and Alaaddinoğlu, E. E. (2015). The effect of platelet-rich fibrin on implant stability. *Int. J. Oral Maxillofac. Implants* 30, 578–582. doi:10.11607/jomi.3897

Öncü, E., Bayram, B., Kantarci, A., Gülsever, S., and Alaaddinoğlu, E. E. (2016). Positive effect of platelet rich fibrin on osseointegration. *Med. Oral Patol. Oral Cir. Bucal* 21 (5), e601–e607. doi:10.4317/medoral.21026

Osman, R. B., and Swain, M. V. (2015). A critical review of dental implant materials with an emphasis on titanium versus zirconia. *Mater. (Basel)* 8, 932–958. doi:10.3390/ma8030932

Panayotov, I. V., Vladimirov, B. S., Dutilleul, P. Y., Levallois, B., and Cuisinier, F. (2015). Strategies for immobilization of bioactive organic molecules on titanium implant surfaces - a review. *Folia Med. Plovdiv.* 57, 11–18. doi:10.1515/folmed-2015-0014

Pang, K., Seo, Y. K., and Lee, J. H. (2021). Effects of the combination of bone morphogenetic protein-2 and nano-hydroxyapatite on the osseointegration of dental implants. *J. Korean Assoc. Oral Maxillofac. Surg.* 47, 454–464. doi:10.5125/jkaoms.2021.47.6.454

Pearce, A. I., Richards, R. G., Milz, S., Schneider, E., and Pearce, S. G. (2007). Animal models for implant biomaterial research in bone: A review. *Eur. Cell. Mat.* 13, 1–10. doi:10.22203/ecm.v013a01

Polimeni, G., Wikesjö, U. M., Susin, C., Qahash, M., Shanaman, R. H., Prasad, H. S., et al. (2010). Alveolar ridge augmentation using implants coated with recombinant human growth/differentiation factor-5: Histologic observations. *J. Clin. Periodontol.* 37, 759–768. Epub 2010 May 25. doi:10.1111/j.1600-051X.2010.01579.x

Puleo, D. A., and Nanci, A. (1999). Understanding and controlling the bone-implant interface. *Biomaterials* 20 (23-24), 2311–2321. doi:10.1016/s0142-9612(99)00160-x

Ramazanoglu, M., Lutz, R., Ergun, C., von Wilmowsky, C., Nkenke, E., and Schlegel, K. A. (2011). The effect of combined delivery of recombinant human bone morphogenetic protein-2 and recombinant human vascular endothelial growth factor 165 from biomimetic calcium-phosphate-coated implants on osseointegration. *Clin. Oral Implants Res.* 22 (12), 1433–1439. doi:10.1111/j.1600-0501.2010.02133.x

Raphel, J., Karlsson, J., Galli, S., Wennerberg, A., Lindsay, C., Haugh, M. G., et al. (2016). Engineered protein coatings to improve the osseointegration of dental and orthopaedic implants. *Biomaterials* 83, 269–282. doi:10.1016/j.biomaterials.2015.12.030

Riool, M., de Breij, A., Drijfhout, J. W., Nibbering, P. H., and Zaat, S. A. J. (2017). Antimicrobial peptides in biomedical device manufacturing. *Front. Chem.* 5, 63. doi:10.3389/fchem.2017.00063

Ruoslahti, E. (1996). RGD and other recognition sequences for integrins. *Annu. Rev. Cell Dev. Biol.* 12, 697–715. doi:10.1146/annurev.cellbio.12.1.697

Russell, R. G. G., Watts, N. B., Ebetino, F. H., and Rogers, M. J. (2008). Mechanisms of action of bisphosphonates: Similarities and differences and their potential influence on clinical efficacy. *Osteoporos. Int.* 19, 733–759. doi:10.1007/s00198-007-0540-8

Shekaran, A., and García, A. J. (2011). Extracellular matrix-mimetic adhesive biomaterials for bone repair. *J. Biomed. Mat. Res. A* 96, 261–272. doi:10.1002/jbm.a.32979

Silva, R. R., Avelino, K. Y., Ribeiro, K. L., Franco, O. L., Oliveira, M. D., and Andrade, C. A. (2016). Chemical immobilization of antimicrobial peptides on biomaterial surfaces. *Front. Biosci.* 8, 453–142. doi:10.2741/s453

Siwakul, P., Sirinnaphakorn, L., Suwanprateep, J., Hayakawa, T., and Pugdee, K. (2021). Cellular responses of histatin-derived peptides immobilized titanium surface using a tresyl chloride-activated method. *Dent. Mat. J.* 40, 307–941. doi:10.4012/dmj.2020-307

Stadlinger, B., Hintze, V., Bierbaum, S., Möller, S., Schulz, M. C., Mai, R., et al. (2012). Biological functionalization of dental implants with collagen and glycosaminoglycans-A comparative study. *J. Biomed. Mat. Res.* 100 (2), 331–341. doi:10.1002/jbm.b.31953

Stadlinger, B., Pilling, E., Huhle, M., Mai, R., Bierbaum, S., Scharnweber, D., et al. (2008). Evaluation of osseointegration of dental implants coated with collagen, chondroitin sulphate and BMP-4: An animal study. *Int. J. Oral Maxillofac. Surg.* 37, 54–59. doi:10.1016/j.ijom.2007.05.024

Stadlinger, B., Pourmand, P., Locher, M. C., and Schulz, M. C. (2012). Systematic review of animal models for the study of implant integration, assessing the influence of material, surface and design. *J. Clin. Periodontol.* 39, 28–36. doi:10.1111/j.1600-051x.2011.01835.x

Stanford, C. M. (2008). Surface modifications of dental implants. *Aust. Dent. J.* 53 (1), S26–S33. doi:10.1111/j.1834-7819.2008.00038.x

Susin, C., Qahash, M., Polimeni, G., Lu, P. H., Prasad, H. S., Rohrer, M. D., et al. (2010). Alveolar ridge augmentation using implants coated with recombinant human bone morphogenetic protein-7 (rhBMP-7/rhOP-1): Histological observations. *J. Clin. Periodontol.* 37, 574–581. doi:10.1111/j.1600-051X.2010.01554.x

Sverzut, A. T., Crippa, G. E., Morra, M., de Oliveira, P. T., Beloti, M. M., and Rosa, A. L. (2012). Effects of type I collagen coating on titanium osseointegration: Histomorphometric, cellular and molecular analyses. *Biomed. Mat.* 7 (3), 035007. doi:10.1088/1748-6041/7/3/035007

Viera-Negron, Y. E., Ruan, W. H., Winger, J. N., Hou, X., Sharawy, M. M., and Borke, J. L. (2008). Effect of ovariectomy and alendronate on implant osseointegration in rat maxillary bone. *J. Oral Implantol.* 34, 76–82. doi:10.1563/1548-1336(2008)34[76:EOOAAO]2.0.CO;2

Wancket, L. M. (2015). Animal models for evaluation of bone implants and devices: Comparative bone structure and common model uses. *Vet. Pathol.* 52, 842–850. doi:10.1177/0300985815593124

Wikesjö, U. M., Huang, Y. H., Xiropaidis, A. V., Sorensen, R. G., Rohrer, M. D., Prasad, H. S., et al. (2008). Bone formation at recombinant human bone morphogenetic protein-2-coated titanium implants in the posterior maxilla (Type IV bone) in non-human primates. *J. Clin. Periodontol.* 35, 992–1000. doi:10.1111/j.1600-051X.2008.01322.x

Wikesjö, U. M., Qahash, M., Polimeni, G., Susin, C., Shanaman, R. H., Rohrer, M. D., et al. (2008). Alveolar ridge augmentation using implants coated with recombinant human bone morphogenetic protein-2: Histologic observations. *J. Clin. Periodontol.* 35, 1001–1010. doi:10.1111/j.1600-051X.2008.01321.x

Wikesjö, U. M., Xiropaidis, A. V., Qahash, M., Lim, W. H., Sorensen, R. G., Rohrer, M. D., et al. (2008). Bone formation at recombinant human bone morphogenetic protein-2-coated titanium implants in the posterior mandible (Type II bone) in dogs. *J. Clin. Periodontol.* 35, 985–991. doi:10.1111/j.1600-051X.2008.01318.x

Xuereb, M., Camilleri, J., and Attard, N. J. (2015). Systematic review of current dental implant coating materials and novel coating techniques. *Int. J. Prosthodont.* 28, 51–59. doi:10.11607/ijp.4124

Yang, G. L., He, F. M., Yang, X. F., Wang, X. X., and Zhao, S. F. (2009). *In vivo* evaluation of bone-bonding ability of RGD-coated porous implant using layer-by-layer electrostatic self-assembly. *J. Biomed. Mat. Res. A* 90, 175–185. doi:10.1002/jbm.a.32055

Yoo, S. Y., Kim, S. K., Heo, S. J., Koak, J. Y., Lee, J. H., and Heo, J. M. (2015). Biochemical responses of anodized titanium implants with a poly(lactide-co-glycolide)/bone morphogenetic protein-2 submicron particle coating. Part 2: An *in vivo* study. *Int. J. Oral Maxillofac. Implants* 30, 754–760. doi:10.11607/jomi.3701b

Zagury, R., Harari, N., Conz, M., Soares, A., and Vidigal, G. (2007). Histomorphometric analyses of bone interface with titanium-aluminum-vanadium and hydroxyapatite- coated implants by biomimetic process. *Implant Dent.* 16, 290–296. doi:10.1097/ID.0b013e3180e9d9ed

Zhang, X., Geng, H., Gong, L., Zhang, Q., Li, H., Zhang, X., et al. (2018). Modification of the surface of titanium with multifunctional chimeric peptides to prevent biofilm formation via inhibition of initial colonizers. *Int. J. Nanomedicine* 13, 5361–5375. doi:10.2147/IJN.S170819

Frontiers in Bioengineering and Biotechnology

TYPE Review
PUBLISHED 29 September 2022
DOI 10.3389/fbioe.2022.950235

OPEN ACCESS

EDITED BY
Yuangang Liu,
Huaqiao University, China

REVIEWED BY
Jie Zheng,
University of Akron, United States
Hong-Hui Wang,
Hunan University, China

*CORRESPONDENCE
Ting Wang,
tingwang@seu.edu.cn

SPECIALTY SECTION
This article was submitted
to Biomaterials,
a section of the journal
Frontiers in Bioengineering
and Biotechnology

RECEIVED 22 May 2022
ACCEPTED 12 September 2022
PUBLISHED 29 September 2022

CITATION
Zhang J, Wang T, Zhang Y, Lu P, Shi N,
Zhu W, Cai C and He N (2022), Soft
integration of a neural cells network and
bionic interfaces.
Front. Bioeng. Biotechnol. 10:950235.
doi: 10.3389/fbioe.2022.950235

Soft integration of a neural cells network and bionic interfaces

Jixiang Zhang[1], Ting Wang[1,2]*, Yixin Zhang[1], Pengyu Lu[1], Neng Shi[1], Weiran Zhu[3], Chenglong Cai[1,2] and Nongyue He[1]

[1]State Key Laboratory of Bioelectronics, National Demonstration Centre for Experimental Biomedical Engineering Education, School of Biological Science and Medical Engineering, Southeast University, Nanjing, China, [2]Southeast University Jiangbei New Area Innovation Institute, Nanjing, China, [3]SceneRay Co., Ltd., Suzhou, China

Both glial cells and neurons can be considered basic computational units in neural networks, and the brain–computer interface (BCI) can play a role in awakening the latency portion and being sensitive to positive feedback through learning. However, high-quality information gained from BCI requires invasive approaches such as microelectrodes implanted under the endocranium. As a hard foreign object in the aqueous microenvironment, the soft cerebral cortex's chronic inflammation state and scar tissue appear subsequently. To avoid the obvious defects caused by hard electrodes, this review focuses on the bioinspired neural interface, guiding and optimizing the implant system for better biocompatibility and accuracy. At the same time, the bionic techniques of signal reception and transmission interfaces are summarized and the structural units with functions similar to nerve cells are introduced. Multiple electrical and electromagnetic transmissions, regulating the secretion of neuromodulators or neurotransmitters *via* nanofluidic channels, have been flexibly applied. The accurate regulation of neural networks from the nanoscale to the cellular reconstruction of protein pathways will make BCI the extension of the brain.

KEYWORDS

brain–computer interface, neural network, glia cell, biointerface, nanoparticle, neuromodulation, bioinspired design

Introduction

The ecosystem of a neural network is composed of neurons and glial cells immersed in an extracellular matrix, and they are extensively connected in the brain. The nucleus, ganglia, and cerebral cortex form an interconnected network (Bostan and Strick, 2018; Greene et al., 2020). Changes in the organization of functional connections allow information to be analyzed and processed, and thus the neural network appears in the brain. The generation of neural networks and signal transmission processes are closely related to electrical and chemical signals. Consciousness and intelligence were considered to be hidden behind the largely associated and well-organized information networks, which have dynamic parallel storage and analysis functions. To better understand the neural network and cure brain diseases, integrated brain–computer interfaces (BCIs) to perform afferent and efferent functions were developed. BCIs could not only replace injured sense organs and improve motor debilities, such as stroke rehabilitation (Biasiucci et al., 2018) that translate neural intentions into movement and are helpful in amyotrophic lateral sclerosis, but also can modulate emotions and memories and monitor brain health, such as tumorigenesis and stroke risks. The BCI plays a core role in mapping neural signals. However, hard BCI brain electrodes can cause a lot of damage to brain tissue, such as scars and inflammation. In this study, we will discuss the ways to realize the bionic neural network information interface, overcoming the long-term defects of scar tissue and losing control of lacking environmental interactions.

Noninvasive BCI systems based on electroencephalogram (EEG) signals will be a strategy to overcome the long-term defects of scar tissue and inflammation. Because of their penetration of the skull through various energy and information patterns, the brain electrode contact interface can be exploited on the knowledge of the original brain physiology. However, their less precision to interact with brain networks led to unsuccessfully applied for precisely timed control tasks. Other noninvasive detections are based on the nutrients sensitive to neurons and blood flow to oxy and deoxygenated hemoglobin; functional magnetic resonance imaging (fMRI) as well as functional near-infrared spectroscopy (fNIRS) are favorable neuroimaging modalities. They are commonly used for confirming brain areas of a functional population of neurons that have coordinated activities in noninvasive BCI systems (Golub et al., 2018).

A more accurate way to effectively find targeted nerve nuclei and observe the patient's response to stimulation was combined using deep brain stimulation and transcranial magnetic stimulation. TMS uses a pulsed magnetic field to influence the membrane potential of nerve cells, causing them to produce induced currents, affecting brain metabolism and electrical activity. DBS records the characteristics of different depths and orbits of the brain to find targeted nerve nuclei and observe the patient's response to stimulation. This EEG scan not only allows the surgeon to pinpoint the right target to place the electrode but it can also serve as a source of energy and information for intracranial implantable therapy. The neural population dynamics based on the aforementioned technology inform the implantation of BCI systems in the functional units of the brain's nucleus and subregions (Trautmann et al., 2021). After that, learning models can effectively meet the demand for the large amount of homogeneous training data (Khalil et al., 2022).

The materials such as intracerebral nano-implants for the brain–computer interface mean a type of information penetration technology. The skull can be penetrated by optical and magnetic approaches, and the afferent and efferent information of the neural network can be realized by the information conversion from the implant to control the action potential of neurons. Nanomaterials have unique characteristics such as similar dimensions to neural functional structures and higher spatiotemporal precision for seamless integration (Yang et al., 2021), biocompatibility, and electrically conductive, as well as energy and information conversion (Chen et al., 2018; Liu et al., 2021). However, its safety to the nervous system remains to be evaluated (Xu et al., 2021). In detail, the instantaneous neuron voltage change caused by action potential is determined by the ion concentration on both sides of the plasma membrane, which carries information by spike potential frequency and can be simplified and presented digitally as the highest fidelity of extra-neural messages. To maintain ionic gradients and then achieve interface digitalization, an energy-consuming process, a constant supply of glucose and oxygen is required for neurons. To achieve digitization, it is important to maintain nutrient supply or to regulate interface nutrient supply because of the maintenance of ion charge gradients during this process.

Apart from the biphase actions of nanoparticles for neurons, glial cells' chemotaxis (Rostene et al., 2007), tissue damage, and inflammation limit the BCI's long-term stability, especially in tracking single neuronal activity (Gu et al., 2021). A biocompatible and perdurable BCI requires chemical, mechanical, and physiological properties of the interface to match the structure and function of the neural network. When it comes to the modifications of the arrays, probes and nanoparticles systems, functional groups, and peptides, modular mechanical, neuromorphic, roughness, and density are supposed to be considered to live with the brain network's cell potential difference of the brain network, hydrophobic lipid membrane, and aqueous environment (Terstappen et al., 2021). Only the integration of neural networks and artificial BCIs can form a long-term brain–computer interface system through the influence of synapses and the reduction of inflammatory responses and chemotaxis of glial cells, such as mimicking synaptic release and enzyme reactions, reducing inflammatory responses, and antagonizing glial chemotaxis. The problem can be ameliorated with anti-inflammatory hormones, and some protein molecules such as enzymes and regulatory factors that have pharmacological effects also need to be considered when connected to neural networks.

Internal information exchanges also stimulate the fusion of the interface and lead to an increase in functional connectivity such as coupling to neurotransmitters or functional electrical stimulation (Biasiucci et al., 2018). The brain is not just layers of cell islands but an intricate relation in different aspects of the nervous system and the overall body. The network receives various kinds of message and constantly modulates itself. The feedback reward system generally exists in the brain for behavior encouragement, strengthened by the release of dopamine. In addition, glutamate is the most common neurotransmitter in neural networks, as a rapid excitatory synaptic connection between two neurons and slowly shaping neuroplasticity related to neuronal development, such as learning and memory. These substances have a simple biosynthetic process, release frequently, and diffuse across the synaptic cleft. Receptors selectively bind to these chemicals and function as changing

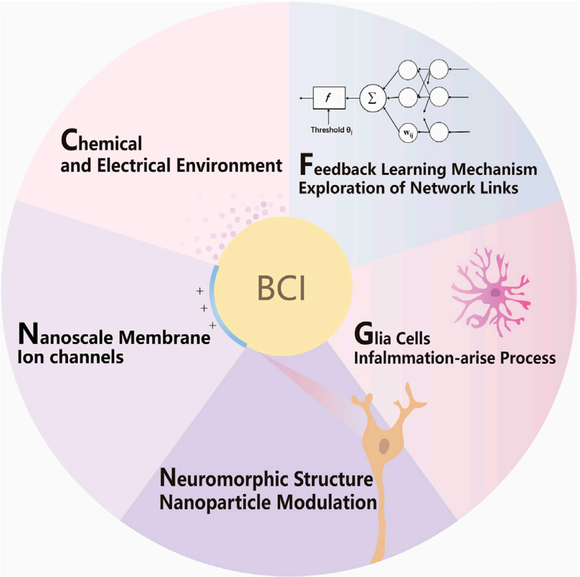

FIGURE 1
Schematic of strategies for molecular, cellular, and network modulation of BCI.

postsynaptic neurons in either excitation or inhibitory way, depolarizing or repolarizing, respectively. These are the zero and ones that have inner similarities to electronic signals, and they will be influenced by the features and chemical environment of neuron interfaces, nanoscale membrane and ion channels, nanoparticle interfaces, glial cells, inflammation-arise process, feedback learning mechanism, and exploration of network links. Accordingly, five aspects of neural network and interface system integration are proposed to promote digital connection to the brain in the following (Figure 1).

As shown in Figure 1, by better fitting bionic interfaces and modulating glial inflammatory responses, researchers can achieve functional manipulation and information reception on single-cell functional systems, thus achieving the purpose of brain–computer interaction bi-directionally and treatment of neurological diseases. The key points are as follows: features and chemical environment of neuron interfaces, nanoscale membrane and ion channels, nanoparticle interfaces, glial cells, inflammation-arise process, feedback learning mechanism, and exploration of network links; a detailed description will be expanded one after another.

Features and chemical environment of neuron interfaces

Stabilization inside and outside the cell is based on concentration gradients and ionic gradients, which are influenced by chemical signals, electrical signals, and nutrition. The homeostasis of the neural environment meets the high metabolic demand due to the blood–brain barrier (BBB) and neurovascular coupling, performing selective substance transport; the latter make sure the activated neural regions with adequate nutrients and acidic metabolites are removed by increased blood flow (Kaplan et al., 2020). In addition, a stable and nutrient-rich internal environment, signal stimulation, and glial microenvironment regulation are the key links to the neuron's survival, especially near the critical interface regions. For example, as a neurotransmitter, dopamine could contribute to the reward system by affecting synaptic conditioning and plasticity, and thus regulate learning, motion control, and moods. At this point, regulation of synaptic weights has been achieved utilizing the neuromorphic interface design and simulation of the dopamine recycle in the synaptic cleft (Keene et al., 2020).

For electrodes, cellular metabolism is associated with the bioelectrochemical process, and certain molecular structures significantly affect electron transfer and absorbed forms. Electrons are transferred to one-electron molecule receptors, such as cytochrome C, to a macroscopic electrode (Bollella & Katz, 2020). The electrostatic attraction of protein residues to the electrode surface with opposite polarity resulted in the fixation of proteins in an electrically active orientation, which promoted direct electron transfer between the redox center and the electrode (Bollella & Katz, 2020). Neuronal morphology electronics with better biocompatibility and relatively low mechanical modulus can imitate subcellular structural features and mechanical properties such as synapse formation and membrane potential. For example, the artificial synapse takes advantage of the dopamine feedback to strengthen the mechanism. The exocytose dopamine at the presynaptic end can be oxidized locally at the postsynaptic gate electrode, resulting in the charge state alteration of the gate electrode and inducing ion flow in the aqueous electrolyte (Yang et al., 2019; Keene et al., 2020; Wei et al., 2021).

As advanced electrodes are much preferred to abandon the hard electrode mode, hydrogels can be used as BCI substrates to simulate the brain's internal environment. Similar mechanical, chemical, and electrical properties effectively reduce the inflammatory response of tissue damage and glial cell aggregation, which is suitable for long-term invasive BMI. The bioadhesive ensures seamless contact with the neuronal network and thus serve as interface materials recording high-quality local field potentials and individual spikes, colocating transmitting laser waveguide stimulation, tin-made microelectrode recording, and fluidic channels such as optic fibers, ionic, electric, and chemical regulation conductor hybrid. In addition, the hardness of the hydrogel varies at different temperatures or hydrate levels, which allows for different shapes and hardness during and after the implantation operation (Sheng et al., 2019; Park et al., 2021). Such BMI can be manufactured by a self-setting process of hydrogel on a microelectrode array (Wang et al., 2022) or the brain tissue surface. Neural interface hydrogels are available in a variety of formulations. Polyethylene glycol and artificial cerebrospinal fluid hydrogels are stretchable, transparent, and ionic conductors and can be made into both ionotropic and optical fibers. In addition, it is reported that polyethylene glycol also has been used to culture neurons for providing a similar environment (Sheng et al., 2019). Furthermore, hydrophilic ultra-small conductive polymer nanoparticles were introduced into the carrageenan–polydopamine–polyacrylamide network. In addition, multifunctional sensing and actuation hydrogel matrix BCI systems are mixed with multimaterial fibers with adaptive bending stiffness adjusted by hydration states. These hydrogel-based brain–computer interfaces are expected to be able to conduct light, electricity, and molecules all at once (Park et al., 2021). Meanwhile, for high conductivity, extensibility, low modulus, and excellent mechanical and electrical stability, catechol functional groups were introduced into the hydrogel to avoid body rejection reaction (Wang et al., 2022), at the same time poly (3,4-ethylene dioxythiophene), poly (styrene sulfonate), or poly (ethylenimine) and partially reduced graphene oxide surface are used for the conductive hydrogel (van de Burgt et al., 2017; Lee et al., 2019; Keene et al., 2020).

Furthermore, widely applied chemogenetics and optogenetics with high cell-type specificity regulating the ion channel structure and potential polarity change can use polyacrylamide hydrogel as optical fibers, performing colocating the site of stimulation and recording. For example, hydrogel, as a soft material with lower glial scars and immune response, could simultaneously stimulate and record neurons utilizing optogenetics (Sheng et al., 2019). Furthermore, cellular-scale semiconductor devices, consisting of light-emitting diodes, actuators, sensors, and silicon devices, can operate precisely in actuation and sensing (Kim et al., 2013).

Nanoscale membrane and ion channels

From the abundant cerebral sulcus to the dendritic spines, certain thresholds are distributed over a wide range of neuronal cell projections. The thresholds on the membrane surface allow the brain to have unique functions. Establishing connections for synaptic-level fusion is the goal to achieve brain–machine interactions. In the change of energy and matter, the membrane is the center of information that can ion flow, electric field change, and other neuron-recognizable information to stimulate the membrane structure, and thus generate artificial neural pathways. Cell membrane regions are basic neural network units for analyzing and transforming information logically, where specialized, and are mainly composed of ion channels and receptor proteins. Key chemical microenvironment, mobility, and ionic gradients are relevant to redox processes, nutrient conversion, enzyme catalysis, glial cell guidance, and ion channels.

The large extension of the neuronal plasma membrane determines polarity conduction and signal processing, where specialized, and are mainly composed of ion channels and receptor proteins. Regarding neurons and glial cells as distributed parallel information processing units, their natural responsivity to various electric stimulus frequencies and chemicals in the membrane structure and aqueous media is performed by protein structure regulation. Interfacing directly with living networks is more than signal acquisition and feedback. Functional membrane structure regulation is also required *via* biochemical signaling activity.

The brain–machine interfaces can intervene in cellular signaling by influencing ion flow across membranes, and the membrane structures of brain cells are rich in function. Neurons and glial cells are just circuit boards or skeletons; specific protein structures are the logic elements on the membrane, such as synaptic structure, receptors, and ion channels. Liquid-ordered microdomains with proteins and lipids called lipid rafts are the basic units, the targets of signal acquisition and intervention, and the smallest regions performing computational functions. Glial cells regulate neuronal membrane proteins through secretion and lipid raft region of glial cells themselves, and neuroglial interactions may also be involved in nervous system functions. These channels, receptors, and enzyme proteins could interact with electrodes. For example, redox enzymes can achieve electronic communication with conductive electrodes *via* electrical, electrochemical, electron transfer mediators cyclic, and direct electron transfer from an enzyme active center to an electrode, and current is generated (Bollella and Katz, 2020).

On the basis of the proximity modulation of the membrane structure, the simulated ion circuit can utilize microfluidic planes of electrolytes in planar and hydrogels, graphene, and hexagonal boron nitride (Hou and Hou, 2021), based on the use of gradients generated by the selective permeability of biological membranes. In biological systems, ions are charge carriers. The action potential across cell membranes is to transmit data based on the time and voltage variant. Thus, the ionic conductivity modulation of the ion environment concludes in nanofluidic iontronics (Yang et al., 2019). Different ion conduction nanofluidic devices not only have signals compatible with neurons but also have working media compatible with the physiological aqueous environment. In natural organisms, ion channels have different structures and shapes. The asymmetric design of geometry and inner surface charge distribution in one-dimensional nanoconfined space can reproduce diode-like ion rectification properties in solution systems. In addition, the biological nanometer channel is dynamical to deformation, the curvature, and adjustable carbon nanotubes for dynamic real-time control of the ion rectifier. In addition, two-dimensional nanomaterials, such as graphene, boron nitride, and molybdenum disulfide, and the emergence of the enlarged translational degree of freedom of ion transport lead to increased interaction between ions, and the interaction forms are more diverse. Moreover, the lag effect of ion motion brings a potential memory effect to the ion circuit, which brings hope for the development and application of brain–computer interface and brain-like computing technology.

The function of the membrane with nanoscale structures can be achieved by proteins and chemical modulation, nanoparticles, *etc.* In addition to complexing in matrices such as artificial hydrogels and thus functioning, they can also naturally adsorb near neuronal and glial cell membrane structures. Therefore, penetrating the neural networks requires surface modifications to bind with nanocarriers that can target neurons and glial membrane or pass through the nanoscale glial blood –brain barrier. The nanocarriers include liposomes, lipid nanoparticles, polymeric particles, micelles, and dendritic molecules, as well as biological vectors such as gene transfer viruses, virus-like particles, and exosomes. For example, adenoviruses target neuronal, astroglia and glioma cells, and their transgene expression lasts for years in the peripheral tissues of primates. They can manufacture but triggers an immune response in the body (Terstappen et al., 2021). Therefore, virus-like particles might be a better choice for controllability and reduced immune response by mimicking neurological latent viruses. In addition, microglia can also be modified by optogenetics to influence chronic pain (Fyfe, 2021), and even improve BCI inflammation state and function by transferring the modulation message. This technique is also frequently used in neuronal manipulation, and in addition inflammation of glial cells will be discussed later. Furthermore, with the acceleration of semiconductor and nanotechnology, such wireless and injectable technics make defined cells manipulation in the deep brain less invasive and removable. In the next part, we will introduce the neuron structure and nanoparticle interfaces in detail.

Neuron structure and nanoparticle interfaces

In most cases, a neuron has a long axon, which transmits electrical signals to other neurons, muscle fibers, or gland cells. Long axons, extensive dendrites, and varying synapses are constantly building up and degenerate. Nerve axons were cables that were wrapped with lipid glial cells and worked as natural output data lines that connect to the outside of the body. Nano-brain-computer interfaces resemble nerve fibers that build artificial membrane synapses and regeneration of axons. Virus-like nanoparticles can be designed to target neuron populations and accurately mediate with optical, magnetic, ultrasonic, chemical, and electrical signals.

Nano-brain-computer interfaces and virus-like nanoparticles are important for neuromodulations. The nanoscale array can directly form junctions with sub-neuron structure, while such accuracy can also be achieved with noninvasive nano modulation. For example, photon absorption elicits conformational changes in membrane proteins that switch ion channels' selectivity, and then comes electrical current. It made precise and versatile neuronal selective manipulation with high resolution in time and space possible to modulate in both excitatory and inhibitory cells *in vivo* within living experimental individuals (Deisseroth, 2015). Since upconversion nanoparticles can absorb certain light of high penetrability at the wavelength of near-infrared and emit visible rays, transcranial near-infrared rays and modified upconversion nanoparticles can mediate optogenetics, initiating the release of dopamine from genetically tagged neurons in an experiment (Chen et al., 2018). And other well-penetrating forms of energy and information such as ultrasound and magnetic fields that can penetrate deeply are converted into physiologically regulated forms of information to achieve noninvasive and precisely combined brain–computer interaction. Such as magnetoelectric nanoparticles, the focused ultrasound that uncage neuromodulatory drugs, and nanoscale piezoelectric materials that transfer acoustic waves into electric fields (Yang et al., 2021). Moreover, attenuated viral or virus-like particles can conduct, for example, photosensitive channel genes, carry nanoparticles to targeted neural populations for manipulation, decipher neuronal connectivity, and perform functional analyses to enable neural information acquisition. Brain–computer interfaces with nanostructures require double-layer membranes and functional protein-coated RNA, *etc.*, which can be modified to target intracranial cells and improve blood–brain permeability. Sensory and motor neurons that extend beyond the skull are the entry point for viruses. The rabies virus spreads from presynaptic neurons to the starter neuron (Vogt, 2019). After entry, the viruses use the axonal transport system for retrograde transport to the brain. Along the axons that cross the blood–brain barrier (BBB), there are glial blood–brain barrier, such as receptor-mediated transcytosis and the use of neurotropic viruses, nanoparticles, and exosomes. To simulate the transport of rabies virus along the axoplasm *via* the natural nerve cell structure, it can be targeted to the neural nucleus by nanoparticle or viral vector; such device delivery requires biomedical materials to achieve. And with the surface-modified APOE peptides, they could target glial cells through the blood–brain barrier *via* LDLR receptors. By actively targeting molecules, adsorption, magnetic and ultrasound mediated trans-BBB can be developed by mimicking bioprocess and using artificially intelligent protein design tools, such as the RVG29 peptide inspired from rabies virus can act on nicotinic acetylcholine receptors to the brain. Surface chemistry, such as electric charge, and chemical groups affect the absorption route into the cell. Targeting ligands, such as antibodies, proteins, nucleic acids, or small molecules, can increase the targeting of the BBB (Terstappen et al., 2021).

In conclusion, targeted nanoparticles, viroid particles, RNA delivery techniques, and exosomes are directly implanted or injected into the brain alone or with BCI. Multifunctional soft substances can be used to promote neuron development and growth *via* various ways such as long-term electrical stimulation, drug-releasing, and scaffold building (Feng et al., 2015). Axons may be possible to regulate gene expression of controlled ion channels or wireless signaling as a signal transfer interface in the brain. Whether using translational nanomaterials, virus-like particles, enzymes or proteins, or photons, they are all means of intervening in neurological interventions that have different interface requirements and therefore need to be examined in practice according to the characteristics of each technology itself.

Brain–computer interface inflammatory response and glial cells

The state of the BCI inflammatory response or the treatment of nervous system diseases is based on regulation of the glial and neuronal state regulation. The glial cells of the neural network affect specific pathways during chronic emotional states or sudden stimulation, and further functional sensitization or degeneration following occurs (Brites and Fernandes, 2015). It was expressed as upregulated astroglial potassium and glycogen synthase kinase 3 and upstream wingless-frizzled signaling pathways (Duman and Voleti, 2012; Cui et al., 2018).

While neurons and their circuits are almost considered to be the basic computational units, glial cells cannot be ignored. They not only have simple protective and nutritional functions, but they are functional partners of neurons. Abnormal glial cell states correspond to synaptic and electrical neuronal excitability (Venkatesh et al., 2019). Astrocytes and microglia play primary roles in synaptic shaping, secreting neuromodulators, ion homeostasis, and the formation of neural networks. To be specific, axon-wrapping glial cells surround axons, with insulating properties, which is due to the high content of lipids in myelin. What's more, with the closed protection of the meninges and blood–brain barrier, the nervous system, and immune system have been previously considered separate while they practically work together to maintain brain health. As a matter of fact, rather than described as displaying immune privilege in the central nervous system (CNS), immunological surveillance and response are frequently carried out, as well as shape the neural network, mostly by microglia, the CNS residents, which have been shown for be essential to homeostasis, development, and neuroinflammation through communications with almost all components, including neurons and glia (Graykowski and Cudaback, 2021). Refined dynamic and localized changes between glial neuro have well cooperated. The microregion of glial cells has a variety of functions in accompanying its local neuronal environment, forming certain structures such as glial processes and dendritic spines. When an injury such as implanted invasive BCI occurs, astrocytes and microglia will form an inflammatory barrier and promote the development of related circuits for sensitive or inhibitory functions (Kofuji and Araque, 2021).

Signals between neurons and glia can significantly seize CNS. Activated by persistent psychosocial or oxidative stressors, a neuronal chronic inflammatory state occurs with synaptic and electrical changes. During the damage process, proliferated microglia are activated to help restore the brain environment, and normally their vast projections constantly surveil and scavenge the brain environment (Graykowski and Cudaback, 2021). However, activated microglia can secrete noxious signals, such as pro-inflammatory cytokines, reactive oxygen species, nitrogen species, and excitatory neurotransmitters, which further aggravate damage. The peripheral inflammatory state mutually promotes neural inflammation, which helps sensitize the CNS to a noxious stimulus. For example, CD11c+ microglia expressed insulin-like growth factor-1 increased when nerve hypersensitivity occurs after an injury; this type of cells and substances help reduce nervous hypersensitivity (Kohno et al., 2022). In addition to releasing neurotransmitters, neurons also release neuromodulators, and the substance and their receptors appear in neurons and glial cells (Rostene et al., 2007), that link and affect their environment. Based on this process, channel proteins that noted expressed in glial cells are actively involved in the dynamic neuroglial interactions (Giaume et al., 2021), such as connexins and gap junction channels. In this case, nanotubes in BCI could play a role as an external control switch that can be designed to regulate glia–glia and neuron–glia interactions. Thus, nanoscale and surface molecular modulations in BCI can be applied to regulate the recovery pathway, glia population differentiation, and further help neuron reconstruction.

Feedback learning mechanism and exploration of network links

A whole BCI system works in the following steps, neuronal signal acquisition, data analysis, and feature extraction by machine learning, then translating to the neural network signals as output from the interface. Machine learning is the key to human–machine signal conversion. Instead of trying to understand the meaning and logic of neural activity patterns, machine learning greatly improves the ability to decode neural activity by identifying and linking the patterns to the user's intent in the face of the problem. For paraplegic patients with spinal cord or motor neuron injury, the motor intention still exists in

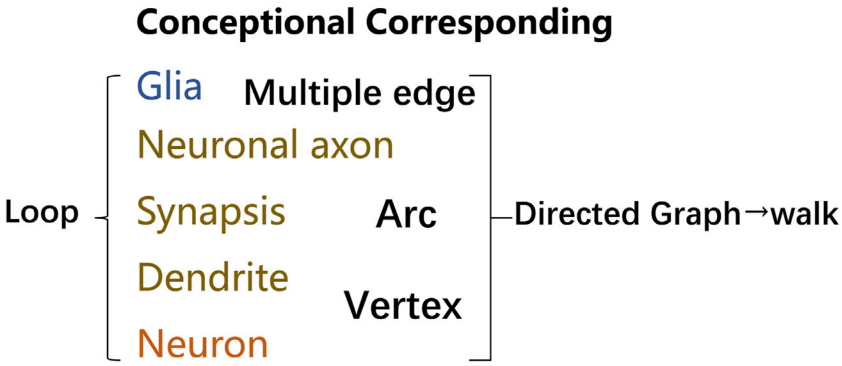

FIGURE 2
Terminology in graph theory corresponding to neural networks. Graphs provide a better way to deal with abstract concepts such as relationships and interactions. Neural loops can be abstracted into graphs utilizing concepts, and graphs made up of vertex and edge may be described analytically or as matrices. Glial cells can be represented as nodes or edges, many of which can correspond to multiple edges, where edges can be directed vectors or arcs. Similarly, dendrites and neurons can be represented as vertex, with edges and nodes labeled with weights that reflect varying degrees of information in positive or negative directions. Neuronal axons can be used as arcs to link different related functional regions, and neural loops can be formed between many neuronal structures. A walk is a finite sequence that takes the form of a graph's vertices and edges. The walk is open if the beginning and last vertices are different. The walk is a closed loop if the initial and final vertex is the same.

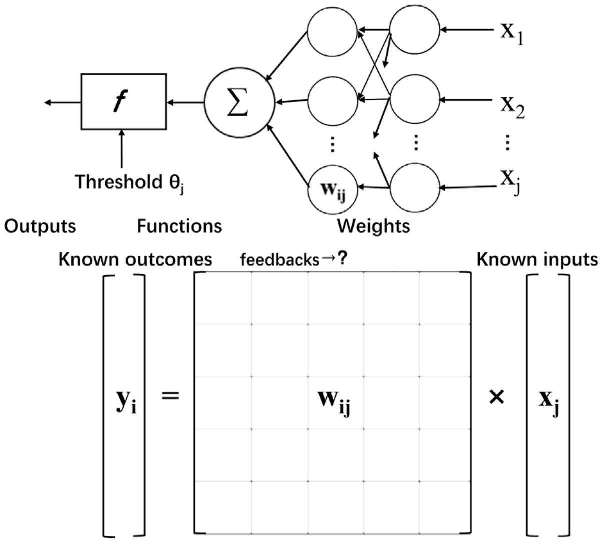

FIGURE 3
Simplified feedback learning process of calculating the unknown neuron value. Similar to solving equations in a matrix with known inputs and outputs, corresponding to received information and learned judgment and behavioral control information, the neural network derives parameter processing information, that is, weights, through feedback.

the brain network after paralysis. By recording neural activity from microelectrode arrays in the premotor area in the cortex while the participant imagines doing a specific activity. Artificial intelligence immediately decodes motor intentions represented by neural activity in the motor cortex and makes it into actual behavior (Willett et al., 2021). However, the information comes from the instantaneous potential changes on a two-dimensional surface, so it is limited to understanding the deeper network functions such as logical thinking and memory.

To further describe the networks, simplified tools for describing net and data structure are seen as essential. Limited to the skull space constraint, unique features along the lines of efficient topology network communication and information processing. And knowing the characteristics of basic elements, modeling networks, and simplifying by mathematical methods can be critical to understanding the networks and how they function mentally. Therefore, a language that clearly describes the structure in neural networks is of urgent need. Graph theory was introduced, which is defined as sets of nodes and edges that represent system elements and their interrelations. Language systems demonstrate the properties of networks, geometry, and spatial anatomical connectivity in the context of structural constraints. The correlated edges in graph theory can indicate the functional correlation between neuronal groups in addition to the neural-directed connections. As shown in Figure 2, through imaging, functional experiments and artificial intelligence analysis, the connection of a neural network can be expressed by the corresponding concepts in graph theory.

In addition, the breakthrough in computer science also provides a new approach to modeling nervous networks. Advances have been made in the application of artificial intelligence, which can sort objects out of raw data by computing, that is, to extract meaning and partly supervised learning. The function that seeks to realize a certain purpose can be visualized in Figure 3. However, the nervous system, especially the human brain, is far more complicated than a single model can convey, especially the dynamic integration on different scales.

Bionic artificial neural network's logical correspondence makes the implementation in brain biomedical interfaces accessible. Signal input and processing breakthroughs are also inspired by mechanisms of brain-like feedback learning. Technically, the brain's information processing ability benefits from the massive parallel and distributed computing model, which means thinking and memory happened simultaneously. In contrast, the computer is composed of independent and fixed CPUs and storage units. Inspired by neural networks, Artificial Neural Network has generated and solved many practical problems. The model is composed of many layers of nodes, also called neurons, connected by tied connections. Each node represents a specific activation function and the connections between nodes are given weighted values *via* feedback. It is an equation solving or function approximation process. By learning about weight through enormous feedback, computers are trained with professional recognition and translation skills. Machines can easily learn to simulate the language with this technic, helping to better shape the interface with functional communication. With the hope of building a hardware neural network interface, attempts have been made to create artificial neural network algorithms.

Once the machine learned the neuronal codes, part of the language spoken by neurons can be programmed and in turn, translated into specific meaning. Now the challenge lies in brain–computer Interface that breaks and expands the physical net limits. Brain–computer interfaces remarkably restore the ability to speak and movement control by training an artificial neural network, which transforms the neural activity into probabilities data of movement intentions.

Conclusion

For invasive BCI systems, good biocompatibility is needed, making it more valuable for us to learn, adapt, and recover various forms of sensory and motor control. Thereby, for example, sensory transduction, control of robotic arms and computers, and even driving (Aflalo et al., 2015) can be reliable throughout the lifetime. In addition, the richness of human sensory forms such as pressure, temperature, vibration, and light form the feeling of touch, warmth, hearing, and vision, which implies a multitude of possibilities for the conversion of signals into neural electrical impulses. And ultrasound, cables, near-infrared light, nano-temperature-controlled channels, and magnetism can all be used as forms of propagating information into the skull. From a functional point of view, brain–computer interface systems can be divided into input for various sensing functions such as somatosensory and special senses such as hearing and vision, and generate motor control such as communication, restoration of hand function, modulation of the autonomic nervous system and even memory and learning, and participation in a variety of functions in the consciousness process. This requires precise control of brain areas and adequate connection to neural networks, forming a similar afferent–transmitter interface between the spinal cord and the brain nerves, where the brain and machine signals are processed, continuously adapted and learned through feedback.

Glial cells play a role in dynamic changes that are related to neuronal function and state, it was important neuronal wiring in the network of neurons and glia, certain information is learned and processed through certain cellular connection structures of neural pathways or the same neurotransmitters, therefore performing specific functions in specialized regions of the complex network. Where neuronal connections depend on information and feedback to survive and establish. This process can be facilitated by a local electrical signals or chemical substances signals but also by optical, acoustical, and magnetic signals through genetic strategy or nanotechnology. In short, with the regulation of glial cells, electronic impulses carrying information, and even accompanied by gene transfer, an efficient interface system may be cultivated. Furthermore, there are many perspectives on the design of the brain–computer interface. If more interfaces are applied to better fit the brain's anatomical structure, currently only a local plane signal, a dynamic and multi-dimensional information network of neurons and glia, the cellular or molecular scale will approach, and more nanoparticle- based empirical models will simplify and create intelligent networks.

After fully interpreting these five-part processes, brain–computer interface technology enables the transformation of signal and regulation from glial cell–mediated nanomaterial to further fit the biological neural network and achieve minimally invasive and higher signal quality from signal relays such as photons, magnetism, and ultrasound to realize the regulation and supplement of brain function. The understanding of the natural structure of the brain can promote optimization of the design and modification and adjustment of functional groups, realize the opening and closing, control and adjustment of ion channels, and clear the operation mode of the bain–computer interface in a stable and accurate brain–computer interaction and self-learning through feedback.

Author contributions

TW directed the project. JZ and TW contributed to the conception and design of the study. JX, YZ, PL, NS, WZ, CC, and, NH performed related experiments and analyzed the data. JZ wrote the first draft of the manuscript. TW wrote sections of the manuscript and acquired funding. All authors contributed to manuscript revision, read, and approved the submitted version.

Funding

The National Key R&D Plan (SQ2021YFA160000, 2017YFA0205304).

Acknowledgments

The authors acknowledge the Southeast University and Nanjing Medical University Cooperation Project.

Conflict of interest

WZ was employed by SceneRay Co., Ltd.

The remaining authors declare that the research was conducted in the absence of any commercial or financial relationships that could be construed as a potential conflict of interest.

Publisher's note

References

Aflalo, T., Kellis, S., Klaes, C., Lee, B., Shi, Y., Pejsa, K., et al. (2015). Decoding motor imagery from the posterior parietal cortex of a tetraplegic human. *Science* 348 (6237), 906–910. doi:10.1126/science.aaa5417

Biasiucci, A., Leeb, R., Iturrate, I., Perdikis, S., Al-Khodairy, A., Corbet, T., et al. (2018). Brain-actuated functional electrical stimulation elicits lasting arm motor recovery after stroke. *Nat. Commun.* 9, 2421. doi:10.1038/s41467-018-04673-z

Bollella, P., and Katz, E. (2020)., 20. Basel), 3517. doi:10.3390/s20123517Enzyme-based biosensors: Tackling electron transfer issues*Sensors*

Bostan, A. C., and Strick, P. L. (2018). The basal ganglia and the cerebellum: nodes in an integrated network. *Nat. Rev. Neurosci.* 19 (6), 338–350. doi:10.1038/s41583-018-0002-7

Brites, D., and Fernandes, A. (2015). Neuroinflammation and depression: Microglia activation, extracellular microvesicles and microRNA dysregulation. *Front. Cell. Neurosci.* 9, 476. doi:10.3389/fncel.2015.00476

Cui, Y., Yang, Y., Ni, Z., Dong, Y., Cai, G., Foncelle, A., et al. (2018). Astroglial Kir4.1 in the lateral habenula drives neuronal bursts in depression. *NATURE* 554, 323–327. doi:10.1038/nature25752

Chen, S., Weitemier, A. Z., Zeng, X., He, L., Wang, X., Tao, Y., et al. (2018). Near-infrared deep brain stimulation via upconversion nanoparticle–mediated optogenetics. *Science* 359, 679–684. doi:10.1126/science.aaq1144

Deisseroth, K. (2015). Optogenetics: 10 years of microbial opsins in neuroscience. *Nat. Neurosci.* 18, 1213–1225. doi:10.1038/nn.4091

Duman, R. S., and Voleti, B. (2012). Signaling pathways underlying the pathophysiology and treatment of depression: Novel mechanisms for rapid-acting agents. *TRENDS Neurosci.* 35, 47–56. doi:10.1016/j.tins.2011.11.004

Feng, Z. Q., Wang, T., Zhao, B., Li, J. C., and Jin, L. (2015). Soft graphene nanofibers designed for the acceleration of nerve growth and development. *Adv. Mat.* 27, 6462–6468. doi:10.1002/adma.201503319

Fyfe, I. (2021). Microglial optogenetics triggers chronic pain in mice. *Nat. Rev. Neurol.* 17, 262. doi:10.1038/s41582-021-00490-z

Giaume, C., Naus, C. C., Saez, J. C., and Leybaert, L. (2021). Glial connexins and pannexins in the healthy and diseased brain. *Physiol. Rev.* 101, 93–145. doi:10.1152/physrev.00043.2018

Golub, M. D., Sadtler, P. T., Oby, E. R., Quick, K. M., Ryu, S. I., Tyler-Kabara, E. C., et al. (2018). Learning by neural reassociation. *Nat. Neurosci.* 21, 607–616. doi:10.1038/s41593-018-0095-3

Graykowski, D., and Cudaback, E. (2021). Don't know what you got till it's gone: Microglial depletion and neurodegeneration. *Neural Regen. Res.* 16, 1921–1927. doi:10.4103/1673-5374.308078

Greene, D. J., Marek, S., Gordon, E. M., Siegel, J. S., Gratton, C., Laumann, T. O., et al. (2020). Integrative and Network-Specific Connectivity of the Basal Ganglia and Thalamus Defined in Individuals. *Neuron* 105 (4), 742. doi:10.1016/j.neuron.2019.11.012

Gu, C., Jiang, J., Tao, T. H., Wei, X., and Sun, L. (2021). Long-term flexible penetrating neural interfaces: Materials, structures, and implantation. *Sci. China Inf. Sci.* 64, 221401. doi:10.1007/s11432-021-3321-7

Hou, Y., and Hou, X. (2021). Bioinspired nanofluidic iontronics. *Science* 373, 628–629. doi:10.1126/science.abj0437

Kaplan, L., Chow, B. W., and Gu, C. (2020). Neuronal regulation of the blood–brain barrier and neurovascular coupling. *Nat. Rev. Neurosci.* 21, 416–432. doi:10.1038/s41583-020-0322-2

Keene, S. T., Lubrano, C., Kazemzadeh, S., Melianas, A., Tuchman, Y., Polino, G., et al. (2020). A biohybrid synapse with neurotransmitter-mediated plasticity. *Nat. Mat.* 19, 969–973. doi:10.1038/s41563-020-0703-y

Khalil, K., Asgher, U., and Ayaz, Y. (2022). Novel fNIRS study on homogeneous symmetric feature-based transfer learning for brain-computer interface. *Sci. Rep.* 12 (1), 3198. doi:10.1038/s41598-022-06805-4

Kim, T. I., Mccall, J. G., Jung, Y. H., Huang, X., Siuda, E. R., Li, Y. H., et al. (2013). Injectable, cellular-scale optoelectronics with applications for wireless optogenetics. *Science* 340, 211–216. doi:10.1126/science.1232437

Kofuji, P., and Araque, A. (2021). Astrocytes control the critical period of circuit wiring. *Sci. (New York, N.Y.)* 373, 29–30. doi:10.1126/science.abj6745

Kohno, K., Shirasaka, R., Yoshihara, K., Mikuriya, S., Tanaka, K., Takanami, K., et al. (2022). A spinal microglia population involved in remitting and relapsing neuropathic pain. *Science* 376, 86–90. doi:10.1126/science.abf6805

Lee, S., Eom, T., Kim, M.-K., Yang, S.-G., and Shim, B. S. (2019). Durable soft neural micro-electrode coating by an electrochemical synthesis of PEDOT:PSS/graphene oxide composites. *Electrochimica Acta* 313, 79–90. doi:10.1016/j.electacta.2019.04.099

Liu, X., Chen, H., Wang, Y., Si, Y., Zhang, H., Li, X., et al. (2021). Near-infrared manipulation of multiple neuronal populations via trichromatic upconversion. *Nat. Commun.* 12, 5662. doi:10.1038/s41467-021-25993-7

Park, S., Yuk, H., Zhao, R., Yim, Y. S., Woldeghebriel, E. W., Kang, J., et al. (2021). Adaptive and multifunctional hydrogel hybrid probes for long-term sensing and modulation of neural activity. *Nat. Commun.* 12, 3435. doi:10.1038/s41467-021-23802-9

Rostene, W., Kitabgi, P., and Melik-Parsadaniantz, S. (2007). Opinion - chemokines: A new class of neuromodulator? *Nat. Rev. Neurosci.* 8, 895–903. doi:10.1038/nrn2255

Sheng, H., Wang, X., Kong, N., XI, W., Yang, H., Wu, X., et al. (2019). Neural interfaces by hydrogels. *Extreme Mech. Lett.* 30, 100510. doi:10.1016/j.eml.2019.100510

Terstappen, G. C., Meyer, A. H., Bell, R. D., and Zhang, W. (2021). Strategies for delivering therapeutics across the blood-brain barrier. *Nat. Rev. Drug Discov.* 20, 362–383. doi:10.1038/s41573-021-00139-y

Trautmann, E. M., O'Shea, D. J., Sun, X., Marshel, J. H., Crow, A., Hsueh, B., et al. (2021). Dendritic calcium signals in rhesus macaque motor cortex drive an optical brain-computer interface. *Nat. Commun.* 12, 3689. doi:10.1038/s41467-021-23884-5

Van De Burgt, Y., Lubberman, E., Fuller, E. J., Keene, S. T., Faria, G. C., Agarwal, S., et al. (2017). A non-volatile organic electrochemical device as a low-voltage artificial synapse for neuromorphic computing. *Nat. Mat.* 16, 414–418. doi:10.1038/nmat4856

Venkatesh, H. S., Morishita, W., Geraghty, A. C., Silverbush, D., Gillespie, S. M., Arzt, M., et al. (2019). Electrical and synaptic integration of glioma into neural circuits. *Nature* 573, 539–545. doi:10.1038/s41586-019-1563-y

Vogt, N. (2019). Dissecting neuronal circuitry. *Nat. Methods* 16 (4), 282. doi:10.1038/s41592-019-0376-0

Wang, X., Sun, X., Gan, D., Soubrier, M., Chiang, H.-Y., Yan, L., et al. (2022). Bioadhesive and conductive hydrogel-integrated brain-machine interfaces for conformal and immune-evasive contact with brain tissue. *Matter* 5, 1204–1223. doi:10.1016/j.matt.2022.01.012

Wei, H. H., Shi, R. C., Sun, L., Yu, H. Y., Gong, J. D., Liu, C., et al. (2021). Mimicking efferent nerves using a graphdiyne-based artificial synapse with multiple ion diffusion dynamics. *Nat. Commun.* 12, 1068. doi:10.1038/s41467-021-21319-9

Willett, F. R., Avansino, D. T., Hochberg, L. R., Henderson, J. M., and Shenoy, K. V. (2021). High-performance brain-to-text communication via handwriting. *Nature* 593, 249–254. doi:10.1038/s41586-021-03506-2

Xu, H., Wang, X., Zhang, X., Cheng, J., Zhang, J., Chen, M., et al. (2021). A deep learning analysis reveals nitrogen-doped graphene quantum dots damage neurons of nematode *Caenorhabditis elegans*. *Nanomater. (Basel)* 11, 3314. doi:10.3390/nano11123314

Yang, X., Mcglynn, E., Das, R., Pasca, S. P., Cui, B., and Heidari, H. (2021). Nanotechnology enables novel modalities for neuromodulation. *Adv. Mat.* 33, e2103208. doi:10.1002/adma.202103208

Yang, X., Zhou, T., Zwang, T. J., Hong, G., Zhao, Y., Viveros, R. D., et al. (2019). Bioinspired neuron-like electronics. *Nat. Mat.* 18, 510–517. doi:10.1038/s41563-019-0292-9

frontiers | Frontiers in Bioengineering and Biotechnology

TYPE Original Research
PUBLISHED 14 November 2022
DOI 10.3389/fbioe.2022.1056652

Check for updates

OPEN ACCESS

EDITED BY
Junchao Wei,
Nanchang University, China

REVIEWED BY
Chao Feng,
Ocean University of China, China
Binghong Luo,
Jinan University, China

*CORRESPONDENCE
Ruimin Long,
simplever@126.com
Jumei Tian,
tjm@xmmc.edu.cn
Jun Zheng,
jason@3dmetalwerks.com

†These authors have contributed equally to this work

SPECIALTY SECTION
This article was submitted to Biomaterials,
a section of the journal
Frontiers in Bioengineering and Biotechnology

RECEIVED 29 September 2022
ACCEPTED 31 October 2022
PUBLISHED 14 November 2022

CITATION
Long R, Shi L, He P, Tian J, Wang S and Zheng J (2022), 3D cell culture based on artificial cells and hydrogel under microgravity for bottom-up microtissue constructs.
Front. Bioeng. Biotechnol. 10:1056652.
doi: 10.3389/fbioe.2022.1056652

3D cell culture based on artificial cells and hydrogel under microgravity for bottom-up microtissue constructs

Ruimin Long[1,2,3]*†, Linrong Shi[1]†, Peng He[1], Jumei Tian[4]*, Shibin Wang[1,3,5] and Jun Zheng[6]*

[1]College of Chemical Engineering, Huaqiao University, Xiamen, China, [2]Engineering Research Center of Artificial Organs and Materials, Ministry of Education, Jinan University, Guangzhou, China, [3]Institute of Pharmaceutical Engineering, Huaqiao University, Xiamen, China, [4]Engineering Research Center of Fujian University for Stomatological Biomaterials, Xiamen Medical College, Xiamen, China, [5]Fujian Provincial Key Laboratory of Biochemical Technology, Huaqiao University, Xiamen, China, [6]College of Materials Science and Engineering, Xiamen University of Technology, Xiamen, China

The use of hydrogel as a filling medium to recombine dispersed microencapsulated cells to form an embedded gel-cell microcapsule complex is a new idea based on bottom-up tissue construction, which is benefit for cell distribution and of great significance for tissue construction research *in vitro*. In this experiment, sodium alginate and chitosan were used as the main materials, rat normal liver cell BRL-3A was used as the model cell to prepare “artificial cells”. Silkworm pupa was used as raw material to extract silk fibroin solution, which was prepared by ultrasound to be the silk fibroin gel; silk fibroin hydrogel-microencapsulated hepatocyte embedded complex was then prepared by using silk fibroin gel as filling medium; the complex was cultured under three modes (static, shaking, and 3D microgravity), and the tissue forming ability of rat hepatocytes was investigated. The results showed that the microgravity culture condition can enhance the cell proliferation and promote the formation of cell colonies in the microcapsules; silk fibroin can form an embedded gel-cell microcapsule complex with microencapsulated cells, which provided mechanical support for the structure of the composite. We hope that this bottom-up construction system will have potential applications in the fields of cell culture and tissue construction.

KEYWORDS

tissue engineering, bottom-up, artificial cell, microgravity culture, hydrogel

Introduction

Compared with two-dimensional culture, three-dimensional culture enables cells to simulate tissue-like structures more effectively and provide optimal simulation microenvironment for cell growth. Besides, microgravity stimulates cell-cell and cell matrix interactions, which promotes the formation of three-dimensional clusters and promotes cell proliferation. For example, Costantini D et al. (Costantini et al., 2019) studied the effects of microgravity on human bile duct trunk/progenitor cells (HBTSCs) and found that stem gene expression in HBTSCs cultured in SMG microgravity conditions was significantly increased compared with HBTSCs cultured under normal gravity control conditions. Zhou X et al. (Zhou et al., 2019) fabricated microencapsulated cells through microcapsules loaded with C5.18 chondrocytes alginate/chitosan prepared by a high-voltage electrostatic method. It could be found from the cell viability (cell proliferation) cell proliferation (AO/EB staining) and cell viability (CCK-8 assay) results that microencapsulated cells had a better cell proliferation under 3D micro-gravity microgravity conditions using bFGF than under 2D conditions (including static and shaking conditions). Mattei C (Mattei et al., 2018) studied the rotating cell culture system and found that microgravity basically supports the generation and maintenance of neurological organs derived from human embryonic stem cells, and can be used as a model for human brain development. In addition, He L et al. (He et al., 2016) confirmed that microgravity conditions promote the proliferation of human dental pulp stem cells compared with normal gravity conditions, thereby effectively forming functional tissues and promoting dental tissue engineering. Other publications also revealed that 3D microgravity culture is benefit for cell propagation (Farid et al., 2018; Sapudom et al., 2021; Zou et al., 2022).

Besides, microencapsulation technology is also used for cell culture. Microcapsules can immobilize plant, microbial or animal cells, as well as enzymes, coenzymes or proteins, in a polymeric hydrogel membrane (Li et al., 2020), which has selective permeability and immunoisolation ability. Only oxygen, nutrients and metabolites can be transported through the membrane, while the IgG is stopped outside. The microcapsules embedded with living cells are also called “artificial cells”, which usually contain biological substances such as cells, DNA, RNA, and protein encapsulated in semipermeable membranes or other compartments. At present, cell microencapsulation technology is considered to be a viable treatment for the therapy of neurological and endocrine diseases (Montanucci et al., 2013). It can also be used for oral probiotic (Mawad et al., 2018) or hyperlipidemic therapy (Song et al., 2017). Furthermore, Zhang X et al. (Zhang et al., 2017) investigated the role of active oyster peptide extract (AOPS) microcapsules formed by microemulsion gelling to prolong their biological activity. The results showed that the AOPS microcapsule can effectively reduce IL-1β and TNFα and increase the levels of ACP and lysozyme for inflammatory cytokines.

Today, tissue engineering has attracted considerable attention. Compared with the traditional top-down approach, which may have the problem of cell distribution to form an organizational structure with complex microstructure features (Luo et al., 2019), modular tissue engineering, also called bottom-up way, is to construct a pseudo-ecological micro-structural unit and then assemble to form a large-scale organization (Nie and Takeuchi, 2018). Okudaira T et al. (Okudaira et al., 2017) used a bottom-up approach to prepare 3D liver tissue from hepatocyte spheroids covering human umbilical vein endothelial cells and NIH/3T3 cells, which had higher liver function activity and higher cell density, and hepatic vascular endothelial cells formed a regular network structure in liver tissue. Luo C et al. (Luo et al., 2019) compared the performance of top-down and bottom-up construction strategies *in vivo*, and the comparative studies showed that bottom-up construction strategy was more effective in the treatment of bone defects *in vivo*.

Therefore, to solve the problem of cell distribution in scaffold and promote the cell growth, a bottom-up strategy based on microcapsule and modular tissue engineering was proposed (Scheme 1). Microcapsules were prepared with sodium alginate and chitosan to encapsulate rat normal liver cell BRL-3A to form “artificial cells”; silk fibroin was used as the filling medium to fix the shape of the obtained silk fibroin hydrogel-artificial cell complex considering that silk fibroin is a commonly available natural biopolymer with suitable properties such as mechanical strength, elasticity, biocompatibility and controllable biodegradability, and has been widely used in tissue regenerations (Kundu et al., 2013; Gomes et al., 2022). Three different culture modes, including static, shaking, and 3D microgravity, were applied to primarily investigate the cell growth and functions.

Materials and methods

Materials

BRL-3A normal rat liver cells were purchased from Shanghai cell bank of Chinese Academy of Sciences, (Shanghai, China). High glucose DMEM medium and trypsin 1:250 were obtained from GIBICO Inc. (United States). Sodium alginate (ALG, A2158), acridine orange (AO) and ethidium bromide (EB) were provided by Sigma Inc. (United States). Chitosan (Chi, M.W. 1 × 10^5 Dalton) was purchased from Golden Shell Biotechnology Co., Ltd. (Zhe Jiang, China). Albumin assay kit and urea assay kit were purchased from Zhongsheng Beikong Biological Co., Ltd. (Shanghai, China). HE kit was obtained from Plylai Biotechnology Co., Ltd. (Beijing, China). EDTA was purchased from Sinopharm Chemical Reagent Co., Ltd. (Shanghai, China).

Preparation of microencapsulated cells

Preparation of microencapsulated cells using high-voltage electrostatic droplet generator (customized by Shanghai University of Technology) was conducted referring the method published elsewhere (Kundu et al., 2013) (Zhou et al., 2018). Briefly, adherently grown BRL-3A cells were digested with trypsin solution and mixed with 1.5% (w/v) sodium alginate solution (previously filtered through 0.8, 0.45, 0.22 μm filter). The volume ratio of the suspension to the Alg solution was 1:4. The cell

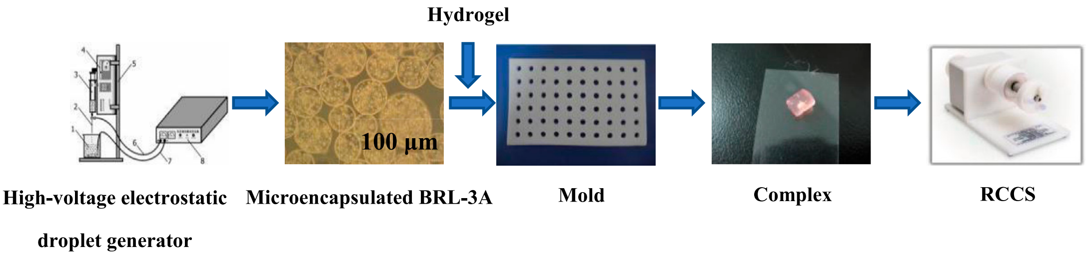

SCHEME 1
The complex was formed by the hydrogel and the microencapsulated BRL-3A cells prepared by the high-voltage electrostatic generator, and then was subjected to tissue construction under microgravity.

suspension was adjusted to 1×10^4/ml and dropped into 1.5% (w/v) calcium chloride solution through a high-voltage electrostatic droplet generator (parameter setting: 7.5 kV, 20 mm/h) to form Alg beads embedded with cells. The obtained beads were coated with a filter-sterilized chitosan solution for 8 min to obtain alginate/chitosan microcapsules, which were then suspended in 0.15% (w/v) Alg solution to form ACA microcapsules (Gomes et al., 2022) (Liu et al., 2015), and the core was liquefied with 1.6% (w/v) sodium citrate. The collected microcapsules were washed with saline, and placed in an incubator containing 5% CO2 at 37°C. The prepared microencapsulated cells were respectively cultured in three modes of static (24-well plate), shaking (Constant temperature incubator shaker, Weide Technology Co., Ltd., Xiamen, China) and microgravity culture system (RCCS-1 rotary microgravity incubator, Yituo Biological Instrument Co., Ltd., Shanghai, China).

Preparation of silk fibroin hydrogel-microencapsulated cell complex

As shown in Scheme 2, firstly, silk fibroin aqueous solution was prepared. Briefly, silk fibroin solution was obtained by degumming, dissolving, dialysis, and concentration. Then the solution was diluted to 5% (w/v), and silk fibroin gelling solution was prepared at ultrasonic power of 200 W and time of 45s. The microcapsules and the solution were mixed at a volume ratio of 1:2. The resulting mixture was kept at room temperature for 5 min to obtain silk fibroin gel-microcapsule complex. The prepared silk fibroin-microencapsulated cell complex was respectively cultured in three modes of static, shaking and microgravity culture system.

AO/EB staining

The suspension of 200 μL microcapsulated cells was mixed with 10 μL AO/EB mixture and incubated for 30 s. Take one drop of the above staining solution and drip it onto a clean glass slide. The sample was immediately observed under confocal laser microscopy (Zeiss, Germany) and 200 × objective microscopy (Zhou et al., 2018) (Zhao and Zhang, 2018).

Determination of albumin secretion

The albumin content of BRL-3A cells in microencapsulated cells and complexes was measured at predetermined times according to the instructions of the albumin assay kit (Zhongsheng Beikong Biotechnology Co., Ltd., Shanghai, China) provided by the company.

Determination of urea synthesis

According to the instructions of the urea detection kit provided by the company (Zhongbei Control Biological Co., Ltd., Shanghai, China), the urea content secreted by microencapsulated cells and BRL-3A cells in the complex was determined respectively at predetermined times.

Statistical analysis

Results were expressed as mean ± standard deviation. Each measurement reported was based on duplicate analysis of at least three independent experiments.

Results and discussion

Microencapsulated BRL-3A cells and their activity

It can be seen from Figure 1 that the prepared calcium alginate/chitosan microcapsules were intact in morphology, good in sphericity, smooth in surface, non-adhesive between capsules, and well dispersed. The cells distributed well within the

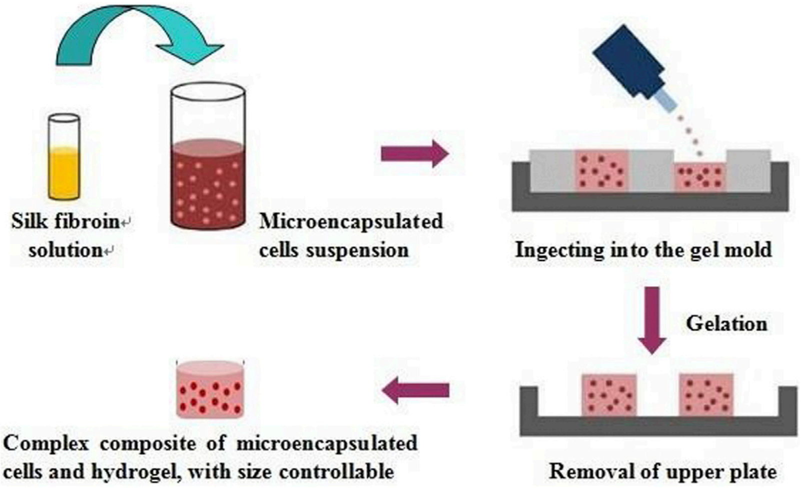

SCHEME 2
The preparation process of the silk fibroin gel and cell microcapsulation composites.

microcapsules. By AO/EB fluorescence staining, it can be clearly seen under the laser confocal microscope that the BRL-3A cells in the microcapsules were almost green, indicating that the cells in the capsule were basically living cells, and the survival rate was high, thereby confirming that the microcapsules did not affect cell survival.

Culture of microencapsulated BRL-3A cells in three culture systems

The microencapsulated BRL-3A cells were cultured in a simulated microgravity culture system for up to 2 weeks. After one week of culture, the cells began to form a spherical shape with a diameter of about 50 μm, and the morphology and size were irregular, as shown in Figure 2D. After two weeks of cultivation, as shown in Figure 2E, the size of the sphere increased gradually, and a small cell mass of 30–50 μm in diameter formed a dense sphere having a diameter of 100–150 μm. Compared with the cell growth in the simulated microgravity culture system, there was no obvious cell colony formation after 2 weeks of static culture of the cells in the microcapsules, and only some cells aggregated toward the edge of the microcapsules (Figure 2H). Under shaking culture conditions, the cells in the microcapsules also did not form cell colonies in the central part, but there was obvious edge aggregation. Most of the cells aggregated toward the edge of the microcapsules, and a small number of small cell colonies were formed (Figure 2J).

In the study of Zhang (Liu et al., 2015) (Zhang et al., 2006), polylysine was used as a membrane material, and

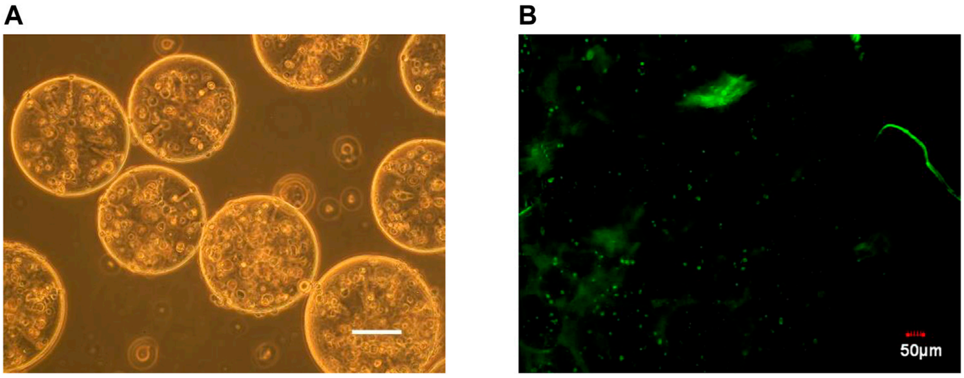

FIGURE 1
Microscopy photograph **(A)** and confocal laser scanning microscope image **(B)** of microencapsulated BRL-3A cells. (×200, left bar: 100 μm).

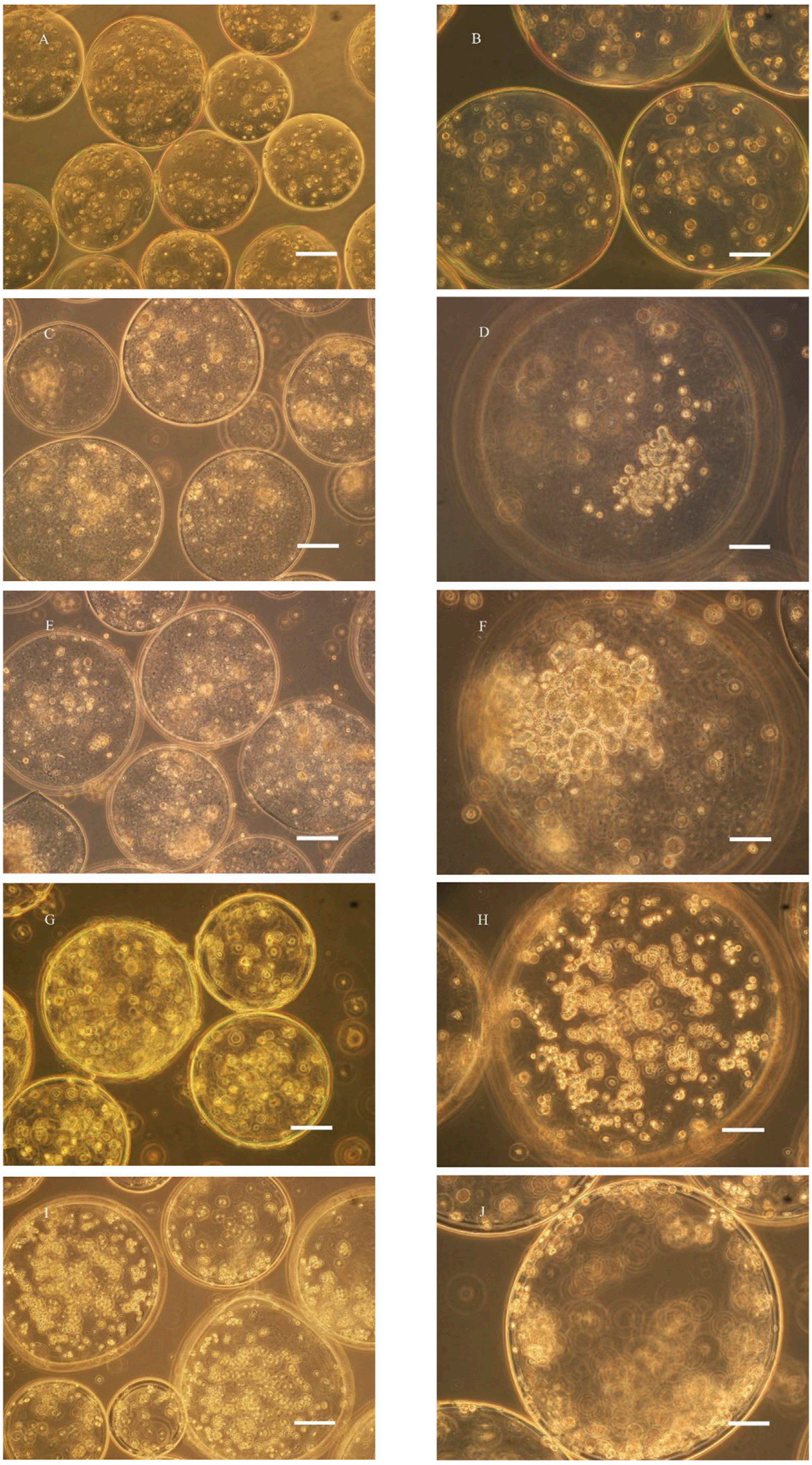

FIGURE 2
Microscopy photograph of microencapsulated BRL-3A cultured in rotary **(C–F)**, static **(G, H)** and shaking **(I, J)** cell culture system (left: ×200, bar: 100 μm; right: ×400, bar: 50 μm; **(A, B)**: 0 d; **(C, D)**: 7 d; **(E–J)**: 14 d).

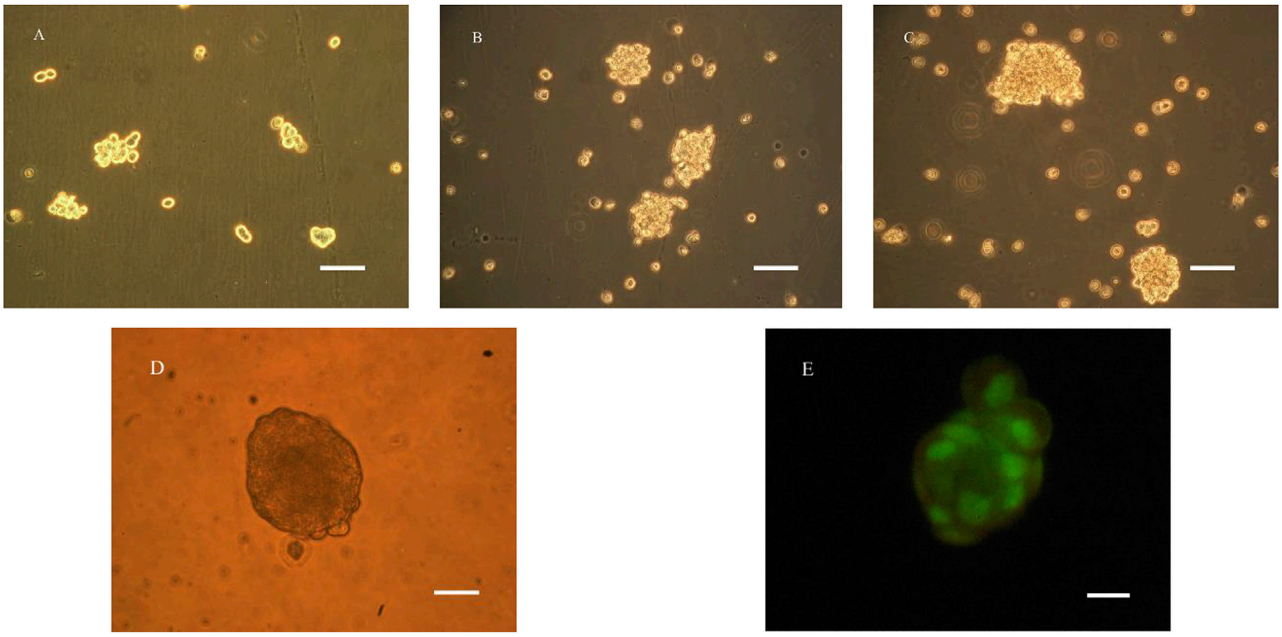

FIGURE 3
Microscopy photograph **(A–E)** and confocal laser scanning microscope image **(E)** of BRL-3A cultured in RCCS **(A)**: 1d, **(B)**: 4d, **(C–E)**: 7d; **(A–C)**: ×200, bar:100 μm; **(D, E)**: ×400, bar:50 μm).

human breast cancer cells and chronic myeloid leukemia cells were embedded with sodium alginate, and cultured with an inducer in a static environment, and formed two weeks later. The cell colonies were about 180 and 70 μm in diameter, and the cell colonies were dense overall, and the cells therein had higher activity. In contrast, microencapsulated BRL-3A cells in static culture failed to express cell colonies after two weeks, while similar results were obtained under simulated microgravity culture. Compared with tumor cells, normal somatic cells have certain difficulties in the formation of tissue-like colonies, and better experimental results can be obtained in the culture system of this experiment, thus highlighting the effectiveness of simulated microgravity culture system in tissue construction.

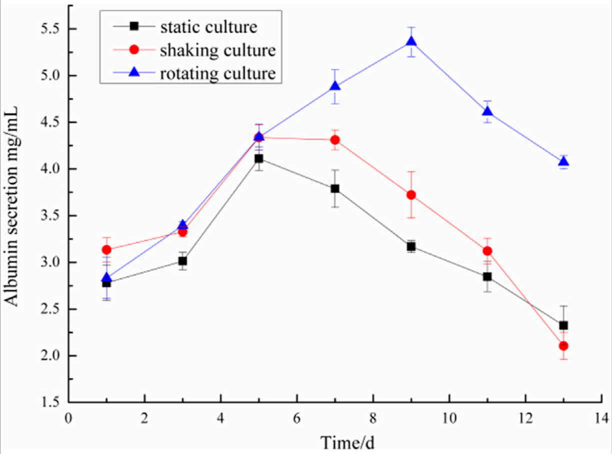

FIGURE 4
Comparison of albumin secretion of microencapsulated BRL-3A.

Culture of BRL-3A cells in 3D microgravity culture system

To further verify the ability of cells to form aggregates under microgravity conditions, we cultured BRL-3A cells in a microgravity system alone as shown below:

Under RCCS culture conditions, liver cells did not attach to the wall and spread, but remained suspended and round. As can be seen from Figure 3A, after 24 h, the liver cells began to form a globular shape, and the shape and size were irregular. After one week of cultivation, as shown in Figure 3C, the size of the globule gradually increased, and a small cell mass of 30–50 μm in diameter formed a dense sphere with a diameter of 100–150 μm. It can be seen by fluorescence staining that the cell colony presented good cell survival phenomenon.

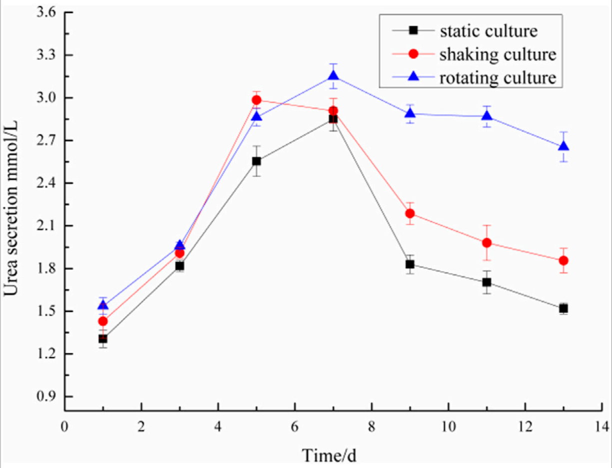

FIGURE 5
Comparison of urea secretion of microencapsulated BRL-3A.

Determination of albumin and urea in microencapsulated BRL-3A cells in three culture systems

Microencapsulated BRL-3A cells were cultured in three ways: static, shaking, and simulated microgravity. Clinically, albumin and urea are main indexes to examine the function of liver. Thus, the metabolism of hepatocytes was examined by detecting the albumin and urea content in the culture medium. The results were shown in Figures 4, 5.

On the first day, the albumin content in the culture medium was about 3.0 mg/ml and the urea content was about 1.4 mmol/L in the three culture modes. With the prolongation of the culture time, especially after 5 days, the metabolic properties of the microencapsulated hepatocytes under the simulated microgravity culture system were different. In the 5th day, the content of albumin synthesized by the three groups of microencapsulated hepatocytes increased, and the albumin content of microencapsulated hepatocytes in the simulated microgravity culture system increased significantly; in the 5th to 13th days, the amount of albumin secreted by microencapsulated hepatocytes in static and shaking culture systems was reduced compared with the previous days, but the microencapsulated hepatocytes under simulated microgravity culture system still showed strong albumin synthesis ability, and the albumin synthesis ability decreased until 10 days later.

In the 2nd to 7th days, the urea content of microencapsulated hepatocytes increased in the three medium culture mode, but after 7 days, the ability of microencapsulated hepatocytes to secrete urea in the static and shaking culture system decreased significantly and the amount of urea secretion decreased; in the 8th to 13th days, the ability of microencapsulated hepatocytes to secrete urea under simulated microgravity culture system decreased, but still maintained a high level. These results indicated that microencapsulated hepatocytes still had strong metabolic functions after long-term culture under simulated microgravity culture system.

Preparation of silk fibroin-microencapsulated cell complex

The prepared silk fibroin solution was mixed with the prepared microencapsulated BRL-3A cells to obtain a silk fibroin-microencapsulated cell complex, and a small-sized block composite was obtained by means of a mould as shown in Figure 6. From the laser confocal microscopy, it can be seen that the BRL-3A cells in the silk fibroin-microencapsulated cell complex had a good survival rate and can be further investigated.

Detection of BRL-3A cell metabolites in complex

It can be seen from Figure 7 that on the first day, the content of synthetic albumin was not high, which is about 0.2 mg/dl; on the third day, the ability to synthesize albumin in the complex has been improved significantly under the microgravity culture system, while the complex in other culture systems has not increased the albumin content obviously; on the fifth day, the ability of the complex to secrete albumin in each culture system was greatly reduced, which indicated that the cell survival rate in the complex decreased; on the seventh day, only the complex under simulated microgravity culture can secrete a small amount of albumin, and the cells in the complex under other culture systems almost had no albumin secretion ability.

The amount of urea secreted in the silk fibroin gel-microencapsulated cell complex under different culture systems was shown in Figure 8, and the results were in accordance with the results of albumin. On the first day, the cells in the complex could secrete urea, and the content was about 1 mg/dl; on the third day, the ability to secrete urea in the complex under microgravity culture system was significantly improved, while the amount of urea secreted in the complex under other culture systems increased slightly; on the fifth day, the ability of the complex to secrete urea decreased in each culture system, indicating that the cell survival rate in the complex decreased; on the seventh day, only a small amount of urea was secreted, including the compound cultured under simulated microgravity.

Compare the albumin and urea secretion from the complex with those from the microcapsules, wen can see that the size plays an important role in mass transfer. For the silk fibroin gel-microencapsulated cell complex, the larger scale hinders the metabolites diffuse from the inside out.

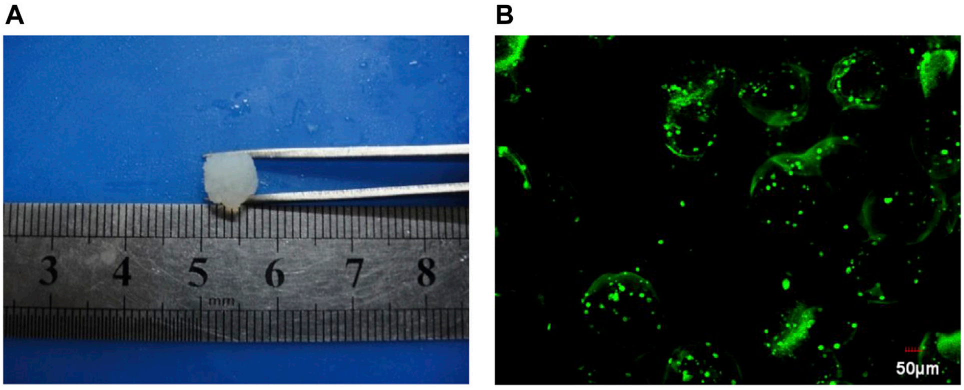

FIGURE 6
The image of gel **(A)** and cell microencapsulation complex under confocal laser scanning **(B)**.

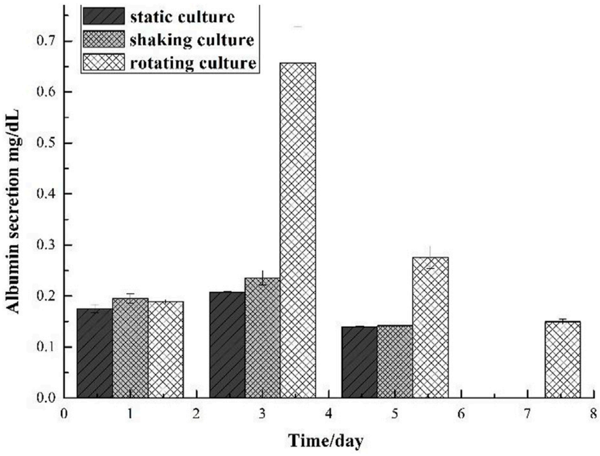

FIGURE 7
Comparison of albumin secretion of gel and cell microcapsulation composites in different culture system.

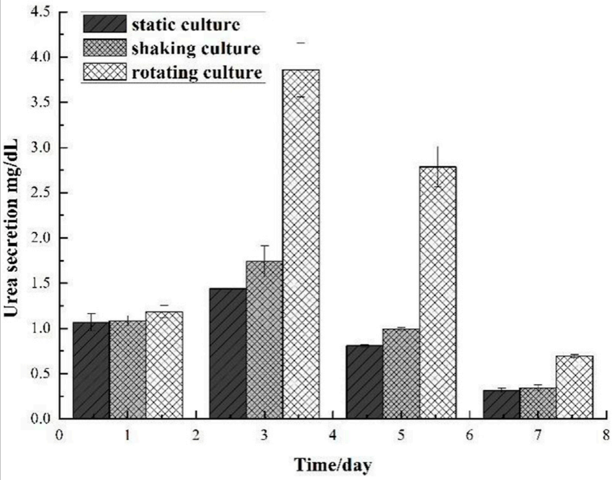

FIGURE 8
Comparison of urea secretion of gel and cell microcapsulation composites in different culture systems.

Conclusion

BRL-3A cells were cells with strong adaptability and rapid proliferation, which were easy to expand *in vitro* and had great expansion potential. The preparation of microencapsulated cells was carried out using the mature preparation process of the laboratory, and the results showed that microencapsulation did not affect cell survival. BRL-3A cells were cultured under simulated microgravity culture system, and the whole cell colonies showed a state of good cell growth. Under this culture system, the time of proliferative ability and metabolic capacity of the cells can be further extended on the basis of microencapsulated hepatocytes. Silk fibroin provided mechanical support for maintaining the structure of the gel-artificial cell complex. Since artificial cells are well distributed in the complex, the demands of high porosity and high connectivity of the traditional tissue engineering scaffolds can be avoided. This complex also has excellent mass transfer properties due to the inner liquification of the artificial cells. This work provides an alternative way for cell culture and tissue construction *in vitro*. However, much work should be done before this strategy being applied in the future. The main problem is that the secretions of albumin and urea from the complex are much fewer than those from the microcapsules. Thus, how to maintain the cell viability for a long period in the complex is a challenge. In the future work, we will attempt to build microvessels at the same time of the microtissue formation to enhance the mass transportation in the microtissues.

Data availability statement

The original contributions presented in the study are included in the article/Supplementary material, further inquiries can be directed to the corresponding authors.

Author contributions

RL, JT, and JZ conceptualized the system and designed the studies. PH performed the experiments with assistance from LS. LS wrote the draft and RL finished the manuscript with assistance from SW for revision.

Funding

This research is also supported by the Program for Innovative Research Team in Science and Technology at Fujian Province University. Financial support from the Open Fund of Engineering Research Center of Artificial Organs and Materials, Ministry of Education, Jinan University, Guangzhou 510632, China (ERCAOM202211), Engineering Research Center of Fujian University for Stomatological Biomaterials (Xiamen Medical College) (XMMC-KQ202101) and the National Natural Science Foundation of China (32171337) is gratefully acknowledged.

Acknowledgments

We thank Instrumental Analysis Center of Huaqiao University for the support of the work.

Conflict of interest

The authors declare that the research was conducted in the absence of any commercial or financial relationships that could be construed as a potential conflict of interest.

Publisher's note

References

Costantini, D., Overi, D., Casadei, L., Cardinale, V., Nevi, L., Carpino, G., et al. (2019). Simulated microgravity promotes the formation of tridimensional cultures and stimulates pluripotency and a glycolytic metabolism in human hepatic and biliary tree stem/progenitor cells. *Sci. Rep.* 9, 5559. doi:10.1038/s41598-019-41908-5

Farid, E., Zahra, H., Seyed, M. T., and Mojtaba, D. (2018). Simulated microgravity condition alters the gene expression of some ECM and adhesion molecules in adipose derived stem cells. *Int. J. Mol. Cell. Med.* 7, 146–157. doi:10.22088/IJMCM.BUMS.7.3.146

Gomes, J. M., Silva, S. S., Fernandes, E. M., Lobo, F. C. M., Martín-Pastor, M., Taboada, P., et al. (2022). Silk fibroin/cholinium gallate-based architectures as therapeutic tools. *Acta Biomater.* 147, 168–184. doi:10.1016/j.actbio.2022.05.020

He, L., Pan, S., Li, Y., Zhang, L., Zhang, W., Yi, H., et al. (2016). Increased proliferation and adhesion properties of human dental pulp stem cells in PLGA scaffolds via simulated microgravity. *Int. Endod. J.* 49, 161–173. doi:10.1111/iej.12441

Kundu, B., Rajkhowa, R., Kundu, S. C., and Wang, X. (2013). Silk fibroin biomaterials for tissue regenerations. *Adv. Drug Deliv. Rev.* 65, 457–470. doi:10.1016/j.addr.2012.09.043

Li, X., Zhao, Z., Yang, Y., Liu, Z., Wang, J., Xu, Y., et al. (2020). Novel β-1, 3-d-glucan porous microcapsule enveloped folate-functionalized liposomes as a Trojan horse for facilitated oral tumor-targeted co-delivery of chemotherapeutic drugs and quantum dots. *J. Mat. Chem. B* 8, 2307–2320. doi:10.1039/c9tb02674f

Liu, Y. G., Tang, X. L., Wang, S. B., Chen, A. Z., Wu, W. G., and Long, R. M. (2015). A novel cartilage tissue construction based on artificial cells and matrix-shaping. *Mat. Lett.* 159, 24–27. doi:10.1016/j.matlet.2015.06.068

Luo, C., Fang, H. M., Li, J. L., Hou, J. F., Yang, J., Yuan, Q., et al. (2019). An *in vivo* comparative study of the gelatin microtissue-based bottom-up strategy and top-down strategy in bone tissue engineering application. *J. Biomed. Mat. Res. A* 107, 678–688. doi:10.1002/jbm.a.36587

Mattei, C., Alshawaf, A., D'Abaco, G., Nayagam, B., and Dottori, M. (2018). Generation of neural organoids from human embryonic stem cells using the rotary cell culture system: Effects of microgravity on neural progenitor cell fate. *Stem Cells Dev.* 27, 848–857. doi:10.1089/scd.2018.0012

Mawad, A., Helmy, Y. A., Shalkami, A. G., Kathayat, D., and Rajashekara, G. (2018). E-coli Nissle microencapsulation in alginate-chitosan nanoparticles and its effect on Campylobacter jejuni *in vitro*. *Appl. Microbiol. Biotechnol.* 102, 10675–10690. doi:10.1007/s00253-018-9417-3

Montanucci, P., Pennoni, I., Pescara, T., Basta, G., and Calafiore, R. (2013). Treatment of diabetes mellitus with microencapsulated fetal human liver (FH-B-TPN) engineered cells. *Biomaterials* 34, 4002–4012. doi:10.1016/j.biomaterials.2013.02.026

Nie, M. H., and Takeuchi, S. (2018). Bottom-up biofabrication using microfluidic techniques. *Biofabrication* 10, 044103. doi:10.1088/1758-5090/aadef9

Okudaira, T., Yabuta, R., Mizumoto, H., and Kajiwara, T. (2017). Fabrication of a fiber-type hepatic tissue by bottom-up method using multilayer spheroids. *J. Biosci. Bioeng.* 123, 739–747. doi:10.1016/j.jbiosc.2017.01.002

Sapudom, J., ElGindi, M., Arnoux, M., Drou, N., Garcia-Sabaté, A., and Teo, J. C. (2021). Fibroblast differentiation and matrix remodeling impaired under simulated microgravity in 3D cell culture model. *Int. J. Mol. Sci.* 22, 11911. doi:10.3390/ijms222111911

Song, J. J., Tian, W. J., Kwok, L. Y., Wang, Y. L., Shang, Y. N., Menghe, B., et al. (2017). Effects of microencapsulated Lactobacillus plantarum LIP-1 on the gut microbiota of hyperlipidaemic rats. *Br. J. Nutr.* 118, 481–492. doi:10.1017/s0007114517002380

Zhang, X. K., Zhang, L., Xu, M. Q., Li, Q., and Miao, R. K. (2017). Synthesis of microencapsulated oyster peptides and its effect on inflammatory cytokines and enzyme levels in mice. *Food Meas.* 11, 610–620. doi:10.1007/s11694-016-9429-6

Zhang, X. L., Wang, W., Xie, Y. B., Zhang, Y., Wang, X. L., Guo, X., et al. (2006). Proliferation, viability, and metabolism of human tumor and normal cells cultured in microcapsule. *Appl. Biochem. Biotechnol.* 134, 61–76. doi:10.1385/abab:134:1:61

Zhao, D., and Zhang, X. Y. (2018). Selenium antagonizes the lead-induced apoptosis of chicken splenic lymphocytes *in vitro* by activating the pi3k/akt pathway. *Biol. Trace Elem. Res.* 182, 119–129. doi:10.1007/s12011-017-1088-x

Zhou, X., Tang, X. L., Long, R. M., Wang, S. B., Wang, P., Cai, D. H., et al. (2019). The influence of bFGF on the fabrication of microencapsulated cartilage cells under different shaking modes. *Polymers* 11, 471. doi:10.3390/polym11030471

Zhou, X., Wu, K. J., Long, R. M., Kankala, R. K., Wang, S. B., and Liu, Y. G. (2018). Preparation of a MVL-Ca-Alg/CS MEMs system with add-on effect for type 2 diabetes treatment. *Int. J. Polym. Mater. Polym. Biomaterials* 67, 823–829. doi:10.1080/00914037.2017.1383249

Zou, Y., Yin, Y., Xiao, Z., Zhao, Y., Han, J., Chen, B., et al. (2022). Transplantation of collagen sponge-based three-dimensional neural stem cells cultured in a RCCS facilitates locomotor functional recovery in spinal cord injury animals. *Biomater. Sci.* 10, 915–924. doi:10.1039/d1bm01744f

frontiers | Frontiers in Bioengineering and Biotechnology

TYPE Original Research
PUBLISHED 09 January 2023
DOI 10.3389/fbioe.2022.1016001

EDITED BY
Junchao Wei,
Nanchang University, China

REVIEWED BY
Meng Tian,
Sichuan University, China
Yuangang Liu,
Huaqiao University, China

*CORRESPONDENCE
Hao Wang,
✉ wanghaosci@163.com

†These authors have contributed equally to this work

SPECIALTY SECTION
This article was submitted to Biomaterials,
a section of the journal
Frontiers in Bioengineering and Biotechnology

RECEIVED 10 August 2022
ACCEPTED 22 November 2022
PUBLISHED 09 January 2023

CITATION
Bai X, Yu J, Xiao J, Wang Y, Li Z and Wang H (2023), Antibacterial intraosseous implant surface coating that responds to changes in the bacterial microenvironment.
Front. Bioeng. Biotechnol. 10:1016001.
doi: 10.3389/fbioe.2022.1016001

Antibacterial intraosseous implant surface coating that responds to changes in the bacterial microenvironment

Xin Bai[1†], Jiawei Yu[2†], Jie Xiao[1], Yanping Wang[1], Zhe Li[1] and Hao Wang[3*]

[1]Jiande First People's Hospital, Hangzhou, Zhejiang, China, [2]Zhuji Affiliated Hospital of Wenzhou Medical University, Shaoxing, Zhejiang, China, [3]Department of Orthopedics, Quanzhou First Hospital Affiliated of Fujian Medical University, Quanzhou, Fujian, China

Bone implant-associated infection is one of the most challenging problems encountered by orthopedic surgeons. There is considerable interest in the development of drug-loaded antibacterial coatings for the surfaces of metal implants. However, it is difficult to achieve the stable local release of an effective drug dose for many antibacterial coatings. In the present study, analyses of the thickness and water contact angle of multiple layers confirmed the successful assembly of multilamellar membrane structures. Measurement of the zone of bacterial inhibition indicated gradual degradation of the (montmorillonite [MMT]/hyaluronic acid [HA])$_{10}$ multilamellar film structure with concentration-dependent degradation during incubation with hyaluronidase solution and *Staphylococcus aureus*. *In vivo* results resembled the *in vitro* results. Overall, the findings confirm that the (MMT/HA-rifampicin)$_{10}$ multilamellar film structure exhibits good antibacterial properties and excellent biocompatibility. Further studies of the clinical potential of the antibacterial coating prepared in this experiment are warranted.

KEYWORDS

infection, antibacterial coating, *Staphylococcus aureus*, layer-by-layer, microenvironment

1 Introduction

Since the introduction of various metallic and non-metallic fixation materials in the field of orthopedics, and particularly with the development of internal and external fixation over the past century, advances in materials science and medical techniques have led to the increasing use of orthopedic surgery (Berger et al., 2016; Li et al., 2017). However, bone and soft tissue infections remain among the most challenging complications of orthopedic surgery (Neumann et al., 2016; Pickett et al., 2018). In cases of open fractures, various fixation devices (e.g., plate screws, external fixation brackets, and intramedullary nails) may contribute to infection (Amerstorfer et al., 2017; Perez-Jorge et al., 2017). Closed fractures have infection rates of approximately 1.5%, whereas open fractures have infection rates of 3–40% (Neumann et al., 2016; Kendall and

Gorgone, 2018). The incidence of trauma-related open fractures is increasing (Tessier et al., 2016). Approximately 60% of open fractures are contaminated by bacteria at the time of injury (Caroom et al., 2018). Fixation-related infections can also cause serious adverse consequences for patients, potentially requiring systemic antibiotics, multiple debridement-and-revision surgeries, extended hospital stays, and/or amputations; they may also result in death (Barnett et al., 2016; Klein et al., 2016). Therefore, fixation-related infections have become a major research focus in the fields of orthopedics, microbiology, biomaterials, and drug development (Jones et al., 2016; Sugii et al., 2017).

The local preventive or therapeutic application of antibiotics has received considerable attention for the treatment of internal fixation-related infections (Flamant et al., 2016). Intravenous infusion of antibiotics based on the results of drug sensitivity testing is a common clinical treatment method, but systemic drug administration can only achieve low concentrations in lesions while potentially damaging areas such as the liver, kidney, and ears (Girmenia and Iori, 2017; Kyriakidis et al., 2017). Therefore, the application of drug-loaded antibacterial coatings on the surfaces of metal implants has been proposed to aid in preventing infection and avoiding side effects associated with systemic administration (Li et al., 2016). Jennings et al. (2015) mixed vancomycin and amikacin into lecithin to form a uniform solution that could coat the surface of titanium metal. They found that the drugs could be stably released for approximately six days, and their system exhibited *in vitro* antibacterial activity against *Staphylococcus aureus*. Braem et al. (2015) used titanium with a pore structure as a drug carrier, then integrated it into a mesoporous SiO_2 diffusion barrier to control drug release on the titanium metal surface. Although this method resolved the problem of drug burst release, the drug release time remained short. Hirschfeld et al. (2017) used plasma vapor deposition to deposit vertically aligned carbon nanotubes approximately 700 nm long and 10–200 nm in diameter on the surface of titanium; the tubes were used to carry rifampicin (RFP). Their experiments confirmed the antibacterial ability of the RFP from these carbon nanotubes against *Staphylococcus epidermidis*. The greatest limitation of using these surface coatings as antibacterial drug carriers is that they generally do not allow the stable local release of effective drug doses. There is often a burst release in the early stages of drug release, and it is difficult to maintain accurate drug release for an extended duration. There has been considerable progress in the construction of stimulus-sensitive drug delivery systems on the surfaces of biological materials (Huang et al., 2016; Wang et al., 2016), and numerous drug delivery systems based on enzymes, temperature, and pH sensitivity have been constructed (Sun et al., 2021). These stimulus-sensitive drug delivery systems can control drug release and avoid drug resistance caused by excessive short-term release or minimal long-term release. The microenvironment of bacterial infection has multiple unique biological characteristics, including the abnormal expression of some enzymes and the specific release of toxins (Wang et al., 2018a). These specific biological characteristics can be used to prepare smart drug delivery systems with appropriate microenvironmental responses to ensure controlled release and accumulation of antibacterial drugs at the site of infection (Aycan and Alemdar, 2018). Layer-by-layer self-assembly based on multisubstance interactions is a useful method for the formation of nanostructured multilamellar films (Chen et al., 2017). External stimuli can achieve the selective embedding of substances and the intelligent controlled release of drugs from multilamellar films (Mable et al., 2018).

S. aureus is the main species of pathogenic bacteria encountered after surgery or trauma and the primary species involved in endosseous implant-related bone, joint, and soft tissue infections (Gundtoft et al., 2017; Araújo et al., 2018). The entry of *S. aureus* into lymphatic vessels or blood can cause sepsis. RFP, which has high antibacterial activity against various Gram-positive bacteria (Branch-Elliman et al., 2017), is a key antibiotic for treating severe *S. aureus* infections. It has an important role in clinical therapy and is an ideal antibiotic for topical application (Downes et al., 2017). During bacterial infection, the surrounding environment secretes large amounts of hyaluronidase (HAS) and phospholipase (Seroussi et al., 2018; Liu et al., 2021). Montmorillonite (MMT)/hyaluronic acid (HA) multilamellar film actively disintegrates in the presence of infection (Wang et al., 2018b). MMT is a typical clay mineral with a unique crystal structure that provides it with a high cation exchange capacity and a high expansion capacity; thus, it is widely used in various fields (Enteshari Najafabadi and Bagheri, 2017). Because of its high specific surface area, MMT can additionally be included in multilamellar films to load drugs at high concentrations and prevent rapid release (Qiao et al., 2016; Chabbi et al., 2018). HA is an acidic mucopolysaccharide that is widely distributed in the human body. It solubilizes readily in water, where it forms an acidic solution with a considerable negative charge. HA has good biocompatibility and various clinical uses (e.g., as a lubricant in joint surgery and a moisturizing agent in eye surgery) (Friedrich and Washburn, 2017; Hwang et al., 2017). In the present study, drug-loaded polyelectrolyte multilayers of $(MMT/HA\text{-}RFP)_{10}$ were fabricated in a layer-by-layer manner and exhibited HAS release-induced degradation in the presence of infection.

2 Materials and methods

2.1 Reagents and materials

MMT was obtained from Zhejiang Sanding Technology Co., Ltd. (Zhejiang, China). HA was purchased from Freda Biochem Co., Ltd. (Shandong, China). RFP and polyethyleneimine (Mw: 25 kDa) were purchased from Sigma-Aldrich (St. Louis, MO,

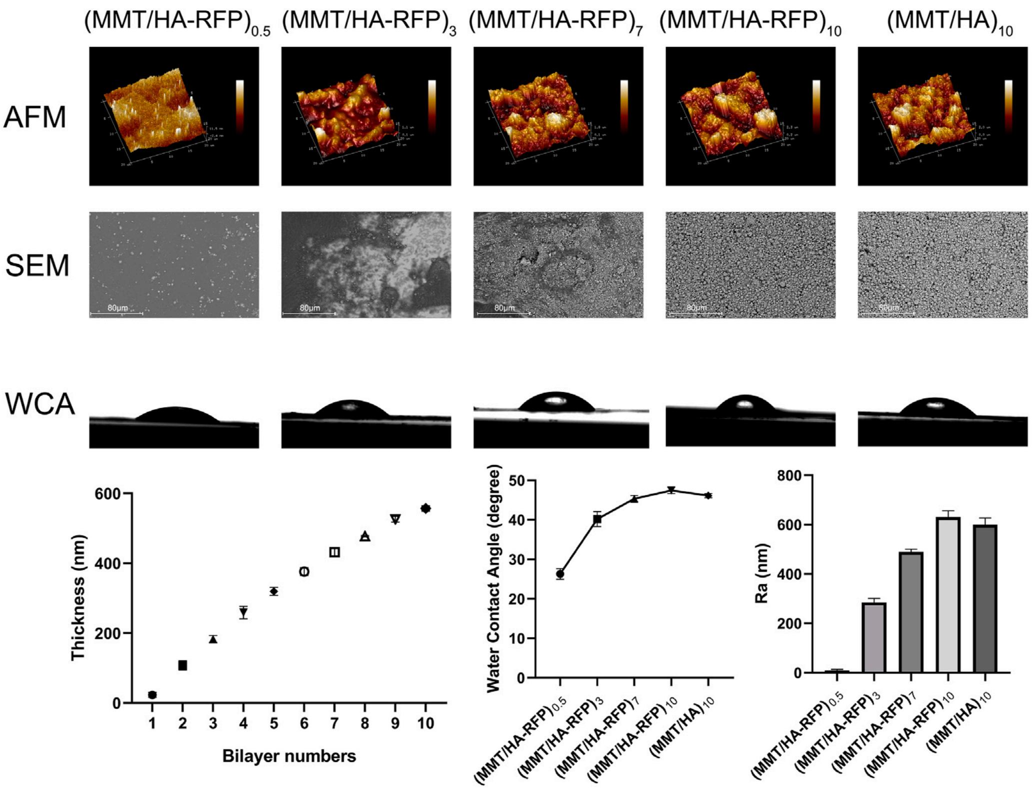

FIGURE 1
Atomic force microscopy (AFM), SEM, water contact angle (WCA), and thickness analysis of multilamellar membrane structures during co-assembly.

United States). Titanium Kirschner wires (K-wires; 1.25 mm) were purchased from MK Medical GmbH & Co. (Emmingen-Liptingen, Baden-Württemberg, Germany). Luria-Bertani agar and Luria-Bertani broth were purchased from Difco Laboratories (Detroit, MI, United States).

2.2 Construction of polyelectrolyte multilayers

The substrates were ultrasonically cleaned in acetone and in ethanol for 2 h each, then dried with compressed air. MMT stock solution (0.5 mg/ml, pH = 2.5) was prepared. Next, HA and RFP were separately dissolved at a concentration of 1.0 mg/ml in deionized water. Before assembly, the reaction solutions were dispersed by ultrasonication for 2 h. All substrates were subsequently deposited in polyethyleneimine solution (3 mg/ml, 20 min) as a precursor, then immersed alternately in MMT solution and HA-RFP solution for 15 min each at room temperature. Finally, the obtained hybrid multilamellar films were dried under a stream of nitrogen gas. This immersion cycle corresponded to the deposition of one bilayer. The above steps were repeated 10 times to yield (MMT/HA-RFP)$_{10}$ multilamellar membrane structures.

2.3 Characterization of materials

We tested the following polymer coatings: (MMT/HA-RFP)$_{0.5}$, (MMT/HA-RFP)$_3$, (MMT/HA-RFP)$_7$, (MMT/HA-RFP)$_{10}$, and (MMT/HA)$_{10}$. The surface roughness of silicon wafers, the substrate material, was measured by atomic force microscopy. Additionally, scanning electron microscopy (SEM) was performed to examine the surface morphology of each sample. To determine the wetting properties of the multilamellar film surfaces, water contact angles were measured using a video optical contact angle measuring

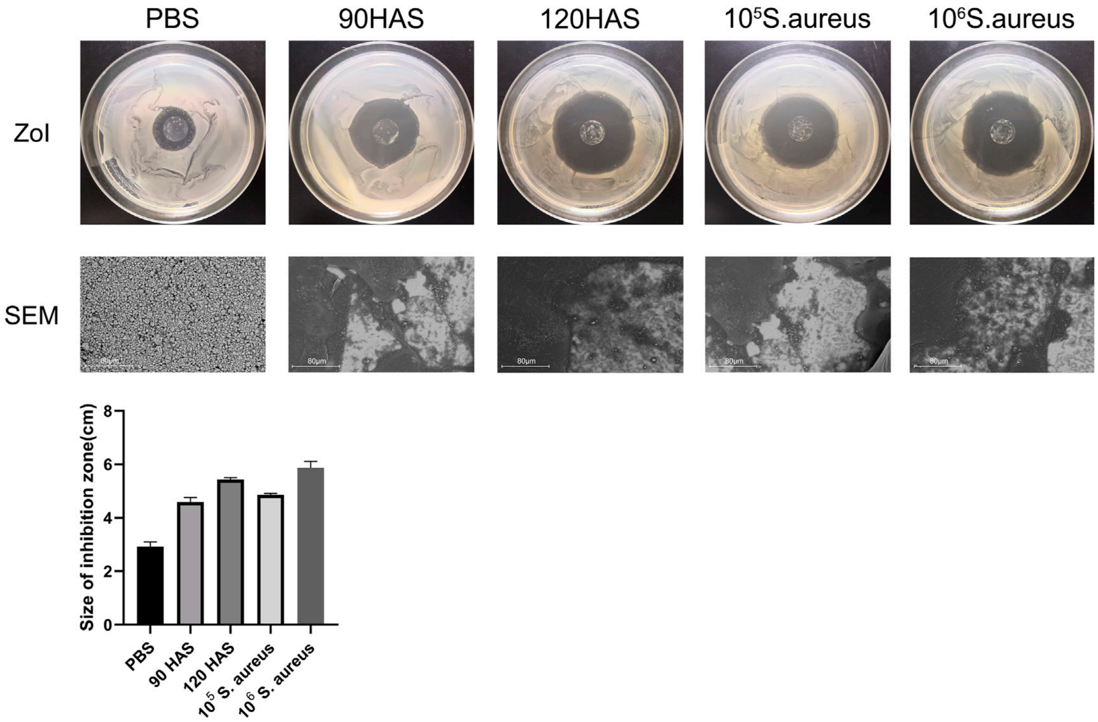

FIGURE 2
ZOI and SEM of (MMT/HA-RFP)$_{10}$ multilamellar film-coated glass slides after immersion in 0.01 M PBS, HAS, and *Staphylococcus aureus* solutions.

device (OCA15pro; DataPhysics Co., Filderstadt, Germany) in air at room temperature (25°C). The mean value of each multilamellar film structure was calculated from the measurements at three different locations. To confirm the successful assembly of multilamellar membrane structures, the thickness of (MMT/HA-RFP)$_n$ deposited in each layer was measured by spectroscopic ellipsometry (M-2000 DITM; J.A. Woollam, Lincoln, NE, United States).

2.4 Zone of inhibition measurement and SEM

Glass slides were selected as the substrate material in this study. Layer-by-layer self-assembled multilamellar films were prepared using the method described above. The multilamellar films were immersed for two days in 0.01 M phosphate-buffered saline (PBS), HAS solution, and *S. aureus* solution. At the end of the soaking period, all samples were removed and dried in an oven. *S. aureus* was grown from broth on nutrient agar, then plated on Luria-Bertani agar. Growth inhibition was verified based on the zone of inhibition (ZOI) after incubation at 37°C for 24 h. SEM was used to examine changes in the (MMT/HA-RFP)$_{10}$ multilamellar coating on the surface of the glass slides.

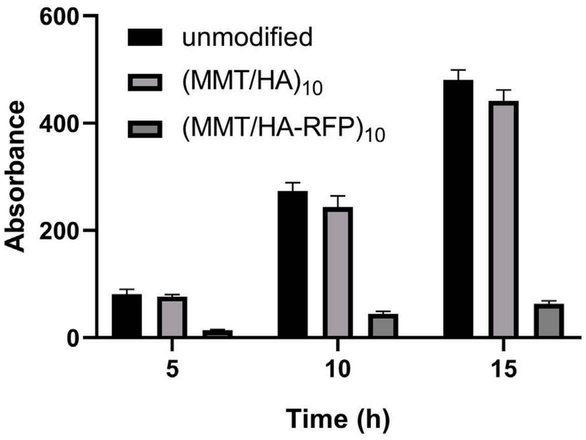

FIGURE 3
Determination of biofilm formation after immersion with unmodified, (MMT/HA)$_{10}$-coated, and (MMT/HA-RFP)$_{10}$ multilamellar film-coated silicon wafers at various time points.

2.5 Assessment of biofilm formation

Unmodified silicon wafers, as well as (MMT/HA)$_{10}$ and (MMT/HA-RFP)$_{10}$ multilamellar film silicon wafers, were

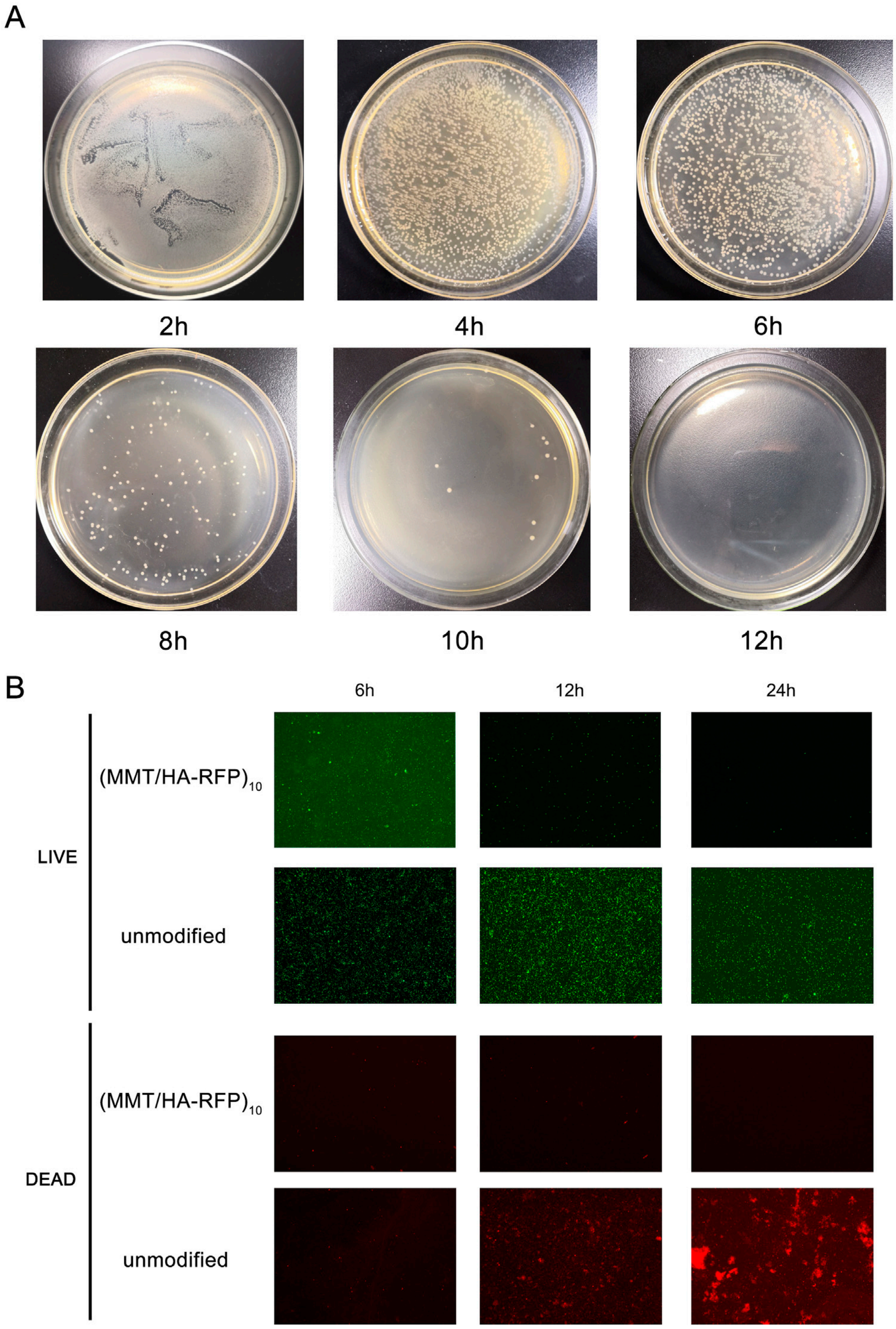

FIGURE 4
(A) Shaking flask culture and **(B)** live/dead staining assay.

prepared as three parallel samples, then immersed in 2 ml of *S. aureus* suspension [10 colony-forming units/ml (Kendall and Gorgone, 2018)] and incubated at 37°C for 5, 10, or 15 h. At preset time points, the surfaces were thoroughly rinsed with PBS. Next, all samples were stained with 1% (wt/vol) crystal violet solution for 15 min, then washed three times with PBS. Finally, 1 ml of 95% (v/v) ethanol was added to each well. The mixture was then incubated for 15 min in the dark and shocked for 10 s

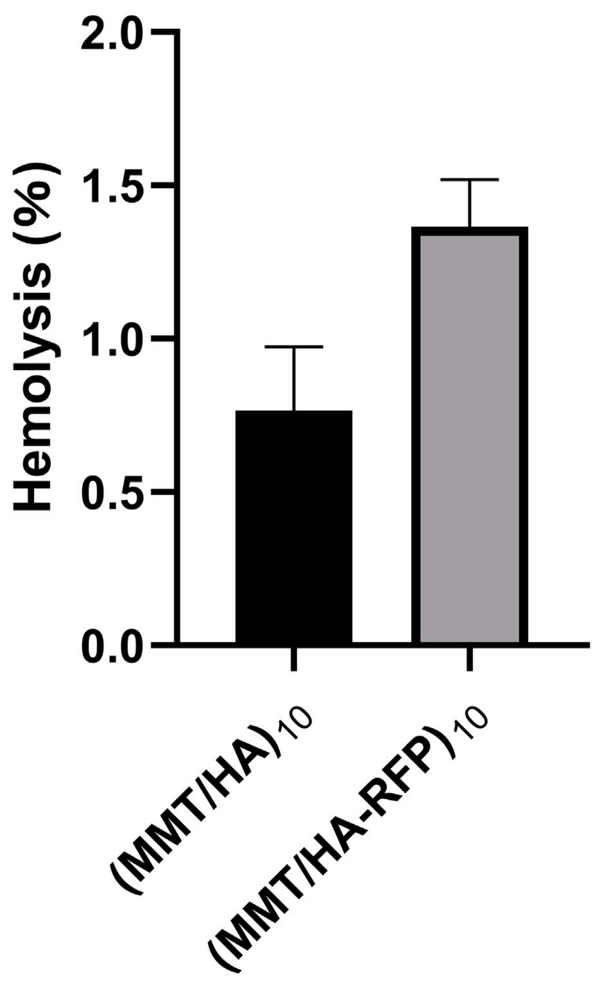

FIGURE 5
Hemolysis rates of $(MMT/HA)_{10}$ and $(MMT/HA\text{-}RFP)_{10}$ multilamellar films.

every 5 min at room temperature. The absorbance at 570 nm (A570) was measured with a microplate reader (BioTek, Winooski, VT, United States).

2.6 Shaking flask culture and live/dead staining assay

The shaking flask culture method was used to comprehensively evaluate the *in vitro* antibacterial properties of the coating. $(MMT/HA\text{-}RFP)_{10}$-coated polydimethylsiloxane was immersed in *S. aureus* solution and cultured. Aliquots of the bacterial solution were collected at specified time points (2 h, 4 h, 6 h, 8 h, 10 h, and 12 h) and diluted; next, they were evenly spread on agar plates, cultured, and counted. For direct analysis of the live/dead populations of bacteria on the surface of $(MMT/HA\text{-}RFP)_{10}$ multilamellar membrane structures, fluorescence microscopy was conducted with live/dead staining. $(MMT/HA\text{-}RFP)_{10}$-coated glass slides and unmodified glass slides were co-cultured with 3 ml of *S. aureus* solution, incubated at 37°C for 6, 12, or 24 h, and then subjected to live/dead staining.

2.7 *In vitro* hemolysis rate

Four ml of fresh anticoagulated rat blood was diluted with 5 ml of normal saline. The multilamellar film was incubated in 10 ml of normal saline (37°C constant temperature water bath, 30 min). Next, 0.2 ml of diluted blood was added by mixing, and the solution was incubated at a constant temperature of 37°C for 60 min. Aliquots of 500 μL were collected and centrifuged at 1,500 rpm for 5 min. The absorbance of the resulting supernatant at 540 nm was measured with an ultraviolet-visible spectrophotometer (PuXi TU-1800; China). In the positive control group, 0.2 ml of diluted blood was added to 10 ml of distilled water; in the negative control group, 0.2 ml of diluted blood was added to 10 ml of 0.9% NaCl solution.

Hemolysis of the multilamellar film was calculated using the following equation:

$$\text{Hemolysis rate } \% = (ODs - ODn)/(ODp - ODn) \times 100$$

where ODs, ODp, and ODn represent the respective absorbance values of the sample, negative control, and positive control groups.

2.8 Animal experiments

2.8.1 Biocompatibility analysis

Thirty male rats (body weight 200 ± 20 g) were obtained from SLAC Laboratory Animal Co., Ltd. (Shanghai, China) for use in this experiment. All experiments were approved by the Animal Research Ethics Committee of the Second Affiliated Hospital (Jiande Branch) of the School of Medicine, Zhejiang University. All rats were housed in an animal room with controlled humidity and temperature, where they were provided with adequate food and water. Unmodified, $(MMT/HA)_{10}$-coated, and $(MMT/HA\text{-}RFP)_{10}$ multilamellar film-coated K-wires were prepared. The rats were randomly divided into three groups (n = 10 per group). For the experimental analysis, the rats were initially anesthetized with 10% chloral hydrate (0.35 ml/100 g). The left knee of each rat was shaved, the overlying fur was removed, and the skin was disinfected. Then, the skin and muscles were cut to expose the tibial plateau. During this procedure, neurovascular injury was avoided when possible. Under sterile conditions, a 0.8-mm K-bit was used to drill vertically into the medullary cavity, and a sterile syringe was used to aspirate bone marrow from the tibia. Unmodified, $(MMT/HA)_{10}$-coated, or $(MMT/HA\text{-}RFP)_{10}$ multilamellar film-coated K-wires were placed in the boreholes according to each rat's group designation. The drilled hole was sealed with bone wax, and the incision was sutured layer by layer. After each rat had regained consciousness, it was

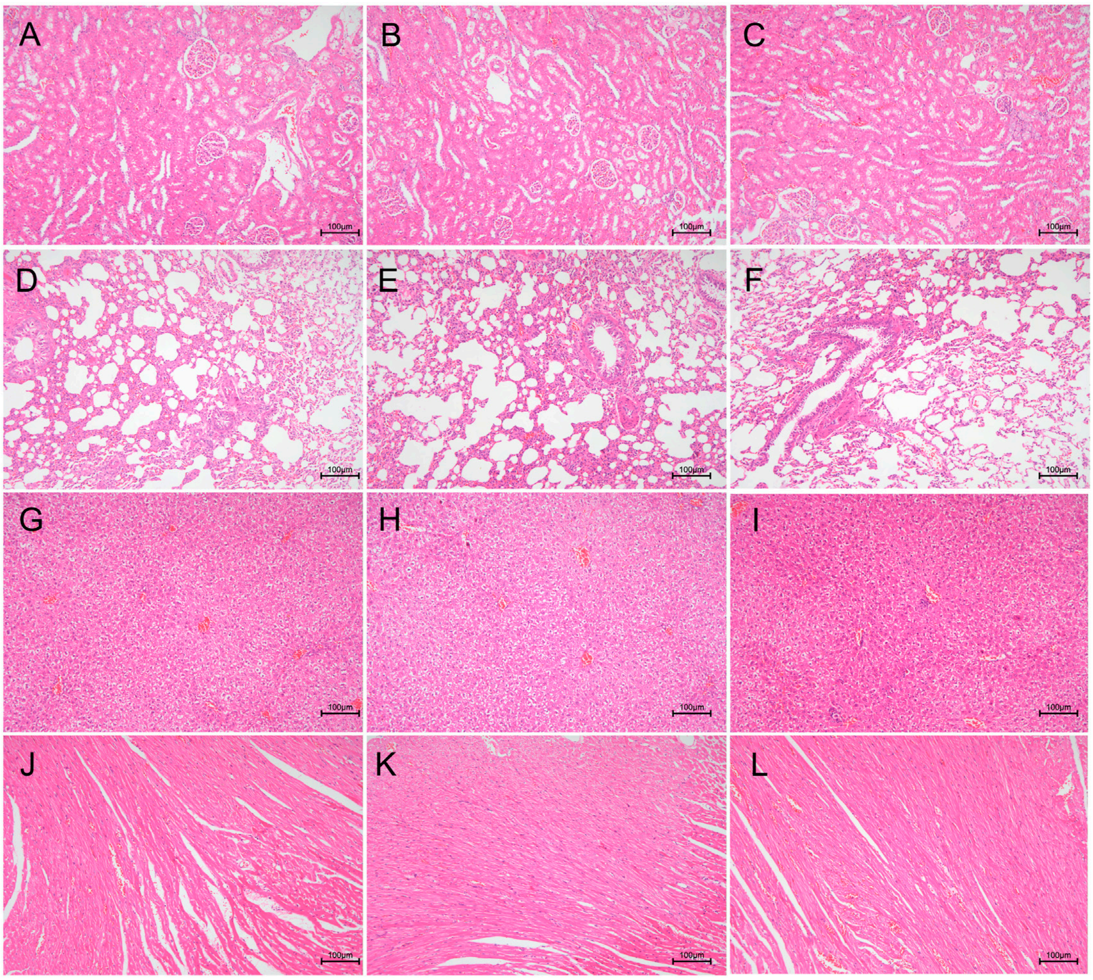

FIGURE 6
Biocompatibility analysis of $(MMT/HA)_{10}$ and $(MMT/HA\text{-}RFP)_{10}$ multilamellar films. H&E staining of rat kidney, lung, liver, and heart. **(A–C)** Kidney in the unmodified, $(MMT/HA)_{10}$, and $(MMT/HA\text{-}RFP)_{10}$ groups, respectively. **(D–F)** Lung in the unmodified, $(MMT/HA)_{10}$, and $(MMT/HA\text{-}RFP)_{10}$ groups, respectively. **(G–I)** Liver in the unmodified, $(MMT/HA)_{10}$, and $(MMT/HA\text{-}RFP)_{10}$ groups, respectively. **(J–L)** Heart in the unmodified, $(MMT/HA)_{10}$, and $(MMT/HA\text{-}RFP)_{10}$ groups, respectively.

maintained in an appropriate environment with adequate food and water. All rats were sacrificed 4 weeks after surgery. Their tissues (lung, kidney, heart, and liver) were cryopreserved, cut into sections, fixed, and stained with hematoxylin and eosin (H&E), in accordance with standard protocols.

2.8.2 *In vivo* antibacterial experiments

Thirty additional rats were used to determine the *in vivo* antimicrobial efficacy of the multilamellar film structure. The animals were divided randomly into three groups (n = 10 per group): 1) an unmodified group, with placement of unmodified K-wires and injection of 10 μL of 10^6 *S. aureus* cells/mL; 2) a $(MMT/HA\text{-}RFP)_{10}$ group, with placement of $(MMT/HA\text{-}RFP)_{10}$-coated K-wires and injection of 10 μL of 10^6 *S. aureus* cells/mL; and 3) a sham group, with placement of unmodified K-wires and without injection of *S. aureus*. For each animal, the drilled hole was sealed with bone wax, and the incision was sutured layer by layer. After each rat had regained consciousness, it was maintained in a standard environment with adequate food and water. The condition of each wound was monitored regularly.

2.8.2.1 Measurement of body temperature and inflammatory index *in vivo*

At regular intervals, each rat's body temperature was monitored and their blood collected from the tail tip to examine white blood cell (WBC) count, as well as levels of high-sensitivity C-reactive protein (hs-CRP), interleukin (IL)-1β, IL-6, and IL-8.

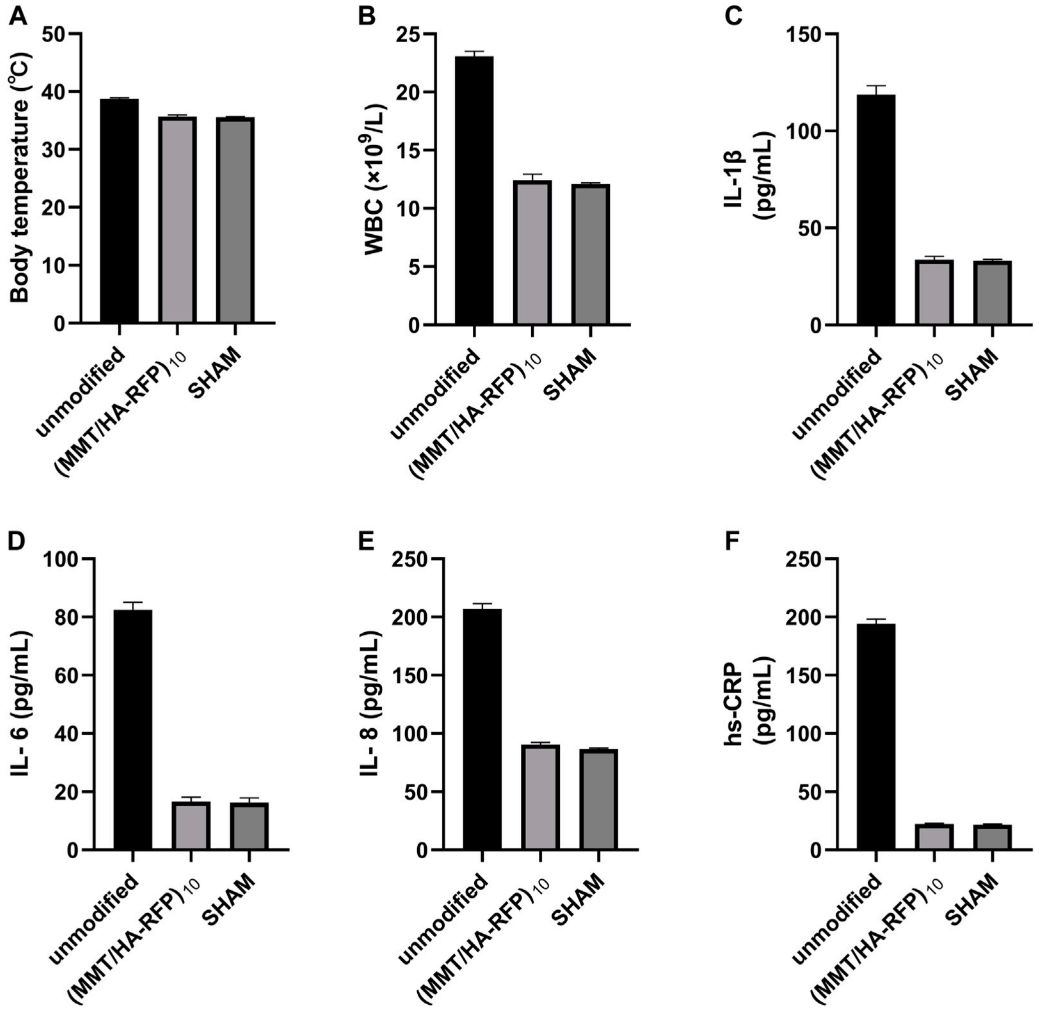

FIGURE 7
(A) Body temperature, **(B)** WBC count, **(C)** IL-1β level, **(D)** IL-6 level, **(E)** IL-8 level, and **(F)** hs-CRP level in rats.

2.8.2.2 Colonies from K-wires and soft tissue

Left tibia specimens were thawed at room temperature, then snap-frozen in liquid nitrogen. The soft tissue was pulverized in sterile PBS for 60 s. Concurrently, the K-wires were sonicated in sterile PBS for 30 min. All procedures were performed in a sterile environment. The fluids from soft tissue and K-wires were diluted in sterile saline, inoculated onto agar plates, and placed in a bacteriological incubator at a constant temperature of 37°C. Finally, the numbers of bacterial colonies on agar plates were counted.

2.8.2.3 X-ray examination

Each rat was euthanized and their left tibia extracted for X-ray examination (current, 250 mA; energy, 45 kV; integration time, 200 ms) (Carestream DRX; Carestream, Rochester, NY, United States). Three deputy chief orthopedic physicians evaluated the tibia destruction, osteolytic lesions, and tissue surrounding the tibia. Then, each tibia was wrapped in saline-saturated gauze and stored at −20°C.

2.8.2.4 Computed tomography examination

Left tibia specimens were thawed at room temperature and their soft tissue removed. Next, the samples were fixed with 4% paraformaldehyde in PBS for 12 h. Tibia lesions were observed by CT (energy, 70 kV at 114 μA; integration time, 300 ms; threshold, 220) (Skyscan 1,173; Skyscan, Kontich, Belgium). A ring with a surface radius of 0.1 mm from the metal implant was evaluated as the volume of interest. CT software was used to analyze bone mineral density (BMD), trabecular bone number (Tb.N),

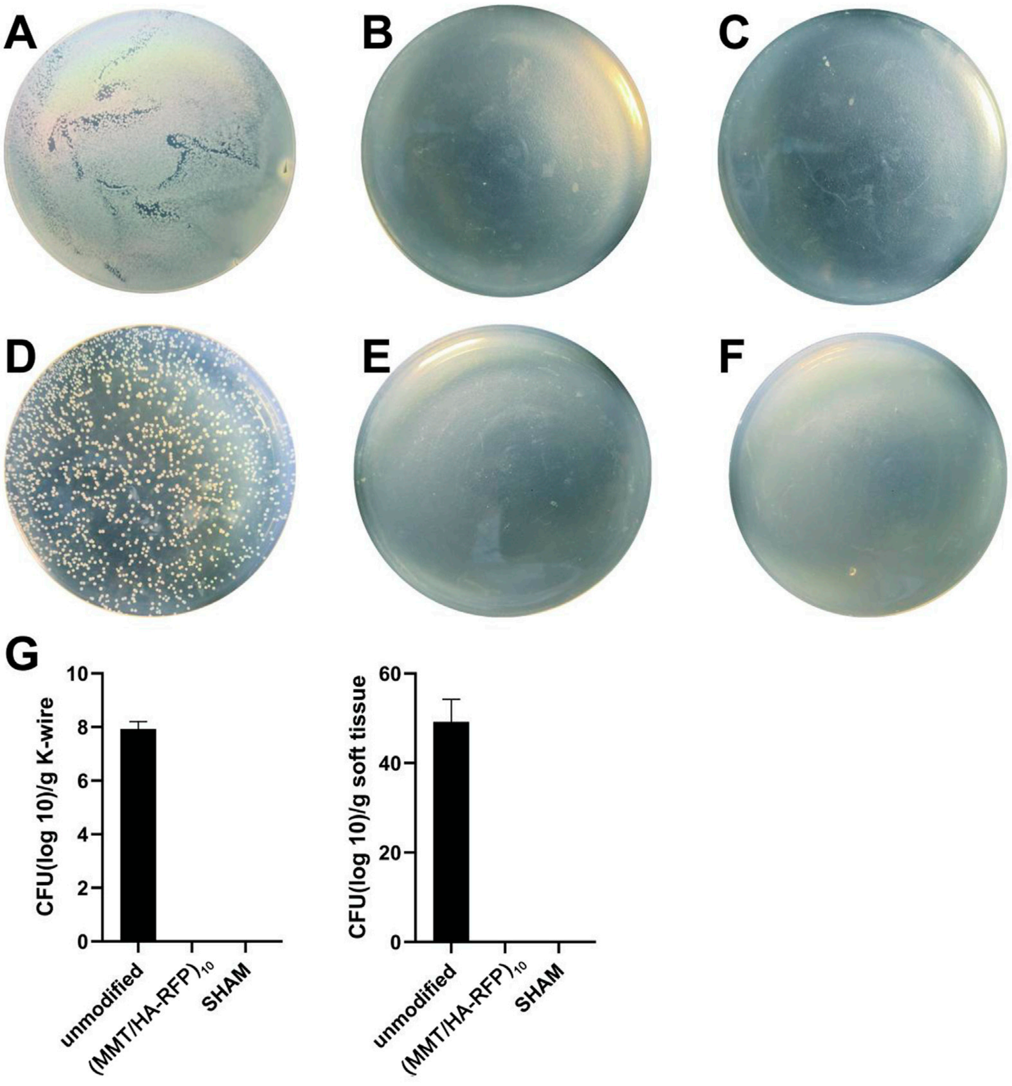

FIGURE 8
Colonies from K-wires: **(A–C)** unmodified, (MMT/HA-RFP)$_{10}$, and sham groups, respectively. Colonies from soft tissue: **(D–F)** unmodified, (MMT/HA-RFP)$_{10}$, and sham groups, respectively. **(G)** Number of colonies in each group.

percentage bone volume (BV/TV), and trabecular thickness (Tb.Th); three-dimensional histograms were also constructed.

2.8.2.5 Tibia specimen bending test

Left tibia specimens were thawed at room temperature and their soft tissue removed. The specimens were subjected to three-point bending tests to determine their integration strength, using an ElectroForce 3200 computer-controlled testing machine (Bose Corp., Eden Prairie, MN, United States); a crosshead speed of 1 mm min−1 was applied until each specimen broke. Finally, the maximum load, maximum strain, maximum bending moment, maximum stress, and bending section modulus were determined for the quantitative analysis of the mechanical strength of each tibia.

2.8.2.6 Histological analysis

Lesions of the tibial metaphysis were fixed with 4% paraformaldehyde for 48 h. Tibia bone specimens were decalcified with ethylenediaminetetraacetic acid solution for

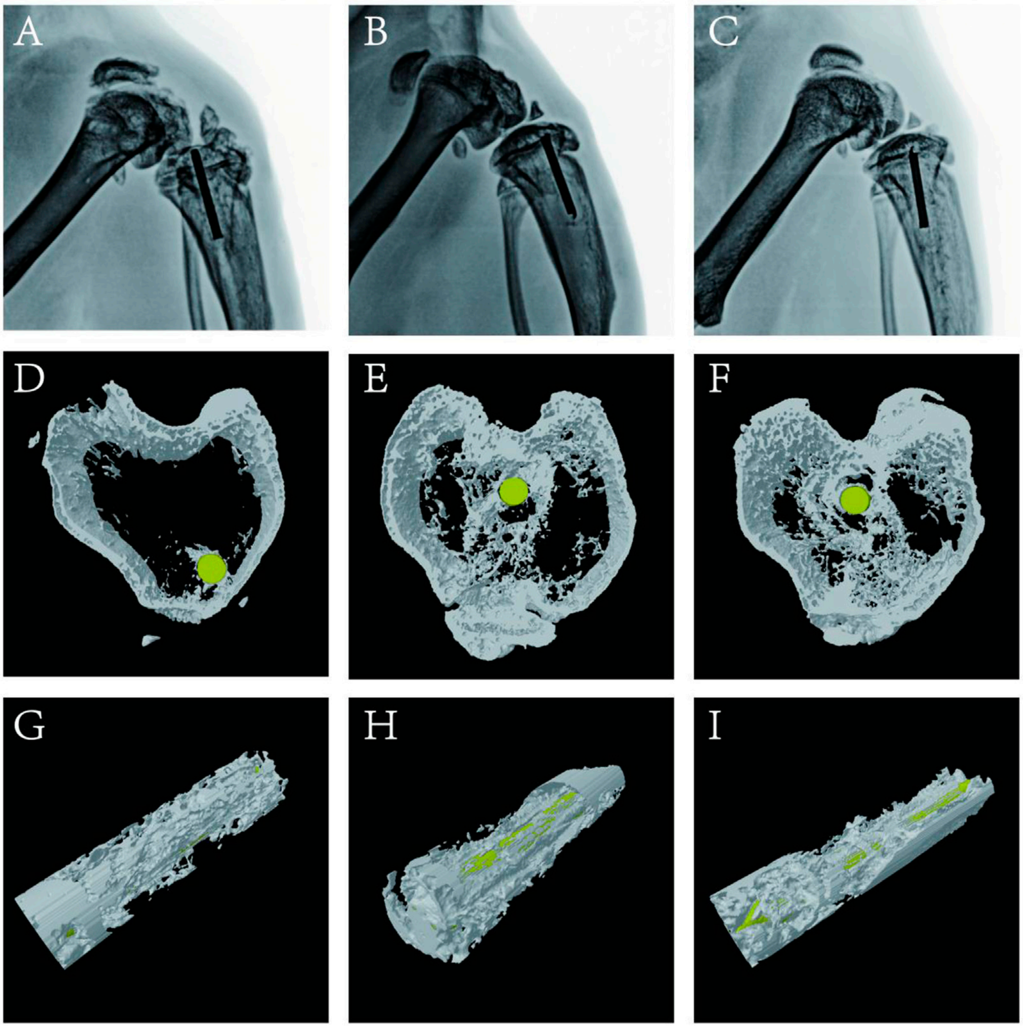

FIGURE 9
X-ray examination: **(A–C)** unmodified, $(MMT/HA\text{-}RFP)_{10}$, and sham groups, respectively. Trabecular distribution: **(D–F)** unmodified, $(MMT/HA\text{-}RFP)_{10}$, and sham groups, respectively. New bone formation surrounding implants: **(G–I)** unmodified, $(MMT/HA\text{-}RFP)_{10}$, and sham groups, respectively.

one month, then embedded in paraffin. The specimens were cut into 5-μm-thick sections; stained with H&E, Masson's trichrome, and toluidine blue; and then observed under a microscope.

2.9 Statistical analysis

Data analyses were performed using SPSS 24.0 (SPSS Inc., Chicago, IL, United States). Multisample means were evaluated by one-way analysis of variance ($\alpha = 0.05$). Comparisons among groups were analyzed by the *t*-test. In all analyses, $p < 0.05$ was considered to indicate statistical significance.

3 Results and discussion

3.1 Characterization of materials

As shown in Figure 1, we measured the roughness of surfaces using atomic force microscopy (AFM). After the coating was deposited, surface roughness increased. More specifically, the $(MMT/HA\text{-}RFP)_{0.5}$ coating had a roughness of 8.70 ± 4.14 nm, and the $(MMT/HA\text{-}RFP)_3$ coating had a roughness of 285.33 ± 12.71 nm. The roughness of the $(MMT/HA\text{-}RFP)_7$ coating was 489.33 ± 9.03 nm, that of the $(MMT/HA\text{-}RFP)_{10}$ coating was 630.00 ± 21.74 nm, and that of the $(MMT/HA)_{10}$ coating was

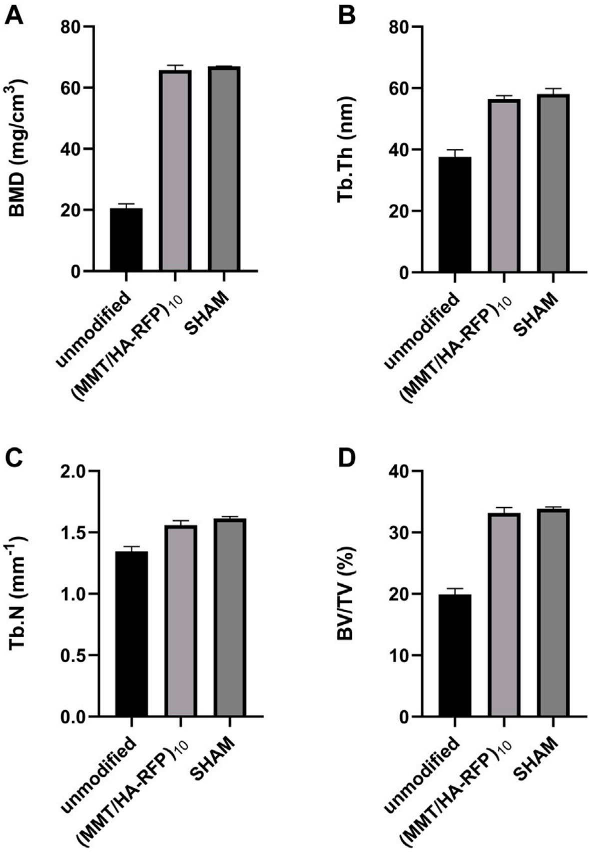

FIGURE 10
Analysis of **(A)** BMD, **(B)** Tb.Th, **(C)** Tb.N, and **(D)** BV/TV in each group.

599.67 ± 22.07 nm. Using SEM, we observed multiple layers on the surface of substrate, with uniform membrane structure. Next, the contact angle was measured to determine the hydrophilicity of each surface. The contact angles were 26.30 ± 1.10° for the $(MMT/HA\text{-}RFP)_{0.5}$ coating, 40.20 ± 1.56° for the $(MMT/HA\text{-}RFP)_3$ coating, 45.37 ± 0.63° for the $(MMT/HA\text{-}RFP)_7$ coating, and 47.43 ± 0.63° for the $(MMT/HA\text{-}RFP)_{10}$ coating. In addition, the contact angle of the $(MMT/HA)_{10}$ coating was 46.13 ± 0.42°. This shows that the material has a hydrophilic surface after coating modification. Many reports have indicated that moderate hydrophilicity could increase the biocompatibility of the material (Bluestein et al., 2017; Hu et al., 2017). Finally, we performed thickness measurements on multilayer structures. The thickness of the multilamellar membrane structures clearly exhibited linear growth as assembly progressed. More specifically, the thickness of the $(MMT/HA\text{-}RFP)_1$ coating was 23.33 ± 5.79 nm. As self-assembly progressed, the $(MMT/HA\text{-}RFP)_5$ coating had a thickness of 319.67 ± 9.46 nm and the $(MMT/HA\text{-}RFP)_{10}$ coating had a thickness of 557.00 ± 5.10 nm.

3.2 ZOI measurement and SEM

The ZOI represents the diameter of the bacteriostatic area, which reflects the antibacterial coating of the multilamellar films. As shown in Figure 2, after immersion in 0.01 M PBS, the ZOI around the multilamellar films was 2.93 ± 0.14 cm, whereas it was 4.59 ± 0.14 cm and 5.43 ± 0.06 cm after immersion in HAS solutions at concentrations of 90 and 120 U/mL, respectively. After multilamellar films had been immersed in solutions containing 105 or 106 colony-forming units/mL of *S. aureus*, the ZOIs were 4.86 ± 0.05 cm and 5.87 ± 0.20 cm, respectively. Changes in the multilamellar coating on the surfaces of glass slides were examined by SEM. Compared with immersion in PBS, the degree of disintegration of the $(MMT/HA\text{-}RFP)_{10}$ multilamellar film structure gradually increased after two days of immersion in solutions with increasing concentrations of HAS and *S. aureus*. The ZOI increase with increasing concentrations of HAS and bacterial solutions may have occurred because the HAS secreted by *S. aureus* promoted the disintegration of the multilamellar film,

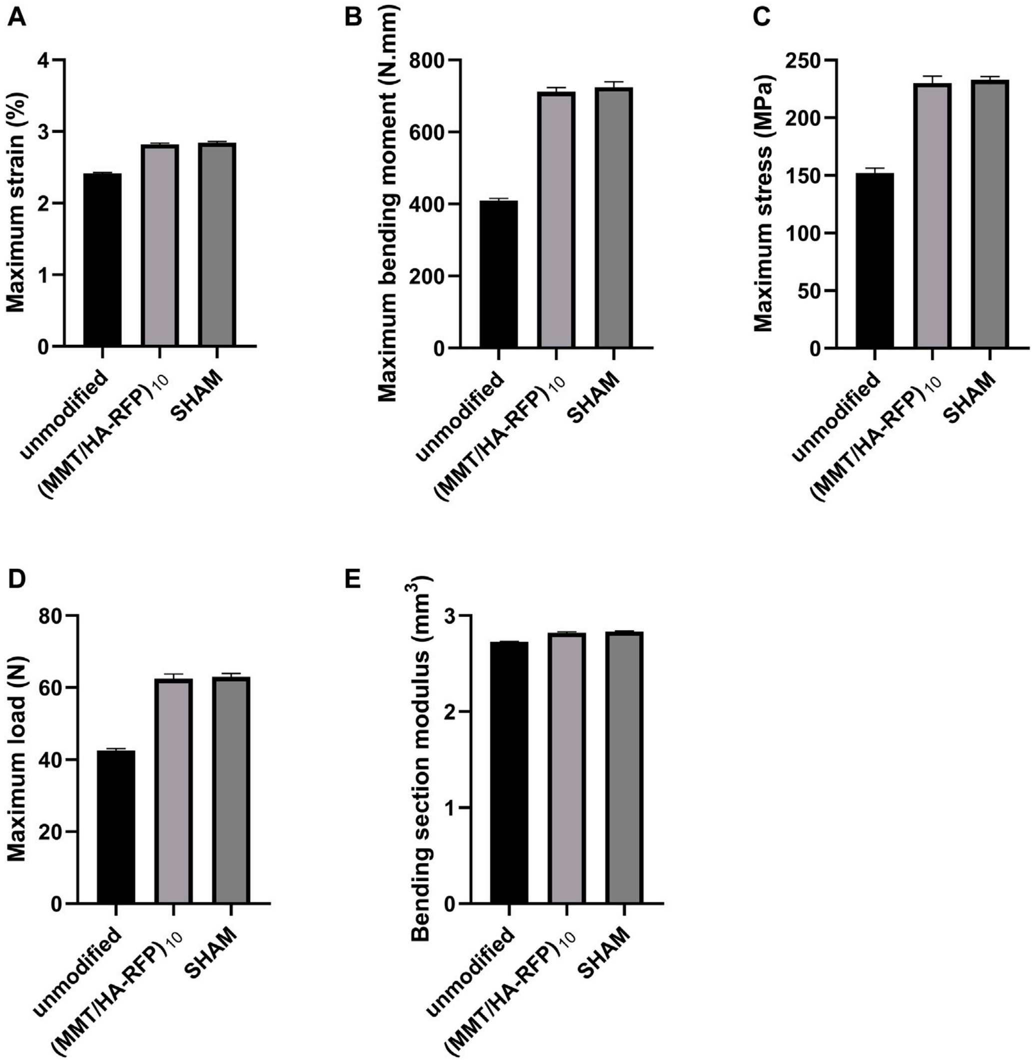

FIGURE 11
Bending tests of tibia specimens: **(A)** maximum strain, **(B)** maximum bending moment, **(C)** maximum stress, **(D)** maximum load, **(E)** bending section modulus.

leading to large amounts of disintegrated film fragments on the surface of the glass slides, and MMT could be loaded with large amounts of the test drug.

3.3 Determination of biofilm formation

Biofilm inhibition activity was assessed by crystal violet staining (Figure 3). The crystal violet absorption by the $(MMT/HA\text{-}RFP)_{10}$ samples was substantially lower than the crystal violet absorption by the unmodified samples at all time points examined (5, 10, and 15 h). With increasing culture time, the crystal violet absorption by all $(MMT/HA\text{-}RFP)_{10}$ samples slowly increased, whereas the crystal violet absorption by unmodified samples substantially increased, confirming that the $(MMT/HA\text{-}RFP)_{10}$ multilamellar film structure had strong biofilm-inhibition effects.

3.4 Shaking flask culture and live/dead staining assay

The number of bacteria was calculated at various time points using the shaking flask method. As shown in Figure 4, the number of bacteria decreased over time, nearly reaching zero at 12 h, indicating that the antibacterial coating can

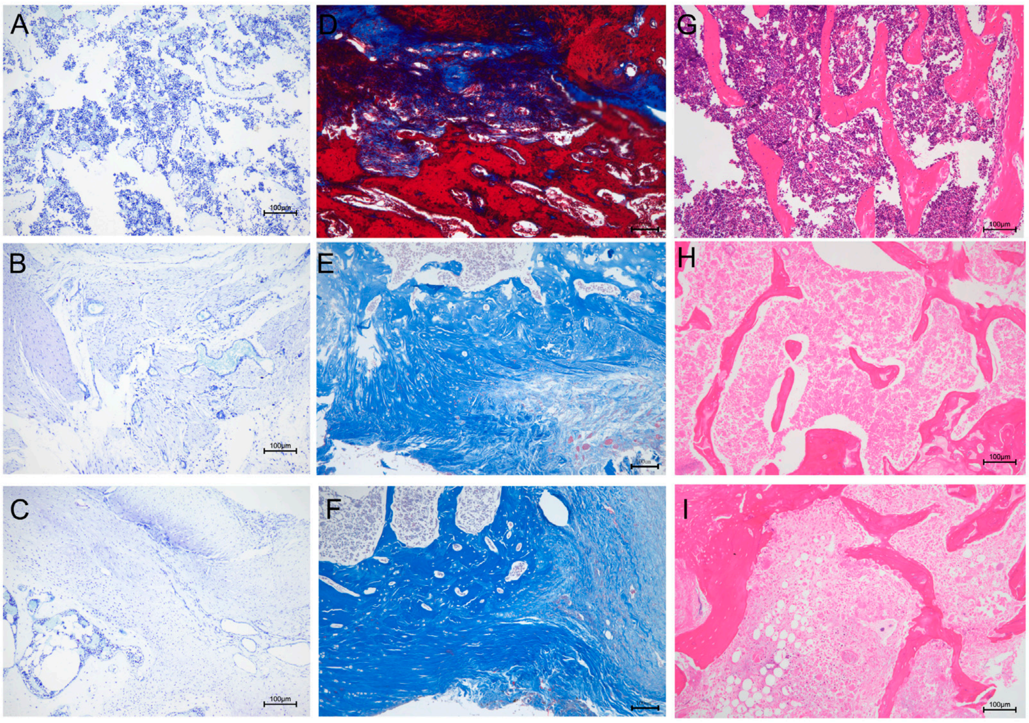

FIGURE 12
Histological analysis. Toluidine blue staining: **(A–C)** unmodified, $(MMT/HA\text{-}RFP)_{10}$, and sham groups, respectively. Masson's trichrome staining: **(D–F)** unmodified, $(MMT/HA\text{-}RFP)_{10}$, and sham groups, respectively. H&E staining: **(G–I)** unmodified, $(MMT/HA\text{-}RFP)_{10}$, and sham groups, respectively.

rapidly and efficiently sterilize bacterial solutions. After 6, 12, and 24 h of coincubation, the numbers of both live (green) and dead (red) bacteria were substantially reduced on the surface of the $(MMT/HA\text{-}RFP)_{10}$ multilamellar film, compared with the unmodified group. These observations indicate that the $(MMT/HA\text{-}RFP)_{10}$ polymer multilamellar film has excellent antibacterial properties. The $(MMT/HA\text{-}RFP)_{10}$ multilamellar membrane structure may also remove some dead bacteria from the surface.

3.5 *In vitro* hemolysis rate

The hemolysis rate represents the degree of damage to red blood cells caused by the test material, which is an important consideration in the experimental analysis of medical materials (Figure 5). The absorbance value of the positive control group (ODp) was 1.225 L/g/cm, whereas the absorbance value of the negative control group (ODn) was 0.001 L/g/cm. The absorbance values of the sample (ODs) were substituted into the formula specified in the Methods to calculate the hemolysis rate. The hemolysis rate of the membrane surface was <5%, consistent with the standard for medical polymer materials, and the multilayer structure fulfilled the requirements of the body environment (Dang et al., 2019).

3.6 Biosafety evaluation

To evaluate the biocompatibility of the $(MMT/HA\text{-}RFP)_{10}$ multilamellar membrane structure, H&E-stained vital organ sections were subjected to histological examination. Heart, liver, lung, and kidney sections from the $(MMT/HA)_{10}$ and $(MMT/HA\text{-}RFP)_{10}$ groups exhibited normal morphology (Figure 6). Therefore, the $(MMT/HA\text{-}RFP)_{10}$ multilamellar membrane structure demonstrated excellent biocompatibility.

3.7 Measurement of body temperature and inflammatory index *in vivo*

A rat infection model was used to explore the *in vivo* antibacterial properties of $(MMT/HA\text{-}RFP)_{10}$ multilamellar films. Body temperature and WBC count, as well as levels of hs-CRP, IL-1β, IL-6, and IL-8, were examined to characterize infection control. At 4 weeks after surgery, body temperature in the sham group was normal (35.57°C ± 0.09°C), whereas body temperature in the unmodified group had significantly increased to 38.73°C ± 0.17°C. However, body temperature in the (MMT/HA-RFP)$_{10}$ group was 35.67°C ± 0.25°C (Figure 7A), presumably because the (MMT/HA-RFP)$_{10}$ multilamellar film released antibiotics that killed bacteria; no rats in that group exhibited postoperative infection. Moreover, WBC count in the unmodified group was elevated at 4 weeks after surgery but within normal limits in the (MMT/HA-RFP)$_{10}$ group (Figure 7B). Similar trends were observed in the levels of IL-1β (Figure 7C), IL-6 (Figure 7D), IL-8 (Figure 7E) and hs-CRP (Figure 7F).

3.8 Colonies isolated from K-wires and soft tissue

Bacteriological examination revealed large amounts of bacteria on K-wires and in soft tissue in the unmodified group (Figures 8A,D), indicating that bacteria spread *via* circulation and multiplied throughout the body. However, there were no bacteria in the (MMT/HA-RFP)$_{10}$ group (Figures 8B,E). As expected, there were also no bacteria in the sham group (Figures 8C,F). Compared with the unmodified group, the surfaces of the K-wires and soft tissue in the (MMT/HA-RFP)$_{10}$ group showed 7.93 ± 0.23 and 49.20 ± 4.12 log reductions of *S. aureus*, respectively (Figure 8G).

3.9 X-ray and CT examination

Bone infection is commonly assessed by X-ray examination in clinical practice (Mistry et al., 2016). Bone in the sham group exhibited excellent structural integrity (Figure 9C), confirming that the surgeries had been performed successfully, animal management was reliable, and no infections had occurred. The unmodified group exhibited bone destruction on the tibial plateau, and the femoral condyle was infected (Figure 9A). These phenomena may have occurred because bacteria multiplied throughout the body and severely damaged the bone structure. Notably, no bone destruction was observed in the (MMT/HA-RFP)$_{10}$ group, despite injection of *S. aureus* into the bone (Figure 9B). To comprehensively assess bone tissue microstructure, three-dimensional histograms were constructed using the software provided with the CT scanner. K-wires appeared yellow on cross-sections of rat tibia. Trabecular bone constitutes the internal extension of cortical bone in the bone marrow cavity. There is an irregular network structure inside, which supports hematopoietic function; this microstructure is extremely difficult to segment within the bone (Kesavan et al., 2017). As shown in Figure 9D, the unmodified group exhibited the widespread rupture and disordered arrangement of trabecular bone. However, the (MMT/HA-RFP)$_{10}$ and sham groups exhibited considerably less trabecular bone destruction (Figures 9E,F). Moreover, minimal new bone formation was visible in the unmodified group (Figure 9G). In contrast, a considerable amount of new bone was detected around implants in the (MMT/HA-RFP)$_{10}$ group; the new bone was in close contact with the implant surface (Figure 9H). Importantly, the findings were similar between the (MMT/HA-RFP)$_{10}$ and sham groups (Figure 9I). Furthermore, micro-CT was performed to quantify BMD, Tb.N, BV/TV, and Tb.Th (Figure 10). In the sham group, the tibia lesions demonstrated normal values of BMD, Tb.N, BV/TV, and Tb.Th. In the unmodified group, the presence of bacteria led to significant decreases in the tibial total BMD, Tb.N, BV/TV, and Tb.Th. Bacterial proliferation affects bone cell growth (Min et al., 2016). Surprisingly, all characteristics in the (MMT/HA-RFP)$_{10}$ group resembled characteristics in the sham group.

3.10 Bending tests of tibia specimens

The three-point bending test was used to examine the integration strength of bone samples in each group through assessments of maximum load, maximum strain, maximum bending moment, maximum stress, and bending section modulus. As shown in Figure 11, tibia lesions in the sham group had normal values for maximum load, maximum strain, maximum bending moment, maximum stress, and bending section modulus. However, all values were significantly lower in the unmodified group. Bacteria can reportedly disrupt homeostatic balance in bone and destroy the integrity of bone microstructure (Raphel et al., 2016). Importantly, all characteristics in the (MMT/HA-RFP)$_{10}$ group resembled characteristics in the sham group, confirming that the (MMT/HA-RFP)$_{10}$ multilamellar membrane structure has good antibacterial properties.

3.11 Histological analysis

We performed further histological analyses by staining bone sections with H&E, Masson's trichrome, and toluidine blue. Toluidine blue staining showed numerous mast cells in the bone tissue of the unmodified group (Figure 12A). Mast cells can release large amounts of inflammatory mediators, such as tumor necrosis factor-α, IL-1, and IL-8 (Delgado et al., 2020). However, inflammatory mast cell infiltration was significantly reduced in the (MMT/HA-RFP)$_{10}$ group (Figure 12B). In the sham group, mast cells were not observed, and the bone tissue structure was normal (Figure 12C). Furthermore, the sections were subjected to Masson's trichrome staining to visualize collagen fibers and assess fibrotic lesions in bone tissue (Griffin et al., 2019). In the unmodified group, most areas were stained red because of infection-induced fibrosis in the bone marrow cavity (Figure 12D). Notably, bone tissue was completely free of fibrotic lesions in the (MMT/HA-RFP)$_{10}$ and sham groups (Figures 12E, 2F). H&E staining revealed that large quantities of inflammatory cells had penetrated the bone trabecula in the unmodified group, which confirmed the presence of bone infection (Figure 12G). However, no inflammatory responses (e.g., swelling or inflammatory cell infiltration) were found in the (MMT/HA-RFP)$_{10}$ and sham groups (Figures 12H,I).

4 Conclusion

In this study, a (MMT/HA-RFP)$_{10}$ multilamellar film structure was successfully prepared from MMT, HA, and RFP; its thickness increased linearly during layer-by-layer assembly. The (MMT/HA-RFP)$_{10}$ multilamellar film structure gradually deteriorated and exhibited concentration-dependent degradation during incubation with solutions containing HAS and *S. aureus*. The (MMT/HA-RFP)$_{10}$ multilamellar film structure showed good antibacterial properties, as determined by analyses of biofilm formation and shaking flask culture. The hemolysis rate highlighted the excellent biocompatibility of this material. (MMT/HA-RFP)$_{10}$ multilamellar film-coated K-wires showed excellent antibacterial properties and excellent biocompatibility *in vivo*. Further studies are needed to fully characterize the clinical potential of this material.

Data availability statement

The original contributions presented in the study are included in the article/Supplementary Material; further inquiries can be directed to the corresponding author.

Ethics statement

The animal study was reviewed and approved by the Animal Research Ethics Committee of the Second Affiliated Hospital (Jiande Branch) of the School of Medicine, Zhejiang University. Written informed consent was obtained from the owners for the participation of their animals in this study.

Author contributions

XB: conceptualization, methodology, software, investigation, formal analysis, writing—original draft; JY: data curation, writing—original draft; JX: visualization, investigation; YW: resources, supervision; ZL: software, validation; HW: conceptualization, funding acquisition, resources, supervision, writing—review and editing).

Acknowledgments

We thank all study participants.

Conflict of interest

The authors declare that the research was conducted in the absence of any commercial or financial relationships that could be construed as a potential conflict of interest.

Publisher's note

References

Amerstorfer, F., Fischerauer, S., Sadoghi, P., Schwantzer, G., Kuehn, K., Leithner, A., et al. (2017). Superficial vancomycin coating of bone cement in orthopedic revision surgery: A safe technique to enhance local antibiotic concentrations. *J. Arthroplasty* 32 (5), 1618–1624. doi:10.1016/j.arth.2016.11.042

Araújo, T., Rodrigues, P., Santos, M., de Oliveira, J., Rosa, L., Bagnato, V., et al. (2018). Reduced methicillin-resistant *Staphylococcus aureus* biofilm formation in bone cavities by photodynamic therapy. *Photodiagnosis Photodyn. Ther.* 21, 219–223. doi:10.1016/j.pdpdt.2017.12.011

Aycan, D., and Alemdar, N. J. C. p. (2018). Development of pH-responsive chitosan-based hydrogel modified with bone ash for controlled release of amoxicillin. *Carbohydr. Polym.* 184, 401–407. doi:10.1016/j.carbpol.2017.12.023

Barnett, S., Peters, D., Hamilton, W., Ziran, N., Gorab, R., and Matta, J. J. T. J. o. a. (2016). Is the anterior approach safe? Early complication rate associated with 5090 consecutive primary total hip arthroplasty procedures performed using the anterior approach. *J. Arthroplasty* 31 (10), 2291–2294. doi:10.1016/j.arth.2015.07.008

Berger, L., Eichler, J., Ryll, E., Fischerauer, S., Raschke, M., Kolbitsch, A., et al. (2016). Advanced interlocking systems to improve heavy-load-bearing characteristics of flexible intramedullary nailing. *Mater. Sci. Eng. C* 68, 358–365. doi:10.1016/j.msec.2016.05.122

Bluestein, B., Reed, J., and Canavan, H. J. A. s. s. (2017). Effect of substrate storage conditions on the stability of "Smart" films used for mammalian cell applications. *Appl. Surf. Sci.* 392, 950–959. doi:10.1016/j.apsusc.2016.07.004

Braem, A., De Cremer, K., Delattin, N., De Brucker, K., Neirinck, B., Vandamme, K., et al. (2015). Novel anti-infective implant substrates: Controlled release of antibiofilm compounds from mesoporous silica-containing macroporous titanium. *Colloids Surfaces B Biointerfaces* 126, 481–488. doi:10.1016/j.colsurfb.2014.12.054

Branch-Elliman, W., Ripollone, J., O'Brien, W., Itani, K., Schweizer, M., Perencevich, E., et al. (2017). Risk of surgical site infection, acute kidney injury, and *Clostridium difficile* infection following antibiotic prophylaxis with vancomycin plus a beta-lactam versus either drug alone: A national propensity-score-adjusted retrospective cohort study. *PLoS Med.* 14 (7), e1002340. doi:10.1371/journal.pmed.1002340

Caroom, C., Moore, D., Mudaliar, N., Winkler, C., Murphree, J., Ratheal, I., et al. (2018). Intrawound vancomycin powder reduces bacterial load in contaminated open fracture model. *J. Orthop. Trauma* 32 (10), 538–541. doi:10.1097/bot.0000000000001259

Chabbi, J., Jennah, O., Katir, N., Lahcini, M., Bousmina, M., and El Kadib, A. J. C. p. (2018). Aldehyde-functionalized chitosan-montmorillonite films as dynamically-assembled, switchable-chemical release bioplastics. *Carbohydr. Polym.* 183, 287–293. doi:10.1016/j.carbpol.2017.12.036

Chen, W., Luo, G., Qiu, W., Lei, Q., Liu, L., Wang, S., et al. (2017). Mesoporous silica-based versatile theranostic nanoplatform constructed by layer-by-layer assembly for excellent photodynamic/chemo therapy. *Biomaterials* 117, 54–65. doi:10.1016/j.biomaterials.2016.11.057

Dang, Q., Li, C., Jin, X., Zhao, Y., and Wang, X. J. C. p. (2019). Heparin as a molecular spacer immobilized on microspheres to improve blood compatibility in hemoperfusion. *Carbohydr. Polym.* 205, 89–97. doi:10.1016/j.carbpol.2018.08.067

Delgado, S., Dehmel, S., Twisterling, E., Wichmann, J., Jonigk, D., Warnecke, G., et al. (2020). Disruptive anti-IgE inhibitors prevent mast cell-dependent early airway response in viable atopic lung tissue. *J. Allergy Clin. Immunol.* 145 (2), 719–722.e1. e1. doi:10.1016/j.jaci.2019.11.002

Downes, K., Cowden, C., Laskin, B., Huang, Y., Gong, W., Bryan, M., et al. (2017). Association of acute kidney injury with concomitant vancomycin and piperacillin/tazobactam treatment among hospitalized children. *JAMA Pediatr.* 171 (12), e173219. doi:10.1001/jamapediatrics.2017.3219

Enteshari Najafabadi, M., and Bagheri, H. J. M. a. (2017). Wireless electrochemical preparation of gradient nanoclusters consisting of copper(II), stearic acid and montmorillonite on a copper wire for headspace in-tube microextraction of chlorobenzenes. *Microchim. Acta* 185 (1), 80. doi:10.1007/s00604-017-2549-9

Flamant, Q., Caravaca, C., Meille, S., Gremillard, L., Chevalier, J., Biotteau-Deheuvels, K., et al. (2016). Selective etching of injection molded zirconia-toughened alumina: Towards osseointegrated and antibacterial ceramic implants. *Acta Biomater.* 46, 308–322. doi:10.1016/j.actbio.2016.09.017

Friedrich, E., and Washburn, N. J. B. (2017). Transport patterns of anti-TNF-α in burn wounds: Therapeutic implications of hyaluronic acid conjugation. *Biomaterials* 114, 10–22. doi:10.1016/j.biomaterials.2016.11.003

Girmenia, C., and Iori, A. J. E. o. o. d. s. (2017). An update on the safety and interactions of antifungal drugs in stem cell transplant recipients. *Expert Opin. Drug Saf.* 16 (3), 329–339. doi:10.1080/14740338.2017.1273900

Griffin, M., Kalaskar, D., and Butler, P. J. J. o. n. (2019). Argon plasma modified nanocomposite polyurethane scaffolds provide an alternative strategy for cartilage tissue engineering. *J. Nanobiotechnology* 17 (1), 51. doi:10.1186/s12951-019-0477-z

Gundtoft, P., Pedersen, A., Schønheyder, H., Møller, J., and Overgaard, S. J. O. (2017). One-year incidence of prosthetic joint infection in total hip arthroplasty: A cohort study with linkage of the Danish hip arthroplasty register and Danish microbiology databases. *Osteoarthr. Cartil.* 25 (5), 685–693. doi:10.1016/j.joca.2016.12.010

Hirschfeld, J., Akinoglu, E., Wirtz, D., Hoerauf, A., Bekeredjian-Ding, I., Jepsen, S., et al. (2017). Long-term release of antibiotics by carbon nanotube-coated titanium alloy surfaces diminish biofilm formation by Staphylococcus epidermidis. *Nanomedicine Nanotechnol. Biol. Med.* 13 (4), 1587–1593. doi:10.1016/j.nano.2017.01.002

Hu, W., Lu, S., Ma, Y., Ren, P., Ma, X., Zhou, N., et al. (2017). Poly(dopamine)-inspired surface functionalization of polypropylene tissue mesh for prevention of intra-peritoneal adhesion formation. *J. Mat. Chem. B* 5 (3), 575–585. doi:10.1039/c6tb02667b

Huang, W., Chen, S., Chiang, W., Huang, C., Lo, C., Chern, C., et al. (2016). Tumor microenvironment-responsive nanoparticle delivery of chemotherapy for enhanced selective cellular uptake and transportation within tumor. *Biomacromolecules* 17 (12), 3883–3892. doi:10.1021/acs.biomac.6b00956

Hwang, D., Kim, H., Li, F., Park, J., Kim, D., Park, J., et al. (2017). *In vivo* visualization of endogenous miR-21 using hyaluronic acid-coated graphene oxide for targeted cancer therapy. *Biomaterials* 121, 144–154. doi:10.1016/j.biomaterials.2016.12.028

Jennings, J., Carpenter, D., Troxel, K., Beenken, K., Smeltzer, M., Courtney, H., et al. (2015). Novel antibiotic-loaded point-of-care implant coating inhibits biofilm. *Clin. Orthop. Relat. Res.* 473 (7), 2270–2282. doi:10.1007/s11999-014-4130-8

Jones, Z., Brooks, A., Ferrell, Z., Grainger, D., and Sinclair, K. J. J. o. b. m. r. P. B. (2016). A resorbable antibiotic eluting bone void filler for periprosthetic joint infection prevention. *J. Biomed. Mat. Res.* 104 (8), 1632–1642. doi:10.1002/jbm.b.33513

Kendall, M., and Gorgone, M. J. I. j. o. s. (2018). Surgical site infection following open reduction and internal fixation of a closed ankle fractures: A retrospective multicenter cohort study. *Int. J. Surg.* 49, 60–61. doi:10.1016/j.ijsu.2017.12.012

Kesavan, C., Bajwa, N., Watt, H., and Mohan, S. J. B. r. (2017). Experimental repetitive mild traumatic brain injury induces deficits in trabecular bone microarchitecture and strength in mice. *Bone Res.* 5, 17042. doi:10.1038/boneres.2017.42

Klein, S., Nurjadi, D., Eigenbrod, T., and Bode, K. J. I. j. o. a. a. (2016). Evaluation of antibiotic resistance to orally administrable antibiotics in staphylococcal bone and joint infections in one of the largest University hospitals in Germany: Is there a role for fusidic acid? *Int. J. Antimicrob. Agents* 47 (2), 155–157. doi:10.1016/j.ijantimicag.2015.12.002

Kyriakidis, I., Tragiannidis, A., Munchen, S., and Groll, A. J. E. o. o. d. s. (2017). Clinical hepatotoxicity associated with antifungal agents. *Expert Opin. Drug Saf.* 16 (2), 149–165. doi:10.1080/14740338.2017.1270264

Li, M., Liu, X., Xu, Z., Yeung, K., Wu, S. J. A. a. m., and interfaces (2016). Dopamine modified organic-inorganic hybrid coating for antimicrobial and osteogenesis. *ACS Appl. Mat. Interfaces* 8 (49), 33972–33981. doi:10.1021/acsami.6b09457

Li, Z., Shizhao, S., Chen, M., Fahlman, B., Liu, D, Bi, H. J. M. s., et al. (2017). *In vitro* and *in vivo* corrosion, mechanical properties and biocompatibility evaluation of MgF 2 -coated Mg-Zn-Zr alloy as cancellous screws. *Mater. Sci. Eng. C* 75, 1268–1280. doi:10.1016/j.msec.2017.02.168

Liu, Y., Chen, D., Zhang, A., Xiao, M., Li, Z., Luo, W., et al. (2021). Composite inclusion complexes containing hyaluronic acid/chitosan nanosystems for dual responsive enrofloxacin release. *Carbohydr. Polym.* 252, 117162. doi:10.1016/j.carbpol.2020.117162

Mable, C., Fielding, L., Derry, M., Mykhaylyk, O., Chambon, P., and Armes, S. J. C. s. (2018). Synthesis and pH-responsive dissociation of framboidal ABC triblock copolymer vesicles in aqueous solution. *Chem. Sci.* 9 (6), 1454–1463. doi:10.1039/c7sc04788f

Min, J., Choi, K., Dreaden, E., Padera, R., Braatz, R., Spector, M., et al. (2016). Designer dual therapy nanolayered implant coatings eradicate biofilms and accelerate bone tissue repair. *ACS Nano* 10 (4), 4441–4450. doi:10.1021/acsnano.6b00087

Mistry, S., Roy, S., Maitra, N., Kundu, B., Chanda, A., Datta, S., et al. (2016). A novel, multi-barrier, drug eluting calcium sulfate/biphasic calcium phosphate biodegradable composite bone cement for treatment of experimental MRSA osteomyelitis in rabbit model. *J. Control. Release* 239, 169–181. doi:10.1016/j.jconrel.2016.08.014

Neumann, M., Strohm, P., Reising, K., Zwingmann, J., Hammer, T., Suedkamp, N. J. S. j. o. t., et al. (2016). Complications after surgical management of distal lower leg fractures. *Scand. J. Trauma Resusc. Emerg. Med.* 24 (1), 146. doi:10.1186/s13049-016-0333-1

Perez-Jorge, C., Arenas, M., Conde, A., Hernández-Lopez, J., de Damborenea, J., Fisher, S., et al. (2017). Bacterial and fungal biofilm formation on anodized titanium alloys with fluorine. *J. Mat. Sci. Mat. Med.* 28 (1), 8. doi:10.1007/s10856-016-5811-5

Pickett, J., Thompson, J., Sadowska, A., Tkaczyk, C., Sellman, B., Minola, A., et al. (2018). Molecularly specific detection of bacterial lipoteichoic acid for diagnosis of prosthetic joint infection of the bone. *Bone Res.* 6, 13. doi:10.1038/s41413-018-0014-y

Qiao, Z., Zhao, S., Wang, J., Wang, S., Wang, Z., and Guiver, M. J. A. C. (2016). A highly permeable aligned montmorillonite mixed-matrix membrane for CO2 separation. *Angew. Chem. Int. Ed.* 55 (32), 9321–9325. doi:10.1002/anie.201603211

Raphel, J., Holodniy, M., Goodman, S., and Heilshorn, S. J. B. (2016). Multifunctional coatings to simultaneously promote osseointegration and prevent infection of orthopedic implants. *Biomaterials* 84, 301–314. doi:10.1016/j.biomaterials.2016.01.016

Seroussi, E., Blum, S., Krifucks, O., Lavon, Y., and Leitner, G. J. P. o. (2018). Application of pancreatic phospholipase A2 for treatment of bovine mastitis. *PLoS ONE* 13 (8), e0203132. doi:10.1371/journal.pone.0203132

Sugii, M., Ferreira, F., Müller, K., Lima, D., Groppo, F., Imasato, H., et al. (2017). Physical, chemical and antimicrobial evaluation of a composite material containing quaternary ammonium salt for braces cementation. *Mater. Sci. Eng. C* 73, 340–346. doi:10.1016/j.msec.2016.12.084

Sun, M., Li, Q., Yu, H., Cheng, J., Wu, N., Shi, W., et al. (2021). Cryo-self-assembled silk fibroin sponge as a biodegradable platform for enzyme-responsive delivery of exosomes. *Bioact. Mat.* 8, 505–514. doi:10.1016/j.bioactmat.2021.06.017

Tessier, J., Moore, B., Putty, B., Gandhi, R., and Duane, T. J. S. i. (2016). Prophylactic gentamicin is not associated with acute kidney injury in patients with open fractures. *Surg. Infect. (Larchmt).* 17 (6), 720–723. doi:10.1089/sur.2015.086

Wang, B., Liu, H., Sun, L., Jin, Y., Ding, X., Li, L., et al. (2018). Construction of high drug loading and enzymatic degradable multilayer films for self-defense drug release and long-term biofilm inhibition. *Biomacromolecules* 19 (1), 85–93. doi:10.1021/acs.biomac.7b01268

Wang, P., Sun, J., Lou, Z., Fan, F., Hu, K., Sun, Y., et al. (2016). Assembly-induced thermogenesis of gold nanoparticles in the presence of alternating magnetic field for controllable drug release of hydrogel. *Adv. Mat.* 28 (48), 10801–10808. doi:10.1002/adma.201603632

Wang, X., Wu, J., Li, P., Wang, L., Zhou, J., Zhang, G., et al. (2018). Microenvironment-Responsive magnetic nanocomposites based on silver nanoparticles/gentamicin for enhanced biofilm disruption by magnetic field. *ACS Appl. Mat. Interfaces* 10 (41), 34905–34915. doi:10.1021/acsami.8b10972

Frontiers in
Bioengineering and Biotechnology

Accelerates the development of therapies, devices, and technologies to improve our lives

A multidisciplinary journal that accelerates the development of biological therapies, devices, processes and technologies to improve our lives by bridging the gap between discoveries and their application.

Discover the latest Research Topics

See more →

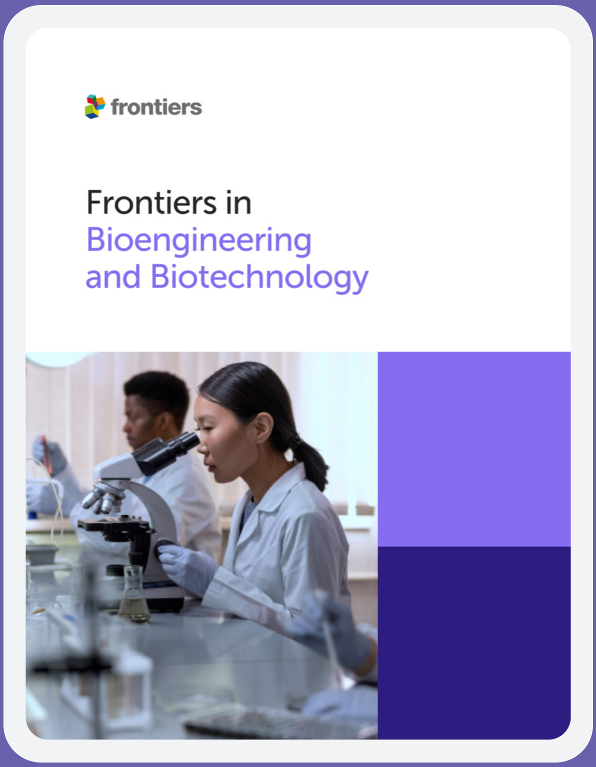

frontiers

Frontiers in
Bioengineering
and Biotechnology

Frontiers

Avenue du Tribunal-Fédéral 34
1005 Lausanne, Switzerland
frontiersin.org

Contact us

+41 (0)21 510 17 00
frontiersin.org/about/contact